Inzicht in elementaire reactieroutes
binnen metaal-organische roosters en zeolieten
op basis van ab initio modellen voor chemische kinetiek

Bridging the Gap between Experiment and Theory
with First-Principles Chemical Kinetics:
Unraveling Reaction Pathways
within Metal-Organic Frameworks and Zeolites

Matthias Vandichel

Promotoren: prof. dr. ir. V. Van Speybroeck, prof. dr. M. Waroquier
Proefschrift ingediend tot het behalen van de graad van
Doctor in de Ingenieurswetenschappen

Vakgroep Toegepaste Fysica
Voorzitter: prof. dr. ir. C. Leys

Vakgroep Fysica en Sterrenkunde
Voorzitter: prof. dr. D. Ryckbosch

Faculteit Ingenieurswetenschappen en Architectuur
Academiejaar 2012 - 2013

UNIVERSITEIT
GENT

ISBN 978-90-8578-546-0
NUR 913, 928
Wettelijk depot: D/2012/10.500/72

Dit onderzoekswerk werd uitgevoerd in het Centrum voor Moleculaire Modellering, onder leiding van prof. dr. ir. Veronique Van Speybroeck en prof. dr. Michel Waroquier.

Mattina

M'illumino
d'immenso

Giuseppe Ungaretti,
26/01/1917,
Santa Maria La Longa

Leden van de examencommissie

Voorzitter

prof. dr. ir. Rik Van de Walle (Universiteit Gent)

Leescommissie

dr. ir. An Ghysels (Universiteit Gent)

dr. German Sastre (Universitat Politècnica de València)

prof. dr. ir. Joris Thybaut (Universiteit Gent)

prof. dr. Michel Waroquier (Universiteit Gent, co-promotor)

Overige leden

prof. dr. ir. Dirk De Vos (Katholieke Universiteit Leuven)

prof. dr. ir. Karen Hemelsoet (Universiteit Gent)

prof. dr. Pascal Van Der Voort (Universiteit Gent)

prof. dr. Dimitri Van Neck (Universiteit Gent)

prof. dr. Rutger van Santen (Technische Universiteit Eindhoven)

prof. dr. ir. Veronique Van Speybroeck (Universiteit Gent, promotor)

prof. dr. ir. Toon Verstraelen (Universiteit Gent)

Contents

Voorwoord xvii

Samenvatting xxi

Summary xxvii

List of abbreviations xxxiii

I Bridging the gap between experiment and theory with first-principles chemical kinetics: Unraveling reaction pathways within MOFs and Zeolites 1

1 General Introduction 3
- 1.1 Overview of ordered nanoporous materials . . . 3
  - 1.1.1 Zeolites . . . 4
  - 1.1.2 Mesoporous materials . . . 5
  - 1.1.3 Metal-Organic Frameworks . . . 6
  - 1.1.4 Differences between MOFs and zeolites . . . 9
- 1.2 Metal-Organic Frameworks . . . 11
  - 1.2.1 A matter of design? . . . 11
  - 1.2.2 Synthesis, pre- and postmodifications . . . 14
  - 1.2.3 Applications . . . 16
- 1.3 The added value of Molecular Modeling within MOF research 21

2 Scope 23

3 Major research results 29
- 3.1 Introductory remarks on the methodology . . . 29
- 3.2 Brønsted catalyzed reactions during the MTO process . . . 31
- 3.3 Epoxidation of cyclohexene on vanadium catalysts . . . 38
  - 3.3.1 Search for the active sites within MIL-47 . . . 39
  - 3.3.2 Catalytic cycles driving the epoxidation reaction on MIL-47's active sites . . . 42
  - 3.3.3 Unraveling of $VO(acac)_2$ as active epoxidation catalyst 45
- 3.4 Activity and selectivity of the citronellal cyclization on Lewis acid MOFs . . . 46

3.4.1 Effects of linker substitution on the Lewis acid UiO-66 46
3.4.2 Activity and selectivity of the citronellal cyclization on various catalysts 51
3.5 Selective adsorption of xylenes in MIL-47 56
3.6 Structural transitions of COMOC-2 56
3.7 Contributions to other research projects 60

4 Conclusions and perspectives 63

II Publications in peer-reviewed journals 67

Paper 1 : Assembly of cyclic hydrocarbons from ethene and propene in acid zeolite catalysis to produce active catalytic sites for MTO conversion 69
Paper 2 : First principle kinetic studies of zeolite-catalyzed methylation reactions 82
Paper 3 : Full theoretical cycle for both ethene and propene formation during methanol-to-olefin conversion in H-ZSM-5 . . . 95
Paper 4 : The remarkable catalytic activity of the saturated metal organic framework V-MIL-47 in the cyclohexene oxidation . . 101
Paper 5 : Mechanistic insight into the cyclohexene epoxidation with $VO(acac)_2$ and *tert*-butyl hydroperoxide 105
Paper 6 : The coordinative saturated vanadium MIL-47 as a low leaching heterogeneous catalyst in the oxidation of cyclohexene 124
Paper 7 : Performance of Vanadium MIL-47 and linker substituted variants as catalysts for oxidation reactions: a combined theoretical and experimental approach 137
Paper 8 : Electronic effects of linker substitution on Lewis acid catalysis with Metal-organic frameworks 151
Paper 9 : Insight into the activity and diastereoselectivity of various Lewis acid catalysts for the citronellal cyclization 169
Paper 10 : Host-guest and guest-guest interactions between xylene isomers confined in the MIL-47(V) pore system 235
Paper 11 : A new V^{IV} based metal-organic framework having framework flexibility and high CO_2 adsorption capacity 249
Paper 12 : Ab initio parametrized force field for the flexible metal-organic framework MIL-53(Al) 293
Paper 13 : Synthesis, characterization and adsorption properties of an amino functionalized Metal Organic Framework: NH_2-MIL-47(V) 309

Paper 14 : Efficient approach for the computational study of alcohol and nitrile adsorption in H-ZSM-5 319
Paper 15 : The effect of confined space on the growth of naphthalenic species in a chabazite-type catalyst: A molecular modeling study 330

A List of publications **337**
A.1 International peer-reviewed journals 337
A.2 Oral contributions 340
A.3 Poster contributions 340

Bibliography **341**

Voorwoord

Nanoporeuze materialen vormen het studieonderwerp van dit doctoraatswerk, vandaar nog even een korte situatieschets van hoe mijn interesse in deze materialen ooit begon ... Als kind ging ik vaak op zoek naar siliciumdioxidekeien, beter gekend als vuurstenen of silex. Al vlug begon ik aan een mineralenverzameling, zij het dan vooral met bergkristal of kwarts in allerlei vormen en kleuren. De stap naar een thesis over poreuze siliciumdioxidehoudende materialen was dus niet zo groot, gezien er ook van deze klasse zeotype materialen natuurlijke varianten bestaan. De meeste zeolieten zijn in feite gewone poreuze siliciumdioxide structuren die aluminiumdefecten bevatten waarvoor een ladingscompensatie nodig is van een tegenion. De zeolieten in waspoeders en waterverzachters bevatten bijvoorbeeld natrium als tegenion, terwijl protonen gebruikt worden voor de zeolieten die zure reacties katalyseren.

In de opleiding voor burgerlijk scheikundig ingenieur werd ons al gewezen op het belang van co-katalysatoren of promotoren die de katalysator nog actiever maken. Zo ook heeft deze doctorandus nood gehad aan promotoren om dit doctoraat te mogen afleggen. Mijn grootste dank en grootste appreciatie gaat dan ook uit naar Veronique en Michel voor de investering van hun tijd en interesse om mijn onderzoeksprojecten samen tot een goed einde te brengen (lees: de vele resultaten te doen convergeren naar wetenschappelijke artikels). Ik ben ervan overtuigd dat we in de komende jaren nog vele interessante onderzoeksdiscussies zullen houden over tal van onderwerpen en jullie mijn enthousiasme voor het construeren van goede samenwerkingsverbanden met experimentele partners enkel zullen aanwakkeren.

Het katalytisch onderzoek dat verricht werd op metaal-organische roosters – bij ons beter bekend als onder de afkorting MOFs – vormde een excellent voorbeeld van zo'n samenwerking tussen experimentele en theoretische groepen. Tijdens mijn doctoraat hebben we zeer intensief samengewerkt met het *Centre for Ordered Materials, Organometallics and Catalysis* (COMOC, prof. Pascal Van Der Voort) voor epoxidatiereacties binnen MOFs en het *Center for Surface Science and Catalysis* (COK, prof. Dirk De Vos) voor Lewis zuurgekatalyseerde reacties binnen MOFs. Ik ben zowel Dirk als Pascal heel dankbaar voor de gevoerde onderzoeksdiscussies en constructieve samenwerking. Verder heeft het regelmatige contact met mijn collegae

van beide onderzoeksgroepen mijn inzicht in de experimentele katalysewereld grondig uitgebreid. Ik vermeld mijn samenwerkingspartners nog even per experimentele groep. Bij COMOC zijn dit Karen Leus, Ying-Ya Liu, Shyam Biswas en Ilke Muylaert, bij het COK Frederik Vermoortele, Ben Van de Voorde, Luc Alaerts en Michael Maes. Een welgemeende dankjewel voor de aangename wetenschappelijke en minder wetenschappelijke gesprekken!

In het Centrum voor Moleculaire Modellering (CMM) doctoreren heeft zo zijn voordelen, gezien expertise op veel vlakken al aanwezig is in de groep, die van persoon tot persoon kan worden overgebracht. Bij deze dank ik het hele CMM, haar huidige leden maar ook de CMM-alumni, gezien zij me ook rechtstreeks of onrechtstreeks hebben geholpen. Bedankt voor jullie assistentiebereidheid! Meer specifiek ben ik enorm veel dank verschuldigd aan Toon Verstraelen en An Ghysels, gezien zij de voortrekkers zijn geweest om een computationele code voor kinetiekbepaling te implementeren in een Pythonprogramma die ik TAMkin heb gedoopt. TAMKin, je hebt mijn computationeel analysewerk veel lichter gemaakt door excelsheets overbodig te maken! Verder ook een groot woord van dank naar David Lesthaeghe, Karen Hemelsoet en Jeroen Van der Mynsbrugge voor de interessante MTO-discussies. Veel dank ook voor mijn VASP-buddies Lennart Joos, Kim Rijpstra en Kurt Lejaeghere. *Muchas gracias* ook voor Wim Dewitte, onze secretaris, die met de glimlach al onze administratie op zich neemt. Tevens is hij een onmisbare factor bij het maken van figuren.

I would further like to thank Joachim Paier and Joachim Sauer for broadening my VASP acquaintance and their hospitality during my stay in Berlin.

It was furthermore a great honour to have dr. German Sastre of the Polytechnic University in València in my reading committee and I hope to have many opportunities for discussion in the near future. Verder dank ik de andere leden van de leescommissie: prof. Joris Thybaut en dr. An Ghysels, met jullie beiden heb ik eigenlijk ook banden op sportief gebied; Joris is meestal één van mijn concurrenten tijdens het maandelijkse exploot rond de Watersportbaan, terwijl ik samen met An soms ontspannende wandelingen in Zwijnaarde maak tussen het werk door. We gaan die tradities zeker in ere proberen te houden! Vooraf werd dit werk – of stukken ervan – ook al eens gelezen door een officieuze leescommissie: Michel, Veronique, Anneleen, Lennart en Thomas. Een dikke merci!

Verder dank ik ook nog de leden van mijn examencommissie die nog niet aan bod kwamen: prof. Rutger van Santen, die als extern jurylid aanwezig was

op mijn interne verdediging, voor de boeiende discussie, prof. Dimitri Van Neck om de rol van secretaris van de examenjury te vervullen en *last but not least* onze decaan, prof. Rik Van de Walle, die de rol van voorzitter op zich nam.

In het derde jaar van mij doctoraat had ik het geluk twee uitmuntende masterthesisstudenten te mogen begeleiden: Thomas Bogaerts en Stijn Cottenie. Ze maakten mijn werk lichter en zwaarder tegelijk door de vele interessante onderzoeksresultaten die ze behaalden, dankjewel!

Op persoonlijk gebied is de lijst van mijn indirecte supporters zelfs nog langer; zo lang dat ik mij zal beperken tot algemene dankzeggingen, gezien ik mogelijks iemand vergeet die toch in de lijst zou horen te staan. Beste vrienden, familie en CMM-leden, bedankt voor jullie aanmoedigingen!

Voor mijn ouders maak ik toch wel een uitzondering, gezien ik hier niet zou gestaan hebben zonder hun steun en inspanningen!

Matthias Noël Jozef Vandichel

Samenvatting

Zeolieten en metaal-organische roosters (MOFs) zijn nanoporeuze materialen met poriegroottes variërend tussen 0.5 en 2 nm. Hun compositie is echter verschillend. Zeolieten bevatten enkel anorganische bouwstenen, die typisch bestaan uit silicium tetraëdrisch omringd met zuurstofatomen. Zeolietroosters kunnen ondermeer katalytisch actief zijn door de aanwezigheid van zure sites (zowel Brønsted als Lewiszure sites). Indien Al-defecten worden ingebouwd, worden Brønsted zure sites gecreëerd. MOFs bevatten net als zeolieten anorganische bouwblokken (diverse metaaloxides), maar deze zijn verder gecoördineerd met organische bouwstenen. Dit hybride karakter maakt MOFs tot een nieuwe klasse van poreuze materialen met tal van eigenschappen: regelbare porositeit (via het gebruik van organische linkers die in grootte variëren), de functionalisering van het interne oppervlak en de structurele flexibiliteit van het rooster. Die eigenschappen zorgen er onder andere voor dat MOFs een extreem rijke adsorbens-adsorbaatchemie hebben. Zeolieten worden gekenmerkt door een relatief beperkte flexibiliteit en een hoge thermische stabiliteit als gevolg van de sterkte van de siliciumzuurstofbindingen (gezien Si-O bindingen behoren tot de sterkst bekende covalente bindingen). Hybride materialen hebben daarentegen betrekkelijk zwakkere bindingen (coördinatieve bindingen, pi-pi interacties, waterstofbruggen, enz.) die verantwoordelijk zijn voor hun intrinsieke structurele flexibiliteit. Daardoor is de chemie van beide klassen van nanoporeuze materialen zeer divers en dit maakt dat de toepassingsmogelijkheden van beide materialen niet volledig overlappen. Juist omdat het onderzoek naar katalyse op nanoporeuze materialen sterk gerelateerd is aan industriële toepassingen, is het ook een zeer dynamische en concurrerende tak binnen de wetenschappelijke onderzoeksgemeenschap. Typische toepassingen van zeolieten zijn katalytische omzettingen en scheidingen die reeds op grote schaal gebruikt worden binnen de industriële context. MOFs worden momenteel hoofdzakelijk getest voor adsorptie, opslag en scheidingen van gasmengsels (bv. H_2, CO_2 en CH_4); toch neemt hun belang in de katalyse tegenwoordig gestaag toe. De centrale thema's in dit proefschrift zijn katalyse en adsorptie in zeolieten en MOFs. De katalytische toepassingen op zeolieten zullen gericht zijn op een aantal belangrijke reacties in het Methanol-To-Olefins (MTO) proces, wat een belangrijk proces is voor de productie van lichte olefines uit methanol. De resultaten binnen deze thesis sluiten nauw aan bij een actieve onderzoekslijn van het Centrum voor Moleculaire Modellering (CMM). Het

onderzoek gerelateerd met MOFs en hun katalytische exploitatie is nog zeer exploratief. Binnen het kader van dit proefschrift wordt via een aantal case studies aangetoond dat deze materialen een groot potentieel hebben voor katalyse en adsorptie. De meeste van de onderzochte items zijn gerelateerd met onderzoeksvragen van experimentatoren waarbij moleculaire modellering de meest geschikte toolbox biedt om deze vragen aan te pakken. Het voorgestelde onderzoekswerk werd derhalve uitgevoerd in samenwerking met prominente experimentele partners. In de meeste gevallen werden de experimenten gelijktijdig met de computationele berekeningen uitgevoerd, wat leidde tot gezamenlijke publicaties.

Kwantummechanica en veeldeeltjes-perturbatietheorie vormen de basis voor elke benadering in de **moleculaire modellering** van chemische systemen waarin elektronische vrijheidsgraden een rol spelen. Zulke ab initio methodes bestaan altijd uit van het oplossen van de veeldeeltjes-Schrödingervergelijking. Vandaag de dag kan een benaderende oplossing van deze vergelijking verkregen worden via golffunctiemethoden (zoals de *Hartree-Fock Theory*, HF) ofwel via dichtheidsfunctionaalmethoden (zoals de *Density Functional Theory*, DFT). Om voldoende elektroncorrelaties op te nemen in het model, zijn post-HF en andere variationele methoden op basis van *Configuration Interaction* (CI) absoluut nodig. Het zijn deze methoden die bijzonder veeleisend zijn in computerkracht. DFT-methoden zijn computationeel veel haalbaarder, hoewel hun resultaat sterk afhangt van de gekozen dichtheidsfunctionaal. In de literatuur zijn veel functionalen beschikbaar, die alle zijn getest in verscheidene studies. Afhankelijk van het toepassingsgebied kan een meer of minder "geschikte" functionaal worden gevonden. Omdat uitgebreide moleculaire systemen nodig zijn om de omgeving waar de katalytische reacties plaatsvinden accuraat te beschrijven, zullen we gebruik maken van DFT-gebaseerde methoden. Een goede beschrijving van de katalytische sites is van groot belang en in periodieke systemen zoals zeolieten en MOFs lijkt het gebruik van periodieke modellen een logische keuze. Deze vertonen echter ook tekortkomingen, waardoor uitgebreide clustermodellen niet a priori kunnen worden uitgesloten. In dit proefschrift worden deze twee benaderingen gebruikt en hun resultaten met elkaar vergeleken. Eens een model is gekozen, kunnen alle nodige eigenschappen in principe worden berekend.
Het CMM heeft een reeks softwaretools ontwikkeld om de post-processing van de simulaties te vergemakkelijken (zie http://molmod.ugent.be/software). Deze softwarepakketten worden binnen het CMM en andere internationale laboratoria op regelmatige basis gebruikt. Ze dienen als een platform voor de berekening van thermodynamische en kinetische coëfficiënten door data-extractie van de numerieke simulaties, gevolgd door normale mode analyse

(NMA) en partitiefunctie-opbouw. Het programma TAMkin ondersteunt een groot aantal verschillende NMA schema's, waaronder de *Partial Hessian Vibrational Analysis* (PHVA) die nodig is voor de berekening van nauwkeurige chemische kinetiek op katalysatormodellen met gefixeerde randatomen. Het merendeel van de reacties bestudeerd in dit proefschrift, gebruikt dit PHVA-schema.

Het doel van deze thesis is het verlenen van inzicht in elementaire reactieroutes die optreden bij katalytische processen binnen MOFs en zeolieten met behulp van moleculaire modelleringstechnieken. Alle inzichten worden bekomen door het berekenen van chemische kinetiek van elementaire reacties. Daarbij wordt ook onderscheid gemaakt tussen intrinsieke en apparente kinetiek afhankelijk van het referentieniveau dat in beschouwing wordt genomen voor de reactanten. In het licht hiervan is het ook van cruciaal belang de geadsorbeerde toestand accuraat te beschrijven. Een specifieke sectie van dit proefschrift handelt over de beschrijving van *host-guest* interacties en adsorpties van gastmoleculen in nanoporeuze roosters. Als gevolg van externe stimuli zoals gastmoleculen vertonen sommige MOFs interessante structurele fenomenen die ook aan bod komen in dit werk. Hierna volgt een kort overzicht van de belangrijkste bestudeerde onderzoeksthema's in dit proefschrift. Een meer uitgebreide presentatie van elk *onderzoeksthema* wordt gegeven in deel I.3, terwijl alle wetenschappelijke publicaties opgenomen zijn in deel II.

Allereerst worden *verscheidene Brønsted zuur gekatalyseerde reacties die optreden tijdens Methanol-To-Olefins (MTO) proces bestudeerd in zeolieten* (**Papers 1-3 en 15**). In een poging om het mechanisme van het MTO-proces te ontrafelen, werd een mogelijke route naar een cyclisch species gemodelleerd uitgaande van bouwstenen zoals etheen en propeen (**Paper 1**). Deze species vormen immers een tussenstap in de vorming van polymethylbenzenen (PMBs). PMBs en alkenen kunnen beide als co-katalysatoren binnen het MTO-proces fungeren en de functie van een methyleringsplatform vervullen. Op zo'n platform worden methyleringsreacties afgewisseld met olefine producerende krakingsreacties. PMBs kunnen uiteindelijk naftalenische cokesprecursoren worden, waarvan is gebleken dat ze minder actief zijn als co-katalysator binnen het zeoliet HSSZ-34 (**Paper 15**). Verder werden berekende kinetische coëfficiënten voor de methylering van verschillende alkenen vergeleken met experimentele data (**Paper 2**). Daaruit bleek dat theoretische berekeningen in staat zijn om reactiesnelheidsconstanten en activeringsenergieën te berekenen met chemische accuraatheid, m.a.w. met een afwijking die kleiner is dan

een factor 10. De combinatie van krakingsreacties met methyleringsreacties maakt de bouw van een katalytische alkeencyclus mogelijk. De haalbaarheid van een lineaire alkeencyclus werd onder andere gepubliceerd in **Paper 3**.

Een tweede belangrijk onderwerp van deze scriptie heeft betrekking op de exploratie van de katalytische eigenschappen in MOFs. In samenwerking met een experimentele partner werden *epoxidatiereacties van cyclohexeen op vanadiumhoudende katalysatoren zoals MIL-47, MIL-47-X en VO(acac)$_2$* onderzocht (**Papers 4-7**). De epoxidatiereacties gaan door via een geconcerteerd reactiemechanisme, zoals voorgesteld door Sharpless, met vanadium alkylperoxo-complexen als actieve site. Na epoxidatie vormt zich een inactief complex dat met het oxidans *tert*-butyl hydroperoxide (TBHP) terug geactiveerd wordt. Merk op dat bij radicaalvormende reacties de oxidatietoestand van vanadium kan veranderen van +IV naar +V en vice versa. Onze theoretische resultaten tonen aan dat de epoxidatiereactie met een $V^{+V}O(OOtBu)$ species het meest dominant is omdat de radicalaire vorming vanuit $V^{+IV}O(OOtBu)$, die ook aanleiding geeft tot de vorming van V^{+V}, lager geactiveerd is dan de epoxidatie. Daardoor zullen actieve species van de vorm $V^{+V}O(OOtBu)$ meestal voor epoxidatie zorgen (**Papers 5, 6**). Naast het gebruik van uitgebreide clustermodellen, zijn ook periodieke berekeningen uitgevoerd op de twee verschillende MIL-47 periodieke slabs (die elk een ander type site voorstellen) waarbij de belangrijkste reactieklassen werden gemodelleerd. Door hun betere omgevingsbeschrijving zijn periodieke codes immers beter aangepast om de meest actieve plaats te bepalen (**Paper 7**). Deze site werd dan verder onderzocht om het effect van elektronenzuigende of elektronenduwende groepen op de linkers te onderzoeken (**Paper 7**). De berekeningen toonden het effect van de linkersubstituenten aan, waarbij zowel experimenteel als theoretisch een lineaire vrije energie relatie gevonden werd tussen Hammett substitutieconstantes (σ_p, σ_m) en de epoxidatiesnelheid van cyclohexeen.
Binnen het thema "Exploratie van katalytische eigenschappen in MOFs", hebben we ook *onderzocht hoe elektronische modulatie van linkersubstituenten X de conversie van de UiO-66-X's beïnvloedt* voor de Lewis zuur gekatalyseerde ringsluitingsreactie van citronellal (**Paper 8**). Ongecoördineerde defectsites zijn aanwezig als de tereftalaatlinkers, die de octaëdrische $Zr_6O_4(OH)_4$-anorganische bouwblokken bijeenhouden, ontbreken. De aanwezigheid van zulke defecten werd geverifieerd via Thermogravimetrische Analyse (TGA) door een experimentele partner. Bovendien bleek uit theoretische berekeningen dat de activiteit van dergelijke defectsites veel hoger is dan deze van volledig verzadigde sites. Ook het gebruik van gefunctionaliseerde linkers kan de katalytische prestaties van de coördinatieve onverzadigde Lewiszure

sites sterk verbeteren. Zo resulteerde de substitutie met een nitro-groep in een 56-voudige toename van de snelheid. Dit effect werd bevestigd via theoretische modellering op een goed gekozen defectsite van een uitgebreid clustermodel: een aanzienlijke toename van zowel de apparente als intrinsieke snelheidscoëfficiënten werd inderdaad waargenomen.
Vervolgens werd de *ringsluiting van citronellal onderzocht op vier verschillende katalysatoren* (**Paper 9**), om de onderliggende parameters van katalysatoractiviteit en -selectiviteit te bepalen. De homogene katalysatoren $ZnBr_2$ en ATPH worden vergeleken met het metaal-organisch rooster Cu_3BTC_2 en een hypothetische nitro-gesubstitueerde variant van Cu_3BTC_2 (Cu_3BTC_2-NO_2). De volgende activiteitsvolgorde werd verkregen: ATPH > Cu_3BTC_2-NO_2 > $ZnBr_2$ > Cu_3BTC_2. Verder kon de initiële selectiviteit theoretisch bepaald worden op basis van het Curtin-Hammettprincipe. Dit stelt dat de productdistributie kinetisch gecontroleerd wordt via het Gibbs vrije energie verschil tussen de transitietoestanden. De berekeningen tonen aan dat een sterkere Lewiszure site aanleiding geeft tot een grotere activiteit. Het Lewiszure karakter van de open metaal sites kan verder worden gemodificeerd door het aanbrengen van elektronenzuigende groepen zoals een nitro groep. Er werd gevonden dat ATPH de hoogste selectiviteit heeft voor cyclizatie naar het belangrijkse isomeer ((-)-isopulegol). Dit is te wijten aan de grote liganden die zorgen voor sterische effecten waardoor het vrije energieverschil tussen de stereoselectieve transitietoestanden meer gunstig wordt voor vorming van isopulegol. Verder werd gevonden dat de selectiviteit daalt bij hogere temperaturen. Een actievere katalysator laat toe bij lagere temperaturen te werken, waardoor hogere selectiviteiten worden bereikt.

Binnen het kader van dit werk werden ook de *host-guest interacties van xyleenisomeren in MIL-47* uitvoerig bestudeerd (**Paper 10**). Periodieke berekeningen werden daarbij gebruikt om bij volledig gevulde poriën van de katalysator de interacties van verscheidende xyleenparen te bepalen. Via energetische berekeningen konden we het experimenteel waargenomen scheidingsgedrag van de xyleenisomeren niet verklaren. De preferentiële adsorptie van orthoxyleen en paraxyleen in het rooster wordt niet waargenomen gezien alle adsorptie-energieën van dezelfde grootteorde zijn. Dit verklaart waarom entropische of pakkingseffecten waarschijnlijk de belangrijkste drijvende krachten zijn voor de adsorptieselectiviteit. Sterk gerelateerd met voorgaand onderwerp zijn structurele transities die kunnen optreden als gevolg externe stimuli, zoals belading met gastmoleculen. In het raam hiervan werden *structurele transities van een nieuwe V^{+IV} gebaseerde MOF, COMOC-2* onderzocht. Deze nieuwe MOF heeft een hoge CO_2-adsorptiecapaciteit. Het materiaal werd eerst gesynthetiseerd door één van onze experimentele partners, en

van zodra de structuur bekend was, onderworpen aan een grondige theoretische studie. Men kan het experimenteel waargenomen ademen of breathing effect van de poriën eenvoudig verklaren (**Paper 11**). De adsorptie- en desorptie-isotherm van CO_2 bij 265 K vertoont een typische hysteresislus, een belangrijke indicatie voor het ademend gedrag van dit materiaal. De *host-guest* interacties van CO_2 zijn namelijk sterk genoeg om de structuur te laten sluiten vanaf een bepaalde CO_2-druk. Verder werd theoretisch inzicht in de porie-ademhaling verkregen met behulp van de climbing Nudged Elastic Band (cNEB) methodologie. Naast een gesloten porievorm, werden ook een "overstretched" gesloten porievorm en een open porievorm theoretisch gevonden. In de open vorm heeft de porie de vorm van een prisma, met als grondvlak een parallellogram. Een vrij energieprofiel kon in functie van de poriehoek (kleine hoek van het parallellogram) worden bepaald, met typische vrije energiebarrières van circa 40 kJ/mol om van de open porievorm naar de gesloten porievorm te gaan. Dit resultaat is bijzonder interessant, aangezien deze transitiebarrières tussen nanoporeuze structuren voor de eerste maal aangetoond zijn. Daarvoor werd immers enkel gefocust op de thermodynamische stabiliteit tussen open en gesloten porievormen.

De belangrijkste conclusie van dit proefschrift is dat moleculaire modellering een volwaardige complementaire positie kan innemen naast experimenteel onderzoek. De voorspelling van chemische kinetiek van reacties in nanoporeuze materialen is bijzonder ambitieus en tot voor kort werden voornamelijk barrières berekend aan de hand van theoretische methoden. In dit proefschrift werden alle conclusies genomen op basis van reactiesnelheidsconstanten, waarvan ook aangetoond werd dat zij met redelijke accuraatheid kunnen voorspeld worden. Zowel theorie als experiment zijn onmisbaar om reactiemechanismen van complexe chemische processen te ontrafelen, zoals deze in de poriën en kooien van de nanoporeuze materialen (zeolieten/MOFs) plaatsvinden. Onderzoek naar de rol van de samenstelling, topologie, zuursterkte, eventuele solventen, enz. kan alleen efficiënt worden aangepakt door een combinatie van experimentele en theoretische inspanningen. Het merendeel van de gepubliceerde artikels in dit proefschrift is inderdaad gezamenlijk met experimentele groepen. Het design van multifunctionele supramoleculaire systemen en de daaropvolgende assemblage van deze op maat gemaakte ongekende materialen wordt een grote uitdaging voor de toekomst. Dit proefschrift kan gezien worden als een bijdrage aan de realisatie van dat ambitieuze doel.
Dit doctoraatswerk zal resulteren in 15 wetenschappelijke publicaties, waarvan 13 gepubliceerd of ter perse en twee in voorbereiding.

Summary

Zeolites and MOFs are ordered nanoporous materials with pore sizes between 0.5 and 2 nm. Their respective compositions are however quite different. Zeolites are constructed from purely inorganic building blocks, typically Si tetrahedrally surrounded with oxygen atoms. Zeolites contain both Brønsted and Lewis acid sites which make them catalytically active. The incorporation of Al-defects in the framework creates such Brønsted acid sites. In contrast to zeolites, which have a purely inorganic character, MOFs constitute a new class of porous materials that exhibit a truly hybrid character, since both inorganic and organic moieties are needed to build up their framework. For MOFs, the combination of tunable porosity and the functionalization of the internal surface together with the structural flexibility of the host (the empty framework) opens the way to an extremely rich host-guest chemistry, putting this class of materials in a unique position. Zeolites on the other hand are characterized by a relatively limited framework flexibility and a high thermal stability due to the strength of the silicon-oxygen bonds (Si-O bonds are among the strongest covalent bonds known). By contrast, hybrid materials have significantly weaker bonds (coordinative bonds, pi-pi stacking, hydrogen bonds, etc.) that are responsible for their intrinsic structural flexibility. This makes the chemistry of both classes of nanoporous materials completely distinctive and the high application potential of both materials is therefore not completely overlapping. As research into catalysis on nanoporous materials is strongly correlated with industrial interests, it is a very dynamic and competitive area. While catalytic conversions and separations are the most frequently used industrial applications of zeolites, future MOF applications lie more in adsorption, storage and separation of gas mixtures (H_2, CO_2, or CH_4), and nowadays their importance in catalysis is steadily increasing.

The central themes in this thesis are catalysis and adsorption in zeolites and MOFs. The catalytic applications of zeolites will be focused on some key reactions in the Methanol-To-Olefins (MTO) process, an important process for the production of light olefins from methanol. The results in this thesis are closely linked to an active on-going research line within the Center for Molecular Modeling (CMM). The research related to MOFs and their catalytic operation is very explorative. Within the framework of this thesis, a number of case studies have shown that these materials have great potential for catalysis and adsorption. Most of the items investigated in this thesis

have originated from research questions posed by experimentalists whereby molecular modeling has provided the most appropriate toolbox to tackle these problems. Therefore, the proposed research work was carried out in collaboration with prominent experimental partners. In most cases experiments were performed at the same time as the computational calculations, resulting in joint publications.

Quantum Mechanics and Many-body Perturbation Theory are the basics behind each approach used in **molecular modeling** in which electronic degrees of freedom play a role. Ab-initio or first-principles methods always consist of solving the many-particle Schrödinger equation. Nowadays, an approximate solution of this equation can be obtained via either wave-function based (such as Hartree-Fock Theory) or density based (such as Density Functional Theory) methods. The first category is very expensive and in large systems even unfeasible, as post-HF or variational CI methods are necessary to incorporate sufficient electron correlations into the model. On the other hand, DFT methods are computationally more feasible but their results largely depend on the choice of the density functional. In literature many functionals are available, which all have been tested in several assessment studies. Due to the size of the model space where the catalytic reactions take place, we will make use of DFT-based methods. A good description of the catalytic environment is of utmost importance, and in periodic systems such as zeolites and MOFs, the use of periodic models seems a logical choice. However, those may also have their shortcomings and therefore extended cluster models can not a priori be rejected. In this thesis, the two approaches will be used and their results compared with each other. Once a model has been chosen, all properties can in principle be evaluated.
The CMM has developed a series of software tools to facilitate the analysis of computational data (see http://molmod.ugent.be/software). These software packages are used on a routine basis within the CMM and other international laboratories. They serve as a platform for the computation of thermodynamic and kinetic coefficients by data extraction, normal mode analysis (NMA) and partition function construction. In particular, TAMkin supports many different NMA schemes: it incorporates the partial hessian vibrational analysis (PHVA) which is required for the calculation of accurate chemical kinetics in constrained catalyst models. Most of the reactions, studied in this PhD thesis, fall into this category.

The purpose of this thesis is to use molecular modeling to provide insight into elementary reaction pathways that occur in catalytic processes in zeolites and MOFs. All insights are obtained by cal-

culating first-principles chemical kinetics of elementary reactions. Both intrinsic and apparent kinetics are calculated, which merely differ by the chosen reference level for the reactants. A specific section of this thesis deals with the description of host-guest interactions and adsorption of guest molecules in nanoporous frameworks. As a result of external stimuli, such as guest molecules, some MOFs exhibit interesting structural phenomena, which in this thesis are also discussed for some specific materials. In the following paragraphs a short overview of the main research *topics* studied in this PhD thesis is presented. A more extended presentation of each research theme is given in Section I.3, while all research articles are taken up in Part II.

First, *various Brønsted acid catalyzed reactions that occur during the Methanol-To-Olefins (MTO) process are studied in zeolites* (**Papers 1-3 and 15**). In an attempt to unravel the mechanism of the MTO process, a preliminary pathway to a 5-membered cyclic species from basic building blocks (ethene, propene) was modeled in HZSM-5 (**Paper 1**). These species are an intermediate step in the formation of polymethylbenzenes (PMBs). PMBs and alkenes can both operate as co-catalysts in the MTO process by acting as methylation scaffolds. Several methylation reactions of those co-catalysts are altered with olefin producing cracking reactions. PMBs might eventually become naphthalenic coke precursors, which have proven to be less active co-catalysts in zeolite HSSZ-34 (**Paper 15**). Furthermore, the calculated kinetic coefficients for alkene methylations were compared with experimental data (**Paper 2**). We found that theoretical calculations are capable of determining the rate constants and activation energies with near chemical accuracy, i.e. with a deviation of less than a factor of 10. The combination of cracking or β-scission reactions with methylation reactions allows the construction of a catalytic alkene cycle. The feasibility of such a linear alkene cycle was published in **Paper 3**.

A second main topic of the thesis concerns the exploration of catalytic properties in MOFs. In collaboration with an experimental partner, *epoxidation reactions of cyclohexene on the vanadium-containing catalysts MIL-47, MIL-47-X and VO(acac)$_2$ are investigated* (**Papers 4-7**). The epoxidation reaction occurs via a concerted Sharpless reaction mechanism with vanadium alkylperoxo complexes as the active complexes. After epoxidation, an inactive complex is formed that can be reactivated by *tert*-butyl hydroperoxide (TBHP) being used as an oxidant. Note that radical decomposition reactions may switch the oxidation state of vanadium from +IV to +V species and vice versa. Our theoretical results reveal that the dominant epoxidation

reaction happens via $V^{+V}O(OOtBu)$ species since the radical generation from $V^{+IV}O(OOtBu)$ is less activated than the epoxidation from $V^{+IV}O(OOtBu)$, which shows that active $V^{+V}O(OOtBu)$ species will be the most abundant epoxidation complexes (**Papers 5-7**). Beside the use of extended cluster models, periodic calculations have also been performed on the parent MIL-47 framework and the most important reaction classes have been modeled. Periodic codes were more suited to determine the most active site (**Paper 7**). This site was then used to investigate the effect of electron withdrawing and donating groups on the linkers (**Paper 7**). The calculations elucidated the effect of linker modifications on the catalytic performance of MIL-47. Experimentally and theoretically, a linear free energy relationship was found between Hammett substituent constants (σ_p, σ_m) of the linker substituents X and the epoxidation rate of cyclohexene.

Within the topic "Exploration of catalytic properties in MOFs", we also investigated *the electronic modulation behaviour of UiO-66-X materials* (**Paper 8**) *for the Lewis acid catalyzed citronellal cyclization.* Uncoordinated defect sites are present as some of the terephthalate linkers, that hold together the octahedral $Zr_6O_4(OH)_4$-inorganic brick, are missing in the framework. The presence of such defect sites was verified by Thermogravimetrical Analysis (TGA) by an experimental partner. Moreover, the activity of such defects sites was shown by theoretical calculations to be much higher than fully saturated sites. Functionalized linkers could greatly enhance the catalyst performance of the coordinatively unsaturated Lewis acid sites. Nitro-group substitution resulted in a 56-fold increase in the rate of the citronellal cyclization. This effect was confirmed by theoretical modeling on a well chosen defect site of an extended cluster model: a substantial increase of both the apparent and intrinsic rate coefficients was indeed observed.

Next, *the citronellal cyclization is studied on four different catalysts* (**Paper 9**), explaining the underlying parameters that determine catalyst activity and selectivity. The homogeneous ATPH and $ZnBr_2$ catalysts are compared with Cu_3BTC_2 and a hypothetical nitro-substituted variant of Cu_3BTC_2 (Cu_3BTC_2-NO_2). The following activity order of the catalysts was obtained: ATPH > Cu_3BTC_2-NO_2 > $ZnBr_2$ > Cu_3BTC_2. Furthermore, the initial selectivity could be calculated theoretically on the basis of the Curtin Hammett principle, stating that the product ratio is kinetically controlled by the difference in free energy between the transition states. The calculations show that stronger Lewis acid sites have an increased activity. The Lewis acid character of the open metal sites may be further modified by the application of electron-withdrawing groups such as a nitro group. ATPH showed the highest selectivity for the cyclization reaction towards the most important isomer ((-)-isopulegol). This is due to the bulky ligands, providing steric ef-

fects so that the free energy difference between the stereoselective transition states increases, which is favorable for the formation of isopulegol. Furthermore, it was found that the selectivity decreases at higher temperatures. A more active catalyst makes it possible to operate at lower temperatures, resulting in the possibility of obtaining higher selectivities.

Within the framework of this PhD, *the adsorptive host-guest interactions for xylene isomers in MIL-47* are studied in great detail (**Paper 10**). Periodic calculations were used for a full description of the catalyst environment when it was fully loaded with xylenes. In the case of the xylenes, the energetics could not explain the experimentally observed separation behaviour of the xylene isomers with a preferential adsorption for orthoxylene and paraxylene, since all adsorption energies lie in the same range. Therefore, entropic effects are likely to be the main driving forces for the adsorption selectivity.

Finally, *the structural transitions of a new material, called COMOC-2, are tackled*. This new V^{+IV} based MOF has been proposed showing framework flexibility and high CO_2 adsorption capacity. The material was first synthesized by one of our experimental partners and has been subjected to a thorough theoretical investigation. As observed experimentally, theory also succeeds in explaining the structural transitions of the breathing framework (**Paper 11**). The adsorption/desorption isotherm of CO_2 at 265 K shows a typical hysteresis loop, revealing the breathing behavior of this material. The host-guest interactions of CO_2 are strong enough to close the structure at a certain CO_2 pressure. Furthermore, insight into the breathing transitions was obtained using the climbing Nudged Elastic Band (cNEB) methodology. Apart from a regular narrow pore form, an overstretched narrow pore configuration was found theoretically. A full free energy profile along the breathing angle of the COMOC-2(V^{+IV}) was determined with free energy barriers of $\sim$40 kJ/mol from the large pore to the narrow pore structures. This result is particularly interesting, since it is the first time that breathing barriers of structures have been reported. Before, focus was laid mainly on the thermodynamical stability between the open and the closed pore forms.

The main conclusion of this PhD work is that molecular modeling has gained a unique complementary position in relation to experimental research. The prediction of chemical kinetics on reactions in nanoporous materials is highly ambitious and up until recently many computational papers, focused solely on the computation of activation barriers. In this thesis, all conclusions were taken on the basis of reaction rate constants, which could be predicted with reasonable accuracy. Both theory and experiment are indispensable to un-

ravel reaction mechanisms of complex chemical processes which only take place in an environment as presented by the pores/cages of a nanoporous material (zeolite/MOF). Study of the role of the composition, topology, acid strength of the host framework, presence of solvents in the pores, etc. on chemical kinetics, can only be tackled efficiently by a combined experimental-theoretical effort. Most of the published articles in this PhD thesis are indeed joint papers with experimental groups. Design of multifunctional supramolecular systems and the subsequent fabrication of these tailor-made unprecedented materials would seem to be as a grand challenge for the future. This thesis makes a contribution to the realization of this ambitious goal.

This PhD work has resulted into 13 published research articles and 2 papers in preparation.

List of abbreviations

AC	Active Complex
acac	acetyl acetonate
ads	adsorbed
app	apparent
ATPH	tris(2,6-diarylphenyloxy)aluminum
BDC	Benzenedicarboxylate or terephthalate
BTC	Benzenetricarboxylate
bwd	backwards
CHA	chabazite (topology)
CMM	Center for Molecular Modeling
cNEB	climbing Nudged Elastic Band
COF	Covalent Organic Framework
COK	Centre for Surface Chemistry and Catalysis
COMOC	Centre for Ordered Materials, Organometallics and Catalysis
CTAC	cetyltriammoniumchloride
DEF	Diethylformamide
DFT	Density Functional Theory
DMF	N,N-dimethylformamide
EPR	Electron Paramagnetic Resonance
FER	Ferrierite
fwd	forward
HKUST	Hong-Kong University of Technology
HP	Hydrocarbon Pool
IC	Inactive Complex
intr	intrinsic
IRMOF	Isoreticular Metal-Organic Framework
IUPAC	International Union of Pure and Applied Chemistry
IZA	International Zeolite Association
LFER	Linear Free Energy Relationship
lp	large pore

MAF	Metal Azolate Framework
MBioF	Metal-Biomolecule Framework
MCM	Mobil Catalytic Material
MIL	Material of l'Institute Lavoisier
MOF	Metal-Organic Framework
MPF	Metal Peptide Framework
MTG	Methanol-To-Gasoline
MTH	Methanol-To-Hydrocarbons
MTO	Methanol-To-Olefins
NMR	Nuclear Magnetic Resonance
np	narrow pore
OMP	Ordered Mesoporous Polymers
PBC	Periodic Boundary Conditions
PCN	Porous Coornation Network
PCP	Porous Coordination Polymer
PHVA	Partial Hessian Vibrational Analysis
PMO	Periodic Mesoporous Organosilica's
PSM	Post Synthetic Modification
SBU	Secondary Building Unit
SDA	Structure Directing Agent
STY	Space-Time Yield
TBHP	*tert*-butyl hydroperoxide
TS	Transition State
TGA	Thermogravimetrical Analysis
UiO	University of Oslo
VC	vacuum
ZIF	Zeolitic Imidazolate Framework
ZMOF	Zeolite-like Metal-Organic Framework
ZSM-5	Zeolite Socony Mobil number 5

Part I

Bridging the gap between experiment and theory with first-principles chemical kinetics: Unraveling reaction pathways within MOFs and Zeolites

1

General Introduction

This chapter highlights the different topics studied in this PhD thesis. Ordered nanoporous materials, more specifically zeolites and Metal-Organic Frameworks (MOFs), have been studied for various reactions by use of first principle chemical kinetics. First, a short overview of the two "nanoporous" families is presented in view of their historical context and their scientific and industrial relevance. Second, MOFs are discussed in depth, focusing on some design-principles related with synthesis and applications.

1.1 Overview of ordered nanoporous materials

The International Union of Pure and Applied Chemistry (IUPAC) classifies nanoporous materials in three classes according to the pore diameter. *Microporous* materials have a pore diameter of 0.2-2 nm, while the pore sizes within *mesoporous* materials lie typically between 2 nm and 50 nm. A third class are the *macroporous* materials, having pore dimensions larger than 50 nm. A short introduction will describe the historical evolutions within the field of ordered nanoporous materials, which has evolved from microporous zeolites to various mesoporous materials and Metal-Organic Frameworks (MOFs). Afterwards, we will focus on the truly crystalline and porous materials, such as zeolites and MOFs, and compare them based on their building blocks, applications and properties.

1.1.1 Zeolites

The research field focusing on the synthesis of new ordered porous materials was initiated in the previous century, yet it has earlier roots. The Swedish mineralogist Axel Frederik Cronstedt was the first to introduce the term zeolite in 1756 [1]. The word zeolite originates from the Greek $\zeta\varepsilon\omega$ (*zeo*, I boil) and $\lambda\iota\theta o\varsigma$ (*lithos*, stone) and explains the observed water evaporation while heating the natural hydrated aluminosilicate minerals. Due to the limited availability of these materials in nature, little efforts have been undertaken to profoundly investigate these materials for a very long time. The two scientists who can justly be regarded as the founders of zeolite synthesis science and practice are Richard Barrer (1910-1996) and Robert Milton (1920-2000). In the early 1940s, Richard Barrer investigated the conversion of known mineral phases under the action of strong salt solutions at fairly high temperatures (ca. 170-270 °C) [2]. Using this approach in 1948, he synthesized the first zeolite unknown as a natural mineral. Robert Milton began his synthesis program in 1949. The use of more reactive starting materials (freshly precipitated aluminosilicate gels) enabled reactions to be carried out under milder conditions. The rate of progress was astonishing. By 1953, Milton and his colleagues had synthesized 20 zeolites, including 14 unknown as natural minerals.

The first synthesis mixtures did only contain inorganic building blocks, until 1961 when two groups proposed recipes with quaternary ammonium cations as templates during the zeolite synthesis [3, 4]. From that point on, the research field escalated with the development of many synthetic zeolites and zeotypes (crystalline aluminophosphates), leading to a wide spectrum of industrial applications [5]. A more detailed historical overview about zeolite synthesis and applications is given by Cundy and Cox [6], while a systematic atlas of zeolite topologies can be found in books [7, 8] or in the online database of the International Zeolite Association [9]. Within this database, zeolites are ordered according to their topology, typically expressed by a 3-letter code.

The most important milestone in the field of zeolite synthesis is the discovery of ZSM-5 (abbreviation of *Zeolite Socony Mobil*), with the MFI-topology. Although ZSM-5 was synthesized in the sixties [10], the patent of the Mobil Oil Corporation dates from 1972 [11, 12]. This material consists of two types of channels perpendicular to each other; zigzag channels and straigth channels (Figure 1.1). Today ZSM-5 and its modifications are considered as the workhorses of the chemical industry for the majority of catalytic conversions and separations [13, 14]. This was the main reason to focus on

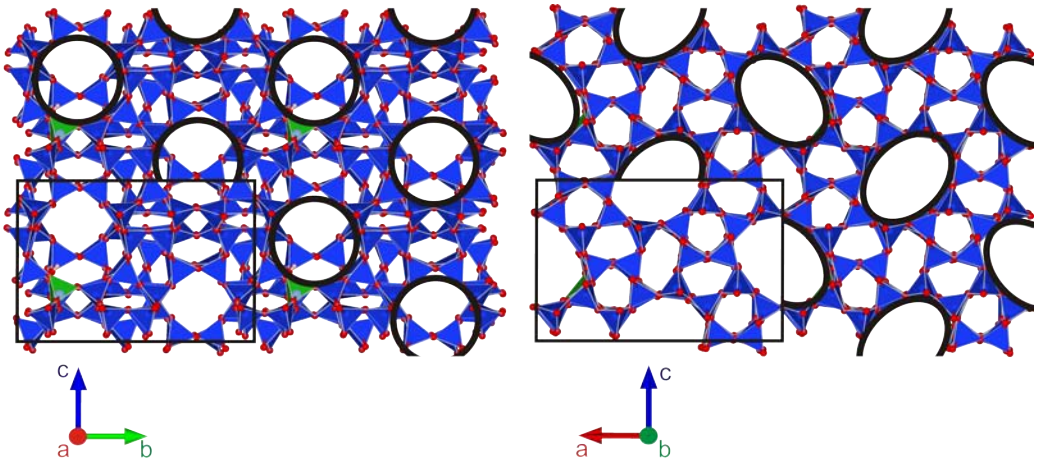

Figure 1.1: Impression of HZSM-5 in a and b direction. The SiO_4 and AlO_4 tetrahedra are respectively indicated in blue and green.

H-ZSM-5 (Brønsted exchanged ZSM-5) within the zeolite part of this work, particularly for modeling reactions taking place in the Methanol-To-Olefins (MTO) process. We have not limited our study to alumino-silicate systems, but also included zeolitic or zeotype materials with other composition such as alumino-phosphates. It is generally accepted that in the near future the H-SAPO-34, with the CHA-topology [9], will be commercially used in the MTO-process [14].

1.1.2 Mesoporous materials

In the search for larger pore materials for the development of other industrial applications, researchers at Mobil Oil Corporation announced in 1992 the direct synthesis of the first family of mesoporous silicates, known as the Mobil Catalytic Materials or MCMs [15, 16]. To form ordered mesopores, large surfactants such as cetyltriammoniumchloride (CTAC) need to be used as templating agents. Although the pores are much larger than zeolite pores, they remain small on the scale of the mesoporous spectrum. A disadvantage of those materials are the thin pore walls of approximately 1 nm in size. This structural limitation also prevents the incorporation of heteroatoms in the wall. Furthermore, the still relatively small pore size of 10 nm limits the size of the molecules that can penetrate into the pores. Other strategies were developed to obtain mesoporous materials [17] that are able to surpass the MCM-materials. We briefly mention the most important ones: SBA-materials [18, 19], Periodic Mesoporous Organosilica's (PMOs) [20, 21, 22],

Ordered Mesoporous Polymers (OMPs) and multifunctional hybrids [23].

Altogether, the discovery of new materials was essential for the progress of industrial technologies, and still today there is a need for microporous materials with new topologies and compositions. In the nineties, also another newborn baby, joined the club of ordered porous materials: the Metal-Organic Frameworks (MOFs).

1.1.3 Metal-Organic Frameworks

Over the past decade, Metal-Organic Frameworks (MOFs) have emerged as an important new class of nanoporous materials [24, 25, 26] and can be considered as the most recent development and challenge in the field of ordered porous materials. In contrast to zeolites, having a purely inorganic character, MOFs constitute a new class of porous materials exhibiting a truly hybrid character, since both inorganic and organic moieties are building blocks constructing their framework. In this way, MOFs bridge the gap between organic polymers and inorganic crystalline zeolites and are sometimes also referred to as a crystalline subclass within the coordination polymers (CPs). The most strict definition would describe MOFs as crystalline, porous and three dimensional lattices consisting of metal(oxide) ions connected by multidentate organic ligands [27, 28]. The first MOF-like materials appeared in 1965 [29, 30, 31], albeit Yaghi and co-workers introduced the abbreviation MOF around 1999 [32]. This material was called MOF-5 and consisted of $[Zn_4O]^{6+}$ tetrahedrons each connected by 6 terephthalate or benzenedicarboxylate $[OOCC_6H_4COO]^{2-}$ anions. Although this zinc cluster – the secondary structure building unit (SBU) – had been known for more than 40 years and was illustrated in widely-read texts such as Wells' Structural Inorganic Chemistry [33], no one before Yaghi thought about replacing the acetic acid by terephthalic acid [28]. Moreover, the designability of MOF-5 was nicely illustrated by the synthesis of an isoreticular series in which pore size and functionality could be varied systematically [34] (Figure 1.2). This example already illustrates how tunable MOFs are.

Apart from the research group of Omar Yaghi, also the groups of Susumu Kitagawa and Gérard Férey pioneered in the synthesis and characterization of those new materials and generated a lot of curiosity within the scientific community, leading to a fully qualified research field with an explosion of papers [36]. Nowadays, MOF-5 [32], HKUST-1 (also known as Cu_3BTC_2) [37], and MIL-53 [38] are well known examples of MOFs, commercially available at the chemical company BASF (Figure 1.3).

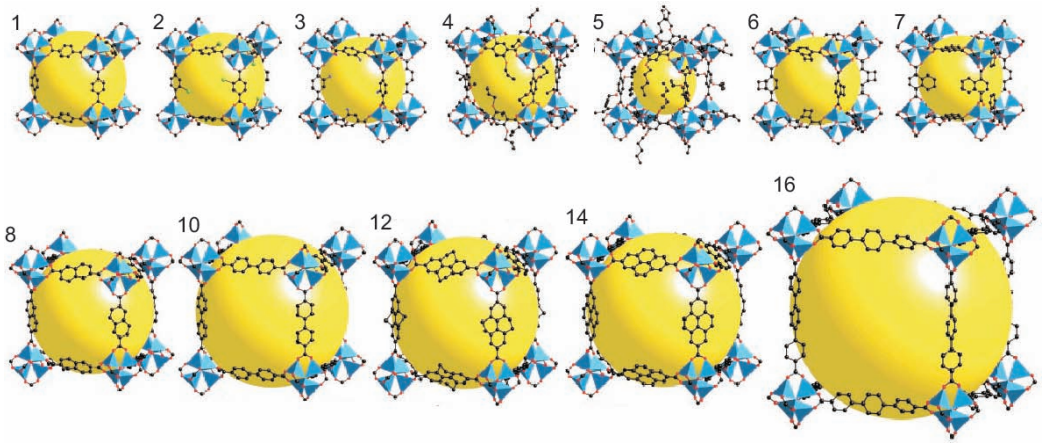

Figure 1.2: A large series of Isoreticular Metal-Organic Frameworks (IRMOFs) has been produced from MOF-5. The organic linkers differ both in functionality of the pendant groups (IRMOF-1 to -7) and in length (IRMOF-8 to -16) [34, 35]. The yellow ball represents the empty void in the structure.

Just like zeolites, MOFs are mostly named with an acronym of the laboratory that reported the first synthesis, followed by a number. Some well-known examples are: MIL (Matériaux de l'Institut Lavoisier) and HKUST (Hong-Kong University of Science and Technology) and so on. However, not all MOFs are called according to their founders [39]: a nomenclature such like Porous Coordination Polymer (PCP) [40], Porous Coordination Network (PCN) [41], ZMOF (Zeolite-like Metal-Organic Framework) [42], ZIF (Zeolitic Imidazolate Framework) [43], MPF (Metal Peptide Framework) [44], MAF (Metal Azolate Framework) [45], COF (Covalent Organic Framework) [46], and bio-MOF or MBioF (Metal-Biomolecule Framework) [47] is commonly accepted.

In 2009, the IUPAC started with a project to make the nomenclature and classification of this type of materials more uniform [48]. A preliminary study proposed a classification according to different criteria, and invites researchers of various fields to take part in the debate on the nomenclature of the hybrid inorganic-organic materials [49]. The studied MOFs within this PhD are UiO-66 [50], MIL-47 [51], Cu_3BTC_2 [37] and COMOC-2 [52]. Modified versions of those MOFs, in which substituted terephthalate linkers were used, have also been investigated in collaboration with experimental partners (see Chapter 2).

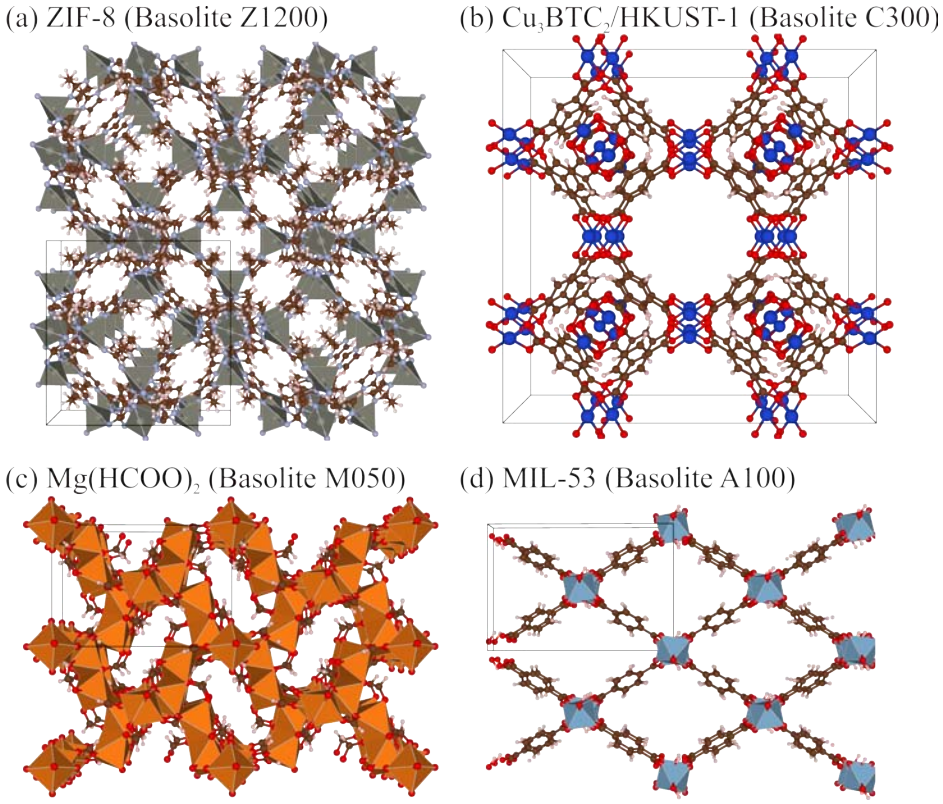

Figure 1.3: Overview of some commercialized MOFs. FeBTC (Basolite F300) and Al-fumarate (Basolite A520) are not shown since the exact structure is not disclosed.

1.1.4 Differences between MOFs and zeolites

As this PhD deals with zeolites and MOFs, it is instructive to summarize the major differences and similarities between those two categories of nanoporous materials. An overview of generalized properties is given in Table 1.1. MOFs can be considered as organic zeolite analogues, as their pore architectures and topologies are similar. Their coordinative bonds connecting the organic linkers with the metals of the inorganic Secondary Building Units (SBUs) are not as strong as the Si-O and Al-O bounds within zeolites. However, for many MOFs their thermal decomposition does not start below 300 °C [53].

The variety of suitable SBUs and linkers, which makes MOFs so characteristic, opens a wide range of new perspectives for more extreme properties, the surface area for instance can extend even beyond 5000 m^2 g^{-1} (Table 1.1). This is the result of enormous pore volumes.

Table 1.1: Overview of the main properties and characteristics of zeolites and MOFs [53, 54].

	Zeolites	**MOFs**
Building blocks	Tetrahedral SiO_2 and AlO_2	Metal(oxide) clusters and organic linkers
Major applications	Separation, catalysis, ion exchange, water treatment	Separation and storage, catalysis, ion exchange, sensing, imaging, drug delivery
Properties		
Lewis acidity	High	Low to medium
Brønsted acidity	Bridging Si(OH)/Al hydroxyl groups	Bridging M(OH)M hydroxyl groups or introduced by PSM[a]
Basicity	Arises from the framework oxygens	Introduced by PSM[a] or directly through linkers
Surface area	Around 200-500 m^2 g^{-1}	Up to 6000 m^2 g^{-1}
Pore volume	Around 0.1-0.5 cm^3 g^{-1}	Over 1 cm^3 g^{-1}
Thermal stability	$>$ 445 °C	$\leq$ 300 °C
Chemical stability	High	Limited and incompatible with certain solvents
Diffusion	Fast for small gas phase molecules and slow in the liquid phase	Strongly influenced by the polarity of linkers
Metal site density	Low	High
Framework defects	Important in many reactions	Expected to play a minor role but sometimes crucial for activity
Active site environment	Mostly hydrophilic but can also be made hydrophobic	Considerably hydrophobic
Poisoning of active sites	Reactivation by thermal treatment	Thermal treatment not valid for catalyst regeneration
Chirality	Not possible or difficult to achieve	Homochiral solids can be obtained from chiral linkers or by PSM[a]

[a]PSM = post-synthetic modifications

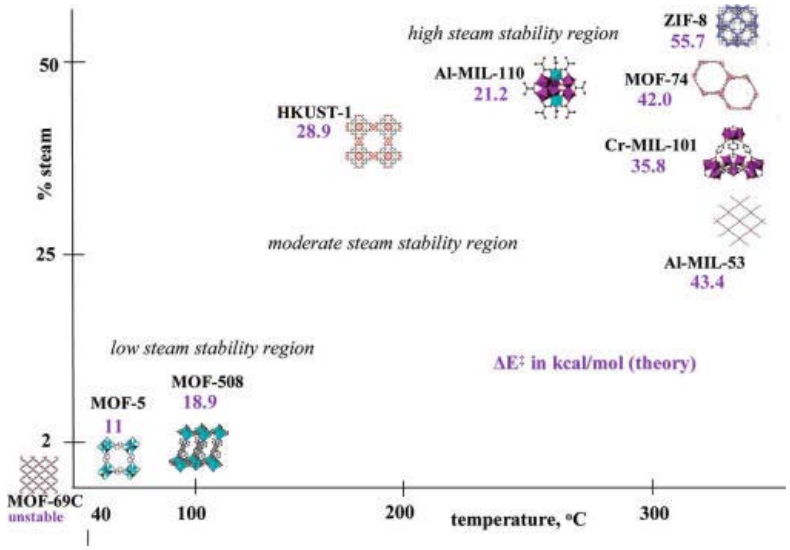

Figure 1.4: Steam stability map for various MOFs. The position of the structure for a given MOF represents its maximum structural stability by XRD measurement, while the energy of activation for ligand displacement by a water molecule determined by molecular modeling is given in kcal/mol [57].

Zeolites are very hydrophilic, as they contain plenty of crystal water molecules after synthesis and calcination steps. Besides Brønsted active sites, generated through acid exchange, zeolites have also a strong Lewis acid character because of uncoordinated Al-sites [55]. MOFs can also contain both types of active sites, as will be described in Section 1.2.3.

Furthermore, some MOFs are chemically unstable in water or solvents, or even at atmospheric moisture [56]. Low et al. [57] have performed a high throughput screening to determine the hydrothermal stability of various materials. Hydrothermal stability is a critical property for commercial sorbents, since they have to be resistant to moisture at process conditions and during regeneration. The screening happened with the experimental steaming method covering broad range of steam levels. Furthermore, the transition state barriers for metal ligand bond breaking with water were determined by theoretical modeling. Good agreement was observed with experimental results (Figure 1.4).

In the following sections, MOFs are discussed more in depth, focusing on some design-principles related with synthesis and applications within adsorption and catalysis (Section 1.2).

1.2 Metal-Organic Frameworks

We have previously shown that MOFs are a fascinating class of crystalline hybrid materials, which are formed by association of metal centers or clusters and organic linker(s). Their construction offers a unique chemical versatility combined with a designable framework and an unprecedentedly large and permanent inner porosity. Since the 1990s, this area of chemistry has experienced an unparalleled growth, witnessed by not only the sheer number of research and review papers published but also by the ever-expanding scope of the research [58]. For more in depth information about MOFs, the reader can consult various general reviews on MOFs that have appeared over the years [27, 40, 59, 36, 31, 60, 61, 62, 63, 64]. Reviews from Kitagawa et al. [40, 61] are more conceptual and written from the broader perspective of coordination polymers while Férey's review [36] is generally considered as a good practical introduction for new researchers within the MOF field. Furthermore, the reviews by Müller et al. [59, 31] are written from industrial viewpoint. For the classification of MOFs in terms of nets we refer the reader to the papers of O'Keeffe et al. [65, 66, 67, 68, 69]. Despite all those efforts, much like with zeolites, the used nomenclature is mostly based on the abbreviation of the inventing research group.

Further in this section, the concept of design is first discussed followed by the evolutions in MOF-synthesis, whereafter the focus is set to the industrially important applications of MOFs: catalysis, gas storage and separation.

1.2.1 A matter of design?

Synthesizing a new structure is like playing with lego-blocks; many different bricks are available to build a certain framework. The inorganic bricks can make coordinations with di-, tri- and tetravalent cations, constructed from a broad range of metals [36]. Another commonly used name for those inorganic bricks is Secondary Building Units (SBUs), of which some of them have been listed [66]. The number of available organic bricks is also simply impressive, some examples can be found in Yaghi's review paper [70]. This number is even drastically increased considering the large choice of functionalized organic linkers, already demonstrated by the isoreticular MOF-5 series (Figure 1.2). Those impressive results seemed to convince the scientific community that a rationalization of the synthesis of MOFs is possible because the large amount of directional information already present in the building blocks would imply that new MOFs can be easily devised [71]. The idea of *tailor-made materials* or *MOFs by design* was therefore often used [72, 69, 70, 73],

but those are in fact misleading terms. This concept led to interesting discussions where the term *design* has been criticized [74, 36, 28]. In the most narrow sense of the word, design implies a creative and original aspect; an architect can design a new house, the height, the size, the arrangement of the rooms, the number and placement of windows and doors, etc. In other words, design can be seen as the realization of our imaginations [36]. But can a chemist really design a MOF? In theory, it is possible to combine linkers and metal ions, but then the reaction should be steered towards the right target compound by adjusting reaction parameters. We would therefore need to rationalize the free energy landscape of that MOF and its inorganic bricks at various reaction conditions. In particular, the crystallization is determined by rather unpredictable parameters, such as solubility products, nucleation and growth rates. In reality, a successful synthetic plan always corresponds to the anticipation (based on a prediction, identification, or intuitive hunch) of a still unknown compound, i.e. a predetermined local minimum on the free-energy hypersurface. The corresponding structures, including possible isomers and polymorphic modifications, equilibrium distances and material properties are inherent to the chemical system and are not accessible to *design*. From this narrow viewpoint, new MOF structures can be discovered, but they can neither be created, nor designed [74, 71]. A few examples that support this view are given.

Figure 1.5 shows two structures with the same chemical formula, resulting in a different structure with the same inorganic SBU, a $[V(OH)]_x^{2+}$-chain. MIL-47(V^{+III}) or MIL-47as[1] is synthesized in water. In contrast, MIL-68(V^{+III}) [75] could be synthesized under solvothermal conditions using a non-aqueous medium. The water is totally substituted by N,N-dimethylformamide (DMF). When both materials are compared on energetic basis, MIL-47(V^{+III}) is 14.2 kJ/mol more stable per $[V(OH)(OOCC_6H_4COO)]$-unit. It would be an interesting experiment to synthesize a phase of MIL-47 around MIL-68 and make multi-phasic MOFs with probably new interesting applications in catalysis and separation [76]. Very recently, V-MIL-101 could also be synthesized by Biswas et al. [77]. This shows that varying the solvent and reaction conditions results in a changed connectivity and different inorganic building blocks. Another example are the Al-pyromellitate frameworks (MIL-118, -120, and -121) which have been found dependent on the pH [78].

Recently, it was also shown that depending on the solvent used, another material could be obtained [79]. A solution of amino-terephthalate linkers, $AlCl_3$ in water resulted in a NH_2-MIL-53(Al) and if the solvent was changed

[1] as = as synthesized

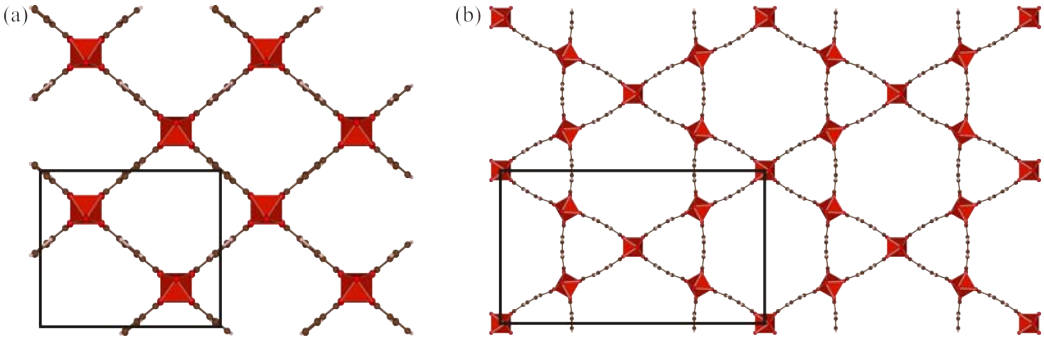

Figure 1.5: Impression of two polymorf structures with $[V(OH)(OOCC_6H_4COO)]$ as crystal chemical formula: (a) MIL-47(V^{+III})[51] and (b) MIL-68(V^{+III})[75].

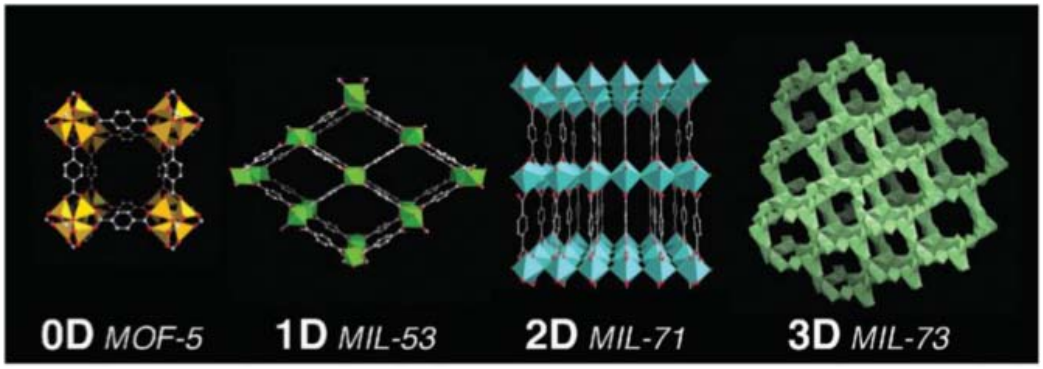

Figure 1.6: Examples of MOFs with various dimensionalities for the inorganic part [36].

to DMF, NH_2-MIL-101(Al) appeared instead. Within this example the inorganic part forms clusters (MIL-101) or chains (MIL-53) dependent on the solvent. This leads to the concept of dimensionality of the inorganic subnetwork within a 3D crystalline MOF. For the topologies of MOF-5, UiO-66, HKUST-1 and MIL-101, the inorganic bricks are clearly separated by organic linkers, the dimensionality of the inorganic part is thus zero as this part is finite. However, there are also hybrid porous solids that possess inorganic parts with a larger dimensionality, giving rise to chains (1D), layers (2D) or even inorganic frameworks (3D) [36]. Examples of MOFs with higher dimensionalities are MIL-47 [51] (1D), MIL-71 [80] (2D) and MIL-73 [81] (3D) (Figure 1.6). Another example of MOFs with a 3D inorganic part, was found by applying a mixed metal composition between Co^{+II} and Ni^{+II} within the synthesis procedure for the full Co-MOF MIL-9.

This study has shown that a set of appropriate mixtures of metal ions allows

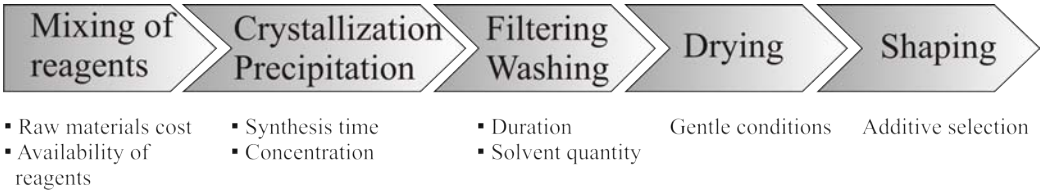

Figure 1.7: Simplified flow diagram of industrial MOF synthesis procedure via the solvothermal route with parameters important for scale-up indicated [86].

the synthesis of different solids with new unforeseen architectures. These results stress once more the difficulty of predicting or controlling inorganic condensation in the field of MOFs [82].

Ideally, synthesis conditions are varied during a high-throughput study. Those studies allow the rapid discovery of structures in function of the different parameters (such as temperature, pH) [83, 84, 78, 85].

1.2.2 Synthesis, pre- and postmodifications

Basically, the hydrothermal synthesis of MOF-materials can be ordered in subsequent processes: (1) mixing of reagents, (2) crystallization or precipitation, (3) filtration and washing, (4) drying, (5) shaping (Figure 1.7). To commercialize MOFs and promote their use for various applications (Section 1.2.3), all of the synthesis processes should be perfectly mastered. Due to the economic reality, only the most cost effective and best performing MOFs will be heading for market [86].

The first syntheses of MOFs happened *solvothermal*, typically by heating salt in solvent for 12-48 h. Although this procedure can yield high quality crystals, it suffers from long reaction times and can be difficult to scale above $\sim$1 g. Solvents, especially the often employed diethylformamide (DEF), can be very expensive and therefore hindering a cost-efficient scale up to industrial proportions. Müller and coworkers at BASF were the first to investigate scale up procedures for MOFs and reported a synthesis of MOF-5 on a 50 g scale that required almost 6 liter of DEF. Therefore, methods that decrease reaction times and the amount of solvent required are highly desirable for laboratory scale experiments, as well as for commercialization of MOF materials [59, 64]. To scale up synthesis from lab scale to industrial scale requires in first instance the maximalization of the space-time yield (STY), which expresses the kilograms of MOF product per cubic meter of reaction mixture per day. Some industrially synthesized MOFs such as Cu_3BTC_2 and MIL-53(Al), sold as respectively Basolite C300 and Basolite A100, are produced at

higher STY's than zeolites (50-150 kg/m^3) [86]. Very recently, the synthesis procedures of Al-fumarate (Basolite A520) and Mg-formate (Basolite M050) were improved, obtaining extremely high STY's of more than 3000 kg/m^3 per day [87]. For the Al-fumarate MOF (Basolite A520), a water based synthesis procedure was developed [88]. Those examples nicely illustrate that MOFs have the ability for large scale synthesis. Furthermore, another important synthesis factor is the solvent. When less solvent is needed, the STY increases and the reactor vessels can be made smaller. It is also desirable to have a solvent which is not too expensive [86].

Besides solvothermal synthesis, new alternative synthesis methods have been developed that might speed up the industrial MOF-synthesis. Those methods may also have a strong impact on reaction time, yields, or particle size and morphology, or may be well suited for the implementation in large-scale processes. Among those are *microwave-assisted*, *electrochemical*, *sonochemical*, and *mechanochemical* synthesis methods [85]. Within these various methods, one can still add extra solvents, structural directing agents (SDAs), mineralizers, inorganic brick-precursors and modulators. Modulators are an excellent example of additives that can increase crystal size, mineralizers (e.g. F^- ions) are used to increase crystallinity and promote crystal growth. In terms of morphology, MOFs are generally obtained as nanoparticles, but also thin films (membranes, coatings, etc.) [89, 90, 91, 92] and even aerogels [93] have been made. A conceptually new technology for membrane synthesis is the direct growth at a liquid-liquid interface, also known as interfacial or biphasic synthesis. This method uses the preferential solubility of the metal salts and linkers in water and organic solvents and has led to the formation of thin films and hollow capsules of HKUST-1 and ZIF-8 [94].

Once synthesis conditions are known that give crystalline structures, pre- and post-modifications can be applied to access more advanced MOFs. One strategy consists in the use of prefunctionalized moieties such as metalloligands [95, 96] introduced prior to or during the MOFs synthesis. Another approach uses substituted ligands prior to the MOFs synthesis [97], which can then be grafted during a post-synthetic modification (PSM) process. Post-synthetic modifications of MOFs and applications thereof have been reviewed several times during the last years [97, 98, 99, 100]. Generally, there are three main ways to postmodify MOFs with other groups: (i) by exploiting host-guest interactions, (ii) based on coordination chemistry, (iii) by making covalent bonds. The latter approach is most straightforward in the generation of new materials. Especially the amino group is suitable for further modification reactions: the reaction with anhydrides or carboxylic acids forms amides [101, 102, 103] and the reaction with aldehydes forms

imines [104]. Amino-groups have even been treated with reactive fosgene derivatives to generate reactive iso(thio)cyanate groups on MIL-53, leading to (thio)urea or (thio)carbamate groups after reactions with respectively amines and alcohols [105]. Other post-synthetic functionalization reactions start from aldehyde [106], hydroxyl [107] or azide groups [108], which include the reduction of aldehyde groups and the formation of imines. There are also direct functionalization procedures to generate nitro- [109], sulfate- [110] and chloromethyl-groups [111] on the MOF-linkers.

Figure 1.8 illustrates an optimization procedure for a certain application screening the performance (for selective adsorption, catalysis, etc.) of several MOFs and their modifications. The modification procedure is iterated until the target criteria are fulfilled (red light). Then, the right material for this particular application is found. If only small improvements are still needed (orange light), one can try to play with PSM to adapt the material based on good theoretical and experimental insight, for example by adjusting linkers or grafting-substituents. Sometimes the material is simply not suited for a certain application (green light), it is better to switch to new materials. Theoretical insight can be used to explain why some materials did not yield satisfactory results, and accordingly, other MOF structures can be suggested for testing in the next iteration loop.

1.2.3 Applications

In contrast to zeolites, MOFs have more potential applications due to their composition, a larger amount of possible structures and hybrid nature. Zeolites have already proven that they can be applied on large scale. In chemical industry they are used for catalysis and separation. In daily life, they are present as ion exchange agent within washing powders and water treatment filters (Table 1.1). Will MOFs also be applied on such a large scale? Initial tests have already indicated some promising results for various applications (Table 1.2). The ambition for the future is to bridge the gap between the state of the art and commercial applications in the domains of energy, chemistry, physics and medicine. This will require efficient and environmentally friendly synthesis procedures. The application spectrum of MOFs is most completely reviewed by Meek and Kuppler [64, 60] (Table 1.2). Beside the applications mentioned in Table 1.2, creative ideas have led to edible MOFs [139], MOFs expanding the lifetime of fruits by capturing ethylene [86], hydrophobic coatings [104], various thin film applications [89], antibacterial agents for water treatment [140], etc. The list is simply amazing and already

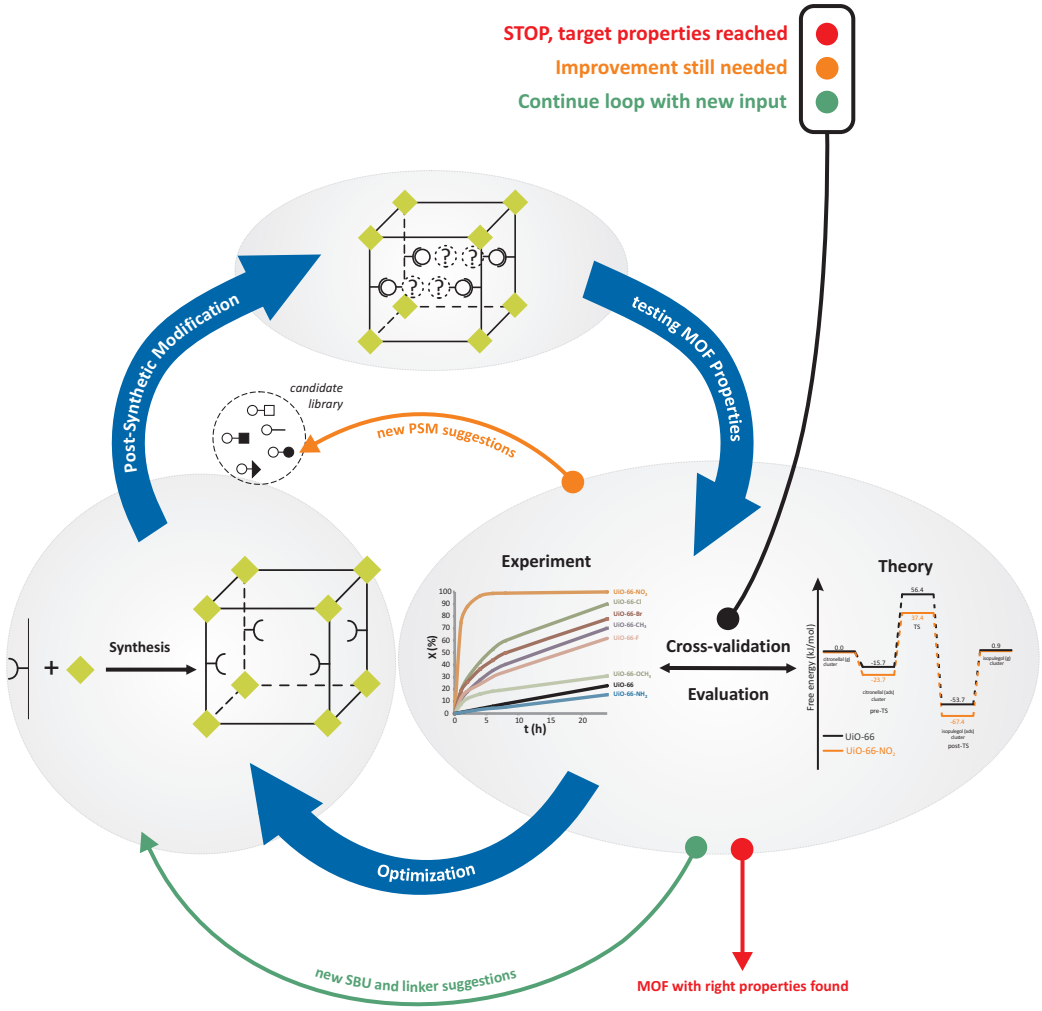

Figure 1.8: Iterative approach for optimization of MOF properties by post-synthetic modification (PSM) and the possible interplay with theoretical modeling (partially based on [98]).

Table 1.2: Overview of the published reviews: different MOF-applications and other specific MOF-related reviews

Applications	**Specific reviews**	**Part of review**
Catalysis	[112, 53, 113, 114, 115, 116]	[64, 117, 31, 60]
Adsorption and Storage	[118, 119, 120, 121, 122, 123]	[124, 60]
Separation	[39, 124]	[89, 64, 117, 60]
Optics and sensing	[125, 126, 127, 128, 129]	[89, 64, 60]
Magnetical/electrical	[130, 131, 132]	[64, 60]
Biomedical	[133]	[64, 60]
Varia	**Reviews**	
MOFs	[27, 40, 59, 36, 31, 60, 61, 63, 64]	
Synthesis	[85]	
Post Synthetic Modifications	[97, 98, 99, 100]	
Thin films	[89, 90, 91, 92]	
Simulations adsorption	[134, 135]	
Metal-azolate frameworks	[136]	
Phosponate frameworks	[137, 138]	

indicates the impact that MOFs will have on our daily lifes. In the next sections, the most important applications for MOFs within chemical industry will be discussed: gas storage, separations and catalysis.

Gas storage

Certain MOFs have a very high surface area making them suited for the storage of various gases: H_2, CO_2, CH_4. Recently, the fear for CO_2 as potentially major cause as global warming agent [141] has led to the development of CO_2 capture principles within academia [142]. Nowadays, also MOF-research is affected by this hype and many structures have already been investigated for CO_2 adsorption [118, 143]. Particularly MOF-74, especially known for its hexagonal honeycomb pattern, seems an interesting material for this application as it has open metal sites that can strongly interact with adsorbate molecules. MOF-74(M) or CPO-27 analogues have been synthesized in various metals (M = Mg [144], Ni [145], Co [146], Zn [147], Mn [148] and Cu [149]) and have strong metal CO_2 bonds upon adsorption. Furthermore, it is possible to obtain an isoreticular MOF-74 series with larger pores [150]. The combined experimental and modeling approaches recently showed that MOF-74 yields a much higher CO_2 uptake at 298 K and 0.1 bar than several other

MOFs such as HKUST-1 [37], ZIF-8 [43], MOF-177 [151], etc. [152]. Even hypothetical MOF-74 variants with other metals have been investigated and assessed by molecular modeling [153]. In terms of volume and mass, capturing all the CO_2 from power plants seems utopic since the amount of material needed would be simply gigantic or we would have to change and consume less energy. But what if we could convert the CO_2 in a useful molecule as formic acid? Recently, this has been achieved by photocatalysis on an amine modified version of MIL-125(Ti) [154]. As triethanolamine (TEOA) was used as sacrificial agent for the conversion of CO_2 into $HCOO^-$ in acetonitrile, we realize that reaction conditions will have to change (other solvent, sacrificial agent) in order to obtain a sustainable process. Nevertheless, cleaner energy producing technologies are also re-developed and heading to market soon [155]. MOFs will be valuable for adsorption, storage and separation of specialty compounds, and could be used in the downstream of chemical refineries. Furthermore, MOFs severely reduce the vessel size needed for H_2 (or CH_4) storage [119, 122]. This could be particularly useful if those materials would be used as energy-carriers for temporal fuel storage. As those applications are likely to be commercialized, the challenge is to find a cheap and well performing MOF that can easily be synthesized. So far, there are no MOFs that meet the DOE targets that should be achieved by 2017. Those are 5.5 wt.-% and 45 g/L at -40-60 ℃ under the maximum delivery pressure of 100 atm. Theoretical calculations have predicted that the target materials should have a high adsorption enthalpy of 15-25 kJ/mol in order to store H_2 at ca. 30 bar, and to release it at ca. 1.5 bar [156, 119]. Methane has a slightly higher adsorption interaction of around 15 kJ/mol on aromatics, which makes it more feasible for storage on MOFs [156] from thermodynamic viewpoint.

Separations

Sometimes, MOFs show a selective adsorption behavior for a mixture of chemical compounds, a property that is needed for separation purposes. Industrial separation processes can take place on the basis of difference in boiling point by distillation. When the boiling points of two compounds are very close to each other, crystallization techniques can be used. Within adsorptive driven separation processes, gas separation is achieved based on the differences in adsorption capability of different components in the adsorbent. The performance is directly determined by the characteristics of the adsorbent in both adsorption equilibrium and kinetics. In addition to acceptable mechanical properties, a promising adsorbent should possess not only good

adsorption capacity and selectivity, but also favorable adsorption kinetics and regenerability [124]. A complete overview of the studied liquid- and gas-phase adsorptive separations is given by Li et al. [39], but we will focus our discussion on underlaying concepts of the separation processes. Nanoporous materials are also able to separate compounds based on (i) shape selectivity (pore size, channel size), (ii) adsorbate packing effects, (iii) framework dynamics (breathing) and (iv) adsorptive host-guest interactions. Some industrially relevant examples of separations are given for each category:

- Due to exquisite *shape-selectivity* within MIL-125(Ti)-NH_2, para-Xylene is selectively adsorbed over other xylenes [157]
- Adsorbate *packing effects* explain the separation of xylene isomers on MIL-47 [158, 159] and MIL-53 [160]
- Different *adsorptive host-guest interactions* lead to separation of ethylbenzene and styrene over MIL-47, MIL-53 [161] and Cu_3BTC_2 [162]

Another more exotic example may arise when adsorption or desorption of guest molecules introduces a structural change of the material (more specifically of the pores), without loss of crystallinity and connectivity, the structural change is referred to as *breathing*. This behavior is seen for example upon adsorption of CO_2 on various materials with the MIL-53(Al)-topology [163, 164, 165, 166, 39]. It was also observed for COMOC-2, having a biphenyl linker [52]. Because of the breathing behavior, the separation between CO_2 and CH_4 is highly enhanced compared to rigid MIL-47 analogues having the same topology. Furthermore, the separation performance of MIL-53(Al) could be increased by amino-substituted linkers [167]; a separation factor larger than 60 was obtained at very low surface coverage, which is significantly larger than the factor of $\sim$5 for the parent MIL-53(Al). A theoretical explanation for this is the enhanced stability of the empty narrow pore structure of MIL-53-NH_2 over the large pore structure; which was not the case in MIL-53(Al) [168]. New selective materials can be designed by combining those insights and results (as in Figure 1.8), using for example substituted biphenyl-linkers within the MIL-53(Al) topology.

Some MOFs can be industrially relevant for new separations. A good example has been demonstrated by De Vos and coworkers [169]. They have recently presented a whole flow scheme for the separation of C_{5+} feedstock, using only three different nanoporous materials: MIL-96, Cu_3BTC_2, and a high silica chabazite zeolite [169].

Catalysis and active site engineering

The metal sites in MOFs are highly dispersed, forming one of the main advantages of MOFs. However, reactions can only take place when the metal sites are accessible or unsaturated. An example of a MOF with unsaturated metal sites is Cu_3BTC_2, active for various *Lewis* catalyzed reactions [170]. MOFs have been synthesized with accessible metal sites in their pores, even if the structure would seem fully coordinated, those defect sites can either be generated by adding a certain modulator during the synthesis or by modifying the MOF-synthesis procedures. Some MOFs, such as MIL-53(Ga) also contain *Brønsted* acid protons that can catalyze the Friedel-Crafts alkylation of biphenyl, even surpassing traditional zeolites (H-Beta, H-mordenite) in activity [171]. In theory, some organic linkers might also display basicity and in this case, the MOF may be used as base catalyst.

1.3 The added value of Molecular Modeling within MOF research

The following indicative examples will show that molecular modeling techniques have already been highly beneficial for experimental research, especially if they are used for structure predictions and further analysis. Férey and coworkers demonstrated already in 2004 the added value of structure predictions; to see which polymorfs can be generated from basis secondary building blocks and organic linkers [172]. In a recent study of Snurr et al. a MOF database was constructed from a library of 102 building blocks. Nearly 140000 hypothetical MOFs were generated and for each one the pore-size distribution, surface area and methane-storage capacity was calculated. For over 300 MOFs, the predicted capacity was larger than that of any known material. One such promising MOF could then be selected to confirm its predicted capacity experimentally [173]. Furthermore, grand canonical Monte Carlo studies have already been widely used to study the adsorption isotherms of compounds within frameworks [174, 175, 176, 177]. Afterwards, the researcher can even construct mixed compound isotherms with the Ideal Adsorbed Solution Theory (IAST) [178, 179], to get an idea of the separation capacities of the materials. Notwithstanding the efforts made in the field of adsorption and structure predictions, the articles about catalytic reactions in MOFs were very scarce as well as the modeling of these reactions. The MOF-research was still in an exploratory phase compared to zeolite-research. The comparison of some MOFs with known homogeneous catalysts was highly

warranted together with theoretical reaction pathways on realistic catalyst models to unravel the reaction pathways. The challenge was taken to study both epoxidation and Lewis acid catalyzed reactions in MOFs as main research topics of this PhD shown further in the Scope (Chapter 2).

2

Scope

Most of the scientific research performed in this PhD thesis has already been published in peer reviewed papers. They can be classified in different categories, as schematically shown in Figures 2.1 and 2.2 (all papers are labeled from 1 to 15 (see Table 2.1)). The main focus of the thesis is on nanoporous materials, which take a prominent place in heterogeneous catalysis. For all reactions chemical kinetics have been evaluated from first-principles and – if available – compared with experimental data. Up until recently many computational papers focused solely on activation barriers, whereas in this study all conclusions have been made on basis of rate constants. In the absence of experimental data in literature new experiments on kinetics have been performed by our experimental partners and the results published in joint experimental-computational papers. The catalytic properties of zeolites and MOFs have been thoroughly investigated for a number of case studies in which the active site consisted of a Brønsted or Lewis acid.

The first part of the thesis focuses on Brønsted acid catalyzed reactions. The methanol-to-olefin (MTO) process is an important industrial process in view of the waning oil reserves and has also been for some years part of an active research line of the CMM. In this process, methanol is converted into hydrocarbons. Within this thesis some specific aspects have been selected that take place in zeolites. Zeolites are used as acid catalysts and should be designed to control the ethene/propene ratio and to suppress secondary reactions that lead to coke formation. In order to meet this goal, insight into the activity and selectivity of individual active sites is necessary, and the crucial role of topology in reaction rates should be unraveled (**Papers 1-3**).

The second part is devoted to two themes, namely to catalytic oxidation reactions in MOFs in collaboration with the experimental COMOC group of

the Ghent University (Prof. Pascal Van Der Voort), and to the development of new methods to enhance the activity and selectivity of MOF catalysts in collaboration with Prof. Dirk De Vos of the Centre for Surface Chemistry and Catalysis, COK, KULeuven. Both research lines have been very successful. The first theme concentrates on oxidation reactions (more precisely cyclohexene epoxidation) in vanadium MOFs (**Papers 4-7**). In the second theme we showed that functionalized linkers can greatly increase the activity of MOF catalysts with coordinatively unsaturated sites. In a series of functionalized Zr-terephthalate materials with the UiO-66 structure, the nature of the active sites and the increase in activity was explicitly predicted theoretically and confirmed experimentally. Citronellal cyclization was taken as a test reaction, and we were pioneers in showing how to increase the activity by modulating the electronic effects via various linker substitutions. These results are presented in a paper published in Angewandte Chemie International Edition (**Papers 8-9**).

Finally, we also explored structural phenomena and adsorption properties of some MOFs. These topics are indirectly related to catalysis research, as before a reaction takes place the guest molecules need to diffuse into the pores and adsorb on the active site. After that the actual reaction may take place. Just as in catalysis, adsorption and diffusion play a crucial role in separation phenomena. Related to those processes, it is important to account for the fact that nanoporous materials are often much more flexible than expected. For MOF materials, a lot of research is performed on structural transitions as a result of external phenomena. In particular the simulation of the selective adsorption of xylene isomers in the MIL-47 pore system (**Paper 10**) was a time-consuming project that was executed in the first half of my PhD, but was very useful for my training and ultimately has given me much greater competency in molecular modeling. To summarize, the research performed in the frame of this thesis can be subdivided into five themes. Within each theme one or more items have been tackled:

1. **Brønsted acid catalyzed reactions within zeotype materials**
   More specifically, some key reactions in unraveling the mechanism of the Methanol-To-Olefins (MTO) process (such as methylation, dimerization, cracking, cyclization) have been investigated (**Papers 1-3**).

2. **Epoxidation reactions of cyclohexene on vanadium catalysts**
   In the context of investigating catalytic properties of MOFs for oxidation reactions, cyclohexene epoxidation has been selected as a reference reaction. This theme gets a lot of attention in this thesis as cyclohexene epoxidation is not only extensively studied on MIL-47 and MIL-47-X

(MIL-47 with linker substituents X) but also on $VO(acac)_2$ in a homogeneous catalysis process (**Papers 4, 5, 6 and 7**). This homogeneous catalyst was selected as it allowed for the plausible reaction mechanisms during cyclohexene epoxidation to be fully unraveled. Also experimentally a lot of resemblances were found between the catalytic activity of MIL-47 and $VO(acac)_2$. Many aspects are discussed within the scope of this theme, such as methodology (cluster versus periodic), structure of the active sites and effect of linker substituents, radical decomposition, etc. In particular the importance of the model choice is emphasized in **Paper 7**, where both periodic and cluster approaches are compared.

3. **Activity and selectivity on the citronellal cyclization on Lewis acid MOFs**
   In this stage of MOF research, experimental groups are increasingly enthusiastic about methods that significantly enhance the activity and selectivity of MOF-catalysts. A nice illustration of this concept is the electronic linker modulation behavior of UiO-66-X materials for Lewis acid catalysis (**Paper 8**). Furthermore, various other catalysts have also been compared for the cyclization of citronellal: ATPH, $ZnBr_2$, Cu_3BTC_2 and Cu_3BTC_2-NO_2 (**Paper 9**).

4. **Adsorptive host-guest interactions**
   Significant attention is given to the xylene adsorption interactions within MIL-47 (**Paper 10**). Contributions to other papers within this theme can also be taken up here (**Paper 13-14**).

5. **Structural transitions of MOFs**
   The breathing modes of a newly synthesized vanadium MOF (COMOC-2) are investigated (**Paper 11**).

An overview of the research articles resulting from this PhD thesis and their modeled topic is given in Table 2.1. In the remainder of Part I of this thesis, we will only highlight the main conclusions of the research forming the core concerns of this PhD study. For the entire contents, technical details concerning the applied methodology, etc., the reader is referred to the respective papers taken up in Part II.

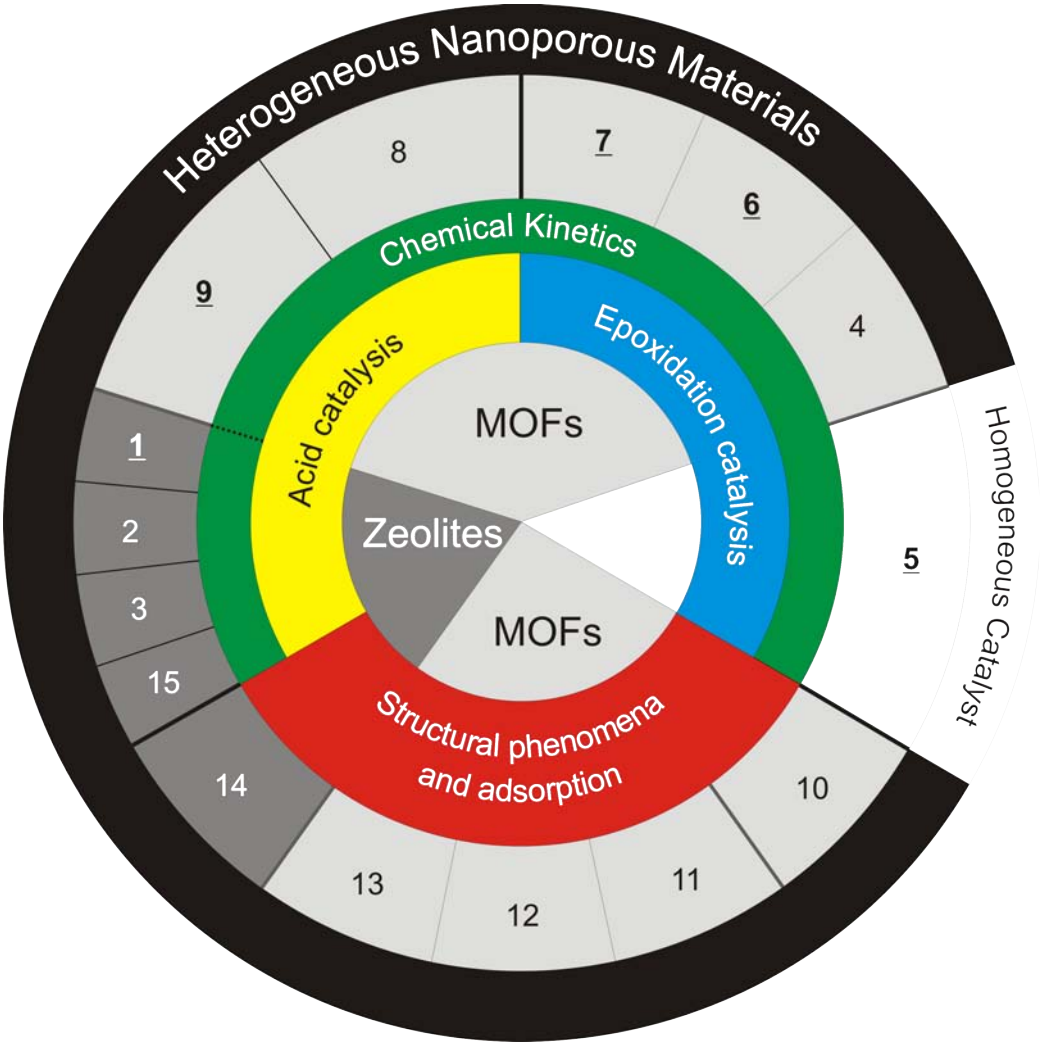

Figure 2.1: Global overview of the papers, resulting from this PhD-work, ordered based on research themes.

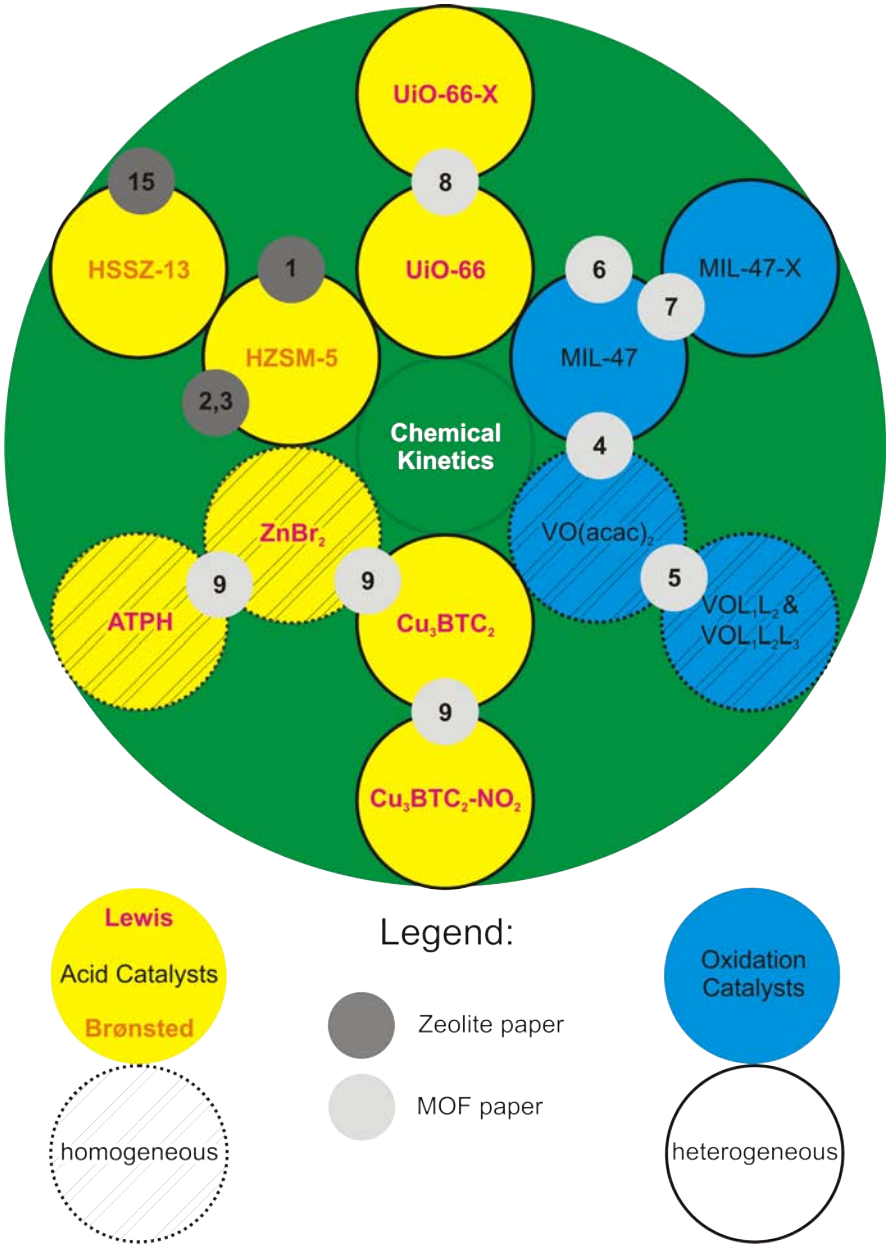

Figure 2.2: Schematical overview of all heterogeneous and homogeneous catalysts used in this PhD thesis for the description of oxidation or acid catalyzed reactions. The labeling of the papers is also given.

Table 2.1: Overview of the papers covering the research done in the frame of this PhD.

	subject	**catalyst**	**Ref.**
Paper 1	Alkene oligomerization, cracking and cyclization	HZSM-5	[180]
Paper 2	Alkene methylation	HZSM-5	[181]
Paper 3	Linear alkene methylation and cracking reactions	HZSM-5	[182]
Paper 4	Initial epoxidation pathways	MIL-47, $VO(acac)_2$	[183]
Paper 5	Epoxidation routes	$VO(acac)_2$	[184]
Paper 6	Epoxidation and radical reactions with TBHP	MIL-47	[185]
Paper 7	Epoxidation and radical reactions with TBHP	MIL-47 and MIL-47-X	in prep.
Paper 8	Citronellal cyclization	UiO-66-X	[186]
Paper 9	Citronellal cyclization	$ZnBr_2$, Cu_3BTC_2, ATPH, Cu_3BTC_2-NO_2	in prep.
Paper 10	Xylene adsorption interactions	MIL-47	[187]
Paper 11	Structural Transitions	COMOC-2	[52]
Paper 12	Force field development	MIL-53	[188]
Paper 13	Adsorption of CH_4 and CO_2	MIL-47-NH_2	[189]
Paper 14	Alcohol and nitrile adsorption	HZSM-5	[190]
Paper 15	Naphthalene methylation	HSSZ-13	[191]

3

Major research results

3.1 Introductory remarks on the methodology

In this PhD thesis, a variety of chemical reactions is studied in various molecular environments. As the bonding pattern changes drastically during a chemical reaction, it is necessary to describe the electronic structure problem from first principles. In quantum chemistry, different methods exist for solving the stationary Schrödinger equation ($\hat{H}\,|\Psi\rangle = E\,|\Psi\rangle$) associated with a molecular system. The two main approaches to solve the electronic structure problem are based on wavefunction methods, such as Hartree-Fock (HF) and Density Functional Theory (DFT) [192]. Due to the size of the model space where catalytic reactions, adsorption of guest molecules or structural transitions take place, we decided to use DFT-based methods, as this is an efficient cost-effective method.

The second problem is the choice of the model for the active site as displayed in Figure 3.1, where a terephthalate defect site is shown for the UiO-66. On the one hand, extended cluster calculations are more established within the community of computational chemistry and therefore a broader variety of density functionals is available and the algorithms to search for transition states are much more developed. On the other hand, periodic simulation codes are based on plane wave basis sets and originate from the solid state community. Since a few years, those codes are also used in catalysis research for typical chemical problems but many hybrid functionals, commonly applied within the computational chemistry community, are not available in periodic codes. Furthermore, the usage of hybrid functionals in periodic codes is computationally very expensive and one needs careful convergence

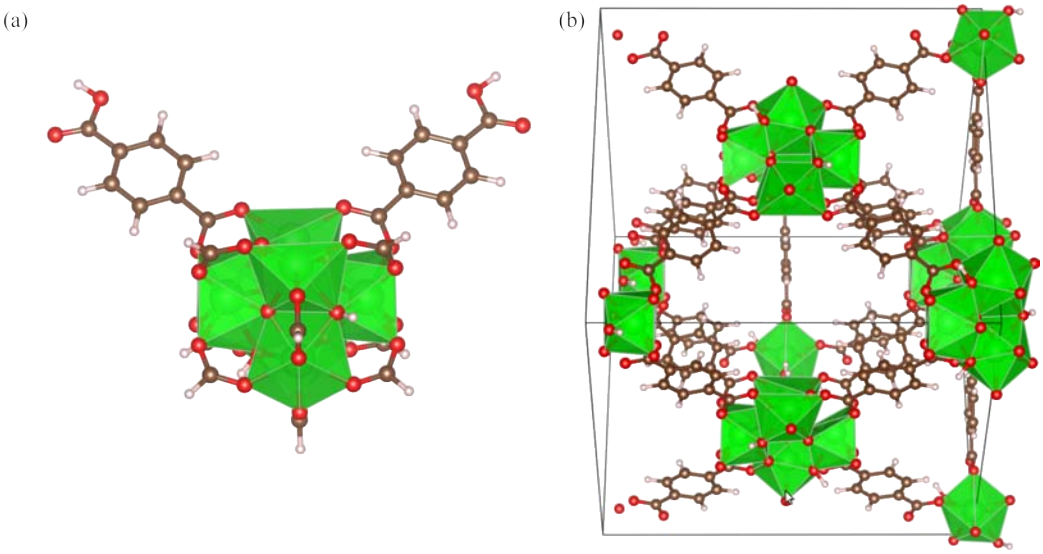

Figure 3.1: A model for a terephthalate defect site: (a) cluster or (b) periodic approach.

checks (k-points, kinetic energy cut off of the plane waves, cell volume, etc.). Additionally, the search for transition states is a non-trivial task. For some case studies, e.g. citronellal cyclization on Cu_3BTC_2, we have tested these periodic procedures. To avoid small residual imaginary frequencies, it was found that very stringent convergence criteria are needed in combination with a high kinetic energy cut off of the plane waves as was also shown by De Moor and co-workers [193]. The development of additional theoretical techniques to speed up this process or to filter the small (real and imaginary) frequencies out of the full Hessian would be interesting for future research. Despite these computational issues which are not in favor of periodic calculations, some problems may not be tackled with cluster calculations. For example, this was the case for the treatment of the structural transitions in COMOC-2. Periodic simulations were also necessary to study adsorption interactions within MIL-47.

The term first-principle chemical kinetics, frequently used in this thesis, refers to the theoretical determination of reaction paths, free energy profiles, rate coefficients, etc., since these descriptors provide inside on the reaction mechanism and allow to validate our theoretical model. The three following paragraphs provide remarks where we should care for when transferring experimental kinetic data to first-principles chemical kinetics and vice versa.

If we compare experimental with theoretical kinetics, we have to be fully aware that we are working with theoretical models, meaning that our models

will not necessarily be representative for all experimentally existing catalytically active sites. Some examples will be given to substantiate this contention: First, the position of Al-sites in the HZSM-5 is normally kinetically controlled during the synthesis of the zeolites [194]. The incorporation of Al is thus not random and can be varied by the synthesis conditions [195]. Our choice to put the Al-defect in the crystallographic T12 [196] is thus somewhat arbitrary, but gives the most accessible proton positions ($T_{12}O_{11}T_{11}$, $T_{12}O_{24}T_{24}$, $T_{12}O_{20}T_{15}$, $T_{12}O_{12}T_{18}$). For all methylation reactions and alkoxide formations, the proton was put on the O_{20} position (**Papers 1-3**). Second, our theoretical model includes just one Al-defect in case of HZSM-5, while there are many other possible active sites present within the materials: e.g. Silanol groups (Si-OH) and Lewis acid sites (Al).

3.2 Brønsted catalyzed reactions within zeotype materials during the MTO process

The accurate prediction of chemical kinetics from first-principles is one of the core businesses of the CMM. In this PhD thesis this unique expertise is used for the investigation of reaction paths in catalytic processes, for searching the active sites in the nanoporous materials under study and for unraveling reaction mechanisms of industrially relevant processes. The contribution of this PhD thesis to catalytic processes over zeolites is restricted to the MTO-process, as the CMM has already built up a longstanding reputation in this research area. The reaction mechanism is complex and is not uniquely determined. The formation of hydrocarbon pool species in the pores of a zeolite (H-ZSM-5 and H-SAPO-34) offers a reaction mechanism that is plausible on the basis of theory and experiment for the conversion of methanol to olefins (ethene, propene, etc.). The unraveling of reaction steps within the Methanol-To-Olefin (MTO) process on H-ZSM-5 has been the topic of my master thesis and I further elaborated on it during my first PhD-year (**Papers 1, 2 and 3**). It was already discovered in 1976 that H-ZSM-5 has the ability to convert methanol to hydrocarbons (MTH) in the range C_{2-10}. Other industrial processes, such as the conversion of methanol to gasoline (MTG) and methanol to olefins (MTO), using other protonated zeolites or zeotypes have been developed since then [197, 198].

For over 30 years, there has been an ongoing dispute on the true nature of the reaction mechanism in MTO catalysis by both experimental and theoretical researchers [199, 200, 201]. Only recently, consensus has been achieved on an indirect olefin-producing cycle rather than direct coupling of C_1 entities (like

methanol or dimethylether) [202, 203, 204]. In this alternative "hydrocarbon pool" (HP) model, the active site of a typical MTO catalyst is composed of a nm-sized inorganic channel or cage with Brønsted acid functionality, containing an essential organic compound, all interacting to form a supramolecular catalyst [205]. In a typical catalytic cycle, the HP species undergoes successive methylation steps by methanol and/or dimethyl ether and subsequently eliminates light olefins such as ethene and propene [206, 207, 208]. Within HZSM-5, this methylation scaffold can either belong to the alkene- or the aromatic-family, implying that a dual-cycle is operative, displayed in Figure 3.2. Based on ^{13}C labeling experiments with methanol, it was stated that the polymethylbenzene cycle yields predominantly ethene, and an alkene cycle yields mainly propene and higher alkenes [209]. This does not explain how the initial hydrocarbon pool compounds (methylbenzenes and alkenes in the case of H-ZSM-5) are generated. The two most plausible pathways are (i) from impurities in the initial methanol feed, e.g. ethanol, propanol or isopropanol, or rather (ii) through the incomplete calcination of templating agents [208]. Internal framework (silanol) defects were recently found to be crucial for the deactivation behavior of the ZSM-5 catalysts [210] and might also play a role within initial and secondary HP formation due to their dehydration potential. However, once full conversion has started, new secondary HP species may arise from primary MTO products like ethene and propene (Figure 3.2).

In **Paper 1**, the formation of those aromatic secondary hydrocarbon pool compounds for methanol-to-olefin conversion (MTO) in H-ZSM-5 is taken as a practical example for the creation of bulky organic compounds trapped in a confined space. The theoretical calculations describe a preliminary pathway to a 5-membered cyclic species from small alkene molecules like ethene and propene (Figure 3.3a). This route involves the following steps: physisorption of a first propene molecule to form a π-complex, alkoxide formation to form a covalently bonded complex, i.e., the n-propoxide, physisorption of a second propene and dimerization to form the 2-hexylcarbenium ion and finally cyclization toward a neutral methylcyclopentane molecule. For all steps, both forward and backward intrinsic reaction rates are given at 673 K.

The reaction rates are in the same order of magnitude as those reported in an earlier modeled methylbenzene cycle for the production of olefins in ZSM-5 [211]. The alkoxide formation and dimerization have similar reaction energies and barriers as the methylation reactions of aromatic species in the same topology. Once this carbenium ion folds up, the ring closure itself is very rapid. Although the total energy barrier for direct cyclization from the 2-hexylcarbenium ion amounts to 69.2 kJ/mol, the free energy barrier is

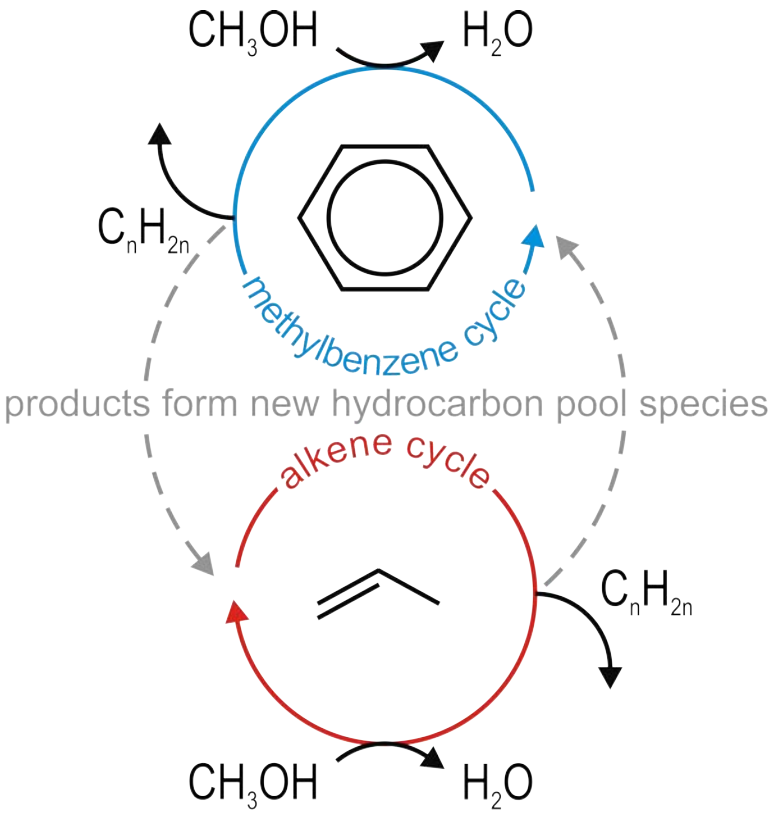

Figure 3.2: Two possible hydrocarbon pool cycles, based on a methylbenzene and alkene organic co-catalyst present in the zeolite pores. Both cycles convert methanol into light olefins and water, but with different ethene/propene selectivities. The two cycles do not operate independently, but are interconnected since the products can either act as new co-catalysts directly (for the alkene cycle) or undergo oligomerization and cyclization to form new aromatic co-catalysts (used in the methylbenzene cycle).

still 88.4 kJ/mol, due to the entropic losses from the folding up towards the transition state [1].

However, to form aromatic hydrocarbons from this 5-membered ring species, we still need to consider several dehydrogenation steps as well as ring expansion. An example of such a route is displayed in Figure 3.3b. Ring expansion towards toluene was studied by McCann et al. [211]. The dehydrogenation reactions require the conversion of alkenes to alkanes. Furthermore, the stepwise propene dimerization reactions are highly favoured over the concerted pathways, making small alkoxide species necessary intermediates within the MTO-process.

Alkene methylation reactions form another reaction class during the MTO-process and have been investigated in depth within **Paper 2**. Theoretical rate constants are compared with the experimental data of Svelle and coworkers [212, 213]. Starting from an adsorbed ^{13}C-labelled methanol molecule, alkene pulses were fed over the reactor at high space velocities to minimize the secondary side product formation. The reaction orders in the alkene and the adsorbed methanol were determined to be 1 and 0 . For the rate equation

$$r = k.p^0_{\text{methanol}} p^1_{\text{alkene}},$$

experimental kinetic coefficients were determined for the tested alkenes. For the methylations of ethene, propene and the butene-fraction relative ratios are found to be k_{ethene}:k_{propene}:$k_{\text{butene-fraction}}$= 1:17:50 at 350 ℃, with respective apparent barriers being 104, 64 and 40 kJ/mol [214].

Since 2-butanol was taken as the butene precursor, the thermodynamic distribution of the alkenes formed needed to be determined. Therefore, the butene conversion was studied at the experimental conditions of the methylation experiment but without the methanol cofeed. At the reaction conditions of methylation, 16% of the linear butenes (originating from 2-butanol) were converted into fractions of isobutene (30%), propene (30%), and pentene (31%). Accordingly, the initial distribution of butenes ($C_4^=$) can be written as follows:

$$C_4^= = 0.84 C_{\text{lin-butenes}} + 0.16(0.30 C_{\text{propene}} + 0.30 C_{\text{isobutene}} + 0.31 C_{\text{pentene}}).$$

The various contributions to the linear butenes were estimated by calculating the corresponding theoretical equilibrium constants between adsorbed

[1] If the 2-hexylcarbenium ion would transform first back to the adsorbed 2-hexene state, this whole cyclization process would be even higher activated

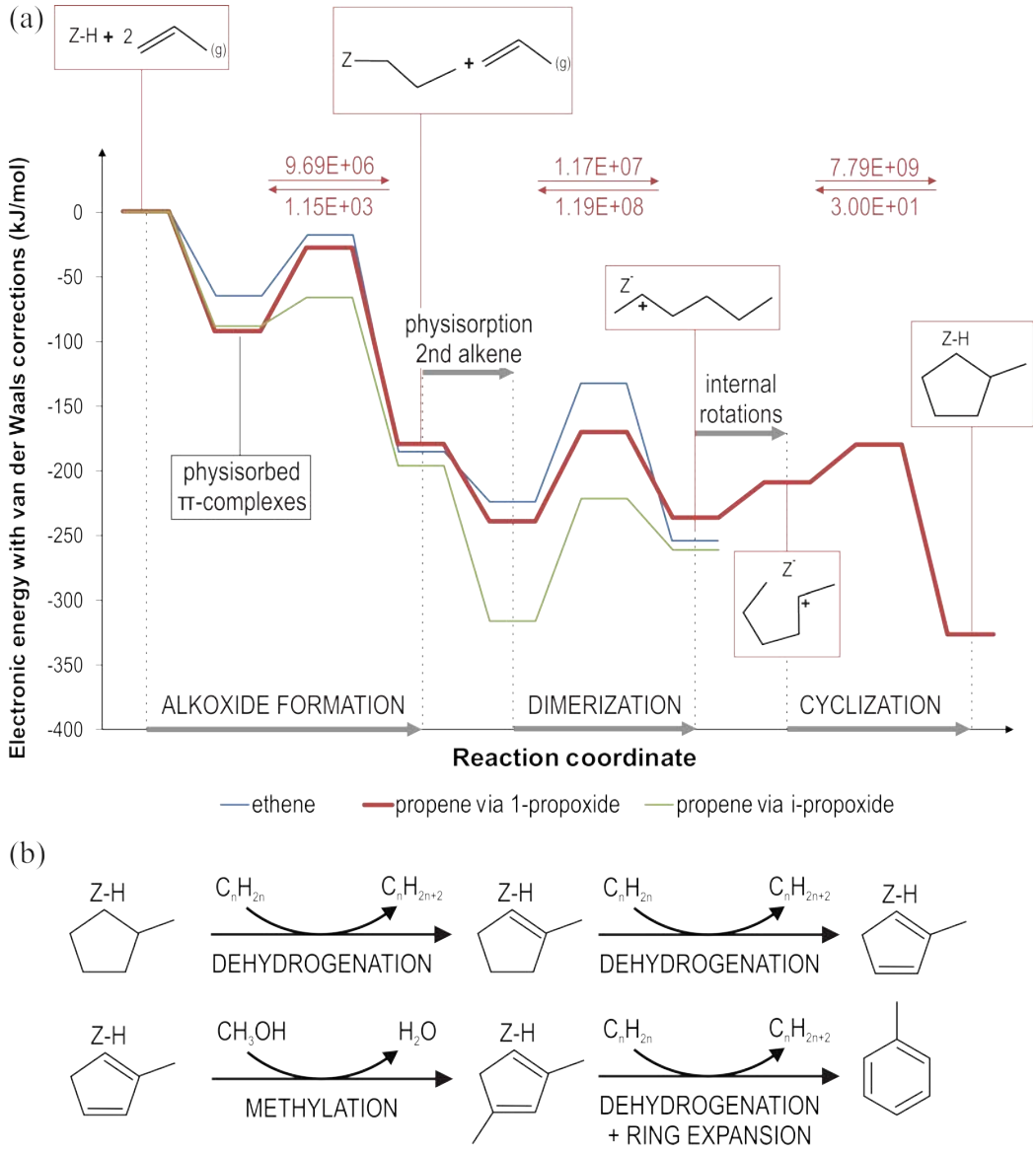

Figure 3.3: (a) Overview of a viable route towards the formation of cyclic species starting from ethene and propene. The red cycle is the most probable pathway and involves physisorption of propene, formation of n-propoxide, additional physisorption of propene, dimerization to form the 2-hexylcarbenium ion and cyclization to methylcyclopentane (intrinsic kinetic coefficients in s^{-1} at 673 K); (b) Other reaction steps that are needed to form an active polymethylbenzenic HP species are dehydrogenation, methylation and ring-expansion.

π-complexes within HZSM-5. This finally yields the following expression for the distribution of butenes:

$$C_4^= = 0.476C_{\mathrm{trans-2-butene}} + 0.066C_{\mathrm{1-butene}} + 0.404C_{\mathrm{cis-2-butene}} + 0.054C_{\mathrm{isobutene}}.$$

Taking into account the van der Waals corrections, the following relative ratios for methylations (k_{ethene}:k_{propene}:k_{butene}) are found, 1:23:1197, which are already in quite good agreement with the experimental values (1:17:50). However, a better experimental agreement is obtained, when some refinements are incorporated, by treating some of the low vibrational modes of the gas phase molecules in a more appropriate way than the standard HO approximation. These internal rotations are more accurately described within the 1D-HR approach. By doing this, the calculated constants are now in a much better quantitative agreement with the experimental data: apparent activation energies of 94, 62 and 37 kJ/mol for ethene, propene, and butene are found, and relative ratios of methylation k_{ethene}:k_{propene}:$k_{\mathrm{butene-fraction}}$ = 1:23:898. Summarizing, the relative rates of methylation for ethene and propene agreed excellent with experimental values, especially after accounting for the full flexibility of the gas phase alkenes using internal rotors.

Only, the theoretical rate for butene methylation remains somewhat overestimated. In the model used, the diffusion is not taken into account. As butenes diffuse slower relative to ethene in H-ZSM-5, this could explain the slight overestimation of butene methylation. Diffusion constants for the various alkenes could have been determined by molecular dynamics; but this is not done and falls beyond the scope of this work.

In **Paper 2** a profound discussion is taken up around the so-called "compensation effect" [215]. As displayed in Figure 6 of **Paper 2**, a clear trend was indeed observed between $\ln(A)$ and E_{a} for the bimolecular kinetic coefficients. While the activation energy systematically decreases when going to longer alkenes giving rise to an increase in the rate, the pre-exponential factor systematically decreases inducing an opposite effect on the rate constant. For the intrinsic pre-exponential factors this trend is not observed and the values are on the same order of magnitude along the whole series of alkenes. This effect is ascribed to a stronger adsorption with longer chain length, due to stronger van der Waals interactions because of additional methylene groups. At the same time a stronger adsorption leads to a higher entropy loss compared to the gas phase as fewer conformations are possible. The whole mechanism is schematically shown in Figure 4 of **Paper 2**.

Going back to the scheme displayed in Figure 3.3a, and focusing on the dimerization process, where the formation of a 2-hexylcarbenium ion occurs

with a reaction rate constant of 1.17E+07 s^{-1}, we notice that the backward reaction, corresponding with β-scission or cracking, is 10 times faster. It implies that a catalytic alkene cycle (Figure 3.2) during MTO conversion is feasible. The full theoretical cycle is elaborated in **Paper 3**.

Starting with a single propene molecule, chain growth proceeds through successive alkene methylation steps by methanol, forming longer alkenes, which can then again be methylated or undergo cracking steps. At 673 K, the β-scission from a 2-hexylcarbenium ion is ten times faster than the reverse reaction of propene dimerization (Figure 3.3a). Therefore, the alkene cycle offers a viable path to the production of olefin products. Methylation of linear alkenes occurs as fast as that of the most active methylbenzenes and is not subject to any steric hindrance. Several cracking steps are possible (depending on the chain length), resulting in the production of both propene and ethene, yet still with a slight preference for propene in our linear-alkene cycle. As isomerization and deprotonation/protonation reactions are extremely fast, they result in a wide variety of linear and branched alkenes. They will be most abundant in an elaborated version of the linear alkene cycle, since those branched alkenes did also display the fastest cracking reactions. The cracking transition state has a secondary carbenium ion character in the case of branched alkenes, while it has a primary carbenium ion character in the case of linear-alkene cracking. Furthermore, the butene distribution does not solely consists of 1-butene, meaning that branched alkenes can already be formed from butene methylation. It is clear that next to the alkene cycle of **Paper 3**, there will be an even faster catalytic cycle governed by branched alkenes such as isobutene and various 2-methyl-pentenes.

It should be stressed that all reactions in this work have been studied by completely taking into account the environment (topology, Brønsted acid strength, composition of the framework, etc.). This is of utmost importance to find all transition states that consist of the protonated structures and also the protonated intermediates along the reaction paths. They are trapped within H-ZSM-5, and appear as stable minima on the electronic energy surface: the protonated methylcyclopropane intermediate in ethene dimerization could be identified (**Paper 1**) and the 2-hexylcarbenium ion has been trapped after dimerization of propene with 1-propoxide (Figure 3.3a). Furthermore, all studied methylation reactions resulted in protonated stable post-transition state products, sometimes even coordinated with water to form an oxonium ion (**Papers 2 and 3**). Nevertheless, deprotonation reactions from those protonated intermediates are exothermal and barely activated. Tuma and Sauer have already shown the preference of protonated isobutyl-carbenium ion intermediate over the alkoxide within H-FER [216]

at ambient conditions. However, the neutral π-complex from isobutene remained the most thermodynamically favoured complex.

It can be concluded that during the MTO-process in HZSM-5 multiple parallel and interlinked routes operate on a competitive basis: methylation, oligomerization, cracking, hydrogenation, dehydrogenation, cyclization, protonation, deprotonation, alkoxide formation, alkyl shifts, etc. Small alkoxide species have been identified as important reaction intermediates. In the future, the role of other methyl sources, such as dimethylether and even methoxy species should be clarified. Another evident next step involves the exploration of other zeotype and zeolite topologies, as the acid strength and cage topology are important factors when chosing the best supramolecular catalyst system for a certain application. For example, an initial study on the coke formation within H-SSZ-13, a zeolite with CHA-topology, is given in **Paper 15**. Various methylations of naphthalenic species are investigated, to find the most plausible pathway towards a species within the sidechain route able to eliminate olefins.

Summarizing, this part of the thesis, devoted to catalysis in zeolites, learns that molecular modeling has become a tool that can be regarded as complementary to the experiment, as the reliability of its predictions is systematically increasing, and as information can be gathered from individual reactions which are not accessible by experiment.

3.3 Epoxidation of cyclohexene on vanadium catalysts

In this PhD, two Vanadium containing catalysts (more in particular the heterogeneous MIL-47 and homogeneous $VO(acac)_2$) have been tested for the epoxidation of cyclohexene with *tert*-butyl hydroperoxide (TBHP) in the solvent chloroform or CH_3Cl. The work was published in four research papers (**Papers 4-7**).

In a preliminary communication (**Paper 4**), the homogeneous $VO(acac)_2$ catalyst has been compared with the metal-organic framework MIL-47 for the epoxidation of cyclohexene using a 70 wt.-% TBHP solution dissolved in water. The cyclohexene conversion and product distribution are found to be very similar. The product spectrum of both V-catalysts is quite broad and apart from cyclohexene oxide **2**, the other main reaction products are cyclohexane-1,2-diol **3**, *tert*-butyl-2-cyclohexenyl-1-peroxide **4** and cyclohexen-2-one **5** (Figure 3.4a). Hot filtration experiments indicated that

MIL-47 was partly a heterogeneous catalyst as the leaching of V-centers amounted to 12.8 % after 1 h of reaction. This problem was resolved in **Paper 6** by working with TBHP dissolved in decane, an apolar solvent. The leaching of V-centers is negligible, preserving the structural integrity of the MIL-47 during successive catalytic runs. Furthermore, the selectivity towards the epoxide was much higher with TBHP/decane in both $VO(acac)_2$ as MIL-47.

In the following, we discuss the structure of the active Vanadium sites, and on the diverse reaction pathways leading to cyclohexene oxidation. EPR and NMR experiments confirm that both V^{+IV} and V^{+V} sites are present during the catalysis [217, 185]. The mechanism can schematically be simplified by the scheme displayed in Figure 3.5. Before starting the actual epoxidation reaction, the V-catalyst needs to be activated with TBHP forming an active complex (AC). The catalytic cycles consist in principle of two main reaction families: the epoxidation of cyclohexene bringing the catalyst into an inactive complex (IC), and the activation of inactive to active complexes through reaction with the oxidant TBHP. Apart from these reaction families, radical decomposition reactions alter the oxidation state of Vanadium, from +IV to +V and vice versa. Those oxidation state transitions do happen much faster in the presence of water, leading to a much higher concentration of radical adduct product **4** when TBHP dissolved in water is used. In the following, the focus will be on unraveling the active V-sites within MIL-47 and afterwards the scheme in Figure 3.5 will be worked out specifically for MIL-47.

3.3.1 Search for the active sites within MIL-47

MIL-47 has $[V^{+IV}O(CO_2C_6H_4CO_2]$ as structural formula. More specifically, this material consists of a porous terephthalate framework built from infinite chains of $V^{4+}O_6$ octahedra and has a three-dimensional orthorhombic structure that exhibits large pores [51]. Every structural unit in MIL-47 contains an O-V^{+IV}=O bridge. The linkage of the V^{+IV} to dicarboxylate groups of the terephthalate linkers results in an octahedral structure unit. Hence each vanadium(+IV) centre is saturated and terephthalic acid linkers need to torn away in order to create active sites forming the active vanadium-alkylperoxo-group. In **Paper 4**, a preliminary catalytic cycle is given based on $VO(acac)_2$ as catalyst, which showed a remarkable resemblance to the MIL-47 catalyst from the experimental results. It has been shown that the removal of an acetylacetonate (acac) ligand is needed to make an active vanadium-alkylperoxo compound, which is able to epoxidize cyclohexene.

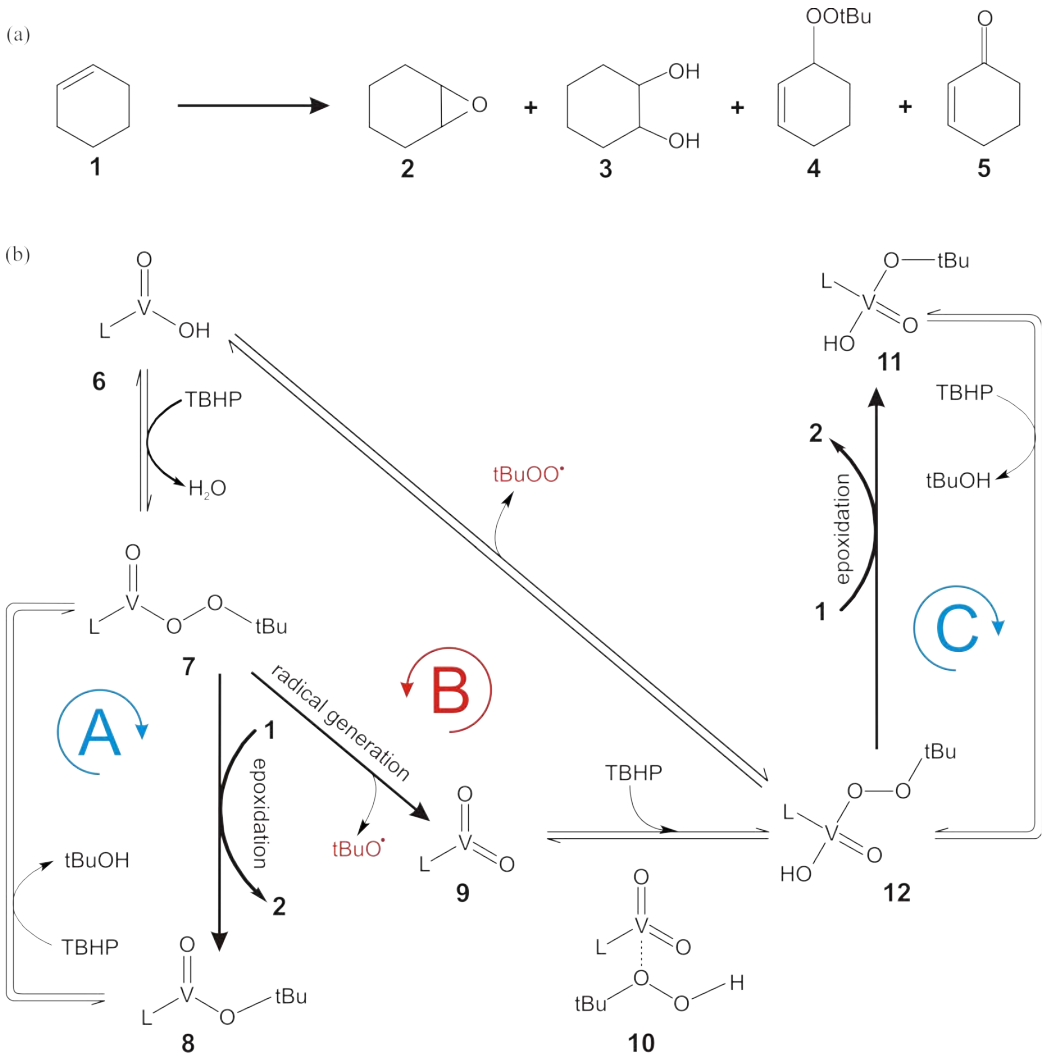

Figure 3.4: (a) Oxidation of cyclohexene **1** to cyclohexene oxide **2** and consecutive ring opening to cyclohexane-1,2-diol **3**, *tert*-butyl-2-cyclohexenyl-1-peroxide **4** and allylic oxidation to 2-cyclohexene-1-one **5**; (b) Two competitive cyclohexene epoxidation pathways (**7** → **8**, **12** → **11**) and radical generation reactions (**7** → **9** and **12** → **6**), allowing transformation of oxidation state from +IV to +V and vice versa.

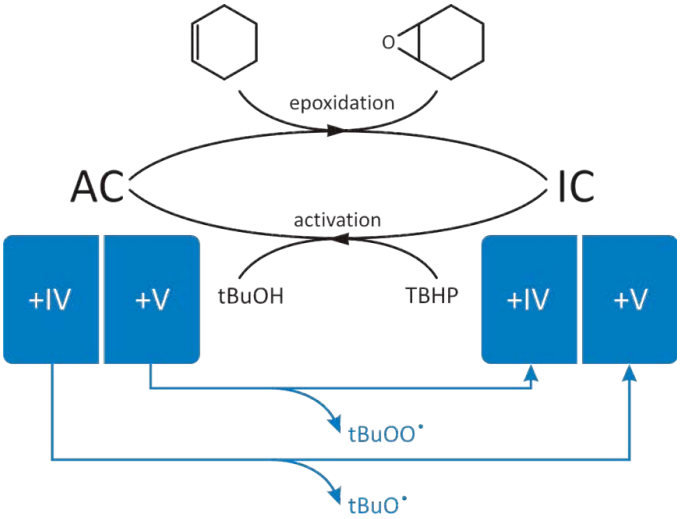

Figure 3.5: Main reaction families of the Vanadium/TBHP catalytic systems for epoxidation of cyclohexene, transforming active complexes (AC) to inactive complexes (IC). The scheme reports *tert*-butanol as most dominant side-product of the activation step. Side reactions in which radicals (tBuOO•, tBuO•) are generated, start as well from active complexes.

Free coordination positions should also be created by ligand removal or by folding one terephthalic acid ligand away from the vanadium center or by removing the bridging oxygen between the neighboring vanadium centers from the O-V=O axis.

In the theoretical modeling, special attention should be drawn in the construction of the extended cluster. In the top of Figure 3.6 it is shown how the cluster is cut out from the crystal. The extended cluster model contains two vanadium atoms, bridged by two terephthalate linkers. On the vanadyl chain only two V=O bonds are maintained, and the continuation to further terephthalate linkers is interrupted and replaced by terminating OH-groups. Figure 3.6 makes also clear that we should discriminate between two effectively different V-sites within MIL-47. They are denoted by type I and type II. In **Papers 5-6** only sites of type I have been investigated in both a constrained[2] and unconstrained extended cluster model. In a more recent study (not yet published - **Paper 7**), however, it has been demonstrated that V-sites of type II are lower in energy than those of type I. Their influence on the kinetics will be discussed later.

[2]The outer carboxyl groups are fixed during the optimization and Hessian calculation

3.3.2 Catalytic cycles driving the epoxidation reaction on MIL-47's active sites

The main pathways that have been modeled in **Papers 6-7** are shown in Figure 3.4b. The reaction cycle starts with an activation step, in which TBHP coordinates with the vanadium center to form an alkylperoxo species **7** (as shown in Figure 3.4b). First, a direct pathway to epoxidation may lead to the formation of cyclohexene oxide **2** and brings the catalyst to a less active complex **8**. Second, a radical mechanism is plausible (**7**→**9** in Figure 3.4b). In this route V^{+V} vanadium complexes **9** are formed by homolytic cleavage of the peroxy linkage which can then be further activated with TBHP. The generated V^{+V} activated complexes **10** and **12** can again epoxidize cyclohexene. Both direct epoxidation (A and C) and radical (B) routes are completed by a regeneration step which closes the cycle (Figure 3.4b)).

In **Paper 6**, the V-site of type I is investigated on both a constrained[3] and unconstrained extended cluster model. For a detailed discussion about the kinetics of each reaction displayed in Figure 3.4b, the reader is referred to **Paper 6**. Summarizing, there are two pathways which are competitive and form a closed cycle of epoxidation and regeneration and wherein the peroxide is systematically used to bring the inactive vanadium complex (species **6**) into an active complex with oxidation state +IV (species **7**) or an active complex with oxidation state +V (species **10** and **12**). The two epoxidation pathways start from a complex with another oxidation state for vanadium, but a switch from one cycle to the other is possible at any time. Once V^{+V} complexes are formed, a return to the V^{+IV}-cycle is possible via the equilibration step (**12**→**6**, which we will call the V^{+V} - V^{+IV} recycling step for further reference. This step is energetically not favored ($\Delta E_{0,r}$ = 132.5 kJ/mol) but becomes possible at temperatures of 323 K due to entropic contributions, that bring the free energy of the reaction to reasonable values of 67-77 kJ/mol. These barriers are of the same order of magnitude as the barriers for epoxidation and are thus competitive with these pathways.

Paper 7 can be regarded as a continuation of **Paper 6** in the sense that the methodology has been extended: the two types of active sites have been modeled in a periodic slab model and the results compared with the cluster calculations. The periodic simulations include a larger part of the active site environment, describing geometrical and electronic effects much better. In this way they give an added value to the discussion, as they provide extra insight in the epoxidation behavior of MIL-47 and are of primordial impor-

[3]The outer carboxyl groups are fixed during the optimization and Hessian calculation

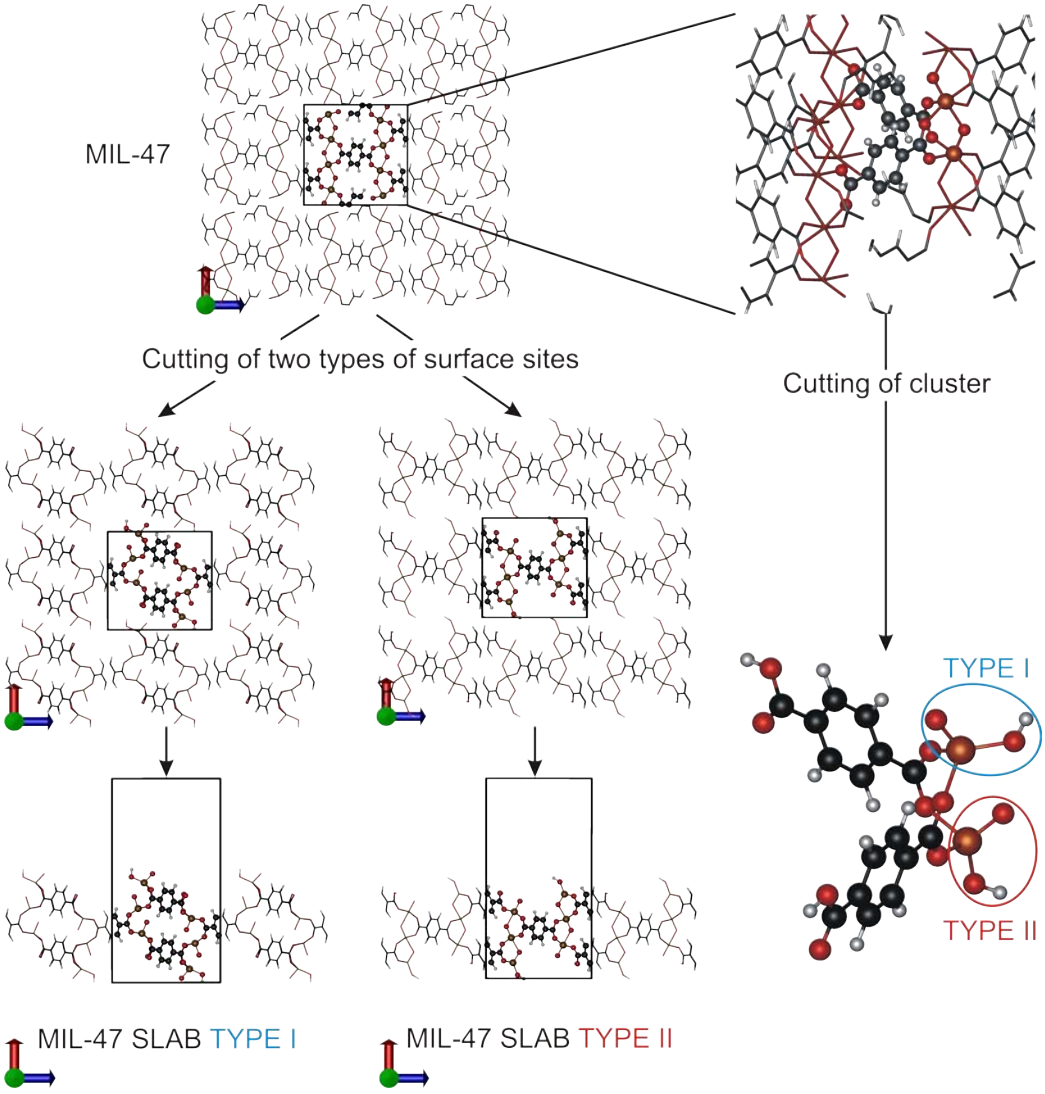

Figure 3.6: Representation of the cutting procedure to obtain periodic slabs or an extended cluster model. There are two possibilities considered for the accessible V-sites within MIL-47.

Table 3.1: Apparent energy and free energy barriers (respectively $\Delta E_0^{\ddagger}$ and $\Delta G_{323}^{\ddagger}$ in kJ/mol) for the modeled reaction of Figure 3.4b.

	Type I			**Type II**		
	7 → 8	**7 → 9**	**12 → 11**	**7 → 8**	**7 → 9**	**12 → 11**
Periodic results on PBE0-D2[a]						
$\Delta E_0^{\ddagger}$		32.6	35.7	11.4	28.1	29.1
$\Delta G_{323}^{\ddagger}$		32.8	90.6	65.8	28.0	87.0
Extended cluster results on PBE0/6-311+g(d,p)-D3[b]						
$\Delta E_0^{\ddagger}$	9.9	53.3	49.7	12.3	53.0	34.1
$\Delta G_{323}^{\ddagger}$	59.8	50.5	114.9	67.5	54.2	89.1
Extended cluster results on B3LYP/6-311+g(d,p)-D3[b]						
$\Delta E_0^{\ddagger}$	-9.2	34.2	33.5	3.5	38.5	22.8
$\Delta G_{323}^{\ddagger}$	40.7	31.4	98.6	58.7	39.7	77.8

[a]Optimization at PBE-D2 with 600eV as the kinetic energy cut off.
[b]Optimization at ONIOM(B3LYP/BS1:B3LYP/3-21g).

tance to identify the exact nature of the active site, which turns out to favour type II. It is the most stable defect site and hence is more resistant to leaching. This is also visible if we compare the transition states for epoxidation from V^{+V} on both types of active sites. The whole scheme of Figure 3.4b has been investigated in the various models; the results (zero point- and free-energy barriers) of the three main steps are collected in Table 3.1. A first inspection of the table learns that the predictions of the barriers of the three investigated reactions are not differing much when changing level of theory, model or active site (**7→9** < **7→8** < **12→11**). A more profound analysis, however, reveals that not all models are consistent in predicting the same dominant paths, although we must be very cautious in drawing conclusions as subtle shifts of some kJ/mol can switch the whole picture of most preferable routes. Periodic calculations seem to prefer type II active sites, but the energy differences leading to this conclusion are small (few kJ/mol).

Are the theoretical predictions in accordance with experiment? We could rely on the kinetic study of the cyclohexene epoxidation with $VO(acac)_2$ by Gould et al. [218] and which was also redone by one of our experimental partners (**Paper 5**). The experiment reports values of 53.1 kJ/mol (43.2 kJ/mol) for the enthalpy of activation while -82.8 J/K/mol (-90.8 J/K/mol) for the entropy of activation. For T=323 K, this results in a Gibbs-free energy of activation of about 80 kJ/mol (72.6 kJ/mol). The values between parentheses

come from the experiment described in **Paper 6**. Apparently, we notice an excellent agreement with the theoretical predictions for the pathway **12**→**11** that proceed through a vanadium in oxidation state +V. This brings us to the very tentative conclusion that the V^{+V} epoxidation reaction is probably the dominant epoxidation reaction, and that $V^{+V}O(OOtBu)$ active species will be the most abundant epoxidation complexes (**Paper 5**).

In the search for a better performance (higher activity) of the catalyst, we investigated the effect of substituted linkers on MIL-47 (**Paper 7**). The substituents such as -F, -Cl and -Br, $-CH_3$, $-NH_2$ did obey a linear free energy relationship shown by a Hammett plot of the conversion towards cyclohexene oxide as a function of σ_p (substitution constant). In general substitution leads to an increased activity relative to the parent MIL-47. Additionally, first-principles kinetic calculations are performed on periodic slab models of MIL-47 and compared with cluster models to determine the most important active site. The periodic models allowed to investigate different types of active sites (type I and II) with more reliable environment description compared to the cluster model. Thermodynamically, alkylperoxo species $V^{+V}O(OOtBu)$ of type II were found to be more stable than active sites of Type I. Overall the difference in free energies of activation between periodic and cluster models is quite similar. Therefore, the effect of linker substitution was investigated on a cluster model of type II. Then, functionalized cluster models were constructed and the rate constants for epoxidation were determined and also compared relative to the epoxidation on a MIL-47 cluster model. A very good qualitative agreement was found on a selection of the substituents (-OH, -Cl, $-NH_2$), for which the epoxidation activity of the functionalized models agreed qualitatively with experiment.

3.3.3 Unraveling of $VO(acac)_2$ as active epoxidation catalyst

Paper 5 reports the epoxidation reaction of cyclohexene for the system vanadyl acetylacetonate ($VO(acac)_2$) as homogeneous catalyst, employing *tert*-butyl hydroperoxide (TBHP) as oxidant. It was our aim to identify the most active species for epoxidation and the most plausible epoxidation mechanism. The reaction mixture is composed of various inactive and active complexes in which vanadium may either have oxidation state +IV or +V. Inactive species are activated with TBHP to form active complexes (Figure 3.5 and 3.4b). After reaction with cyclohexene each active species transforms

back into an inactive complex which may be reactivated again. Stepovik et al. showed that the acetylacetonate (Hacac) rapidly oxidizes to acetate (HOAc) in the presence of TBHP [219]. The reaction mixture is thus quite complex containing hydroxyl ($^{-}$OH)), acetyl acetonate (acac), acetate ($^{-}$OAc) or *tert*-butoxide ($^{-}$OtBu) anions as ligands. Various ligand exchange reactions may thus occur among active and inactive complexes. Radical decomposition reactions allow transforming V^{+IV} to V^{+V} species and vice versa. As a result a free energy diagram was constructed for the various species bearing either oxidation state +IV and +V. The change in oxidation state was modeled through radical decomposition pathways. Our results show that the most abundant vanadium +IV species are VO(acac)(OOtBu), VO(acac)(OtBu)-TBHP and V(OH)(acac)(OtBu)(OOtBu) whereas for vanadium +V species complexes of the type $VO(L_1)(L_2)(OOtBu)$ are energetically preferred, with L_1 and L_2 one of the above mentioned ligands. To unravel the nature of the most plausible epoxidation mechanism, first-principles chemical kinetics calculations have been performed on all proposed epoxidation pathways. Our results allow to conclude that the concerted Sharpless mechanism is preferred and that alkylperoxo species $V^{+IV}O(L)(OOtBu)$ and $V^{+V}O(L_1)(L_2)(OOtBu)$ species are most abundant within the family of V^{+IV} and V^{+V} active species respectively. At the onset of the catalytic cycle vanadium +IV species may play an active role but as the reaction proceeds, reaction mechanisms that involve vanadium +V species are preferred as the acetyl acetonate is readily oxidized into acetic acid.

3.4 Activity and selectivity of the citronellal cyclization on Lewis acid MOFs

3.4.1 Effects of linker substitution on the Lewis acid UiO-66

The structure of the metal-organic framework UiO-66 has been reported first in 2008 [50] and because of its remarkable thermal stability, has awakened an enormous interest of the MOF community. UiO-66 is a Zr-MOF with benzene-1,4-dicarboxylate (BDC) linkers. Changing the linker to biphenyl or terphenyl dicarboxylate (BPDC or TPDC) other ultimately stable structures have been constructed. Various studies on modified Zr-MOF materials have been performed [220, 103, 221, 222, 223, 224]. In **Paper 8** a series of functionalized Zr-terephthalate materials with the UiO-66 structure has been

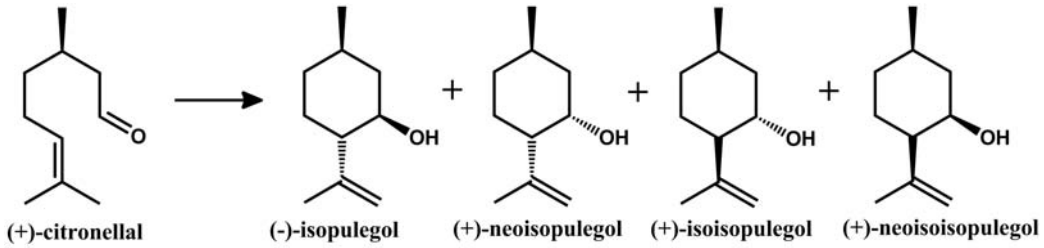

Figure 3.7: Cyclization of (+)-citronellal to isopulegol and its isomers.

investigated. UiO-66 materials were synthesized with 8 different benzene-1,4-dicarboxylate linkers (BDC-X; X = H, NH_2, CH_3, OCH_3, F, Cl, Br or NO_2). To test the effect of the substituents on the activity, the cyclization of citronellal was selected first (Figure 3.7). This carbonyl-ene reaction is of commercial interest since the isopulegol product is a direct precursor of synthetic menthol. (-)-Menthol, a particular isomer of menthol, is one of the most important flavoring chemicals used today and an important ingredient in chewing gums, shampoos, pharmaceuticals and more.

The selectivity for the isopulegol isomers depends strongly on the Lewis acidity of the active site [170]. Before reaction, each catalyst was activated at 493 K to remove residual solvent molecules. For UiO-66 type Zr-terephthalates, this results in a dehydration of the $Zr_6O_4(OH)_4$ cluster, with the formation of Zr_6O_6 [50]. Conversion profiles for reactions in toluene are given in Figure 3.8a. Initial rate constants could be obtained from linear fitting to conversion curves at t=0. Next, we attempted to correlate the activity to the electronic nature of the ligands, as expressed in Hammett's σ-values. The choice of a suitable type of σ-value is not obvious, since each substituent is either ortho or meta to a Zr-coordinating carboxylate group. An excellent correlation was found by plotting $\log(k_X)$, in the σ_m value of each substituent, which includes both inductive and resonance contributions [225]. The $\log(k)$ values correlate positively with σ_m, resulting in a linear-free energy relationship (LFER, $\log(\frac{k_X}{k_H}) = \rho.\sigma_m$) with $\sigma = 2.35$ (Figure 3.8b). Thus, Lewis acid sites are stronger in materials with an electron-withdrawing group close to the Zr-site.

In order to rationalize the electronic modulation of the active sites, molecular modeling calculations were performed to predict rates for the citronellal cyclization on UiO-66 and UiO-66-NO_2. First-principles kinetic calculations were performed on an extended cluster that is representative for the active site environment in the catalyst. Four different clusters were built as possible active sites: hydrated ($Zr_6O_4(OH)_4$) and dehydrated (Zr_6O_6) clusters

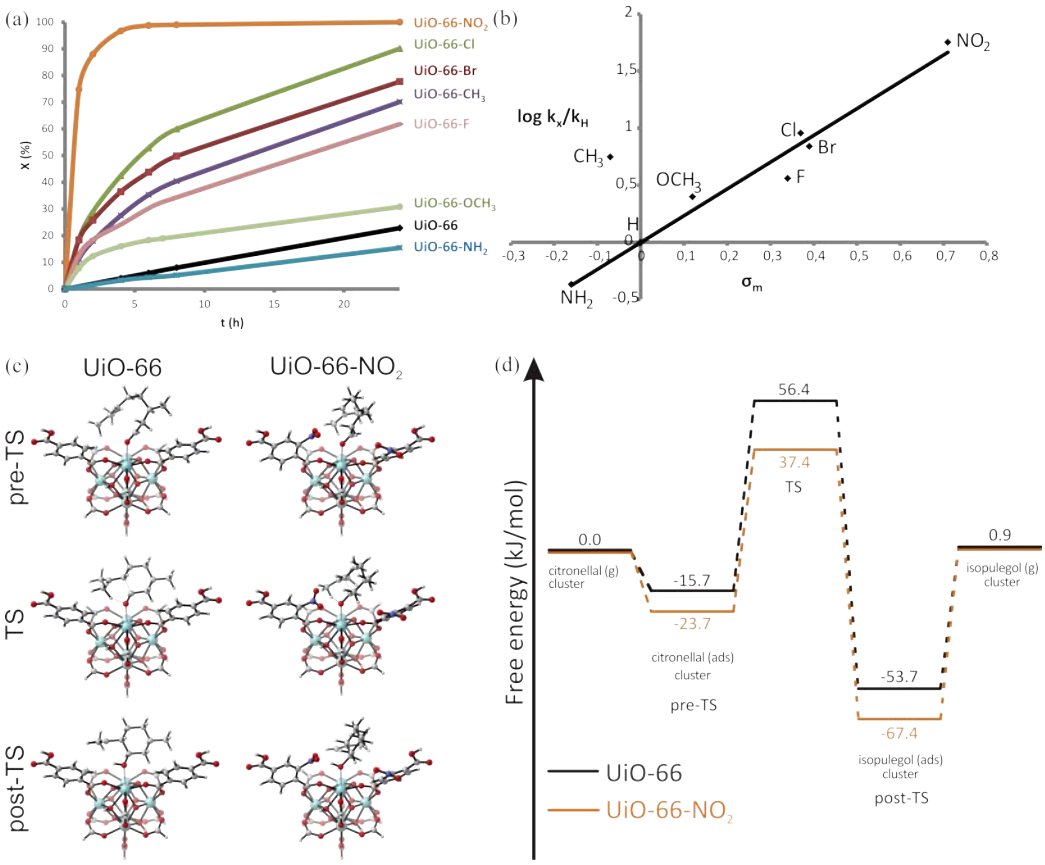

Figure 3.8: (a) Conversion of citronellal over UiO-66-X vs. time (solvent = toluene, 373 K, citronellal : Zr = 10); (b) Hammett plot for the cyclization of citronellal with different UiO-66-X catalysts; (c) Critical points along the reaction profile of citronellal towards isopulegol, for (left) UiO-66, and (right) UiO-66-NO_2. One carboxylate linker has been omitted from the cluster. From top to bottom, the figures correspond to the adsorbed state of citronellal, the transition state for cyclization and the adsorbed isopulegol product state. Interactions between the hydrogen atoms of citronellal and the nitro groups at distances < 3 Å are indicated with green lines; (d) Gibbs free energy profiles, calculated at 373 K, for citronellal cyclization to isopulegol.

with 12 carboxylate linkers. We refer to the Supporting Information of our ANIE communication (**Paper 8**), that we have included in the thesis, for the ultimate structure of the active site in the Zr-clusters.

Reasonable transition states were only found for the Zr-clusters in which at least one terephthalate linker was missing, both for UiO-66 and UiO-66-NO_2. This is in complete agreement with data from Thermogravimetrical Analysis (TGA), indicating only 8-10 terephthalate ligands per Zr_6-cluster instead of 12. Such a linker deficiency was previously also suggested in literature [220], and allows the identification of coordinatively unsaturated Zr-centers as the active sites.

Extended cluster models with one missing linker, both for UiO-66 and UiO-66-NO_2, were therefore used as models in the rest of the study. Since isopulegol is the most abundant product, the mechanism of its formation was studied in detail. A variety of different transition states were found which differ in the adsorption mode of citronellal. To understand the rate increase induced by the nitro group, we discuss only the two most stable transition states, for UiO-66 and UiO-66-NO_2 respectively. Critical points and the corresponding free energy profile along the reaction pathway are shown in Figure 3.8c-d. The extended cluster state of the catalyst and citronellal in the gas phase is chosen as a reference level.

Citronellal is more strongly adsorbed on the nitro-modified cluster, with free energies of adsorption of -15.7 and -23.7 kJ/mol for UiO-66 and UiO-66-NO_2, respectively (Table 3.2). The Zr-site with nitro-substituted linkers clearly is a stronger Lewis acid, as reflected in shorter distances between the carbonyl oxygen atom of citronellal and Zr (2.367 Å and 2.320 Å for UiO-66 and UiO-66-NO_2. In addition, the NO_2-groups strongly interact with some hydrogen atoms of the adsorbate in the pre-reactive complex, the transition state and adsorbed product state, as shown in Figure 3.8c. The theoretically obtained transition states suggest a concerted mechanism in which the carbon-carbon bond formation and the proton transfer occur in the same reaction step, although not completely synchronously. For the nitro-modified cluster, the same features as in the adsorbed state are observed, overall leading to a more stabilized transition state. Indeed, the difference between the Gibbs free energy barriers amounts to $\sim$19 kJ/mol.

In order to quantify the relative rates on UiO-66 and UiO-66-NO_2, both intrinsic and apparent kinetics were evaluated, which merely differ in the reference level chosen for the reactants. The intrinsic analysis starts from the pre-transition state reactants, which is the local reactant minimum closest

to the transition state, while the apparent analysis starts from the UiO-66 cluster and citronellal in the gas phase [181]. The calculated kinetic data are collected in Table 3.2, together with the enthalpic and entropic contributions to the Gibbs free energies. Both apparent and intrinsic kinetic coefficients are higher in the case of UiO-66-NO_2, predicting a citronellal cyclization which is 35 times faster intrinsically. Using apparent kinetics, which additionally take into account the extra stabilization of the adsorbed citronellal on the nitro cluster, an acceleration factor of 460 is obtained.

Table 3.2: Kinetic data for the citronellal cyclization to isopulegol at 373 K. Free energy, enthalpic and entropic contributions in the adsorbed state (ads) and in the transition state (‡) (kJ/mol). The rate constants (k_{373}^{fwd}) are given in units of $m^3.mol^{-1}.s^{-1}$ for the apparent kinetics and in s^{-1} for the intrinsic kinetics. The relative rates of UiO-66-NO_2 versus UiO-66 are also given. The used level of theory is B3LYP/6-31+G(d)-D3//B3LYP/4-31G*.

		$\Delta G_{373}^{\mathrm{ads}}$	$\Delta H_{373}^{\mathrm{ads}}$	$-T.\Delta S_{373}^{\mathrm{ads}}$	
Pre-TS	UiO-66	-15.7	-88.6	72.9	
	UiO-66-NO_2	-23.7	-104.0	80.4	
		$\Delta G_{373}^{\ddagger}$	$\Delta H_{373}^{\ddagger}$	$-T.\Delta S_{373}^{\ddagger}$	k_{373}^{fwd}
Apparent kinetics	UiO-66	56.4	-44.2	100.6	3.03E+03
	UiO-66-NO_2	37.4	-67.8	105.2	1.40E+06
Relative ratio					460
Intrinsic kinetics	UiO-66	72.1	44.4	27.8	6.15E+02
	UiO-66-NO_2	61.1	36.4	24.7	2.17E+04
Relative ratio					35

The partition of the free energies into enthalpic and entropic contributions along the reaction path, shows that the nitro-substituted cluster yields both a higher adsorption enthalpy (-104 versus -89 kJ/mol) and a lower intrinsic enthalpy barrier (36 versus 44 kJ/mol). In UiO-66-NO_2, the adsorption is stronger due to the stronger Lewis acidity, and additionally, the transition state is stabilized due to preferred electrostatic interactions between the adsorbate and the nitro groups.

The differences in entropic contributions between the two clusters are less pronounced. For the adsorption step a slightly higher entropy contribution is obtained for the substituted cluster (80 versus 73 kJ/mol) due to more steric hindrance in the nitro cluster. The overall acceleration is thus governed by the enthalpic preference both in adsorbed and transition state for the nitro-substituted cluster.

In conclusion, we have shown that it is possible to increase the activity of MOF catalysts strongly with coordinatively unsaturated sites by using different functionalized linkers. A clear LFER was found between the electronic nature of the linker substituents and the reaction rate in the carbonyl-ene reaction, and the concept was extended to other Lewis acid reactions. This is the very first LFER ever observed for MOF catalysts. Molecular modeling indicated that the citronellal cyclization happens through a concerted mechanism in which the carbon-carbon bond formation and the proton transfer occur in the same reaction step. Nitro-substitution strongly increases the rate of the citronellal cyclization as it lowers the adsorption and activation free energy of the reaction. The predicted rate acceleration by theory nicely corresponds to the experimentally observed ratio of about 60 at 373 K.

3.4.2 Activity and selectivity of the citronellal cyclization on various catalysts

This section describes the most important research results obtained in **Paper 9**. The cyclization of citronellal over various Lewis acid catalyts is also studied, but with the major goal to unravel the effects leading to an active and selective catalyst. Most synthetic processes to produce (-)-menthol have the cyclization of (+)-citronellal as an intermediate step on a Lewis acid catalyst. The cyclization of (+)-citronellal leads to the formation of four different isopulegol isomers, as displayed in Figure 3.7. Of these, only (-)-isopulegol can, be hydrogenated to (-)-menthol. To find an active and selective heterogeneous catalyst for the citronellal cyclization, industrially used homogeneous catalysts $ZnBr_2$ and ATPH have been compared with the metal-organic frameworks Cu_3BTC_2 and Cu_3BTC_2-NO_2. ATPH is a bulky homogeneous catalyst which is very selective towards the major isomer of pulegol, $ZnBr_2$ is the standard homogeneous catalyst used in many industrial processes but with selectivities of circa 90 % at room temperature. Cu_3BTC_2 is a heterogeneous catalyst with open metal centers. First, the activity of the various catalysts has been compared. Therefore, the free energy profiles of the cyclization of citronellal towards isopulegol were calculated and also compared with experimental kinetic data (Figure 3.9).

The gas phase cyclization has the highest free energy barrier of 136.1 kJ/mol, which can be decoupled into enthalpy and entropy contributions amounting to 105.7 kJ/mol and 30.4 kJ/mol, respectively. As the free energy barrier is a measure for the catalytic activity, the catalyst can be ordered from least active to most active: Cu_3BTC_2, $ZnBr_2$, Cu_3BTC_2-NO_2 and ATPH. The

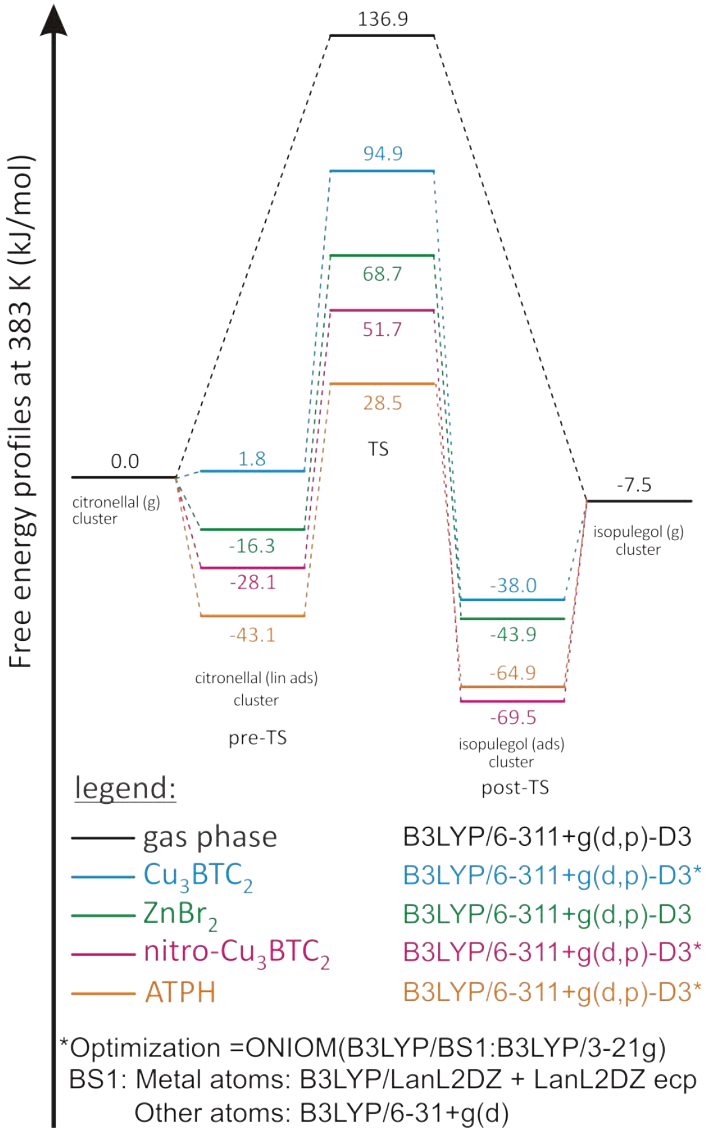

Figure 3.9: Gibbs free energy profiles, calculated at 383 K, for citronellal cyclization to isopulegol on various catalysts. The used level of theory for the energetics was B3LYP/6-311+g(d,p)-D3

entropic contributions to the free energy are expected to rise when using a catalyst, so the decrease in free energy barrier should be the result of a lower enthalpy barrier. A more detailed overview of the enthalpy and entropy contributions to the free energy are given in Table 3.3.

Table 3.3: Kinetic data for the citronellal cyclization to isopulegol at 373 K. Free energy, enthalpic and entropic contributions in the adsorbed state (ads) are given for linearly adsorbed citronellal (ads,citro) and adsorbed isopulegol (ads,iso). Those contributions are also given in the transition state (‡) (kJ/mol). The rate constants (k_{373}^{fwd}) are given in units of $\mathrm{m^3.mol^{-1}.s^{-1}}$ for the apparent kinetics and in $\mathrm{s^{-1}}$ for the intrinsic kinetics. The relative rates are also given.

Adsorption	$\Delta G_{373}^{\mathrm{ads,citro}}$	$\Delta H_{373}^{\mathrm{ads,citro}}$	$-T.\Delta S_{373}^{\mathrm{ads,citro}}$	
Cu_3BTC_2	-0.28	-79.57	79.29	
$ZnBr_2$	-17.36	-58.39	41.03	
Cu_3BTC_2-NO_2	-30.50	-115.81	85.31	
ATPH	-44.93	-113.40	68.47	
Desorption	$\Delta G_{373}^{\mathrm{ads,iso}}$	$\Delta H_{373}^{\mathrm{ads,iso}}$	$-T.\Delta S_{373}^{\mathrm{ads,iso}}$	
Cu_3BTC_2	32.31	99.34	-67.03	
$ZnBr_2$	37.72	83.30	-45.58	
Cu_3BTC_2-NO_2	64.02	137.85	-73.83	
ATPH	59.33	165.50	-70.90	
Intrinsic kinetics	$\Delta G_{373}^{\ddagger,\mathrm{intr}}$	$\Delta H_{373}^{\ddagger,\mathrm{intr}}$	$-T.\Delta S_{373}^{\ddagger,\mathrm{intr}}$	$k_{373}^{\mathrm{fwd,intr}}$
Cu_3BTC_2	92.66	77.55	15.11	8.22E-01
$ZnBr_2$	83.97	45.30	38.67	1.36E+01
Cu_3BTC_2-NO_2	79.39	60.90	18.49	5.92E+01
ATPH	71.91	33.30	38.61	6.62E+02
Apparent kinetics	$\Delta G_{373}^{\ddagger,\mathrm{app}}$	$\Delta H_{373}^{\ddagger,\mathrm{app}}$	$-T.\Delta S_{373}^{\ddagger,\mathrm{app}}$	$k_{373}^{\mathrm{fwd,app}}$
gas phase	136.06	105.66	30.40	6.88E-07
Cu_3BTC_2	92.38	-2.02	94.40	2.75E-02
$ZnBr_2$	66.61	-13.10	79.71	1.12E+02
Cu_3BTC_2-NO_2	48.89	-54.91	103.80	3.38E+04
ATPH	26.98	-80.10	107.08	3.96E+07

The stronger citronellal is adsorbed on the Lewis active site, the faster the reaction proceeds. A stronger Lewis acid site, activated the carbonyl bond more strongly. As a result the carbon of the carbonyl bond has a larger partial positive charge and is more prone to nucleophilic attack of the intramolecular carbon-carbon double bond.

To compare with experimentally observed kinetics, we have determined the

Table 3.4: Overview of the theoretical and experimental selectivity distributions on various catalysts. S_{exp} represents the initial experimental selectivity where the selectivity for the two less formed isomers of pulegol (neoisoisopulegol and isoisopulegol) are added. S_{ini} and S_{TPE} respresent the theoretical initial selectivity and the thermodynamic equilibrium of the pulegol isomers.

	T (K)	S_{exp}	S_{ini}	S_{TPE}
Without	298	-	90.6/8.4/0.9/0.1	77.0/20.0/2.7/0.3
catalyst	373	-	80.1/15.3/3.9/0.7	71.2/23.3/4.8/0.7
Cu_3BTC_2	373	73/20.8/6.2	85.9/4.4/9.6/0.1[a]	
	373	73/20.8/6.2	83.5/12.1/4.1/0.2[b]	
$ZnBr_2$	373	88/7.4/4.6	81.6/15.3/2.8/0.2	
	298	87.5/7.4/5.1	86.9/11.8/1.3/0.1	
ATPH	298	97.9/1.1/1.0	95.4/0.1/4.6/0.0	
Selectivity distribution for the [a] periodic model, [b] extended cluster model				

Table 3.5: Comparison of experimental and theoretical ratios of kinetic rate constants between the various catalysts. Theoretical results are on the B3LYP/6-311+g(d,p)-D3 level of theory and are based on the intrinsic rate coefficients. The number between brackets is hypothetical and is obtained when augmenting the efficiency of the Cu-BTC catalyst by using crystal particles of size 2 μm.

	Experiment	Theory
$k_{ZnBr_2}/k_{Cu_3BTC_2}$ (T=373 K)	252 (68)	16.5
k_{ATPH}/k_{ZnBr_2} (T=298 K)	4	129

relative ratios between kinetic rate constants of various catalysts both theoretically and experimentally. The results are given in Table 3.5. However, the experimental rate constants should be corrected with a sort of an efficiency factor correcting for the amount of active metal sites that is really accessible to allow a quantitative comparison of the ratios in Table 3.5.

At second instance the catalysts were compared with respect to their selectivity towards (-)-isopulegol. ATPH is the most selective catalyst, followed by $ZnBr_2$. The least selective catalyst is Cu_3BTC_2 (Table 3.4). We also modeled the theoretical selectivities. Therefore it was essential to generate a representative set of stereoselective transition states. At second instance the free energies between all these transition states were calculated and based on these values we could predict theoretically the initial selectivity using the

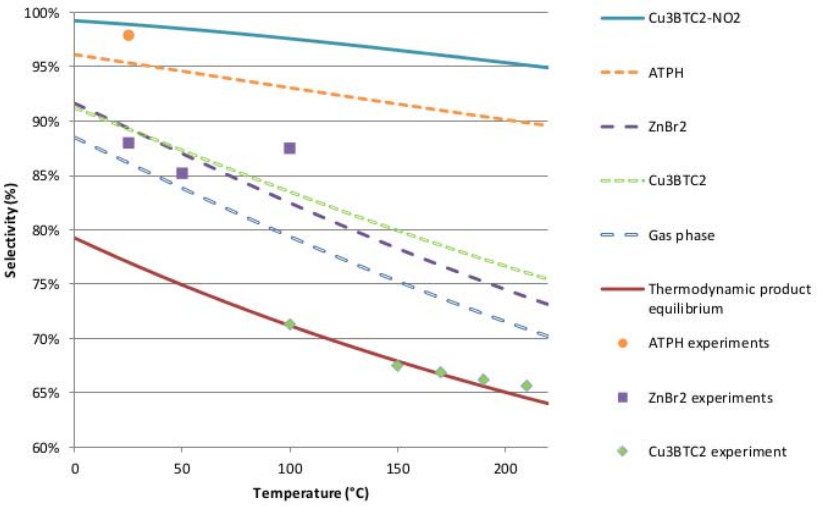

Figure 3.10: Modeled isopulegol selectivity on various catalysts ($ZnBr_2$, Cu_3BTC_2, gas phase, Cu_3BTC_2-NO_2) in relation with the thermodynamic product selectivity.

Curtin Hammett principle. Our theoretical selectivities correspond quite well with the experimental values, providing evidence for the proposed theoretical model. Furthermore, we found that the selectivity towards isopulegol decreased in terms of temperature. Thus the more active the catalysts, the lower the operation temperatures and the higher the finally obtained selectivities. This is especially true for ATPH. Moreover, the selectivity distribution in function of temperature was found to be kinetically driven for $ZnBr_2$ and ATPH, and thermodynamically driven for Cu_3BTC_2. The selectivity towards isopulegol (S_{iso}), as modeled on cluster models is given in Figure 3.10.

Generalizing, the following statements could be proven with regard to the isopulegol selectivity: (1) a high catalyst activity allows working at lower temperatures and improves the selectivity (2) introducing steric factors increases the selectivity (compare S_{iso} for Cu_3BTC_2 and Cu_3BTC_2-NO_2). The hypothetically constructed active site for Cu_3BTC_2-NO_2 forms a nice example of those two guidelines: by the addition of the nitro-groups, the catalyst activity increases (lower activation enthalpy) and transition states towards the unwanted isomers are made impossibly or difficult to occur (entropic contribution to the free energy raises). However, since the isopulegol isomers can not diffuse out of the very selective hypothetical Cu_3BTC_2-NO_2, isoreticular MOFs with larger pores or similar active sites should be constructed.

3.5 Selective adsorption of xylenes in MIL-47

The porous MIL-47 material shows a selective adsorption behavior for para, ortho, and meta-isomers of xylenes, making the material a serious candidate for separation applications [158, 159, 160]. The origin of the selectivity lies in the differences in interactions (energetic) and confining/packing (entropic) inside the pores. In **Paper 10** the xylene-framework interactions and the xylene-xylene interactions are investigated with quantum mechanical calculations, using a dispersion corrected density functional and periodic boundary conditions to describe the crystal.

First, the strength and geometrical characteristics of the optimal xylene-xylene interactions are quantified by studying the pure and mixed pairs in gas phase. An extended set of initial structures is created and optimized to sample as many relative orientations and distances as possible. Next, the pairs are brought in the pores of MIL-47. The interaction with the terephthalic linkers and other xylenes increases the stacking energy in gas phase (-31.7 kJ/mol per pair) by roughly a factor four in the fully-loaded state (-58.3 kJ/mol per xylene). Our decomposition of the adsorption energy shows various trends in the contributing xylene-xylene interactions. The energetics could not explain the experimentally observed separation of xylene isomers with a preferential adsorption for orthoxylene and paraxylene, since all adsorption energies lie in the same range. Therefore, entropic effects are likely the main driving forces for the adsorption selectivity. This has two implications. First, sampling of configurational space (more specifically, different positioning of xylenes within MIL-47) should be adequately performed to assess the entropic effects (based on the possibilities for positioning in the xylene pair, the pores and also mixing effects), which can only be obtained with molecular dynamics or Monte Carlo simulations [226, 174, 175, 176, 177]. Secondly, since the accuracy of the energetics is of subordinary importance to the sampling, it is expected that reasonable results can be obtained with classical force-fields. Whereas force-fields are less accurate than an ab-initio treatment, they allow considerably longer sampling times because of the reduced computational cost.

3.6 Structural transitions of COMOC-2

A few intriguing structures are those whose pore dimensions may change without breaking chemical bonds within the framework, triggered by host-guest interactions at a certain temperature or pressure. This type of frame-

work dynamics has often been referred to as *breathing* [38, 227]. Beside *breathing*, there are other dynamics possible within some MOFs; such as intraframework dynamics, gate opening phenomena, negative thermal expansion and swelling [228]. A well studied example of such flexible coordination compounds is the series of MIL-53, originally developed by Férey's group, $M^{III}(OH)(BDC)$ (M^{III}= Al, Cr, Fe, Ga, Sc and In; BDC^{2-} = 1,4-benzenedicarboxylate) [38, 229, 230, 231, 232, 233]. An isostructural analogue of MIL-53 is MIL-47. The main difference between both isostructures lies in the nature of the metal centres and in the presence of -OH groups: while the MIL-53 structure is known with a variety of M^{+III} ions, the MIL-47 framework is only described for the V^{+IV} ion. In MIL-47, the V-centers are present as vanadyl species ($V^{+IV}O(BDC)$). The difference in flexibility between both structures was explained [234] by the presence of -OH groups on M^{+III} sites, whereas the V^{+IV} has a V=O bond. These -OH groups may strongly interact with different adsorbates, inducing structural transformations. Recently, it was shown that a certain degree of flexibility can be induced in the MIL-47 structure by controlling the oxidation state of the V-centers, going from pure V^{+III} to mixed V^{+IV}/V^{+III} valence states [234].

In **Paper 11**, a new V^{+IV}-MOF was synthesized and characterized; having the topology of the parent MIL-47, but with larger biphenyl linkers, which make COMOC-2 flexible again. In order to verify the structural transformation of COMOC-2(V^{+IV}), CO_2 and CH_4 sorption isotherms were measured (Figure 3.11a). The adsorption isotherms at 303 K for both CO_2 and CH_4 show a type I shape, with a capacity of 4.8 mmol CO_2 g^{-1} at 25 bar and 1.4 mmol CH_4 g^{-1} at 27 bar. In contrast, at 265 K, a different behaviour is observed. In the CO_2 sorption isotherm at ca. 12.5 bar, a sudden increase in adsorption is noted, reaching 14 mmol g^{-1} at 28 bar. Two distinct steps are clearly observed, revealing a breathing of the framework. Desorption occurs with a large hysteresis loop. The presence of this loop is explained with the stress model developed by Neimark et al. [235] According to this model, structural transition or phase transformation, i.e. the breathing effect, occurs when a certain critical stress threshold is reached. As a consequence, the structural transition pressure depends on the stress threshold. As the stress threshold is different for the various phases, a hysteresis occurs in the adsorption-desorption process. Also at this lower temperature, CH_4 presents a type I isotherm without any hysteresis loop. The distinctive adsorption step of COMOC-2(V^{+IV}) at 265 K for CO_2 is similar to the CO_2 adsorption behavior of MIL-53 at 304 K [163].

To further unravel the mechanism inducing the breathing, we decided to study the free energy profile along the breathing mode of the empty COMOC-

2(V^{IV}) by means of first-principles calculations. For MIL-53, Walker et al. showed that a subtle interplay between dispersion forces and entropic factors controlled the inherent bistable behaviour of the material [236]. Along the same line, Stavitski et al. used dispersion corrected first-principles calculations to describe the breathing in the amine modified MIL-53(Al) framework [168]. Very recently, Triguero et al. presented a stochastic model of *breathing* transitions in MIL-53. They concluded that (at the level of the crystal) these transformations occur via layer-by-layer shear [237]. We have determined a full free energy profile along the breathing angle of the COMOC-2(V^{+IV}) structure using the climbing Nudged Elastic Band (cNEB) methodology [238]. As the morphology of the free energy profile did not change much with temperature, just the energy profile at 0 K is shown in Figure 3.11. We were able to find three stable minima: the narrow pore (np), the large pore (lp) and an overstretched narrow pore (np') form, as indicated in Figure 3.11b.

The two narrow pore forms are different in geometry (Figure 3.11b), and their unit cell can be seen as a very narrow pore structure (vnp) as observed in anhydrous MOFs by the group of Férey [239], as the theoretical models have been modeled in the complete absence of water. In complete agreement with earlier work of Walker et al. [236], inclusion of dispersion corrections [240, 241, 242] is needed to have realistic energy differences between lp and np forms. Without dispersion interactions, the three minima are not found. As frequency calculations were performed for every point along the profile, we were able to determine the entropic contributions and to plot the free energy profiles in terms of various temperatures (**Paper 11**).

Detailed results show that the free energy barrier for the lp $\rightarrow$ np phase transition is more or less constant with temperature, varying between 36 and 42 kJ/mol. The free energy difference between the narrow pore forms decreases from 38.3 to 27.2 kJ/mol when increasing the temperature from 0 to 650 K. The theoretically determined free energy profiles of the empty host show that COMOC-2(V^{+IV}) has the intrinsic potential for showing a tri-stable behavior, favoring the large pore structure when temperature rises. Experimentally, we can only observe the breathing behavior when it occurs in an applied pressure range. It is dependent on the strength of the host-guest interactions of guest molecules. For a molecule such as CO_2 (exhibiting strong interactions with the pore walls), the free energy barrier towards the narrow pore may already be overcome at 1 bar, whereas for the more inert CH_4 molecule, the closed form is never observed within the studied pressure window. As our simulations were performed without guest molecules, we cannot correlate the pore angle and lattice parameters for the np and lp

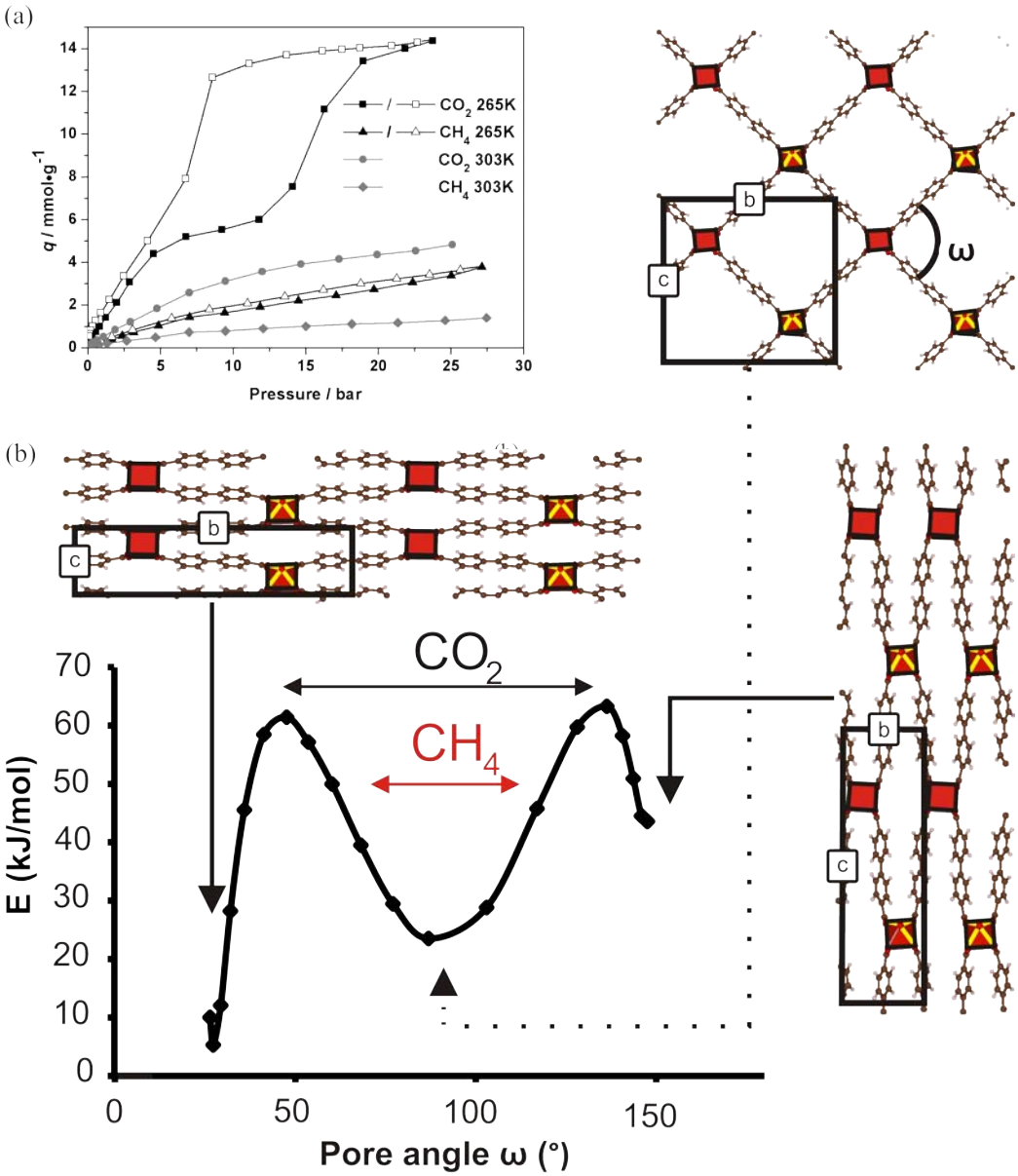

Figure 3.11: (a) The adsorption isotherms indicate that breathing occurs for CO_2 at lower temperatures; (b) The modelled energy profile in function of the pore angle ω for COMOC-2(V^{+IV}). For the empty framework, three different minima are shown in schematic view, representing the different pore forms: np, lp and np'.

forms with the experimental values. In particular, the theoretical lattice parameter along the c-axis for the np form is smaller than the experimental value, since the np form may not fully close due to the presence of adsorbate molecules.

In conclusion, a new V^{+IV} carboxylate MOF COMOC-2 having the same framework topology as MIL-47 was synthesized and fully characterized. Unlike MIL-47, COMOC-2(V^{+IV}) shows a breathing effect upon gas and vapor sorption at mild conditions. Similar to MIL-53, the sorption isotherms of CO_2 and CH_4 display a different shape at specific temperatures. The theoretically determined free energy profile along the pore angle indicates a tri-stable behavior of the material. Apart from a regular np form, an overstretched narrow pore configuration was theoretically found. Furthermore, this is the *first time* that breathing barriers have been reported, since researchers had mainly focused on the thermodynamical stability between open and closed pore forms. The climbing Nudged Elastic Band (cNEB) method thus has the intrinsic potential in predicting structural transitions within various materials, although it comes with a high computational cost. Future work will concentrate on the better understanding of the underlaying mechanism of phase transitions within MOFs by various other adsorbates, targeting potential applications in selective gas adsorption and molecular sensing.

3.7 Contributions to other research projects

One of the main CMM research lines within nanoporous materials is focused on the development of a new generation of force fields, which can be used in MOFs. Very recently a new force field has been proposed in our group for the flexible metal-organic framework MIL-53(Al), which is calibrated using density functional theory calculations on non-periodic clusters (**Paper 12**). The new force field, predicts geometries and cell parameters that compare well with the experimental values both for the large and narrow pore phases. The energy profile along the breathing mode of the empty material reveals the existence of two minima, which confirms the intrinsic bistable behaviour of the MIL-53. Even without the stimulus of external guest molecules the material may transform from the large pore (lp) to the narrow pore (np) phase. The relative stability of the two phases critically depends on the vdW parameters as the MM3 dispersion interaction has the tendency to overstabilize the np phase. My contribution to this work was limited to periodic DFT calculations which were needed to fit the Pauli repulsion parameters within the Force Field.

In **Paper 13**, the metal-organic framework MIL-47 and its amino-substituted variant MIL-47-NH_2 have been compared for their adsorption properties. The CO_2 and CH_4 adsorption properties have been evaluated and compared to MIL-47, showing that both MOFs have a similar adsorption capacity and affinity for CO_2. This is a strong indication that the amino groups only enhance the CO_2 adsorption in MOFs, if they influence the flexibility of the network. DFT-based molecular modeling calculations were performed to obtain more insight into the adsorption positions for CO_2 in NH_2-MIL-47. DFT calculations confirm that the amino groups provide a more enhanced adsorption of CO_2 compared to CH_4. However, the separation performance of this rigid MIL-47-NH_2 framework is significantly lower compared to MIL-53(Al)-NH_2 [167], where a separation factor larger than 60 was obtained at very low surface coverage, which is significantly larger than the factor of $\sim$5 for the parent MIL-53(Al). A theoretical explanation for this is that amino-substitution enhances the stability of the empty narrow pore structure of MIL-53-NH_2 over the large pore structure; which was not the case in MIL-53(Al) [168]. It is concluded that amino groups only enhance the CO_2 adsorption in MOFs, if they influence the flexibility of the network.

In **Paper 14**, we report the adsorption of water, alcohols, and nitriles at the bridging Brønsted sites of H-ZSM-5, using both cluster and periodic models to account for the zeolite environment. Since catalytic processes start with the adsorption of guest molecules inside the pores of an acidic zeolite catalyst, a proper estimate of the adsorption enthalpy is of paramount importance. Stabilization of the adsorption complexes comes from hydrogen bonding between the guest molecule and the framework, and van der Waals interactions of the adsorbate with the pore walls. Both large cluster and periodic calculations were performed. Large-cluster calculations with different DFT methods, are tested for their ability to reproduce the experimental heats of adsorption available in the literature [243] (Table 3.6). When dispersion corrections are added, the experimental adsorption is both qualitatively and quantitatively reproduced. In the periodic calculations including dispersion corrections throughout the geometry optimizations, ion-pair complexes were obtained for methanol, ethanol and propanol, resulting in two fairly similar hydrogen bonds (average length 1.50 Å) between the protonated alcohol and two framework oxygens adjacent to the aluminum defect of H-ZSM-5. Whether ion-pair complexes appear as stationary points or not, most likely depends at least in part on the level of theory used. In particular, the addition of D-corrections and the kinetic energy cutoff might have an important influence on the result. Nguyen et al. recently reported both hydrogen bonded and protonated complexes for primary alcohols in H-ZSM-5, based

on periodic PBE-D2 calculations using a cutoff energy of 400 eV [244]. In contrast, we have found only protonated complexes by applying a higher kinetic energy cut off. Unraveling the true nature of the adsorbed species – oxonium ion or hydrogen-bonded complex – should be elucidated by more advanced molecular modeling techniques.

Table 3.6: Adsorption enthalpies at 400 K calculated using different DFT methods with dispersion corrections (in kJ/mol).

	B3LYP-D3	M06-2X-D3	PBE-D2	PBE-D3	PBE-D2 pbc[b]	experimental[c]
H_2O	-90	-88	-87	-91	-89	-90 ± 10
CH_3OH	-111	-101	-108	-112	-125	-115 ± 5
CH_3CH_2OH	-132	-120	-124	-129	-141	-130 ± 5
$CH_3(CH_2)_2OH$	-152	-134	-140	-148	-	-145 ± 5
CH_3CN	-110	-98	-102	-104	-108	-110 ± 5
CH_3CH_2CN	-127	-108	-116	-120	-112	-120 ± 5
$CH_3(CH_2)_2CN$	-144	-121	-128	-137	-139	-145 ± 5
$(CH_3)_2CHCN$	-139	-115	-125	-130	-	-130 ± 5

[a] All cluster calculations were performed using the 6-31+g(d) basis set.
[b] Periodic results obtained using a kinetic energy cutoff of 600 eV.
[c] Experimental values from Lee et al. [243].

A proper account of dispersion interactions is indispensable to describe the experimental trend across a series of adsorbates of increasing size, i.e., an increase in adsorption enthalpy by 10-15 kJ/mol for each additional carbon atom. The well-known B3LYP and PBE functionals are completely inadequate to determine adsorption enthalpies for the alcohols and nitriles and are effectively unable to distinguish between alcohols or nitriles of different size. M06-2X, which was parametrized to include weak interactions, was still found to underestimate the adsorption enthalpy for the adsorbates considered in this study. Moreover, the deviation from the experimental trend increases with increasing adsorbate size. For all three functionals, however, the deficiency can be remedied by adding dispersion correction terms as proposed by Grimme. The extended-cluster model offers an attractive alternative to periodic simulations on the entire H-ZSM-5 unit cell, resulting in virtually identical final adsorption enthalpies, while avoiding both the larger computational expense and technical difficulties associated with periodic calculations.

4

Conclusions and perspectives

In this thesis molecular modeling techniques have been used to obtain insight into reaction pathways of catalytic reactions in nanoporous materials. In particular, reactions taking place in zeolites on Brønsted acid sites and reactions taking place in MOFs on saturated and unsaturated metal centers operating as epoxidation or Lewis acid catalysts, were studied. The research has been performed in close collaboration with experimental partners and most research questions were inspired by experimental findings which needed additional and fundamental understanding. All conclusions in this thesis have been made on the basis of first-principles chemical kinetics, i.e. full calculation of the reaction rate constants including reaction barriers and pre-exponential factors. In addition both intrinsic and apparent kinetic data have been modeled, which is crucial if a decent comparison with experimental data has to be made. The last aspect means that the research had to be extended to the description of adsorption phenomena as guest molecules first need to diffuse into the pores of the materials and adsorb before any reaction can take place. Nanoporous materials are often more flexible than expected at first sight. This is especially true for Metal-Organic Frameworks, which may be extremely flexible and undergo phase transitions upon exposure to external stimuli such as temperature, adsorption of guest molecules. Some aspects of these phenomena have also been tackled in this thesis.

The thesis covers several important case studies which are situated in zeolite and MOF catalytic research. Overall, we can conclude that molecular modeling techniques have matured to a level where chemical kinetics may be determined with "near chemical accuracy". Practically this means that chemical rate constants were predicted for several case studies that agree within a factor ten with experimentally determined values. This was explicitly shown for the methylations of olefins in ZSM-5, however, more research

is needed to generalize these conclusions to other systems. Compared to the status of theoretical modeling techniques up until a few years ago, this may be regarded as a major step forward for catalysis research in nanoporous materials. This progress may partly be ascribed to the development of more accurate models to treat the electronic structure of catalytic systems in a computationally efficient way. Nowadays various models are available that make it possible to treat long range non-bonding interactions in a fairly accurate way. Within this thesis no new theoretical models were developed but various contempory functionals were tested for accuracy on large catalytic systems. For the description of entropy contributions or the pre-exponential factor of the rate constants, a static approach and a normal mode analysis were adopted. Of course this approach has its limitations such as the efficient treatment of low-lying vibrational contributions. However, the determination of the full Hessian for the large systems under consideration was already quite challenging and time-consuming. This is especially true for periodic calculations.

Indeed, roughly speaking, there are two approaches to model the active site in nanoporous materials. One can either use an extended cluster model – that is cut from the periodic structure – or a fully periodic model. Both methodologies may account appropriately for molecular environment and topology effects provided that the cluster taken into account is large enough. Extended cluster calculations are more established within the community of computational chemistry and therefore a broader variety of density functionals is available and the algorithms to search for transition states are much more developed. Periodic simulation codes are based on plane wave basis sets and originate from the solid state community. Since a few years, those codes are also used in catalysis research for typical chemical problems but many hybrid functionals, commonly applied within the computational chemistry community, are not available. The calculations are also extremely time consuming and the search for transition states is a non-trivial task. For some case studies, we have tested these periodic procedures. To obtain all positive frequencies, it was found that very stringent convergence criteria are needed in combination with a high kinetic energy cut off for the plane waves. The development of additional theoretical techniques to speed up this process or to filter the small positive/negative frequencies out of the full Hessian would be interesting for future research. Despite these computational issues which are not in favor of periodic calculations, some problems may not be tackled with cluster calculations. For example, this was the case for the treatment of the structural transitions in COMOC-2. For the MIL-47 epoxidation cat-

alyst, it is also not possible to discriminate between all active sites when solely using cluster techniques. Most probably a complementary approach between both models will be necessary in the future and many developers of periodic codes are now also actively involved in catalysis research. This has already led to the implementation of computationally expensive methodologies into periodic simulation codes, such as Möller Plesset perturbation theory (for example MP2), coupled cluster, Random Phase Approximation (RPA), Coulomb screened Green function methods (GW), etc.

All phenomena described in this thesis are based on static calculations, that rely on the determination of a few points on the potential energy surface. Afterwards, temperature corrections were taken into account to obtain free energies, as a comparison with experimental data can only be based on the free energies. This approach has been found mostly sufficient for the problems at hand, but some effects such as diffusion effects, accounting for various active sites, solvent effects, etc. may not be treated accurately within such schemes. Computational methods are needed that enable the screening of a larger part of the potential energy surface. This is typically done with molecular dynamics or Monte Carlo methods. Chemical reactions are however rare events and special techniques are needed to overcome the reaction barriers. One method that has gained quite some popularity is the metadynamics technique that determines a large fraction of the energy landscape in a configuration space of collective variables. These methods are also computationally very expensive and it is not yet possible to explore with first-principles methods the full free energy surface associated with a catalytic reaction. Accurate force fields are desperately needed to tackle such problems.

Apart from determining accurate chemical rate constants for reactions, we also included in the thesis a selectivity study on the enantioselective cyclization of the citronellal molecule. Such computational selectivity studies are hardly found in literature, as the problem at hand is extremely challenging. The final result of the correct prediction of the selectivity profile depends on some small free energy differences between a set of diastereoselective transition states. First of all, it is necessary to generate an almost complete set of transition states and secondly one needs to determine the small free energy difference accurately enough. For the cyclization of citronellal, we succeeded quite well in reproducing and understanding the experimentally determined selectivities. The functional used seemed to work quite well for the problems at hand. Further research is certainly needed in this area, as molecular modeling can help to understand the factors contributing to the

high enantioselectivity of reactions on certain catalysts.

By means of some important case studies within catalysis research, this thesis has clearly demonstrated how molecular modeling can help to understand the reaction mechanisms, the nature of the active site and the factors contributing to selectivity of enantioselective catalysts. The presented research has been conducted in close synergy with various experimental partners. Such a complementary approach is necessary if a deeper understanding of the catalytic system is to be attained. By adopting such an approach, molecular modeling can and will be able to help design good catalysts for given catalytic processes. The continuous synergy between experimentalists and theoreticians is of utmost importance for the design of new improved catalysts.

Part II

Publications in peer-reviewed journals

Paper 1

Assembly of cyclic hydrocarbons from ethene and propene in acid zeolite catalysis to produce active catalytic sites for MTO conversion

Matthias Vandichel, David Lesthaeghe, Jeroen Van der Mynsbrugge, Michel Waroquier and Veronique Van Speybroeck

Journal of Catalysis, 2010, 271, 67 - 78

Copyright 2010 by Elsevier.

Journal of Catalysis 271 (2010) 67–78

Contents lists available at ScienceDirect

Journal of Catalysis

journal homepage: www.elsevier.com/locate/jcat

Assembly of cyclic hydrocarbons from ethene and propene in acid zeolite catalysis to produce active catalytic sites for MTO conversion

Matthias Vandichel, David Lesthaeghe, Jeroen Van der Mynsbrugge, Michel Waroquier, Veronique Van Speybroeck *

Center for Molecular Modeling, QCMM Alliance Ghent – Brussels, Ghent University, Technologiepark 903, 9052 Zwijnaarde, Belgium

ARTICLE INFO

Article history:
Received 29 October 2009
Revised 13 January 2010
Accepted 1 February 2010
Available online 15 March 2010

Keywords:
Cyclization
Oligomerization
Molecular modeling
DFT-D
MTO
Methanol to olefins
ZSM-5
Zeolite
Chemical kinetics
Dispersion interactions

ABSTRACT

The formation of cyclic hydrocarbons from smaller building blocks such as ethene and propene is investigated in protonated ZSM-5, using a 2-layered ONIOM(B3LYP/6-31+g(d):HF/6-31+g(d)) approach and an additional Grimme-type van der Waals dispersion correction term to account for the long-range dispersion interactions. These cyclic species form precursors for active hydrocarbon pool species and play a key role in activating the acidic zeolite host for successful methanol-to-olefin (MTO) conversion. Starting from trace amounts of ethene and propene that are formed during an initial induction period or during the active phase, dimerization reactions allow for rapid chain growth. The products of these reactions can be neutral alkenes, framework-bound alkoxide species or intermediate carbenium ions, depending on the zeolite environment taken into account. On the basis of rate constants for successive reaction steps, a viable route toward cyclization is proposed, which starts from the formation of a framework-bound propoxide from propene, followed by dimerization with an additional propene molecule to form the 2-hexyl carbenium ion which finally undergoes ring closure to yield methylcyclopentane. This cyclic species in turn forms a precursor for either an active hydrocarbon pool compound or for deactivating coke deposit.
© 2010 Elsevier Inc. All rights reserved.

1. Introduction

In this study, the formation of hydrocarbon pool compounds for methanol-to-olefin conversion (MTO) in acid zeolites [1] is taken as a practical example for the creation of bulky organic compounds trapped in a confined space. For over 30 years, there has been an ongoing dispute on the true nature of the reaction mechanism in MTO catalysis by both experimental and theoretical researchers [2–4]. Only recently, consensus has been achieved on an indirect olefin-producing cycle over direct coupling of C1 entities (like methanol or dimethylether) [5–7]. In this alternative "hydrocarbon pool" (HP) model, the active site of a typical MTO catalyst is composed of a nm-sized inorganic channel or cage with a Brønsted acid proton, containing an essential organic compound, all interacting to form a supramolecular catalyst [8]. In a typical catalytic cycle, the HP species undergoes successive methylation steps by methanol and/or dimethyl ether and subsequently eliminates light olefins like ethene and propene [9–11].

The most often observed hydrocarbon pool species to date have been typically polymethylbenzenes, though linear alkenes might also function as active organic species during the MTO cycle [12]. Various related cyclic cationic intermediates have also been identified by in situ NMR spectroscopy during MTO conversion [13–15].

It remains unclear when and how these cocatalytic hydrocarbon pool compounds are formed either (i) from impurities in the initial methanol feed, e.g., ethanol, propanol or isopropanol, or rather (ii) through the incomplete calcination of templating agents, or, once full conversion has started, even (iii) from primary MTO products like ethene and propene [11]. Fig. 1 shows compressed two-dimensional views of a catalyst particle (CHA-topology) during its lifetime [8]. The catalyst bed initially shows no activity because no cages contain any HP species. During the kinetic induction period, sufficient methylbenzenes are formed to generate an active MTO catalyst, resulting in primary formation of ethene and propene. This paper, however, will focus on the creation of secondary hydrocarbon pool compounds from these trace amounts of ethene and propene that were already generated in the preceding stage. During the active phase, a large number of HP species are present due to such secondary formation routes of cyclic intermediates. As time progresses, these species evolve into bicyclic species, which are less active toward olefin formation [16]. Finally, at the end of the catalyst lifetime, mass transport is severely restricted when as much as half of the cages contain polycyclic aromatic compounds. While the reactions studied in this paper are mainly

* Corresponding author. Fax: +32 9 264 66 97.
E-mail address: Veronique.VanSpeybroeck@UGent.be (V. Van Speybroeck).

0021-9517/$ - see front matter © 2010 Elsevier Inc. All rights reserved.
doi:10.1016/j.jcat.2010.02.001

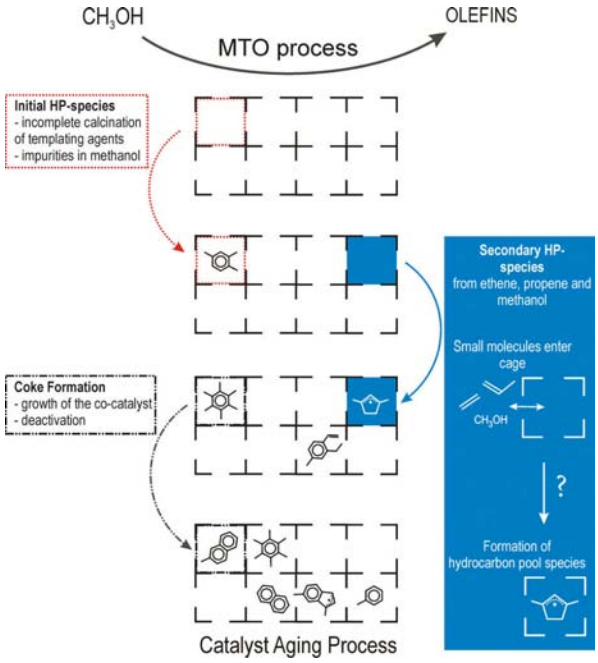

Fig. 1. Two-dimensional views of a catalyst particle during its lifetime [8].

targeted at generating active sites, they are ultimately also relevant for the process of deactivation.

Polymethylbenzenes (PMBs) have been commonly regarded as the most important hydrocarbon pool species, independent of the employed zeolite, though experimental evidence was mainly found in zeolites H-beta [14,17,18] and H-SAPO-34 [19,20]. In H-ZSM-5, however, recent experiments have led to the proposal of a dual cycle mechanism, in which the polymethylbenzene cycle competes with a parallel alkene cycle [12,21]: lower methylbenzenes favor the formation of ethene, while the alkene cycle, consisting of successive methylation and cracking reactions, looks more appropriate for yielding propene and higher alkenes. The role of alkenes such as propene can be twofold: various methylation and dimerization reactions can lead to the formation of secondary cyclic HP species but also to the formation of higher alkenes, which can further be cracked into the main product distribution olefins. Recently a low-energy pathway for the production of the major olefins in ZSM-5 was identified by means of theoretical calculations [22].

In this article, we will focus on the formation of cyclic hydrocarbons from primary ethene and propene molecules [21]. A range of reactions, such as alkoxide formation, oligomerization and cyclization, has been theoretically evaluated. We will deduce how various oligomerization reactions occur and weigh them off against homologation by successive methylation as studied in other work [23]. Since the HP intermediates are often cationic in nature and quite bulky compared with typical zeolite pore dimensions, the stabilizing and steric effects of the zeolite topology must be taken into account in the analysis. We have previously shown that the topology is of utmost importance: some reaction steps become feasible only when the molecular environment is taken into account [24,25]. Taking this into consideration, our results are based on large zeolite clusters which account for the MFI topology of H-ZSM-5.

Another factor that cannot be neglected is the effect of dispersion interactions. Recently, Svelle and coworkers showed that enthalpy barriers for methylation reactions of various olefins in H-ZSM-5 could be calculated with near chemical accuracy [23]. It was shown that dispersion interactions can add up to 20 kJ/mol for energy barriers and to 70 kJ/mol for physisorption energies [23,26], depending on the specific reaction under study. To account for these potentially important long-range effects, we have added an empirical dispersion term to the energies obtained from density functional theory (DFT) calculations. This approach as developed by Grimme and coworkers – often referred to as the DFT-D approach – has been shown to improve accuracy on a variety of systems [27]. All our conclusions will be drawn on reaction barriers as well as on rate coefficients.

Based on the obtained results, we will propose a new low-energy pathway to cyclization which does not assume prior dehydrogenation. While it is obvious that a myriad of reaction cycles could form cyclic intermediates, this study proposes one plausible route

without claiming exclusivity. Basically, this study is a proof of concept for the formation of secondary HP species from already formed olefinic species.

It is important to note that, next to being catalytically active species, these cyclic hydrocarbon pool compounds are also coke precursors. Formation of this species will, therefore, not only provide an active catalyst, but also ultimately deactivate it again [28] (as also illustrated in Fig. 1).

2. Methodology

Geometry optimizations were first performed on pentatetrahedral (5T) clusters with the Gaussian 03 package [29] at the B3LYP/6-31+g(d) level of theory [30–32]. Consequently, transition states of 5T cluster results were used as an initial guess for the transition state in the zeolite environment. Starting from transition state geometries, the quasi-IRC approach allowed the product geometries to be acquired [33]. In the quasi-IRC approach, the geometry of the transition state is slightly perturbed in the direction of the reactants and products followed by full geometry optimizations. This procedure ensures that reactants and products are linked by the same correct transition state. An 8T:46T ONIOM method was used on a cluster cut out of the MFI crystallographic structure of ZSM-5 [24,34,35]. The active site was located at the T12 position [36] at the intersection of the straight and sinusoidal channels, which allows bigger molecules to be formed through bulky transition states. The outer hydrogen atoms of the cluster were constrained in space to prevent unphysical deformations due to the neglect of the full molecular environment. All stationary points and transition states were further localized using the ONIOM(B3LYP/6-31+g(d):MNDO) method, in which the high level is composed of an 8T cluster, and the rest of the cluster is treated at the lower level. The true nature of the stationary points was confirmed by a normal mode analysis, which yields only positive frequencies for all minima and only one negative frequency for each transition state. These energies were refined by single-point energy calculations on the stationary points using the ONIOM(B3LYP/6-31+g(d):HF/6-31+g(d)) level of theory. As shown previously by Svelle and coworkers [23] on the methylation of various olefins in H-ZSM-5, dispersion interactions cannot be neglected for the type of reactions under consideration in this paper. A computationally feasible method to introduce these energy contributions is by adding an empirical $-C_6R^{-6}$ correction to the energy obtained from the Density Functional Theory calculations. This is called the DFT-D approach and provides high accuracy in a variety of simulations [27,37]. For some of the methylation reactions studied by Svelle and coworkers [23], our method gives values that are in very good agreement with the periodic calculations using the PBE functional and augmented with the semi-empirical dispersion term.

Using standard notation LOT-E//LOT-G (LOT-E and LOT-G being the electronic levels of theory used for the energetics and geometry optimizations, respectively), all results discussed in this paper are obtained with the method which is denoted as ONIOM(B3LYP/6-31+g(d):HF/6-31+g(d)) – D//ONIOM(B3LYP/6-31+g(d):MNDO) [38,39]. The van der Waals correction in conjunction with the B3LYP functional as developed by Grimme [37] was calculated using the ORCA program [40]. The above scheme is a viable alternative to more computationally expensive periodic calculations, as also demonstrated by other studies [16,23,41].

The 46T clusters are constrained by the outer hydrogen atoms to prevent unphysical deformation of the cluster. We used the PHVA method [42–46] as previously applied for kinetics [16,25]. This procedure is now implemented in an in-house developed software module TAMKIN, which will be released shortly [47]. Rate coefficients k were obtained by using transition state theory (TST) by calculating the partition functions at 673 K. For an estimation of the uncertainties on the pre-exponential factor A and activation energy E_a in a temperature interval from 623 to 723 K, we refer to the Supporting Information.

3. Results and discussion

The cyclization of olefin-like species is not straightforward as it involves a variety of reactions that add up to a complex reaction network. Starting from the olefins already formed in the zeolite cages, following reaction families can be distinguished (as schematically shown in Fig. 2):

(i) oligomerization to higher olefins,
(ii) isomerization,
(iii) cracking of higher olefins,
(iv) cyclization and
(v) dehydrogenative aromatization.

In this paper, we will only study (i) chain growth through oligomerization and (iv) cyclization of the formed chain, labeled as reaction classes A and B, respectively, in Fig. 2. The oligomerization reactions studied in this work include the coupling of two C2 species and a variety of couplings between two C3 species.

Several other types of chain growth mechanisms have been already thoroughly investigated: methylation of alkenes by methanol [23,33,48–52] or oligomerization of ethene and propene [53]. Svelle et al. [51] found experimental proof that propene dimerization might dominate over chain growth by successive methylation. The obtained longer alkene can be dehydrogenated, followed by a diene cyclization [54–59] or can form a naphthene by cyclization prior to further dehydrogenation steps to yield catalytically active species [25].

It has been shown both experimentally [60] and theoretically [61,62] that the stable intermediates resulting from olefin chemisorption form covalent bonds with the basic oxygen atoms, leading to the formation of framework-bound alkoxides rather than free carbenium ions, depending on both olefin size and the local geometry of the active site. Therefore, alkoxide formation of ethene and

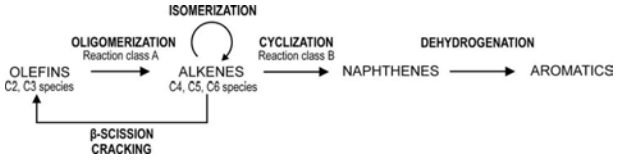

Fig. 2. Overview of various reaction classes for alkene conversion in acidic zeolites.

propene will be studied as they are possible intermediate steps for the oligomerization reactions.

3.1. Reaction class A: alkoxide formation and oligomerization

Chain growth mainly occurs through dimerization of olefins formed during the primary induction phase [51]. The possible ethene dimerization and propene dimerization reaction steps will be investigated and serve as a general model for other oligomerization reactions. Two different mechanism types should be considered: concerted and stepwise [53]. In the concerted coupling of alkenes, protonation and C–C coupling occur simultaneously, while the stepwise oligomerization proceeds via initial alkoxide formation [63,64] followed by C–C bond formation. Dimerization reactions have been modeled earlier on 4T clusters, but it is still unclear how the surrounding framework affects the reaction kinetics [53]. Cracking reactions, which are in fact the reverse process of dimerization reactions, have also been modeled in gas phase or on small clusters [65–67]. In Fig. 3, a summary of the studied dimerization reactions is shown.

3.1.1. Alkoxide formation (reactions A1, A2 and A3)

In what follows we will give a short overview of what has already been published in literature on alkoxide formation and of what can serve as a guideline for the validation of our results presented in this article.

The interaction of the olefin double bond with the zeolite Brønsted acid site results in the formation of a physisorbed π-complex. The alkoxide formation is considered at a Brønsted acid site associated with the T12 crystallographic position. Moreover, the physisorbed π-complex is located at the oxygen situated right at the intersection of the sinusoidal and straight channel and represents the most accessible site for adsorption in the ZSM-5 lattice. Earlier calculations by Bhan et al. [63] studied the influence of the location of both the framework aluminum and the charge-compensating proton on physisorption and chemisorption of propene. They confirmed that the T12 location used in this work is the most

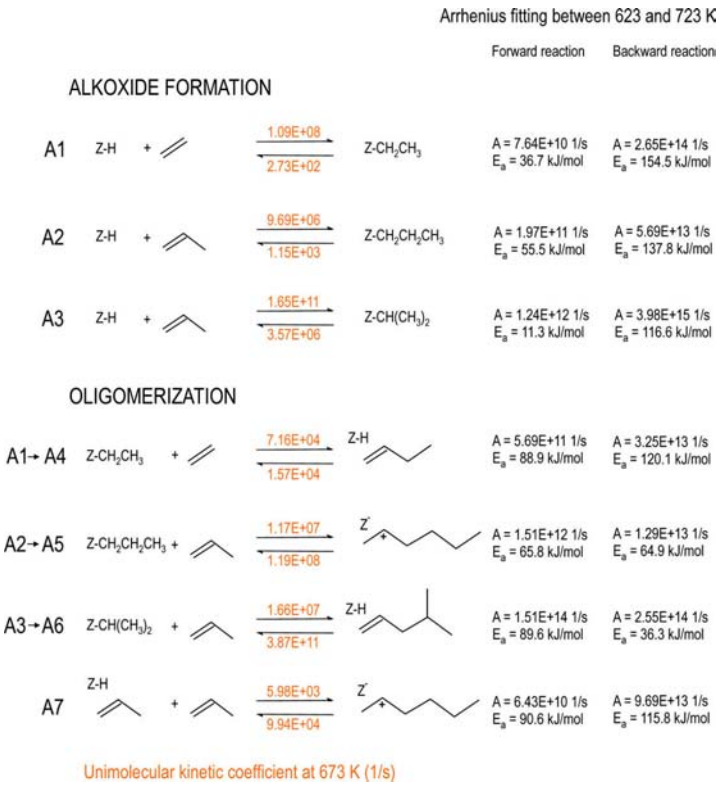

Fig. 3. Investigated oligomerization reactions with kinetic coefficients at 673 K and fitted Arrhenius parameters in the temperature interval 623–723 K calculated on a 46T cluster at the ONIOM(B3LYP/6-31+g(d):HF/6-31+g(d)) – D level of theory including van der Waals corrections.

preferable position for the acidic proton. A recent combined experimental and theoretical study by Sklenak and coworkers showed that the actual distribution of aluminum in MFI is not random and is controlled by the actual conditions of the zeolite synthesis procedure [68]. The T12 position imposes the least steric constraints for formation of bulky intermediates and was therefore used in our theoretical calculations.

The mechanism for alkoxide formation has been studied before by a variety of theoretical models. The results are heavily dependent on the theoretical method used and the model size used to model the solid catalyst [61,62,69,70]. The mechanism of alkoxide formation is schematically depicted in Fig. 4: starting from the physisorbed complex, protonation of the olefin through a carbenium-like transition state results in the formation of chemisorbed covalently bonded alkoxide species. Previous theoretical results showed that the stability of the formed alkoxide is primarily determined by the olefin size [61,63], whereas the activation energies for protonation are determined by the order of stability of primary, secondary and tertiary carbenium-like transition states. Stabilization of the transition state is also determined by electrostatic interactions and might also be influenced by dispersion interactions, which have been unaccounted for so far in ZSM-5. Sauer and coworkers found that for the protonation of isobutene, both the dispersion corrections and the entropic contributions are important to decide on the stability of carbenium ions. At temperatures higher than 120 K, the tert-butyl cation was found to be more stable over the chemisorbed species [26,71].

Experimental evidence has been given for the existence of the physisorbed π-complex and alkoxide by studying the oligomerization reactions of ethene and propene by means of fast FTIR spectroscopy [72]. A downward shift of the O–H stretching frequency was observed of 389 1/cm by interaction of ethene with the Brønsted acidic site at small contact times during which no protonation of the olefin had occurred. Similarly, a downward shift of 11 1/cm for the C=C double bond frequency in ethene was noticed when brought in contact with the acidic site compared with the gas phase spectrum. Our theoretical calculations were able to fairly well reproduce these shifts: predictions of 334 and 10 1/cm were found for the O–H and C=C frequency shifts with respect to the corresponding vibrations in an empty zeolite and a gas phase ethene molecule. The small downward shift of the double bond frequency can be attributed to the reduced density of charge of the carbon–carbon double bond, while the O–H stretch is shifted due to interaction of the acidic proton with the carbon–carbon double bond to form hydrogen-bonded precursor complexes or physisorbed π-complexes.

The physisorption energies of ethene and propene are given in Table 1. As all physisorbed complexes were found by performing a quasi-IRC calculation from the transition state for protonation, the values for the physisorbed complex derived from the i-propoxide are slightly different than the value derived from 1-propoxide. In all geometries of the physisorbed complexes, the bridging hydroxyl is closer to the primary carbon atom that is going to be protonated than to the carbon atom that will interact with the basic oxygen (see Fig. 4). The physisorbed energies without van der Waals corrections amount to −28.3 and −41.3 kJ/mol which are in relatively good agreement with the results found by Bhan et al. [63] and Zheng et al. [73]. All of these physisorption energies are, however, too small compared to experimental data due to the neglect of dispersion interactions as will be shown later in this section [74]. The larger value for propene can be attributed to two effects. Firstly, the interaction with the acidic proton is stronger: the distance between the Brønsted acidic proton and the primary carbon atom that is going to be protonated (C_a in Fig. 4) amounts to 2.341 and 2.083 Å for ethene and propene respectively, whereas the distance between the other carbon atom (C_b in Fig. 4) and the acid site is more or less similar for ethene and propene. Secondly, coordination of the methyl group with the basic oxygen next

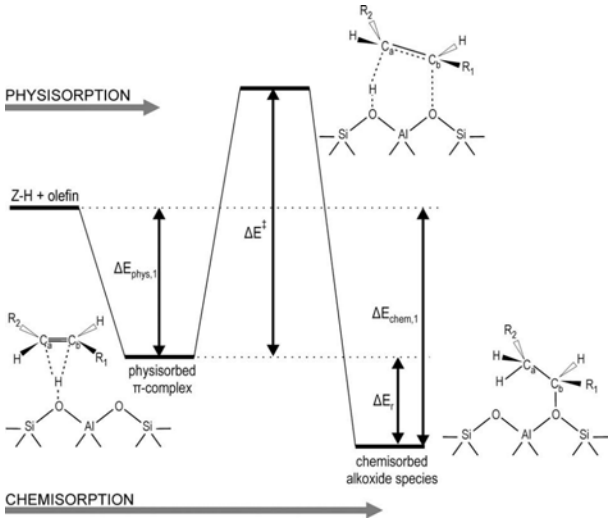

Fig. 4. Energy diagram for alkoxide formation.

Table 1
Electronic energies (in kJ/mol) of various consecutive steps: alkoxide formation, dimerization and cyclization.

Alkoxide formation	$\Delta E^{\ddagger}$	ΔE_r	$\Delta E_{phys,1}$	$\Delta E_{chem,1}$
	Without van der Waals correction			
A1 (ethoxide formation)	56.3	−104.0	−28.3	−132.3
A2 (*n*-propoxide formation)	75.3	−69.6	−41.3	−110.9
A3 (i-propoxide formation)	31.3	−81.3	−38.5	−119.8
	With van der Waals correction			
A1 (ethoxide formation)	47.3	−120.6	−64.6	−185.2
A2 (*n*-propoxide formation)	64.4	−86.9	−92.4	−179.4
A3 (i-propoxide formation)	22.1	−107.9	−88.1	−196.0
Dimerization (stepwise)	$\Delta E^{\ddagger}$	ΔE_r	$\Delta E_{phys,2}$	
	Without van der Waals correction			
A4 (1-butene formation)	101.1	−32.6	−8.9	
A5 (2-hexyl carbenium ion formation)	83.5	17.3	0.6	
A6 (4-methyl-1-pentene formation)	94.7	43.1	−58.0	
	With van der Waals correction			
A4 (1-butene formation)	91.7	−30.3	−38.8	
A5 (2-hexyl carbenium ion formation)	68.8	2.8	−59.6	
A6 (4-methyl-1-pentene formation)	94.3	54.6	−119.4	
Dimerization (concerted)	$\Delta E^{\ddagger}$	ΔE_r		
	Without van der Waals correction			
A7 (2-hexyl carbenium ion formation)	111.1	−5.4		
	With van der Waals correction			
A7 (2-hexyl carbenium ion formation)	98.5	−26.8		
Cyclization	$\Delta E^{\ddagger}$	ΔE_r		
	Without van der Waals correction			
B1 (methylcyclopentene formation)	37.1	−126.5		
B2	155.6	33.9		
B3	72.3	3.2		
	With van der Waals correction			
B1	29.1	−117.0		
B2	165.2	111.7		
B3	70.1	5.4		

$\Delta E^{\ddagger}$ is the electronic energy difference between transition state and reactants. ΔE_r (reaction energy) is the energy difference between the products and reactants. $\Delta E_{phys,1}$ and ΔE_{chem} are the physisorption and chemisorption energies without temperature corrections calculated relative to the gas phase olefins and the empty zeolite cluster as defined in Fig. 4. $\Delta E_{phys,2}$ is the physisorption energy of the second alkene calculated relative to the gas phase olefin and the already formed alkoxide. All energies are calculated at the ONIOM(B3LYP/6-31+g(d):HF/6-31+g(d)) level of theory with and without inclusion of van der Waals corrections.

to the aluminum site results in additional stabilization. Boronat et al. found smaller values ranging from −8 to −16 kJ/mol in mordenite [61]. This confirms that the physisorption energy critically depends on the zeolite topology. The effect of dispersion interaction is considerable, contributing to an extra stabilization of −36.2 and −51.2 kJ/mol for ethene and propene, respectively. This gives final physisorption energies of −64.6 and −92.4 kJ/mol for ethene and propene. Sauer et al. also found dispersion corrections of this order of magnitude for the π-physisorbed butene complex in ferrierite (−78 kJ/mol) [26]. Our results also show that the dispersion interactions are dependent on the size of the hydrocarbon considered [75–78], which was also found by De Moor et al. on basis of QM-Pot(MP2//B3LYP) calculations in faujasite [79].

The reaction barriers without ZPVE corrections for alkoxide formation are also given in Table 1. For the formation of ethoxide, *n*-propoxide and i-propoxide, they amount to 56.3, 75.3 and 31.3 kJ/mol without inclusion of van der Waals corrections. The reaction is concerted: the primary carbon atom (or secondary in case of i-propoxide formation) is protonated by the zeolite, and simultaneously the positive charge on the other carbon atom of the double bond interacts with one of the basic oxygens of the zeolite, resulting in the formation of a covalently bonded alkoxide complex. The reaction barrier is directly related to the ability of this carbon atom to stabilize the positive charge. Hence, the barrier for formation of i-propoxide is smaller than for ethoxide, corresponding with a secondary and primary carbenium ion in the transition state. The effect of van der Waals interactions is quite uniform for all three alkoxide formations, lowering the reaction barriers (without ZPVE) by approximately 10 kJ/mol.

The stability of the finally formed alkoxides is marked by the olefin size, which predicts ethoxide to be more stable than i-propoxide followed by *n*-propoxide. The effect of dispersion interactions on the covalently bonded complex is substantial, yielding corrections from −16.6 to −26.6 kJ/mol. These results show that the formation of the i-propoxide is kinetically favored over the *n*-propoxide complex under the same reaction conditions. Also, thermodynamically i-propoxide is slightly preferred over *n*-propoxide, which can be deduced from the total chemisorption energies of −179.4 and −196.0 kJ/mol, respectively.

3.1.2. Stepwise dimerization (reactions A4, A5, A6)

Three stepwise dimerization reactions (A4–A6) were considered as shown in Fig. 3: dimerization of ethene and two dimerizations of propene. The latter reaction can start from the *n*-propoxide or i-propoxide. All three reactions require physisorption of a second alkene to the alkoxide. The physisorption energies of this step ($\Delta E_{phys,2}$) are given in Table 1 with and without van der Waals interactions. As for the physisorption of the first alkene, the values without dispersion interactions are seriously underestimated. For ethene and propene physisorption, van der Waals corrections of around 30 kJ/mol and 60 kJ/mol are found. In the work of Svelle et al. [53], values were found of around 0–5 kJ/mol with DFT schemes and 15–20 kJ/mol at the post-Hartree Fock level but with usage of a small 4T cluster. The geometries of the physisorbed complexes illustrate that various van der Waals contacts are made not only with the basic oxygen atoms next to the aluminum site but also with other framework oxygen atoms.

The various physisorption energies point toward a very stable i-propoxide co-adsorbed with a propene intermediate, from which only slow reactions can be expected.

After physisorption of the second alkene, the next step of the stepwise dimerization is the formation of a new C–C bond. For coupling between ethoxide and ethene, the reaction profile is shown in Fig. 5.

Without inclusion of an extended cluster model for the zeolite framework (but using a small 5T cluster instead), butene was not formed, but proton back donation to the cluster resulted in the formation of methylcyclopropane instead [53]. This cyclopropane species can easily undergo opening by protonation (the activation barrier for this additional reaction turns out to be 85.2 kJ/mol). These results correspond to earlier theoretical findings of Svelle et al. [53] and Frash et al. [65] who also found the cyclopropane intermediates as stable intermediates when small clusters were used. When an extended cluster model is considered, as in Fig. 5b, we did not find this methylcyclopropane intermediate, yet a similar structure did appear along the optimization of the products as corner-protonated methylcyclopropane. However, this is not a stationary point on the potential energy surface, and the proton on the edge undergoes a barrierless shift [80,81], which results in an automatic opening of the ring structure (Fig. 5b and c).

Depending on the method employed, the (protonated) methylcyclopropane might be a stable intermediate, albeit in a shallow potential well. Anderson and Klinowski [82] reported ^{13}C MAS NMR results, in which there is a weak signal intensity for cyclopropane during the conversion of methanol in gasoline over ZSM-5. Protonated alkylcyclopropane has also been reported earlier in modeling papers on the skeletal isomerization of alkenes [80,83].

From the transition states for dimerization, at least two possible products might be envisaged: a neutral alkene by direct back

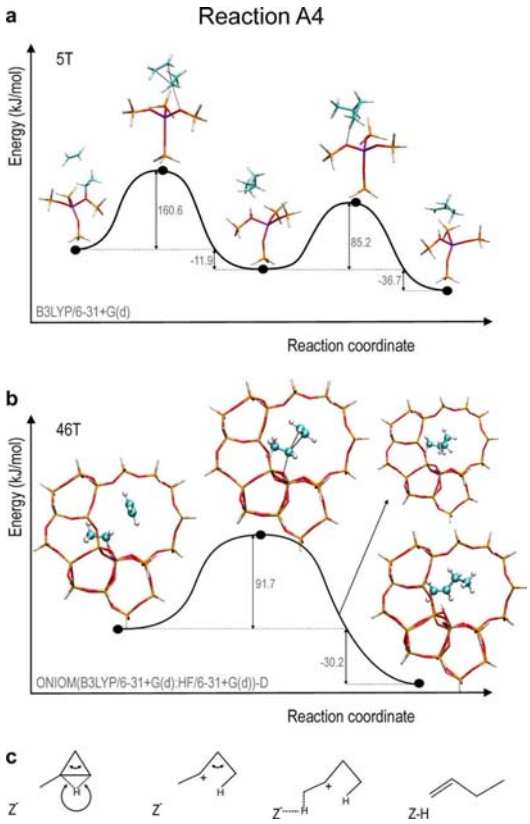

Fig. 5. (a) Visualization of the stepwise ethene dimerization on a 5T cluster; (b) energy diagram of the stepwise ethene dimerization in zeolite environment (Reaction A4); (c) schematic representation of the post-transition state optimization after stepwise coupling of two ethene molecules.

donation of a proton to the zeolite or a butoxide species. We used the quasi-IRC approach to pinpoint the products corresponding to the transition state and found 1-butene as shown in Fig. 5. To compare the stability of the neutral alkene and the alkoxide, we also calculated the energy of 1-butoxide. This covalently bonded complex is 50.8 kJ/mol (not included in Table 1) more stable than the π-complex if van der Waals interactions are taken into account. Without these dispersive forces, the difference only amounts to 10.2 kJ/mol. These results are in line with the earlier results on alkoxide formation, and the transformation from the π-complex to a covalently bonded alkoxide complex should occur easily.

Similar reaction profiles were determined for stepwise dimerization of propene, starting either from *n*-propoxide or i-propoxide. The transition states for carbon–carbon bond formation demonstrate in both cases a preference for attack at the unsubstituted end of the olefin, giving rise to formally secondary carbenium ions rather than primary ones (as illustrated in Fig. 6). While calculations without explicit inclusion of the framework resulted in only neutral products [53], this was not the case when extended models for the zeolite structure were considered, which has the potential to stabilize carbenium ions [24]. The two obtained products were, respectively, the 2-hexyl carbenium ion (Reaction A5) and 4-methylpentene (Reaction A6). These results show that nature of the formed products depends on the specific hydrocarbon, the zeolite structure's ability to stabilize various intermediates and the degree at which the structure has been taken into account.

The energy barriers for the stepwise dimerizations are given in Table 1 with and without van der Waals corrections. To rationalize the importance of each of the consecutive steps, the complete potential energy surface has been shown graphically in Fig. 7.

The alkoxide formation steps are relatively fast for both ethene and propene, with formation of the i-propoxide being the fastest. Adsorption of the second alkene produces a very stable intermediate "i-propoxide + propene". The fastest oligomerization route is

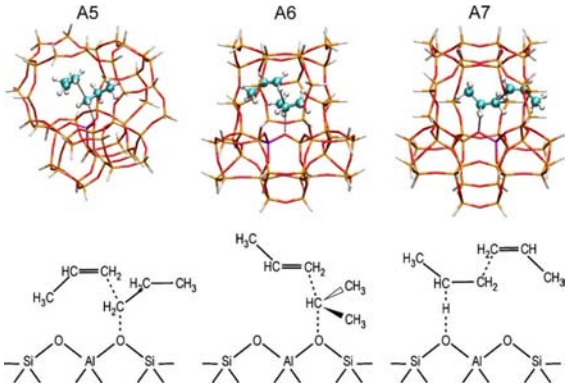

Fig. 6. Visualization of the transition states for propene dimerization. (TS-A5) Stepwise mechanism from a primary propoxide; (TS-A6) stepwise mechanism from a secondary propoxide; (TS-A7) concerted mechanism with a formally primary carbenium ion in the transition state.

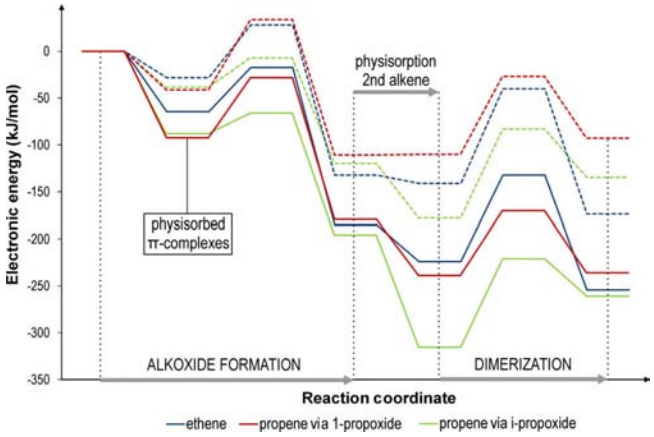

Fig. 7. Energy profiles of the alkoxide formation and subsequent oligomerization reactions of ethene and propene. The energy levels are calculated relative to the gas phase olefins and the empty zeolite cluster, based on electronic energies at the ONIOM(B3LYP/6-31+g(d):HF/6-31+g(d)) level of theory, with (solid line) and without inclusion (dashed line) of van der Waals corrections.

the stepwise dimerization of propene producing the 2-hexylcarbenium ion. However, the oligomerization of ethene to form 1-butene is competitive taking into account alkoxide formation and second physisorption of the alkene. The stepwise oligomerization starting from i-propoxide to form the 4-methyl-1-pentene (A6) is less viable. Although the forward activation energy of 89.6 kJ/mol (see Fig. 3) suggests a rapid transformation at the considered reaction conditions, the backward reaction is much lower activated (36.3 kJ/mol), which shifts the equilibrium toward the i-propoxide. This is evidenced by the equilibrium constants ($K = k_{forward}/k_{backward}$) of reactions A5 and A6 which amount to, respectively, 10^{-1} and 10^{-4}. Therefore, further cyclization and oligomerization from the intermediate "i-propoxide + propene" can be excluded.

From a methodological point of view, it is interesting to compare the potential energy surface with and without van der Waals interactions. In general, the activation energies and reaction energies starting from already adsorbed species (so-called intrinsic barriers) are only subject to relatively small changes. The largest influence is found for each physisorption step of a new reaction partner.

Finally, we will also compare chain growth processes via dimerization versus growth through methylation reactions. The

methylation starts from a physisorbed methanol molecule and an alkene. The respective barriers for methylation of ethene and propene with inclusion of van der Waals interactions are found to be 84.0 and 74.7 kJ/mol. It seems that chain growth will occur along both possible pathways, and for definitive conclusions also intermediate physisorption states should be considered.

3.1.3. Concerted propene dimerization (reaction A7)

As an alternative for the stepwise oligomerization, a concerted reaction pathway might be possible, during which the protonation of the first alkene and carbon–carbon bond formation occur simultaneously. For propene, there are two possible sites of protonation leading to the formation of a formally primary or secondary carbenium ion in the transition state. The transition state with a secondary carbenium ion, as seen on a 4T cluster [53], evolves into the transition state for stepwise dimerization when the zeolite environment is taken into account. The transition state through a formally primary carbenium ion could be located and is visualized in Fig. 7 (Reaction A7). When applying a quasi-IRC approach to the transition state, the formed product was the 2-hexyl carbenium ion which was also found as a result of the stepwise dimerization. The IRC toward the reactants evolved into a structure for which one propene molecule left the cluster. This is an artifact of our 46T cluster, which could not prevent the diffusion of one propene molecule out of the 46T cluster when applying quasi-IRC toward the reactants. To get better predictions of the forward reaction barrier of the concerted route, we used a slightly larger perturbation of the transition state in order to keep both propene molecules physisorbed inside the cluster.

The rate coefficient for the backward cracking reaction (Reaction A7 in Fig. 3) is two orders of magnitude larger than for the forward reaction. The stepwise dimerization to 2-hexylcarbenium ion (Reaction A5 in Fig. 3) will be preferred over the concerted reaction. Also, the forward reaction rate is even four orders of magnitude larger. In addition, the cracking reactions prefer a stepwise mechanism as well.

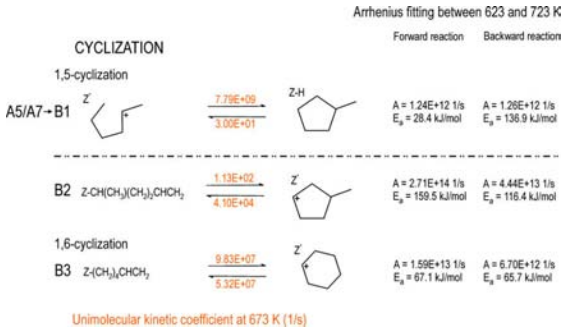

Fig. 8. Cyclization reactions with kinetic coefficients at 673 K.

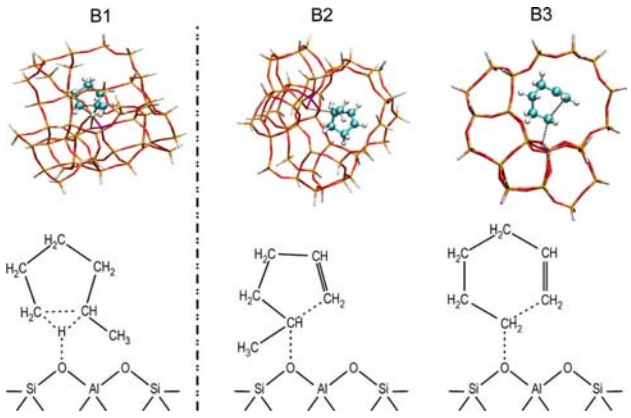

Fig. 9. Visualization of the transition states for cyclization in this study. (TS-B1) cyclization of the 2-hexyl carbenium ion; (TS-B2) cyclization from a secondary alkoxide of hexadiene; (TS-B3) cyclization from a primary alkoxide of hexadiene.

In summary, the theoretical results indicate fast cracking steps at 673 K of alkenes (protonated or non-protonated) in the MFI topology of ZSM-5. This result is in agreement with the recent dual cycle proposal for the MTO process, in which C_{3+} alkenes are possible hydrocarbon pool species [21]. For the oligomerization, our results indicate that, like for the ethene dimerization, propene dimerization also preferably proceeds via a stepwise mechanism.

3.2. Reaction class B: cyclization

Cyclization of the obtained C_6 species yields precursors to methylbenzenes, which have been proven to be active hydrocarbon pool compounds in H-ZSM-5 [12]. The previously studied oligomerization reactions starting from propene show that the 2-hexylcarbenium ion is a likely intermediate. This result allows us to propose a new route to cyclization starting from this carbenium ion and which does not assume any prior dehydrogenation. As schematically proposed by Haw et al., dehydrogenation occurs more easily after cyclization [8]. This would predominantly occur with the assistance of propene and would also explain the formation of alkanes during the MTO process.

Earlier investigations into cyclization [54,55,59] have shown that dienes or trienes might also be precursors for the cyclization reaction. Joshi et al. studied C6, C7 and C8 diene cyclization in H-ZSM-5 theoretically using a hybrid QM/MM approach [57,58]. They found that the barriers for 1,6-cyclization are lower for the larger dienes, as they proceed through a secondary carbenium ion-like transition state, whereas the C6 diene cyclization involves a primary carbenium ion-like transition state. In order to compare cyclization of the 2-hexylcarbenium ion intermediate of this work with the cyclization of the dienes, we have also calculated the cyclization starting from 1,5-hexadiene as suggested in [57] at the level of theory used for all reactions in this paper. The three cyclization reactions considered here are summarized in Fig. 8 (Reactions B1–B3). A visualization of the corresponding transition states is given in Fig. 9.

We first consider cyclization starting from the 2-hexyl carbenium ion, which is a secondary carbenium ion and is formed as a stable product for two different propene dimerization reactions (A5 and A7). A scan along the transition state coordinate was applied to find a direct cyclization route. Fig. 9B1 visualizes this direct 1,5-cyclization transition state. Prior to the transition state, the original 2-hexyl carbenium ion needs to undergo various internal rearrangements to evolve into conformation which is suitable for cyclization. This conformation is slightly less favorable in energy (27 kJ/mol) compared to the linear chain, but under the reaction conditions here these rearrangements are expected to occur easily. During the transition state a proton hops and bonds with one of the basic oxygen atoms on the aluminum tetrahedron and simultaneously the ring closes. The transition state is schematically depicted in Fig. 9. The product after cyclization is a neutral species, i.e., methylcyclopentane. The electronic reaction barriers given in Table 1 and the rate constants shown in Fig. 8 indicate a rapid and irreversible cyclization step. As matter of comparison with the work of Joshi [56,57], we also studied the cyclization of dienes. This reaction starts from a protonated hexadiene which then forms an alkoxide. Cyclization can start from a secondary hexadiene alkoxide (Reaction B2) or from a primary hexadiene alkoxide (Reaction B3). These results show that the 1,6-cyclization starting from a primary alkoxide is strongly favored over the 1,5-cyclization via a secondary alkoxide, which could be expected as secondary alkoxides are more easily formed but are also more stable [84], and thus less reactive for following cyclizations (Fig. 6). All kinetic parameters and reaction barriers show that the newly proposed cyclization starting from the 2-hexyl carbenium ion without prior dehydrogenation is preferred over cyclization of dienes.

3.3. Global scheme for formation of cyclic species

Fig. 10 gives an overview of the studied reactions and highlights in red a viable route toward formation of a 5-membered cyclic species, i.e., methylcyclopentane. The route involves following steps: physisorption of a first propene molecule to form a π-complex,

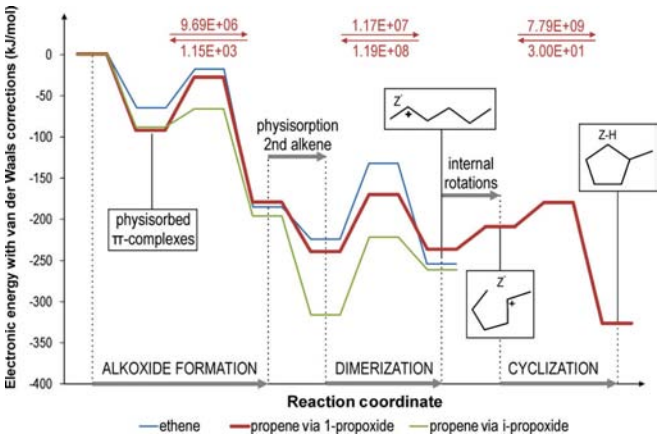

Fig. 10. Overview of a viable route toward the formation of cyclic species starting from ethene and propene. The red cycle is the most probable pathway and involves physisorption of propene, formation of *n*-propoxide, additional physisorption of propene, dimerization to form the 2-hexylcarbenium ion and cyclization to methylcyclopentane.

alkoxide formation to form a covalently bonded complex, i.e., the *n*-propoxide, physisorption of a second propene and dimerization to form the 2-hexylcarbenium ion and finally cyclization toward a neutral methylcyclopentane molecule. For all steps, both forward and backward reaction rates are given at 673 K. The reaction rates are in the same order of magnitude as the ones reported in our full cycle for the production of olefins in ZSM-5 [25]. The alkoxide formation and dimerization are in the same order of magnitude as methylation reactions of aromatic species in the same topology. The ring closure itself is very rapid.

However, to form aromatic hydrocarbons from this 5-membered ring species, we need ring expansion (as studied in [25]) as well as dehydrogenation. Additional research on the dehydrogenation of those cyclic rings might be useful. This step could occur through carbenium ions which provide cracking pathways of larger hydrocarbons at MTO temperatures [80].

Two more hydrogen abstractions lead to the formation of a dimethylcyclopentadienylium ion, a species signaling the end of the induction period in the MTO process in H-ZSM-5 and starting a new working cycle toward olefin protonation [13]. Such cationic 5-membered ring species have already been shown to expand into 6-membered rings [25] and form part of the active methylbenzene hydrocarbon pool cycle. As proposed and described by Haw and Marcus [8], propene could play a crucial role in ring dehydrogenation steps. Moreover, the ultimate clue of the active nature of this species as organic cocatalyst is proven by its occurrence in a recently calculated catalytic cycle in H-ZSM-5 [25].

4. Conclusions

The formation of cyclic hydrocarbons from ethene and propene building blocks was investigated in protonated ZSM-5 using a 2-layered ONIOM approach and taking into account dispersive interactions. These cyclic molecules are crucial in the MTO process, as they form precursors for both active cocatalysts and deactivating coke. Once a sufficient number of initial ethene and propene molecules are formed during the induction period, the rapid formation of new hydrocarbon pool species will bring the protonated zeolite to an active working MTO catalyst, during which methanol is converted into ethene and propene, generating even more active centers, up until the catalyst deactivates.

We performed theoretical calculations to describe a preliminary pathway to cyclic species from small alkene molecules like ethene and propene. By taking the zeolite environment into account, the factual role of the methylcyclopropane intermediate in ethene dimerization could be identified. For further growth of the chain, the calculated kinetic coefficients indicate that stepwise propene dimerization occurs faster than ethene dimerization. The ethoxide formation is rapid, but the dimerization proceeds more slowly. Propene dimerization could result in stable charged species like the 2-hexyl carbenium ion, from which a new rapid cyclization route is proposed. Our calculations further demonstrate the importance of the zeolite environment and the importance of dispersion interactions on the stability of specific intermediates on the potential energy surface. It was found that without accounting for the zeolite cage, some intermediates may be identified which are not stable in the MFI topology of H-ZSM-5. The effect of dispersive interactions was most pronounced for each physisorption step where corrections varying between 30 and 60 kJ/mol were noted.

The reactions studied provide a link between both catalytic cycles proposed in the hydrocarbon pool concept, which has been deemed crucial toward product control [12,21]. Future work should be focused on the dehydrogenation step, which ultimately leads to aromatic hydrocarbon pool compounds. This type of reactions will also be of utmost importance for the formation of a second ring, creating naphthalenic coke precursors [8,28,85,86].

Acknowledgments

This work is supported by the Fund for Scientific Research - Flanders (FWO), the research Board of Ghent University, and BELSPO in the frame of IAP 6/27. Computational resources and services used in this work were provided by Ghent University.

Appendix A. Supplementary data

Supplementary data associated with this article can be found, in the online version, at doi:10.1016/j.jcat.2010.02.001.

References

[1] M. Stocker, Microporous and Mesoporous Materials 29 (1999) 3–48.
[2] J.F. Haw, D.M. Marcus, P.W. Kletnieks, Journal of Catalysis 244 (2006) 130–133.
[3] Y.J. Jiang, W. Wang, V.R.R. Marthala, J. Huang, B. Sulikowski, M. Hunger, Journal of Catalysis 244 (2006) 134–136.
[4] Y.J. Jiang, W. Wang, V.R.R. Marthala, J. Huang, B. Sulikowski, M. Hunger, Journal of Catalysis 238 (2006) 21–27.
[5] D. Lesthaeghe, V. Van Speybroeck, G.B. Marin, M. Waroquier, Angewandte Chemie – International Edition 45 (2006) 1714–1719.
[6] D. Lesthaeghe, V. Van Speybroeck, G.B. Marin, M. Waroquier, Chemical Physics Letters 417 (2006) 309–315.
[7] W.G. Song, D.M. Marcus, H. Fu, J.O. Ehresmann, J.F. Haw, Journal of the American Chemical Society 124 (2002) 3844–3845.
[8] J.F. Haw, D.M. Marcus, Topics in Catalysis 34 (2005) 41–48.
[9] I.M. Dahl, S. Kolboe, Catalysis Letters 20 (1993) 329–336.
[10] R.M. Dessau, Journal of Catalysis 99 (1986) 111–116.
[11] J.F. Haw, W.G. Song, D.M. Marcus, J.B. Nicholas, Accounts of Chemical Research 36 (2003) 317–326.
[12] S. Svelle, F. Joensen, J. Nerlov, U. Olsbye, K.P. Lillerud, S. Kolboe, M. Bjorgen, Journal of the American Chemical Society 128 (2006) 14770–14771.
[13] J.F. Haw, J.B. Nicholas, W.G. Song, F. Deng, Z.K. Wang, T. Xu, C.S. Heneghan, Journal of the American Chemical Society 122 (2000) 4763–4775.
[14] A. Sassi, M.A. Wildman, H.J. Ahn, P. Prasad, J.B. Nicholas, J.F. Haw, Journal of Physical Chemistry B 106 (2002) 2294–2303.
[15] T. Xu, D.H. Barich, P.W. Goguen, W.G. Song, Z.K. Wang, J.B. Nicholas, J.F. Haw, Journal of the American Chemical Society 120 (1998) 4025–4026.
[16] K. Hemelsoet, A. Nollet, M. Vandichel, D. Lesthaeghe, V. Van Speybroeck, M. Waroquier, ChemCatChem 1 (2009) 373–378.
[17] M. Bjorgen, U. Olsbye, D. Petersen, S. Kolboe, Journal of Catalysis 221 (2004) 1–10.
[18] M. Bjorgen, F. Bonino, S. Kolboe, K.P. Lillerud, A. Zecchina, S. Bordiga, Journal of the American Chemical Society 125 (2003) 15863–15868.
[19] B. Arstad, S. Kolboe, Catalysis Letters 71 (2001) 209–212.
[20] W.G. Song, J.F. Haw, J.B. Nicholas, C.S. Heneghan, Journal of the American Chemical Society 122 (2000) 10726–10727.
[21] M. Bjorgen, S. Svelle, F. Joensen, J. Nerlov, S. Kolboe, F. Bonino, L. Palumbo, S. Bordiga, U. Olsbye, Journal of Catalysis 249 (2007) 195–207.
[22] D. Lesthaeghe, J. Van der Mynsbrugge, M. Vandichel, V. Van Speybroeck, M. Waroquier, manuscript in revision.
[23] S. Svelle, C. Tuma, X. Rozanska, T. Kerber, J. Sauer, Journal of the American Chemical Society 131 (2009) 816–825.
[24] D. Lesthaeghe, B. De Sterck, V. Van Speybroeck, G.B. Marin, M. Waroquier, Angewandte Chemie – International Edition 46 (2007) 1311–1314.
[25] D.M. McCann, D. Lesthaeghe, P.W. Kletnieks, D.R. Guenther, M.J. Hayman, V. Van Speybroeck, M. Waroquier, J.F. Haw, Angewandte Chemie – International Edition 47 (2008) 5179–5182.
[26] C. Tuma, J. Sauer, Physical Chemistry Chemical Physics 8 (2006) 3955–3965.
[27] S. Grimme, J. Antony, T. Schwabe, C. Muck-Lichtenfeld, Organic & Biomolecular Chemistry 5 (2007) 741–758.
[28] D. Mores, E. Stavitski, M.H.F. Kox, J. Kornatowski, U. Olsbye, B.M. Weckhuysen, Chemistry A European Journal 14 (2008) 11320–11327.
[29] M.J. Frisch, G.W. Trucks, H.B. Schlegel, G.E. Scuseria, M.A. Robb, J.R. Cheeseman, J.A. Montgomery, Jr., T. Vreven, K.N. Kudin, J.C. Burant, J.M. Millam, S.S. Iyengar, J. Tomasi, V. Barone, B. Mennucci, M. Cossi, G. Scalmani, N. Rega, G.A. Petersson, H. Nakatsuji, M. Hada, M. Ehara, K. Toyota, R. Fukuda, J. Hasegawa, M. Ishida, T. Nakajima, Y. Honda, O. Kitao, H. Nakai, M. Klene, X. Li, J.E. Knox, H.P. Hratchian, J.B. Cross, V. Bakken, C. Adamo, J. Jaramillo, R. Gomperts, R.E. Stratmann, O. Yazyev, A.J. Austin, R. Cammi, C. Pomelli, J.W. Ochterski, P.Y. Ayala, K. Morokuma, G.A. Voth, P. Salvador, J.J. Dannenberg, V.G. Zakrzewski, S. Dapprich, A.D. Daniels, M.C. Strain, O. Farkas, D.K. Malick, A.D. Rabuck, K. Raghavachari, J.B. Foresman, J.V. Ortiz, Q. Cui, A.G. Baboul, S. Clifford, J. Cioslowski, B.B. Stefanov, G. Liu, A. Liashenko, P. Piskorz, I. Komaromi, R.L. Martin, D.J. Fox, T. Keith, M.A. Al-Laham, C.Y. Peng, A. Nanayakkara, M. Challacombe, P.M.W. Gill, B. Johnson, W. Chen, M.W. Wong, C. Gonzalez, J.A. Pople, Gaussian 03, Revision E.01, Wallingford CT, 2004.

[30] A.D. Becke, Journal of Chemical Physics 98 (1993) 5648–5652.
[31] D. Lesthaeghe, V. Van Speybroeck, M. Waroquier, Journal of the American Chemical Society 126 (2004) 9162–9163.
[32] S.A. Zygmunt, R.M. Mueller, L.A. Curtiss, L.E. Iton, Journal of Molecular Structure – Theochem 430 (1998) 9–16.
[33] S. Svelle, S. Kolboe, U. Olsbye, O. Swang, Journal of Physical Chemistry B 107 (2003) 5251–5260.
[34] D. Lesthaeghe, G. Delcour, V. Van Speybroeck, G.B. Marin, M. Waroquier, Microporous and Mesoporous Materials 96 (2006) 350–356.
[35] C. Raksakoon, J. Limtrakul, Journal of Molecular Structure – Theochem 631 (2003) 147–156.
[36] H. Vankoningsveld, H. Vanbekkum, J.C. Jansen, Acta Crystallographica Section B – Structural Communications 43 (1987) 127–132.
[37] S. Grimme, Journal of Computational Chemistry 25 (2004) 1463–1473.
[38] J.T. Fermann, T. Moniz, O. Kiowski, T.J. McIntire, S.M. Auerbach, T. Vreven, M.J. Frisch, Journal of Chemical Theory and Computation 1 (2005) 1232–1239.
[39] X. Solans-Monfort, M. Sodupe, V. Branchadell, J. Sauer, R. Orlando, P. Ugliengo, Journal of Physical Chemistry B 109 (2005) 3539–3545.
[40] ORCA 2.6.35ed. <http://www.thch.uni-bonn.de/tc/orca/>.
[41] D. Lesthaeghe, A. Horré, M. Waroquier, G.B. Marin, V. Van Speybroeck, Chemistry – A European Journal 15 (2009) 10803–10808.
[42] A. Ghysels, V. Van Speybroeck, T. Verstraelen, D. Van Neck, M. Waroquier, Journal of Chemical Theory and Computation 4 (2008) 614–625.
[43] A. Ghysels, V. Van Speybroeck, E. Pauwels, D. Van Neck, B.R. Brooks, M. Waroquier, Journal of Chemical Theory and Computation 5 (2009) 1203–1215.
[44] A. Ghysels, V. Van Speybroeck, E. Pauwels, S. Catak, B.R. Brooks, D. Van Neck, M. Waroquier, Journal of Computational Chemistry 31 (2009) 994–1007.
[45] A. Ghysels, D. Van Neck, M. Waroquier, Journal of Chemical Physics 127 (2007) 164108.
[46] A. Ghysels, D. Van Neck, V. Van Speybroeck, T. Verstraelen, M. Waroquier, Journal of Chemical Physics 126 (2007) 224102.
[47] CMM Code 2008–2009. <http://molmod.ugent.be/code/wiki> (accessed 26.10.09).
[48] Z.M. Cui, Q. Liu, Z. Ma, S.W. Bian, W.G. Song, Journal of Catalysis 258 (2008) 83–86.
[49] S. Svelle, B. Arstad, S. Kolboe, O. Swang, Journal of Physical Chemistry B 107 (2003) 9281–9289.
[50] S. Svelle, S. Kolboe, O. Swang, U. Olsbye, Journal of Physical Chemistry B 109 (2005) 12874–12878.
[51] S. Svelle, P.A. Ronning, S. Kolboe, Journal of Catalysis 224 (2004) 115–123.
[52] S. Svelle, P.O. Ronning, U. Olsbye, S. Kolboe, Journal of Catalysis 234 (2005) 385–400.
[53] S. Svelle, S. Kolboe, O. Swang, Journal of Physical Chemistry B 108 (2004) 2953–2962.
[54] D.V. Dass, A.L. Odell, Journal of Catalysis 113 (1988) 259–262.
[55] G. Giannetto, R. Monque, R. Galiasso, Catalysis Reviews – Science and Engineering 36 (1994) 271–304.
[56] Y.V. Joshi, A. Bhan, K.T. Thomson, Journal of Physical Chemistry B 108 (2004) 971–980.
[57] Y.V. Joshi, K.T. Thomson, Journal of Catalysis 230 (2005) 440–463.
[58] Y.V. Joshi, K.T. Thomson, Journal of Physical Chemistry C 112 (2008) 12825–12833.
[59] P. Meriaudeau, C. Naccache, Catalysis Reviews – Science and Engineering 39 (1997) 5–48.
[60] J.F. Haw, B.R. Richardson, I.S. Oshiro, N.D. Lazo, J.A. Speed, Journal of the American Chemical Society 111 (1989) 2052–2058.
[61] M. Boronat, P.M. Viruela, A. Corma, Journal of the American Chemical Society 126 (2004) 3300–3309.
[62] V.B. Kazansky, Accounts of Chemical Research 24 (1991) 379–383.
[63] A. Bhan, Y.V. Joshi, W.N. Delgass, K.T. Thomson, Journal of Physical Chemistry B 107 (2003) 10476–10487.
[64] D. Lesthaeghe, V. Van Speybroeck, G.B. Marin, M. Waroquier, Journal of Physical Chemistry B 109 (2005) 7952–7960.
[65] M.V. Frash, V.B. Kazansky, A.M. Rigby, R.A. van Santen, Journal of Physical Chemistry B 102 (1998) 2232–2238.
[66] Q.B. Li, A.L.L. East, Canadian Journal of Chemistry – Revue Canadienne De Chimie 84 (2006) 1159–1166.
[67] Q.B. Li, K.C. Hunter, A.L.L. East, Journal of Physical Chemistry A 109 (2005) 6223–6231.
[68] S. Sklenak, J. Dedecek, C.B. Li, B. Wichterlova, V. Gabova, M. Sierka, J. Sauer, Angewandte Chemie – International Edition 46 (2007) 7286–7289.
[69] M. Boronat, P. Viruela, A. Corma, Journal of Physical Chemistry A 102 (1998) 982–989.
[70] X. Rozanska, R.A. van Santen, T. Demuth, F. Hutschka, J. Hafner, Journal of Physical Chemistry B 107 (2003) 1309–1315.
[71] C. Tuma, J. Sauer, Angewandte Chemie – International Edition 44 (2005) 4769–4771.
[72] G. Spoto, S. Bordiga, G. Ricchiardi, D. Scarano, A. Zecchina, E. Borello, Journal of the Chemical Society, Faraday Transactions 90 (1994) 2827–2835.
[73] A.M. Zheng, S.B. Liu, F. Deng, Microporous and Mesoporous Materials 121 (2009) 158–165.
[74] P.E. Sinclair, A. de Vries, P. Sherwood, C.R.A. Catlow, R.A. van Santen, Journal of the Chemical Society, Faraday Transactions 94 (1998) 3401–3408.
[75] F. Eder, J.A. Lercher, Zeolites 18 (1997) 75–81.
[76] F. Eder, M. Stockenhuber, J.A. Lercher, Journal of Physical Chemistry B 101 (1997) 5414–5419.
[77] J.F. Denayer, G.V. Baron, J.A. Martens, P.A. Jacobs, Journal of Physical Chemistry B 102 (1998) 3077–3081.
[78] J.F.M. Denayer, G.V. Baron, Adsorption-Journal of the International Adsorption Society 3 (1997) 251–265.
[79] B.A. De Moor, M.F. Reyniers, M. Sierka, J. Sauer, G.B. Marin, Journal of Physical Chemistry C 112 (2008) 11796–11812.
[80] A. Boronat, A. Corma, Applied Catalysis A – General 336 (2008) 2–10.
[81] K.B. Wiberg, S.R. Kass, Journal of the American Chemical Society 107 (1985) 988–995.
[82] M.W. Anderson, J. Klinowski, Journal of the American Chemical Society 112 (1990) 10–16.
[83] T. Demuth, X. Rozanska, L. Benco, J. Hafner, R.A. van Santen, H. Toulhoat, Journal of Catalysis 214 (2003) 68–77.
[84] M. Boronat, C.M. Zicovich-Wilson, P. Viruela, A. Corma, Journal of Physical Chemistry B 105 (2001) 11169–11177.
[85] F. Bleken, M. Bjørgen, L. Palumbo, S. Bordiga, S. Svelle, K.-P. Lillerud, U. Olsbye, Topics in Catalysis 52 (2009) 218–228.
[86] L. Palumbo, F. Bonino, P. Beato, M. Bjorgen, A. Zecchina, S. Bordiga, The Journal of Physical Chemistry C 112 (2008) 9710–9716.

Paper 2

First principle kinetic studies of zeolite-catalyzed methylation reactions

Veronique Van Speybroeck, Jeroen Van der Mynsbrugge, Matthias Vandichel, Karen Hemelsoet, David Lesthaeghe, An Ghysels, Guy B. Marin and Michel Waroquier

Journal of the American Chemical Society, 2011, 133, 888 - 899

Copyright 2010 by the American Chemical Society.

JACS
JOURNAL OF THE AMERICAN CHEMICAL SOCIETY
ARTICLE
pubs.acs.org/JACS

First Principle Kinetic Studies of Zeolite-Catalyzed Methylation Reactions

Veronique Van Speybroeck,*[,†] Jeroen Van der Mynsbrugge,[†] Matthias Vandichel,[†] Karen Hemelsoet,[†] David Lesthaeghe,[†] An Ghysels,[†] Guy B. Marin,[‡] and Michel Waroquier[†]

[†]Center for Molecular Modeling (CMM), Ghent University, Technologiepark 903, 9052 Zwijnaarde, Belgium, and QCMM—Alliance, Ghent-Brussels, Belgium

[‡]Laboratory of Chemical Technology (LCT), Krijgslaan 281-S5, 9000 Gent, Belgium

Supporting Information

ABSTRACT: Methylations of ethene, propene, and butene by methanol over the acidic microporous H-ZSM-5 catalyst are studied by means of state of the art computational techniques, to derive Arrhenius plots and rate constants from first principles that can directly be compared with the experimental data. For these key elementary reactions in the methanol to hydrocarbons (MTH) process, direct kinetic data became available only recently [*J. Catal.* **2005**, *224*, 115−123; *J. Catal.* **2005**, *234*, 385−400]. At 350 °C, apparent activation energies of 103, 69, and 45 kJ/mol and rate constants of 2.6×10^{-4}, 4.5×10^{-3}, and 1.3×10^{-2} mol/(g h mbar) for ethene, propene, and butene were derived, giving following relative ratios for methylation $k_{ethene}/k_{propene}/k_{butene}$ = 1:17:50. In this work, rate constants including pre-exponential factors are calculated which give very good agreement with the experimental data: apparent activation energies of 94, 62, and 37 kJ/mol for ethene, propene, and butene are found, and relative ratios of methylation $k_{ethene}/k_{propene}/k_{butene}$ = 1:23:763. The entropies of gas phase alkenes are underestimated in the harmonic oscillator approximation due to the occurrence of internal rotations. These low vibrational modes were substituted by manually constructed partition functions. Overall, the absolute reaction rates can be calculated with near chemical accuracy, and qualitative trends are very well reproduced. In addition, the proposed scheme is computationally very efficient and constitutes significant progress in kinetic modeling of reactions in heterogeneous catalysis.

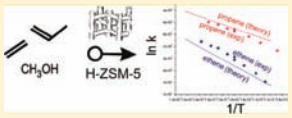

1. INTRODUCTION

Recently, the rate of alkene methylations by methanol in acidic nanoporous H-ZSM-5 were measured by Svelle and co-workers.[1,2] The ability of H-ZSM-5 to convert methanol to hydrocarbons (MTH) in the range C_2-C_{10} and water was already discovered in 1976. Other industrial processes, such as the conversion of methanol to gasoline (MTG) and methanol to olefins (MTO), also using other protonated zeolites have been developed since then. The MTO process is one of the most prominent technologies in the petrochemical industry to bypass crude oil as a fundamental feedstock which is very significant in view of the waning oil reserves. Methanol can be made from synthesis gas, which in turn can be formed from almost any gasifiable carbonaceous species, such as natural gas, coal, biomass, and waste. In all proposed reaction cycles for the MTO process, methylation reactions of various hydrocarbons have been shown to be key reaction steps of the process.[3−6] Depending on the topology and hydrocarbon species to be methylated, intrinsic barriers may vary between 60 and 180 kJ/mol and are non-negligible.[7,8] Also, other reactions required for olefin formation may be equally highly activated.[5,9] Nevertheless, understanding the methylation reactions of various alkenes is of utmost importance for the control of the MTO process; therefore, various efforts have been conducted to understand this elementary step both from experimental and theoretical points of view.[1,2,10,11]

The reaction mechanism responsible for the formation of hydrocarbons has been shown to be tremendously difficult to unravel.[12,13] Historically, direct mechanisms in which two methanol molecules couple to form the initial C−C bond were believed. For a while it seemed that there were multiple possibilities for direct conversion of methanol to ethene. In the late 1990s reasonable evidence was given by a variety of theoretical calculations for partial pathways of the direct mechanisms.[14] It is noteworthy that, despite the methodology used, there was a consensus that in the pre-equilibrium phase dimethylether and framework-bound methoxide groups were formed.[15] These pathways were facilitated by assisting molecules such as methanol or water, giving overall higher rate constants. However, when all of the individual reactions which were scattered through the literature were consistently combined, it was found that all direct mechanisms failed.[16] A complete overview of all theoretical contributions was given by some of the current authors.[17]

Currently, there is a consensus that an alternative hydrocarbon pool mechanism operates in which an organic reaction center in the zeolite pores acts as a cocatalyst.[13,18−21] Herein, certain hydrocarbons are stabilized in the pores of the zeolite, which undergo successive methylation steps by methanol and/or dimethylether and subsequently eliminate light olefins like ethene and propene. Combined experimental and theoretical studies have shown that the reaction rates are much higher compared to all direct mechanisms, provided the reaction intermediates are properly stabilized by the zeolite environment.[3,5]

At the same time, alkenes, which are important components in the product stream, may be methylated by methanol, once or several times,

Received: August 24, 2010
Published: December 23, 2010

 © 2010 American Chemical Society

thereby creating longer alkenes that are easily cracked to smaller alkenes that are again methylated.[22,23] Recent experimental results revived this old proposal of successive methylation and cracking reactions of C_3^+-alkenes, providing a parallel route for the production of light olefins in zeolite H-ZSM-5. It was proposed that in H-ZSM-5 ethene is formed solely from lower methylbenzenes, while propene and higher alkenes would be formed from alkene methylation and interconversion.[24]

In view of the importance of the methylation reactions for the above-mentioned industrial processes, experimental efforts have been conducted to directly measure the rate of methylation. The rate of alkene methylations is not easily monitored due to the occurrence of various side reactions such as alkene interconversions, not caused by methanol methylations. Various side reactions could eventually also lead to deactivation of the catalyst.[25] By utilizing a reaction system consisting of [^{13}C]methanol and [^{12}C]alkene, and choosing the conditions so that secondary reactions are inhibited, direct measurement of the rates of methylations was possible.[1,2] A very small amount of catalyst (2.5 mg) and extremely high reactant (mixture of methanol and short chain olefin) feed rate were used in their experiments, so that secondary reactions were limited. An interesting, yet other, approach to inhibit secondary reactions and to assess the influence of olefin homologations was followed by Song et al.[26,27] By usage of the smaller pore zeolite ZSM-22, these authors observed direct homologations of simple olefins such as ethene, propene, butene, and styrene. As the current contribution focuses on direct comparison with experimental kinetic data, we have chosen the results of Svelle et al. for the theoretical benchmarking.[1,2] The reaction order for the methylation of ethene to form propene has been found to be one with respect to ethene and zero with respect to methanol. This means that all sites are covered by methanol, and these supramolecular sites (zeolite + methanol) undergo a bimolecular reaction with ethene. Measurements have been carried out over an extended range of temperatures allowing the construction of an Arrhenius plot in the temperature range between 305 and 410 °C which covers realistic and practical MTH conditions. Although a lot of experimental studies are available on catalytic reactions in acidic zeolites, actual Arrhenius plots and rate constants that can be used to benchmark theoretical calculations are hard to find.[28−31] The above-mentioned experimental kinetic data are thus very valuable not only from the application side but also to benchmark theoretical kinetic models.

As experimental kinetic data on individual reactions are very hard to obtain, there is an ongoing quest to determine reaction rates from a theoretical point of view with high accuracy and in a computationally efficient manner. First principle determination of reaction rates would mean a huge step forward to understand complex reaction networks in heterogeneous catalysis. However, the accurate determination of reaction rates in zeolitic systems remains a challenge. A large amount of papers are available discussing various mechanistic aspects of catalytic reactions in porous materials, and reaction barriers are nowadays frequently reported, but the extension toward reaction rates that can directly be compared to experimental data is seldom made. Very recently, Svelle and co-workers showed that enthalpy barriers for individual reactions in heterogeneous catalysis could be calculated with near chemical accuracy.[10] These authors used a multistep approach that relies on a series of MP2 energy calculations on a variety of clusters of increasing size and on periodic DFT calculations which enable production of an approximate MP2 energy estimate of the system with periodic boundary conditions. This work of Svelle and co-workers can on its own be considered as a landmark paper. The proposed methodology is however computationally very demanding, and with current computational resources, it cannot be applied routinely on a large set of individual reaction steps. In addition to studying reaction networks in zeolites, pre-exponential factors are also needed, as are rate constants at operating conditions. Therefore, also the molecular partition functions are needed, which are determined by all possible atomic motions.[32] These quantities

Scheme 1. Methylation of Alkenes with Methanol

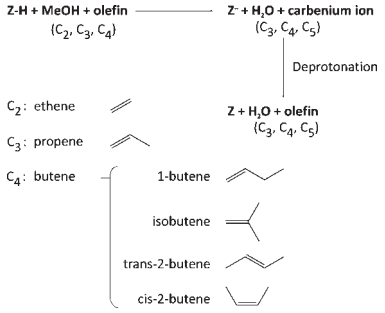

are mostly calculated in the harmonic oscillator (HO) approximation, which reaches its limits for large amplitude vibrations such as internal rotations, adsorption modes, and lattice vibrations. Within this approach, all motions of the guest molecules relative to the zeolite are considered to be frustrated, corresponding to an immobile adsorbate.[33] Recently, De Moor et al. showed that physisorption entropies of alkanes and alkenes could be calculated accurately if some of the low vibrational modes corresponding to translation and rotation of the adsorbate are replaced by "free" translation and rotation modes.[34]

In this paper, methylations of a series of alkenes (Scheme 1) with methanol are studied by means of state of the art computational techniques, to derive from first principles Arrhenius plots that can directly be compared with the experimental data as measured by Svelle and co-workers.[1,2] We have chosen methanol as a methylating agent to be able to compare decently with earlier theoretical studies. However, it cannot be excluded that dimethylether, which is in equilibrium with methanol at MTO reaction conditions, will also perform the methylation and will most probably be slightly more reactive.[35] All experimental kinetic data were referred to the adsorbed state of methanol and the olefin in the gas phase and are denoted as apparent kinetic data. (A general energy scheme for the methylation reactions under study is shown in Figure 1.) In view of this, it is of utmost importance to get a proper description of the adsorption energies. As shown by Svelle and co-workers for some of the reactions also considered in this paper, a proper account of nonbonding interactions is crucial to obtain a reliable prediction of these adsorption enthalpies.[10] Depending on the adsorbate, the corrections due to dispersive interactions range from 30 to 70 kJ/mol (for methanol and butene, respectively). The intrinsic kinetic data can be derived from these measured data by correcting for the olefin adsorption free energy. In earlier publications, we reported theoretically determined kinetics for various reactions relevant for the MTO process.[4−6,9,16,36] Those kinetic data were calculated in an intrinsic fashion, i.e., referred to the fully adsorbed prereactive complex. Due to an efficient canceling of errors in the fully adsorbed complex and transition state, the effect of dispersive interactions was assumed to be of less importance. However, when comparing theoretical rate constants with experimental data, the adsorption step cannot be neglected and van der Waals corrections should be accounted for.[4,10]

This is the approach followed in this paper: reaction rates are calculated that are directly comparable to experimental data. To the best of our knowledge, this it the first time such a comparison is conducted for elementary reactions in the MTO process. Only very recently Hansen et al. conducted a comparative study between experimental and theoretical Arrhenius plots for the alkylation of benzene.[37] The comparison in that study with experimental data was however less straightforward

Journal of the American Chemical Society ARTICLE

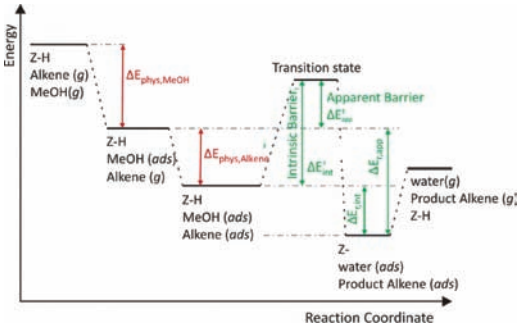

Figure 1. Energy diagram for methylation reaction of olefins in acidic zeolites.

as the mechanism of the reaction was not fully clear. When conducting such a comparative study between theoretical and experimental kinetic data, it is important to determine to what extent the theoretical data are able to capture the experimental trends and whether the HO approximation succeeds in describing the pre-exponential factor correctly.

Benchmarking between theoretical and experimental data can be performed by directly comparing absolute values for rate constants. This is often done by introducing a factor ($f_k = k_{theory}/k_{experiment}$) which is characteristic for the deviation between theory and experiment. This approach was followed for various reactions taking place in the gas phase, and a deviation of a factor of 10 ($0.1 \leq f_k \leq 10$) was generally accepted as "accurate".[38] In this paper we keep the same criterion to assign the label "kinetic accuracy". For gas phase reactions it has already been proven very difficult to achieve the kinetic accuracy.[38−41]

In addition to explicitly comparing theoretical and experimental Arrhenius plots, it is even more interesting to deduce correct qualitative trends. Interestingly, Svelle and co-workers report in a second paper kinetic studies on methylations of other alkenes such as propene and butene and determined the following ratios for the methylation of ethene, propene, and butene, $k_{ethene}:k_{propene}:k_{butene}$ = 1:17:50.[2] These ratios are based on apparent rate constants. The reproduction of these relative rate constants and qualitative trends is even more important than the quantitative reproduction of kinetic data. Before shifting to the actual discussion, the following point is worth mentioning: at 350 °C apparent activation energies of 103, 69, and 45 kJ/mol were measured for ethene, propene, and butene. (Apparent activation energies of 109 and 103 kJ/mol for the methylation of ethene were given in refs 1 and 2, respectively. Throughout this manuscript we used the value of 103 kJ/mol as it was also obtained by fitting a linear function to the measured values of the rate constants. The latter experimental values were provided by Dr. Svelle.) On the basis of these relative differences between the activation energies, the relative apparent rates of methylations (1:17:50) cannot be explained. Our results will show whether the entropic effects are able to capture the experimentally observed relative rates of methylation.

2. COMPUTATIONAL DETAILS

For various key reactions in the MTO process the effect of topology on the chemical kinetics was unambiguously proven to be of utmost importance both experimentally and theoretically.[3,26,42] Theoretically,, various methodologies can be adopted to account for the material's topology. In the work of Svelle and co-workers, periodic calculations were performed taking into account the entire H-ZSM-5 unit cell. In this work, all calculations were performed on a 46 T finite zeolite cluster cut out of the MFI crystallographic structure of ZSM-5.[3,43,44] From a computational technical point of view, the location of transition states and interpretation of the normal modes is substantially simpler in a cluster approach compared to a periodic approach.[45,46]

The active site was located at the T_{12} position[47] at the intersection of the straight and sinusoidal channels, which prevents any effects of transition-state-shape selectivity as also bigger molecules can be formed on this location. A recent combined experimental and theoretical study by Sklenak and co-workers showed that the actual distribution of aluminum in MFI is not random and is controlled by the actual conditions of the zeolite synthesis procedure.[48]

The outer hydrogen atoms of the cluster were constrained in space to prevent unphysical deformations due to the neglect of the full molecular environment. Structures for starting geometries were built using the in-house developed software package ZEOBUILDER.[49,50]

All stationary points and transition states were localized using the ONIOM(B3LYP/6-31+g(d):MNDO) method in which the high level is composed of an 8T cluster and the rest of the cluster is treated at the lower level using the Gaussian03 software.[51−53]

The true nature of the stationary points was confirmed by a normal-mode analysis, which yields only positive frequencies for all minima and only one negative frequency for each transition state. Starting from transition state geometries, the quasi-IRC approach allowed the product and reactant geometries to be acquired.[54] In the quasi-IRC approach the geometry of the transition state is slightly perturbed in the direction of the reactants and products. Subsequent full geometry optimizations yield the reactants and products directly linking the transition state.

Subsequently, single-point calculations at the ONIOM(B3LYP/6-31+g(d):HF/6-31+g(d)) level of theory were performed, which was first benchmarked by Solans-Monfort et al. and Fermann et al.[55,56] The current study provides additional evidence for the proposed methodology, provided dispersion effects are also accounted for. The energies were further refined by including van der Waals interactions at the B3LYP-D level of theory with the Orca software package.[57] This is a computationally adequate method to introduce dispersion interaction by adding

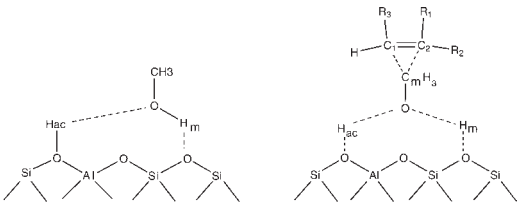

Figure 2. Schematic representation of methanol adsorbed in zeolite H-ZSM-5 and the transition state for methylation of ethene.

an empirical $-C_6R^{-6}$ correction to the energy obtained from the density functional theory calculations. This is called the DFT-D approach and provides high accuracy in a variety of simulations.[58−60] Using standard notation LOT-E//LOT-G (LOT-E and LOT-G being the electronic levels of theory used for the energetics and geometry optimizations, respectively), most of the results in this paper are obtained using the ONIOM(B3LYP/6-31+g(d):HF/6-31+g(d))-D//ONIOM(B3LYP/6-31+g(d):MNDO) level of theory. Further in this manuscript we will use the shorthand notation Cluster B3LYP-D for this method. However, to compare the energies obtained using the cluster methodology with those obtained in a periodic code,[10] also some single point calculations were performed using the Perdew−Burke−Ernzerhof (PBE) exchange-correlation functional.[61,62]

Another aspect which should be considered for the refinements of the single point energies are the errors caused by the usage of incomplete atomic basis sets, which is usually referred to as the basis set superposition error (BSSE). The most common method to remedy this effect is the usage of the counterpoise (CP) correction.[63−65] This method however usually overestimates the BSSE and is not applicable in the intramolecular case.[66] Within the context of the DFT-D approach it was suggested by Grimme not to apply the CP correction as long as properly polarized triple-ζ AO basis sets are employed.[60] We have additionally performed single point energy calculations using the 6-311++g(d,p) basis set and compared the results with the 6-31+g(d) basis set to assess the effect of the basis sets.

The 46T clusters are constrained by the outer hydrogen atoms to prevent unphysical deformation of the cluster during the geometry optimization, due to the neglect of the full material's environment. All other atoms were allowed to relax, so that the zeolite framework could fully adapt to the adsorbed species.

We used the partial Hessian vibrational analysis (PHVA) method for the frequency calculation as previously applied for kinetics by some of the authors.[67−71] Only the outer hydrogens which were used to saturate the cluster were given an infinite mass. This procedure is now implemented in an in-house developed software module TAMkin.[49,72]

Partition functions are calculated in the temperature range which is experimentally relevant (305 and 410 °C), and rate coefficients were obtained by using transition-state theory (TST). More details are outlined in section 3.3.2

3. RESULTS AND DISCUSSION

3.1. Adsorption of Methanol and Alkenes. The adsorption mode of methanol in ZSM-5 was already studied by various authors with a variety of theoretical techniques.[10,31,73,74] Therefore, we will only briefly summarize our results. A schematic representation of the adsorption mode of methanol is shown in Figure 2.

Table 1. Electronic Energies (kJ/mol) without Zero Point Energies (ZPE) of Various Consecutive Steps for the Methylation Reactions[a]

alkene	$\Delta E_{phys,MeOH}$	$\Delta E_{phys,alkene}$	$\Delta E_{int}^{\ddagger}$	$\Delta E_{r,int}$	$\Delta E_{app}^{\ddagger}$	$\Delta E_{r,app}$
	−97.27					
ethene		−10.35	84.03	28.58	73.68	18.18
propene		−33.38	74.72	21.79	41.34	−11.59
1-butene		−53.20	62.74	−125.51[b]	9.54	−178.71[b]
isobutene		−49.03	71.94	−35.69	22.91	−84.71
trans-2-butene		−53.84	71.49	11.86	17.65	−41.98
cis-2-butene		−53.54	63.95	−3.10	10.40	−56.64

[a] $\Delta E_{phys,MeOH}$, $\Delta E_{phys,alkene}$, $\Delta E_{int}^{\ddagger}$, $\Delta E_{r,int}$, $\Delta E_{app}^{\ddagger}$, and $\Delta E_{r,int}$ are the various energy contributions defined in Figure 1 and are calculated at the ONIOM(B3LYP/6-31+g(d):HF/6-31+g(d)) level of theory with inclusion of van der Waals corrections. [b] For 1-butene an oxonium ion was obtained which explains the large stabilization of the products.

Methanol is adsorbed end-on forming two hydrogen bonds, a strong one between the acidic proton and the methanol oxygen and another between the methanol hydroxyl proton and a zeolite oxygen. Earlier studies investigated the possible protonation of methanol, but the results showed that methanol exists in its neutral form.[73]

All experimentally determined kinetic data are referred to the adsorbed state of methanol; therefore, a discussion on the physisorption energy of methanol is warranted. An experimental study by Lee and co-workers determined differential heat of adsorption for a series of alcohols, nitriles, water, and diethyl ether in H-ZSM-5 and silicalite.[75] The experimental adsorption energy of methanol was determined to be -115 ± 5 kJ/mol (H-ZSM-5, Si/Al = 26) at 400 K. Our theoretical estimate for the adsorption enthalpy at 400 K amounts to −97 kJ/mol. This number includes a dispersive correction according to the Grimme scheme of −34 kJ/mol. As expected, the physisorption energies are too small without the van der Waals corrections. Depending on the topology and on the adsorbate the corrections may vary from −30 to −80 kJ/mol.[76,77]

The next step in the discussed methylation reactions is the coadsorption of the alkene molecule. For the calculation of the kinetics and the comparison with the experimental data, this state is less relevant, as all experimental data are referred to the state in which only methanol is adsorbed. For completeness we give our calculated values in Table 1 (column $\Delta E_{phys,alkene}$). These values include the dispersion corrections; a similar table without the van der Waals corrections is given in Table S.1 of the Supporting Information.

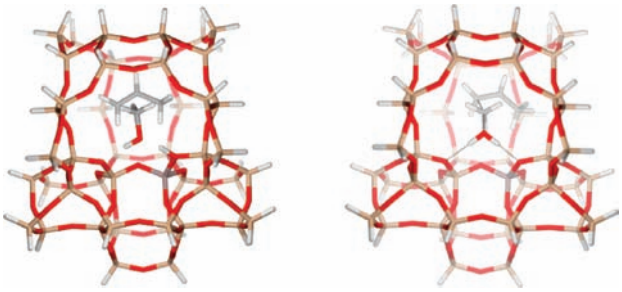

Figure 3. Reactant and transition state geometries for the methylation of propene.

DFT completely fails in describing these intermediates in which no specific interactions with methanol or the zeolite are involved. Without the dispersive corrections, the expected trend with respect to hydrocarbon size is not found, as all physisorption energies are more or less the same (18−25 kJ/mol).[78−80] With inclusion of the dispersion correction suggested by Grimme, the values become negative, and also the influence of the hydrocarbon number is present. No direct experimental values of the coadsorption energies of alkenes are available; only indirect comparisons can be made with adsorption energies in silicalite-1, the silicate version of ZSM-5.[81] For a more in-depth discussion we refer to Svelle et al.[10] Our adsorption energies even with inclusion of the dispersion term are about 20 kJ/mol smaller than the values given in the work of Svelle et al. which were obtained with the periodic PBE-D approach. This energy level in which the alkene is not directly interacting with the acidic site but rather with the surrounding zeolite wall and the methanol is expected to be most prone to errors due to our model as a large part of the zeolite wall is described at the lower level of theory in our two level cluster approach. However, for the further determination of the apparent reaction kinetics this state is not used anymore as will be discussed further.

3.2. Methylation Reactions. *Transition State Geometries.* In the transition state, methanol is protonated by the zeolite acidic proton (H_{ac} in Figure 2), the O−C methanol bond is significantly stretched, and a formal methyl cation leaves the methanol and moves toward the alkene double bond. Simultaneously, a water molecule is formed, which makes a hydrogen bond with an oxygen next to the aluminum site and another oxygen not directly connected to the aluminum defect. A schematic representation of the transition state is shown in Figure 2, and the transition state geometry for the methylation of propene is shown in Figure 3. The methyl group is transferred in a typical S_N2 type fashion through an umbrella-like inversion. For methylations of large polymethylbenzenes, transition-state-shape selectivity can become important as the zeolite cage cannot accommodate these undistorted S_N2-type transition states. In our case, where only small alkenes are studied, these effects were not seen.[3,74]

In order to obtain more insight into the geometries of the transition states for the series of studied alkenes, some critical distances are tabulated in Table S.2 of the Supporting Information. The atom labeling scheme is given in Figure 2. For the substituted alkenes, the attack mode of the methyl cation toward the double bond is unsymmetrical. The methyl cation attacks the less substituted carbon of the double bond to form secondary or tertiary carbenium ions. Alternatively, the transition state occurs via a protonated cyclopropyl species (PCP), which was the case for ethene. For ethene and trans-2-butene in which the alkene double bond is symmetrically substituted, the methyl group is again almost symmetrically located between the double bond (this can be verified by comparing the C_m-C_1 and C_m-C_2 distances).

Products. The immediate products of the methylation reactions are carbenium ions and water (Scheme 1). The former ions are quickly deprotonated in a second step to form the neutral alkenes. In the case of propene, 1-butene, *trans*-2-butene, and *cis*-2-butene secondary carbenium ions are formed, whereas for isobutene a tertiary carbenium ion is formed. There have been many discussions on the existence of such cations in zeolites.[82−84] Also, theoretically no definite answer was obtained as the stabilization of the carbenium ions is also determined by the electrostatic interactions and dispersion interactions with the rest of the framework. These factors were up to recently not properly accounted for in many theoretical models. More recently, Sauer and co-workers showed that the stability of carbenium ions is also largely determined by entropic contributions.[76,85] In this study, the presence of water appeared to have a dual effect on the existence of cationic species. On one hand, the water molecule functions as a wedge that separates the cation and the cluster. The strong hydrogen bond interactions between the water molecule and the cluster lower the proton affinity of the latter, which reduces the probability of deprotonation. On the other hand, when the positive charge of the carbenium ion is not efficiently shielded from the water molecule, a much more stable oxonium ion is formed. This effect was observed in the case of 1-butene, in which we did not succeed in locating the stationary point corresponding with the carbenium ion. In the cases where the carbenium ions could be located as stable minima, the geometry points out that these species are elusive (e.g., sharp $C_1C_2C_{methanol}$ angles are found (around 75°)). Consequently, the following deprotonations to form the neutral species are very fast reaction steps, with reaction barriers on the order of 5−10 kJ/mol.[3] Detailed reaction schemes are given in Figure S.1 of the Supporting Information.

In the case of methylation of ethene, a protonated cyclopropane species is formed, which is a stable minimum on the

Table 2. Comparison between Various Methodologies for the Calculation of Apparent Barriers for Methylation Reactions

apparent barriers (kJ/mol)	ethene	propene	*trans*-2-butene
periodic PBE-D[a]	75.0	40.0	12.0
Cluster B3LYP- D[b]	73.7	41.3	17.7
Cluster PBE- D[c]	65.2	27.6	17.2
eomposite method[d]	94.0	66.7	37.9
experiment[e]	94.0	54.0	30.0

[a] Values taken from Svelle et al. [10] [b] Cluster B3LYP- D is a shorthand notation for Cluster ONIOM(B3lyp/6-31+G(d):HF/6-31+G(d)). [c] Cluster PBE- D is a shorthand notation for Cluster ONIOM(PBE/6-31+G(d):HF/6-31+G(d)). [d] Composite method referred as final energy barrier in Table 6 of Svelle et al.[10] [e] Estimated from experimental enthalpies (refs 1 and 2) by subtracting zero point energies and finite temperature corrections.

potential energy surface.[36] This species is also an elusive intermediate, which can also be deduced from geometrical parameters (e.g., the C_1-C_{ml} and C_2-C_m distances amount to 1.68 and 1.81 Å). Various scans were performed to simulate direct deprotonation of this species to form the neutral alkene, but they all resulted in the formation of a primary propoxide first which then deprotonates. The formation of various alkoxides from olefins and the reverse step which is relevant here was already studied using the same methodology in ref 36. Also, in earlier studies no primary propyl cation could be found, and it was concluded that only the corner-protonated cyclopropane cation and the secondary propyl cation exist as stable minima on the potential energy suface.[11,86]

3.3. Chemical Kinetics . *3.3.1. Electronic Energies.* Table 1 gives an overview of the electronic energies of various consecutive steps for the methylation reactions defined in Figure 1. Similar values but without inclusion of dispersion are given in Table S.1 of the Supporting Information. In addition, Table 2 gives selected values for the apparent energy barriers as published in Svelle et al. together with some of our values.[10] A more complete table with all our values including those without dispersion and including values obtained with other basis sets is given in Table S.3 of the Supporting Information.

The apparent barriers without inclusion of the van der Waals dispersion term do not show the correct qualitative trend (Table S.1). In the series ethene, propene, 1-butene, isobutene, *trans*-2-butene, and *cis*-2-butene all barriers are in the same order of magnitude (125, 112, 100, 111, 110, and 102 kJ/mol). Introduction of the dispersion term allows differentiating between the activation barriers of the various alkenes, giving values of 74, 41, 10, 23, 18, 10 kJ/mol for the aforementioned series of alkenes.

Another interesting feature concerns the van der Waals influence on the intrinsic barriers and intrinsic reaction energies which turn out to be less affected by the dispersion effects than the apparent barriers. The van der Waals corrections are much more uniform along the reaction coordinate when starting from the complex in which all reactants are already adsorbed. This gives a substantial canceling of errors giving intrinsic barriers which are less affected by the dispersion term. This effect is independent of the system under study, since only small changes of 10 kJ/mol were also observed for intrinsic reaction barriers for a variety of reactions involving methylbenzenes.[6,9]

It is now interesting to compare our cluster calculations with the earlier obtained periodic results on some of the reactions considered here (Table 2). Table 2 also includes the "final energy barriers" from ref10 which were obtained using a composite method that accounts for both the long-range correlation effects and the effects of the topology in a very systematic way.

Our DFT-D results obtained from large cluster calculations (46T) are remarkably close to the periodic PBE calculations with dispersion correction (periodic PBE-D compared to Cluster B3LYP-D). The periodic PBE-D prediction for the apparent barriers for methylation of ethene, propene, and *trans*-2-butene are, respectively, 75, 40, and 12 kJ/mol and almost coincide with those obtained with the Cluster B3LYP-D calculations of this work, 74, 41, and 18 kJ/mol. The PBE results obtained with our cluster and small basis set, and including dispersion corrections (Cluster PBE-D), give 65 kJ/mol for the apparent barrier for the methylation of ethene. This value is slightly smaller than the corresponding B3LYP value. This underestimation even with the inclusion of the semiempirical correction for dispersion is typical for GGA-type functionals and PBE in particular.[87] Some additional calculations were performed to test the sensitivity of the barriers with respect to basis set and functional (Table S.3 of SI). These results show that the apparent barriers are only moderately dependent on the basis set. These results give evidence that the size of our cluster is sufficiently large to mimic the periodic limit results.

All previous barriers are still about 20 kJ/mol lower than the barriers obtained with the composite method of ref 10. The composite method goes toward the benchmark values in a very systematic way but is also computationally much more expensive. Overall, the results for the methylation of propene and *trans*-2-butene with the other basis sets and functionals show that the overall qualtitative trend remains the same irrespective of the level of theory used for the single point energy calculations. Therefore, the here proposed Cluster B3LYP-D method is a reasonable compromise between accuracy and computational efficiency.

3.3.2. Reaction Rate Constants. Before discussing the differences in reaction rate constants for the various alkenes, we first describe the methodology used to compare the theoretically determined rate constants with the experimental data for the methylation of ethene. For this reaction, the reaction conditions were controlled in such a way to make the methylation of ethene the most prominent reaction, and thus, the rate of methylation could be measured. It was found that the reaction is zero order with respect to methanol and first order with respect to ethene and could be described by the following kinetic equation:[1,2]

$$r = k\, p^{0}_{\text{methanol}}\, p^{1}_{\text{ethene}} \qquad (1)$$

with p_{methanol} and p_{ethene} as the partial pressures of methanol and ethene, respectively.

It was found that the rate of formation of clean methylation product is 0.013 mol/ (g_{catalyst} h) at 350 °C. With a partial pressure of 50 mbar of ethene this gives a rate constant k of 2.6×10^{-4} mol/(g_{catalyst} h mbar). The experimentally found zero- and first-order behavior with respect to methanol and ethene means that, in the observed experimental range, methanol is adsorbed on all acid sites and ethene is extremely sparsely adsorbed. [We also calculated the adsorption terms for methanol which are normally figuring in a typical Langmuir–Hinshelwood–Hougen–Watson (LHHW) kinetic equation. The results confirmed that the proposed kinetic equation (eq 1) is a very good description of the here described reaction mechanism.]. It was noted that this rate equation may break down when $p_{\text{methanol}} \ll 20$mbar

Table 3. Activation Energies, Pre-Exponential Factors, and Rate Constants for the Methylation Reactions

	with dispersion						
	unimolecular			bimolecular			
	A (1/s)	E_a (kJ/mol)	k (350 °C) (1/s)	A (m^3/mol/s)	E_a (kJ/mol)	k (350 °C) (m^3/mol/s)	exptl[c] $E_{a,exp}$ (350 °C)
ethene	1.1×10^{11}	86.9	5.5×10^{5}	9.1×10^{5}	94.1	1.2×10^{-2}	103
propene	6.4×10^{11}	77.7	2.0×10^{5}	4.3×10^{4}	62.0	2.7×10^{-1}	69
1-butene	8.3×10^{11}	65.4	2.8×10^{6}	9.8×10^{3} (2.4×10^{3})[b]	30.5 (29.5)	2.7×10^{1} (7.9 10°) [b]	
iso-butene	2.2×10^{12}	75.3	1.1×10^{6}	2.9×10^{4} (2.0×10^{4}) [b]	44.4 (44.2)	5.5 10° (3.9 10°) [b]	
trans-2-butene	5.8×10^{11}	75.2	2.9×10^{5}	6.6×10^{3} (2.6×10^{3}) [b]	39.3 (39.5)	3.4 10° (1.3 10°) [b]	
cis-2-butene	8.9×10^{11}	67.1	2.1×10^{6}	1.1×10^{4} (2.7×10^{4}) [b]	31.5 (34.0)	2.6×10^{1} (3.8×10^{1}) [b]	
butene(av)[a]			1.6×10^{6}		36.4 (36.8)	1.6×10^{1} (1.3×10^{1}) [b]	45
butene(dist)[a]			1.2×10^{6}			1.4×10^{1} (1.7×10^{1}) [b]	
$k_{propene}/k_{ethene}$			36			23	17
$k_{butene(av)}/k_{ethene}$			283			1307 (763)	50
$k_{butene(dist)}/k_{ethene}$			225			1197 (898)	

[a] Butene(average) is obtained by taking an average of the rate constants of the various isomers; butene(distribution) is obtained by using eq 3. [b] Values between parentheses are obtained by replacing the harmonic oscillator partition functions of internal rotors in the gas phase molecules with manually constructed partition function using the 1D-HR approximation. [c] Values taken from ref 2.

and when $p_{ethene} \gg$ 100mbar. For the methylations of propene and butene rate constants of 4.5×10^{-3} mol/(g h mbar) and 1.3×10^{-2} mol/(g h mbar) were found at 350 °C giving following relative ratios for methylation k_{ethene}:$k_{propene}$:k_{butene} = 1:17:50.

Theoretically, the rate constants can be modeled using various methodologies. A first procedure involves the calculation of unimolecular reaction rates, in which the entire supramolecular complex (cage + contents) is handled as a single molecule. In our case, the reactant level would correspond to the zeolite cluster with one acidic site, on which both methanol and ethene are physisorbed (referred as Z-H, MeOH(ads), Alkene(ads) in Figure 1). These reaction rates then have units of 1/s and are not directly comparable to the experimentally determined rates but are very useful when evaluating qualitative differences between various competitive reactions in a reaction cycle. This was the procedure that was used in earlier work of some of the authors.[4−6,9,36] We will refer to these rates as intrinsic reaction rates.

To obtain rates which are directly comparable to the observed experimental data, the theoretical rates should be determined from a reactant level in which only methanol is physisorbed (referred as Z-H, MeOH(ads), Alkene(g) in Figure 1). In this case, bimolecular transition state theory should be applied giving a rate constant which is given by the following formula:

$$k_{Z-H,\,MeOH(ads),\,Alkene(g)} = \frac{k_B T}{h} \frac{q_{TS}^{\ddagger}}{q_{Z-H,\,MeOH(ads)} q_{Alkene(g)}} \exp(-\Delta E_{app}^{\ddagger}/RT) \quad (2)$$

As our calculations are performed on a 46T cluster with one acidic site, the obtained rate constant are normalized per active site. Experimentally, the rates are given per gram catalyst. Our values can be converted to the experimentally observed values by taking into account the Si/Al ratio. For the H-ZSM-5 sample used in the experiments the Si/Al ratio was 45, giving 2.21×10^{20} active sites per gram catalyst.

Table 3 gives an overview of the activation energies, pre-exponential factors, and rate constants for the methylations of ethene, propene, and butene calculated both in an unimolecular and bimolecular fashion and with inclusion of van der Waals corrections. The values without taking into account van der Waals corrections are given in Table S.4 of the Supporting Information. The final values of the activation energies and pre-exponential factors are obtained by fitting a linear function through the values of $k(T)$ obtained at different temperatures within the temperature interval 300−450 °C. Alternatively, the kinetic parameters could be obtained by using the so-called thermodynamic approach in which the activation energy is given by the standard enthalpy of activation plus $2 \times RT$ for a bimolecular reaction. This was the approach followed in ref 10 and for sake of comparison we also calculated for the methylation of ethene the kinetic parameters using this approach. These data are taken up in Table S.5 of the Supporting Information. Comparison between the fitted Arrhenius parameters and the thermodynamically derived Arrhenius parameters shows that both approaches give nearly identical values provided the correct thermal corrections to the enthalpy barrier which are derived from the vibrational motion are taken into account.

For butene, several isomers can contribute in various amounts to the experimentally observed rate. The most simple solution to account for the various isomers is to take an average of the calculated rate constants of 1-butene, *trans*-2-butene, isobutene, and *cis*-2-butene. Alternately, a distribution of various butenes can be used along the lines explained in refs 1,2. In that experimental work 0.013 mbar [^{12}C] butene and 50 mbar [^{13}C] methanol were coreacted at 350 °C over 2.5 mg of H-ZSM-5 catalyst. 2-Butanol was taken as the butene precursor, which is instantaneously transformed into water and linear butenes. In order to have an idea of the distribution of the various butene isomers, the butene conversion was studied at the same experimental conditions as during the methylation experiment but without the methanol cofeed. At the reaction conditions of methylation 16% of the linear butenes (originating from 2-butanol) were converted into fractions of isobutene (30%),

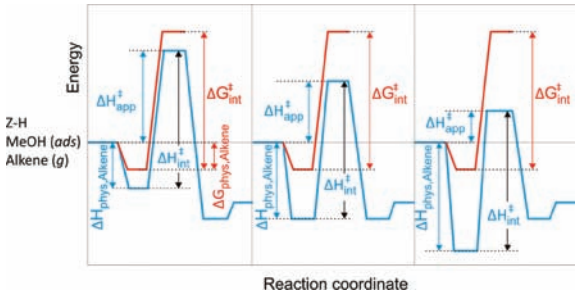

Figure 4. Schematic illustration of the change in the apparent standard enthalpy of activation ($\Delta H^{\ddagger}_{app}$) as the adsorption enthalpy ($\Delta H_{phys.alkene}$, blue curve) increases, whereas the intrinsic standard enthalpy of activation ($\Delta H^{\ddagger}_{int}$) and the free energy of activation ($\Delta G^{\ddagger}_{int}$) are held constant. Also, the free energy of adsorption $\Delta G_{phys.alkene}$ and free energy of activation $\Delta G^{\ddagger}_{int}$ are shown (red curve).

propene (30%), and pentene (31%). Accordingly the distribution of butenes can be written as follows:

$$C_{butene} = 0.84 \times (C_{lin\text{-}butenes}) + 0.16 \times (0.30 \times C_{propene} + 0.30 \times C_{isobutene} + 0.31 \times C_{pentene})$$

The various contributions to the linear butenes was estimated by calculating the corresponding equilibrium constants. This finally yields the following expression for the distribution of butenes:

$$C_{butene} = 0.476 \times C_{trans\text{-}2\text{-}butene} + 0.066 \times C_{1\text{-}butene} + 0.404 \times C_{cis\text{-}2\text{-}butene} + 0.054 \times C_{isobutene} \quad (3)$$

Both values are taken up in Table 3 indicated by butene-(averaged) and butene(distribution). Instead of using the arithmetic mean as used here, also the approach suggested by Alberty could have been used in which the total molecular partition function of the isomer group is approximated as the sum of the partition functions of the individual isomers.[88] The results in Table 3 show that the detailed approach of the butene isomers only marginally affects the final kinetic results for butene. Therefore, the approach of Alberty was not explicitly considered here.

Although the unimolecular reaction rates cannot be directly compared to experimental rates, it is interesting to note that the increase in methylation rate of butene versus ethene and propene versus ethene is in quite good agreement with the experimental determined qualtitative trend ($k_{propene}/k_{ethene}$ = 34 and $k_{butene(dist)}/k_{ethene}$ = 89 without van der Waals corrections and $k_{propene}/k_{ethene}$ = 36 and $k_{butene(dist)}/k_{ethene}$ = 225 with van der Waals correction). Also, without van der Waals corrections the relative ratios are of the correct order of magnitude, which is probably ascribed to a compensation of errors along the reaction path. This conclusion cannot be generalized as it depends largely on the reactive species that need to be adsorbed during the reaction cycle.

Experimentally the apparent activation energies were determined as 103, 69, and 45 kJ/mol for ethene, propene, and butene at 350 °C. Our theoretical estimates (with van der Waals corrections) are in very good agreement with the experimentally determined values giving activation energies of 94, 62, and 36 kJ/mol. The activation energies without the van der Waals corrections are largely overshot, due to neglect of dispersion interaction, which is more pronounced for the larger alkenes (see Table S.4). In conclusion, the qualitative behavior in methylation rate constants between the various alkenes is not correctly described without taking into account the dispersion correction. According to this calculation scheme the methylation of ethene would be the fastest. As here the transition state is referred to the state into which only methanol is adsorbed and a gas phase alkene [Z-H, MeOH(ads), Alkene(g)] the compensation of errors mentioned for the intrinsic barriers does not hold.

The overall rate is determined by both the activation energy and pre-exponential factor. Whereas the activation energy systematically decreases when going to longer alkenes giving rise to an increase in the rate, the pre-exponential factor also decreases inducing an opposite effect on the rate constant. For the intrinsic pre-exponential factors this trend is not observed and the values are on the same order of magnitude along the whole series of alkenes. These observations are in line with the so-called "compensation effect", which has been the subject of a lot of debate.[89,90] For the reactivity of alkane cracking reactions, it was shown that the true activation energy is virtually invariant with the alkane chain length, despite the rapid decrease in the apparent activation energy.[91] This effect is ascribed to a stronger adsorption (increase in the absolute value of the enthalpy of adsorption) with longer chain length, due to additional stronger van der Waals interactions of additional methylene groups. At the same time a stronger adsorption leads to a higher entropy loss (lower adsorption entropy) compared to the gas phase as fewer conformations are possible.

This leads to a compensation of both effects in the total free energy of adsorption.[78] This compensation effect on the overall reaction kinetics is illustrated in Figure 4 assuming that the intrinsic free energy of activation remains constant. As the adsorption enthalpy becomes larger, the apparent activation energy decreases but the free energy of adsorption remains nearly constant due to the compensating entropy effect. Such compensation effects were demonstrated computationally by Smit et al. by means of Monte Carlo simulations of free energies of adsorption and also experimentally by adsorption studies.[80,89,92−97] Also noteworthy is the experimental paper by Van Santen and

co-workers, who were able to explicitly determine entropic and enthalpic effects for the n-hexane hydroisomerization on a variety of different zeolites and also clearly observe a compensation effect.[98]

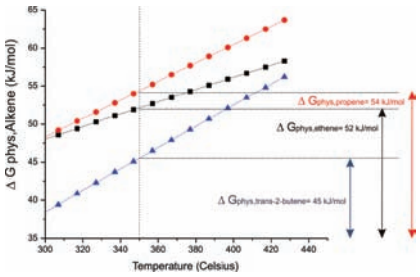

Figure 5. $\Delta G_{phys,alkene}$ for ethene, propene, and *trans*-2-butene.

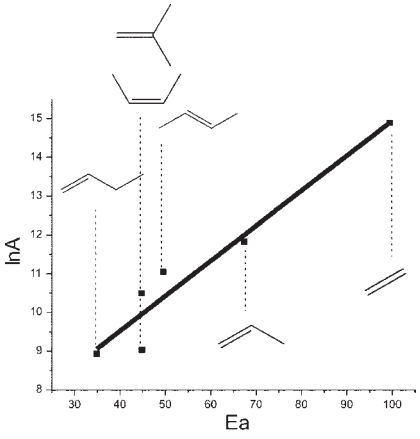

Figure 6. Constable plot (ln A versus *E*a) for the studied methylation reactions (R^2 value = 0.9322).

The values for the enthalpy, entropy, and free energy of adsorption in our case are given in Table S.6 of the Supporting Information within the temperature interval 300−450 °C. In addition, the free energy of adsorption ($\Delta G_{phys,alkene}$) is plotted for ethene, propene, and *trans*-2-butene in Figure 5. Our values show that for ethene and propene compensation is almost complete at the temperature of 350 °C whereas for trans-2-butene only a partial compensation of entropy and enthalpy contributions occurs for the here studied reactions.

This can also be deduced from rate eq 2: The reacting gas phase molecules have more degrees of freedom as the carbon number increases and the denominator in eq 2 becomes larger, giving an overall decrease in the pre-exponential factor. Thus, for the studied reactions, a positive compensation between the pre-exponential factor and activation energy is found. The associated plot of ln A versus E_a is shown in Figure 6. Such a linear dependency between the pre-exponential factor and activation energy is often referred to as the Cremer−Constable relation.[89]

Apart from the compensation effect which is dependent on the alkene chain length, also the diffusion properties might affect the experimentally determined reaction rates. It can be anticipated that diffusion limitations become more important for longer alkenes. Such effects are not accounted for in the estimated rates of this paper, which implies that our rates are somewhat overestimated. For butene such diffusion effects might start to play a role. The calculation, however, of the diffusion correction is beyond the scope of this paper.[92]

Within the calculation scheme with van der Waals corrections, the following relative ratios for methylations (k_{ethene}:$k_{propene}$:k_{butene}) are found, 1:23:1197, which are already in quite good agreement with the experimental values (1:17:50). These relative ratios can however be refined by treating some of the low vibrational modes of the gas phase molecules in a more appropriate way than the standard HO approximation. These internal rotations are more accurately described within the 1D-HR approach. It is now generally accepted that the entropy of gas phase molecules with a substantial amount of flexibility is underestimated in the harmonic oscillator approximation.[99−101] For propene such an approach is less relevant as only the methyl rotor is present in the molecule. The treatment of this motion beyond the harmonic oscillator approximation hardly affects the entropy of the molecule. For the various isomers of butene, however, internal rotations may affect the value of the molecular partition function substantially. For each of these motions, a relaxed rotational potential energy scan was determined, which then served as an input for the calculation of the hindered rotor partition function as explained in ref 99. An overview of the low amplitude motions that have been treated within the 1D-HR

Table 4. Comparative Table between Theoretical and Experimental Values[a]

	theory			experiment[b]			
	A	E_a	k(350 °C)	A	E_a	k(350 °C)	$k_{theory}/k_{experiment}$
ethene	1.3×10^4	94.1	1.7×10^{-4}	1.2×10^5	103	2.6×10^{-4}	0.7
propene	6.3×10^2	62.0	3.9×10^{-3}	2.0×10^3	69	4.5×10^{-3}	0.9
butene	2.0×10^2	36.8	2.4×10^{-1}		45	1.3×10^{-2}	18.1

[a] Values of k are given in units of mol/(g h mbar). The original theoretical rate constant in units of m^3/mol/s is converted by applying a factor of 0.0146 at 350 °C. The pre-exponential factor for butene is not given as substantial deviations from linearity were obtained. The apparent activation of energy of 45 kJ/mol for butene was obtained by linear fitting in the temperature range 295−400° C in which the methylation reaction is closest to first order with respect to the alkene pressure and zero order with respect to methanol. [b] Values taken from ref 2.

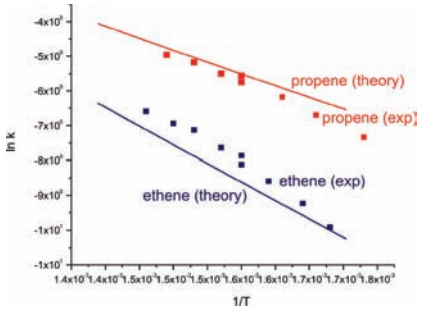

Figure 7. Theoretically and experimentally determined Arrhenius plots.

approximation for 1-butene and the associated rotational potential for the ethylene rotation is given in Figure S.2 of the Supporting Information. For 1-butene the largest correction is found giving an increase of the gas phase partition function of about 3 or an increase of the entropy at 298.15 K of about 10 J/(mol K). For the other isomers the corrections are much smaller, as again only methyl rotations are involved. These refinements give the following relative ratios for methylations of alkenes k_{ethene}:$k_{propene}$:k_{butene} = 1:23:898, which agree better with the experimental values.

Finally, it is interesting to compare the absolute experimental rates with the theoretical predictions (Table 4). Our theoretical estimates of the reaction rates are very close to the experimentally observed values and reach "kinetic accuracy" for ethene and propene. For butene the theoretical value is slightly overestimated ($k_{theory}/k_{experiment}$ = 18). Also, experimentally those values were prone to more uncertainty as substantial deviations from linearity were observed. Both the experimental and theoretical determined Arrhenius plots are shown in Figure 7. Given the complexity of the systems treated here, the agreement between theory and experiment is truly outstanding. This is a huge step forward for theoretical predictions of zeolite-catalyzed reactions. As the scheme is computationally also very attractive, it is thus feasible to predict with high accuracy rates of individual reactions in complex reaction networks.

4. CONCLUSIONS

In this paper, reaction rates of methylation of ethene, propene, and butene by methanol over the acidic microporous H-ZSM-5 catalyst were studied by means of various computational methologies. The reactions are important for a variety of industrial processes such as MTH, MTG, and MTO. Monitoring rates of individual reactions is experimentally very difficult due to the occurrence of various side reactions. For the title reactions accurate experimental rates are available, and therefore, they are ideally suited to benchmark theoretical methodologies. The topology of the material was taken into account by a cluster approach in which a finite cluster was cut from the periodic materials structure. Dispersive interactions have been found to be very important to describe accurately the adsorbed states and thus also to describe "apparent kinetics".

The activation energies have been found to be in excellent agreement with the experimentally derived values and reach the level of "chemical accuracy" (deviations between 0 and 10 kJ/mol).

The relative rates of methylation among various alkenes have been found in excellent agreement with the experimental values, especially after accounting for the full flexibility of the gas phase alkenes using internal rotors.

The absolute values of the rate constants are very close to the experimental values and reach "kinetic accuracy" (deviations of less than a factor 10). The proposed method is computationally very attractive and can be applied routinely to reaction cycles applicable in heterogeneous catalysis. This is a huge step forward for theoretical predictions of zeolite-catalyzed reactions, and it shows that theoretical methods are a viable alternative to estimate kinetics of elementary reactions that cannot easily be monitored experimentally. With respect to this particular type of reaction studied here, it might be interesting to study also other topologies such as ZSM-22 for which experimental homologation reactions without side reactions were observed due to the limited pore size of this particular zeolite.[102] Also, the influence of other methylating agents such as dimethylether might be interesting for future research.

■ ASSOCIATED CONTENT

Supporting Information. Complete ref 51; electronic energies (kJ/mol) of various consecutive steps for the methylation reactions without dispersion corrections, negative frequencies, and some critical distances of transition state geometries for methylations of various alkenes; comparison between various methodologies for the calculation of apparent barriers for methylation reactions; activation energies, pre-exponential factors, and rate constants for the methylation reactions without dispersion; Arrhenius parameters according to the thermodynamic approach for the methylation of ethene; adsorption enthalpies, entropies, and free energies for ethene, propene, and *trans*-2-butene (in kJ/mol); reaction schemes for methylations of various alkenes; overview of the low amplitude motions that have been treated within the 1D-HR approximation for 1-butene and the associated rotational potential for the ethylene rotation; absolute energies (in Hartrees) and optimized geometries in Cartesian coordinates of all calculated structures. This material is available free of charge via the Internet at http://pubs.acs.org.

■ AUTHOR INFORMATION

Corresponding Author
Veronique.vanspeybroeck@ugent.be

■ ACKNOWLEDGMENT

This work is supported by the Fund for Scientific Research—Flanders (FWO), the Research Board of Ghent University (BOF), and BELSPO in the frame of IAP/6/27. Funding was also received from the European Research Council under the European Community's Seventh Framework Programme [FP7(2007-2013) ERC grant agreement number 240483]. We would like to thank J. Sauer (Humboldt-Universität zu Berlin, Institüt fur Chemie, Berlin) for fruitful discussions and S. Svelle (inGAP Center of Research Based Innovation, Department of Chemistry, University of Oslo) for providing us with the raw experimental data that were published in refs 1 and 2.

REFERENCES

(1) Svelle, S.; Ronning, P. A.; Kolboe, S. *J. Catal.* **2004,** *224*, 115–123.
(2) Svelle, S.; Ronning, P. O.; Olsbye, U.; Kolboe, S. *J. Catal.* **2005,** *234*, 385–400.
(3) Lesthaeghe, D.; De Sterck, B.; Van Speybroeck, V.; Marin, G. B.; Waroquier, M. *Angew. Chem., Int. Ed.* **2007,** *46*, 1311–1314.
(4) Lesthaeghe, D.; Van der Mynsbrugge, J.; Vandichel, M.; Waroquier, M.; Van Speybroeck, V. *ChemCatChem* **2010**, DOI: 10.1002/cctc.201000286.
(5) McCann, D. M.; Lesthaeghe, D.; Kletnieks, P. W.; Guenther, D. R.; Hayman, M. J.; Van Speybroeck, V.; Waroquier, M.; Haw, J. F. *Angew. Chem., Int. Ed.* **2008,** *47*, 5179–5182.
(6) Hemelsoet, K.; Nollet, A.; Vandichel, M.; Lesthaeghe, D.; Van Speybroeck, V.; Waroquier, M. *ChemCatChem* **2009,** *1*, 373–378.
(7) Bjorgen, M. *J. Catal.* **2010,** *275*, 170–180.
(8) Bjorgen, M.; Olsbye, U.; Petersen, D.; Kolboe, S. *J. Catal.* **2004,** *221*, 1–10.
(9) Lesthaeghe, D.; Horre, A.; Waroquier, M.; Marin, G. B.; Van Speybroeck, V. *Chem.—Eur. J.* **2009,** *15*, 10803–10808.
(10) Svelle, S.; Tuma, C.; Rozanska, X.; Kerber, T.; Sauer, J. *J. Am. Chem. Soc.* **2009,** *131*, 816–825.
(11) Svelle, S.; Arstad, B.; Kolboe, S.; Swang, O. *J. Phys. Chem. B* **2003,** *107*, 9281–9289.
(12) Stocker, M. *Microporous Mesoporous Mater.* **1999,** *29*, 3–48.
(13) Song, W. G.; Marcus, D. M.; Fu, H.; Ehresmann, J. O.; Haw, J. F. *J. Am. Chem. Soc.* **2002,** *124*, 3844–3845.
(14) Blaszkowski, S. R.; vanSanten, R. A. *J. Am. Chem. Soc.* **1997,** *119*, 5020–5027.
(15) Blaszkowski, S. R.; vanSanten, R. A. *J. Phys. Chem. B* **1997,** *101*, 2292–2305.
(16) Lesthaeghe, D.; Van Speybroeck, V.; Marin, G. B.; Waroquier, M. *Angew. Chem., Int. Ed.* **2006,** *45*, 1714–1719.
(17) Lesthaeghe, D.; Van Speybroeck, V.; Marin, G. B.; Waroquier, M. *Ind. Eng. Chem. Res.* **2007,** *46*, 8832–8838.
(18) Haw, J. F.; Song, W. G.; Marcus, D. M.; Nicholas, J. B. *Acc. Chem. Res.* **2003,** *36*, 317–326.
(19) Dahl, I. M.; Kolboe, S. *Catal. Lett.* **1993,** *20*, 329–336.
(20) Dahl, I. M.; Kolboe, S. *J. Catal.* **1994,** *149*, 458–464.
(21) Dahl, I. M.; Kolboe, S. *J. Catal.* **1996,** *161*, 304–309.
(22) Dessau, R. M. *J. Catal.* **1986,** *99*, 111–116.
(23) Dessau, R. M.; Lapierre, R. B. *J. Catal.* **1982,** *78*, 136–141.
(24) Svelle, S.; Joensen, F.; Nerlov, J.; Olsbye, U.; Lillerud, K. P.; Kolboe, S.; Bjorgen, M. *J. Am. Chem. Soc.* **2006,** *128*, 14770–14771.
(25) Mores, D.; Stavitski, E.; Kox, M. H. F.; Kornatowski, J.; Olsbye, U.; Weckhuysen, B. M. *Chem.—Eur. J.* **2008,** *14*, 11320–11327.
(26) Cui, Z. M.; Liu, Q.; Song, W. G.; Wan, L. J. *Angew. Chem., Int. Ed.* **2006,** *45*, 6512–6515.
(27) Cui, Z. M.; Liu, Q.; Ma, Z.; Bian, S. W.; Song, W. G. *J. Catal.* **2008,** *258*, 83–86.
(28) Vos, A. M.; De Proft, F.; Schoonheydt, R. A.; Geerlings, P. *Chem. Commun.* **2001,** 1108–1109.
(29) Vos, A. M.; Nulens, K. H. L.; De Proft, F.; Schoonheydt, R. A.; Geerlings, P. *J. Phys. Chem. B* **2002,** *106*, 2026–2034.
(30) Vos, A. M.; Schoonheydt, R. A.; De Proft, F.; Geerlings, P. *J. Phys. Chem. B* **2003,** *107*, 2001–2008.
(31) Vos, A. M.; Rozanska, X.; Schoonheydt, R. A.; van Santen, R. A.; Hutschka, F.; Hafner, J. *J. Am. Chem. Soc.* **2001,** *123*, 2799–2809.
(32) McQuarrie, D. A.; Simon, J. D. *Physical Chemistry, A Molecular Approach*; University Science Books: Sausalito, CA, 1997.
(33) Dumesic, J. A.; Rudd, D. F.; Aparico, L. M.; Rekoske, J. E.; Treviño, A. A. *The Microkinetics of Heterogeneous Catalysis*; American Chemical Society: Washington, DC, 1993.
(34) De Moor, B. A.; Reyniers, M. F.; Marin, G. B. *Phys. Chem. Chem. Phys.* **2009,** *11*, 2939–2958.
(35) Svelle, S.; Kolboe, S.; Swang, O.; Olsbye, U. *J. Phys. Chem. B* **2005,** *109*, 12874–12878.
(36) Vandichel, M.; Lesthaeghe, D.; Van der Mynsbrugge, J.; Waroquier, M.; Van Speybroeck, V. *J. Catal.* **2010,** *271*, 67–78.
(37) Hansen, N.; Kerber, T.; Sauer, J.; Bell, A. T.; Keil, F. J. *J. Am. Chem. Soc.* **2010,** *132*, 11525–11538.
(38) Van Speybroeck, V.; Van Cauter, K.; Coussens, B.; Waroquier, M. *ChemPhysChem* **2005,** *6*, 180–189.
(39) Vandeputte, A. G.; Sabbe, M. K.; Reyniers, M. F.; Van Speybroeck, V.; Waroquier, M.; Marin, G. B. *J. Phys. Chem. A* **2007,** *111*, 11771–11786.
(40) Sabbe, M. K.; Vandeputte, A. G.; Reyniers, M. F. O.; Van Speybroeck, V.; Waroquier, M.; Marin, G. B. *J. Phys. Chem. A* **2007,** *111*, 8416–8428.
(41) Hemelsoet, K.; Moran, D.; Van Speybroeck, V.; Waroquier, M.; Radom, L. *J. Phys. Chem. A* **2006,** *110*, 8942–8951.
(42) Lesthaeghe, D.; Van Speybroeck, V.; Waroquier, M. *Phys. Chem. Chem. Phys.* **2009,** *11*, 5222–5226.
(43) Lesthaeghe, D.; Delcour, G.; Van Speybroeck, V.; Marin, G. B.; Waroquier, M. *Microporous Mesoporous Mater.* **2006,** *96*, 350–356.
(44) Lesthaeghe, D.; Van Speybroeck, V.; Marin, G. B.; Waroquier, M. *Chem. Phys. Lett.* **2006,** *417*, 309–315.
(45) Trygubenko, S. A.; Wales, D. J. *J. Chem. Phys.* **2004,** *120*, 2082–2094.
(46) Henkelman, G.; Uberuaga, B. P.; Jonsson, H. *J. Chem. Phys.* **2000**, *113*, 9901–9904.
(47) Vankoningsveld, H.; Vanbekkum, H.; Jansen, J. C. *Acta Crystallogr., Sect. B, Struct. Sci.* **1987,** *43*, 127–132.
(48) Sklenak, S.; Dedecek, J.; Li, C. B.; Wichterlova, B.; Gabova, V.; Sierka, M.; Sauer, J. *Angew. Chem., Int. Ed.* **2007,** *46*, 7286–7289.
(49) *CMM Code;* http://molmod.ugent.be/code/wiki.
(50) Verstraelen, T.; Van Speybroeck, V.; Waroquier, M. *J. Chem. Inf. Model.* **2008,** *48*, 1530–1541.
(51) Frisch, M. J.; et al. *Gaussian03*; Gaussian, Inc.: Wallingford, CT, 2004.
(52) Becke, A. D. *J. Chem. Phys.* **1993,** *98*, 5648–5652.
(53) Zygmunt, S. A.; Mueller, R. M.; Curtiss, L. A.; Iton, L. E. *THEOCHEM* **1998,** *430*, 9–16.
(54) Svelle, S.; Kolboe, S.; Olsbye, U.; Swang, O. *J. Phys. Chem. B* **2003,** *107*, 5251–5260.
(55) Fermann, J. T.; Moniz, T.; Kiowski, O.; McIntire, T. J.; Auerbach, S. M.; Vreven, T.; Frisch, M. J. *J. Chem. Theory Comput.* **2005,** *1*, 1232–1239.
(56) Solans-Monfort, X.; Sodupe, M.; Branchadell, V.; Sauer, J.; Orlando, R.; Ugliengo, P. *J. Phys. Chem. B* **2005,** *109*, 3539–3545.
(57) *ORCA. 2.6.35ed.*; http://www.thch.uni-bonn.de/tc/orca/.
(58) Grimme, S. *J. Comput. Chem.* **2004,** *25*, 1463–1473.
(59) Grimme, S.; Antony, J.; Schwabe, T.; Muck-Lichtenfeld, C. *Org. Biomol. Chem.* **2007,** *5*, 741–758.
(60) Grimme, S. *J. Comput. Chem.* **2006,** *27*, 1787–1799.
(61) Perdew, J. P.; Burke, K.; Ernzerhof, M. *Phys. Rev. Lett.* **1996,** *77*, 3865–3868.
(62) Perdew, J. P.; Burke, K.; Ernzerhof, M. *Phys. Rev. Lett.* **1997,** *78*, 1396–1396.
(63) Boys, S. F.; Bernardi, F. *Mol. Phys.* **1970,** *19*, 553–&.
(64) Jansen, H. B.; Ros, P. *Chem. Phys. Lett.* **1969,** *3*, 140–143.
(65) Vanduijneveldt, F. B.; Vanduijneveldtvanderijdt, J.; Vanlenthe, J. H. *Chem. Rev.* **1994,** *94*, 1873–1885.
(66) Jensen, F. *J. Chem. Theory Comput.* **2010,** *6*, 100–106.
(67) Ghysels, A.; Van Neck, D.; Van Speybroeck, V.; Verstraelen, T.; Waroquier, M. *J. Chem. Phys.* **2007,** *126*, 224102.
(68) Ghysels, A.; Van Neck, D.; Waroquier, M. *J. Chem. Phys.* **2007,** *127*, 164108.
(69) Ghysels, A.; Van Speybroeck, V.; Pauwels, E.; Catak, S.; Brooks, B. R.; Van Neck, D.; Waroquier, M. *J. Comput. Chem.* **2010,** *31*, 994–1007.
(70) Ghysels, A.; Van Speybroeck, V.; Pauwels, E.; Van Neck, D.; Brooks, B. R.; Waroquier, M. *J. Chem. Theory Comput.* **2009,** *5*, 1203–1215.
(71) Ghysels, A.; Van Speybroeck, V.; Verstraelen, T.; Van Neck, D.; Waroquier, M. *J. Chem. Theory Comput.* **2008,** *4*, 614–625.

(72) Ghysels, A.; Verstraelen, T.; Hemelsoet, K.; Waroquier, M.; Van Speybroeck, V. *J. Chem. Inf. Model.* **2010,** *50,* 1736–1750.
(73) Haase, F.; Sauer, J. *Microporous Mesoporous Mater.* **2000,** *35*−*6,* 379–385.
(74) Lesthaeghe, D.; Van Speybroeck, V.; Marin, G. B.; Waroquier, M. *J. Phys. Chem. B* **2005,** *109,* 7952–7960.
(75) Lee, C. C.; Gorte, R. J.; Farneth, W. E. *J. Phys. Chem. B* **1997,** *101,* 3811–3817.
(76) Tuma, C.; Sauer, J. *Phys. Chem. Chem. Phys.* **2006,** *8,* 3955–3965.
(77) De Moor, B. A.; Reyniers, M. F.; Sierka, M.; Sauer, J.; Marin, G. B. *J. Phys. Chem. C* **2008,** *112,* 11796–11812.
(78) Denayer, J. F.; Baron, G. V.; Martens, J. A.; Jacobs, P. A. *J. Phys. Chem. B* **1998,** *102,* 3077–3081.
(79) Eder, F.; Lercher, J. A. *Zeolites* **1997,** *18,* 75–81.
(80) Eder, F.; Stockenhuber, M.; Lercher, J. A. *J. Phys. Chem. B* **1997,** *101,* 5414–5419.
(81) Jakobtorweihen, S.; Hansen, N.; Keil, F. J. *Mol. Phys.* **2005,** *103,* 471–489.
(82) Martens, J. A.; Jacobs, P. A.; van Bekkum, H.; Flanigan, E. M.; Jansen, J. C. *Stud. Surf. Sci. Catal.* **2001,** *137,* 633–671.
(83) Kazansky, V. B. *Catal. Today* **1999,** *51,* 419–434.
(84) Boronat, M.; Corma, A. *Appl. Catal., A* **2008,** *336,* 2–10.
(85) Tuma, C.; Sauer, J. *Angew. Chem., Int. Ed.* **2005,** *44,* 4769–4771.
(86) Koch, W.; Liu, B.; Schleyer, P. V. *J. Am. Chem. Soc.* **1989,** *111,* 3479–3480.
(87) Zhang, Y. K.; Pan, W.; Yang, W. T. *J. Chem. Phys.* **1997,** *107,* 7921–7925.
(88) Alberty, R. A. *J. Chem. Educ.* **1988,** *65,* 409–413.
(89) Bond, G. C.; Keane, M. A.; Kral, H.; Lercher, J. A. *Catal. Rev.*—*Sci. Eng.* **2000,** *42,* 323–383.
(90) Gounder, R.; Iglesia, E. *J. Am. Chem. Soc.* **2009,** *131,* 1958–1971.
(91) Haag, W. O. In *Zeolites and Related Microporous Materials: State of the Art 1994*; Weitkamp, J., Karge, H. G., Pfeifer, H., Holderich, W., Eds.; 1994, pp 1375−1394.
(92) Smit, B.; Maesen, T. L. M. *Chem. Rev.* **2008,** *108,* 4125–4184.
(93) Denayer, J. F.; Souverijns, W.; Jacobs, P. A.; Martens, J. A.; Baron, G. V. *J. Phys. Chem. B* **1998,** *102,* 4588–4597.
(94) Ruthven, D. M.; Kaul, B. K. *Adsorpt.-J. Int. Adsorpt. Soc.* **1998,** *4,* 269–273.
(95) Tielens, F.; Denayer, J. F. M.; Daems, I.; Baron, G. V.; Mortier, W. J.; Geerlings, P. *J. Phys. Chem. B* **2003,** *107,* 11065–11071.
(96) Atkinson, D.; Curthoys, G. *J. Chem. Soc., Faraday Trans. I* **1981,** *77,* 897–907.
(97) Wender, A.; Barreau, A.; Lefebvre, C.; Di Lella, A.; Boutin, A.; Ungerer, P.; Fuchs, A. H. *Adsorpt.-J. Int. Adsorpt. Soc.* **2007,** *13,* 439–451.
(98) de Gauw, F.; van Grondelle, J.; van Santen, R. A. *J. Catal.* **2002,** *206,* 295–304.
(99) Van Speybroeck, V.; Van Neck, D.; Waroquier, M.; Wauters, S.; Saeys, M.; Marin, G. B. *J. Phys. Chem. A* **2000,** *104,* 10939–10950.
(100) Van Speybroeck, V.; Vansteenkiste, P.; Van Neck, D.; Waroquier, M. *Chem. Phys. Lett.* **2005,** *402,* 479–484.
(101) Vansteenkiste, P.; Van Speybroeck, V.; Marin, G. B.; Waroquier, M. *J. Phys. Chem. A* **2003,** *107,* 3139–3145.
(102) Teketel, S.; Olsbye, U.; Lillerud, K. P.; Beato, P.; Svelle, S. *Microporous Mesoporous Mater.* **2010,** *136,* 33–41.

Paper 3

Full theoretical cycle for both ethene and propene formation during methanol-to-olefin conversion in H-ZSM-5

David Lesthaeghe, Jeroen Van der Mynsbrugge, Matthias Vandichel, Michel Waroquier and Veronique Van Speybroeck

ChemCatChem, 2011, 3, 208 - 212

Copyright 2011 by Wiley-VCH Verlag GmbH& Co. KGaA, Weinheim.

CHEMCATCHEM

DOI: 10.1002/cctc.201000286

Full Theoretical Cycle for both Ethene and Propene Formation during Methanol-to-Olefin Conversion in H-ZSM-5

David Lesthaeghe, Jeroen Van der Mynsbrugge, Matthias Vandichel, Michel Waroquier, and Veronique Van Speybroeck*[a]

The methanol-to-olefin (MTO) process, catalyzed by acidic zeolites such as H-ZSM-5, provides an increasingly important alternative to the production of light olefins from crude oil. However, the various mechanistic proposals for methanol-to-olefin conversion have been strongly disputed for the past several decades. This work provides theoretical evidence that the experimentally suggested 'alkene cycle', part of a co-catalytic hydrocarbon pool, offers a viable path to the production of both propene and ethene, in stark contrast to the often-proposed direct mechanisms. This specific proposal hinges on repeated methylation reactions of alkenes, starting from propene, which occur easily within the zeolite environment. Subsequent cracking steps regenerate the original propene molecule, while also forming new propene and ethene molecules as primary products. Because the host framework stabilizes intermediate carbenium ions, isomerization and deprotonation reactions are extremely fast. Combined with earlier joint experimental and theoretical work on polymethylbenzenes as active hydrocarbon pool species, it is clear that, in zeolite H-ZSM-5, multiple parallel and interlinked routes operate on a competitive basis.

Introduction

To meet the ever increasing demand for oil-based chemicals despite waning oil reserves, the development of new technologies from alternative feedstock is a general concern for both scientific and industrial communities. One of the most prominent emerging technologies is the methanol-to-olefin (MTO) process, catalyzed by acidic zeolites, such as H-ZSM-5, or by nanoporous zeotype materials, such as H-SAPO-34.[1] Herein, we report on a complete route from a theoretical viewpoint of the recently proposed 'alkene route,'[2] in which alkenes act as essential co-catalysts in addition to the zeolite framework. This hypothesis provides a complete, viable low-energy pathway to both ethene and propene production in H-ZSM-5.

Despite considerable effort from experimental and theoretical research, the reaction mechanism of the MTO process has proven to be extremely difficult to unravel, ever since its discovery in the 1970s.[1] Recent interest in the mechanism was fueled by a surge in oil prices; MTO conversion allows the petrochemical industry to bypass crude oil as a fundamental feedstock. Methanol can be made from synthesis gas, which in turn can be formed from almost any gasifiable carbonaceous species, such as natural gas, coal, biomass and organic waste. The MTO process converts methanol into light olefins, such as ethene and propene, which serve as basic building blocks for the entire petrochemical industry and polymerization processes in particular. As a result, ethene and propene are increasingly in demand.

Historically, almost all attention focused on 'direct mechanisms', for which C–C coupling occurs from C_1 species, such as methanol and dimethyl ether, only. In the last decade, however, intensive experimental[3,4] and theoretical[5–7] research has shown that the direct routes do not explain the initial C–C coupling, opening the door to new mechanistic proposals. The most recent experimental developments strongly support an alternative 'hydrocarbon pool' mechanism,[8] in which organic reaction centers in the zeolite pores act as olefin-producing co-catalysts. The basic ideas were originally proposed in the 1980s and 1990s by Dessau, Dahl, and Kolboe,[9,10] but have since remained largely ignored by the scientific community. The failure of the direct routes and additional experimental proof for the hydrocarbon pool mechanism has reignited interest in the proposed hydrocarbon pool mechanism.[11–13]

In a recent joint experimental/theoretical effort, we managed to construct a complete working catalytic cycle based on methylbenzenes as crucial hydrocarbon pool species in H-ZSM-5 following the 'paring' route' and producing isobutene.[14] The experimentally observed energy barriers were significantly lower than those calculated for the direct routes.[6] However, this type of cycle has so far failed to theoretically explain the ethene production witnessed in H-ZSM-5, as energy barriers for ethene elimination in the 'side-chain' route were found to be too high.[15] To our knowledge, no full cycle producing

[a] Dr. D. Lesthaeghe, J. Van der Mynsbrugge, M. Vandichel, Prof. Dr. M. Waroquier, Prof. Dr. V. Van Speybroeck
Center for Molecular Modeling, QCMM Alliance Ghent–Brussels
Ghent University, Technologiepark 903, 9052 Zwijnaarde (Belgium)
Fax: (+32) 9-264-66-97
E-mail: veronique.vanspeybroeck@ugent.be

Supporting information for this article is available on the WWW under http://dx.doi.org/10.1002/cctc.201000286.

 WILEY ONLINE LIBRARY © 2011 Wiley-VCH Verlag GmbH & Co. KGaA, Weinheim

ethene has been theoretically validated, though fragmented reaction steps have been documented before.

Polymethylbenzenes might not be the only active hydrocarbon pool species toward olefin formation, even though they have long been commonly regarded as the most important hydrocarbon pool species. While this probably still holds for zeolites with the BEA or CHA topology, recent experiments have shown that the archetypical MTO catalyst H-ZSM-5 (with more limited space in the MFI-topology) could form an important exception. Svelle et al. demonstrated that the higher methylbenzenes, normally the most active species, are virtually unreactive in the pores of H-ZSM-5.[16] Molecular simulations show that this is mainly due to transition state shape selectivity; the narrow channels and restricted space at channel intersections limit the reactivity of bulky methylbenzenes.[17] The original proposal by Dessau, based on successive methylation and cracking reactions of C_{3+} alkenes, was revived through ^{13}C labeling experiments,[9] providing a parallel route for the production of light olefins on zeolite H-ZSM-5. In more detailed research by Svelle et al., ethene appeared to be formed solely from the lower methylbenzenes (on the basis of equal ^{13}C incorporation in ethene and lower methylbenzenes), whereas propene and higher alkenes would be formed from alkene methylation and interconversion.[18]

These observations led to the proposal of a complete dual cycle mechanism, in which a polymethylbenzene cycle would yield predominantly ethene, and an alkene cycle would mainly yield propene and higher alkenes (Scheme 1). These cycles are

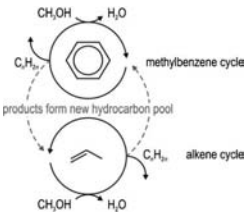

Scheme 1. Two possible hydrocarbon pool cycles, based on a methylbenzene and alkene organic co-catalyst present in the zeolite pores. Both cycles convert methanol into light olefins and water, but with different ethene/propene selectivities. The two cycles do not operate independently, but are interconnected since the products can either act as new co-catalysts directly (for the alkene cycle) or undergo oligomerization and cyclization to form new aromatic co-catalysts (used in the methylbenzene cycle).

interconnected since the polymethylbenzene cycle also produces propene as a product (which can act directly as a co-catalyst in the alkene cycle),[14] and conversely propene molecules can oligomerize to form a new polymethylbenzene catalyst, as has been shown from theoretical viewpoint.[19]

Such a dual cycle might eventually allow full control of the propene-to-ethene ratio, for which a thorough understanding and comparison of all elementary steps is of the utmost importance. In this study, the elementary reactions of the C_{3+} alkene cycle are modeled using quantum chemical techniques to identify a complete pathway with low energy barriers (for more information on the level of theory, see the Methods section and Refs. [20] and [21]). To verify whether olefin formation proceeds along this route and whether propene formation is indeed preferred to ethene formation, the previously suggested cycle[16] is extended so that no a priori assumptions are made regarding the nature of the products formed. However, some limitations have been made towards branching intermediates to prevent an excessively complicated scheme. The main questions to be answered from a theoretical perspective are the following: Can the alkene proposal be considered a viable olefin-producing route? How does it relate to the direct mechanisms and to the methylbenzene route? How might it influence the ethene/propene product selectivity?

Results and Discussion

A simplified picture of the studied cycle is shown in Scheme 2. Starting with a single propene molecule, chain growth proceeds through successive methylation steps by methanol

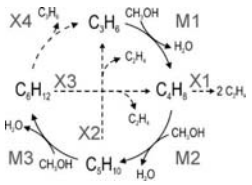

Scheme 2. Full catalytic cycle near an acid site in zeolite ZSM-5, starting from propene (top). Several methylation steps by methanol (M1–M3) provide chain growth, whereas cracking steps (X1–X3) form new ethene and propene products and replenish the original hydrocarbon pool.

(M1–M3), finally forming hexene. For clarity, only methylation of 1-alkenes, through which no branching of the carbon skeleton occurs, is considered in this study. Accordingly, isomerization reactions that ensure a proper placement of the double bond need to be taken into account before each methylation. Ultimately, the cracking of these longer alkenes (reactions X1–X4) results in the production of light olefins, notably ethene and propene.

We chose to limit the calculations to linear alkenes to prevent excessive cluttering of the reaction diagrams. This choice was based on the fact that branched molecules will crack more easily than linear molecules,[22] which makes the reaction barriers considered in this study representative of the upper limit of such reactions. If a full cycle for linear alkenes proves to be fully operational, branched alkenes will only speed up the process. For a detailed theoretical study on the methylation to *trans*-2-butene, we refer to earlier work.[21]

Most of the reactions under study herein have already been studied theoretically,[19,23–26] albeit on varying levels of theory and using a wide scale of theoretical methods, ranging from

 © 2011 Wiley-VCH Verlag GmbH & Co. KGaA, Weinheim

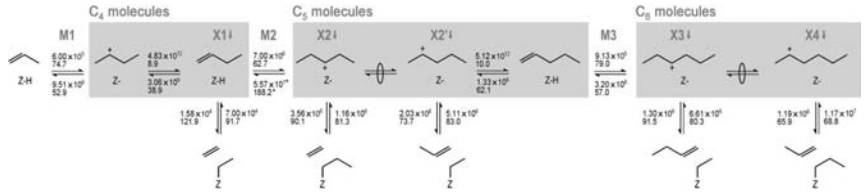

Scheme 3. Overview of the full alkene cycle forming both alkenes and alkoxides: methylation steps (M1–M3, shown horizontally) and cracking steps (X1–X4, shown vertically) correspond to those in Scheme 2. Numbers refer to reaction rates at 673 K (in s^{-1}, top value) and reaction barriers (in kJ mol^{-1}, bottom value).

small cluster calculations to full periodic calculations, rendering direct comparison almost impossible. Even though isolated steps might be feasible, it remains unclear whether a complete route is a solid alternative to the direct mechanisms. Therefore, our goal in this work is to treat all reactions uniformly, including the effect of the surrounding zeolite framework, and fill in the missing gaps. This approach allows full comparison between the various reaction types, as well as with previous work on the methylbenzene hydrocarbon pool.

Scheme 3 gives a more detailed overview of the full cycle, expanded from Scheme 2. Full details on how reaction rates and barriers were calculated can be found in the Methods section and in previous work.[21]

Methylation

The reaction barriers for methylation of alkenes (60–80 kJ mol^{-1}) are lower than those previously reported for methylation of higher polymethylbenzenes (±150 kJ mol^{-1}) in H-ZSM-5 (horizontal arrows in Scheme 3, reactions M1–M3).[14,17] The latter values were obtained without dispersion interactions, but these corrections typically lie in the range of 20–30 kJ mol^{-1} for methylation reactions, thus making them still larger than the here obtained values.[15,17,23] The reaction barriers in the MFI topology depend largely on the number of methyl substituents, as reported previously.[17] The here-obtained values fall in exactly the same range as those for the methylation of -hexamethylbenzene in the CHA topology of H-SSZ-13 (the aluminosilicate analogue of SAPO-34) or the lower methylbenzenes in H-ZSM-5 (also in the range of 60–80 kJ mol^{-1}).[17] As far as methylation is concerned, the small alkenes seem to be very similar in reactivity compared to the active methylbenzenes, and much higher in reactivity compared to relatively inactive higher methylbenzenes when space constraints are imposed. These results demonstrate that methylation of alkenes and methylbenzenes will be competitive and dependent on the available species within the zeolite pores.

The resulting product species is a secondary carbenium ion (Scheme 3), which is easily deprotonated to form the subsequent alkene; barriers are no higher than 10 kJ mol^{-1}. These low barriers for deprotonation were already obtained without any assistance of the residual water molecule. There is one notable exception: the intrinsic reaction coordinate (IRC) calculation reveals that, after methylation of butene, the residual water molecule attaches to the carbenium ion, forming an oxonium ion instead (Scheme 3, asterisk for the reverse reaction M2). This structure is shown in Figure 1. The observed additional stabilizing effect will be further investigated in future work, as it suggests that the abundance of water molecules within the zeolite cages will assist in stabilizing crucial carbenium ion intermediates. The deprotonation steps have not been explicitly labeled in Scheme 2, and are shown within the grey boxes in Scheme 3 (energy barriers of 8.9 and 10.0 kJ mol^{-1}).

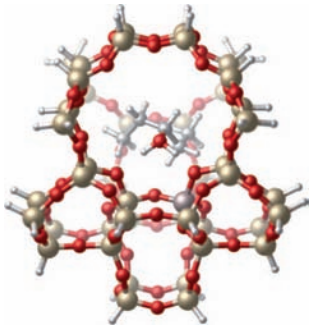

Figure 1. The product for the second methylation reaction (M2) within the ZSM-5 framework. The oxygen atom from the water molecule coordinates with the positively charged carbon atom, further stabilizing this species.

Isomerization

Isomerization can occur both in a one-step and a two-step (through an intermediate alkoxide)[28] procedure starting from neutral molecules. However, to date, isomerization studies have always been considered from neutral species. Using the products obtained from the preceding steps, we know that secondary carbenium ions are formed after the methylation step. These ions can undergo intramolecular hydride shifts which are virtually barrierless (10–15 kJ mol^{-1}) even outside the

 © 2011 Wiley-VCH Verlag GmbH & Co. KGaA, Weinheim

zeolite environment and lead to an equilibrium between different secondary carbenium ions of the same chain length, which is completely in line with experimental observations.[29] Because the carbon number does not change, these hydride shift reactions can be found as barrierless reactions alongside the deprotonation reactions (Scheme 3, grey boxes). Combined with the equally fast deprotonation steps (barriers around 10 kJ mol^{-1}), the double bond can be reasonably assumed to be in any desired position, fully allowing the construction of the simplified complete cycle consisting solely of linear alkenes in this study. Of course, it is important to restate that branched alkenes will be formed as well and actually will be preferential methylation products. Furthermore, they are believed to crack more easily as stated earlier, and will, therefore, have even lower energy barriers.

Cracking

Once the chain reaches the desired length, ethene and propene can be formed through cracking reactions (Scheme 3, reactions X1–X4), even for linear alkenes. β-Scission on a secondary carbenium ion was the main cracking reaction modeled in this study but, alternatively, cracking can also occur through a protonated cyclopropyl species (PCP). Cracking of alkenes with five or more carbon atoms seems to occur readily (barriers of 70–90 kJ mol^{-1}), with the β-scission mechanism being generally favored over the PCP-type mechanism. The cracking products appear both as alkenes and as framework-bound alkoxides, requiring an additional desorption step; the latter step has already been elaborately documented.[19,28]

Our theoretical results reveal that cracking of longer alkenes to form propene (Schemes 2 and 3; X2, X2′, and X4,) is generally faster than that to form ethene (X1 and X3), confirming the experimentally observed predominant propene selectivity of this route, yet not completely excluding residual ethene formation along this route either. This is in total agreement with previous experimental work on alkene cracking within acidic zeolites[29] and also with the observation that the alkene route would be propene heavy in comparison to other hydrocarbon pool cycles.[16,18,30] Taking into account the possibility of alkene formation from polymethylbenzenes, we observe a delicate balance for product selectivity based on the size and shape of the nanometer-sized pores. Since none of the considered steps has excessively high energy barriers, we can also conclude that the propene route is a viable olefin-producing route from theoretical viewpoint as well, confirming the recent experimental statements.[16]

Conclusions

In summary, our theoretical calculations have shown that the alkene cycle offers a viable path to the production of both major olefin products. Methylation occurs equally as fast as that of the most active methylbenzenes, but is not subject to any steric hindrance. Several cracking steps are possible depending on chain length, resulting in the production of not only propene but also ethene, yet still with a slight preference for the former. Isomerization and deprotonation reactions are extremely fast, which will result in a wide variety of linear and branched alkenes formed. Going beyond our earlier theoretical work on the polymethylbenzenes as active hydrocarbon pool molecules, we can conclude that, in H-ZSM-5, multiple parallel and interlinked routes operate on a competitive basis. Although these routes are based on totally different hydrocarbon pool co-catalysts, the most active routes show similar energy barriers for the rate determining steps.

With respect to our choice to only consider linear alkenes, we can firmly conclude that the alkene route is definitely an active olefin-producing route. Since cracking steps occur faster for branched alkenes, any similar route containing branched alkenes along the way is likely to have even lower energy barriers. We also note that the energy barrier for cracking of linear alkenes becomes competitive with the energy barrier for methylation once we reach a linear C_6 molecule. This might indicate that the most effective route for linear alkenes would consist of 3 subsequent methylation steps, after which the molecule cracks into two propene species. Reaction rates can not easily be compared between these two reaction families, since they will be dependent on the methanol and water concentrations in the pores. Nevertheless, comparison with experimental data shows that the calculated energy barriers are highly accurate with this level of theory.[21]

Additional insights into these parallel cycles, and into the role of the zeolite framework on their relative productivity, might lead to the highly coveted control over the ethene/propene ratio. Additionally, favoring the alkene route over the methylbenzene route could also provide a means to prevent coke formation and delay ultimate deactivation of the catalyst,[17,19] since this route is less likely to form diffusion-limiting polyaromatics.

Theoretical methods

All geometries were optimized at the ONIOM(B3LYP/6-31g(d):MNDO) level of theory on a large 8T:46T H-ZSM-5 cluster with the Gaussian03 software.[31] Saturating hydrogen atoms were held fixed to mimic crystallographic behavior. Subsequently single-point calculations at the ONIOM(B3LYP/6-31g(d):HF/6-31g(d)) level of theory were performed. These energies were further refined by including van der Waals corrections at the B3LYP-D level of theory with the Orca software package.[32] A similar level of theory was used for the paring route and side-chain route in the polymethylbenzene cycle. The paring route still lacked dispersion corrections, but both for the side-chain route and the alkene route, we found dispersion corrections to be mainly significant for adsorption energies, but less so for reaction barriers (typical changes of up to 10 kJ mol^{-1}). Kinetic coefficients were obtained using classical TST and the PHVA methods[33] as used in previous work.[14] Only with the surrounding zeolite environment did secondary carbenium ions occur as minima, albeit in a shallow potential well. For visualization and kinetic analysis, we used in-house developed software programs,[34,35] as well as CYLview.[36]

The computational method employed herein, which was also used in previous work,[14,15] has recently been the subject of an extensive theoretical benchmarking study,[21] going beyond the original level-of-theory study for ONIOM calculations in zeolites in 2005.[20] More

 © 2011 Wiley-VCH Verlag GmbH & Co. KGaA, Weinheim

specifically, for the methylation reactions studied in this paper (M1–M2), the obtained results are very close to extremely high-level periodic results and experimental observations,[24] especially when the DFT-D corrections are included. Compared to the landmark benchmarking study by Sauer and co-workers,[24] this method has the additional advantage that it is computationally very efficient and allows for a wide range of reactions to be studied within a realistic computational time frame. In a recent study on related reactions, a variety of other theoretical procedures and functionals were also tested.[37]

Acknowledgements

This work was supported by the Fund for Scientific Research Flanders (FWO-Vlaanderen), the Research Board of Ghent University (BOF) and BELSPO, in the framework of the IAP 6/27. Computational resources and services used in this work were provided by Ghent University. Funding was also received from the European Research Council under the European Community's Seventh Framework Programme (FP7(2007-2013) ERC grant agreement number 240483).

Keywords: density functional calculations · heterogeneous catalysis · hydrocarbons · kinetics · zeolites

[1] M. Stöcker, *Microporous Mesoporous Mater.* **1999**, *29*, 3 – 48.
[2] M. Bjorgen, S. Svelle, F. Joensen, J. Nerlov, S. Kolboe, F. Bonino, L. Palumbo, S. Bordiga, U. Olsbye, *J. Catal.* **2007**, *249*, 195 – 207.
[3] W. G. Song, D. M. Marcus, H. Fu, J. O. Ehresmann, J. F. Haw, *J. Am. Chem. Soc.* **2002**, *124*, 3844 – 3845.
[4] D. M. Marcus, K. A. McLachlan, M. A. Wildman, J. O. Ehresmann, P. W. Kletnieks, J. F. Haw, *Angew. Chem.* **2006**, *118*, 3205 – 3208; *Angew. Chem. Int. Ed.* **2006**, *45*, 3133 – 3136.
[5] D. Lesthaeghe, V. Van Speybroeck, G. B. Marin, M. Waroquier, *Ind. Eng. Chem. Res.* **2007**, *46*, 8832 – 8838.
[6] D. Lesthaeghe, V. Van Speybroeck, G. B. Marin, M. Waroquier, *Angew. Chem.* **2006**, *118*, 1746 – 1751; *Angew. Chem. Int. Ed.* **2006**, *45*, 1714 – 1719.
[7] D. Lesthaeghe, V. Van Speybroeck, G. B. Marin, M. Waroquier, *Chem. Phys. Lett.* **2006**, *417*, 309 – 315.
[8] J. F. Haw, D. M. Marcus, *Top. Catal.* **2005**, *34*, 41 – 48.
[9] R. M. Dessau, *J. Catal.* **1986**, *99*, 111 – 116.
[10] I. M. Dahl, S. Kolboe, *J. Catal.* **1994**, *149*, 458 – 464.
[11] W. G. Song, J. F. Haw, J. B. Nicholas, C. S. Heneghan, *J. Am. Chem. Soc.* **2000**, *122*, 10726 – 10727.
[12] J. F. Haw, W. G. Song, D. M. Marcus, J. B. Nicholas, *Acc. Chem. Res.* **2003**, *36*, 317 – 326.
[13] U. Olsbye, M. Bjorgen, S. Svelle, K. P. Lillerud, S. Kolboe, *Catal. Today* **2005**, *106*, 108 – 111.
[14] D. M. McCann, D. Lesthaeghe, P. W. Kletnieks, D. R. Guenther, M. J. Hayman, V. Van Speybroeck, M. Waroquier, J. F. Haw, *Angew. Chem.* **2008**, *120*, 5257 – 5260; *Angew. Chem. Int. Ed.* **2008**, *47*, 5179 – 5182.
[15] D. Lesthaeghe, A. Horré, M. Waroquier, G. B. Marin, V. Van Speybroeck, *Chem. Eur. J.* **2009**, *15*, 10803 – 10808.
[16] S. Svelle, F. Joensen, J. Nerlov, U. Olsbye, K. P. Lillerud, S. Kolboe, M. Bjorgen, *J. Am. Chem. Soc.* **2006**, *128*, 14770 – 14771.
[17] D. Lesthaeghe, B. De Sterck, V. Van Speybroeck, G. B. Marin, M. Waroquier, *Angew. Chem.* **2007**, *119*, 1333 – 1336; *Angew. Chem. Int. Ed.* **2007**, *46*, 1311 – 1314.
[18] S. Svelle, U. Olsbye, F. Joensen, M. Bjorgen, *J. Phys. Chem. C* **2007**, *111*, 17981 – 17984.
[19] M. Vandichel, D. Lesthaeghe, J. Van der Mynsbrugge, M. Waroquier, V. Van Speybroeck, *J. Catal.* **2010**, *271*, 67 – 78.
[20] X. Solans-Monfort, M. Sodupe, V. Branchadell, J. Sauer, R. Orlando, P. Ugliengo, *J. Phys. Chem. B* **2005**, *109*, 3539 – 3545.
[21] V. Van Speybroeck, J. Van der Mynsbrugge, M. Vandichel, K. Hemelsoet, D. Lesthaeghe, A. Ghysels, G. B. Marin, M. Waroquier, unpublished results.
[22] T. Wakayama, H. Matsuhashi, *J. Mol. Catal. A: Chem.* **2005**, *239*, 32 – 40.
[23] S. Svelle, B. Arstad, S. Kolboe, O. Swang, *J. Phys. Chem. B* **2003**, *107*, 9281 – 9289.
[24] S. Svelle, C. Tuma, X. Rozanska, T. Kerber, J. Sauer, *J. Am. Chem. Soc.* **2009**, *131*, 816 – 825.
[25] Y.-X. Sun, J. Yang, L.-F. Zhao, J.-X. Dai, H. Sun, *J. Phys. Chem. C* **2010**, *114*, 5975 – 5984.
[26] S. Svelle, S. Kolboe, O. Swang, U. Olsbye, *J. Phys. Chem. B* **2005**, *109*, 12874 – 12878.
[27] K. Hemelsoet, A. Nollet, M. Vandichel, D. Lesthaeghe, V. Van Speybroeck, M. Waroquier, *ChemCatChem* **2009**, *1*, 373 – 378.
[28] A. Bhan, Y. V. Joshi, W. N. Delgass, K. T. Thomson, *J. Phys. Chem. B* **2003**, *107*, 10476 – 10487.
[29] Y. V. Kissin, *Catal. Rev. Sci. Eng.* **2001**, *43*, 85 – 146.
[30] M. Bjørgen, F. Joensen, K. P. Lillerud, U. Olsbye, S. Svelle, *Catal. Today* **2009**, *142*, 90 – 97.
[31] *Gaussian 03*, Revision C.02, M. J. Frisch, G. W. Trucks, H. B. Schlegel, G. E. Scuseria, M. A. Robb, J. R. Cheeseman, J. A. Montgomery, T. Vreven, K. N. Kudin, J. C. Burant, J. M. Millam, S. S. Iyengar, J. Tomasi, V. Barone, B. Mennucci, M. Cossi, G. Scalmani, N. Rega, G. A. Petersson, H. Nakatsuji, M. Hada, M. Ehara, K. Toyota, R. Fukuda, J. Hasegawa, M. Ishida, T. Nakajima, Y. Honda, O. Kitao, H. Nakai, M. Klene, X. Li, J. E. Knox, H. P. Hratchian, J. B. Cross, V. Bakken, C. Adamo, J. Jaramillo, R. Gomperts, R. E. Stratmann, O. Yazyev, A. J. Austin, R. Cammi, C. Pomelli, J. W. Ochterski, P. Y. Ayala, K. Morokuma, G. A. Voth, P. Salvador, J. J. Dannenberg, V. G. Zakrzewski, S. Dapprich, A. D. Daniels, M. C. Strain, O. Farkas, D. K. Malick, A. D. Rabuck, K. Raghavachari, J. B. Foresman, J. V. Ortiz, Q. Cui, A. G. Baboul, S. Clifford, J. Cioslowski, B. B. Stefanov, G. Liu, A. Liashenko, P. Piskorz, I. Komaromi, R. L. Martin, D. J. Fox, T. Keith, A. Laham, C. Y. Peng, A. Nanayakkara, M. Challacombe, P. M. W. Gill, B. Johnson, W. Chen, M. W. Wong, C. Gonzalez, J. A. Pople, Gaussian, Inc., Wallingford CT, **2003**.
[32] *Orca version 2.7.0*, F.Neese, University of Bonn, Germany, **2008**.
[33] A. Ghysels, D. Van Neck, V. Van Speybroeck, T. Verstraelen, M. Waroquier, *J. Chem. Phys.* **2007**, *126*, 224102.
[34] A. Ghysels, T. Verstraelen, K. Hemelsoet, V. Van Speybroeck, M. Waroquier, *J. Chem. Inf. Model.* **2010**, *50*, 1736 – 1750.
[35] T. Verstraelen, V. Van Speybroeck, M. Waroquier, *J. Chem. Inf. Model.* **2008**, *48*, 1530 – 1541.
[36] CYLview BETA 1.0, Copyright **2006–2008** Claude Y. Legault.
[37] B. Chan, L. Radom, *Can. J. Chem.* **2010**, *88*, 866 – 876.

Received: August 17, 2010
Published online on November 9, 2010

 © 2011 Wiley-VCH Verlag GmbH & Co. KGaA, Weinheim

Paper 4

The remarkable catalytic activity of the saturated metal organic framework V-MIL-47 in the cyclohexene oxidation

Karen Leus, Ilke Muylaert, Matthias Vandichel, Guy B. Marin, Michel Waroquier, Veronique Van Speybroeck and Pascal Van Der Voort

Chemical Communications, 2010, 46, 5085 - 5087

Copyright 2010 by The Royal Society of Chemistry.

COMMUNICATION www.rsc.org/chemcomm | ChemComm

The remarkable catalytic activity of the saturated metal organic framework V-MIL-47 in the cyclohexene oxidation†

Karen Leus,[a] Ilke Muylaert,[a] Matthias Vandichel,[b] Guy B. Marin,[c] Michel Waroquier,[b] Veronique Van Speybroeck*[b] and Pascal Van Der Voort*[a]

Received 20th May 2010, Accepted 4th June 2010
First published as an Advance Article on the web 18th June 2010
DOI: 10.1039/c0cc01506g

The remarkable catalytic activity of the saturated metal organic framework MIL-47 in the epoxidation of cyclohexene is elucidated by means of both experimental results and theoretical calculations.

Metal organic frameworks (MOFs) are crystalline porous solids composed of a three-dimensional network of metal ions held in place by multidentate organic molecules.[1,2] Recently, the catalytic applications of MOFs have been reviewed by Hupp *et al.* and Farrusseng *et al.*[3,4] However, catalytic reaction mechanisms in metal organic frameworks and in particular at saturated coordinated centres are still poorly understood.

In this study, we describe the high catalytic activity of a coordinative saturated V-MOF in the liquid phase oxidation of cyclohexene. The metal organic framework MIL-47 consists of a porous terephthalate framework built from infinite chains of $V^{4+}O_6$ octahedra and has a three-dimensional orthorhombic structure that exhibits large pores.[5] Every structure unit in MIL-47 contains an O–V^{+IV}–O bridge. The linkage of the V^{+IV} to dicarboxylate groups of the terephthalate linkers results in an octahedral structure unit. Hence each vanadium(+IV) centre is saturated.

The selective oxidation of cyclohexene is particularly interesting as it can yield, depending on the catalyst and the reaction conditions, several products as shown in Scheme 1. In this study, the reaction was carried out with *tert*-butyl hydroperoxide (70 wt% TBHP in water) as oxidant and chloroform as solvent. The internal standard used was 1,2,4-trichlorobenzene. The molar ratios were chloroform : cyclohexene : TBHP : 1,2,4-trichlorobenzene = 462 : 1 : 2 : 1. The reaction temperature was kept constant at 323 K. Samples were taken out from the reaction mixture at certain times and analyzed by gas chromatography. Next, MIL-47 was compared with a homogeneous vanadium catalyst vanadyl acetylacetonate $VO(acac)_2$. Prior to the reaction, all the catalysts were dried under vacuum. Blank tests were performed without catalyst and no cyclohexene conversion was observed.

[a] *Department of Inorganic and Physical Chemistry, Centre for Ordered Materials, Organometallics and Catalysis, Ghent University, Krijgslaan 281-S3, 9000 Ghent, Belgium. E-mail: pascal.vandervoort@ugent.be*
[b] *Centre for Molecular Modeling, Ghent University, Technologiepark 903, 9052 Zwijnaarde, Belgium. E-mail: Veronique.vanspeybroeck@ugent.be*
[c] *Laboratory for Chemical Technology, Ghent University, Krijgslaan 281-S5, 9000 Ghent, Belgium*
† Electronic supplementary information (ESI) available: XRF analysis, nitrogen adsorption isotherms, XRD patterns, experimental and computational details. See DOI: 10.1039/c0cc01506g

Fig. 1 depicts the cyclohexene conversion and the detailed product distributions for MIL-47 and the homogeneous $VO(acac)_2$ catalyst. In both reactions, we used an identical amount of V-sites (0.4 mmol, 0.095 g MIL-47 and 0.106 g $VO(acac)_2$). The four main reaction products formed are cyclohexene oxide **2**, cyclohexane-1,2-diol **3**, *tert*-butyl-2-cyclohexenyl-1-peroxide **4** and 2-cyclohexen-1-one **5**. From these figures it can be seen that the homogeneous catalyst $VO(acac)_2$ and the MIL-47 show high reaction rates for the conversion of cyclohexene. The initial turnover frequencies considered at the first 20 min are 57 h^{-1} and 43 h^{-1} for the $VO(acac)_2$ and the MIL-47 respectively. Both catalysts showed an almost linear conversion rate during the first 2 h of reaction and finally topped out at 60% conversion. The turnover numbers calculated at the end of the reaction were 62 and 68 for $VO(acac)_2$ and MIL-47 respectively. Moreover, considering the product distributions, truly interesting similarities between both catalysts are observed.

Firstly, the cyclohexene oxide is formed during the first 2 h and is topped out at 15%, but its yield decreases with increasing reaction time. At the same time and at the same reaction rate the oxide is decreasing, the cyclohexane-1,2-diol formation is observed, indicating a consecutive reaction is taking place. After 5 h, the diol formation reaches a plateau at 15%. Additionally, both catalysts produce a significant amount of *tert*-butyl-2-cyclohexenyl-1-peroxide **4** (30%) as determined by GC-GC-TOF-MS and a minimal amount of 2-cyclohexen-1-one **5** (5%).

In order to examine the heterogeneity of the catalytic reaction, a hot filtration experiment was performed. The catalyst was separated from the reaction mixture after 1 h using a combined nylon-membrane filter. Fig. 2 presents the conversion curve of cyclohexene in the presence of MIL-47 and the cyclohexene conversion after filtration. Also the sum of products **2**, **3** and **5** is shown with and without the hot filtration. It is clear from this figure that both the conversion of cyclohexene and the formation of oxidized products are strongly reduced after filtration of the catalyst. This indicates that the catalytic reaction is predominantly heterogeneous. There is however some homogeneous catalytic activity left. This activity is due to a combination of radical mechanisms

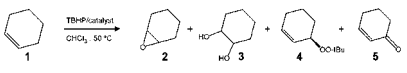

Scheme 1

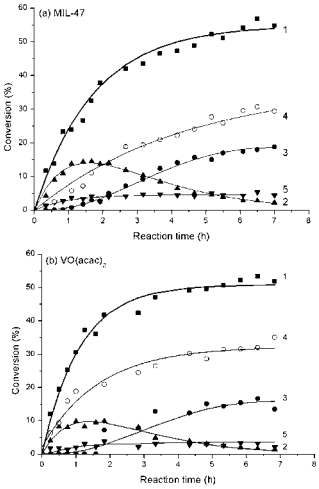

Fig. 1 Total cyclohexene conversion and detailed product distribution in the cyclohexene oxidation with (a) MIL-47 and (b) $VO(acac)_2$ in chloroform with *tert*-butyl hydroperoxide (70 wt% solution in water) at 323 K. The numbers of the curves correspond with the numbers in Scheme 1.

(formation of product **4** occurs *via* radical pathways (*vide infra*)) and leached V. By XRF analysis we have determined that 12.8% of the V-sites have leached out after 1 h of reaction (see Fig. S.1 in the supplementary information†). Finally, we also show the catalytic conversion caused by dissolving exactly the amount of $VO(acac)_2$ that corresponds to the 12.8% leached V-sites (▼). This leads however to only 5% conversion.

Furthermore, the stability and the regenerability in terms of morphology and catalytic performance of MIL-47 were studied. The original synthesized MOF exhibits a specific surface area around 800 $m^2\ g^{-1}$. After the first catalytic run, the pores are completely clogged by organic compounds. Subsequently, MIL-47 was regenerated by a treatment in a tubular furnace under a nitrogen flow at 523 K for four hours to remove the organic compounds.

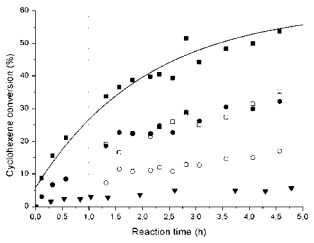

Fig. 2 Hot filtration experiment. Cyclohexene conversion (■) and yield of oxidized products (●) as a function of time. Cyclohexene conversion (□) and yield of oxidized products (○) after filtration of the catalyst. The catalytic activity of $VO(acac)_2$ corresponding to the 12.8% leached V-sites (▼).

After this calcination treatment the porosity was completely regenerated as can be seen in Fig. S.2.† Additionally, X-ray diffraction (XRD) patterns show that the crystalline structure of MIL-47 is preserved after regeneration (see Fig. S.3†). Finally, the catalytic activity of MIL-47 is tested in a second catalytic run, in which 27 mg catalyst was recovered and used. In order to make a fair comparison, we also show first runs, using respectively 20 mg and 40 mg catalyst, in Fig. 3. Although the kinetics are initially different, the final conversion in the second run does not show any significant loss of activity.

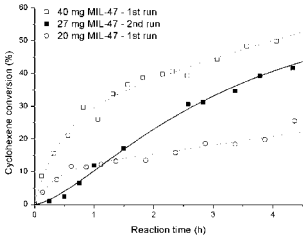

Fig. 3 Cyclohexene conversion for MIL-47 in its first run with (□) 40 mg MIL-47, (○) 20 mg MIL-47 catalyst mass and (■) after regeneration with 27 mg MIL-47.

Besides MIL-47, two other V catalysts are tested for the oxidation of cyclohexene, namely the supported VO_x/SiO_2 and the microporous crystalline VAPO-5. The latter is a crystalline AlPO zeotype, containing vanadium(+IV) centres. We observed that VAPO-5 is completely catalytically inactive for the oxidation of cyclohexene. This observation is consistent with other research, outlining that VAPO-5 (and more generally MeAPOs) are not suitable as catalysts for liquid phase oxidation reactions.[6]

The supported VO_x/SiO_2 catalyst shows a good conversion in a first run (see Fig. S.4†). However, after the first catalytic run, 40% of the vanadium was leached from the silica supported catalyst and no cyclohexene conversion was observed in its second run, indicating the reaction occurs basically homogeneously.

To get more insight into the possible reaction mechanisms and intermediates, theoretical calculations were performed on the $VO(acac)_2$ catalyst, which showed a remarkable resemblance to the MIL-47 catalyst from the experimental results. A comparison of the optimized geometries of the $VO(acac)_2$ system with the XRD data of the MIL-47 indicates that the surroundings of the vanadium atom are very similar geometrically wise (Fig. 4). The initial coordination of TBHP with vanadium is expected to occur in a similar fashion apart from steric constraints. More information on the computational details can be found in the supporting information.† The formation of the epoxide, the diol and the peroxide will

 This journal is © The Royal Society of Chemistry 2010

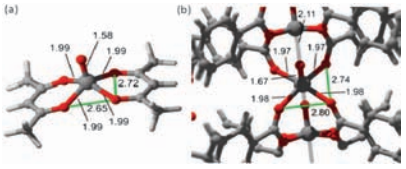

Fig. 4 Comparison of distances (in Å) for (a) the homogeneous $VO(acac)_2$ system and (b) the metal organic framework MIL-47.

now be discussed. Because the ketone is not present in large quantities, this reaction pathway will not be considered here.

Fig. 5 shows the epoxidation pathway with $VO(acac)_2$ with the final regeneration step of the catalyst included. The reaction cycle starts with an activation step (**A**) in which TBHP coordinates with $VO(acac)_2$. Here, an alkylperoxo species, namely VO(acac)(OOtBu), is formed. All attempts to model an epoxidation cycle on a complex with two acac ligands failed, which suggests that first vacant coordination sites need to be generated, in accordance with earlier literature data on the activity of peroxo and alkylperoxo species for oxidations.[7] In a second step the actual epoxidation (**E**) towards cyclohexene oxide can occur easily with an activation barrier of 55.9 kJ mol^{-1} calculated at the B3LYP/6-311 + g(3df,2p) level of theory. This step is irreversible which can be deduced from the reverse barrier which is very high (236.8 kJ mol^{-1}). After epoxidation, Hacac can coordinate back to the vanadium centre and cyclohexene oxide is split off (**P**). Notice that a similar ligand exchange with cyclohexene oxide could also occur with other species present in the reaction medium (tBuOH, H_2O, TBHP). The final regeneration step occurs fast *via* a proton transfer reaction. Both activation (**A**) and production (**P**) are endothermic from our calculations but the equilibrium could significantly shift on inclusion of a larger molecular environment.

In the case of the $VO(acac)_2$ catalysts substantial amounts of acetic acids are formed upon decomposition of Hacac with TBHP.[8] The subsequent formation of the cyclohexane-1,2-diol can be explained by opening of the epoxide ring by an acid catalyzed hydrolysis mechanism.[9] In the MIL-47, a small fraction of terephthalic acid is anticipated to catalyze the opening of the epoxide ring.

During the first catalytic cycle, a majority of the reaction product is *tert*-butyl-2-cyclohexenyl-1-peroxide. This product is formed due to a radical reaction pathway between the substrate and the oxidant TBHP and has been recently observed for unsaturated Co-MOFs.[10] Freely diffusing peroxy radicals can be generated by a variety of mechanisms in which the oxidation state of vanadium changes.

Similar reaction pathways in the MIL-47 system can be considered, provided one terephthalic acid ligand folds away from the vanadium centre to create a vacancy for the coordination of a TBHP molecule. Subsequently, the actual epoxidation can occur. Further theoretical modelling is in progress to fully investigate the proposed reactions in the MIL-47.

In conclusion, the saturated metal organic framework MIL-47 is catalytically active in the oxidation of cyclohexene,

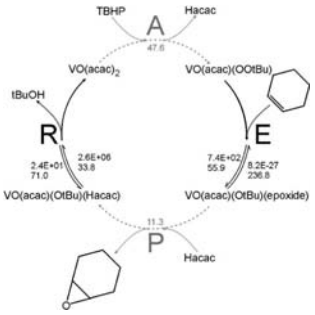

Fig. 5 $VO(acac)_2$ epoxidation cycle. Gray numbers indicate reaction energies (kJ mol^{-1}), while black numbers indicate reaction barriers (bottom, kJ mol^{-1}) and reaction rates (top, s^{-1}).

showing a similar catalytic activity and product distribution to the homogeneous vanadium complex $VO(acac)_2$. Hot filtration experiments show that the oxidation catalysis occurs predominantly heterogeneously. MIL-47 can be regenerated and reused. Theoretical calculations on the $VO(acac)_2$ system give insights into the reaction pathways towards the reaction products and reveal that the successful epoxidation is accompanied by a linker exchange with TBHP. A similar mobility of the terephthalic linkers is required to explain the high catalytic activity of the saturated vanadium centre in MIL-47.

This research is co-funded by Ghent University, GOA grant no. 01G00710 and Methusalem grant no. 01M00409, BELSPO in the frame of IAP 6/27 and the European Research Council (FP7(2007–2013) ERC grant no. 240483). I.M. acknowledges the IWT grant no. IWT/SB/71325. We are grateful to Steven Pijl for his experimental help with the GC-GC-TOF-MS measurement and to Jan Musschoot for the XRF analysis.

Notes and references

1 N. L. Rosi, J. Eckert, M. Eddaoudi, D. T. Vodak, J. Kim, M. O'Keeffe and O. M. Yaghi, *Science*, 2003, **300**, 1127.
2 G. Férey, *Chem. Soc. Rev.*, 2008, **37**, 191.
3 (*a*) J. Lee, O. K. Farha, J. Roberts, K. A. Scheidt, S. T. Nguyen and J. T. Hupp, *Chem. Soc. Rev.*, 2009, **38**, 1450; (*b*) J. Perles, N. Snejko, M. Iglesias and M. A. Monge, *J. Mater. Chem.*, 2009, **19**, 6504; (*c*) F. Gandara, E. G. Puebla, M. Iglesias, D. M. Proserpio, N. Snejko and M. A. Monge, *Chem. Mater.*, 2009, **21**, 655; (*d*) M. C. Bernini, F. Gandara, M. Iglesias, N. Snejko, E. Gutierrez-Puebla, E. V. Brusau, G. E. Narda and M. A. Monge, *Chem.–Eur. J.*, 2009, **15**, 4896.
4 D. Farrusseng, S. Aguado and C. Pinel, *Angew. Chem., Int. Ed.*, 2009, **48**, 7502.
5 K. Barthelet, J. Marrot, D. Riou and G. Férey, *Angew. Chem., Int. Ed.*, 2002, **41**, 281.
6 M. J. Haanepen, A. M. ElemansMehring and J. H. C. Van Hooff, *Appl. Catal., A*, 1997, **152**, 203.
7 E. P. Talsi, V. D. Chinakov, V. P. Babenko and K. I. Zamaraev, *J. Mol. Catal.*, 1993, **81**, 235; H. Mimoun, M. Mignard, P. Brechot and L. Saussine, *J. Am. Chem. Soc.*, 1986, **108**, 3711.
8 L. Stepovik and M. Gulenova, *Russ. J. Gen. Chem.*, 2009, **79**, 1663.
9 A. Lundin, I. Panas and E. Ahlberg, *J. Phys. Chem. A*, 2007, **111**, 9087.
10 M. Tonigold, Y. Lu, B. Bredenkötter, B. Rieger, S. Bahnmüller, J. Hitzbleck, G. Langstein and D. Volkmer, *Angew. Chem., Int. Ed.*, 2009, **48**, 7546.

Paper 5

Mechanistic insight into the cyclohexene epoxidation with $VO(acac)_2$ and *tert*-butyl hydroperoxide

Matthias Vandichel, Karen Leus, Pascal Van Der Voort,
Michel Waroquier and Veronique Van Speybroeck

Journal of Catalysis, 2012, 294, 1-18

Copyright 2012 by Elsevier.

Journal of Catalysis 294 (2012) 1–18

Contents lists available at SciVerse ScienceDirect

Journal of Catalysis

journal homepage: www.elsevier.com/locate/jcat

Mechanistic insight into the cyclohexene epoxidation with $VO(acac)_2$ and *tert*-butyl hydroperoxide

Matthias Vandichel [a], Karen Leus [b], Pascal Van Der Voort [b], Michel Waroquier [a,*], Veronique Van Speybroeck [a,*]

[a] Center for Molecular Modeling, Ghent University, Technologiepark 903, 9052 Zwijnaarde, Belgium
[b] Department of Inorganic and Physical Chemistry, Center for Ordered Materials, Organometallics and Catalysis, Ghent University, Krijgslaan 281 – Building S3, 9000 Gent, Belgium

ARTICLE INFO

Article history:
Received 23 February 2012
Revised 4 May 2012
Accepted 2 June 2012
Available online 9 August 2012

Keywords:
Catalysis
Epoxidation
Vanadyl acetylacetonate ($VO(acac)_2$)
tert-Butyl hydroperoxide (TBHP)
Cyclohexene
DFT
Chemical kinetics
Rate constants

ABSTRACT

The epoxidation reaction of cyclohexene is investigated for the catalytic system vanadyl acetylacetonate ($VO(acac)_2$) with *tert*-butyl hydroperoxide (TBHP) as oxidant with the aim to identify the most active species for epoxidation and to retrieve insight into the most plausible epoxidation mechanism. The reaction mixture is composed of various inactive and active complexes in which vanadium may either have oxidation state +IV or +V. Inactive species are activated with TBHP to form active complexes. After reaction with cyclohexene, each active species transforms back into an inactive complex that may be reactivated again. The reaction mixture is quite complex containing hydroxyl, acetyl acetonate, acetate, or a *tert*-butoxide anion as ligands, and thus, various ligand exchange reactions may occur among active and inactive complexes. Also, radical decomposition reactions allow transforming V^{+IV} to V^{+V} species. To obtain insight into the most abundant active complexes, each of previous transformation steps has been modeled through thermodynamic equilibrium steps. To unravel the nature of the most plausible epoxidation mechanism, first principle chemical kinetics calculations have been performed on all proposed epoxidation pathways. Our results allow to conclude that the concerted Sharpless mechanism is the preferred reaction mechanism and that alkylperoxo species $V^{+IV}O(L)(OOtBu)$ and $V^{+V}O(L_1)(L_2)(OOtBu)$ species are most abundant. At the onset of the catalytic cycle, vanadium +IV species may play an active role, but as the reaction proceeds, reaction mechanisms that involve vanadium +V species are preferred as the acetyl acetonate is readily oxidized. Additionally, an experimental IR and kinetic study has been performed to give a qualitative composition of the reaction mixture and to obtain experimental kinetic data for comparison with our theoretical values. The agreement between theory and experiment is satisfactory.

© 2012 Elsevier Inc. All rights reserved.

1. Introduction

(Cyclo)alkene epoxidation is a key transformation in organic synthesis both on an academic and industrial scale for the production of various chemicals. Many catalytic systems based on transition-metal complexes of Mo, Ti, W, and V have been reported and found to be very effective and selective for the epoxidation of a wide range of (cyclo)alkenes using hydroperoxides as oxidant [1–3]. The reaction chemistry of vanadyl acetylacetonate ($VO(acac)_2$) as catalyst for the oxidation of cyclohexene with hydrogen peroxide or *tert*-butyl hydroperoxide (TBHP) as oxidant has been the subject of several experimental studies [4–8]. Recently, the homogeneous $VO(acac)_2$/TBHP system and the porous metal organic framework–type catalyst MIL-47 [9] have been compared for their cyclohexene epoxidation activity, and they showed similar conversion patterns [10,11]. In view of our interest in both the homogeneous ($VO(acac)_2$) system and the heterogeneous epoxidation cycles on MIL-47, it is important to obtain mechanistic insight into the plethora of reactions possible for the $VO(acac)_2$/TBHP system. Herein, we have investigated various epoxidation pathways for this catalytic system theoretically. Additionally new kinetic experiments were performed to compare the theoretical kinetic data with the experimentally observed trends. The investigated reaction routes are as complete as possible, taking into account vanadium species in oxidation state +IV and +V, with a variety of ligands and with the additional account of reaction that allow changing the oxidation state. To the best of our knowledge, no full mechanistic proposal of all possible reactions has been proposed, but yet there are a series of experimental and theoretical studies providing very relevant information.

The $VO(acac)_2$/TBHP system has already received considerable attention due to a variety of interesting applications. More

* Corresponding authors.
E-mail addresses: michel.waroquier@ugent.be (M. Waroquier), veronique.vanspeybroeck@ugent.be (V. Van Speybroeck).

0021-9517/$ - see front matter © 2012 Elsevier Inc. All rights reserved.
http://dx.doi.org/10.1016/j.jcat.2012.06.002

information can be found in vanadium chemistry reviews [12–15] but some interesting highlights on applications are given hereafter. $VO(acac)_2$ is readily oxidized to V^{+V} complexes upon treatment with a peroxide and vanadium(V) complexes have been found to act as catalyst precursors in various oxidation reactions such as bromination reactions, epoxidations of alkenes and allylic alcohols, oxidations of sulfides to sulfoxides and sulfones, hydroxylations of alkanes and arenes, and oxidations of primary and secondary alcohols to the corresponding aldehydes and ketones [13,15]. The $VO(acac)_2$-catalyzed epoxidation of allylic alcohols with alkyl hydroperoxides provides a useful route to epoxidize alcohols [4,15–17]. By using proline-derived hydroxamic acids as chiral ligands, even higher enantioselectivities (up to 80% enantiomeric excess) could be achieved [12,17]. Furthermore, the $VO(acac)_2$/TBHP/ligand system allows the highly chemoselective mono-epoxidation of olefinic alcohols like geraniol [18,19], as unfunctionalized alkenes react more slowly with this system. The active species have been identified in stoichiometric reactions as mononuclear oxoperoxovanadium(V) complexes, of which some have been structurally characterized [20]. The catalyst $VO(acac)_2$ forms different complexes, and experimental studies have been conducted to demonstrate the various transformations $VO(acac)_2$ undergoes upon treatment with TBHP.

$VO(acac)_2$ is rapidly converted to vanadate esters $(VO(OR)_{3-x}(OOR)_x$, with R = *tert*-butyl and $x \in \{1,2,3\}$) in the presence of TBHP, and the oxidation products were found to be also acidic, just as Hacac [7,21,22]. Upon treating $VO(acac)_2$ with an excess of TBHP, typically in the proportion of $VO(acac)_2$:TBHP > 10 as in mild oxidation conditions (benzene, 20 °C), acetylacetonate (acac)-ligands are eliminated and oxidized. In all cases, these reactions are exothermic. The most abundant oxidation product of Hacac was found to be acetic acid (HOAc) [7,23]. Furthermore, certain studies have tried to unravel the initial steps in the reaction of $VO(acac)_2$ with TBHP [7,8]. The active intermediates were widely accepted to be vanadium(+V) alkylperoxo complexes in the $VO(acac)_2$/TBHP [4,16,17,22] and $VO(acac)_2$/TBHP/ligand [24–28] catalytic systems. More specifically, Talsi et al. [8] investigated the role of alkylperoxo complexes for the cyclohexene epoxidation with organic hydroperoxides in the presence of $VO(acac)_2$ in detail by NMR and EPR. Experimentally, V^{+V} alkylperoxo species ($V^{+V}O(OOtBu)$) have been thought to epoxidize cyclohexene [8]. Those alkylperoxo species are also able to oxidize cyclohexane, but only through radical generation via the equilibrium $V^{+V}O(OOR) \leftrightarrow V^{+IV}O + \cdot OOR$. Moreover, when cyclohexene is added to the $VO(acac)_2$/TBHP system, it is converted in various products [10] (see Scheme 1). The desired product is usually cyclohexene oxide **2** which consecutively converts into cyclohexane-1, 2-diol **3** in presence of water and acid, while *tert*-butyl-2-cyclohexenyl-1-peroxide **4** and 2-cyclohexene-1-one **5** are byproducts formed by radical side reactions and alcohol oxidations. Here, we will exclusively focus on the epoxidation mechanism for unfunctionalized alkenes, so the species active for epoxidation need to be identified.

From a computational point of view, there are to the best of our knowledge no theoretical investigations on the epoxidation reaction with THBP on vanadium species so far. It might be anticipated that similarities will be present with the epoxidation reaction cycle in which hydrogen peroxide is used, but still some differences might occur due to the more bulky TBHP molecule. Apart from this, some interesting computational studies on the vanadium-catalyzed olefin epoxidation are available, which all use hydrogen peroxide H_2O_2 as oxidant [29–32]. We particularly mention the work of Kuznetsov et al. [31] where different pathways of the reaction of divanadium-substituted polyoxotungstate with hydrogen peroxide and olefin were studied using DFT methods and where the role of solvent is also taken into account with explicit water molecules or a polarizable continuum model with acetonitrile as solvent.

Another recent theoretical study concerns the epoxidation of olefins catalyzed by vanadium-salan complexes [32]. Therein, three main routes were investigated, that is, the Mimoun, the Sharpless, and the biradical mechanisms. In that case, it was found that the epoxidation of the VO-salan complexes preferably happens via a concerted Sharpless route [33]. Bühl et al. [29] came to the same conclusion in their study on $[VO(O_2)_2(Im)]^-$ species solvated in water, where also the effect of various substituents was tested in relation to the barrier for epoxidation and ^{51}V-NMR shift. In another recent study, Kirilova et al. [34] presented a kinetic scheme for oxidations in the vanadate/pyrazine-2-carboxylic acid (PCA) system. The mechanism of radical generation was studied, as these catalytic systems activate C–H bonds via such radical pathways. The generation of both ·OH and ·OOH radicals was modeled via thermodynamic equilibrium steps of various catalytic cycles containing both +IV and +V species. Side reactions such as keton formation from an alcohol have been modeled in detail by Sauer and coworkers on vanadium surfaces [35–38]. During this reaction, the oxidation state of the vanadium goes from +V to +III. Therefore, the broken symmetry approach has been applied for the description of the transition state for the keton formation [35].

Molecular modeling of the homogeneous epoxidation of cyclohexene with $VO(acac)_2$/TBHP is very complex due to the presence of multiple complexes that can be formed [8,21]. The cyclohexene conversion also changes with reaction time, as more and more byproducts are formed such as *tert*-butanol (tBuOH) and *tert*-butyl-2-cyclohexenyl-1-peroxide **4**, inhibiting further conversion [8]. In addition, this distribution can be affected by solvents, pH, addition of ligands, usage of radical-catching species, etc.

The aim of this study is twofold: (1) identifying the most abundant, active epoxidation complexes and (2) investigating the probability of various proposed reaction mechanisms and eventually establish the most plausible one. To achieve this goal, a whole family of active and inactive complexes that can either have oxidation state +IV or +V for vanadium have been considered, where also the ligand has been varied. The transformation among the different species has been modeled as thermodynamic equilibrium steps. After that, first principle chemical kinetic data have been calculated for each of the active species and for each of the proposed mechanistic cycles in literature. To cross-validate our theoretical data with experiments, also new experimental kinetic data have been produced. As such, this study should allow to provide a nearly complete picture of the epoxidation of cyclohexene through the homogeneous catalytic $VO(acac)_2$/TBHP system.

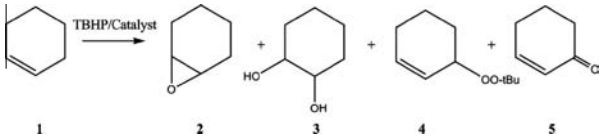

Scheme 1. Possible reaction products formed during the oxidation of cyclohexene with $VO(acac)_2$ as a catalyst and TBHP as oxidant.

2. Overview of epoxidation mechanisms and various active and inactive complexes

2.1. Active versus inactive complexes

Before starting the actual epoxidation reaction, the $VO(acac)_2$ needs to be brought into an active complex (AC) after reaction with the oxidant TBHP. There are various possibilities for the generation of active species, which will be outlined below. The whole catalytic cycle consists in the principle of two main reaction families: the epoxidation of cyclohexene bringing the catalyst into an inactive complex (IC) and the activation of inactive to active complexes through reaction with the oxidant TBHP. Apart from these reaction families, radical decomposition reactions allow altering the oxidation state from +IV to +V or vice versa. These main categories are schematically shown in Fig. 1.

2.1.1. Initial activation of $VO(acac)_2$

One possibility for generating active complexes was suggested by Stepovik [7] and is illustrated in Fig. 2. In this picture, $VO(acac)_2$ **6** looses one of its acetylacetonate ligands with formation of Hacac **9**, which may further oxidize to acetic acid (HOAc) [7,23]. This reaction is irreversible due to the strong exothermic nature of the reaction (reaction energy of −1172 kJ/mol at 0 K) and the escape of the CO_2. As such, Hacac will become less abundant as the catalytic cycle of epoxidation evolves and is responsible for the presence of acetic acid in the reaction mixture. HOAc may then play a significant role in the further catalytic system through ligand exchange reactions, as will be explained further in this paper. Apart from this activation step that occurs initially, a variety of other activation steps have been considered in this paper which will be discussed further in this section.

2.1.2. Radical decomposition of active complexes

The vanadium +IV alkylperoxo complex **8** of Fig. 2 is one possible active complex, but in the early stages of the epoxidation reaction with an excess of TBHP in the reagent mixture, various radical decomposition pathways may also occur. Some examples of such pathways are shown in Fig. 3, although these are only illustrative examples and are far from unique. They allow transforming $V^{+IV} \rightarrow V^{+V}$, giving rise to the alkylperoxo species of the type $VO(acac)_2OOR$ (R = H or tBu), which were observed in the experimental work of Talsi et al. [8]. However, in the absence of spin traps (in benzene at 20 °C), the EPR spectrum measured just after the mixing of reagents shows a signal that could be assigned to the coordinated $VO(acac)_2$ – TBHP complex with vanadium in oxidation state +IV. Hence, this work gives evidence that both +IV and +V vanadium alkylperoxo complexes are present during the reaction of $VO(acac)_2$ with TBHP. An excess of TBHP in the reagent mixture also lead to the complete disappearance of the V^{+IV} signal in the EPR spectrum. These observations point toward the existence of radical decomposition mechanisms. The examples given in Fig. 3a concern a homolytic cleavage of the peroxy linkage of the alkylperoxocomplex **10** with formation of a tBuO· radical and a dioxo-complex **11**. The equilibrium displayed in Fig. 3b suggests a correlation between the concentration of the active $VO(L_1)(L_2)(OOtBu)$ complex and that of tBuOO· as most stable free radical in solution, which is indeed observed in the work of Talsi [8].

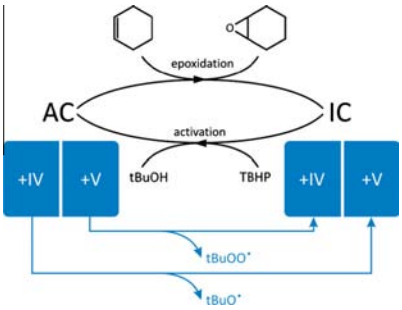

Fig. 1. Main reaction families of the $VO(acac)_2$/TBHP catalytic system for epoxidation of cyclohexene, transforming active complexes (AC) to inactive complexes (IC). The scheme reports *tert*-butanol as most dominant side-product of the activation step. Side reactions where radicals (tBuOO·, tBuO·) are generated, start as well from active complexes.

Previous examples given in Fig. 3a and **b** are non-restrictive, and both V^{+IV} and V^{+V} monoperoxo complexes can be formed by various reaction mechanisms for example by ligand exchange. The most straightforward choice for the ligand L represents an acetyl acetonate (acac) ligand, but the concept may easily be generalized with other ligands such as hydroxyl, acetate, or a *tert*-butoxide anion which are schematically represented in Fig. 3c. Indeed, from the NMR spectra reported in the work of Talsi [8], evidence was given for other vanadium +V complexes, for instance, species with one or more hydroxyl groups as ligands. Ligand exchange reactions lie on the origin of the formation of other active complexes with various ligands. A more general representation of all considered active and inactive complexes in this work is given in Fig. 4 and will be discussed further below. The proposed reactions and equilibrium steps for changing the oxidation state are completely equivalent with similar work done by Kirilova et al. [34].

2.1.3. Activation reactions

After epoxidation, the active complexes (AC) turn back into inactive complexes (IC), and in order to react with cyclohexene, they need to be reactivated. This activation step occurs *in situ* by activation reactions with the help of the peroxides HOOR after which active complexes (AC) are formed again, as schematically shown in Fig. 1. The most relevant structures for inactive and active complexes are given in Fig. 4. The transformation from active to inactive and vice versa is described as thermodynamic equilibrium steps. Generic structures for the various types of inactive complexes (IC) are represented by the compounds **13** and **15** for V^{+IV} and **11** and **18** for V^{+V} in Fig. 4. Active vanadium peroxy compounds may be formed by coordination with the alkyl hydroperoxide (complexes **14** and **17**), by ligand exchange reactions with the alkyl hydroperoxide (complexes **10**, **16**, **19,** and **12**) and as the result of TBHP addition to a V=O bond (complexes **12**(L_2 = OH) and **20**) (see Fig. 4).

2.1.4. Gibbs free-energy surfaces for inactive (IC) and active complexes (AC)

As already mentioned, all inactive (IC) and active complexes (AC) are linked with each other through equilibrium steps. A generic scheme is shown in Fig. 5. Most of them are generated by ligand-exchange reactions. The monoperoxo species **21** are not formed by simple exchange reactions, but further details on their formation will be given in Section 5.3.

2.2. Epoxidation mechanism

Once the active complexes are formed, epoxidation of cyclohexene may take place. Hereafter, we give an overview of all possible epoxidation mechanisms of mono-vanadium complexes with peroxides H_2O_2 or TBHP as oxidant (represented by the notation ROOH

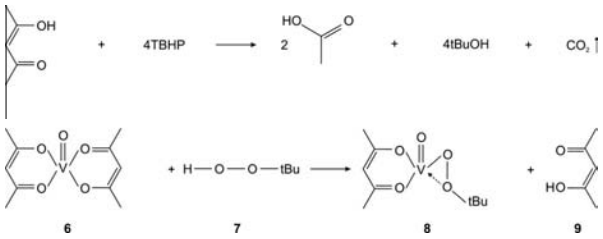

Fig. 2. Ligand exchange in the initial stage of the catalytic cycle forming an active complex 8.

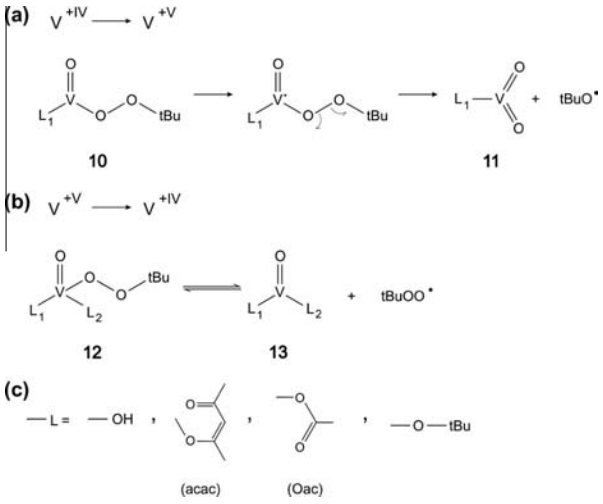

Fig. 3. Example of possible radical decomposition reactions: (a) oxidation of V^{+IV} in an alkylperoxocomplex induced by homolytic cleavage of the peroxy linkage; (b) formation of the peroxy radical and an inactive V^{+IV} complex; (c) ligand choices throughout this paper.

with R = H or tBu), which were already suggested in literature. All mechanistic proposals start from active mono-vanadium complexes that have either oxidation number +IV or +V. They are schematically represented in Fig. 6. Three reaction classes are distinguished, which are labeled by roman numbers **I**, **II,** and **III** and which are viable both for vanadium in oxidation state +IV and +V. For each of the reaction families, a schematic representation of the transition state is also given.

Within reaction family **I**, the peroxide is coordinated with the metal. This mechanism was already proposed in the early seventies [4,39–43]. In mechanism **Ia,** the electron-deficient oxygen of the hydroperoxide ROOH is placed in the vicinity of the double bond in the transition state. As such, the epoxidation reaction is favored over the decomposition of the hydroperoxide. A hydrogen transfer occurs from the coordinated peroxide to the oxo-ligand in the vanadium complex. Mechanism **Ib** differs only slightly from **Ia**. In this case, the peroxide hydrogen undergoes a transfer to a ligand (L_2 in Fig. 6) with the cleavage of the metal–ligand bond. It might be anticipated that reaction families **Ia** and **Ib** would not be preferred in case TBHP is used as oxidant due to the bulkiness of this species and the steric hindrance with the various ligands. It was already reported earlier that those mechanisms fail to explain the exceptional epoxidation reactivity of allylic alcohols [4,16,42], although the validity of this reaction class will be investigated by modeling for each of the involved species thermodynamic and kinetic data.

In the second class **II**, the intermediate is a monoperoxo complex where the (cyclo)alkene attacks the peroxo-ligand. It is a concerted one-step process and is called a Sharpless-type mechanism [16,33,44]. This mechanism enables to explain the exceptional epoxidation reactivity observed for allylic alcohols. The direction of approach is now ideal for an allylic alcohol, which is simultaneously coordinated through its hydroxyl group to the vanadium center (see **IIa** and **IIb** in Fig. 6).

The third class of epoxidation reactions **III** starts from peroxo species **21** as active oxidant. There are many mechanisms possible

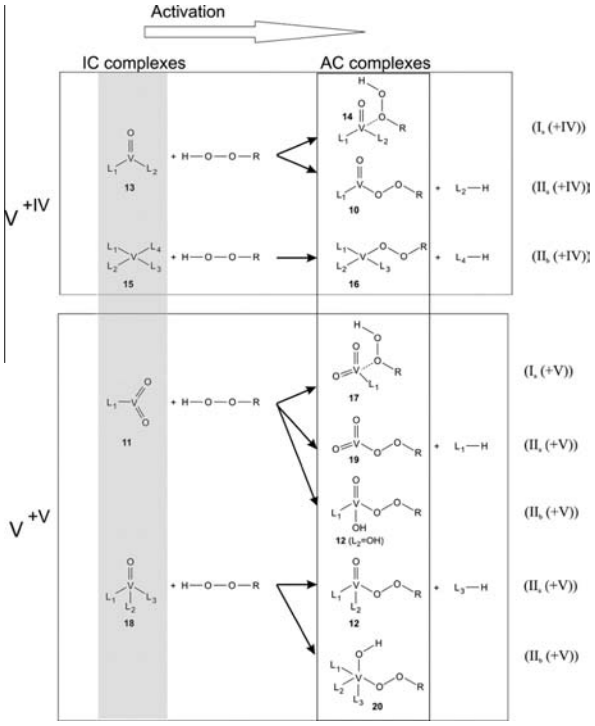

Fig. 4. Generic structures for the inactive complexes are given in the gray-shaded region. Activation steps to the formation of active complexes take place after reaction with TBHP. Once the active complexes are formed, they may undergo epoxidation along various mechanistic cycles that are indicated with Roman indices in the figure. The different classes Ia, Ib, IIa, IIb, and III of reaction mechanisms are defined in Fig. 6.

to form this high energetic species from the reaction of TBHP with the oxometal group of the catalyst. Plausible routes have been proposed by Chong and Sharpless [44], and some of them will be discussed later in the paper. The occurrence of peroxo complexes of the type **21** with vanadium in oxidation number +IV is less probable, as these complexes require an excess of the peroxide, and under these circumstances, we may expect oxidation of V^{+IV} to V^{+V}.

Apart from the three mechanisms, there also exists another mechanism – the so-called Mimoun-type mechanism [45] – in which the (cyclo)alkene first coordinates with the metal before reacting with the peroxide, followed by the formation of a five-membered cyclic intermediate that decomposes to epoxide and catalyst. The Mimoun-type mechanism has been intensively studied by Kuznetsov and Pessoa [32] in the olefin epoxidation catalyzed by a vanadium-salan complex. However, they found no stable π-complexes for the coordination of the double bond of the alkene with the metal, and this is probably due to the high oxidation state of the transition metal. In addition, the activation barrier to form a five-membered metallocyclic intermediate turns out to be too high. They conclude that the Mimoun-type mechanism may be ruled out. Therefore, the Mimoun mechanism will not be further examined in this work and focus will be made on the Sharpless-type mechanism.

The mechanisms taken up in Fig. 6 are meant to give a global overview of various mechanistic proposals for epoxidation starting from a mixture of active complexes. Those complexes that are not figuring in the scheme are either energetically too activated or show a structure with too many ligands hindering any flexibility for further reaction. In addition, almost all active complexes are linked through reaction equilibriums – they will be discussed later – and in this respect structures that are not taken up in the scheme can in most cases be brought back to one of the classes sketched in Fig. 6.

In view of all these considerations, it is obvious that the total number of possible active complexes (AC) may be very high. This is especially true when taking into account all possible ligand combinations that can be formed. Realistic choices for ligands in this epoxidation study with $VO(acac)_2$ are given in Fig. 2c. Each AC generates its own reaction kinetics. To prevent unnecessary transition state computations for reactions that are unlikely to occur, we exclude the possibility that the acetyl acetonate and acetate ligand appears twice in the same monovanadium complex. Also experimentally, it

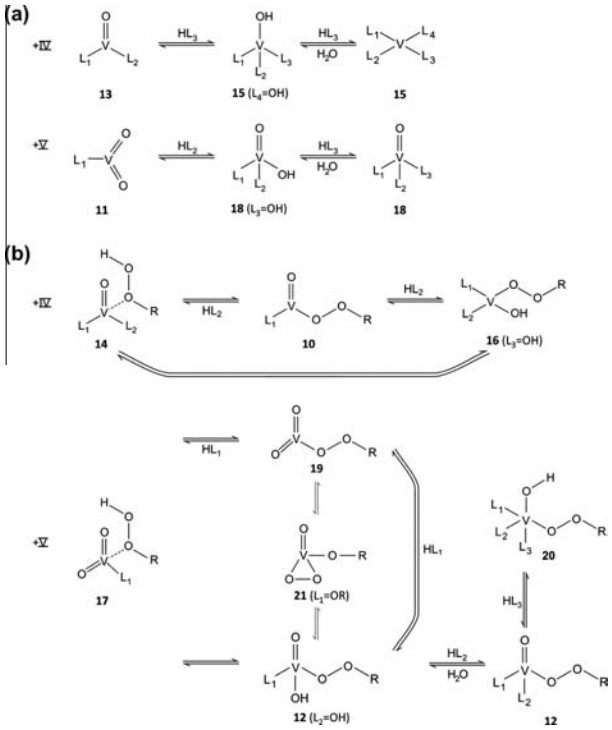

Fig. 5. (a) Equilibrium steps between different inactive complexes (IC). (b) Equilibrium steps between various active complexes (AC).

was shown that $VO(acac)_2(OOR)$ could not be responsible for the catalytic activity in epoxidation of cyclohexene [8].

3. Computational methods

The proposed catalytic cycles for the homogenous epoxidation of cyclohexene ($VO(acac)_2$ + TBHP) were studied theoretically by means of Density Functional Theory (DFT). All intermediates and transition states were fully optimized at the DFT level of theory using the B3LYP hybrid functional [46,47] and usage of the Gaussian03 package [48]. The double-zeta Pople basis set 6-31 + G(d) was used for all the atoms except for vanadium, for which the LANL2DZ effective core potential, and basis set was applied [49]. This combined basis set is abbreviated by BS1 in the following. The frequencies were calculated at the same level of theory as the geometry optimizations and confirmed that all structures were either local minima on the potential energy surface or transition states. Afterward, the energies were refined by single-point energy calculations at the B3LYP/6-311 + g(3df,2p) level of theory. This type of procedure is commonly used in theoretical calculations on transition metal catalysis [34,50,51]. Furthermore, also the van der Waals corrections as developed by Grimme were included [52]. More specifically, the dispersion corrections are calculated according to the third version of Grimme [53] by using the ORCA program [54]. Using standard notation "LOT-E"//"LOT-G" (LOT-E and LOT-G being the electronic levels of theory used for the energy and geometry optimizations, respectively), all results discussed in this paper are obtained with the method denoted as "B3LYP/6-311 + g(3df,2p)-D3//B3LYP/BS1."

In this paper, both the unimolecular and bimolecular rate coefficients will be determined for the epoxidation reaction. Both approaches differ by the reference level that is used for the reactants [55]. A schematic energy diagram for the epoxidation reaction of cyclohexene is given in Fig. 6. In case of the intrinsic approach, one starts from the reactant level where the various reacting species are fully adsorbed at the active complex (referred as pre-reactive complex in Fig. 7). In case of the bimolecular approach, the reactant level is taken as the active vanadium complex (AC) with cyclohexene in the gasphase.

All considered reactions are strongly exothermic, which is reflected in a high backward reaction barrier (in most cases even higher than 200 kJ/mol). Therefore, only the forward reaction will be considered in the main paper (backward reaction parameters can be found in Supporting information). In order to find the correct pre-reactive complex, IRC calculations were performed starting from the transition states. All reaction rate constants are

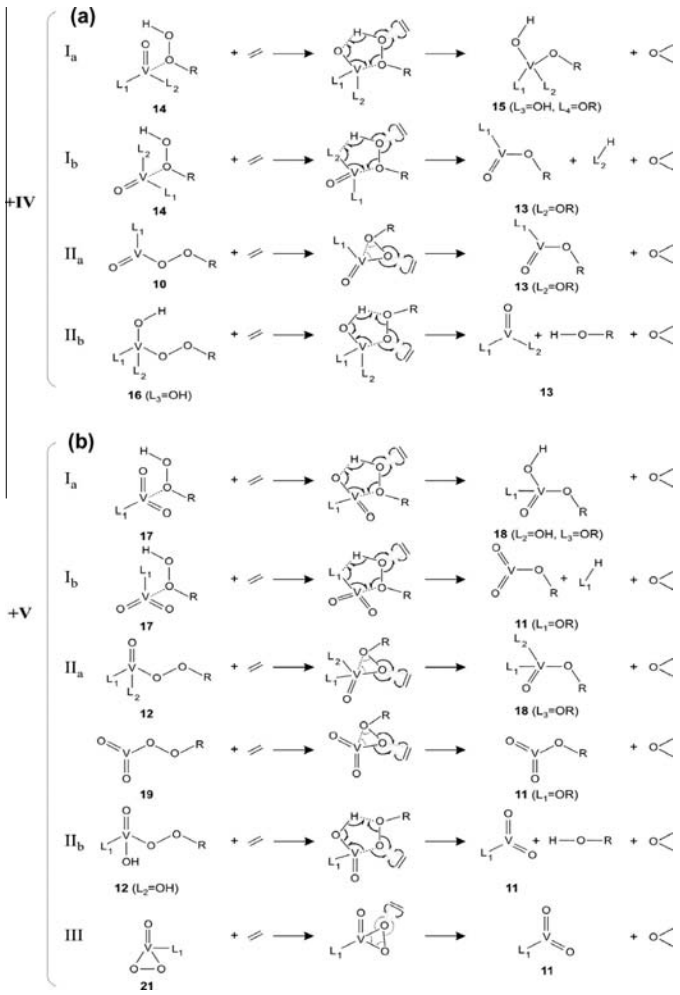

Fig. 6. Various reaction mechanisms for the epoxidation reaction. Both vanadium species in oxidation state +IV and +V are taken up.

obtained using classical transition state theory. Within the unimolecular approach, this gives following expression for the rate coefficient k_{uni} (s^{-1}):

$$k_{fwd,uni}(T) = \frac{q_{TS}(T)}{q_R(T)} \exp\left(-\frac{\Delta E^{\ddagger}_{0,int}}{RT}\right) \quad (1)$$

with $\Delta E^{\ddagger}_{0,int}$ the intrinsic reaction barrier at 0 K (Fig. 7).

Within the bimolecular approach, the reactants consist of cyclohexene (CH) and an activated complex (AC), and the rate constant $k_{fwd,bi}$ ($m^3\ mol^{-1}\ s^{-1}$) is given by the following expression:

$$k_{fwd,bi}(T) = \frac{q_{TS}(T)}{q_{AC}(T)\,q_{CH}(T)} V \exp\left(-\frac{\Delta E^{\ddagger}_{0,app}}{RT}\right) \quad (2)$$

with $\Delta E^{\ddagger}_{0,app}$ the apparent reaction barrier at 0 K (Fig. 7).

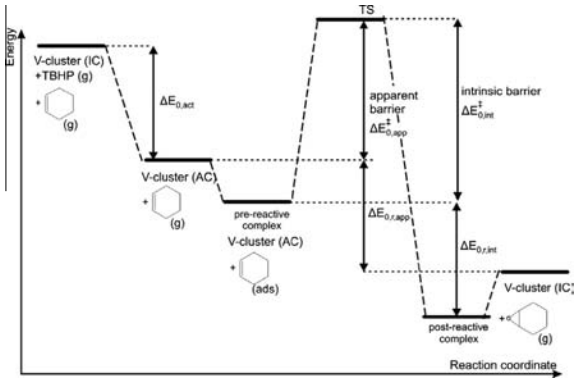

Fig. 7. Schematical energy diagram for the epoxidation reaction of cyclohexene and an active mono-vanadium peroxo complex. For an unimolecular approach, relevant energies are the intrinsic barrier $\Delta E^{\ddagger}_{0,int}$, and the reaction energy $\Delta E_{0,r,int}$ referred to the fully physisorbed pre-reactive of post-reactive complex. For a bimolecular description, the apparent energy barriers $\Delta E^{\ddagger}_{0,app}$ and apparent reaction energies $\Delta E_{0,r,app}$ are used. $\Delta E_{0,r,act}$ is the energy difference between the inactive complex and the activated complex.

All other reactions in the catalytic cycle apart from the epoxidation reaction are described as equilibrium steps. Fast equilibrium processes exist between the various species belonging to the family of inactive (Fig. 5a) and active complexes (Fig. 5b), which in turn are subdivided into vanadium +IV or vanadium +V classes. A third class of equilibrium processes concerns the activation reactions (Fig. 4) connecting the family of inactive to the family of the active species. In all equilibrium steps, the oxidation state of the vanadium is kept fixed (+IV or +V), and transition between vanadium complexes with different oxidation number only takes place via radical decomposition reactions as outlined in Fig. 3. Most of the equilibrium reactions represent ligand exchange reactions. In this last category, the equilibrium coefficient is calculated as follows:

$$K_P\ (T) = \frac{q_B\ (T) \cdot q_{HL2}\ (T)}{q_A\ (T) \cdot q_{HL1}\ (T)} \cdot \exp\left(-\frac{\Delta E_{0,r}}{RT}\right) = \exp\left(-\frac{\Delta G_{323,r}}{RT}\right), \qquad (3)$$

for the reaction schematically written by complex A + HL_1 complex B + HL_2.

Herein, $\Delta E_{0,r}$ and $\Delta E_{323,r}$ represent respectively the reaction energy at 0 K and the Gibbs free energy at 323 K.

The calculation procedures for all rate coefficients k and K are now implemented in an in-house developed software module TAMKIN [56].

4. Experimental characterization and kinetics for epoxidation of cyclohexene

This experimental section contains an infrared (IR) and gas chromatography (GC) study carried out to characterize various species present in the reaction mixture. The results on the UV–Vis and GC are taken up in the SI. Additionally, experimental kinetic parameters for the epoxidation of cyclohexene have been determined, which can then directly be compared with the theoretically determined rates.

4.1. IR

The IR measurements were recorded on a Bruker EQUINOX 55 FTIR spectrometer. The liquid samples were measured between KBr plates at room temperature. An accumulation of 100 scans was done of each sample. Three samples with increasing V/TBHP ratio were prepared in a mixture of 0.0055 mol catalyst with *tert*-butyl hydroperoxide (TBHP) solved in decane. Their specific composition is tabulated in Table 1. The samples are presented with increasing amount of oxidant.

Fig. 8 presents the liquid-phase infrared spectra of the mixtures described in Table 1, measured within a few minutes after mixing the ingredients at room temperature. It is not surprising that these infrared spectra are very rich, as they contain a mixture of several infrared active species. As a consequence, the vibrations that are typical for acetylacetonate ligands (1562 cm^{-1} for the C═O and 1526 cm^{-1} for the conjugated C═C stretch) [57] are overwhelmed by other vibrations, for example the CH_2 deformation of decane (solvent of TBHP) and CH_3—C deformation of TBHP, both located around 1500 cm^{-1}. However, there is a clear window around 1700 cm^{-1} and the C═O stretch vibration that is very typical of the acetate can be nicely seen at 1715 cm^{-1} [58]. The peak intensity of the acetate clearly increases by raising the amount of TBHP. So, if more oxidant is added, then more acetylacetonate ligands oxidize toward acetate esters and acetic acid. This is a nice experimental validation of the proposal of Stepovik [7] to initially generate active complexes (Fig. 1).

In order to strengthen the experimental validation, we repeated the experiment with two different solvents: toluene and acetonitrile. The results are reported in the SI, but confirm the experiment with chloroform as solvent.

4.2. Kinetic study

An experimental setup has been established to determine kinetic parameters for the epoxidation of cyclohexene. Therefore,

Table 1
Composition of the liquid samples.

	Ratio V/TBHP	TBHP (mol)	$VO(acac)_2$ (mol)	Chloroform (mL)
Sample 1	2	0.00275	0.0055	10
Sample 2	2/1.5	0.00412	0.0055	10
Sample 3	0.5	0.0110	0.0055	10

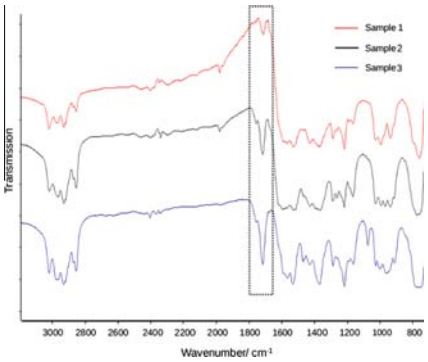

Fig. 8. IR spectra of samples 1 to 3 with the composition described in Table 1.

experiments have been performed at different temperatures, with varying cyclohexene and *tert*-butyl hydroperoxide concentration, working in diluted conditions (solvent: chloroform). For extended details, for example experimental setup and different initial concentrations, we refer to the Supporting Information.

The cyclohexene epoxidation rate R is assumed to be first order in the cyclohexene concentration [CH] and the concentration of all active vanadium species [V^{AC}]:

$$R = \frac{d[\mathrm{CH-ox}]}{dt} = k \cdot [\mathrm{CH}] \cdot [V^{AC}] \quad (4)$$

with k, the rate coefficient for the epoxidation reaction of cyclohexene ($m^3\ mol^{-1}\ s^{-1}$) toward cyclohexene oxide **2**. An equilibrium is further assumed between the active vanadium (V^{AC}) and the inactive vanadium (V^{IC}) species. (This will be extensively discussed in the theoretical results section.) Activation of the inactive complexes takes place after reaction with TBHP:

$$V^{IC} + \mathrm{TBHP} \rightleftharpoons V^{AC}$$

The corresponding equilibrium coefficient K_{act} ($m^3\ mol^{-1}$) for this activation reaction is easily calculated as:

$$K_{act} = \frac{[V^{AC}]}{[V^{IC}] \cdot [\mathrm{TBHP}]} \quad (5)$$

Assuming a constant total concentration of vanadium $[V^0] = [V^{IC}] + [V^{AC}]$, which is determined by the initial vanadium concentration, a straightforward calculation leads to an expression of the cyclohexene epoxidation rate R in terms of the concentration of the vanadium catalyst, cyclohexene and the peroxide:

$$R = \frac{k \cdot [\mathrm{CH}] \cdot K_{act} \cdot [V^0] \cdot [\mathrm{TBHP}]}{1 + K_{act} \cdot [\mathrm{TBHP}]} \quad (6)$$

in agreement with what has been reported by Gould et al. [4].

The initial rate R_0 is obtained after considering the initial concentration of cyclohexene $[CH]_0$ in the reaction mixture.

Equation. (6) is rewritten as:

$$Y = k \cdot [V^0] \cdot K_{act} - K_{act} \cdot X \quad (7)$$

with $Y = \frac{R_0}{[\mathrm{TBHP}]_0 [\mathrm{CH}]_0}$ and $X = \frac{R_0}{[\mathrm{CH}]_0}$

A plot Y versus X represents a Hofstee-type plot. The intersection with the Y-axis, obtained after extrapolation of the rate data, yields the value of the rate constant k. The absolute value of the slope represents the equilibrium constant K_{act}. Measurements have been done at different temperatures and results are summarized in Table 2. For each temperature, different runs have been performed with different concentrations of cyclohexene $[CH]_0$ and TBHP $[TBHP]_0$. The Hofstee plots at the various temperatures are given in Fig. S.3 of the Supporting Information. The rate constants k derived from the Hofstee plots for the four temperatures are used as input for an Arrhenius plot of $\ln(k)$ versus 1/T. It closely approaches a straight line (Fig. 9) indicating that the extrapolation procedure used to obtain the rates k is free from large random errors. The Arrhenius plot predicts an average pre-exponential factor A of 2.36E+07 $m^3\ mol^{-1}\ s^{-1}$ and an activation energy E_a of 48.6 kJ/mol. These kinetic parameters should be regarded as average parameters of all possible active vanadium species, leading to the epoxidation of cyclohexene. The values in Table 2 are in close agreement with those of the paper of Gould et al. [4], also taking in mind that we have been working at other reaction conditions (solvent, different concentrations of cyclohexene, vanadium, and TBHP; Supporting Information for details). Moreover, we could also extract more information from the experiment. The standard enthalpy of activation at 323 K is found to be 43.2 kJ/mol (for a bimolecular reaction $\Delta H^{\ddagger}_{323} = E_a - 2\,RT$). The entropic contribution $\Delta S^{\ddagger}_{323}$ amounts to −90.8 J/mol/K, yielding a Gibbs free-energy difference $\Delta G^{\ddagger}_{323}$ for the epoxidation reaction of 72.6 kJ/mol. These are interesting values to be compared with the theoretical predictions (see Section 5.7).

The kinetic data obtained here will be validated with the epoxidation mechanisms that are found to be most probable from our theoretical calculations.

5. Results and discussion on the theoretical calculations

The complete catalytic cycle, including activation, epoxidation, and change in oxidation state through radical decomposition reactions is now studied theoretically for all active complexes and ligands as introduced in Section 2. This section is structured as follows: First, the thermodynamic equilibriums between various active complexes are discussed, followed by a similar discussion on the inactive complexes. Then, the activation steps allowing the transformation of inactive to active complexes are modeled through thermodynamic equilibrium steps. First principle chemical kinetics are determined for all proposed epoxidation pathways (Fig. 6) in Section 5.4. In Section 5.5, we also discuss the radical decomposition pathways that allow to change the oxidation state. At the end of this section, our kinetic data on the most abundant species and most probable epoxidation mechanisms are compared with available experimental data from literature and the experimental data from this work.

5.1. Equilibrium between active complexes (AC)

The different equilibriums occurring among the active complexes are schematically displayed in Fig. 5b. For the vanadium +IV complexes, three different types of active complexes are considered corresponding to species **10**, **14,** and **16**(L_3 = OH), which were already introduced in Fig. 4. They may transform into each other

Table 2
Overview of the rate constant and equilibrium constant K_p between active and inactive vanadium complexes at different temperatures.

	337 K	331 K	321 K	313 K	323 K
k ($m^3\ mol^{-1}\ s^{-1}$)	7.4E−04	4.9E−04	2.9E−04	1.9E−04	2.13E−04[a]
K_{act} ($m^3\ mol^{-1}$)	3.18E−03	4.90E−03	8.56E−03	1.79E−02	1.03E−02[a]

[a] Experimental value from [4].

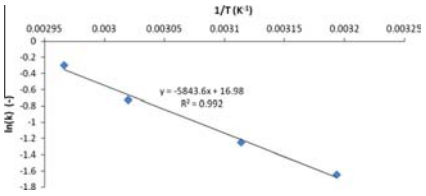

Fig. 9. Arrhenius plot: ln (k) versus 1/T.

through ligand interchanges and by proton hops. With the introduction of four ligands (OH, acac, OAc, and OtBu as introduced in Fig. 3c) the number of different complexes may become very high. To keep this number within reasonable limits, we restricted the calculation of equilibrium steps among active complexes bearing only one acac or OAc ligand per complex, which is a reasonable assumption taking into account the bulkiness of the TBHP as oxidant. The choice of the four ligands is evident, since acetic acid (HOAc) is formed during the oxidation of acetyl acetonate (Hacac), as already mentioned in Section 2, which was also confirmed by the experimental IR measurement. In addition, the acetate ligand (OAc) prefers a bidendate ligand coordination with vanadium in most of the complexes.

The equilibrium constants for each of these steps were calculated according to the procedure outlined in the computational section. The results for the equilibrium constants and the associated free energies are schematically shown in Fig. 10a. The complex VO(acac)(OOtBu) **10** is taken as a reference for the free energies for all species bearing vanadium in oxidation state +IV. Vertical moves in the scheme correspond to the complexes of the same type VO(L_1)(OOtBu) but with ligand exchange. The other complexes **14** and **16**(L_3 = OH) contain an additional ligand L_2. In the scheme of Fig. 10a only those complexes are retained which are energetically closest to VO(acac)(OOtBu) complex. The latter is the most favored active V^{+IV} compound resulting from the calculations. The notation used for the identification of the other complexes is straightforward: V(OH)(OH)(acac)(OOtBu) stands for active compound **16** with two OH ligands and an acetyl acetonate ligand.

Similarly, for vanadium +V complexes, a selection of equilibrium steps is given in Fig. 10b. The selection is made on basis of the same criterion as for the vanadium +IV complexes. In this case, complex VO(acac)(OH)(OOtBu) belonging to compound family **12** is taken as the reference, although it does not correspond to the most stable complex. From that starting point, all combinations L_1 and L_2 are considered according to the imposed restrictions on the ligand choices. By subsequent ligand exchange reactions, all active V^{+V} complexes taken up in Fig. 5b are reached. On basis of the Gibbs free-energy profiles (at 323 K), complex VO(OtBu)(OtBu)(OOtBu) turns out to be energetically the most favorable compound (indicated in the bottom right of Fig. 10b). Any complex of family **12** formed during the catalytic cycle will finally evolve into the complex where all passive ligands are replaced by OtBu. These ligand exchange reactions require the presence of *tert*-butanol, but since the concentration of this alcohol is systematically increasing with reaction time, theory will predict complex VO(OtBu)(OtBu)(OOtBu) as the most abundant active species, and this is in complete agreement with experimental observations.

The same conclusion cannot entirely be drawn for the vanadium +IV complexes. The scheme in Fig. 10a predicts VO(acac)(OOtBu) and V(OH)(OtBu)(acac)(OOtBu) as most favorable active compounds. The complex with two OtBu ligands suffers from a slightly higher free energy of about 25 kJ/mol, which is still reasonable. The corresponding VO(OtBu)(OOtBu) alkylperoxo complex with a V=O ligand is substantially higher activated (about 50 kJ/mol). It confirms that in the first catalytic cycle, active species with a bidentate ligand coordinating to vanadium V^{+IV} are present in this complex mechanism of subsequent epoxidation and activation processes. This is partly also the case in the catalytic cycle with V^{+V} as active species, but less significant. In the vanadium +V complexes, there is clear ligand preference for *tert*-butanol. The gain in free energy with respect to the other ligands amounts to 20 kJ/mol or more. On the other hand, within the complexes coordinated with TBHP (compound family **17**), the bidendate ligands (acac and OAc) turn out to be the most favorable ligands.

Another relevant remark resulting from experimental work is the strong preference of acetic acid for coordination with vanadium. Theoretically, this preference is not that pronounced but it cannot be excluded on energetic grounds. In addition, further ligand exchange reactions on complexes containing acac ligands with water or *tert*-butanol will release Hacac, which is not stable against oxidation and rapidly oxidizes toward acetate acid and release of CO_2 gas. With increasing reaction time, the appearance of OAc-containing active vanadium complexes in the reagent mixture will obviously grow.

5.2. Equilibrium between inactive complexes (IC)

Similarly as for the active complexes, equilibriums between inactive complexes have also been investigated. A scheme similar as Fig. 10 has been constructed based on the different equilibrium steps displayed in Fig. 5a. As it does not reveal new conclusions fundamentally different from those drawn for the active species, the scheme is taken up in the S.I. under Fig. S.4. The Gibbs free-energy differences are listed for each path on the surface of inactive complexes and are of practical use to extract the Gibbs free activation energy required for activating any inactive species to a specific active species. The procedure will be outlined in the remainder of the paper.

5.3. Activation from inactive to active complexes

Inactive complexes are activated to active complexes after reaction with TBHP. The different classes are depicted in Fig. 4. These activation reactions are described as equilibrium steps. In the early stages of epoxidation, also the reaction given in Fig. 2 where the $VO(acac)_2$ catalyst is activated with TBHP is relevant. This equilibrium step belongs to the class **13** + TBHP → **10** + HL_2 (Fig. 4). A Gibbs free-energy difference of +44.5 kJ/mol is found at 323 K, but since Hacac oxidizes fastly with a strong exothermic reaction energy of −1171 kJ/mol, the reaction becomes irreversible. Acetic acid – one of the end products of the oxidation of Hacac – will grow in importance in the reagent mixture and hence in ligand exchange reactions between the various vanadium complexes.

The Gibbs free energies differences between active complex and inactive complexes at 323 K are tabulated in the first two column of Tables 3 and 4, and these will further be referred as activation free energies, that is, $\Delta G_{323,act}$, referring to the activation step of inactive to active complexes. Table 3 contains all vanadium species in oxidation state +IV, whereas Table 4 contains the species in oxidation state +V. Two inactive compounds are chosen as reference level for the activation free energies, that is, VO(acac)(OH) **13**(L_1 = acac, L_2 = OH) and V(OH)(OtBu)(OtBu)(OtBu) **15** for the inactive V^{+IV} species and VO_2(acac) **11**(L_1 = acac) and VO(OtBu)(OtBu)(OtBu) **18**(L_1 = OtBu, L_2 = OtBu, L_3 = OtBu) for the inactive V^{+V} species. In the early stages of the reaction, one could expect that inactive complexes with an acetyl acetonate ligand will certainly be abundantly present in the reagent mixture (they are also

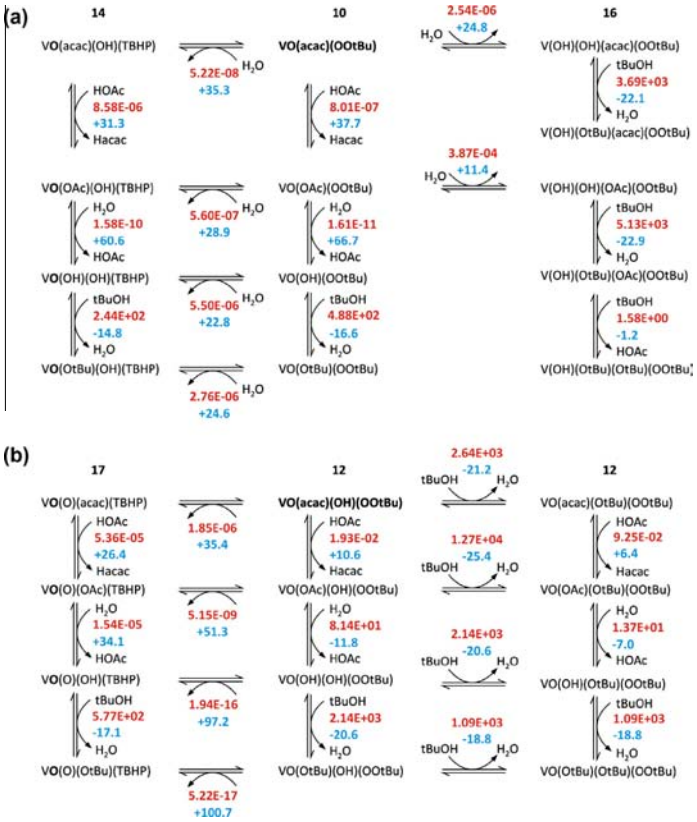

Fig. 10. a) Scheme displaying a selection of equilibrium steps between active V^{+IV} epoxidation complexes of the types 14, 10, and 16(L_3 = OH). Complex VO(acac)(OOtBu) is taken as the reference for the indication of the free energies and is indicated in bold. b) Equilibriums between active V^{+V} epoxidation complexes of the types 17 and 12. Complex VO(acac)(OH)(OOtBu) is taken as the reference for the indication of the free energies and is indicated in bold. The equilibrium coefficients $K_P(T)$ are indicated in red belonging to a temperature of 323 K. Also, the Gibbs free-energy differences ΔG_{323K} (in kJ/mol) are reported (blue). All data were calculated on the B3LYP/6-311 + g(3df,2p)-D3 level of theory for the energetics.

energetically favored on the free-energy surface (Fig. S.4). The second reference species are inactive complexes, which will become more and more dominant in the course of the epoxidation reaction, due to the increasing amount of *tert*-butanol in the reagent mixture, and the fact that these complexes are energetically the most favored on the Gibbs free-energy surface at 323 K. A schematic figure representing the class of active and inactive complexes for the various oxidation states and the reference species is given in Fig. 11.

To obtain a complete picture of the activation process, only one activation free energy is needed together with the free-energy differences among all active and inactive complexes. For example, to activate the reference inactive complex VO(acac)(OH) **13**(L_1 = acac, L_2 = OH) (which will be called IC1) to the corresponding activated complex VO(acac)(OH)-TBHP **14**, a free-energy difference of −4.2 kJ/mol is obtained (first line Table 3). With the additional knowledge of the free-energy differences between the various inactive complexes and active complexes, a complete picture of all transformations between inactive and active complexes can be obtained. The activation free energies tabulated in Table 3 and 4 represent actually the Gibbs free-energy difference required for activating reference compound IC1 to any active complex ACi after reaction with TBHP. Summarizing, the knowledge of the Gibbs free-energy surfaces corresponding to the respective inactive (Fig. S.4) and active complexes (Fig. 10) and the knowledge of only one activation step are sufficient to construct the entire energetic balance for each active species ready for epoxidation.

In order to determine the fastest epoxidation reaction mechanism, we need a complete energetic balance of all active

Table 3
Free energies for activation steps from inactive to active complexes and kinetics for epoxidation reactions starting from active V^{+IV} complexes. The activation free energies $\Delta G^{IC1}_{323,act}$ and $\Delta G^{IC2}_{323,act}$ are referred to VO(acac)(OH) and V(OH)(OtBu)(OtBu)(OtBu), respectively, and represent free-energy differences between active and inactive complexes. $\Delta E^{\ddagger}_{0,app}$ and $\Delta G_{323,app}$ are the electronic activation energy for epoxidation reaction and the activation free-energy for epoxidation as defined in Fig. 7. $\Delta E_{0,r,app}$ and $\Delta G_{323,r,app}$ are the electronic energy differences between product and reactant of epoxidation including zero-point vibrational energies and the free-energy differences between product and reactant of epoxidation at 323 K. Results are on the B3LYP/6–311+g(3df,2p)-D3 level of theory. All energies in kJ/mol.

	Activation Steps		*Epoxidation Reactions*					
	$\Delta G^{IC1}_{323,ac}$	$\Delta G^{IC2}_{323,act}$	$\Delta E^{\ddagger}_{0,app}$	$\Delta G^{\ddagger}_{323,app}$	$\Delta E_{0,r,app}$	$\Delta G_{323,r,app}$	k_{bi} (m^3 mol^{-1} s^{-1})	$\Delta G^{IC1}_{323,act+epox}$
	13–>14	15–>14	reaction mechanism Ia					
V**O**(acac)(OH)–TBHP	−4.2	6.3	42.1	97.3	−174.2	−172.6	3.34E−05	93.1
V**O**(acac)(OtBu)–TBHP	−13.4	−3.0	45.9	103.3	−182.4	−180.8	3.49E−06	89.9
V**O**(OAc)(OH)–TBHP	27.1	37.6	31.5	86.6	−188.6	−186.8	1.77E−03	113.8
V**O**(OAc)(OtBu)–TBHP	17.4	27.8	33.7	90.2	−196.4	−195.8	4.67E−04	107.6
V**O**(OH)(OH)–TBHP	87.8	98.2	22.0	74.9	−248.7	−249.0	1.36E−01	162.7
V**O**(OtBu)(OH)–TBHP	73.0	83.4	20.2	76.0	−252.8	−249.5	9.21E−02	149.0
V**O**(OtBu)(OtBu)–TBHP	60.1	70.5	20.3	76.5	−256.4	−252.6	7.51E−02	136.6
	13–>14	15–>14	reaction mechanism Ib					
VO(acac)(**O**H)–TBHP	−25.9	−15.4	36.9	92.0	−171.3	−170.0	2.36E−04	66.2
VO(acac)(**O**H)–TBHP endo	−25.9	−15.4	37.5	92.4	−171.3	−170.0	2.01E−04	66.6
VO(acac)(**O**tBu)–TBHP	−30.8	−20.3	41.3	98.7	−182.4	−181.5	1.97E−05	67.9
VO(OAc)(**O**H)–TBHP	4.6	15.0	24.6	78.9	−113.8	−162.6	3.08E−02	83.5
VO(OAc)(**O**H)–TBHP radical	4.6	15.0	25.1	78.8	−122.4	−126.9	3.23E−02	83.4
VO(OAc)(**O**tBu)–TBHP	−4.6	5.8	26.6	85.0	−94.2	−153.4	3.21E−03	80.4
VO(OH)(**O**H)–TBHP radical	66.4	76.9	−0.5	38.5	−195.4	−197.3	1.06E+05	104.9
	13–>10	15–>10	reaction mechanism IIa					
VO(acac)(OOtBu)	−39.4	−29.0	14.6	68.4	−152.6	−159.3	1.55E+00	29.0
VO(OAc)(OOtBu)	−1.7	8.7	8.9	61.4	−151.7	−156.3	2.09E+01	59.7
VO(OH)(OOtBu)	65.0	75.4	7.9	58.4	−146.9	−154.3	6.46E+01	123.4
VO(OtBu)(OOtBu)	48.4	58.8	8.6	59.8	−147.8	−157.0	3.77E+01	108.2
	13–>16	15–>16	reaction mechanism IIb					
V(OH)(acac)(OH)(OOtBu)	−14.6	−4.2	82.5	143.5	−116.2	−167.5	1.12E−12	128.9
V(OH)(acac)(OtBu)(OOtBu)	−36.7	−26.2	100.3	164.6	−106.4	−162.1	4.29E−16	127.9
V(OH)(OAc)(OH)(OOtBu)	9.6	20.0	78.8	139.3	−99.7	−150.0	5.25E−12	148.9
V(OH)(OAc)(OtBu)(OOtBu)	−13.3	−2.9	91.8	154.6	−90.8	−144.7	1.78E−14	141.3

compounds, which can be deduced following the procedure explained in Fig. 11. However, not all equilibriums are displayed on the Gibbs free-energy surfaces for active complexes (Fig. 10). The two highly active peroxo vanadium complexes VO(OO)(OH) **21**(L_1 = OH) and VO(OO)(OOtBu) **22** are not taken up in the general scheme of Fig. 4 but may result from active dioxo V^{+V} complexes, such as complexes **17** and **19**. An example of a possible mechanism to these active peroxo complexes is demonstrated in Fig. 12. The scheme starts from the active dioxo V^{+V} complex **17** VO(O)(OH)-TBHP that transforms into the peroxo complex **21**(L_1 = OtBu) after spatial reorientation of the coordinated TBHP and release of water. In general, complexes **17** and also complex **21** VO(OO)(OH) are substantially higher in energy than the most stable active complex (VO(OtBu)(OtBu)(OOtBu)) with energy differences of the order of 150 kJ/mol. In order to make these active species and subsequent epoxidation reaction plausible in the overall reaction scheme, a substantial higher epoxidation rate would be required. We will discuss these issues in following section.

Careful inspection of the activation free energies for both V^{+IV} complexes coordinated with TBHP learns that the formation of active complexes ready for epoxidation pathways **Ib** is preferred over **Ia**, and the formation of some active complexes ready for pathways **IIa** and **IIb** is also preferred over **Ia**. For V^{+V} complexes, there is clearly a preference for the formation of active complexes of epoxidation pathways **IIa** and **IIb**. However, to make conclusions about the preferred epoxidation pathways, also Gibbs free-energy barriers for epoxidation need to be taken into consideration.

5.4. Epoxidation reactions

Epoxidation transition states have been theoretically modeled for each active species, and the various reaction mechanisms proposed in Fig. 4. 3-D representations of the transition states are shown in Fig. 13. In Tables 3 and 4 the apparent kinetic data are taken up, that is, where the reference level is taken as the active vanadium complex and cyclohexene in the gas phase. For completeness, we also report the unimolecular kinetic data in Tables S.3 and S.4 of the Supporting Information. The list of active species is almost complete and comprises all ligand combinations with exception of twice the acac and OAc ligands in the same mono-vanadium complex. In this context, it is also worthwhile to note that even an excess of TBHP will never restore $VO(acac)_2(OOtBu)$ as active complex, fully in line with the experimental findings reported by Talsi [8], due to the irreversible oxidation of the acac ligand into acetic acid.

Inspection of the Tables 3 and 4 learns that the energy barriers may vary drastically going from nearly zero to about 130 kJ/mol. To discriminate between plausible epoxidation pathways, taking into account both the abundance of the active species and the rate constant for epoxidation, we introduced a global free-energy barrier ($\Delta G^{IC1}_{323,act+epox}$) that is defined as the sum of the activation free energy ($\Delta G^{IC1}_{323,act}$) and the epoxidation free-energy barrier ($\Delta G^{\ddagger}_{323,app}$)). For V^{+V} species, a similar quantity $\Delta G^{IC3}_{323,act+epox}$ is introduced.

Within the class of V^{+IV} complexes, species VO(acac)(OOtBu) appears as one of the favorable active complexes ($\Delta G^{IC1}_{323,act}$ = −39.4 kJ/mol), which furthermore has one of the lowest activation free-energy barriers for epoxidation $\Delta G^{\ddagger}_{323,app}$ = 68.4 kJ/mol) or a bimolecular epoxidation rate of 1.55 m^3 mol^{-1} s^{-1}. This favorable reaction cycle falls into the class of the Sharpless reaction mechanism **IIa** and will be one of the dominant reaction paths for the epoxidation of cyclohexene over $VO(acac)_2$ catalysts. This is certainly the case in the early stages of the epoxidation process, but since any release of Hacac in a ligand exchange reaction will

Table 4
Free energies for activation steps from inactive to active complexes and kinetics for epoxidation reactions starting from active V^{+V} complexes. The activation free energies $\Delta G^{IC3}_{323,act}$ and $\Delta G^{IC4}_{323,act}$ are referred to VO_2(acac) (IC3) and VO(OtBu)(OtBu)(OtBu) (IC4), respectively, and represent free-energy differences between active and inactive complexes. $\Delta E^{\ddagger}_{0,app}$ and $\Delta G^{\ddagger}_{323,app}$ are the electronic activation energy for epoxidation reaction and the activation free-energy for epoxidation as defined in Fig. 7. $\Delta E_{0,r,app}$ and $\Delta G_{323,r,app}$ are the electronic energy differences between product and reactant of epoxidation including zero-point vibrational energies and the free-energy differences between product and reactant of epoxidation at 323 K. Results are on the B3LYP/6–311+g(3df,2p)-D3 level of theory. All energies in kJ/mol.

	$\Delta G^{IC3}_{323,ac}$	$\Delta G^{IC4}_{323,act}$	$\Delta E^{\ddagger}_{0,app}$	$\Delta G^{\ddagger}_{323,app}$	$\Delta E_{0,r,app}$	$\Delta G_{323,r,app}$	k_{bi} (m^3 mol^{-1} s^{-1})	$\Delta G^{IC3}_{323,act+epox}$
	11– > 17	18– > 17	reaction mechanism Ia					
V**O**(O)(acac)—TBHP	−9.3	85.6	39.1	94.2	−214.6	−212.4	1.05E−04	84.9
V**O**(O)(acac)—TBHP endo	−9.3	85.6	35.2	91.6	−214.6	−212.4	2.71E−04	82.4
V**O**(O)(OAc)—TBHP	17.1	112.0	22.1	78.9	−246.5	−245.3	3.15E−02	96.0
V**O**(O)(OAc)—TBHP endo	17.1	112.0	17.3	75.2	−246.5	−245.3	1.22E−01	92.4
V**O**(O)(OH)—TBHP	51.2	146.1	8.9	59.9	−286.9	−287.9	3.62E+01	111.2
V**O**(O)(OH)—TBHP endo	51.2	146.1	1.4	54.6	−176.1	−179.3	2.66E+02	105.8
V**O**(O)(OtBu)—TBHP	34.2	129.0	8.8	61.9	−289.1	−288.4	1.74E+01	96.1
V**O**(O)(OtBu)—TBHP endo	34.2	129.0	2.2	56.3	−289.1	−288.4	1.39E+02	90.5
	11–>17	18–>17	reaction mechanism Ib					
VO(O)(**O**Ac)—TBHP	26.7	121.6	7.2	64.3	−205.8	−198.8	7.21E+00	91.0
VO(O)(**O**H)—TBHP	58.4	153.3	−0.4	52.2	−183.6	−186.5	6.55E+02	110.6
VO(O)(**O**tBu)—TBHP	43.7	138.6	1.0	52.8	−202.8	−202.1	5.15E+02	96.6
	11–>12	18–>12	reaction mechanism IIa					
VO(acac)(OH)(OOtBu)	−44.7	50.2	48.8	108.7	−185.8	−184.1	4.74E−07	64.0
VO(acac)(OtBu)(OOtBu)	−65.9	29.0	47.7	109.5	−178.7	−174.7	3.47E−07	46.8
VO(OAc)(OH)(OOtBu)	−34.1	60.7	22.2	80.9	−192.3	−190.9	1.47E−02	57.1
VO(OAc)(OAc)(OOtBu)	−21.2	73.6	14.3	78.3	−195.6	−197.7	3.85E−02	34.0
VO(OAc)(OtBu)(OOtBu)	−59.5	35.4	34.5	93.50	−192.4	−189.2	1.36E−04	56.3
VO(OH)(OH)(OOtBu)	−46.0	48.9	49.2	102.3	−190.0	−190.7	5.06E−06	41.2
VO(OtBu)(OH)(OOtBu)	−66.5	28.4	48.5	107.7	−188.4	−187.7	6.82E−07	31.0
VO(OtBu)(OtBu)(OOtBu)	−85.3	9.6	53.9	116.3	−188.4	−191.7	2.80E−08	43.6
	11–>12	18–>12	reaction mechanism IIb					
VO(OH)[acac)(OOtBu)	−44.7	50.2	107.6	168.6	−88.3	−137.4	9.64E−17	123.9
VO(OH)(OAc)(OOtBu)	−34.1	60.8	103.1	162.1	−30.8	−79.8	1.07E−15	128.0
VO(OH)(OH)(OOtBu)	−45.9	48.9	120.9	175.2	77.8	25.8	8.19E−18	129.3
VO(OH)(OtBu)(OOtBu)	−66.5	28.4	125.9	181.9	80.4	24.8	6.94E−19	115.3
	11–>	18–>	reaction mechanism III					
VO(OO)(OOtBu) **22**	26.7	121.6	7.8	58.2	−155.9	−159.2	1.39E+02	84.9
VO_2(OOtBu) **19**	97.1	192.0	−9.0	41.7	−134.2	−136.8	6.46E+04	138.8
VO(OO)(OH) **21**(L_1 = OH)	73.5	168.4	11.1	59.9	−95.4	−93.6	7.32E+01	133.4
VO(OO)(OtBu) **21**(L_1 = OtBu)	49.6	144.5	15.8	66.8	−89.9	−89.3	2.79E+00	116.4

irreversibly transform the acetyl acetonate acid into acetate acid this reaction path will decrease in importance. Within the same reaction family also, species VO(OAc)(OOtBu) results in a low global free-energy barrier for epoxidation ($\Delta G^{IC1}_{323,act+epox} = 59.7$) and will generate favorable epoxidation paths.

On basis of our kinetic and thermodynamic data, reaction mechanism **IIb** is ruled out as a probably reaction cycle for epoxidation. This is an immediate result from the high (free) energy barriers for epoxidation. The active complexes of the type **16** for V^{+IV} (and also type **12** for V^{+V} (see Fig. 3) have not the most ideal configuration to epoxidize the double bond in cyclohexene, although their free energies for formation predict a relatively high abundance. Also, the reaction mechanism **Ia** is not regarded as very plausible for epoxidation.

To a large extent, the same conclusions can be drawn for the class of the V^{+V} complexes: reaction mechanism **IIb** exhibits extremely low reaction rates despite the high probability for the formation of active complexes leading to this route, while the most preferred epoxidation mechanism is manifestly **IIa** with total free energies of activation + epoxidation that vary between 31 and 64 kJ/mol, which is by far 30 kJ/mol lower in energy than all other $\Delta G^{IC3}_{323,act+epox}$ predictions. When studying the values within this class in more details, it becomes apparent that the reaction rates for epoxidation may vary substantially with orders of magnitude depending on the choice of the ligands L_1 and L_2 in the active complex family VO(L_1)(L_2)(OOtBu) **12**. It is striking that acetyl acetonate and OtBu ligands hinder the epoxidation with low rate constants around 10^{-7} m^3 mol^{-1} s^{-1} despite their thermodynamical assignment as most favorable V^{+V} complexes (Fig. 10 and first column of Table 4). Largest reaction rates (of about 10^{-2} m^3 mol^{-1} s^{-1}) correspond with species containing the acetate ligand. Those complexes are thermodynamically slightly less favorable than the former with OtBu ligands, but the large reaction rate constant largely compensates this effect. The corresponding transition state is also shown in Fig. 13. Furthermore, this means that acetic acid can also be added experimentally to the solution, to fasten the epoxidation reaction, hereby confirming the previous experimental studies on the acceleration effect of acetic acid [59,60].

The reaction mechanisms **Ia** and **Ib** use TBHP-coordinated complexes. The individual reaction rates for epoxidation of complexes of family **17** are relatively high. Also, here acetate as ligand predicts the highest rate constant within this **Ia** reaction mechanism (see Table 2). However, thermodynamically, the formation of the active complexes is not preferred especially compared with the active complexes of family **12**. However, species of the type **17** are also formed via radical decomposition from active V^{+IV} coordinated complexes of type **14** following the mechanism outlined in Fig. 3. In this respect, VO(O)(L_1)(TBHP) **17** complexes can be more present than predicted according to the equilibrium steps sketched in Fig. 10. More information about the radical decomposition steps will be given further in this paper.

For complexes **17** involved in the reaction mechanisms **Ia** and **Ib**, several transition states were possible that mainly differ in the stereochemical position of the ligands on the active complexes.

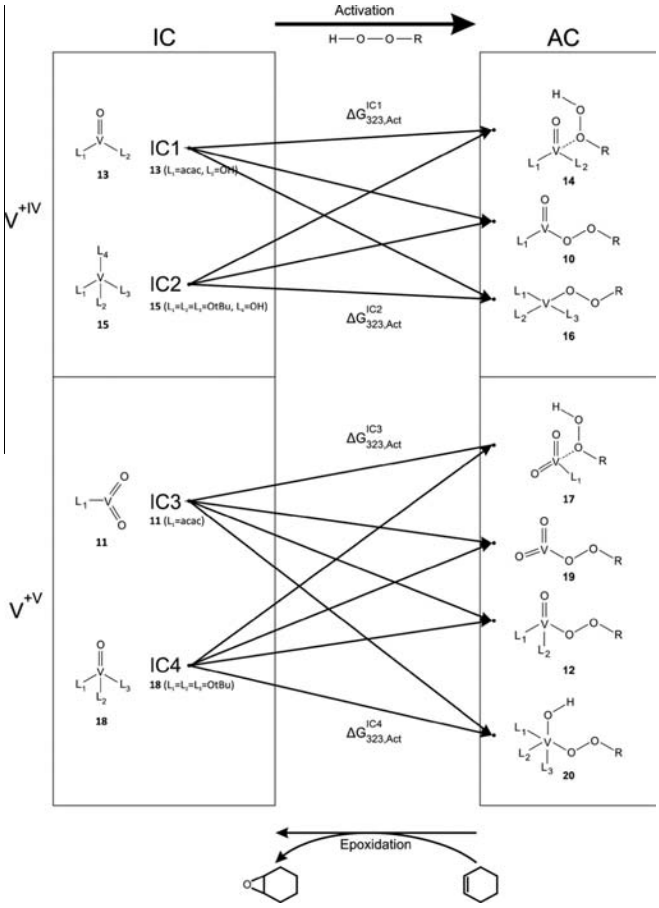

Fig. 11. Schematic representation of the class of active and inactive complexes for the various oxidation states and the reference species, IC1, IC2, IC3, and IC4, are defined as VO(acac)(OH), V(OH)(OtBu)(OtBu)(OtBu), VO_2(acac), and VO(OtBu)(OtBu)(OtBu).

We calculated transition states with an *endo* and *exo* position of the coordinated cyclohexene with respect to the vanadium dioxocompound. They are illustrated in Fig. S.5 in the Supporting Information. The *endo*-TS predicts a slightly smaller energy barrier (Table 4), but does not alter the overall conclusions.

Epoxidations according to mechanism **III** which start from peroxo species of types **19**, **21,** or **22** are characterized by a high rate of epoxidation. This is especially true for the peroxo complex VO_2(OOtBu) **19** that has actually the highest rate of epoxidation (6.4E+04 m^3 mol^{-1} s^{-1}). Some characteristic transition states are given in Fig. 14. Apart from the possible mechanisms for the formation of these active complexes, (given in Fig. 12) also other routes produce peroxovanadium species from the reaction of TBHP with the oxometal group of the catalyst, as proposed for example by Chong and Sharpless [44], although thermodynamically the formation of these complexes is not favored, as already mentioned earlier. For example, the Gibbs free-energy difference between species **19** and the most stable species VO(OtBu)(OtBu)(OOtBu) amounts to 182.5 kJ/mol, which can readily be deduced from the equilibrium steps displayed in Figs. 10 and 12. As such, overall mechanism **III** is not preferred with global free energies ($\Delta G^{IC3}_{323,act+epox}$) amounting to about 130 kJ/mol.

Finally, the major end product of the epoxidation reaction in the vanadium/TBHP catalytic system is *tert*-butanol beside the

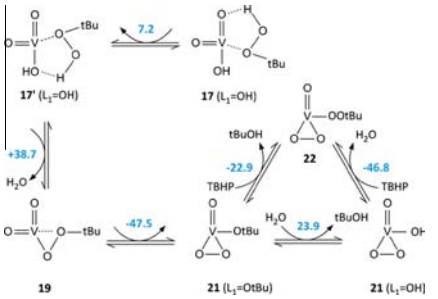

Fig. 12. A plausible pathway starting from an abundant V^{+V} inactive complex 18 to the highly activated peroxo complex 21. The Gibbs free-energy differences (in kJ/mol) of the displayed equilibriums are reported in blue belonging to a temperature of 323 K. (For interpretation of the references to colour in this figure legend, the reader is referred to the web version of this article.)

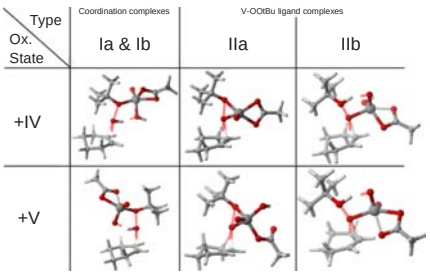

Fig. 13. Transition states for the mechanism types I and II with acetate ligands.

cyclohexene oxide. On the other hand, *tert*-butanol is also involved in multiple ligand exchange reactions on both inactive and active equilibrium free-energy surfaces. As the reaction time increases, high yields of tBuOH will be observed and will prevail in the reagent mixture, leading to less active species.

5.5. Coordination with water and tert-butanol

All equilibrium reactions on the Gibbs free-energy surfaces for active and inactive complexes, displayed in Fig. 10 and Figure S.4, and activation reactions (IC → AC) are modeled without coordination with water or *tert*-butanol. They could heavily affect the Gibbs free energy of the exchange ligand reactions or others, but the overall picture will not be affected. To illustrate with an example, we concentrate on the activation step from the inactive complex VO(OH)(OH)(OH) **18** to the active complex VO_2(OH)-TBHP **17**. Without coordination with water – following the lines as applied in the previous sections – the Gibbs free-energy difference between VO(OH)(OH)(OH) **18** and IC4 amounts to -61.2 kJ/mol (can be readily deduced from the Gibbs free-energy surface in Fig. S.4). Table 4 learns that the activation of IC4 to active complex VO_2(OH)-TBHP **17** requires an energy of 146.1 kJ/mol. Fig. 15 describes the same activation step from VO(OH)(OH)(OH) to VO_2(OH)-TBHP **17** but now via species **11** coordinated with water. This path leads to the same result. But we also learn that the complex **11**(L_1 = OH) coordinated with water is of about 100 kJ/mol more bound than the uncoordinated complex. Summarizing, a whole description of each complex coordinated with water or *tert*-butanol will not alter the conclusions made in the previous sections. We have preferred not to take them into consideration, as they will disturb the transparency of the discussion.

5.6. Radical decomposition reactions

In the previous discussion, V^{+IV} and V^{+V} species were treated as two independent families that could undergo epoxidation. However, they can mutually transform into each other by radical decomposition reactions, as already illustrated in Fig. 3. The $V^{+IV} \rightarrow V^{+V}$ oxidation happens by the production of tBuO· radicals, while the reverse transfer takes place by the production of tBuOO· radicals.

Some catalytic cycles for the interconversion of +IV and +V vanadium species were already investigated for the above-mentioned Vanadate/PCA system [34]. The proposed mechanism for radical generation with TBHP is completely analogous as that applied in this work (Fig. 3).

Table 5 gives an overview of reaction energies and reaction kinetics for the various radical decomposition reactions displayed in Fig. 3. We first concentrate on the generation of the tBuO· radical yielding V^{+V} species. The reaction energies show a strong dependence on the ligand choice. With an acac ligand in the complex, the reaction is thermodynamically favored for the formation of tBuO· giving a reaction free energy of -22 kJ/mol, whereas with all other ligands, this value becomes positive. These results are in agreement with our earlier published data, where a vanadium cluster with two terephthalate linkers was used to simulate the MIL-47 framework [11]. In that case, a reaction free energy was calculated of −34.7 kJ/mol. For monodentate ligands, such as the hydroxyl and *tert*-butoxide anion, the reaction takes values of about 35 kJ/mol. The observed trends can be related to the type of coordination of bidentate and monodentate ligands. The first one is tetrahedrally coordinated in the vanadium VO_2(L) complex and are more stabilized with respect to trigonal planar-coordinated species. On the other hand, the electronic activation barrier for the cleavage of the peroxide bond varies only slightly in terms of other ligands with values ranging from 30 to 40 kJ/mol. The reason for the apparently different behavior of the reaction energy should rather be searched in the different spatial coordination of the ligand with the metal. One should however be careful in analyzing the exact values for the free energies for the radical decomposition reaction $VO(L_1)(OOtBu) \rightarrow VO_2(L_1) + tBuO^{\cdot}$, as in reality these reactions take place in a reagent mixture with solvent, water, acids, alcohols, etc. If we reexamine the above reaction but now with the product coordinated with water, the reaction energy becomes negative in all cases. If we start from an already water-coordinated species $VO(L_1)(OOtBu)(H_2O)$ forming the coordinated $VO_2(L_1)(H_2O)$, the reaction energy is still exothermic ($\Delta G_{323,r,app} = -42.4$ kJ/mol for L_1 = OH)), whereas the electronic barrier remains nearly the same (31.8 kJ/mol). These results indicate the reaction is thermodynamically driven if coordinating ligands are present.

Summarizing, the obtained thermodynamic and kinetic data confirm that in all stages of the epoxidation reactions the transformation $V^{+IV} \rightarrow V^{+V}$ will certainly take place.

Apart from the transformation from $V^{+IV} \rightarrow V^{+V}$ species through oxidation, also V^{+V} species may transform back into V^{+IV} complexes (Fig. 3b). In Leus and Vandichel et al. [11], it has been found that the reaction free energy for this step is competitive (around 37 kJ/mol) with epoxidation reactions. In Table 5, we also report the reaction energies, but in contrast to the MIL-47 cluster, these "recycling" reactions become less probable when bidentate ligands

Fig. 14. Transition states for epoxidation starting from peroxo complexes.

are replaced by monodentate ligands. With the systematic increase of *tert*-butanol in the reagent mixture together with the decrease of Hacac, we could expect that the transformation of V^{+V} to V^{+IV} species will mainly occur during the early stages of the epoxidation, but that this recycling process will become less important as the reaction proceeds. We also investigated the effect of the coordination with water on the reaction free energies in the process $V^{+V} \rightarrow V^{+IV}$. In contrast to the $V^{+IV} \rightarrow V^{+V}$ radical decomposition, this has little influence on the thermodynamics. If the transformation would take place, it is most preferred for complexes with acac ligands. As these ligands are also readily consumed during the reaction cycle by oxidation (Fig. 2), the probability of going back to the oxidation state +IV is less probable as the reaction proceeds.

With the generation of tBuOO· radicals in the catalytic cycle highly active species are formed which can epoxidize cyclohexene following the so-called Twigg mechanism [61]. We did the calculation and found that the Twigg epoxidation mechanism turned out to be not favorable: First, an intermediate of alkoxy radical type is formed with a high reaction free-energy barrier of 92.4 kJ/mol and finally the epoxidation with a barrier of 30.3 kJ/mol. In view of these findings, this specific epoxidation path can be seen as a minor route toward cyclohexene oxide. The interested reader is referred to our earlier work [11] for more details on this mechanism.

5.7. Comparison with experiment

The free-energy barrier ($\Delta G^{\ddagger} = \Delta H^{\ddagger} - T \cdot \Delta S^{\ddagger}$) for experimental epoxidation is estimated to be 79.9 ± 4.2 kJ/mol (323 K) by Gould et al. [4], obtained from fitting specific rate constants k (s^{-1}) at different temperatures. The value of 72.6 kJ/mol, obtained in our experimental study, closely resembles the Gould estimate [4] and appears to be in good agreement with some free-energy barriers reported in Tables 3 and 4. However, it should be verified whether the active vanadium complexes, predicting correct epoxidation reaction rates, can indeed be formed on thermodynamical grounds.

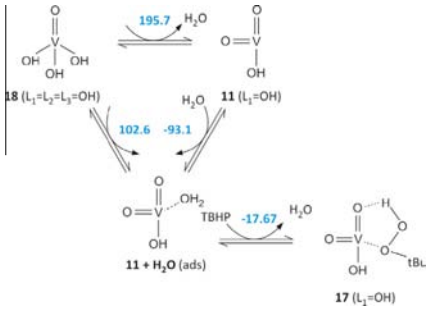

Fig. 15. Activation of the complex VO(O)(OH) coordinated with water to active complex VO(O)(OH) coordinated with TBHP.

In order to validate the theory with experiment, we therefore consider two plausible routes toward epoxidation starting from the catalyst $VO(acac)_2$ in its initial stage. In both plausible routes, the epoxidation occurs via the **IIb** mechanism, which indeed was identified as the most plausible one. First, we consider an example belonging to the family of V^{+IV} complexes, as they are probably present in the early stages of the reaction cycle. $VO(acac)_2$ is an inactive complex of type **13** with two acetylacetonate linkers. The early stage of the epoxidation process, the activation of $VO(acac)_2$ to VO(acac)(OOtBu) with TBHP (as schematically shown in Fig. 2) requires a Gibbs free energy of 44.5 kJ/mol which will be easily composed after "traveling" over the IC surface (Fig. S.4) to reach IC1 or IC2, and by the use of the activation energy as reported in Table 3. Afterward, species **10** VO(acac)(OOtBu) follows route **IIa** with an apparent free-energy reaction barrier that amounts to 68.4 kJ/mol, which is in nice agreement with the experimental prediction, but thermodynamically, the increase of 44.5 kJ/mol should be overcome. Initially, this might occur through coupling with a highly exothermal reaction as the oxidation of Hacac. However, the subsequent epoxidation reaction now starts from VO(acac)(OtBu) **13** as inactive species, which is then activated with the formation of active species VO(acac)(OOtBu) and is preferred on the free-energy surface by about −22.8 kJ/mol (easily deduced from Fig. S.4). This means that as the catalytic cycle proceeds, this reaction path becomes more plausible and in agreement with experiment. Reaction mechanism **IIa** offers more active species, which in average give apparent free energies for epoxidation, which are in close agreement with the experimental prediction.

The second example focuses on a V^{+V} complexes, which may be formed after a radical decomposition pathway. The pathway differs from the previous one in that VO(acac)(OOtBu) now oxidizes to $VO_2(acac)$ (**11**(L_1 = acac) after reaction with TBHP with formation of tBuO· radical. It further undergoes an activation step to the desired active species VO(OAc)(OAc)(OOtBu) which corresponds to a free-energy change of −21.2 kJ/mol. The required free-energy barrier of 78.3 kJ/mol for epoxidation matches fairly well the experimental value.

Of course, the previous examples are indicative but demonstrate that the selected preferred reaction pathways that all occur through mechanism **IIa** (the Sharpless mechanism) give free energies of epoxidation that are fairly close to the experimental values. On the basis of our simulations, we cannot exclude the other pathways, as our model does not include any time dependence. It only evaluates the theoretical reaction rate and/or Gibbs free energy for any route that can take place. A kinetic model could be constructed based on some particular selection of plausible reaction routes and assumption of initial concentrations of all relevant ingredients. It falls, however, outside the scope of this work. Nevertheless, one can readily see that the favored pathways lead to an increased release of *tert*-butanol, which has a deactivating effect.

Table 5
Radical decomposition following scheme given in Fig. 3a and b. $\Delta E_0^{\ddagger}$ and $\Delta G_{323}^{\ddagger\,\dagger}$ are the electronic reaction barrier and corresponding Gibbs free-energy barrier. $\Delta E_{0,r,app}$ and $\Delta G_{323,r,app}$ are the electronic energy differences between products and reactant including zero-point vibrational energies and the corresponding Gibbs free-energy differences at 323 K. Results are on the B3LYP/6–311+g(3df,2p)-D3 level of theory. All energies in kJ/mol.

		$V^{+IV} \rightarrow V^{+V}$		
10 → 11 + tBuO·				
$VO(L_1)(OOtBu) \rightarrow VO_2(L_1) + tBuO\cdot$				
L_1	$\Delta E_0^{\ddagger}$	$\Delta G_{323}^{\ddagger}$	$\Delta E_{0,r,app}$	$\Delta G_{323,r,app}$
acac	38.5	38.8	33.6	−22.2
OAc	38.4	33.5	62.8	8.3
OH	30.9	31.3	90.3	35.3
OtBu	29.6	30.4	85.8	30.4
$VO(L_1)(OOtBu) + H_2O \rightarrow VO_2(L_1)(H_2O) + tBuO\cdot$				
acac			−9.4	−24.4
OAc			−18.3	−30.6
OH			−44.4	−57.8
OtBu			−45.3	−56.0
$VO(L_1)(OOtBu)(H_2O) \rightarrow VO_2(L_1)(H_2O) + tBuO\cdot$				
OH	31.8	32.1	13.6	−42.4
OtBu	30.9	30.0	9.9	−47.8
		$V^{+V} \rightarrow V^{+IV}$		
12 → 13 + tBuOO·				
$VO(L_1)(L_2)(OOtBu) \rightarrow VO(L_1)(L_2) + tBuOO\cdot$				
L_1	L_2		$\Delta E_{0,r,app}$	$\Delta G_{323,r,app}$
acac	OtBu		135.3	72.1
OAc	OtBu		167.0	106.4
OH	OtBu		248.3	182.2
OtBu	OtBu		253.7	181.6
$12 + H_2O \rightarrow 13–H_2O + tBuOO\cdot$				
$VO(L_1)(L_2)(OOtBu) + H_2O \rightarrow VO(L_1)(L_2)(H_2O) + tBuOO\cdot$				
Acac	OtBu		86.7	75.0
OAc	OtBu		111.4	99.1
OH	OtBu		184.8	167.1
OtBu	OtBu		192.1	167.7

6. Conclusions

The epoxidation reaction of cyclohexene has been investigated theoretically for the system $VO(acac)_2$ with *tert*-butyl hydroperoxide. The overall reaction cycle consists of a variety of steps: First, the catalyst needs to be brought into an active form through interaction with the oxidant, and after that, the epoxidation reaction might occur through a variety of possible reaction mechanisms. Next, the catalyst is brought back into an inactive form and needs to be reactivated again through activation steps with the oxidant. This reaction cycle is valid both for vanadium species in oxidation state +IV and +V and change of oxidation state is also possible through radical decomposition reactions. In order to get a complete picture of the reaction cycle, the Gibbs free energies for all these hops among the various species have been modeled as thermodynamic equilibrium steps. As a result a free energy diagram was constructed for the various species bearing either oxidation state +IV or +V. The change in oxidation state was modeled through radical decomposition pathways for which also the kinetics was modeled. Our results show that the most abundant vanadium +IV species are VO(acac)(OOtBu), VO(acac)(OtBu)-TBHP, and V(OH)(acac)(OtBu)(OOtBu), whereas for vanadium +V species, complexes of the type $VO(L_1)(L_2)(OOtBu)$ are energetically preferred. To draw conclusions on the actual epoxidation mechanisms, we calculated first-principles chemical kinetics for a broad variety of earlier proposed epoxidation mechanisms. Our results show that for both oxidation states of vanadium, the concerted Sharpless mechanism is preferred. This conclusion is made based on both the abundance of the active species ready for epoxidation along this pathway and their rate constant. For some species, high rate constants were found, and this was particularly true for peroxo complexes of the type $VO_2(OOtBu)$, but as there is a lot of free energy required to form these compounds, such reaction pathways are finally not preferred. The calculations do not reveal a particular ligand preference for monovanadium complexes leading to cyclohexene epoxidation, but the bidentate coordination of acetic acid (HOAc) with the vanadium catalyst is in most cases favorable.

Transitions from the V^{+IV} platform to V^{+V} platform and vice versa take place via radical decomposition pathways. Our calculations reveal that such transitions from V^{+IV} to V^{+V} complexes occur rather easily but the reverse transformation from V^{+V} to V^{+IV} complexes may only occur in the early stages of the catalytic epoxidation process due to the presence of Hacac as a ligand, required to keep the energy barrier low enough. With the systematic decrease of Hacac and herewith coupled increase of *tert*-butanol in the reagent mixture, the recycling reaction bringing V^{+V} complexes back to coordination number +IV becomes seriously hindered. The calculations also reveal that the radicals tBuOO· and tBuO· produced during these radical decomposition reactions do not play a significant role in the epoxidation process of cyclohexene itself, but are dominant in the formation of by-products and in particular the adduct *tert*-butyl-2-cyclohexenyl-1-peroxide. Thus, the so-called Twiggs mechanism where direct epoxidation occurs with the radical tBuOO· is not preferred.

A comparative study with similar calculations on Vanadium-MIL-47 catalysts learns that large similarities are observed, but also some significant differences. In particular, the mutual V^{+IV}–V^{+V} conversion in the entire catalytic cycle is more present in case of heterogeneous catalysis. And this is probably due to the more persistent presence of the terephthalate ligands in the active catalytic site.

This study is not able to give an accurate prediction of various species in function of the reaction time. Such study requires the initial concentrations of all ingredients in the reaction mixture and solving the microkinetic network of coupled reactions in the function of the reaction time. In view of the huge number of plausible routes, such study falls outside the scope of this paper.

Acknowledgments

This research is co-funded by the Ghent University, GOA Grant No. 01G00710, BELSPO in the frame of IAP 6/27 and the European Research Council (FP7(2007–2013) ERC Grant No. 240483). M.V. thanks the research board of Ghent University (BOF). K.L. is grateful to the Long Term Structural Methusalem Grant No. 01M00409 Funding by the Flemish Government. The authors would like to thank Ying-Ya Liu for her help and comments concerning the UV–Vis spectra. The computational resources and services used in this work were provided by Ghent University (Stevin Supercomputer Infrastructure).

Appendix A. Supplementary material

Supplementary data associated with this article can be found, in the online version, at http://dx.doi.org/10.1016/j.jcat.2012.06.002.

References

[1] D.E. De Vos, B.F. Sels, P.A. Jacobs, Adv. Catal. 46 (2001) 1–87.
[2] D.E. De Vos, B.F. Sels, P.A. Jacobs, Adv. Synth. Catal. 345 (2003) 457–473.
[3] K.A. Jorgensen, Chem. Rev. 89 (1989) 431–458.
[4] E.S. Gould, R.R. Hiatt, K.C. Irwin, J. Am. Chem. Soc. 90 (1968). 4573.
[5] H.E.B. Lempers, A. Ripolles i Garcia, R.A. Sheldon, J. Organic Chem. 63 (1998) 1408–1413.
[6] C.K. Sams, K.A. Jorgensen, Acta Chem. Scand. 49 (1995) 839–847.

[7] L. Stepovik, M. Gulenova, Russ. J. Gen. Chem. 79 (2009) 1663–1670.
[8] E.P. Talsi, V.D. Chinakov, V.P. Babenko, K.I. Zamaraev, J. Mol. Catal. 81 (1993) 235–254.
[9] K. Barthelet, J. Marrot, D. Riou, G. Férey, Angew. Chem. Int. Ed. 41 (2002) 281–284.
[10] K. Leus, I. Muylaert, M. Vandichel, G.B. Marin, M. Waroquier, V. Van Speybroeck, P. Van der Voort, Chem. Commun. 46 (2010) 5085–5087.
[11] K. Leus, M. Vandichel, Y.Y. Liu, I. Muylaert, J. Musschoot, S. Pyl, H. Vrielinck, G.B. Marin, C. Detavernier, P.V. Wiper, Y.Z. Khimyak, M. Waroquier, V. Van Speybroeck, P. Van der Voort, J. Catal. 285 (2012) 196–207.
[12] C. Bolm, Coord. Chem. Rev. 237 (2003) 245–256.
[13] A. Butler, M.J. Clague, G.E. Meister, Chem. Rev. 94 (1994) 625–638.
[14] T. Hirao, Chem. Rev. 97 (1997) 2707–2724.
[15] A.G.J. Ligtenbarg, R. Hage, B.L. Feringa, Coord. Chem. Rev. 237 (2003) 89–101.
[16] K.B. Sharpless, R.C. Michaels, J. Am. Chem. Soc. 95 (1973) 6136–6137.
[17] K.B. Sharpless, T.R. Verhoeven, Aldrichim. Acta 12 (1979) 63.
[18] T. Itoh, K. Jitsukawa, K. Kaneda, S. Teranishi, J. Am. Chem. Soc. 101 (1979) 159–169.
[19] B.E. Rossiter, T.R. Verhoeven, K.B. Sharpless, Tetrahedron Lett. (1979) 4733–4736.
[20] H. Mimoun, L. Saussine, E. Daire, M. Postel, J. Fischer, R. Weiss, J. Am. Chem. Soc. 105 (1983) 3101–3110.
[21] S. Cenci, F. Difuria, G. Modena, R. Curci, J.O. Edwards, J. Chem. Soc. – Perkin Trans. 2 (1978) 979–984.
[22] R. Curci, F. Difuria, R. Testi, G. Modena, J. Chem. Soc. – Perkin Trans. 2 (1974) 752–757.
[23] D.E. Babushkin, E.P. Talsi, Reaction Kinet. Catal. Lett. 71 (2000) 115–120.
[24] H. Mimoun, Catal. Today 1 (1987) 281–295.
[25] H. Mimoun, M. Mignard, P. Brechot, L. Saussine, J. Am. Chem. Soc. 108 (1986) 3711–3718.
[26] Y. Hoshino, H. Yamamoto, J. Am. Chem. Soc. 122 (2000) 10452–10453.
[27] K.P. Bryliakov, N.N. Karpyshev, S.A. Fominsky, A.G. Tolstikov, E.P. Talsi, J. Mol. Catal. A: Chem. 171 (2001) 73–80.
[28] K.P. Bryliakov, E.P. Talsi, S.N. Stas'ko, O.A. Kholdeeva, S.A. Popov, A.V. Tkachev, J. Mol. Catal. A: Chem. 194 (2003) 79–88.
[29] M. Buhl, R. Schurhammer, P. Imhof, J. Am. Chem. Soc. 126 (2004) 3310–3320.
[30] Y. Nakagawa, N. Mizuno, Inorg. Chem. 46 (2007) 1727–1736.
[31] A.E. Kuznetsov, Y.V. Geletii, C.L. Hill, K. Morokuma, D.G. Musaev, Inorg. Chem. 48 (2009) 1871–1878.
[32] M.L. Kuznetsov, J.C. Pessoa, Dalton Trans. (2009) 5460–5468.
[33] K.B. Sharples, D.R. Williams, J.M. Townsend, J. Am. Chem. Soc. 94 (1972) 295–296.
[34] M.V. Kirillova, M.L. Kuznetsov, V.B. Romakh, L.S. Shul'pina, J. da Silva, A.J.L. Pombeiro, G.B. Shul'pin, J. Catal. 267 (2009) 140–157.
[35] J. Dobler, M. Pritzsche, J. Sauer, J. Am. Chem. Soc. 127 (2005) 10861–10868.
[36] X. Rozanska, J. Sauer, Int. J. Quant. Chem. 108 (2008) 2223–2229.
[37] D. Goebke, Y. Romanyshyn, S. Guimond, J.M. Sturm, H. Kuhlenbeck, J. Dobler, U. Reinhardt, M.V. Ganduglia-Pirovano, J. Sauer, H.J. Freund, Angew. Chem. Int. Ed. 48 (2009) 3695–3698.
[38] J.M. Sturm, D. Gobke, H. Kuhlenbeck, J. Dobler, U. Reinhardt, M.V. Ganduglia-Pirovano, J. Sauer, H.J. Freund, Phys. Chem. Chem. Phys. 11 (2009) 3290–3299.
[39] R.A. Sheldon, Recueil Des Travaux Chimiques Des Pays-Bas-J. Roy. Netherlands Chem. Soc. 92 (1973) 253–266.
[40] R.A. Sheldon, J.A. Vandoorn, C.W.A. Schram, A.J. Dejong, J. Catal. 31 (1973) 438–443.
[41] M.N. Sheng, J.G. Zajacek, Adv. Chem. Ser. (1968) 418.
[42] M.N. Sheng, J.G. Zajacek, J. Organic Chem. 35 (1979) 1843–1893.
[43] C.C. Su, J.W. Reed, E.S. Gould, Inorg. Chem. 12 (1973) 337–342.
[44] A.O. Chong, K.B. Sharpless, J. Organic Chem. 42 (1977) 1587–1590.
[45] H. Mimoun, I.S.de. Roch, L. Sajus, Tetrahedron 26 (1970) 37–50.
[46] A.D. Becke, J. Chem. Phys. 98 (1993) 5648–5652.
[47] C.T. Lee, W.T. Yang, R.G. Parr, Phys. Rev. B 37 (1988) 785–789.
[48] M.J. Frisch, G.W. Trucks, H.B. Schlegel, G.E. Scuseria, M.A. Robb, J.R. Cheeseman, J. Montgomery, J.A.T. Vreven, K.N. Kudin, J.C. Burant, J.M. Millam, S.S. Iyengar, J. Tomasi, V. Barone, B. Mennucci, M. Cossi, G. Scalmani, N. Rega, G.A. Petersson, H. Nakatsuji, M. Hada, M. Ehara, K. Toyota, R. Fukuda, J. Hasegawa, M. Ishida, T. Nakajima, Y. Honda, O. Kitao, H. Nakai, M. Klene, X. Li, J.E. Knox, H.P. Hratchian, J.B. Cross, V. Bakken, C. Adamo, J.J. an, d.R. Gomperts, R.E. Stratmann, O. Yazyev, A.J. Austin, R. Cammi, C. Pomelli, J.W. Ochterski, P.Y. Ayala, K. Morokuma, G.A. Voth, P. Salvador, J.J. Dannenberg, V.G. Zakrzewski, S. Dapprich, A.D. Daniels, M.C. Strain, O. Farkas, D.K. Malick, A.D. Rabuck, K. Raghavachari, J.B. Foresman, J.V. Ortiz, Q. Cui, A.G. Baboul, S. Clifford, J. Cioslowski, B.B. Stefanov, G. Liu, A. Liashenko, P.P.I. Komaromi, R.L. Martin, D.J. Fox, T. Keith, M.A. Al-Laham, C.Y. Peng, A. Nanayakkara, M. Challacombe, P.M.W. Gill, B. Johnson, W. Chen, M.W. Wong, C. Gonzalez, J.A. Pople, Gaussian 03, Revision D.01, 2004.
[49] P.J. Hay, W.R. Wadt, J. Chem. Phys. 82 (1985) 270–283.
[50] S. Shaik, S. Cohen, Y. Wang, H. Chen, D. Kumar, W. Thiel, Chem. Rev. 110 (2009) 949–1017.
[51] A. Lundin, I. Panas, E. Ahlbergt, J. Phys. Chem. A 111 (2007) 9080–9086.
[52] S. Grimme, J. Comput. Chem. 25 (2004) 1463–1473.
[53] S. Grimme, J. Antony, S. Ehrlich, H. Krieg, J. Chem. Phys. 132 (2010).
[54] ORCA. 2.8.0ed. <http://www.thch.uni-bonn.de/tc/orca/>.
[55] V. Van Speybroeck, J. Van der Mynsbrugge, M. Vandichel, K. Hemelsoet, D. Lesthaeghe, A. Ghysels, G.B. Marin, M. Waroquier, J. Am. Chem. Soc. 133 (2011) 888–899.
[56] A. Ghysels, T. Verstraelen, K. Hemelsoet, M. Waroquier, V. Van Speybroeck, J. Chem. Inform. Model. 50 (2010) 1736–1750.
[57] B. Vlckova, B. Strauch, M. Horak, Collect. Czechoslovak Chem. Commun. 52 (1987) 686–695.
[58] L.J. Bellamy, The Infrared Spectra of Complex Molecules: Advances in Infrared Group Frequencies, vol. 2, Chapman and Hall, 1980.
[59] E.C.E. Rosenthal, H.L. Cui, M. Hummert, Inorg. Chem. Commun. 11 (2008) 918–920.
[60] S. Vayssie, H. Elias, Liebigs Ann.-Recl. (1997) 2567–2572.
[61] D.E. Vansickle, F.R. Mayo, R.M. Arluck, J. Am. Chem. Soc. 87 (1965) 4824–4832.

Paper 6

The coordinative saturated vanadium MIL-47 as a low leaching heterogeneous catalyst in the oxidation of cyclohexene

Karen Leus*, Matthias Vandichel*, Ying-Ya Liu, Ilke Muylaert, Jan Musschoot, Henk Vrielinck, Freddy Callens, Guy B. Marin, Christophe Detavernier, Yaroslav Z. Khimyak, Michel Waroquier, Veronique Van Speybroeck and Pascal Van Der Voort

Journal of Catalysis, 2012, 285, 196 - 207

Copyright 2012 by Elsevier.

* = equal first author

Journal of Catalysis 285 (2012) 196–207

Contents lists available at SciVerse ScienceDirect

Journal of Catalysis

journal homepage: www.elsevier.com/locate/jcat

The coordinatively saturated vanadium MIL-47 as a low leaching heterogeneous catalyst in the oxidation of cyclohexene

Karen Leus [a,1], Matthias Vandichel [b,1], Ying-Ya Liu [a], Ilke Muylaert [a], Jan Musschoot [c], Steven Pyl [d], Henk Vrielinck [c], Freddy Callens [c], Guy B. Marin [d], Christophe Detavernier [c], Paul V. Wiper [e], Yaroslav Z. Khimyak [e], Michel Waroquier [b], Veronique Van Speybroeck [b,*], Pascal Van Der Voort [a,*]

[a] Department of Inorganic and Physical Chemistry, Center for Ordered Materials, Organometallics and Catalysis, Ghent University, Krijgslaan 281-S3, 9000 Ghent, Belgium
[b] Center for Molecular Modeling, Ghent University, Technologiepark 903, 9052 Zwijnaarde, Belgium
[c] Department of Solid State Sciences, Ghent University, Krijgslaan 281-S1, 9000 Ghent, Belgium
[d] Laboratory for Chemical Technology, Ghent University, Krijgslaan 281-S5, 9000 Ghent, Belgium
[e] Department of Chemistry, University of Liverpool, Liverpool L69 3BX, United Kingdom

ARTICLE INFO

Article history:
Received 9 August 2011
Revised 12 September 2011
Accepted 13 September 2011
Available online 19 October 2011

Keywords:
Metal Organic Frameworks
Vanadium
Oxidation catalysis
DFT-D
Epoxidation

ABSTRACT

A Metal Organic Framework, containing coordinatively saturated V^{+IV} sites linked together by terephthalic linkers (V-MIL-47), is evaluated as a catalyst in the epoxidation of cyclohexene. Different solvents and conditions are tested and compared. If the oxidant TBHP is dissolved in water, a significant leaching of V-species into the solution is observed, and also radical pathways are prominently operative leading to the formation of an adduct between the peroxide and cyclohexene. If, however, the oxidant is dissolved in decane, leaching is negligible and the structural integrity of the V-MIL-47 is maintained during successive runs. The selectivity toward the epoxide is very high in these circumstances. Extensive computational modeling is performed to show that several reaction cycles are possible. EPR and NMR measurements confirm that at least two parallel catalytic cycles are co-existing: one with V^{+IV} sites and one with pre-oxidized V^{+V} sites, and this is in complete agreement with the theoretical predictions.
© 2011 Elsevier Inc. All rights reserved.

1. Introduction

Metal Organic Frameworks (MOFs) have received an enormous amount of attention over the last decade, as they are considered as the newest generation of porous materials [1,2]. This type of materials is constructed by linking organic ligands with metal ions or metal clusters to form infinite network structures. The porosity, structure, and functionality of the MOF can be tuned by varying the linkers (bridging ligands) and/or the metal centers. MOFs are promising materials for applications in gas adsorption [3,4], separation [5], and catalysis [6–8]. By introducing catalytically active metal-connecting points or functional groups into the highly porous MOF structure, MOFs exhibit clear advantages in heterogeneous catalysis. Moreover, unlike traditional immobilized catalysts [9–11], the active catalytic sites in MOFs are well protected by the coordination bonds that prevent leaching to a higher extent. Although the research in this field is relatively new, MOFs have been studied as catalysts in hydrogenation and oxidation reactions [12–18], enantioselective reactions [19–21], photocatalysis [22], carbonyl cyanosilylation [23–25], hydrodesulfurization [26], and esterification [27].

Catalytic studies on the oxidation of cyclohexene in MOFs have already been published by several groups. For example, the group of Rosseinsky [28] has reported a post-modification procedure of the IRMOF-3 framework with $VO(acac)_2$. They carried out a preliminary catalytic investigation on this modified MOF structure for the oxidation of cyclohexene with *tert*-butylhydroperoxide (TBHP) as the oxidant. Volkmer and co-workers [14] have designed and synthesized a MOF containing unsaturated cobalt sites, namely MFU-1. MFU-1 showed a cyclohexene conversion of 22.5% after 22 h of reaction (theoretically maximum 50% conversion), with *tert*-butyl-2-cyclohexenyl-1-peroxide as the main product (66% selectivity). Garcia et al. recently published a review on the use of MOFs as oxidation catalysts [29]. Recent studies by us [30] have focused on the catalytic performance of a saturated vanadium MOF, namely MIL-47 $V^{IV}O(CO_2–C_6H_4–CO_2)$ [31].

As can be seen from Fig. 1, MIL-47 has a three-dimensional framework, where each V^{+IV} center is coordinated to four oxygen atoms from four carboxylate groups, and to two oxygen atoms on the O–V–O axis, thus forming a saturated octahedral coordination node. The nodes are further connected by sharing the carboxylate linkers and thus grow into a three-dimensional framework. 1D rhombus

* Corresponding authors. Fax: +32 9 264 49 83 (P. Van Der Voort), +32 9 264 65 60 (V. Van Speybroeck).
E-mail addresses: Veronique.VanSpeybroeck@UGent.be (V. Van Speybroeck), Pascal.Vandervoort@ugent.be (P. Van Der Voort).
[1] Both authors contributed equally to this work.

0021-9517/$ - see front matter © 2011 Elsevier Inc. All rights reserved.
doi:10.1016/j.jcat.2011.09.014

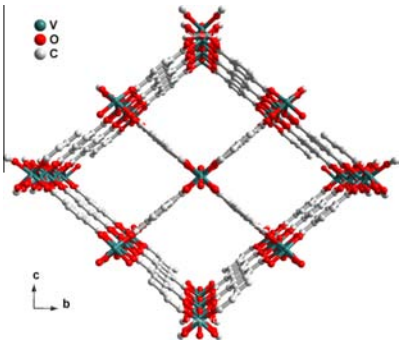

Fig. 1. Perspective view of the structure of MIL-47.

channels are along the *a* axis with sizes of about 10.5 × 11.0 Å (Van der Waals radii excluded) for the channel windows. The structure shows good thermal stability (stable up to 350 °C in air).

Recently, we published the first catalytic evaluation of V-MIL-47 in the liquid phase oxidation of cyclohexene, using TBHP in water as the oxidant and chloroform as the solvent [30]. In general, the liquid phase oxidation of cyclohexene can produce one or more of following products as shown in Scheme 1.

In this paper, we have extended our earlier work to a more in-depth mechanistic study. We examine the catalytic performance of MIL-47 in water and water-free media. In each medium, two catalyst loadings will be considered: 0.11 mmol and 0.42 mmol V-centers in the total reaction mixture. The catalytic activity of the MIL-47 is compared to the homogeneous catalyst $VO(acac)_2$. In order to fully unravel possible reaction mechanisms, which are operative in the MIL-47, an extensive ab initio computational study has been conducted. The nature of the active site is investigated by studying a variety of possible reaction cycles that might occur in the cyclohexene oxidation. Some active sites start from vanadium in oxidation state (+IV) where others produce first vanadium in oxidation state (+V). EPR and NMR measurements were also performed to determine the presence and activity of vanadium in both oxidation states.

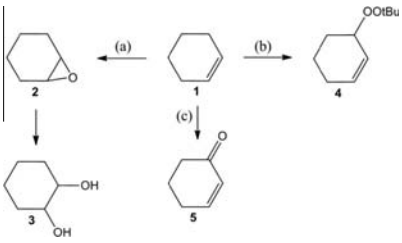

Scheme 1. Oxidation of cyclohexene **1** toward the main reaction products: (a) epoxidation to cyclohexene oxide **2** and consecutive ring opening to cyclohexane-1,2-diol **3**, (b) radical pathway to *tert*-butyl-2-cyclohexenyl-1-peroxide **4** and (c) allylic oxidation to 2-cyclohexene-1-one **5**.

2. Experimental: materials and methods

2.1. General procedures

All chemicals for the synthesis of MIL-47 and the catalytic tests were purchased from Sigma Aldrich (unless otherwise noted) and used without further purification. An ultra-fast GC equipped with a flame ionization detector (FID) and a 5% diphenyl/95% polydimethylsiloxane column with 10 m length and 0.10 mm internal diameter was used to follow the conversions of the products during the catalytic tests. Helium was used as carrier gas, and the flow rate was programmed as 0.8 mL/min. The reaction products were identified with a TRACE GC × GC (Thermo, Interscience), coupled to a TEMPUS TOF-MS detector (Thermo, Interscience). The first column consists of a dimethyl polysiloxane package and has a length of 50 m, with an internal diameter of 0.25 mm, whereas the second column has a length of 2 m with an internal diameter of 0.15 mm. The package of the latter is a 50% phenyl polysilphenylene-siloxane. Helium was used as carrier gas with a constant flow (1.8 mL/min).

X-ray fluorescence (XRF) measurements were performed with an ARTAX (Bruker) Peltier cooled silicon drift detector, using a Mo X-ray source. The detector was placed above the surface of the solution. Spectra were accumulated during 200 s. The system was calibrated by measuring the XRF spectra of different aqueous-based solutions of $VO(acac)_2$ and $Co(NO_3)_2{\cdot}6H_2O$ with known V/Co ratios. Nitrogen adsorption experiments were carried out at −196 °C using a Belsorp-mini II gas analyzer. Prior to analysis, the samples were dried overnight under vacuum at 120 °C to remove adsorbed water. X-ray powder diffraction (XRPD) patterns were collected on a ARL X'TRA X-ray diffractometer with Cu Ka radiation of 0.15418 nm wavelength and a solid-state detector. Electron paramagnetic resonance (EPR) spectra of dry powders were recorded at room temperature with a Bruker ESP300E X-band (9.77 GHz) spectrometer, equipped with a HP5350B frequency counter and a ER035 M gaussmeter. Standard NMR sample tubes (4 mm inner diameter) were filled to a height of approximately 5 mm, and for comparison of intensities, the spectra were divided by the powder mass. For all spectra, the magnetic field was modulated at 100 kHz with an amplitude of 0.2 mT, and the microwave power was set to 2 mW, avoiding saturation.

2.2. Synthesis of MIL-47

MIL-47 was synthesized according to a synthesis route described in literature [31]. Typically, 1.37 g VCl_3 and 0.36 g terephthalic acid were mixed together with 15.7 mL of deionised H_2O. The resulting mixture was transferred into a Teflon-lined stainless autoclave for 4 days at 200 °C. The as-synthesized MIL-47 was filtered, washed with acetone, and calcined for 21 h 30 min at 300 °C to remove free terephthalic acid from the pores. Typical synthesis yield is approximately 15%.

2.3. General procedure for the cyclohexene oxidation

During a typical catalytic test, a 100-mL round-bottom flask was charged with 30 mL of chloroform (anhydrous) used as solvent, 5 mL of cyclohexene, and 6.2 mL of 1,2,4-trichlorobenzene (used as internal standard for the GC analysis). The oxidants used in this paper were *tert*-butylhydroperoxide (TBHP) in water (70%) and TBHP 5.5 M in decane. The molar ratio cyclohexene/oxidant was 1/2. All the catalytic tests were performed at a temperature of 50 °C and with an Ar-containing balloon on top of the condenser. Blank reactions at this temperature showed no catalytic conversion of cyclohexene.

The reaction mixture was stirred under an inert argon atmosphere until a plateau was reached in the cyclohexene conversion. Aliquots were gradually taken out of the mixture, diluted with 500 μl ethylacetate, and subsequently analyzed by GC-FID and GC × GC TOF-MS. After a catalytic run, the catalyst was recovered by filtration on a combined nylon-membrane filter, washed with acetone, and vacuum dried overnight. The filtrate was analyzed by XRF to determine the leached vanadium.

3. Experimental results

3.1. Characterization

In this paper, we will compare the catalytic performance of MIL-47 in water and water-free media. A thorough study of the catalytic performance of MIL-47 is presented, together with a spectroscopic study and a computational model.

3.1.1. Characterization of the catalyst

The MIL-47 had an average Langmuir surface area of 1225 m^2/g and a pore volume of 0.38 ml/g. Only batches of MIL-47 that diverted less than 5% from these values were used in this work. The value of 1225 m^2/g is consistent with literature [31].

The XRPD pattern of the synthesized MIL-47 is presented in Fig. 2 and compared to the XRPD pattern, generated from the original CIF-file [31]. The experimental XRPD pattern of MIL-47 matches perfectly with the simulated pattern, confirming the phase purity of the synthesized MIL-47. Some differences in reflection intensities between the simulated and experimental pattern are due to the variation in crystal orientation of the micro crystals.

3.1.2. The catalytic performance of MIL-47 in the oxidation of cyclohexene

In Fig. 3, the catalytic performance of MIL-47 is shown using respectively TBHP/water (left) and TBHP/decane (right) as oxidant. In this figure, two catalyst loadings (0.11 mmol and 0.42 mmol of V-centers) are considered. The reader should pay attention to the differences in the timescale of the *x*-axes, as all experiments were performed until a linear plateau in the conversion was reached or until a maximum time of 82 h.

Several general trends can be deducted from Fig. 3. (1) Convergence regimes for cyclohexene conversion are reached in all cases, provided sufficient large reaction time is taken into account. (2) The conversion tends toward 80% at the end of the reaction. The lower conversion in Fig. 3c is probably due to a too short reaction time. (3) In the initial stages, the cyclohexene conversion is almost linear in all cases. There are, however, differences in the slope of these linear sections: the 0.42 mmol V catalytic systems start clearly the fastest (approximately 20% conversion per hour for TBHP in water and 7% conversion per hour of TBHP in decane) whereas the 0.11 mmol V systems start much slower (~4% conversion per hour for the TBHP in water and even slower for the TBHP in decane). (4) In the systems that use TBHP in water, the cyclohexene oxide attains a maximum, after which the concentration gradually returns to zero. This is partly due to the transformation of the epoxide **2** into the diol **3** resulting from the reaction with water and terephthalic acid (as shown in Scheme 1). (5) The byproduct **4**, formed via radicalar pathways, grows systematically and exceeds the concentration of the epoxide after sufficient long reaction times. The crossing of those two yields occurs at relative short reaction times for the TBHP in water systems and is heavily delayed by using the TBHP in decane. This is due to the particular role of water in the reaction medium in stabilizing the radical intermediates (see computational discussion, Section 3.2). (6) The formation of the ketone **5** is marginal in all cases. (7) During the first 7 h of reaction, the selectivity toward the cyclohexene oxide is almost 100% in the 0.11 mmol V-sites with TBHP in water system. After that, the product distribution changes. The cyclohexene oxide reaches a maximum of 38% after 25 h of reaction. After that, the cyclohexane-1,2-diol **3** starts to be produced, and the *tert*-butyl-2-cyclohexenyl-1-peroxide **4** becomes dominant (see Table 1).

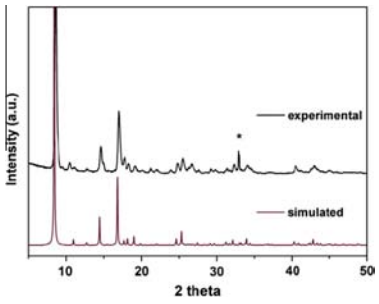

Fig. 2. XRPD patterns of MIL-47 (experimental and simulated [31]) (* is due to the background of the sample holder at an angle of 32.9°).

The faster kinetics observed in Fig. 3c compared to Fig. 3a are mainly due to the higher V-loading. But in both cases, also a significant amount of leached V is observed. Our earlier work [30] showed that after 1 h of catalysis, 12.8% of the V is leached out of the structure with 0.11 mmol of V-sites.

In order to reduce this leaching, the catalytic performance of MIL-47 in the oxidation of cyclohexene was analyzed with TBHP/decane as oxidant (see Fig. 3b and d). When the catalytic performance of MIL-47 in the water-based media is compared to the water-free media, then it is clear that the cyclohexene conversion is approximately 30% after 7 h of reaction with TBHP/decane as oxidant, while the total cyclohexene conversion in the water dissolved TBHP system is much higher in the initial stage (55% after 7 h of reaction). Furthermore, it is interesting to note that, as the conversion is lower, the selectivity toward the cyclohexene oxide is remarkably higher. In Table 1, the selectivity toward the cyclohexene oxide with TBHP/water and TBHP/decane as oxidant is shown for each V-loading, together with the TON and TOF of MIL-47 and $VO(acac)_2$. This Table 1 shows that the selectivity in TBHP/decane is significantly higher compared to the water-based equivalent.

The presence of water during the catalytic test clearly affects both the rate of the epoxidation reaction and the stabilization of radical species toward the formation of the adduct **4.** More details about the reaction mechanisms for both systems are given in the computational sections (vide infra). The former effect might be partly due to vanadium leaching. Only a negligible amount (<3%) of vanadium was leached out of the structure when TBHP/decane was used as oxidant after 7 h of reaction, whereas with TBHP/water, after the same time, a V-leaching of almost 50% was observed.

3.1.3. Catalytic performance of $VO(acac)_2$ in the oxidation of cyclohexene

Next, the catalytic performance of MIL-47 in TBHP/water and TBHP/decane as oxidant was compared with the homogeneous catalyst $VO(acac)_2$ in identical conditions and V-loadings. In Fig. 4, the cyclohexene conversion and yield of cyclohexene oxide **2**, cyclohexane-1,2-diol **3,** and the *tert*-butyl-2-cyclohexenyl-1-peroxide

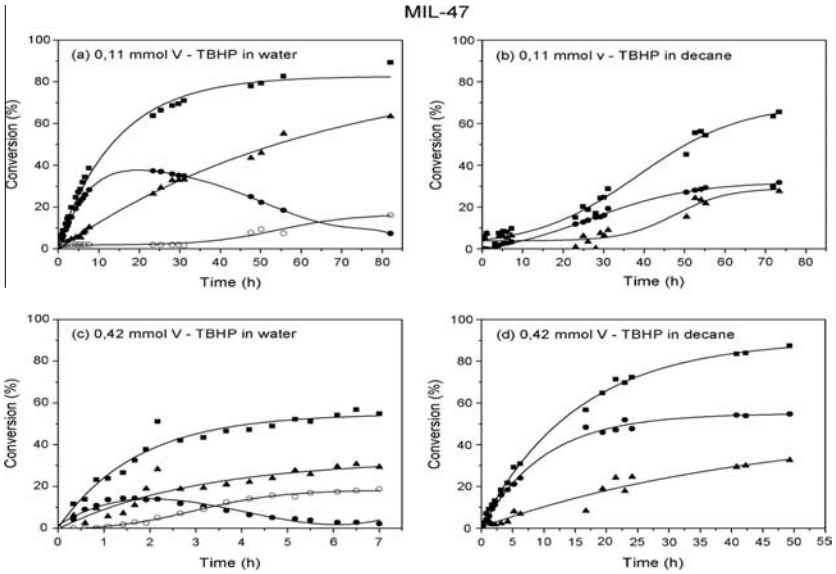

Fig. 3. Cyclohexene (**1**) conversion (■) and the yield of cyclohexene oxide (**2**) (●), *tert*-butyl-2-cyclohexenyl-1-peroxide (**4**) (▲) and cyclohexane-1,2-diol (**3**) (○) for MIL-47 in TBHP/water (Left) with 0.11 mmol V-sites (a) and 0.42 mmol V-sites (c); and for MIL-47 in TBHP/decane (Right) with 0.11 mmol V-sites (b) and 0.42 mmol V-sites (d). No cyclohexane-1,2-diol (○) is formed when TBHP in decane is used. The production of 2-cyclohexene-1-one is in all cases less than 5%, for the clarity of the figure this is not shown.

Table 1
Selectivity toward the cyclohexene oxide with TBHP/water and TBHP/decane as oxidant for each V-loading and the TON and TOF of MIL-47 and $VO(acac)_2$.

V-loading (mmol)	Oxidant	Catalyst	TON[a]	TOF (h^{-1})[b]	Selectivity[c]
0.11	TBHP/water	MIL-47	150	30	70
0.42	TBHP/water	MIL-47	67	29	43
0.11	TBHP/decane	MIL-47	42	37	63
0.42	TBHP/decane	MIL-47	28	8	83
0.11	TBHP/water	$VO(acac)_2$	169	44	70
0.42	TBHP/water	$VO(acac)_2$	62	57	25
0.11	TBHP/decane	$VO(acac)_2$	112	35	87
0.42	TBHP/decane	$VO(acac)_2$	74	48	78

[a] TON was calculated after 7 h.
[b] TOF was calculated after 30 min.
[c] The selectivity toward the cyclohexene oxide calculated at 40% cyclohexene conversion.

4 is shown for the $VO(acac)_2$ catalyst respectively in the water and water-free medium for total V-loadings of 0.11 and 0.42 mmol. The reader is again reminded that the *x*-axes have different timescales.

The homogeneous catalyst shows a similar behavior as MIL-47 in the water-based oxidant. Firstly, the cyclohexene conversions reach a plateau after approximately the same time (80% after 70 h for 0.11 mmol and 55% after 7 h of catalysis for 0.42 mmol V-sites). Secondly, for both V-loadings, the cyclohexene oxide **2** attains a maximum after 20 h for the 0.11 mmol V and 2 h for the 0.42 mmol V when the cyclohexane-1,2-diol **3** starts to be produced and the *tert*-butyl-2-cyclohexenyl-1-peroxide **4** becomes the main product. However, comparison of the homogeneous catalyst with the MIL-47 for TBHP/decane as oxidant clearly shows some differences. For the $VO(acac)_2$, the cyclohexene conversion is much faster compared to the MIL-47. After 7 h of reaction, a cyclohexene conversion of 65% is observed for the 0.42 mmol V-sites compared to 30% for the microporous MOF. Likewise, with the lower V content, it can be seen that the cyclohexene conversion is much slower compared to the $VO(acac)_2$ catalyst. Nevertheless, the selectivity of both catalysts toward cyclohexene oxide is more or less the same as can be seen from Table 1.

3.1.4. Stability and regenerability of the catalyst

The crystalline structure of the MOF was examined by X-ray diffraction to verify the stability of the MOF after a catalytic run. In Fig. 5, the XRPD pattern of MIL-47 is shown before and after a

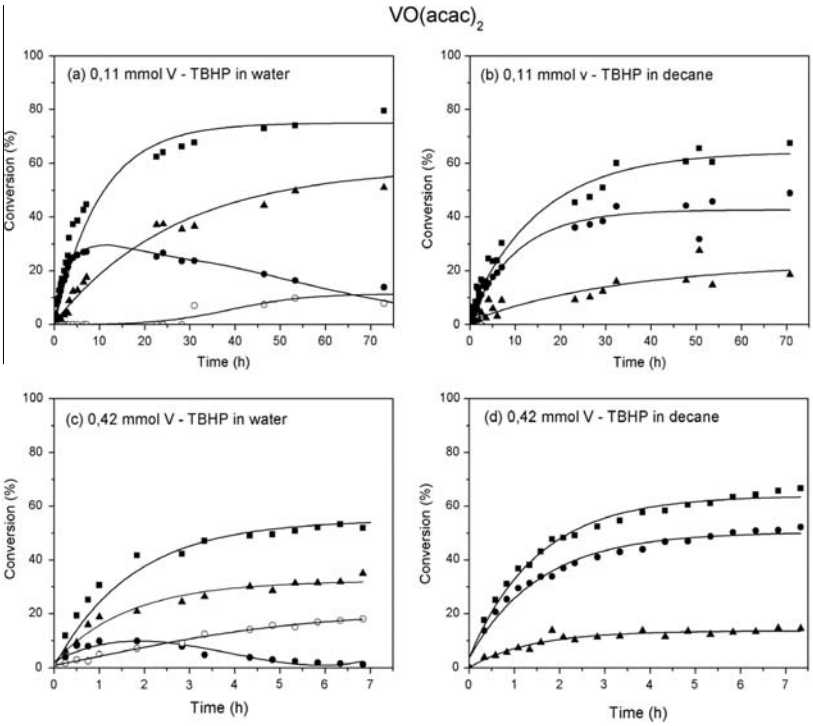

Fig. 4. Cyclohexene (**1**) conversion (■) and the yield of cyclohexene oxide (**2**) (●), *tert*-butyl-2-cyclohexenyl-1-peroxide (**4**) (▲) and cyclohexane-1,2-diol (**3**) (○) for $VO(acac)_2$ in TBHP/water (left) with 0.11 mmol V-sites (a) and 0.42 mmol V-sites (c); and for $VO(acac)_2$ in TBHP/decane (right) with 0.11 mmol V-sites (b) and 0.42 mmol V-sites (d). No cyclohexane-1,2-diol (○) is formed when TBHP/decane is used. The production of 2-cyclohexene-1-one is in all cases less than 5%, for the clarity of the figure this is not shown.

catalytic run, using TBHP/water or TBHP/decane as oxidant at a temperature of 50 °C. Furthermore, the XRPD pattern of the organic linker in MIL-47 (terephthalic acid or BDC, benzene dicarboxylic acid) is shown. As can be seen from this figure, the XRPD pattern of the MIL-47 after a first catalytic run with TBHP in water as oxidant (Fig. 5c) changes significantly compared to the original XRPD pattern (Fig. 5a). Especially, some new diffraction peaks, which can be assigned to the BDC linkers, appear after a first catalytic run. This observation indicates that the structure partially decomposes in the TBHP/water system. This also explains the significant V-leaching that has been observed. Subsequently, MIL-47 was regenerated by a treatment in a tubular furnace under a nitrogen flow at 150 °C for 4 h to remove the organic compounds inside the pores. After this extra step, the structure of MIL-47 was regained as shown in Fig. 5d.

Comparison of the XRPD pattern of MIL-47 before and after a catalytic run, using TBHP in decane (Fig. 5a and b) as oxidant, however, clearly demonstrates that in a water-free medium, the structural integrity of the MOF is entirely preserved. No peaks of free BDC can be observed, and no additional treatment is required to remove these free linkers.

To test the regenerability of the catalyst, four consecutive catalytic runs have been performed in TBHP/decane as oxidant. During each catalytic cycle, the cyclohexene conversion was monitored during at least 6 h. The XRPD patterns of the original MIL-47 and after each run are shown in Fig. 6. As can be seen from this figure, MIL-47 preserves its crystalline structure during these additional runs. The lower signal to noise ratio in run IV is due to the tiny amount of sample that was left for analysis.

In Table 2, the TON and TOF values are shown for MIL-47 in the four consecutive runs. Furthermore, the percentage of leached V in the filtrate is given after each catalytic test. Only in the first cycle, a negligible amount of leached V was observed (<3%), whereas in the following cycles, no leaching was detected. The TON and TOF drop after the first run but remain relatively constant during the next additional cycles. This observation can be explained by the fact that after each run, still some organic compounds of the previous catalytic test clog the pores. This was supported by nitrogen adsorption measurements that showed that the surface area of MIL-47 after a first run dropped from 1225 m^2/g to approximately 500 m^2/g; this will surely lead to a decrease of the reaction rate in the additional runs. We have shown previously [30] that even in

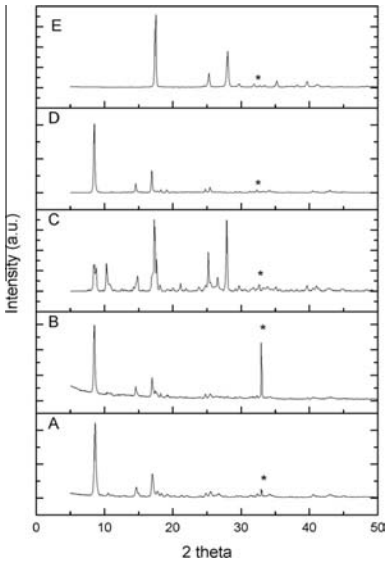

Fig. 5. XRPD pattern of (a) MIL-47, (b) MIL-47 after catalysis with TBHP in decane as oxidant, (c) MIL-47 after catalysis with TBHP in water as oxidant, (d) MIL-47 after regeneration and (e) terephthalic acid (* is due to the background of the sample holder at an angle of 32.9°).

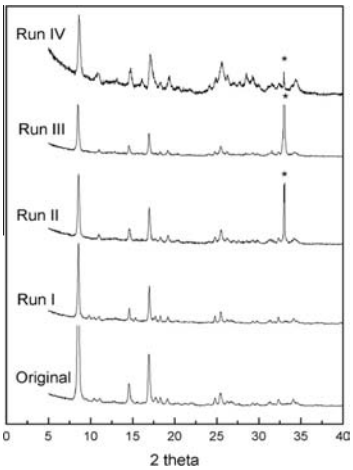

Fig. 6. XRPD pattern of the original MIL-47 before catalysis and the XRPD pattern of MIL-47 after the first, second, third and fourth catalytic run (* is due to the background of the sample holder at an angle of 32.9°).

Table 2
TOF, TON and the percentage of leached V for the consecutive catalytic runs with TBHP/decane as oxidant.

	TON[a]	TOF[b] (h^{-1})	Leaching (%)
Run I	23	7.8	<3
Run II	14	4.8	0
Run III	15.3	2.9	0
Run IV	12.7	3	0

[a] TOF was calculated after 38 min;
[b] TON was calculated after 6 h.

conditions of severe leaching (TBHP in water), still these leached out species are relatively inert for the epoxidation mechanism as the building of epoxide stops immediately after the hot filtration of the catalysts; whereas the radical formation of the adduct **4** continues.

3.1.5. EPR and NMR results

In Fig. 7, the results of room temperature EPR measurements on dry powders of MIL-47 are shown as a function of catalytic reaction time for MIL-47 in TBHP/decane. The inset displays the EPR spectra of the MIL-47 powder and the ML-47 powder after 3 h of catalytic performance. Both spectra appear as broad lines and can be well-fitted by single Lorentzians. The position, which is practically the same in the two spectra, is compatible with a signal assignation to V^{+IV} ($g = 1.96$) [32]. The absence of ^{51}V hyperfine structure is attributed to spin–spin interactions between the close-by V^{+IV} ions in the MIL-47 structure. The width of the spectra, however, is a point of significant difference between the spectra, which will be further addressed in a future investigation.

In the present study, we are mainly interested in the evolution of the total spectral intensity. This was evaluated by double integration of the field-modulated spectra. In order to avoid possible influences of broad background signals, the total intensities were also calculated from the area of the best-fit Lorentzian to the singly integrated spectra. Intensities were normalized to that of the calcined MIL-47 powder. As seen in Fig. 7, the two methods lead essentially to the same conclusions. Within the investigated range of catalytic reaction times, the spectra experience an intensity drop

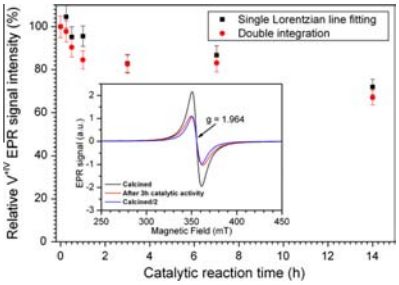

Fig. 7. Catalytic reaction time evolution of the intensity of the EPR spectrum for the MIL-47 in TBHP/decane system. EPR spectra were recorded on dry powders and intensities were evaluated by single Lorentzian fitting to the singly integrated spectra and by double integration. All intensities were normalized to that of the calcined MIL-47. Inset-EPR spectra for calcined MIL-47 (black) and after 3 h of catalytic reaction in the MIL-47/TBHP/decane system (red). For better comparison of the line widths of the EPR spectra, the spectrum of calcined MIL-47 divided by 2 in intensity is shown in blue. (For interpretation of the references to color in this figure legend, the reader is referred to the web version of this article.)

by 20–30%, suggesting that approximately this percentage of the V^{+IV} centers observable with EPR is oxidized to V^{+V}. The major part of the intensity decrease is observed in the first few hours (1–3 h). In the later stages, the EPR intensity seems to stabilize or at least to change far more slowly.

The structural changes around vanadium sites upon calcination of the initial framework are confirmed by ^{51}V solid-state NMR. Due to the paramagnetism of V in the calcined material, a very broad featureless spectrum was recorded. After catalysis, clear presence of V^{+V} in the species is detected and the spectrum profile is reminiscent of that reported for other materials containing V^{+V} species. The spectral profile is consistent with reported complexes containing V^{+V} species [33]. The changes in the environment of vanadium centers after catalysis are reflected in the ^{1}H–13C CP/MAS spectra as much broader peaks are observed for the calcined solids (spectra are shown in the ESI).

3.2. Discussion: theoretical results on reactive pathways for epoxidation

This computational section aims at: (i) defining the active sites for catalysis, (ii) introducing a finite cluster representing the active site within the MIL-47, (iii) proposing plausible reaction pathways for the epoxidation of cyclohexene, and (iv) elucidating the role of the solvent (water versus decane) on the product selectivity in the cyclohexene conversion, as observed in experiment.

3.2.1. Selection of the cluster model

In an undamaged saturated MIL-47 framework, the coordination sphere around the metal ion is completely blocked by the organic linkers, leaving no free positions available for substrate chemisorptions. In our earlier theoretical modeling work on the homogeneous $VO(acac)_2$ catalyst, we found that first vacant coordination sites should be created to activate the catalyst [30]. This is in accordance with earlier literature data [34]. For the MIL-47, free coordination positions should also be created by ligand removal or by folding one terephthalic acid ligand away from the vanadium center or by removing bridging oxygen between the neighboring vanadium centers from the O–V–O axis. In view of these structural defects in the periodic structure, we opted to simulate the reaction pathways in a cluster model. The numerical algorithms to search for transition states are better established in the computational programs used for the cluster calculations compared with their periodic equivalents. Of course the cluster should be chosen large enough to represent the real active environment within the MIL-47 topology. In view of this, we propose the extended cluster model as displayed in Fig. 8. This model contains two vanadium atoms, bridged by two terephthalate linkers. On the vanadyl chain, only two V=O bonds are maintained, and the continuation to further terephthalate linkers is interrupted and replaced by terminating OH-groups. Starting from this cluster, one can search for the optimized geometry by relaxing all atoms or by fixing the outer carboxyl oxygen atoms at their crystal positions to prevent unphysical deformation of the cluster, while relaxing all other atoms during the geometry optimization. When taking into account dispersion interactions, the constrained geometry is favored by about 42 kJ/mol. Moreover, the obtained result is a realistic representation of the actual molecular environment around the active site in the MIL-47. The MIL-47 (with V^{+IV}) is one of the MOF structures that only shows a small degree of flexibility, and thus, this model should be well suited. Although for completeness, we also performed all calculations in the model in which all atoms are relaxed, allowing as such too much conformational flexibility. In particular, the angle between the two terephthalate planes containing the two terephthalic linkers changes largely during such computational protocol. While this particular angle amounts to 98.5° when the outer atoms are fixed, this angle increases by 12° in the completely unconstrained model. The other geometrical parameters are not substantially different, even the distance between the two V-centers remains almost unaltered for both cluster models (3.80 versus 3.81 Å, compared to 3.42 Å in the MIL-47 crystal). As will be seen later, the deviancy in spatial orientation of the linkers leads to important changes in the kinetics of the reactions with non-negligible impact on the preferential pathways.

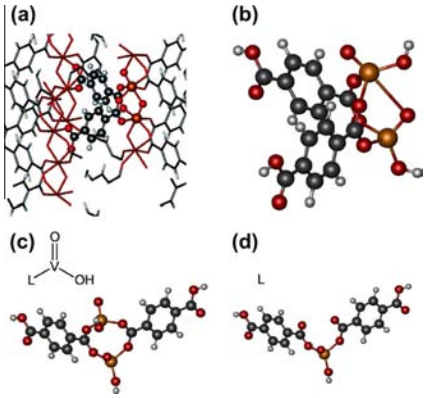

Fig. 8. (a) selected cluster (in balls) in the MIL-47 crystal structure, (b) cluster cut out from the crystal as indicated in (a) is now terminated with hydrogens and is chosen large enough to represent the active site in MIL-47, (c) schematical representation of the extended cluster as displayed in (c), (d) bidentate ligand represented by L. Geometry following the unconstrained model for (c) and (d).

The cluster model is schematically shown in Fig. 8c, where L represents a bidentate ligand (Fig. 8d) and hence shows a twofold coordination with V. Notice that the ligand L in the cluster model contains also a V atom, but this site is not regarded as catalytically active during the simulations. The upper vanadium atom as shown in Fig. 8c is taken as the active catalytic center. Both vanadium atoms have oxidation state +IV in the starting cluster model.

3.2.2. Possible reaction pathways toward formation of cyclohexene oxide

The reaction cycle starts with an activation step, in which TBHP coordinates with the vanadium center to form an alkylperoxo species **7** (as shown in Scheme 2). The two most probable reaction routes toward epoxidation starting from this complex are displayed in Scheme 2. First, a direct pathway to epoxidation leads to the formation of cyclohexene oxide **2** and brings the catalyst to a less active complex **8**. Secondly, a radical mechanism is plausible (indicated as "radical" in Scheme 2). In this route, +V vanadium complexes **9** are formed by homolytic cleavage of the peroxy linkage that can then be further activated with TBHP. The generated V^{+V}-activated complexes **10** and **12** can again epoxidize cyclohexene. Both direct and radical routes are completed by a regeneration step that closes the cycle.

Apart from the complexes given in Scheme 2, other possible V^{+V} (OOtBu) complexes can be formed, which also lead to cyclohexene epoxidation. All these plausible pathways have been investigated in this work, but they turned out to be not competitive with respect to those taken up in Scheme 2. We disregard them from further discussion.

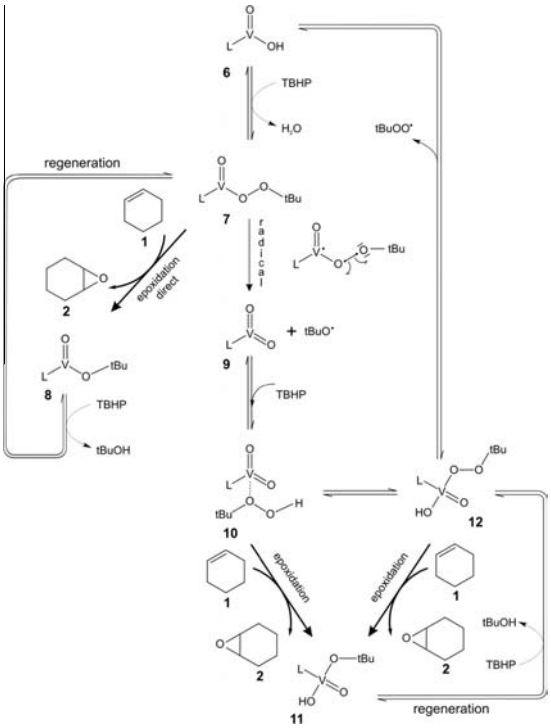

Scheme 2. Two competitive cyclohexene epoxidation pathways for MIL-47 (direct and radical).

3.2.2.1. Reaction kinetics: direct versus radical pathway. For each reaction path energy barriers, Gibbs-free energies at 323 K and reaction rates have been computed in the two models for geometry optimization (unconstrained versus constrained) as outlined before. The results are given in Table 3. All energetics have been calculated within the B3LYP/6-311 + g(3df,2p)-D3//B3LYP/6-31 + g(d) level of theory. The B3LYP/6-311 + g(3df,2p) energies were further refined by including van der Waals interactions at the B3LYP-D3 level of theory with the Orca software package [35]. For the constrained model, we used the partial Hessian vibrational analysis (PHVA) method for the frequency calculations making use of the in-house developed software module TAMkin [36,37]. The outer oxygen atoms, which were used to fix the cluster, were given an infinite mass [38–42]. All structures for starting geometries were built using ZEOBUILDER [37,43].

The kinetics for all epoxidation reactions are obtained using the bimolecular approach in which the two reactants are treated in gas phase. In this case, bimolecular transition state theory should be applied as outlined in Supporting Information. More details are also given by Van Speybroeck et al. [44] on the computational procedures for discriminating between intrinsic and apparent reaction kinetics.

To give an idea on the values of the physisorption energy for the various species, the complete energy diagram is taken up in Fig. 9 for the direct path 7 → 8.

The physisorption energy of cyclohexene is of about −28 kJ/mol, while −70 kJ/mol for the epoxide. However, the position of the cyclohexene/epoxide in the adsorbed complex and the way these molecules are coordinated with the V-center is not always uniquely determined, and therefore, the reaction kinetics is performed starting from the gas-phase species in this study.

The direct epoxidation reaction 7 → 8 is irreversible as can easily be seen from the energy diagram of Fig. 9. Similar large reaction energies are observed for the other epoxidation reactions. Therefore, only the rate constants for the forward reactions are taken up in Table 3. For convenience of the reader, the backward reaction barriers and Gibbs-free energies are also tabulated in Table S1.

The transition state of the direct epoxidation reaction 7 → 8 is given in Fig. 11a. The cyclohexene molecule is located in the free spot that extends to a whole hemisphere in front of the two remaining linkers and the t-butoxy group, stressing once more that the epoxidation reaction can only take place if some ligands are removed.

Table 3
Energy barriers and Gibbs-free energy barriers for the epoxidation reactions (bimolecular) and the radical decomposition (unimolecular). Also the reaction energies are reported, as well the reaction Gibbs-free energies at 323 K.

	Unimolecular			Bimolecular				
	$\Delta E^{\ddagger}_{0,intr}$ (kJ/mol)	$\Delta G^{\ddagger}_{323,intr}$ (kJ/mol)	$k^{unimol}_{323,intr}$ (s^{-1})	$\Delta E^{\ddagger}_{0,app}$ (kJ/mol)	$\Delta G^{\ddagger}_{323,app}$ (kJ/mol)	$k^{binol}_{323,app}$ ($m^3\,mol^{-1}\,s^{-1}$)	$\Delta E_{0,r}$ (kJ/mol)	$\Delta G_{323,r}$ (kJ/mol)
Unconstrained model								
Direct 7 → 8	–	–	–	−2.8	46.3	5.71E+03	−157.7	−174.8
Radical 7 → 9	37.1	32.9	3.22E+07	–	–	–	28.5	−34.7
10 → 11	–	–	–	35.1	89.6	5.73E−04	−219.4	−213.3
12 → 11	–	–	–	26.8	82.9	6.97E−03	−191.9	−187.2
Constrained model								
Direct 7 → 8	27.4	40.3	2.02E+06	−1.0	48.9	2.19E+03	−157.3	−171.2
Radical 7 → 9	38.0	35.2	1.37E+07	–	–	–	23.8	−37.3
10 → 11	–	–	–	29.1	90.2	4.69E−04	−226.5	−220.3
12 → 11	–	–	–	41.9	107.0	8.87E−07	−189.8	−177.8

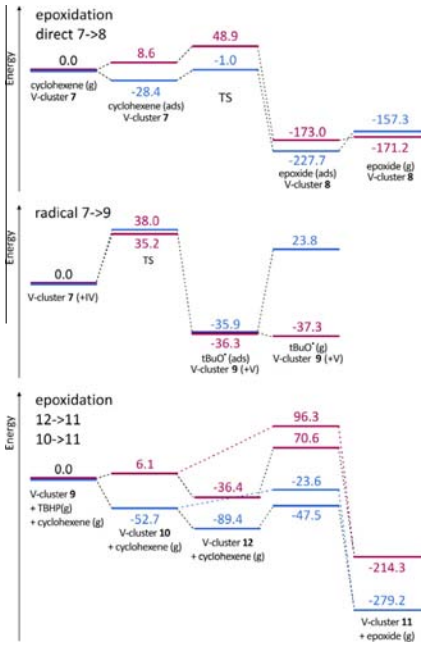

Fig. 9. Energy diagram for the direct epoxidation reaction 7 → 8, the radical reaction pathway 7 → 9 and the subsequent epoxidation reactions 10 → 11 and 12 → 11. Energies (at 0 K) are given in blue, Gibbs-free energies at 323 K are given in red. All energies in kJ/mol. The V-cluster appears as an activated complex in the reactants and as an inactivated complex in the products. In radical reaction 7 → 9 the oxidation number of vanadium changes from +IV to +V. Both energy (at 0 K) and Gibbs-free energy (at 323 K) profiles are drawn relative with respect to the first level in each scheme. Numerical results are obtained using the constrained cluster model. (For interpretation of the references to color in this figure legend, the reader is referred to the web version of this article.)

The constrained and unconstrained models predict nearly the same reaction barriers and entropic contributions (see Table 3) as the geometries resulting from the models only differ in the spatial orientation of the two remaining linkers. The energy diagram of Fig. 9 learns that the reaction is strongly exergonic and thus irreversible.

The direct route **7** → **8** is highly favored on basis of the energy barriers and Gibbs-free energies of activation. The reactions **10** → **11** and **12** → **11** are higher activated (90.2 kJ/mol and 107.0 kJ/mol versus 48.9 kJ/mol for the Gibbs-free energy of activation $\Delta G^{\ddagger}_{323,app}$ following the constrained model Table 3) but are thermodynamically driven as the product **11** is very stable (Gibbs reaction-free energies of −220.3 and −177.8 kJ/mol). The epoxidation reactions **10** → **11** and **12** → **11** are initiated by a radical decomposition **7** → **9** thereby bringing the active V-site into an oxidation state +V followed by a reaction of the originally inactive V-complex **9** with TBHP to an active complex **10** or **12**. The radical decomposition (**7** → **9**) is modeled as an unimolecular process with a reaction barrier of 37–38 kJ/mol or a Gibbs-free energy barrier of 33–35 kJ/mol at 323 K, which thus slightly decreases with temperature. This reaction will certainly take place, and in addition, it is also thermodynamically favored as the reaction becomes more and more exergonic with temperature due to entropic effects (see Fig. 9). Some transformations taken up in Scheme 2 are modeled as equilibration steps and the values are taken up in Table 4. Starting from complex **9**, an equilibration step occurs in which the TBHP coordinates with species **9**, to form another V^{+V} species **10**. This step is thermodynamically controlled toward species **10** at lower temperatures. Species **10** can further transform to species **12**, in which TBHP covalently bonds to the vanadium center. The equilibrium of this step lies in the direction of V-cluster **12**. From species **10** and **12** that are both V^{+V} species, the epoxidation of cyclohexene can be initiated.

Overall, the whole reaction cycle starting from **7** to **11** is very exothermic and also irreversible as the backward reactions have very high activation barriers (up to 300 kJ/mol (see Table S1)). In this "radical" pathway, which allows transformation of oxidation state from +IV to +V for vanadium, one of the epoxidation reactions **10** → **11** and **12** → **11** becomes the rate determining step.

They are higher activated but eventually become also important as this reaction cycle is thermodynamically controlled.

The reaction **12** → **11** requires some special interest as the results are more sensitive to the particular model used for the kinetics calculations, i.e., constrained versus unconstrained. In contrast

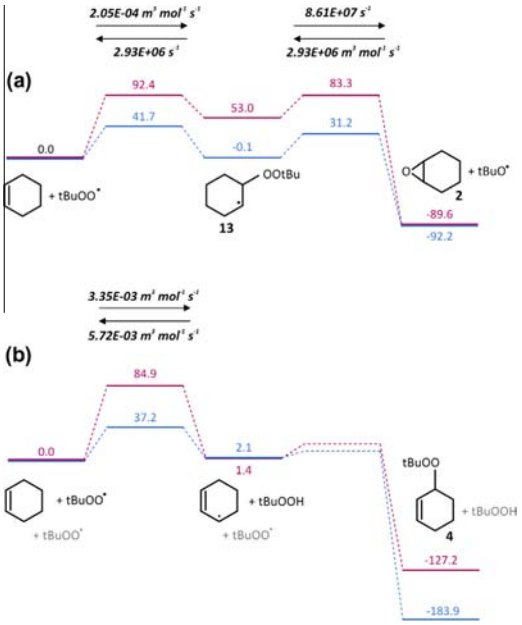

Fig. 10. Energy profiles for the reaction between cyclohexene and the *tert*-butylperoxy radical. Energies (at 0 K) are given in blue, Gibbs-free energies at 323 K are given in red. All energies in kJ/mol. (a) Pathway a leading to formation of cyclohexene oxide. (b) Pathway b leading to formation of the adduct **4**. Electronic energies at 0 K are indicated in red. Energies in kJ/mol. (For interpretation of the references to color in this figure legend, the reader is referred to the web version of this article.)

to the direct pathway **7** → **8** with a V^{+IV} active complex, steric hindrance lies now on the origin of the significant increase of the barrier in the constrained cluster model. In this V^{+V} complex (Fig. 11d), the position of the cyclohexene in the transition state is slightly different with that in the V^{+IV} complex (Fig. 11a). In addition, the free spot for the coordination of cyclohexene is more limited in the V^{+V} complex, and in the constrained model, one of the linkers causes a steric repulsive effect on the cyclohexene, inducing an asymmetric spatial position with respect to the oxygen of the V-complex. This unphysical situation causes too high barriers. Realistically, the values will lie in between the values of the two models and overall the conclusions on the most preferable pathway to epoxidation are not altered. The two geometries of the transition state are visualized in Fig. 11c and d where we can easily see that in the unconstrained case, the position of the linker is more relaxed allowing the cyclohexene to take the most favorable position in the transition state.

The regeneration reactions with TBHP go smoothly as they are mostly thermodynamically driven (see Table 4).

It is now interesting to couple our theoretical results to the available experimental data. The quantitative values of our calculations can indirectly be validated with the results of a kinetic study on the epoxidation of cyclohexene with $VO(acac)_2$. Gould et al. [45] suggested that vanadium is probably converted to the +V oxidation state and remains in that state throughout. This is in full agreement with the situation encountered in the epoxidation reactions **10** → **11** and **12** → **11**. The experiment reports values of 53.1 kJ/mol for the enthalpy of activation and −82.8 J/K/mol for the entropy of activation. For T = 323 K, this results to a Gibbs-free energy of activation of about 80 kJ/mol, which is in excellent agreement with the theoretical predictions for the pathways **10** → **11** and **12** → **11**, which proceed through a vanadium in oxidation state +V.

Summarizing, there are two pathways which are competitive and which form a closed cycle of epoxidation and regeneration and wherein the peroxide is systematically used to bring the inactive vanadium complex (species **6**) into an active complex with oxidation state +IV (species **7**) or an active complex with oxidation state +V (species **10** and **12**). The two epoxidation pathways start from a complex with another oxidation state for vanadium, but a switch from one cycle to the other is possible at any time. Once V^{+V} complexes are formed, a return to the V^{+IV}-cycle is possible via the equilibration step **12** → **6**, which we will call the V^{+V}–V^{+IV} recycling step for further reference. This step is energetically not favored ($\Delta E_{0,r}$ = 132–135 kJ/mol in Table 4) but becomes possible at temperatures of 323 K due to entropic contributions, which bring the free energy of reaction to reasonable values 67–77 kJ/mol. These barriers are of the same order as the barriers for epoxidation and are thus competitive with these pathways.

Thus far, no solvent effects have been taken into account. In the experimental part, the catalytic activity of the MIL-47 has been investigated with TBHP dissolved in water or in decane. One of the main differences was the much larger initiation time for cyclohexene conversion with decane as solvent. The proposed reaction scheme may serve to explain some of the experimental findings. The reaction cycle can only start once free coordination positions are created, either by folding a ligand away or by removing a

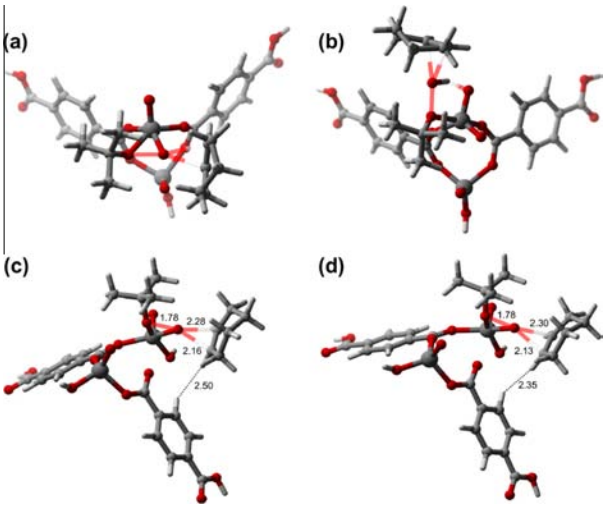

Fig. 11. Transition states of the three epoxidation reactions: (a) direct pathway 7 → 8, (b) pathway 10 → 11, (c) and (d) pathway 12 → 11. Use of the unconstrained model in (a)–(c); use of the constrained model in (d).

Table 4
Thermodynamical parameters for the reactions modeled as equilibrium steps. $\Delta E_{0,r}$ represents the reaction energy corrected with zero-point energies and dispersion, $\Delta G_{323,r}$ the reaction-free energy at 323 K. The equilibrium constant K_{323} at 323 K is obtained after a fitting procedure between 273 and 373 K.

	$\Delta E_{0,r}$ (kJ/mol)	$\Delta G_{323,r}$ (kJ/mol)	K_{323}	$[K_{323}]$
Unconstrained model				
6 → 7	−59.8	−40.8	3.96E+06	–
8 → 7 (regeneration)	−27.5	−7.4	1.55E+01	–
11 → 12 (regeneration)	6.7	5.0	1.53E−01	–
9 → 10	−64.7	−4.8	1.60E−01	$m^3\ mol^{-1}$
10 → 12	−27.5	−26.1	1.67E+04	–
12 → 6 (V^{+V}–V^{+IV} recycling)	132.2	67.6	4.41E−10	m^{-3} mol
Constrained model				
6 → 7	−60.3	−42.3	7.02E+06	–
8 → 7 (regeneration)	−27.9	−10.9	5.73E+01	–
11 → 12 (regeneration)	4.6	−4.3	4.94E+00	–
9 → 10	−52.7	6.1	2.74E−03	$m^3\ mol^{-1}$
10 → 12	−36.7	−42.5	7.54E+06	–
12 → 6 (V^{+V}–V^{+IV} recycling)	134.6	77.2	1.21E−11	m^{-3} mol

terephthalic acid from vanadium. The structure **6** in scheme 2 can be created by cleaving a terephthalate–vanadium bond and replacing the ligand by a hydroxyl group. Such hydroxyl groups can easily be introduced in a water-based medium and thus water helps in creating free coordination sites, enhancing the initial rate of cyclohexene conversion. In case of decane as solvent, such sites of type **6** are not formed as this solvent has no OH-group present. In this case, the activation should be induced by TBHP itself. This can either lead to the cleavage of a vanadium bond and an oxygen of the carboxylate group to form complex **7** immediately but also other species such as VO(L)(OtBu) could be formed, which can by ligand exchange with TBHP form the active species **7**. Therefore, one can anticipate that the initiation time for epoxidation is larger in case of decane, as TBHP takes also an active role in the activation period. These findings are compatible with the observation that the measured experimental diffraction pattern does not change after reaction with TBHP/decane + cyclohexene. The bulk structure remains better conserved during the reaction cycle, whereas in case of water, more vanadium/terephthalic acid bonds are broken. The diffraction pattern of the catalyst with TBHP/water after catalysis (see Fig. 5c) shows a broadening of the peaks that might be ascribed to further structure deterioration.

Another feature observed experimentally is the formation of side products, such as diols, adducts, and cyclohexenones, which are manifestly present after a short reaction time on a MIL-47 catalyst with a V-loading of 0.42 mmol and with TBHP dissolved in water. The experiment with TBHP in decane as oxidant does not reveal any relevant by-product formation. The formation of the *tert*-butyl-2-cyclohexenyl-1-peroxide **4** must be ascribed to radical pathways between the substrate and the oxidant TBHP and was recently further investigated for unsaturated Co-MOFs [14,46]. Freely diffusing peroxy radicals can be generated by a variety of mechanisms in which the oxidation state of vanadium changes. It is well known that radicals are better stabilized in water than in decane and thus such radical pathways are more prominent present in such polarisable media. Also the radicals tBuO• and tBuOO•, appearing in some pathways of Scheme 2, lie on the origin of the formation of the side products, and in particular that of the adduct **4** as schematically shown in Fig. 10 (pathway b). An enhanced concentration of radicals leads to more termination reactions and hence a larger production of adducts. The increasing concentration of the of *tert*-butylperoxy radical tBuOO• requires some attention, as it is also able to directly epoxidize cyclohexene following the so-called Twigg mechanism as reported by Van Sickle et al. [47] (pathway a in Fig. 10). We examine the two competitive pathways. In the first, a radical addition reaction takes place creating an intermediate cyclohexenyl radical **13** followed by cleavage of the

tert-butylperoxy radical and formation of cyclohexene oxide. The energy profile is displayed in Fig. 10 (pathway a). The radical addition reaction shows a high free-energy barrier, while the reaction is strongly endergonic, indicating that the backward reaction (dissociation) goes much faster than the forward reaction (association). In pathway b, a hydrogen abstraction occurs from the allylic position of cyclohexene forming the 3-cyclohexenyl radical, which can rapidly recombine with another *tert*-butylperoxy radical yielding the adduct **4**. The hydrogen abstraction also requires a high energy barrier (only 8 kJ/mol lower than in pathway a). The subsequent radical recombination reaction goes quite quickly since the reaction energy is strongly negative and heavily thermodynamically driven. These theoretical findings are in complete agreement with the suggestions made in a recent experimental work of Tonigold et al. [46] where pathway b has been proposed as the major pathway. Concluding, without excluding the direct epoxidation of cyclohexene by the *tert*-butylperoxy radical tBuOO•, the radical pathway will favor the adduct formation.

4. Conclusions

This study reveals that V-MIL-47 can be a highly selective catalyst in the epoxidation of cyclohexene using TBHP as the oxidant. Water should be avoided as the solvent for the peroxide, as it enhances strongly the leaching of the V-centers and as it accelerates an unwanted radical side reaction, forming an adduct between the peroxide and cyclohexene.

When decane is used to dissolve the peroxide, the MIL-47 is a highly selective catalyst toward the epoxide, especially in the first linear regime of conversion. The leaching of V-centers is negligible in that case and the structural integrity of the MOF is preserved during successive runs. Computational studies show that several catalytic pathways co-exist and compete with each other, but every catalytic cycle starts with the breaking of two V-terephthalic bonds to coordinate with the peroxide. EPR and NMR studies confirm that approximately 20% of the V^{+IV} sites are oxidized to V^{+V} in the first minutes of the catalytic reaction and remain relatively constant afterward.

Acknowledgments

K.L. is grateful to the Long Term Structural Methusalem Grant Nr. 01M00409 Funding by the Flemish Government. M.V. thanks the research board of Ghent University (BOF). I.M. thanks the Institute for the Promotion of Innovation through Science and Technology in Flanders (IWT Vlaanderen). Furthermore, this research is co-funded by the Ghent University, GOA Grant Nr. 01G00710, BELSPO in the frame of IAP 6/27 and the European Research Council (FP7(2007-2013) ERC Grant Nr. 240483). Computational resources (Stevin Supercomputer Infrastructure) and services were provided by Ghent University.

Appendix A. Supplementary material

Supplementary data associated with this article can be found, in the online version, at doi:10.1016/j.jcat.2011.09.014.

References

[1] B.F. Hoskins, R.J. Robson, J. Am. Chem. Soc. 112 (1990) 1546.
[2] H. Li, M. Eddaoudi, M. O'Keeffe, O.M. Yaghi, Nature 402 (1999) 276.
[3] N.L. Rosi, J. Eckert, M. Eddaoudi, D.T. Vodak, J. Kim, M. O'Keeffe, O.M. Yaghi, Science 300 (2003) 1127.
[4] L.J. Murray, M. Dinca, J.R. Long, Chem. Soc. Rev. 38 (2009) 1294.
[5] L. Pan, B. Parker, X.Y. Huang, D.H. Olson, J. Lee, J. Li, J. Am. Chem. Soc. 128 (2006) 4180.
[6] J. Perles, M. Iglesias, M.A. Martin-Luengo, M.A. Monge, C. Ruiz-Valero, N. Snejko, Chem. Mater. 17 (2005) 5837.
[7] D. Farrusseng, S. Aguado, C. Pinel, Angew. Chem. Int. Ed. 48 (2009) 7502.
[8] A. Corma, H. Garcia, F.X.L. Xamena, Chem. Rev. 110 (2010) 4606.
[9] P. Van der Voort, M.G. White, E.F. Vansant, Langmuir 14 (1998) 106.
[10] G. Catana, R.R. Rao, B.M. Weckhuysen, P. Van Der Voort, E. Vansant, R.A. Schoonheydt, J. Phys. Chem. B 102 (1998) 8005.
[11] P. Van Der Voort, M. Baltes, E.F. Vansant, Catal. Today 68 (2001) 119.
[12] A. Henschel, K. Gedrich, R. Kraehnert, S. Kaskel, Chem. Commun. (2008) 4192.
[13] N.V. Maksimchuk, K.A. Kovalenko, S.S. Arzumanov, Y.A. Chesalov, M.S. Melgunov, A.G. Stepanov, V.P. Fedin, O.A. Kholdeeva, Inorg. Chem. 49 (2010) 2920.
[14] M. Tonigold, Y. Lu, B. Bredenkötter, B. Rieger, S. Bahnmüller, J. Hitzbleck, G. Langstein, D. Volkmer, Angew. Chem. Int. Ed. 48 (2009) 7546.
[15] N.V. Maksimchuk, M.N. Timofeeva, M.S. Melgunov, A.N. Shmakov, Y.A. Chesalov, D.N. Dybtsev, V.P. Fedin, O.A. Kholdeeva, J. Catal. 257 (2008) 315.
[16] H. Garcia, A. Dhakshinamoorthy, M. Alvaro, Chem. – A Eur. J. 17 (2011) 6256–6262.
[17] H. Garcia, A. Dhakshinamoorthy, M. Alvaro, Chemcatchem 2 (2010) 1438–1443.
[18] F.X.L.I. Xamena, O. Casanova, R.G. Tailleur, H. Garcia, A. Corma, J. Catal. 255 (2008) 220–227.
[19] J.S. Seo, D. Whang, H. Lee, S.I. Jun, J. Oh, Y.J. Jeon, K. Kim, Nature 404 (2000) 982.
[20] L.Q. Ma, C. Abney, W.B. Lin, Chem. Soc. Rev. 38 (2009) 1248.
[21] C.D. Wu, A. Hu, L. Zhang, W.B. Lin, J. Am. Chem. Soc. 127 (2005) 8940.
[22] L.L. Wen, F. Wang, J. Feng, K.L. Lv, C.G. Wang, D.F. Li, Cryst. Growth Des. 9 (2009) 3581.
[23] P. Phuengphai, S. Youngme, P. Gamez, J. Reedijk, Dalton T. 39 (2010) 7936.
[24] S. Neogi, M.K. Sharma, P.K. Bharadwaj, J. Mol. Catal. A – Chem. 299 (2009) 1.
[25] S. Horike, M. Dinca, K. Tamaki, J.R. Long, J. Am. Chem. Soc. 130 (2008) 5854.
[26] F. Gandara, E.G. Puebla, M. Iglesias, D.M. Proserpio, N. Snejko, M.A. Monge, Chem. Mater. 21 (2009) 655.
[27] J. Juan-Alcaniz, E.V. Ramos Fernandez, U. Lafont, J. Gascon, F. Kapteijn, J. Catal. 269 (2010) 229.
[28] M.J. Ingleson, J.P. Barrio, J.B. Guilbaud, Y.Z. Khimyak, M.J. Rosseinsky, Chem. Commun. (2008) 2680.
[29] A. Dhakshinamoorthy, M. Alvaro, H. Garcia, Catal. Sci. Technol. 1 (2011) 856–867.
[30] K. Leus, I. Muylaert, M. Vandichel, G.B. Marin, M. Waroquier, V. Van Speybroeck, P. Van der Voort, Chem. Commun. 46 (2010) 5085.
[31] K. Barthelet, J. Marrot, D. Riou, G. Ferey, Angew. Chem. Int. Ed. 41 (2001) 281.
[32] A. Brückner, Top Catal. 38 (1–3) (2006) 133.
[33] A. Fenn, M. Wächtler, T. Gutmann, H. Breitzke, A. Buchholz, I. Lippold, W. Plass, G. Buntkowsky, Solid State Nucl. Mag. 36 (2009) 192.
[34] (a) E.P. Talsi, V.D. Chinakov, V.P. Babenko, K.I. Zamaraev, J. Mol. Catal. 81 (1993) 235;
(b) H. Mimoun, M. Mignard, P. Brechot, L. Saussine, J. Am. Chem. Soc. 108 (1986) 3711.
[35] ORCA. 2.6.35ed. <http://www.thch.uni-bonn.de/tc/orca/>.
[36] A. Ghysels, T. Verstraelen, K. Hemelsoet, M. Waroquier, V. Van Speybroeck, J. Chem. Inf. Model. 50 (2010) 1736.
[37] CMM Code. <http://molmod.ugent.be/code/wiki>.
[38] A. Ghysels, D. Van Neck, V. Van Speybroeck, T. Verstraelen, M. Waroquier, J. Chem. Phys. 126 (2007) 224102.
[39] A. Ghysels, D Van Neck, M. Waroquier, J. Chem. Phys. 127 (2007) 164108.
[40] A. Ghysels, V. Van Speybroeck, T. Verstraelen, D. Van Neck, M. Waroquier, J. Chem. Theory Comput. 4 (2008) 614.
[41] A. Ghysels, V. Van Speybroeck, E. Pauwels, D. Van Neck, B.R. Brooks, M. Waroquier, J. Chem. Theory Comput. 5 (2009) 1203.
[42] A. Ghysels, V. Van Speybroeck, E. Pauwels, S. Catak, B.R. Brooks, D. Van Neck, M. Waroquier, J. Comput. Chem. 31 (2010) 994.
[43] T. Verstraelen, V. Van Speybroeck, M. Waroquier, J. Chem. Inf. Model. 48 (2008) 1530.
[44] V. Van Speybroeck, J. Van der Mynsbrugge, M. Vandichel, K. Hemelsoet, D. Lesthaeghe, A. Ghysels, G.B. Marin, M. Waroquier, J. Am. Chem. Soc. 133 (4) (2011) 888.
[45] E.S. Gould, R.R. Hiatt, K.C. Irwin, J. Am. Chem. Soc. 90 (1980) 4573.
[46] M. Tonigold, Y. Lu, A. Mavrandonakis, A. Puls, R. Staudt, J. Mollmer, J. Sauer, D. Volkmer, Chem. Eur. J. 17 (2011) 8671.
[47] D.E. Van Sickle, F.R. Mayo, R.M. Arluck, J. Am. Chem. Soc. 87 (21) (1965) 4824.

Paper 7

Performance of Vanadium MIL-47 and linker substituted variants as catalysts for oxidation reactions: a combined theoretical and experimental approach

Matthias Vandichel, Shyam Biswas, Karen Leus, Joachim Paier, Joachim Sauer, Pascal Van Der Voort, Michel Waroquier and Veronique Van Speybroeck

in preparation

DOI: 10.1002/cplu.200((will be filled in by the editorial staff))

Performance of Vanadium MIL-47 and linker substituted variants as catalyst for oxidation reactions: a combined theoretical and experimental approach.

Matthias Vandichel,[a]* Shyam Biswas,[b] Karen Leus,[b] Joachim Paier,[c] Joachim Sauer,[c] Pascal Van Der Voort,[b]* Michel Waroquier[a]* and Veronique Van Speybroeck,[a]*

Dedication ((optional))

The epoxidation of cyclohexene is investigated on a metal organic framework MIL-47 containing saturated V^{+IV} sites linked with terephthalate linkers, that are functionalized (X-MIL-47, X=-OH, -F, -Cl, -Br, $-CH_3$, $-NH_2$). Experimental catalytic tests are performed on the X-MIL-47 materials to elucidate the effect of linker substitution on the conversion patterns. A quantitative structure activity relationship between the X-MIL-47 materials was found for the initial conversion of cyclohexene to cyclohexene oxide. The substituents such as -F, -Cl and -Br, $-CH_3$, $-NH_2$ obeyed a Hammett equation as a function of σ_p (substituent constant). A second Hammett plot as a function of σ_m could be constructed for the monoatomic substituents and for the multi-atomic substituents, separately. In general substituents led to an increased activity relative to the parent MIL-47. Additionally, first principle kinetic calculations are performed on periodic slab models of MIL-47 and compared with cluster models to determine the most important active site. An alkylperoxo species $V^{+V}O(OOtBu)$ (of slab type II) is identified as most abundant and therefore most active as epoxidation site. Accordingly, such a cluster model was selected for further investigation as the most representative model for the heterogeneous epoxidation on MIL-47 and X-MIL-47. Then, functionalized cluster models were constructed with the most extreme performing substituents (-OH, $-NH_2$) and also for Cl as an example of the halogen substituents. The epoxidation activity of the functionalized models agreed qualitatively and quantitatively with experiment, confirming the relevance of our theoretical active site model as a typical active site within the material.

1. Introduction

Over the past decade, Metal Organic Frameworks (MOFs) have emerged as an important new class of nanoporous materials and can be considered as the most recent development and challenge in the field of ordered porous materials [1]. This new class of porous materials has a truly hybrid character, since both inorganic and organic moieties are necessary to build up the framework. In this way, MOFs can provide a bridge between organic polymers and inorganic crystalline zeolites and are sometimes also referred to as a crystalline subclass within the porous coordination polymers (PCPs). Since the 1990s, this area of chemistry has experienced an almost unparalleled growth, witnessed not only by a large number of research and review papers published but also by the ever-expanding scope of the research [2]. MOFs have been reviewed both from a general perspective [1, 3] as more application-related. The MOF-applications have been extensively studied for adsorption and gas storage [4], separation [5], catalysis [6], optics and sensing [7], electrical/magnetica properties [8]. Recently MOFs are also examined for biomedical applications such as controlled drug delivery [9].

In view of the broad variety of applications, more and more attempts are investigated to tune the properties of MOFs at the nanoscale level. Various studies have appeared in which the organic linkers are functionalized but without altering the original topology of the material. A variety of case studies have appeared to date of which we will mention some of them here to set the scene. The prototype MOF-5, which is constructed from octahedral Zn-O-C clusters and benzene linkers, was functionalized with the organic groups -Br, $-NH_2$, $-OC_3H_7$, OC_5H_{11}, $-C_2H_4$ [10] and particularly IRMOF-6 proved to be beneficial for methane storage. Another example is the work of

[a] *ir. M. Vandichel, prof. M. Waroquier, prof V. Van Speybroeck*
Center for Molecular Modeling, Universiteit Gent
Technologiepark 903, B-9052 Zwijnaarde (Belgium)
Matthias.Vandichel@Ugent.be, Michel.Waroquier@Ugent.be, Veronique.VanSpeybroeck@Ugent.be
[b] *dr. S. Biswas, K. Leus, prof. P. Van Der Voort*
COMOC - Centre for Ordered Materials, Organometallics and Catalysis, Universiteit Gent
Krijgslaan 281-S3, B-9000 Gent (Belgium)
Pascal.VanDerVoort@Ugent.be
[c] *dr. J. Paier, prof. J. Sauer*
Institut für Chemie, Humboldt-Universität zu Berlin
Unter den Linden 6, D-10099 Berlin (Germany)

Supporting information for this article is available on the WWW under http://dx.doi.org/10.1002/cplu.200xxxxxx.

Serra-Crespo et al. in which a pure phase amine functionalized MIL-101(Al) was synthesized and found to be an excellent candidate for the selective adsorption of CO_2 from methane and N_2 [11]. Various studies on the substituted versions of MIL-53(Fe) [12] and MIL-53(Al) [13] are also interesting, as they have shown different adsorption isotherms and breathing behavior compared to parent MIL-53. The functionalization was particularly explored for sorption and separation studies of molecules such as CO_2, CH_4, etc. Very recently, the UiO-66-X series was investigated for both CO_2/CH_4 separation and catalysis. Grand Canonical Monte Carlo calculations showed that $–SO_3H$ and $–CO_2H$ functionalized materials exhibit the highest selectivity for CO_2/CH_4 separation [14]. With respect to catalysis, some of the present authors have shown a remarkable influence of electronic linker modulations of the UiO-66 (UiO-66-X) material on the catalytic activity for the citronellal cyclization [15]. Functionalized linkers could greatly enhance the catalyst performance of the coordinatively unsaturated Lewis acid sites. Nitro-group substitution resulted in a 56-fold increase in rate. This effect was confirmed by theoretical modeling on a well chosen defect site, and resulted in substantial lowering of both the apparent and intrinsic free-energy barrier.

Metal-organic frameworks (MOFs) have also been explored as heterogeneous catalysts for oxidations using hydroperoxides or molecular oxygen. An excellent review on this item was recently given by Garcia and co-workers [6b]. In our previous work [16], we have studied the catalytic performance of a coordinatively saturated V-MOF; V-MIL-47 [17], for the liquid phase oxidation of cyclohexene with *tert*-butyl hydroperoxide (TBHP) as oxidant. Apart from cyclohexene oxide **2**, the product spectrum also consisted of the consecutively formed cyclohexane-1,2-diol **3** and (radical) side products as *tert*-butyl-2-cyclohexenyl-1-peroxide **4** and cyclohexen-2-one **5** (Figure 1a). The catalyst is believed to act partly heterogeneous, which is confirmed by the hot filtration experiments [16a]. After hot filtration of the catalyst, the conversion towards the epoxide almost stops while the radical products are still formed. This could be due to the presence of radical pathways that are also able to produce epoxide and secondly due to leached V-sites in solution [16b]. In a recent theoretical study, we performed a complete mechanistic study on the possible epoxidation pathways for the homogeneous $VO(acac)_2$ system [18]. Our results allowed to conclude that the concerted Sharpless mechanism is preferred and that alkylperoxo species $V^{+V}O(L_1)(L_2)(OOtBu)$ species are most abundant as epoxidation catalyst (L_1, L_2 = OH, acac, Oac and OtBu).

The aim of this study is twofold: First, special attention is devoted to the methodology (cluster versus periodic approaches) to describe the structure of the most active catalytic sites in MIL-47. Second, the effects of linker substitution on the epoxidation performance of the vanadium catalyst MIL-47 [17] in a combined experimental-computational effort. Modifications with both an electron withdrawing (-OH, -F, -Cl, -Br) and electron donating ($-CH_3$, $-NH_2$) are investigated. To the best of our knowledge the functionalized MIL-47 series have not been studied for this purpose. The MIL-47 structure consists of a three-dimensional framework, where each V^{+IV} centre is coordinated to four oxygen atoms from four different carboxylate groups and two oxygen atoms from the vanadyl V=O-V=O chain. As such vanadium is fully saturated in an octahedral coordination mode.

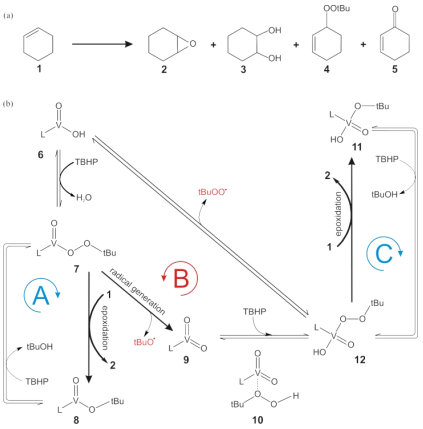

Figure 1. (a) Oxidation of cyclohexene **1** to cyclohexene oxide **2** and the consecutive ring opening to cyclohexane-1,2-diol **3**, *tert*-butyl-2-cyclohexenyl-1-peroxide **4** and allylic oxidation to 2-cyclohexene-1-one **5**; (b) Two competitive cyclohexene epoxidation pathways (**7** → **8**, **12** → **11**) and radical generation reactions (**7** → **9** and **12** → **6**), allowing transformation of oxidation state from +IV to +V and vice versa. L represents the two terephthalate ligands to which the vanadyl oxygens are coordinated.

The main pathways that have been modelled in previous work of the authors [16b] are shown in Figure 1b. The reaction cycle starts with an activation step, in which TBHP coordinates with the vanadium center to form an alkylperoxo species **7**. First, a direct pathway to epoxidation may lead to the formation of cyclohexene oxide **2** and brings the catalyst to a less active complex **8**. Second, a radical mechanism is plausible (**7→9** in Figure 1b). In this route V^{+V} vanadium complexes **9** are formed by homolytic cleavage of the peroxo linkage, which can then be further activated with TBHP. The generated V^{+V} activated complexes **10** and **12** can again epoxidize cyclohexene. Both direct epoxidations (A and C) and radical (B) routes are completed by a regeneration step which closes the cycle (Figure 1b). Many more reactive pathways can occur through the catalytic cycle but the considered pathways here are selected as a proof of principle to determine an accurate catalyst model and investigate the influence of linker substitution. A complete overview of all possible epoxidation pathways may be found in our earlier study on $VO(acac)_2$ [18]. The epoxidation reactions (**7→8**, **10→11**, **12→11**) and radical generation reactions (**7→9**, **11→7**) were calculated previously on extended cluster models [16b] (Figure 1b). In this study, the reaction **10→11** was omitted, as it required a higher free

energy barrier [16b]. It is more likely that complex **10**, would react further to complex **12**, forming the active V^{+V} epoxidation species.

In this work the methodology for a theoretical investigation of the epoxidation reactions has been extended. The reactions have been modelled in a periodic model in the search for the most appropriate active site, and the results are compared with the cluster calculations. The periodic simulations include a larger part of the active site environment, describing geometrical and electronic effects much better. They give a significant added value to the discussion, as they provide extra insight in the epoxidation behaviour of the MIL-47 catalyst and are of primordial importance to identify the exact nature of the active site. However, they are computationally very demanding and therefore restricted to the parent MIL-47. Once the structure of the most active site has been determined, this model was used for the construction of cluster models of substituted X-MIL-47 catalysts. As experimental data on cyclohexene conversion in functionalized X-MIL-47 are missing in literature, these materials were also synthesized and catalytic tests were performed and carefully compared with the results obtained on the parent MIL-47. The combined theoretical and experimental approach will provide us a full understanding of the functionalization on the epoxidation activity of MIL-47.

2. Results and Discussion

2.1. Experimental results

To investigate the influence of substituents on the catalytic performance, a set of catalytic experiments were carried out on the parent MIL-47 and X-MIL-47 series (X= -OH, -Br, -Cl, -F, -CH_3, -NH_2). The time-conversion plot for the formation of cyclohexene oxide in first catalytic runs is shown in Figure 2. The values of TON, TOF and vanadium leaching for the catalysts are presented in Table 1. Due to the high values of vanadium leaching obtained after 6 h for all the compounds except MIL-47 and NH_2-MIL-47, only the first hour of the catalytic tests can be assumed to be mainly heterogeneous. During this period, the conversion of cyclohexene to cyclohexene oxide, the TOF values follows a trend: OH-MIL-47 > Br-MIL-47 > Cl-MIL-47 > F-MIL-47 > CH_3-MIL-47 > NH_2-MIL-47 > MIL-47. Thus, all the substituted X-MIL-47 catalysts show higher activity towards the formation of cyclohexene oxide compared to the parent MIL-47, indicating a significant effect of the functionalization on the catalytic performance. This trend of catalytic activity was attempted to correlate with the electronic effect of the grafted functional groups. In essence, a Hammett-type structure-activity linear free energy relationship (LFER) was established using the experimental rate constants (k_X) and Hammett's σ_p (substituent constant)[19] values of the substituents. The plot of $\log(k_X/k_H)$ versus σ_p resulted in a Hammett-Taft equation [20] (Figure 3a) of the type: $\log(k_X/k_H) = \rho\sigma_p + E_S$ with $\rho = 0.64$ and $E_S = 0.66$, where ρ and E_S represent reaction constant and steric substituent constant, respectively. Only the –OH functionalized MIL-47 and the unsubstituted MIL-47 show a significant deviation from the linear fit, which is not surprising as the para substituent constant σ_p is not representative for ortho substitution of an hydroxyl group due to strong hydrogen bonds with the oxygens of the dicarboxylate groups of the terephthalate linkers. In the vicinity of an active Vanadium center, the hydrogen bond withdraws electron density from the carboxyl group, which in turn has an electron withdrawing effect on vanadium. For an hydroxyl group in ortho position with respect to the carboxyl group near the active site, the Hammett substituent constant for –OH should be large and positive, and hence removes the apparent discrepancy in Figure 3a for the –OH result. It fully explains the large rate increase measured experimentally for cyclohexene conversion on MIL-47-OH.

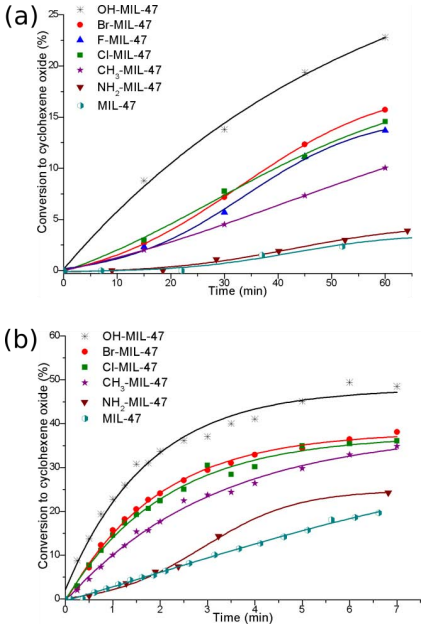

Figure 2a-b. Catalytic conversion of cyclohexene to cyclohexene oxide for MIL-47 in comparison with substituted MIL-47. TBHP in decane as oxidant was used with chloroform as solvent.

For the other substituents the Hammett relationship holds well. They reveal a strong indication that the substituent lying in *ortho*-position relative to the active site has the most influence on the catalytic behaviour. In particular, the steric substituent constant E_S is here dominant as it enhances the rate constant k_X with a factor 4.6 for all substituents. It provides an extra stabilization of the transition state during the epoxidation reaction. We stress here the relatively small value

of the reaction constant ρ, causing a rate increase limited to barely 1.4 for the electron-withdrawing groups Br and Cl. Whether steric effects of substituents influence the enthalpic or the entropic contribution of the reaction rate will be discussed in the theoretical section.

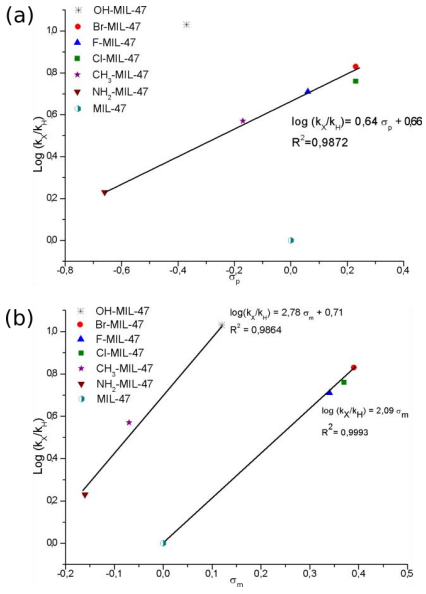

Figure 3a-b: Hammett plots for the cyclohexene epoxidation on different X-MIL-47 catalysts as a function of the substituent values σ for substituents at para (a) and meta postion (b) of the active site.

Recently, the UiO-66-X series was tested for the cyclization of citronellal. It was found that the defect linkers were responsible for the catalytic activity. For the UiO-66-X series, a Hammett equation as a function of σ_m [21] could be found, where electron withdrawing substituents lead to an increased rate and electron donating substituents to a decreased rate. However, the electronic modulation effect on the conversion was higher than in case of the epoxidation on X-MIL-47: a reaction constant ρ = 2.35 was found instead of 0.64. Furthermore, the Hammett-Taft equation did not lead to any steric substituent effect (E_S = 0). Those results were not surprising, since the substituents in meta position with respect to the carboxyl group connected to the active Zr site cannot have much steric influence on the transition state. Applying the same procedure for the epoxidation reaction in X-MIL-47, we get Hammett plots as displayed in Figure 3b. The linear fit through the points belonging to mono-atomic substituents goes through the origin of the plot, and gives evidence that no steric effects are playing a role (*E*s = 0). On the contrary, in the case of multi-atomic substituents, such as -OH, -NH_2 and -CH_3, a steric substituent coefficient of *E*s = 0.71 is observed, which is of the same order of magnitude as for substituents in the ortho position.

After longer periods some catalysts become more active but this may be ascribed to the formation of more defects in the material and larger amounts of leached vanadium centers. At this point, homogeneous pathways may also contribute to the higher activity. Although NH_2-MIL-47 showed much less leaching compared to the other substituted X-MIL-47 after 6h of conversion, this did not lead to a decreased initial activity for NH_2-MIL-47. The initial amount of active sites in the X-MIL-47 materials should thus be similar.

Table 1. TOF, TON and the percentage of leached V for the consecutive catalytic runs with TBHP/decane as oxidant.

	TON_{ox}[a]	TOF_{ox} (h^{-1})[b]	leaching (%)[c]	mmol V
MIL-47- 1st run [16b]	17.8	2.6	< 3	0.46
MIL-47- 2nd run [16b]	8.3	1.4	0.0	0.33
MIL-47-NH_2-1st run	29.7	4.4	10.2	0.38
MIL-47-NH_2-2nd run	53.7	9.0	8.8	0.13
MIL-47-OH-1st run	43.1	27.2	<15	0.42
MIL-47-F-1st run	-	13.1	>30	0.43
MIL-47-Cl-1st run	36.3	14.8	>30	0.42
MIL-47-Br-1st run	41.3	17.3	>30	0.42
MIL-47-CH_3-1st run	33.7	9.5	>30	0.41

[a] TON_{ox} values were calculated after 6 h; [b] TOF_{ox} values were calculated after 30 min. All the TON_{ox} and TOF_{ox} values were calculated based on the conversion to cyclohexene oxide. [c] Amount of vanadium leaching was determined after 6 h.

2.2. Theoretical Results

2.2.1. Periodic slab model and cluster model to represent the active sites

In an undamaged fully saturated MIL-47 framework, the coordination sphere around vanadyl $(V=O)^{2+}$ is completely blocked by terephthalate linkers, leaving no free position for substrate chemisorptions or reactions. The catalytic activity of the material for cyclohexene epoxidation with TBHP needs to be explained by structural defects, making the vanadium sites available for reaction with TBHP. Those defects can be present at the surface of the material, but they can also be generated internally by the removal of two terephthalic acid molecules that are both connected to the same vanadium centre. In this study, we will limit ourselves to two possible defects, namely the defects parallel with the 100 crystal plane according to the crystallographic information file provided by Barthelet et al. [17].

The periodic slab models were created by cutting two terephthalic acids and two vanadium atoms from the optimized MIL-47 unit cell (Figure 4). Subsequently two unsaturated vanadium atoms at the end of the vanadyl chain were terminated with -OH groups, maintaining the +IV oxidation state for the vanadium atoms. Depending on the cutting procedure, either a slab of Type I or Type II was formed (Figure 4). However to allow a comparison with previous

cluster based calculations, also an extended cluster model, as constructed previously [16b], was considered. To allow an energetic comparison between the two sites, a vacuum layer is included in the model to prevent artificial interactions between the terminal hydroxyls and the interrupted vanadyl chain. The periodic slab models are able to determine differences in stabilities of Type I and Type II active sites. The periodic slab of Type II was found to be around 66 kJ/mol more stable than the slab of Type I based on PBE-D2 calculations. As two defect sites are present in each periodic slab, this difference amounts to 33 kJ/mol per active site. This can probably be ascribed to some extra interaction between the terminating vanadyl oxygen and the saturated hydrogen terminating the carboxyl group as shown in Figure 4. In the following section, the two periodic slabs which are models for two types of active sites, will be used to investigate the reaction kinetics of the cyclohexene oxidation. Also a thorough comparison with kinetic results obtained from cluster models will be considered.

2.2.2. Cluster versus periodic approach for cyclohexene oxidation on MIL-47.

The reaction kinetics have been calculated for the three main reaction classes A, B and C in both periodic and cluster models and for various levels of theory. Only a selection of the theoretical results is taken up in Table 2; for completeness all the other results are given in the Supporting Information. In the periodic model the geometries have been established within the PBE exchange correlation functional. Further computational details are given in the Computational and Experimental Section. Energy predictions for reactants and transition states are refined by applying the hybrid functional PBE0 with inclusion of D2 dispersion corrections. Both PBE as PBE0 results are taken up in the Supporting Information. Note that the reaction kinetics for the epoxidation reaction **7→8** could not be derived correctly in the periodic calculation due to the existence of a negative frequency which could not be removed. The Gibbs free energies show the same qualitative trend for the two functionals favouring at most the radical generation reaction **7→9**, but the absolute values are deviating a lot. PBE predictions for apparent barriers are mostly underestimated [22], which is typical for GGA-type functionals [23] even with inclusion of the semi-empirical correction for dispersion. PBE0 is much more reliable for chemical kinetics, and can best be compared with values predicted by other hybrid functionals, such like B3LYP. For that reason we only retain the VASP-PBE0-D2 results for further assessment and comparison with the extended cluster calculations. Zero point and free energy barriers of the three main reactions are collected in Table 2. Regardless of the level of theory or type of active site, our results show that the radical generation reaction **7→9** is the fastest, followed by the epoxidation on a vanadium +IV site **7→8** and that the **12→11** is the slowest reaction. Periodic calculations seem to prefer type II active sites for the epoxidation reactions, but the energy differences of some few kJ/mol are such that we may not exclude active catalytic centers of type I in an overall assessment.

Table 2: Apparent energy and free energy barriers (respectively $\Delta E^{\ddagger}_{0}$ and $\Delta G^{\ddagger}_{323}$ in kJ/mol) for the reaction routes A, B and C. (a) Optimization at PBE-D2, (b) Optimization at ONIOM(B3LYP/BS1:B3LYP/6-31g), (c) results from Vandichel et al. [18].

	Type I			**Type II**		
	7 → 8	7 → 9	12→ 11	7 → 8	7 → 9	12→ 11
(a) Periodic results : PBE0-D2						
$\Delta E^{\ddagger}_{0}$		32.6	35.7	11.4	28.1	29.1
$\Delta G^{\ddagger}_{323}$		32.8	90.6	65.8	28.0	87.0
(b) Extended cluster results : PBE0/6-311+g(d,p)-D3						
$\Delta E^{\ddagger}_{0}$	9.9	53.3	49.7	12.3	53.0	34.1
$\Delta G^{\ddagger}_{323}$	59.8	50.5	114.9	67.5	54.2	89.1
(b) Extended cluster results : B3LYP/6-311+g(d,p)-D3						
$\Delta E^{\ddagger}_{0}$	-9.2	34.2	33.5	3.5	38.5	22.8
$\Delta G^{\ddagger}_{323}$	40.7	31.4	98.6	58.7	39.7	77.8
(c) Homogeneous catalytic conversion with $VO(acac)_2$ B3LYP/6-311+g(3df,2p)-D3						
	L = acac			**L=OAc**		
	7 → 8	7 → 9	12→ 11	7 → 8	7 → 9	12→ 11
$\Delta E^{\ddagger}_{0}$	14.6	38.5	48.8	8.9	38.4	22.2
$\Delta G^{\ddagger}_{323}$	68.4	38.8	108.7	61.4	33.5	80.9

Inspection of the extended cluster results, using the same functional PBE0 but with D3 dispersion corrections, learns that the largest deviations with the periodic calculations are observed in the barrier of the radical decomposition reaction switching the oxidation state for Vanadium from +IV to +V. Periodic calculations predict barriers of circa 30 kJ/mol, independent of the structure of the active site, but obviously much smaller than the 53 kJ/mol predicted in the cluster model using the same density functional. This is remarkable as the epoxidation barriers agree quite fairly (for Type II). To elucidate this remarkable discrepancy, we display the transition state structures for both active sites in the periodic slab in Figure 5 (the extended cluster TS structures are taken up in Figure S.2). For the radical decomposition reaction **7→9**, the breaking O-O distances amount to 1.65 Å and 1.63 Å for Type I and II in the periodic model, compared with 1.79 Å and 1.80 Å in the cluster model. This could probably be ascribed to the environment which is different in both approaches, allowing the oxidant TBHP to come closer to the vanadium catalyst in the periodic model. However, the use of another DFT method (B3LYP/6-311+g(d,p)-D3 level of theory) in the extended cluster models generates much lower free energy barriers of 31.4 and 39.7 kJ/mol, which are now much more in agreement with the periodic predictions of 32.8 and 28.0 kJ/mol at the PBE0-D2 level of theory compared to the results at the PBE0/6-311+g(d,p)-D3 level of theory. It illustrates once more that

small geometry differences of the breaking of O-O bond in the transition state may cause significant shifts in the barriers.

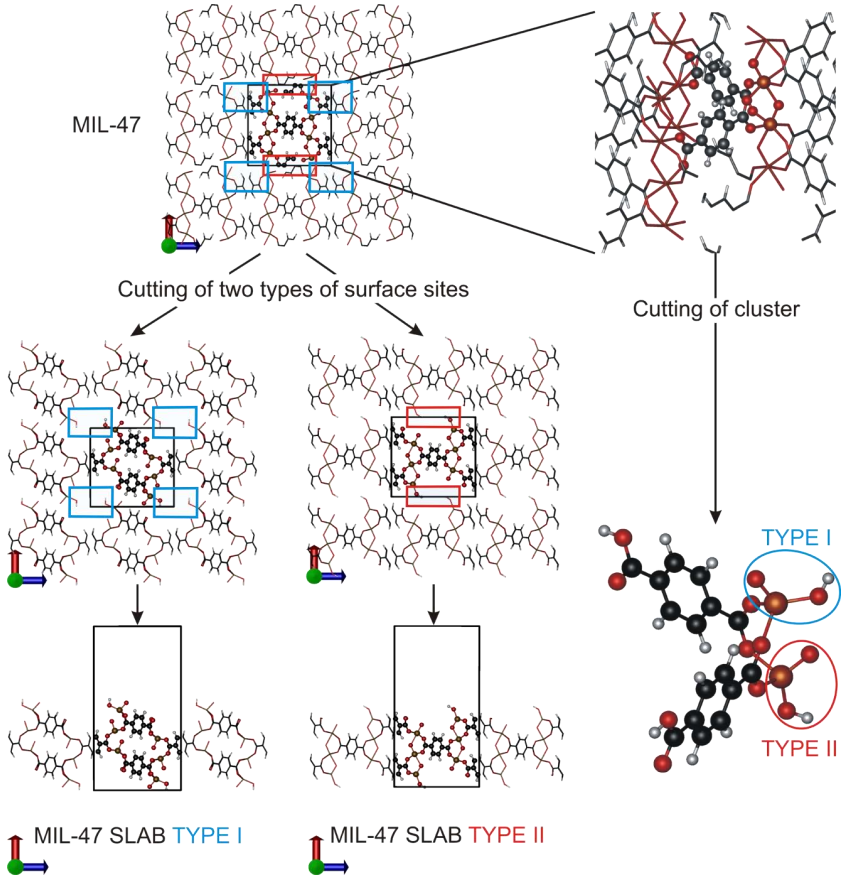

Figure 4: Two types of defects are constructed for MIL-47. In case of the periodic models, those can be separated in two different slab models (Type I an d Type II), while both types of active sites are present in the cluster model. The cutting procedure of the periodic slabs to obtain both types of active sites, can be followed by the rectangles, that display where terephthalate linkers and vanadyl groups are cut.

On the contrary, free energy barriers for the two epoxidation reactions, predicted by the periodic and extended cluster calculations using the same DFT functional, agree quite well with each other, especially for the reactions taking place on active site of type II. Reactions, starting from active V^{+IV} species (**7** → **8**), seem to be favoured. This trend is even more pronounced for epoxidation reactions occurring at active site of type I, where they become competitive with the radical generation $V^{+IV} \rightarrow V^{+V}$ (difference in free energy barrier of about 9 kJ/mol). Use of another hybrid functional does not change the overall picture. On basis of the numerical kinetic results reported in Table 2, one could discuss the different plausible reaction pathways for cyclohexene epoxidation in MIL-47, as schematically shown in Figure 1. Both epoxidation reactions **7** → **8** and **12** → **11** are very exergonic and thus irreversible. Starting from a Vanadium +IV active species 7 the kinetics predict some preference to a radical decomposition bringing V^{+IV} into an oxidation state +V, followed by a reaction of the originally inactive V-complex **9** with TBHP to an active complex **10** or **12**. The epoxidation can then be initiated but the

activation energy is high (of about 100 kJ/mol) and a V^{+V} – V^{+IV} recycling step **12→6** is not excluded. This energy step is energetically not favoured (free energy barrier of 77.2 kJ/mol), but is even lower than the **12 → 11** epoxidation reaction. On the other hand, it should also be stressed that a catalytic cycle within the V^{+IV} complexes is by far not excluded as **7 → 8** is thermodynamically driven as the product **8** is very stable (we refer to results of ref. [16b]. Concluding, all the pathways A, B, C together with the recycling step 12 → 6 are very competitive.

Regarding the catalytic properties of the two reaction sites I and II, it was already mentioned that type II sites are thermodynamically more stable than type I sites. For the reactions with V^{+IV} species, cluster calculations give advantage to active sites of type I (lower free energy barriers), while the catalytic cycle for V^{+V} species is energetically more favourable for sites of type II. It is hard to make a best choice for the active site with the highest performance.

We also include the electronic energy barriers in Table 2, to get insight in the entropic contributions, which turn out to be significant in the determination of the reaction rate for the epoxidation. Some energy barriers are negative as all barriers are referred to the separate reactants (apparent kinetics).

In a recent paper of the authors the cyclohexene epoxidation has been investigated for the homogeneous catalytic system $VO(acac)_2$ with TBHP as oxidant. It is an extensive theoretical study involving all possible reaction paths leading to the epoxidation mechanism, taking into account various ligand exchange reactions, taking place among the active and inactive complexes in which vanadium may either have oxidation state +IV or +V. Also radical decomposition reactions transforming V^{+IV} to V^{+V} species and vice versa, have been taken into account in the extended model space of active and inactive complexes with ligands varying from hydroxyl (-OH), acetyl acetonate (-acac), acetate (-OAc), or *tert*-butoxide anion (-OtBu). A comparison between both studies is instructive as the similarities are large: only the ligand L differs substantially. In the current study the ligand is bidentate and contains two terephthalate linkers, simulating the topology in some way, while in ref. [18] the ligand is essentially smaller. We can assume that the acetyl acetonate (-acac) and acetate (-OAc) are the best comparison with the terephthalic acid ligand in the extended cluster calculation. The energy barriers of these two selected active species are also reported in Table 2. They should best be compared with the B3LYP results of the extended cluster calculations. An overall conclusion is that the numbers do not differ a lot: barriers are slightly higher than in the heterogeneous catalyst. With the acetate ligand the agreement is even striking.

Concluding, the periodic calculations confirm that extended cluster calculations perform even well, provided that the active site environment is sufficiently described. An undamaged saturated MIL-47 framework is catalytically inactive, and organic linkers should be removed to allow free positions for substrate chemisorptions. The channels of the MOF (of about 10.5 x 11.0 Å) are such that the oxidant and the cyclohexene molecule can easily diffuse through them and that the vanadium metal can exert its catalytic activity when the coordination sphere around the metal ion is not completely blocked by the terephthalate linkers. Confinement effects are rather limited and are not essential to take place the epoxidation reactions. This does not mean that the environment (surroundings of the active site) does not play any role. The presence and spatial orientation of the terephthalate linkers may affect the epoxidation rate constant by a factor of 1000 (corresponding with a variation of 25 kJ/mol in Gibbs free energy barrier), although MIL-47 is one of the MOF structures showing a small degree of flexibility. The results discussed in the study on the homogeneous catalytic system $VO(acac)_2$ point toward similar findings. It can be stated that the leaching of the active site is probably easier in case of type I active sites, as there is already one vanadium-linker bond broken in the transition state. This could be an argument to promote active sites of type II to be used in the remainder of this paper, where focus will be made on the effect of linker substituents.

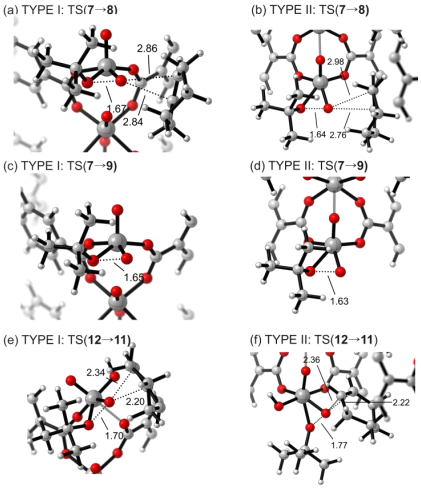

Figure 5 a-f: Transition states for the three main reactions in the periodic slab. Distances related to the oxygen transfer during either epoxide formation or radical generation are indicated.

As the free energy barriers for the bimolecular epoxidation reaction from $V^{+IV}O(OOtBu)$ are always larger than those for the unimolecular radical generation regardless of the level of theory, model or type of active site used (**7→9** < **7→8**), the epoxidation route via the $V^{+V}O(OOtBu)$ species **12** will be dominant. Therefore, the effect of linker substitution should be investigated on the epoxidation reaction of species **12** on an active site of Type II (Figure 6a).

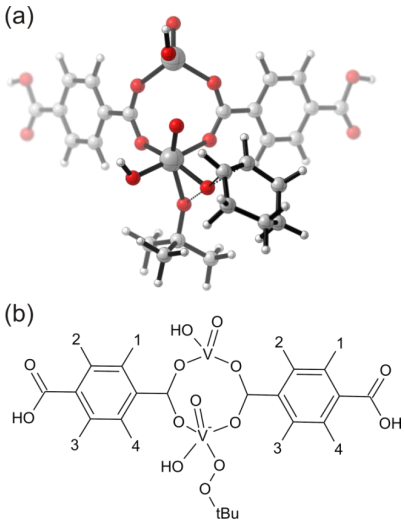

Figure 6: (a) Investigated epoxidation transition state on the MIL-47 cluster; (b) The X-MIL-47 cluster models consider four substitution positions 1-4. For example, within CL-NH_2-1, the amino-substituents are placed in position 1 and hydrogens on positions 2-4.

Summarizing, the comparative study between cluster versus periodic models and Type I versus Type II active sites, shows that the relative rates of the various reactions is maintained regardless of the model.

Periodic simulations include a larger portion of the molecular environment which leads to slightly different transition states. However the extended cluster model considered in our previous work, is also able to capture the expected chemical trends for the epoxidation pathways. Given these findings, we will investigate the effect of linker substitutions on the epoxidation pathways using the extended cluster model in the following section. However, in the remainder of the paper we will only consider Type II as active site, as this one is thermodynamically favoured. Additionally we will further investigate the effect of linker substitution on the reaction **12->11.** When inspecting the general reaction scheme presented in Figure 1(b) together with the free energy barriers presented in Table 2, it is obvious that the unimolecular radical regeneration pathway 7->9 is always faster than the bimolecular epoxidation pathway 7->8. Thus in the overall reaction scheme, the epoxidation route via the $V^{+V}O(OOtBu)$ species **12** will be dominant. These findings are in agreement with our earlier presented theoretical study on all epoxidation pathways for the $VO(acac)_2$ catalyts. As the reaction proceeds, preference will be given to epoxidation pathways starting from vanadium +V species.

2.2.3. Construction of the cluster models for X-MIL-47

The influence of electron withdrawing and donating groups in the linkers is tested by constructing substituted cluster models. These models are further denoted as CL-X-*i* (X=OH, Cl, NH_2) and *i* is representative for the position of the substituent) in the remainder of the paper (Figure 6) whereas the unsubstituted reference cluster is denoted as the CL. In principle the substituents may be placed at various positions as indicated in Figure 6b. However, to obtain an averaged result of the electronic effect of the substituents, one functional group was placed in the ortho-position relative to the active site whereas the other substituent was placed in the meta position. For example if a substituent is placed at position “2”, this substituent is in ortho position with respect to vanadium for one linker whereas in the other linker it is positioned meta with respect to vanadium. In general there are more combinations possible, such as models where the substituents are in ortho position in both linkers, but these are not explicitly considered here. The model considered here is expected to give an averaged effect of the electronic effects of the substituents on the electronic configuration of the active sites. The procedure followed here is similar with the earlier procedure followed for the UiO-66 material [21]. We did however consider for each substituent four possible clusters corresponding to positions “1”, “2”, “3” and “4” in Figure 6b.

During the geometry optimization of all stable points or transition states, all atoms were allowed to relax. In our earlier work on the parent MIL-47 material the effect of partially constrained part of the cluster was investigated [16b]. For the reactions studied here we found that the kinetic and thermodynamic data obtained in the unconstrained or constrained model are very similar.

To obtain consistent theoretical data along the various reaction profiles, the following computational procedure was applied: first the transition states for the epoxidation were located and in a second step, the cyclohexene molecule was removed. Next, the transition state was slightly perturbed and reoptimized in order to obtain the $LV^{+V}O(OOtBu)$ clusters (Figure 6b). Depending on the specific substitution place of the functional group, the energies will vary among the different considered clusters. Table 3 gives the relative free energies between the various CL-X-I models where i=1,2,3 corresponding to species of type $V^{+V}O(OOtBu)$. In all cases positions 3 and 4 are slightly preferred. This may be understood as these positions are closest to the vanadium of the active site (bottom vanadium in Figure 7b) and thus stronger interaction is expected with the active site and with the (OOtBu) group.

2.3. Epoxidation reaction kinetics for X-MIL-47

The transition states for the reaction **12->11** for the epoxidation on the parent MIL-47 cluster and some of the substituted clusters are shown in Figure 7a and 7b. The *tert*-butoxy group is coordinated with one vanadium center whereas the cyclohexene is located in a free spot in front of the two linkers. This particular transition state which involves quite bulky groups from all reactants, stresses once more that structural defects need to be introduced into the periodic structure to allow enough space for the reaction to take place. In the case of the hydroxo-clusters (Figure 7b), the hydrogens of the OH-groups provide extra stabilization for the transition state by hydrogen bondings which are formed in the epoxidation transition states. The obtained kinetic data are collected in Table 4, together with the enthalpic and entropic contributions to the Gibbs free energies. All energies are referred to the separated reactants and thus apparent reaction kinetics is obtained.

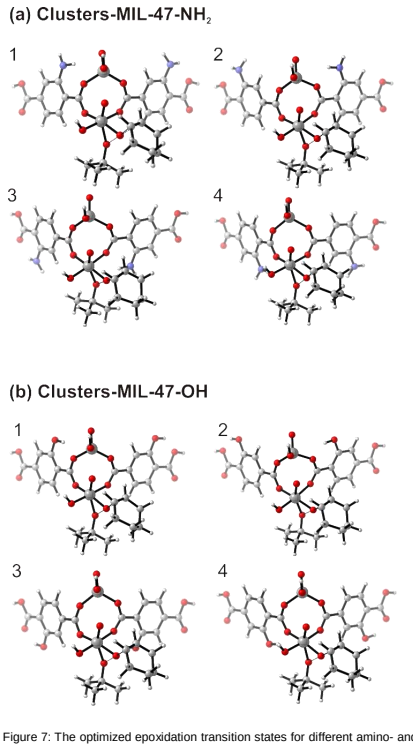

Figure 7: The optimized epoxidation transition states for different amino- and hydroxo-substituted clusters

On basis of the theoretical results it is not possible to definitely conclude that one particular substituent increases or decreases the catalytic activity of the substituted MIL-47 materials. Depending on the particular substituent position the free energy is higher or lower with respect to the unsubstituted cluster model. Only for substitutions with chlorine, all free energy barriers are about 3 kJ/mol lower than the values obtained for the parent MIL-47 material. Experimentally it was indeed found that substituents with an electron withdrawing (-F, -Cl, -Br) character were more active than groups with an electron donating character (-CH_3, -NH_2). Experimentally it was also found that all substituents follow the linear equation for $\log(k_X/k_H)$ as a function of σ_p except -OH. Normally, -OH has an electron withdrawing effect in meta position and an electron donating effect in para position (σ_p = -0.37). As this group does not obey the linear equation for $\log(k_X/k_H)$ as a function of σ_P, an explanation is warranted. In section 2.1, we have already indicated that the -OH group might withdraw electron density from the carboxyl group due to hydrogen bonding with this group. The optimized transition states on our theoretical models (Figure 9b) do indeed confirm this if the -OH groups stand in ortho position to the carboxyl group connected to the active site.

Table 3. Thermodynamic data for the equilibria between the $V^{+V}O(OOtBu)$ clusters at 323 K. Free energy (ΔG), enthalpy (ΔH) and entropic contributions (-T.ΔS) between the clusters CL-X-*i* are given in kJ/mol. The equilibrium constants K_{323} are given in units of s^{-1}.

	ΔG (kJ/mol)	ΔH (kJ/mol)	-T.ΔS (kJ/mol)	K_{323} (s^{-1})
CL-NH_2-1→2	-4,5	-2,3	-2,3	5,41E+00
CL-NH_2-1→3	-15,9	-16,9	1,0	3,75E+02
CL-NH_2-1→4	-19,6	-20,9	1,4	1,46E+03
CL-Cl-1→2	-1,7	-4,5	2,8	1,86E+00
CL-Cl-1→3	-1,7	-2,6	0,8	1,92E+00
CL-Cl-1→4	-3,8	-4,1	0,3	4,11E+00
CL-OH-1→2	-0,5	-3,7	3,2	1,22E+00
CL-OH-1→3	-23,6	-25,7	2,1	6,48E+03
CL-OH-1→4	-22,5	-29,2	6,6	4,40E+03

Table 4. Kinetic data for the epoxidation reaction of a substituted $V^{+V}O(OOtBu)$ cluster representing X-MIL-47 (X = -NH_2, -Cl and -OH) with cyclohexene at 323 K. Free energy (ΔG), enthalpy (ΔH) and entropic contributions (-T.ΔS) between reactants and transition state (‡) are given in kJ/mol. The forward rate constants *k* are given in units of $m^3mol^{-1}s^{-1}$ (apparent kinetics).

	$\Delta G^{\ddagger}$ (kJ/mol)	$\Delta H^{\ddagger}$ (kJ/mol)	$-T.\Delta S^{\ddagger}$ (kJ/mol)	k_{323}^{fwd} ($m^3mol^{-1}s^{-1}$)	$\log(k_X/k_H)$ (-)
CL	86,2	28,9	57,4	2,01E-03	0.0
CL -NH_2-1	85,0	27,6	57,4	3,16E-03	0,20
CL -NH_2-2	89,4	30,5	59,0	6,18E-04	-0,51
CL -NH_2-3	76,5	18,4	58,1	7,70E-02	1,58
CL -NH_2-4	93,1	36,5	56,6	1,55E-04	-1,11
CL -Cl-1	83,4	26,9	56,5	5,78E-03	0,46
CL -Cl-2	83,3	28,3	55,0	6,05E-03	0,48
CL -Cl-3	82,3	23,5	58,8	8,83E-03	0,64
CL -Cl-4	83,8	28,0	55,8	5,01E-03	0,40
CL -OH-1	85,4	26,6	58,8	2,72E-03	0,13
CL -OH-2	84,6	27,1	57,5	3,67E-03	0,26
CL -OH-3	74,3	20,7	53,6	1,72E-01	1,93
CL -OH-4	90,8	29,9	60,9	3,73E-04	-0,73

To compare the theoretical epoxidation rates on four different catalyst cluster models corresponding to different positions of the substituents with the initial experimental rates (Table 4), we applied a averaging procedure. Therefore, the stability of the various clusters is taken into account (Table 3) and the relative rates for the various clusters is used, as given in following equation for the average kinetic rate constant $< k_X >$:

$$< k_X >= \frac{\sum_i K_i k_{i,X}}{4\sum_i K_i},$$

With K_i, the equilibrium constant to form CL-X-*i* and $k_{i,X}$ the epoxidation rate constants for cyclohexene with CL-X-*i*.

The averaged theoretical rate constants are compared with the experimental values in Table 5. The agreement between the theoretical $\log(k_X/k_H)$ and the experimental $\log(TOF_X/TOF_H)$ values for all tested variants of the epoxidation reaction on MIL-47, NH_2-MIL-47 and OH-MIL-47 is quite satisfactory. This shows that our theoretical catalyst model is able to explain the effect of electronic modulation if we have similar amount of active sites in the experimental catalysts during the initial cyclohexene conversion. The modeled substituent combinations were selected as a representative set to describe the effect of electronic linker modulation. In reality more combinations would have to be taken into account but this is beyond the scope of the present paper.

Table 5. Comparison of experimental and theoretical kinetic data for the epoxidation reaction at 323 K on X-MIL-47 (X = -NH_2, -Cl and -OH) and substituted $V^{+V}O$(OOtBu) clusters respectively.

X	TOF (h^{-1})	<k>[a] ($m^3mol^{-1}s^{-1}$)	$\log(TOF_X/TOF_H)$	$\log(k_X/k_H)$
NH_2	4,4	3,95E-03	0,23	0,29
H	2,6	2,01E-03	0,00	0,00
Cl	14,8	1,36E-02	0,76	0,83
OH	27,2	1,78E-02	1,03	0,95

[a] Mean values determined based on the equilibrium between the $V^{+V}O$(OOtBu)-X-*i* complexes

Conclusion

In this work, we have tested the effect of linker modifications on the metal organic framework MIL-47, containing coordinatively saturated V^{+IV} sites linked by terephthalate linkers for the epoxidation reaction of cyclohexene. The substituents such as -F, -Cl and –Br, -CH_3, -NH_2 did obey a linear free energy relationship shown by a Hammett plot of the conversion towards cyclohexene oxide as a function of σ_p (substitution constant). The OH-substituent is normally an electron donating substituent (as $\sigma_p < 0$), yet in ortho-postion to the carboxyl group connected to the active site the H-bond that is formed with the carboxyl group withdraws electron density from that carboxyl group. OH-MIL-47 therefore did not obey the Hammett plot. In general substitution leads to an increased activity relative to the parent MIL-47. Additionally, first principle kinetic calculations are performed on periodic slab models of MIL-47 and compared with cluster models to determine the most important active site. The periodic models allowed to investigate different types of active sites (type I and II) with more reliable environment description compared to the cluster model. Thermodynamically alkylperoxo species $V^{+V}O$(OOtBu) of type II were found to be more stable than active sites of Type I. Overall the difference in free energies of activation between periodic and cluster models are quite similar. Therefore the effect of linker substitution was investigated on a cluster model of type II. Then, functionalized cluster models were constructed and the rate constants for epoxidation were determined and also compared relative to the epoxidation on a MIL-47 cluster model. A very good qualitative agreement was found on a selection of the substituents (-OH, -Cl, -NH_2), for which the epoxidation activity of the functionalized models agreed qualitatively with experiment.

Computational and Experimental Section

1. Computational methods

1.1. Periodic calculations

Periodic DFT calculations were carried out in the Vienna Ab Initio Simulation Package (VASP) [24]. For all periodic simulations, the Brillouin zone sampling was restricted to the Γ-point. Furthermore, the PBE exchange correlation functional of Perdew, Burke and Ernzerhof was applied [25] for optimization together van der Waals corrections of type D2 [26] as implemented in the VASP 5.2.12. The projector augmented wave approximation (PAW) [27] together with a plane wave basis set (kinetic energy cutoff of 600 eV) was used. The RMM-DIIS algorithm was chosen as optimizer to converge the atomic forces below 0.01 eV/Å. A Gaussian smearing [24b] of 0.01 eV was also applied.
First, the cell vectors of MIL-47 are optimized starting from XRD-data [17]. Second, the periodic slabs are constructed (see Section 2.1 and Figure 2), maintaining the unit cell parameters throughout the whole computational study. The atoms within each periodic slab are allowed to move freely upon optimization of the slab. For the reaction pathways only the active site and the neighboring terephthalic groups were relaxed. During this partial optimization approach, the atomic forces are converged below 0.003 eV/Å (the structures can be found in supporting information). Next, a partial vibrational analysis was performed, including only the active site which consisted of the central vanadium atom and nearest neighbors together with the reactive area (cyclohexene + tBuOO-complexes). Displacements in a, b and c-axis of ±0.015 Å were used in the subsequent partial Hessian calculation. The nature of the minima and transition states was very carefully checked and when residual imaginary frequencies were still present, the following strategies were used to get rid of them: (1) the convergence criterion for the electronic self-consistent field (SCF) problem is increased from 10^{-6} up to 10^{-10} eV [28], (2) a small displacement along the trajectory of the imaginary frequency followed by a re-optimization of the found minimum. We refer to the Supporting Information for all structures subjected to the partial hessian calculation.
All systems contained V^{+IV} atoms, which were modeled in their high spin state, as this is anticipated to have a negligible effect on the energy barriers of the material. The optimized geometries are used for single point optimization at the PBE0-D2 level, employing a normal kinetic energy cut off (400 eV) and SCF-criterion (10^{-5} eV). The dispersion part of the energy [26].

1.2. Extended cluster calculations on the various reaction within catalytic cycle

Previously, a cluster model [16b] has already been investigated by some of the present authors, containing two active sites, of which

only one was investigated. The constrained character of the MOF could be preserved by fixing the outer carboxyl oxygen atoms. For the optimization of the geometries, an ONIOM approach was used to accurately describe the active site $(VO(COO))_2$ and the reacting molecules on a high level of theory and the surrounding linkers at a lower level of theory (Figure 2). Geometry optimizations were performed with the Gaussian09 package [31] using the B3LYP hybrid functional [29]. Within the high level part, the double-zeta Pople basis set 6–31+G(d) was used for all high level atoms except for Cu, for which the LANL2DZ effective core potential and basis set was applied [30]. For the sake of clarity, this combined basis will be abbreviated as BS1. Furthermore, the lower level part was described at B3LYP/3-21g. The general optimization procedure can thus be abbreviated as ONIOM(b3lyp/BS1:b3lyp/3-21g). Afterwards, energy refinements, including the third version of dispersion corrections according to Grimme [31], were executed at three different levels of theory: B3LYP/6-311+g(d,p)-D3, PBE/6-311+g(d,p)-D3 and PBE0/6-311+g(d,p)-D3 to allow for a good comparison with the energetics of the periodic simulations at the PBE-D2 and PBE0-D2 level of theory. Note that transition state geometries of both calculation types did vary a bit (compare Figure 6 and 7).

The procedure for the extended cluster calculations on the substituted X-MIL-47 is very similar. Only the application of an ONIOM approach was however omitted to have a more reliable optimization of the substituent groups. Using the standard notation "LOT-E"//"LOT-G" (LOT-E and LOT-G are the electronic levels of theory used for the energy and geometry optimizations, respectively), all results discussed in this paper are obtained with the method denoted as "B3LYP/6-311+g(d,p)-D3//B3LYP/BS1". The calculation of all kinetic and thermodynamic parameters was performed using the in-house developed software module TAMkin [31].

In both cluster and periodic approaches, the Partial Hessian Vibrational Analysis (PHVA) method [32], as implemented in the in-house developed post-processing toolkit TAMKIN [31], was then used for the frequency calculation, required to determine computationally the kinetics of the studied reactions. The PHVA method was already successfully applied in previous first principles studies on kinetics [16b, 22, 33]. Use of PHVA is recommended in the constrained cluster calculations, as the outer carboxyl oxygens, have been fixed at their crystallographic position. In case of the periodic calculations, only a partial hessian was constructed with finite differences to save computational time. The program ZEOBUILDER was used for the construction of initial geometries for the periodic calculations [34].

2. Experimental set up

2.1. Synthesis and activation of X-MIL-47 materials

MIL-47 was synthesized according to a synthesis route described in literature [17]. X-MIL-47 compounds were prepared in a rapid microwave-assisted method as described below.

Synthesis of MIL-47-NH_2-as:
A mixture of VCl_3 (267 mg, 1.74 mmol) and 2-aminoterephthalic acid (308 mg, 1.74 mmol) in 3 mL of water was placed in a Pyrex tube (10 mL). The tube was sealed and heated in a microwave synthesizer (CEM, Discover S) to 150 ºC at 150 W, held under these conditions for 20 min with stirring, then cooled to room temperature. The greenish yellow precipitate was collected by filtration, and dried in air.

Synthesis of MIL-47-F-as:
A mixture of VCl_3 (100 mg, 0.64 mmol) and 2-fluoroterephthalic acid (117 mg, 0.64 mmol) in 2 mL of water was placed in a Pyrex tube (10 mL). The tube was sealed and heated in a microwave synthesizer (CEM, Discover S) to 170 ºC at 150 W, held under these conditions for 30 min with stirring, then cooled to room temperature. The greenish yellow precipitate was collected by filtration, and dried in air.

Synthesis of MIL-47-Cl-as:
This compound was obtained as a greenish yellow powder by the procedure described for MIL-47-F, except the linker used was 2-chloroterephthalic acid (156 mg, 0.64 mmol) instead of 2-fluoroterephthalic acid.

Synthesis of MIL-47-Br-as:
This compound was obtained as a greenish yellow powder by the procedure described for MIL-47-F, except the linker used was 2-bromoterephthalic acid (156 mg, 0.64 mmol) instead of 2-fluoroterephthalic acid.

Synthesis of MIL-47-CH_3-as:
This compound was obtained as a greenish yellow powder by the procedure described for MIL-47-F, except the linker used was 2-methylterephthalic acid (115 mg, 0.64 mmol) instead of 2-fluoroterephthalic acid and the temperature used was 150 ºC instead of 170 ºC.

Synthesis of MIL-47-OH-as:
This compound was obtained as a greenish yellow powder by the procedure described for MIL-47-F, except the linker used was 2-hydroxyterephthalic acid (116 mg, 0.64 mmol) instead of 2-fluoroterephthalic acid.

Activation of X-MIL-47-as:
A suspension of each of MIL-47-NH_2-as and MIL-47-Cl-as in DMF was heated (125 ºC, 1.5 h, MIL-47-NH2-as; 150 ºC, 5 h, MIL-47-Cl-as) in an oil bath. The filtered solids were heated (80 °C, 2 h, MIL-47-NH_2-as; 320 °C, 24 h, MIL-47-Cl-as) under dynamic vacuum to get the activated forms of the compounds. Slow heating ramp (ca. 0.33 °C min^{-1}) to 80 °C, before being held at this temp for 2 h, is crucial to activate the MIL-47-NH_2-as sample.

Each of MIL-47-Br-as, MIL-47-CH_3-as and MIL-47-OH-as was directly heated (300 °C, MIL-47-Br-as; 300 °C, MIL-47-CH_3-as; 280 °C, 5-OH-as) under dynamic vacuum for 24 h to obtain the evacuated forms of the compounds.

The MIL-47 sample, synthesized by using conventional electric heating, was calcined at 300 °C for 21.5 h in air atmosphere to get the thermally activated compound.

2.2. Catalytic tests

During a typical catalytic test, a 100-mL round-bottom flask was charged with 30 mL of chloroform (anhydrous) used as solvent, 5 mL of cyclohexene and 6.2 mL of 1,2,4-trichlorobenzene (used as internal standard for the GC analysis). The oxidant used in this paper was *tert*-butylhydroperoxide (TBHP) dissolved as a 5.5 M solution in decane. The latter was chosen as oxidant due to the instability of MIL-47 in TBHP in water [16a]. The molar ratio cyclohexene/oxidant was 1/2. All the catalytic tests were performed at a temperature of 50 °C and with an Ar-containing balloon on top of the condenser. Blank reactions at this temperature showed no catalytic conversion of cyclohexene.

The reaction mixture was stirred under an inert argon atmosphere. Aliquots were gradually taken out of the mixture, diluted with 500 µl ethylacetate, and subsequently analyzed by a GC-FID. After a catalytic run, the catalyst was recovered by filtration on a combined nylon-membrane filter, washed several times with acetone, and vacuum dried overnight. The filtrate was analyzed by XRF to determine the leached vanadium. To eliminate experimental noise and GC errors, a polynomial fit (of order 4) through the cyclohexene conversion was performed to determine the turnover frequency (TOF) and the turnover number (TON) were calculated after respectively 30min and 6h reaction time. In a similar fashion, the amount of cyclohexene oxide produced per catalytic site per hour was also calculated (TON_{ox}, h^{-1}) after 30min to determine the average epoxidation rate per catalyst MIL-47.

Acknowledgements

MVD was funded by the research board of the Ghent University. VVS, PVDV, SB acknowledge funding obtained

from the the Ghent University by the GOA grant nr. 01G00710. KL acknowledges funding obtained from the Methusalem grant nr. 01M00409. VVS and MW acknowledge BELSPO in the frame of IAP 6/2.. VVS acknowledges funding from the the European Research Council under the European Community's Seventh Framework Programme [FP7(2007-2013) ERC grant agreement number 240483]. Computational resources and services were provided by Ghent University (Stevin Supercomputer Infrastructure).

Keywords: chemical kinetics • epoxidation • X-MIL-47 •linker substituents • MOF

[1] a) J. L. C. Rowsell, O. M. Yaghi, *Micropor Mesopor Mat* **2004**, *73*, 3-14; b) S. Kitagawa, R. Kitaura, S. Noro, *Angew Chem Int Edit* **2004**, *43*, 2334-2375; c) G. Férey, *Chem. Soc. Rev.* **2008**, *37*, 191-214.

[2] H.-C. Zhou, J. R. Long, O. M. Yaghi, *Chemical Reviews* **2012**, *112*, 673-674.

[3] a) S. T. Meek, J. A. Greathouse, M. D. Allendorf, *Adv. Mater.* **2011**, *23*, 249-267; b) R. J. Kuppler, D. J. Timmons, Q. R. Fang, J. R. Li, T. A. Makal, M. D. Young, D. Q. Yuan, D. Zhao, W. J. Zhuang, H. C. Zhou, *Coordin Chem Rev* **2009**, *253*, 3042-3066; c) S. Horike, S. Shimomura, S. Kitagawa, *Nat Chem* **2009**, *1*, 695-704; dU. Mueller, M. Schubert, F. Teich, H. Puetter, K. Schierle-Arndt, J. Pastre, *J. Mater. Chem.* **2006**, *16*, 626-636.

[4] a) K. Sumida, D. L. Rogow, J. A. Mason, T. M. McDonald, E. D. Bloch, Z. R. Herm, T.-H. Bae, J. R. Long, *Chemical Reviews* **2012**, *112*, 724-781; b) M. P. Suh, H. J. Park, T. K. Prasad, D.-W. Lim, *Chemical Reviews* **2012**, *112*, 782-835; c) H. Wu, Q. Gong, D. H. Olson, J. Li, *Chemical Reviews* **2012**, *112*, 836-868; d) G. Férey, C. Serre, T. Devic, G. Maurin, H. Jobic, P. L. Llewellyn, G. De Weireld, A. Vimont, M. Daturi, J.-S. Chang, *Chem. Soc. Rev.* **2011**, *40*, 550-562; e) L. J. Murray, M. Dinca, J. R. Long, *Chem. Soc. Rev.* **2009**, *38*, 1294-1314; f) S. S. Han, J. L. Mendoza-Cortes, W. A. Goddard Iii, *Chem. Soc. Rev.* **2009**, *38*, 1460-1476.

[5] a) J.-R. Li, J. Sculley, H.-C. Zhou, *Chemical Reviews* **2012**, *112*, 869-932; b) J.-R. Li, R. J. Kuppler, H.-C. Zhou, *Chem. Soc. Rev.* **2009**, *38*, 1477-1504.

[6] a) M. Yoon, R. Srirambalaji, K. Kim, *Chemical Reviews* **2012**, *112*, 1196-1231; b) A. Dhakshinamoorthy, M. Alvaro, H. Garcia, *Catal Sci Technol* **2011**, *1*, 856-867; c) J. Lee, O. K. Farha, J. Roberts, K. A. Scheidt, S. T. Nguyen, J. T. Hupp, *Chem. Soc. Rev.* **2009**, *38*, 1450-1459; d) D. Farrusseng, S. Aguado, C. Pinel, *Angew Chem Int Edit* **2009**, *48*, 7502-7513.

[7] a) Y. Cui, Y. Yue, G. Qian, B. Chen, *Chemical Reviews* **2012**, *112*, 1126-1162; b) L. E. Kreno, K. Leong, O. K. Farha, M. Allendorf, R. P. Van Duyne, J. T. Hupp, *Chemical Reviews* **2012**, *112*, 1105-1125; c) C. Wang, T. Zhang, W. Lin, *Chemical Reviews* **2012**, *112*, 1084-1104; d) J. Rocha, L. D. Carlos, F. A. A. Paz, D. Ananias, *Chem. Soc. Rev.* **2011**, *40*, 926-940; e) M. D. Allendorf, C. A. Bauer, R. K. Bhakta, R. J. T. Houk, *Chem. Soc. Rev.* **2009**, *38*, 1330-1352.

[8] a) W. Zhang, R.-G. Xiong, *Chemical Reviews* **2012**, *112*, 1163-1195; b) M. Clemente-Leon, E. Coronado, C. Marti-Gastaldo, F. M. Romero, *Chem. Soc. Rev.* **2011**, *40*, 473-497; c) M. Kurmoo, *Chem. Soc. Rev.* **2009**, *38*, 1353-1379.

[9] P. Horcajada, R. Gref, T. Baati, P. K. Allan, G. Maurin, P. Couvreur, G. Férey, R. E. Morris, C. Serre, *Chemical Reviews* **2012**, *112*, 1232-1268.

[10] M. Eddaoudi, J. Kim, N. Rosi, D. Vodak, J. Wachter, M. O'Keeffe, O. M. Yaghi, *Science* **2002**, *295*, 469-472.

[11] P. Serra-Crespo, E. V. Ramos-Fernandez, J. Gascon, F. Kapteijn, *Chem. Mat.* **2011**, *23*, 2565-2572.

[12] T. Devic, P. Horcajada, C. Serre, F. Salles, G. Maurin, B. Moulin, D. Heurtaux, G. Clet, A. Vimont, J. M. Greneche, B. Le Ouay, F. Moreau, E. Magnier, Y. Filinchuk, J. Marrot, J. C. Lavalley, M. Daturi, G. Ferey, *J. Am. Chem. Soc.* **2010**, *132*, 1127-1136.

[13] S. Biswas, T. Ahnfeldt, N. Stock, *Inorg Chem* **2011**, *50*, 9518-9526.

[14] Q. Yang, A. D. Wiersum, P. L. Llewellyn, V. Guillerm, C. Serre, G. Maurin, *Chemical Communications* **2011**, *47*, 9603-9605.

[15] F. Vermoortele, M. Vandichel, B. Van de Voorde, R. Ameloot, M. Waroquier, V. Van Speybroeck, D. E. De Vos, *Angewandte Chemie International Edition* **2012**, *51*, 4887-4890.

[16] a) K. Leus, I. Muylaert, M. Vandichel, G. B. Marin, M. Waroquier, V. Van Speybroeck, P. Van der Voort, *Chemical Communications* **2010**, *46*, 5085-5087; b) K. Leus, M. Vandichel, Y. Y. Liu, I. Muylaert, J. Musschoot, S. Pyl, H. Vrielinck, G. B. Marin, C. Detavernier, P. V. Wiper, Y. Z. Khimyak, M. Waroquier, V. Van Speybroeck, P. Van der Voort, *Journal of Catalysis* **2012**, *285*, 196–207.

[17] K. Barthelet, J. Marrot, D. Riou, G. Ferey, *Angew Chem Int Edit* **2002**, *41*, 281-+.

[18] M. Vandichel, K. Leus, P. Van der Voort, M. Waroquier, V. Van Speybroeck, *Journal of Catalysis* **2012**, *in press, DOI:10.1016/j.jcat.2012.06.002*.

[19] C. Hansch, A. Leo, R. W. Taft, *Chemical Reviews* **1991**, *91*, 165-195.

[20] R. W. Taft, *J. Am. Chem. Soc.* **1952**, *74*, 3120-3128.

[21] F. Vermoortele, M. Vandichel, B. Van de Voorde, R. Ameloot, M. Waroquier, V. Van Speybroeck, D. E. De Vos, *Angewandte Chemie* **2012**, *51*, 4887-4890.

[22] V. Van Speybroeck, J. Van der Mynsbrugge, M. Vandichel, K. Hemelsoet, D. Lesthaeghe, A. Ghysels, G. B. Marin, M. Waroquier, *J. Am. Chem. Soc.* **2011**, *133*, 888-899.

[23] Y. Zhang, W. Pan, W. Yang, *The Journal of Chemical Physics* **1997**, *107*, 7921-7925.

[24] a) G. Kresse, J. Furthmüller, *Physical Review B* **1996**, *54*, 11169; b) G. Kresse, J. Furthmüller, *Comput. Mat. Sci.* **1996**, *6*, 15; cG. Kresse, J. Hafner, *Physical Review B* **1993**, *47*, 558; dG. Kresse, J. Hafner, *Physical Review B* **1994**, *49*, 14251.

[25] a) J. P. Perdew, K. Burke, M. Ernzerhof, *Phys. Rev. Lett.* **1996**, *77*, 3865; b) J. P. Perdew, K. Burke, M. Ernzerhof, *Phys. Rev. Lett.* **1997**, *78*, 1396.

[26] S. Grimme, *J. Comput. Chem.* **2006**, *27*, 1787-1799.

[27] P. E. Blöchl, *Physical Review B* **1994**, *50*, 17953.

[28] B. A. De Moor, A. Ghysels, M. F. Reyniers, V. Van Speybroeck, M. Waroquier, G. B. Marin, *J. Chem. Theory Comput.* **2011**, *7*, 1090-1101.

[29] a) A. D. Becke, *Journal of Chemical Physics* **1993**, *98*, 5648-5652; b) C. T. Lee, W. T. Yang, R. G. Parr, *Physical Review B* **1988**, *37*, 785-789.

[30] P. J. Hay, W. R. Wadt, *Journal of Chemical Physics* **1985**, *82*, 270-283.

[31] A. Ghysels, T. Verstraelen, K. Hemelsoet, M. Waroquier, V. Van Speybroeck, *Journal of Chemical Information and Modeling* **2010**, *50*, 1736-1750.

[32] a) A. Ghysels, D. Van Neck, M. Waroquier, *Journal of Chemical Physics* **2007**, *127*, 164108; b) A. Ghysels, V. Van Speybroeck, T. Verstraelen, D. Van Neck, M. Waroquier, *Journal of Chemical Theory and Computation* **2008**, *4*, 614-625; c) A. Ghysels, V. Van Speybroeck, E. Pauwels, D. Van Neck, B. R. Brooks, M. Waroquier, *Journal of Chemical Theory and Computation* **2009**, *5*, 1203-1215.

[33] M. Vandichel, D. Lesthaeghe, J. Van der Mynsbrugge, M. Waroquier, V. Van Speybroeck, *Journal of Catalysis* **2010**, *271*, 67-78.

[34] T. Verstraelen, V. Van Speybroeck, M. Waroquier, *Journal of Chemical Information and Modeling* **2008**, *48*, 1530-1541.

Received: ((will be filled in by the editorial staff))
Published online: ((will be filled in by the editorial staff))

FULL PAPER

The epoxidation of cyclohexene is studied on functionalized versions of the metal organic framework MIL-47 containing V^{+IV} sites. All investigated substituted X-MIL-47 frameworks (X= NH_2, CH_3, F, Cl, Br, OH) led to an increased conversion to cyclohexene oxide. A linear free energy relationship was found between centers.

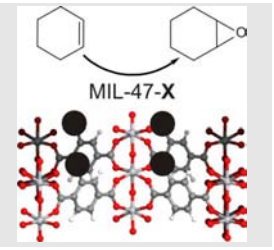

Matthias Vandichel, Shyam Biswas, Karen Leus, Joachim Paier, Joachim Sauer, Pascal Van Der Voort,* Michel Waroquier* and Veronique Van Speybroeck,**

Page No. – Page No.

Substitution of MIL-47 leads to an increased catalytic activity for the epoxidation of cyclohexene.

Paper 8

Electronic effects of linker substitution on Lewis acid catalysis with Metal-organic frameworks

Frederik Vermoortele, Matthias Vandichel, Ben Van de Voorde, Rob Ameloot, Michel Waroquier, Veronique Van Speybroeck and Dirk E. De Vos

Angewandte Chemie International Edition, 2012, 51, 4887 - 4890

Copyright 2012 by Wiley-VCH Verlag GmbH& Co. KGaA, Weinheim.

Angewandte International Edition Chemie

DOI: 10.1002/anie.201108565

Metal–Organic Frameworks

Electronic Effects of Linker Substitution on Lewis Acid Catalysis with Metal–Organic Frameworks**

Frederik Vermoortele, Matthias Vandichel, Ben Van de Voorde, Rob Ameloot, Michel Waroquier, Veronique Van Speybroeck, and Dirk E. De Vos**

Metal–organic frameworks (MOFs) are hybrid porous materials which hold great promise in adsorptive separation,[1] where selectivity is controlled by channel size and shape,[2] hardness or softness of exposed framework ions,[3a–b] framework hydrophobicity, and so on.[3c] They are attracting increasing interest in catalysis.[4] Some catalytic MOFs, like HKUST-1 and the Fe-trimesate MIL-100,[5] have open metal sites at structural nodes. In other cases, homogeneous catalysts, such as Mn Schiff bases, are integrated in the struts between the nodes,[6] so that molecular catalysts are isolated in an inert porous matrix.

In homogeneous catalysis, steric and electronic ligand effects are decisive for activity and stereoselectivity, and in some cases quantitative linear free-energy relationships (LFER) have been found between characteristics like the enantiomeric ratio and the stereo-electronic substituent parameters.[7] For heterogeneous catalysts, it is less obvious to establish quantitative structure–activity relationships. For some zeolites, the number and nature of the isomorphously substituting cations affect the number and strength of the Brønsted or Lewis acid sites; however, the effects are not always easily rationalized due to site heterogeneity.[8] Although the effect of cation variation on catalytic activity has been shown for MOFs,[4d] there are no systematic studies on the effects of framework substitution on the catalytic activity of the structural ions. Here we demonstrate that the concept of electronic modulation of the active site can be transferred from the familiar paradigm of homogeneous catalysis to catalytic frameworks of the MOF type. For a series of functionalized Zr terephthalate materials with UiO-66 structure,[9] the activity in Lewis acid catalyzed reactions can be much more effectively tuned than in inorganic porous solids, and a Hammett-type structure–activity LFER is readily identified. To support this concept, molecular modeling calculations were performed to calculate rates for individual reactions at various modified sites.

In the cubic Zr terephthalate UiO-66, each $Zr_6O_4(OH)_4$ octahedron is surrounded by maximally 12 terephthalate linkers, resulting in large octahedral and small tetrahedral cages. UiO-66 materials were synthesized with eight benzene-1,4-dicarboxylates (BDC-X; X = H, NH_2, CH_3, OCH_3, F, Cl, Br, NO_2). To test the effect of the substituents, the cyclization of citronellal was selected (Scheme 1). The isopulegol product

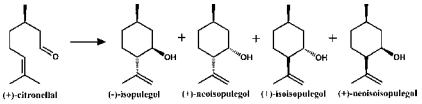

Scheme 1. Cyclization of (+)-citronellal to isopulegol and its isomers.

of this carbonyl-ene reaction is a precursor of synthetic menthol. The selectivity for the isopulegol isomers depends strongly on the Lewis acidity of the active site.[10] Before reaction, each catalyst was activated at 493 K. For UiO-66 materials, this results in dehydration of the $Zr_6O_4(OH)_4$ cluster, with formation of Zr_6O_6.[9a] Conversion profiles for reactions in toluene are given in Figure 1.

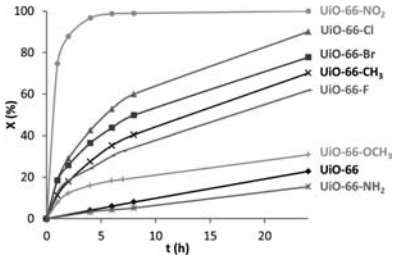

Figure 1. Conversion of citronellal over UiO-66-X versus time (toluene, 373 K, citronellal:Zr = 10).

[*] F. Vermoortele, B. Van de Voorde, Dr. R. Ameloot, Prof. D. E. De Vos
Centre for Surface Chemistry and Catalysis
Katholieke Universiteit Leuven
Kasteelpark Arenberg 23, 3001 Leuven (Belgium)
E-mail: dirk.devos@biw.kuleuven.be
M. Vandichel, Prof. M. Waroquier, Prof. V. Van Speybroeck
Center for Molecular Modeling, Universiteit Gent
Technologiepark 903, 9052 Zwijnaarde (Belgium)
E-mail: veronique.vanspeybroeck@ugent.be

[**] We are grateful to FWO, the Belspo (IAP 6/27), to KULeuven (CASAS Methusalem grant) and the Research Board of Ghent University (BOF) for project support. Funding was also received from the European Research Council under the European Community's Seventh Framework Programme [FP7(2007-2013) ERC grant agreement number 240483]. R.A. is a post-doctoral fellow of FWO. The computational resources were provided by Ghent University (Stevin Supercomputer Infrastructure).

Supporting information for this article (synthesis procedures, characterization, experimental methods, and information on the computational procedures) is available on the WWW under http://dx.doi.org/10.1002/anie.201108565.

 © 2012 Wiley-VCH Verlag GmbH & Co. KGaA, Weinheim

While all materials are active, the rate is dramatically enhanced by electron-withdrawing groups on the linker (F, Cl, Br, NO_2). UiO-66-NO_2 is by far the most active material, reaching full conversion after only 6 h. The reaction is first-order in citronellal (for more details see Supporting Information), and calculated rate constants are listed in Table 1.

Table 1: Reaction rate constants k_X, relative initial rates with respect to the unfunctionalized material, and isopulegol selectivities at maximum conversion for the different UiO-66-X.

Catalyst	k_X [h^{-1}]	Relative reaction rate	Selectivity to isopulegol [%]
UiO-66-NH_2	0.005	0.43	75
UiO-66-H	0.012	1	75
UiO-66-OCH_3	0.030	2.5	70
UiO-66-F	0.043	3.6	82
UiO-66-CH_3	0.067	5.6	74
UiO-66-Br	0.083	6.9	77
UiO-66-Cl	0.108	9.0	78
UiO-66-NO_2	0.673	56	81

Remarkably, introduction of a nitro group results in a 56-fold increase in rate, which clearly points to electronic active site modulation. The substituent effect is also apparent in the selectivities (Table 1); the highest values are observed for catalysts bearing electron-withdrawing groups.[10,11]

Reference experiments with the corresponding linkers proved that the activity is due to the MOFs, and not to residual linkers (Supporting Information Table S1). In all materials, activity is independent of crystal size, which implies that all catalytic sites equally contribute to the activity (Supporting Information Figures S3 and S4). While a perfectly crystalline UiO-66 material should have all Zr ions fully coordinated, detailed study of the thermogravimetric analysis profiles revealed that of the 12 linkers surrounding each cluster, approximately three are systematically missing for the real materials (Supporting Information Table S2).[9b] Such linker deficiency allows coordinatively unsaturated sites on Zr to be identified as the active sites. We attempted to correlate the activity to electronic effects of the linkers using Hammett's σ values. The choice of a suitable type of σ value is not obvious, since each substituent is either *ortho* or *meta* to a Zr-coordinating carboxylate group. An excellent correlation was found by plotting $\log k_X$ values from Table 1 versus the σ_m values, including inductive and resonance contributions.[12] The strong positive correlation of the $\log k$ values with σ_m results in a LFER ($\log(k_X/k_H) = \rho\sigma_m$) with $\rho = 2.35$ (Figure 2). Thus, Lewis acid sites are stronger in materials with an electron-withdrawing group close to the Zr site.

To check whether these trends are general, the Oppenauer oxidation of geraniol by furfural was studied (Figure 3). This hydride-transfer reaction requires simultaneous coordination of an alcohol and a carbonyl compound to a Lewis acid site.[13] While the kinetics are substantially more complex, it is immediately obvious that a similarly large rate increase is realized when a MOF with electron-withdrawing substituents is used.

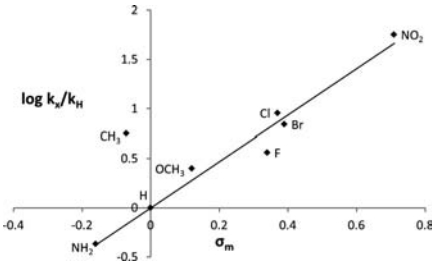

Figure 2. Hammett plot for cyclization of citronellal with different UiO-66-X catalysts.

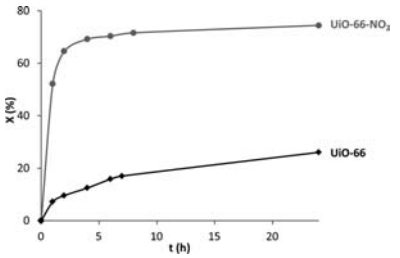

Figure 3. Conversion of geraniol in the Oppenauer oxidation with furfural over UiO-66 and UiO-66-NO_2 (toluene, 368 K, geraniol:Zr = 10).

To rationalize the electronic modulation of the active sites, molecular modeling calculations were performed to predict rates for citronellal cyclization on UiO-66 and UiO-66-NO_2. First-principles kinetic calculations were performed on an extended cluster which is representative for the active site environment. As possible active sites, four different clusters were built (Supporting Information Figure S5). Reasonable transition states were only found for Zr clusters in which at least one terephthalate was missing (Supporting Information Figure S6 and Table S3). Clusters with one missing linker were therefore used as models for both UiO-66 and UiO-66-NO_2 (Supporting Information Figure S7). As isopulegol is the most abundant product, the mechanism of its formation was studied in detail. A variety of different transition states were found which differ in the adsorption mode of citronellal; only the two most stable transition states are discussed. Critical points and the corresponding free-energy profile along the reaction pathway are shown in Figures 4 and 5. As a reference level the extended cluster state of the catalyst and citronellal in the gas phase was chosen.

Citronellal is slightly more strongly adsorbed on the nitro-modified cluster, with free energies of adsorption of −15.7 and −23.7 kJ mol^{-1} for UiO-66 and UiO-66-NO_2, respectively

 © 2012 Wiley-VCH Verlag GmbH & Co. KGaA, Weinheim

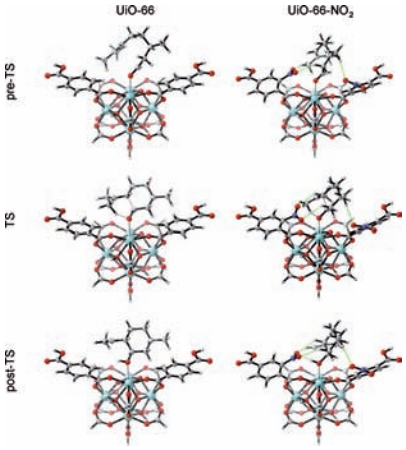

Figure 4. Critical points along the reaction profile of citronellal towards isopulegol for UiO-66 (left) and UiO-66-NO_2 (right). One carboxylate linker has been omitted from the cluster. From top to bottom, the figures correspond to the adsorbed state of citronellal, the transition state for cyclization, and the adsorbed isopulegol product state. Interactions between the hydrogen atoms of citronellal and the nitro groups at distances shorter than 3 Å are indicated by green lines.

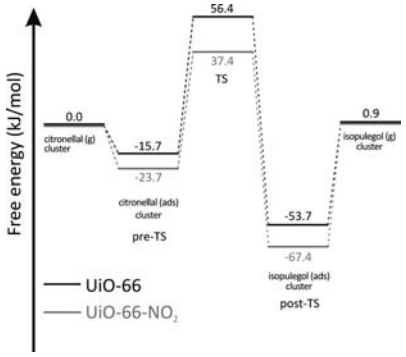

Figure 5. Gibbs free-energy profiles, calculated at 373 K, for citronellal cyclization to isopulegol.

(Table 2). The Zr site with nitro-substituted linkers is clearly a stronger Lewis acid, as reflected in shorter distances between the carbonyl oxygen atom of citronellal and Zr (Supporting Information Table S4). In addition, the NO_2 groups strongly interact with some hydrogen atoms of the adsorbate in the pre-reactive complex, the transition state, and adsorbed-product state (Figure 5). The theoretically

Table 2: Kinetic data for citronellal cyclization to isopulegol at 373 K.[a]

		ΔG^{ads}_{373}	ΔH^{ads}_{373}	$-T\Delta S^{ads}_{373}$	
pre-TS	UiO-66	−15.7	−88.6	72.9	
	UiO-66-NO_2	−23.7	−104	80.4	
		$\Delta G^{\ddagger}_{373}$	$\Delta H^{\ddagger}_{373}$	$-T\Delta S^{\ddagger}_{373}$	k^{fwd}_{373}
apparent kinetics	UiO-66	56.4	−44.2	100.6	3.03×10^{3}
	UiO-66-NO_2	37.4	−67.8	105.2	1.40×10^{6}
	relative ratio				460
intrinsic kinetics	UiO-66	72.1	44.4	27.8	6.15×10^{2}
	UiO-66-NO_2	61.1	36.4	24.7	2.17×10^{4}
	relative ratio				35

[a] Free energy and enthalpic and entropic contributions in the adsorbed state (ads) and in the transition state (‡) [kJ mol^{-1}]. The rate constants (k^{fwd}_{373}) are given in units of m^3 mol^{-1} s^{-1} for the apparent kinetics and in s^{-1} for the intrinsic kinetics. The relative rates of UiO-66-NO_2 versus UiO-66 are also given.

obtained transition states point towards a concerted mechanism in which carbon–carbon bond formation and proton transfer occur in the same reaction step, albeit not completely synchronously, as evidenced by inspecting the distances of these crucial bonds in the transition state (Supporting Information Table S4). For the nitro-modified cluster, the same features as in the adsorbed state are observed, and lead overall to a more stabilized transition state. Indeed the difference between the Gibbs free-energy barriers amounts to about 19 kJ mol^{-1}.

To quantify the relative rates on UiO-66 and UiO-66-NO_2, both intrinsic and apparent kinetics were evaluated, which merely differ in the reference level chosen for the reactants. The intrinsic analysis starts from the pre-transition state reactants, which is the local reactant minimum closest to the transition state, while the apparent analysis starts from the UiO-66 cluster and citronellal in the gas phase.[14] The calculated kinetic data are collected in Table 2, together with the enthalpic and entropic contributions to the Gibbs free energies. Both apparent and intrinsic kinetic coefficients are higher in the case of UiO-66-NO_2. Intrinsically, the calculations predict citronellal cyclization which is a factor of 35 faster. Using apparent kinetics, which additionally take into account the extra stabilization of the adsorbed citronellal on the nitro cluster, an acceleration factor of 460 is obtained. The partition of the free energies into enthalpic and entropic contributions along the reaction path shows that the nitro-substituted cluster yields both a higher adsorption enthalpy (−104 vs. −89 kJ mol^{-1}) and a lower intrinsic enthalpy barrier (36 vs. 44 kJ mol^{-1}). In UiO-66-NO_2, adsorption is stronger due to the stronger Lewis acidity, and, additionally, the transition state is stabilized due to preferred electrostatic interactions between the adsorbate and the nitro groups. The overall acceleration seems to be governed by the enthalpic preference both in adsorbed and transition state for the nitro-substituted cluster, rather than by entropic effects.

In conclusion, the activity of MOF catalysts with coordinatively unsaturated sites can be strongly increased by using functionalized linkers. A clear LFER was found between the electronic nature of the linker substituents and the reaction

 © 2012 Wiley-VCH Verlag GmbH & Co. KGaA, Weinheim

rate in a carbonyl-ene reaction, and the concept was extended to other Lewis acid reactions. This is the first LFER ever observed for MOF catalysts. Molecular modeling indicated that nitro substitution lowers the adsorption and activation free energy of the reaction. The predicted rate acceleration nicely corresponds to the experimentally observed ratio of about 60 at 373 K. The substituents not only alter the Lewis acidic properties but also induce additional stabilizing or destabilizing effects on the reactants depending on their electronic properties.

Received: December 5, 2011
Published online: April 5, 2012

Keywords: heterogeneous catalysis · Lewis acidity · metal–organic framework · structure–activity relationships · substituent effects

[1] a) J.-R. Li, R. J. Kuppler, H.-C. Zhou, *Chem. Soc. Rev.* **2009**, *38*, 1477; b) P. L. Llewellyn, S. Bourrelly, C. Serre, Y. Filinchuk, G. Ferey, *Angew. Chem.* **2006**, *118*, 7915; *Angew. Chem. Int. Ed.* **2006**, *45*, 7751; c) L. Alaerts, C. Kirschhock, M. Maes, M. van der Veen, V. Finsy, A. Depla, J. Martens, G. Baron, J. Denayer, D. De Vos, *Angew. Chem.* **2007**, *119*, 4371; *Angew. Chem. Int. Ed.* **2007**, *46*, 4293.

[2] a) L. Pan, D. H. Olson, L. R. Ciemnolonski, R. Heddy, J. Li, *Angew. Chem.* **2006**, *118*, 632; *Angew. Chem. Int. Ed.* **2006**, *45*, 616; b) L. Hamon, P. L. Llewellyn, T. Devic, A. Ghoufi, G. Clet, V. Guillerm, G. D. Pirngruber, G. Maurin, C. Serre, G. Driver, W. van Beek, E. Jolimaitre, A. Vimont, M. Daturi, G. Férey, *J. Am. Chem. Soc.* **2009**, *131*, 17490; c) S. Bourrelly, P. L. Llewellyn, C. Serre, F. Millange, T. Loiseau, G. Férey, *J. Am. Chem. Soc.* **2005**, *127*, 13519.

[3] a) M. Maes, M. Trekels, M. Boulhout, S. Schouteden, F. Vermoortele, L. Alaerts, D. Heurtaux, Y.-K. Seo, Y. K. Hwang, J.-S. Chang, I. Beurroies, R. Denoyel, K. Temst, A. Vantomme, P. Horcajada, C. Serre, D. E. De Vos, *Angew. Chem.* **2011**, *123*, 4296; *Angew. Chem. Int. Ed.* **2011**, *50*, 4210; b) J. W. Yoon, Y.-K. Seo, Y. K. Hwang, J.-S. Chang, H. Leclerc, S. Wuttke, P. Bazin, A. Vimont, M. Daturi, E. Bloch, P. L. Llewellyn, C. Serre, P. Horcajada, J.-M. Grenèche, A. E. Rodrigues, G. Férey, *Angew. Chem.* **2010**, *122*, 6085; *Angew. Chem. Int. Ed.* **2010**, *49*, 5949; c) J. Cousin Saint Remi, T. Remy, V. Van Hunskerken, S. van de Perre, T. Duerinck, M. Maes, D. E. De Vos, E. Gobechiya, C. E. A. Kirschhock, G. V. Baron, J. F. M. Denayer, *ChemSusChem* **2011**, *4*, 1074.

[4] a) B. Kesanli, W. Lin, *Coord. Chem. Rev.* **2003**, *246*, 305; b) L. Q. Ma, C. Abney, W. Lin, *Chem. Soc. Rev.* **2009**, *38*, 1248; c) D. Farrusseng, S. Aguado, C. Pinel, *Angew. Chem.* **2009**, *121*, 7638; *Angew. Chem. Int. Ed.* **2009**, *48*, 7502; d) U. Ravon, G. Chaplais, C. Chizallet, B. Seyyedi, F. Bonino, S. Bordiga, N. Bats, D. Farrusseng, *ChemCatChem* **2010**, *2*, 1235.

[5] a) S. S.-Y. Chui, S. M.-F. Lo, J. P. H. Charmant, A. G. Orpen, I. D. Williams, *Science* **1999**, *283*, 1148; b) P. Horcajada, S. Surblé, C. Serre, D. Hong, Y. Seo, J. Chang, J. M. Greneche, I. Margiolaki, G. Férey, *Chem. Commun.* **2007**, 2820.

[6] a) S.-H. Cho, T. Gadzikwa, M. Afshari, S. T. Nguyen, J. T. Hupp, *Eur. J. Inorg. Chem.* **2007**, 4863; b) S.-H. Cho, B. Q. Ma, S. T. Nguyen, J. T. Hupp, T. E. Albrecht-Schmitt, *Chem. Commun.* **2006**, 2563; c) F. Song, C. Wang, J. M. Falkowski, L. Ma, W. Lin, *J. Am. Chem. Soc.* **2010**, *132*, 15390.

[7] a) E. N. Jacobsen, W. Zhang, M. L. Güler, *J. Am. Chem. Soc.* **1991**, *113*, 6703; b) M. Palucki, N. S. Finney, P. J. Pospisil, M. L. Güler, T. Ishida, E. N. Jacobsen, *J. Am. Chem. Soc.* **1998**, *120*, 948; c) K. H. Jensen, M. S. Sigman, *Angew. Chem.* **2007**, *119*, 4832; *Angew. Chem. Int. Ed.* **2007**, *46*, 4748; d) J. J. Miller, M. S. Sigman, *Angew. Chem.* **2008**, *120*, 783; *Angew. Chem. Int. Ed.* **2008**, *47*, 771.

[8] a) G. Busca, M. Bevilacqua, T. Armaroli, M. Trombetta, *Stud. Surf. Sci. Catal.* **2002**, *142*, 975; b) J. Datka, B. Gil, A. Kubacka, *Zeolites* **1996**, *17*, 428.

[9] a) J. H. Cavka, S. Jakobsen, U. Olsbye, N. Guillou, C. Lamberti, S. Bordiga, K. P. Lillerud, *J. Am. Chem. Soc.* **2008**, *130*, 13850; b) L. Valenzano, B. Civarelli, S. Chavan, S. Bordiga, M. H. Nilsen, S. Jakobsen, K. P. Lillerud, C. Lamberti, *Chem. Mater.* **2011**, *23*, 1700; c) S. J. Garibay, S. M. Cohen, *Chem. Commun.* **2010**, *46*, 7700; d) M. Kim, S. J. Garibay, S. M. Cohen, *Inorg. Chem.* **2011**, *50*, 729; e) C. Zlotea, D. Phanon, M. Mazaj, D. Heurtaux, V. Guillerm, C. Serre, P. Horcajada, T. Devic, E. Magnier, F. Cuevas, G. Férey, P. L. Llewellyn, M. Latroche, *Dalton Trans.* **2011**, *40*, 4879; f) F. Vermoortele, R. Ameloot, A. Vimont, C. Serre, D. E. De Vos, *Chem. Commun.* **2011**, *47*, 1521; g) C. Wang, Z. Xie, K. E. deKrafft, W. Lin, *J. Am. Chem. Soc.* **2011**, *133*, 13445; h) A. Schaatte, P. Roy, A. Godt, J. Lippke, F. Waltz, M. Wiebcke, P. Behrens, *Chem. Eur. J.* **2011**, *17*, 6643.

[10] L. Alaerts, E. Séguin, H. Poelman, F. Thibault-Starzyk, P. A. Jacobs, D. E. De Vos, *Chem. Eur. J.* **2006**, *12*, 7353.

[11] M. Smith, J. March, *March's Advanced Organic Chemistry: Reactions, Mechanisms, and Structure*, 6th ed., Wiley, Hoboken, **2007**.

[12] C. Hansch, A. Leo, R. W. Taft, *Chem. Rev.* **1991**, *91*, 165.

[13] G. E. Dobereiner, R. H. Crabtree, *Chem. Rev.* **2010**, *110*, 681.

[14] V. Van Speybroeck, J. Van der Mynsbrugge, M. Vandichel, K. Hemelsoet, D. Lesthaeghe, A. Ghysels, G. B. Marin, M. Waroquier, *J. Am. Chem. Soc.* **2011**, *133*, 888.

 © 2012 Wiley-VCH Verlag GmbH & Co. KGaA, Weinheim

Angewandte Chemie
Eine Zeitschrift der Gesellschaft Deutscher Chemiker

Supporting Information

© Wiley-VCH 2012

69451 Weinheim, Germany

Electronic Effects of Linker Substitution on Lewis Acid Catalysis with Metal–Organic Frameworks**

Frederik Vermoortele, Matthias Vandichel, Ben Van de Voorde, Rob Ameloot, Michel Waroquier, Veronique Van Speybroeck, and Dirk E. De Vos**

anie_201108565_sm_miscellaneous_information.pdf

Supporting information

1. Synthesis of ligands and materials characterization

2-fluoroterephthalic acid

Fluoroterephthalic acid was obtained by hydrolyzing dimethyl 2-fluoroterephthalate (ABCR) according to following procedure: 0.256 g dimethyl 2-fluoroterephthalate (1.37 mmol) was added to a solution of 0.48 g NaOH (13.7 mmol) in 25 ml water and heated at 353 K for 30 min. After cooling down to 293 K, HCl (37 wt. % in water) was added dropwise till pH=1. 2-Fluoroterephthalic acid was recovered as a white powder, which was thoroughly washed with water and dried at 348 K under vacuum overnight. Yield: 0.196 g (88%).

2-methoxyterephthalic acid

Methoxyterephthalic acid was synthesized following a literature procedure [1]. In short, a mixture of 6.2 g 2,5-dimethylanisole (ABCR), 31.6 g potassium permanganate (UCB) and distilled water (200 mL) was refluxed for 5 h. After cooling down to room temperature, the mixture was filtered and washed with water. HCl was added dropwise to the filtrate; the white precipitate was collected by filtration, washed with water and dried under vacuum. The product was obtained as white solid. Yield: 4.48 g (50%).

2-Chloroterephthalic acid and 2-methylterepthalic acid were synthesized following a literature procedure [2].

Synthesis of UiO-66-X

The different UiO-66-X materials were synthesized from an equimolar solution (1.5 mM) of $ZrCl_4$, the (functionalized) terephthalic acid and H_2O in DMF. The solution was poured in a Schott bottle and placed in an oven at 393 K for 10-24 h. After the synthesis, the MOF was recovered by centrifugation.

The synthesis of UiO-66-OCH_3 was carried out at 353 K, as an amorphous phase was formed at 393 K.

To remove all unreacted species, the material was washed with DMF, redispersed in hot DMF and placed in an ultrasonic bath. After recovery of the material, it was dispersed in a large amount of methanol (typically 100ml per g solid), to remove DMF molecules from the pores. X-ray diffractograms are virtually identical for all materials, proving that they are isostructural, with the extra substituents incorporated in an essentially random way (Figure S1).

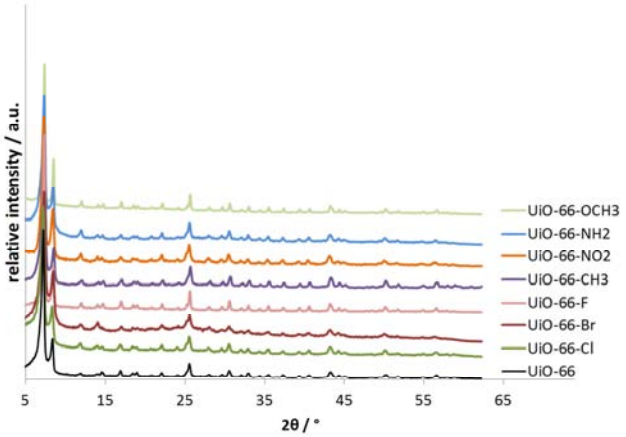

Figure S1. XRD reflection patterns of the substituted UiO-66-X materials.

TGA-analysis

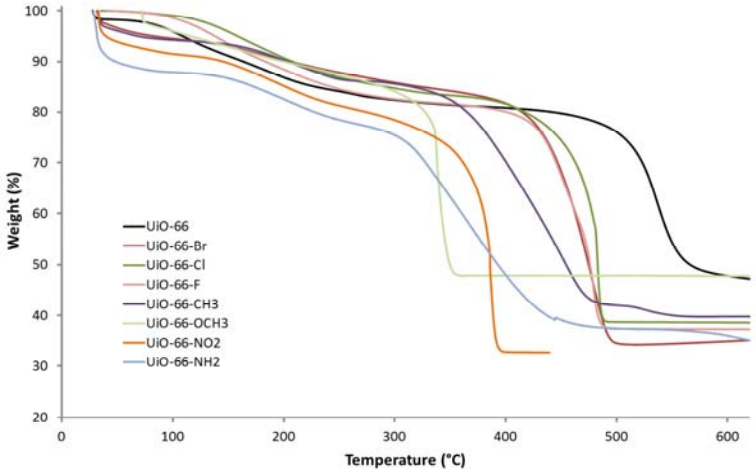

Figure S2. TGA of UiO-66-X under O_2 (heating rate of 5°C per minute).

As can be inferred from the TGA curves of the functionalized UiO-66 materials, the incorporation of the different ligands has a major influence on the thermal stability. Nevertheless, thermal stability of the materials seems guaranteed up to at least 573K, except for UiO-66-NH_2, which starts to decompose at around 548K.

SEM-micrographs

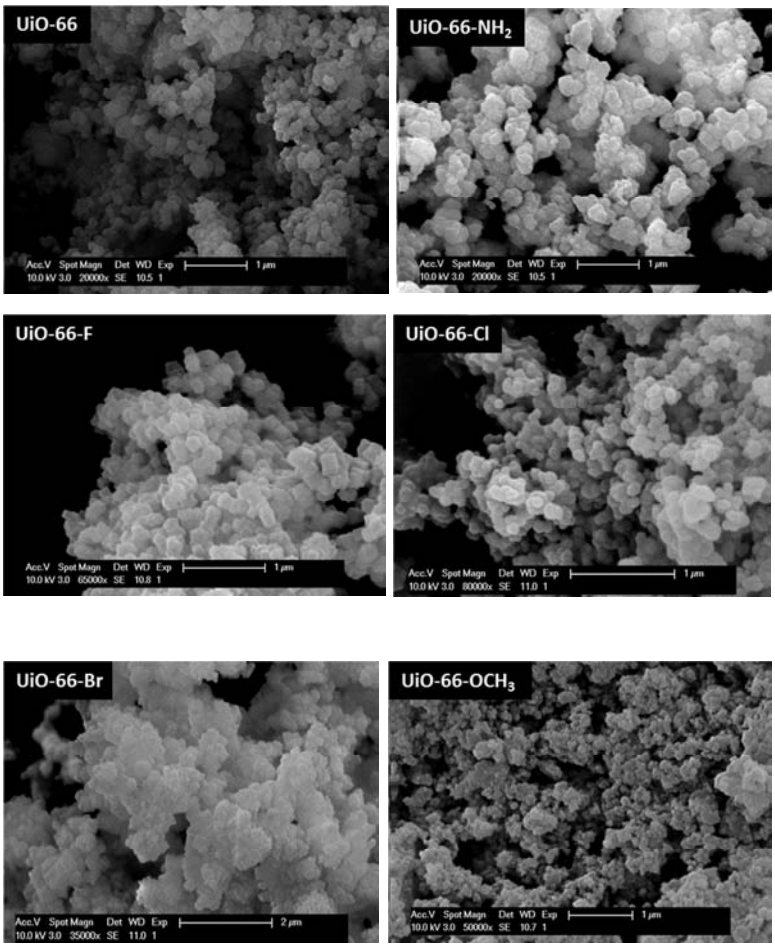

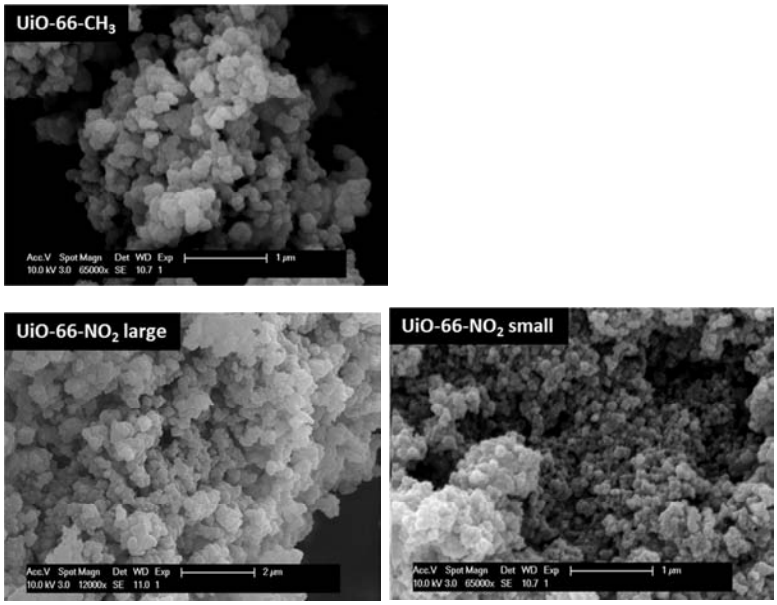

Figure S3. SEM-pictures of UiO-66-X.

2. Catalytic test

Before reaction, each catalyst was dried at 493K to remove residual solvent molecules; catalytic reactions were carried out in 10 ml glass crimp cap reactors loaded with 75 mg catalyst. A solution of citronellal in 5 ml toluene was added. For each catalyst, a citronellal to Zr ratio of 10 was used as to compare the activity of each catalyst. After introduction of the reaction mixture the vessels were placed in an aluminium heating block (at 373K) placed on a stirrer. Reaction samples were filtered through a 0.2 µm filter and analyzed with a Shimadzu 2010 GC equipped with a FID detector and an CP SIL-WAX-CB 57 column.

3. Influence of particle size on catalytic performance

Any quantification of the relation between activity and electronic characteristics will require that all sites, whether at the external surface or in the pores, contribute equally to the activity, implying chemical rather than diffusional control. Particle sizes of the tested catalysts are in the 50-300 nm range (Figure S3), which should permit fast diffusion to all active sites. For the most active catalyst, UiO-66-NO2, a batch with even smaller crystals was obtained by quickly cooling the synthesis mixture immediately at the onset of nucleation (after 90 min). Figure S4 shows that the activity is independent of crystal size, proving again that all active sites are used for citronellal conversion.

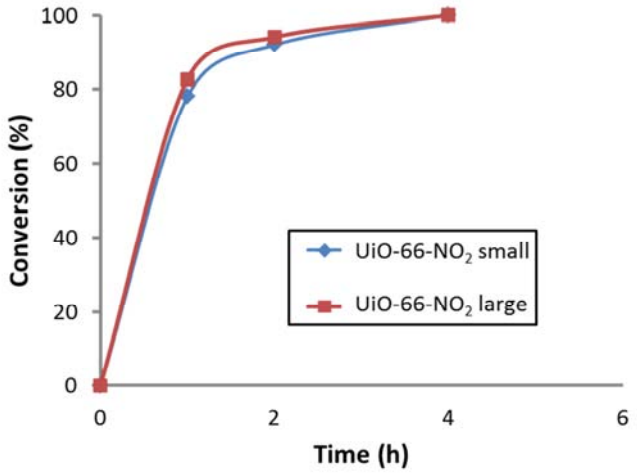

Figure S4. Influence of the particle size of UiO-66-NO_2 on the conversion of citronellal.

4. Catalytic activity of the functionalized ligands

To exclude that the activity or selectivity variations would arise from residual acids in the pores, the activity of the linkers as such was also probed (Table S1). The cyclization of citronellal was carried out using a citronellal : ligand ratio of 10. Only with nitroterephthalic acid a small conversion was noted, however with poor selectivity, showing that the activities and their variations arise specifically from the combination of Zr and the linkers.

Table S1. Conversion of citronellal and selectivity for isopulegol using functionalized BDC ligands as catalysts.

ligand	24h conversion (%)	selectivity (%)
BDC	0.5	67
NH_2-BDC	0.8	71
Br-BDC	1.5	63
Cl-BDC	2.6	60
NO_2-BDC	14.3	52

5. Details on the TGA analysis; linker deficiency

TGA-analysis was used to calculate the average number of missing terephthalates around the hexanuclear Zr clusters. The calculation of the linker deficiency was performed as described in literature [4]. In none of the materials, the Zr clusters are surrounded by the theoretical number of 12 terephthalate linkers, as has also been described in the literature for the unsubstituted UiO-66 [4].

The coordination numbers of the Zr-cluster varied between 8 and 10 (Table S2).

Table S2. Average number of terephthalates around the Zr-cluster in the different UiO-66-X materials.

Material	Average Coordination #
UiO-66	8
UiO-66-Br	9
UiO-66-Cl	9
UiO-66-F	10
UiO-66-CH_3	9
UiO-66-OCH_3	8
UiO-66-NH_2	8
UiO-66-NO_2	8

It seems that the nature of the substituent does not have a specific influence on the extent of linker deficiency. The linker deficiency gives rise to the presence of Lewis acid coordinatively unsaturated sites on Zr.

6. Calculation of the reaction rate constants

Reaction rates were calculated from initial kinetic observations, at low conversion of citronellal. Straight lines were obtained when ln[citronellal] was plotted *vs*. time. First order rate constants k_X were calculated from the slope of these plots according to

$$\ln [A] = \ln [A]_0 - k_X\, t$$

in which A = citronellal.

7. The nature of the active sites

In order to unravel the difference in activity between the substituted and unsubstituted UiO-66 catalysts, various active sites were considered. It has been reported in literature [3] that a pretreatment of the framework under deep vacuum at elevated temperatures leads to a dehydration of the inorganic brick of UiO-66. During this process, the $Zr_6O_4(OH)_4$ core, in which each zirconium atom is eight-coordinated, is transformed to a Zr_6O_6 core, with each zirconium atom in a seven-coordinated state, which results in open coordination sites by removal of the hydroxyl groups.
Another possibility, which is also supported by TGA observations (see 5.), is that the inorganic cluster is not fully coordinated with terephthalate linkers after crystallization. In the ideal structure, every Zr_6-cluster is surrounded by 12 terephthalate ligands. Recently, it was reported that UiO-66 can exhibit linker deficiencies, which also create open metal sites for reaction [4]. In order to explore the nature of the active sites, an initial modeling study was performed on four different clusters.

7.1. Initial cluster study for identifying active sites for the citronellal cyclization

A simplified cluster model was constructed to explore various possible active sites for the catalytic reaction, by replacing the terephthalates by formates ($HCOO^-$) yielding a cluster which is computationally feasible. This results in $Zr_6O_4(OH)_4(HCOO)_{12}$ and $Zr_6O_6(HCOO)_{12}$ as our basic cluster models, which represent resp. the hydrated and dehydrated form (clusters A and B in Figure S5) Clusters with missing linkers were also constructed (clusters C and D in Figure S5), lacking respectively one and three formate groups. In cluster C, one carboxylate linker bridging two adjacent Zr atoms is missing. In cluster D, three carboxylates bridging three Zr atoms on one face of the Zr_6 octahedron are omitted, which could be representative for a framework termination at the outer surface.

In a next step transition states for the citronellal cyclization towards isopulegol were localized on each of the four clusters using geometry optimizations at the b3lyp/4-31g* level of theory. These are shown in Figure S6. The apparent kinetic results, i.e. referring to citronellal in the gas phase and the isolated cluster, were then determined at the b3lyp/4-31g*-D3 level of theory (Table S4). The kinetic data show that the reaction rates for the fully hydrated cluster A without missing carboxylate linkers are much too low to be realistic. Dehydration (cluster B) leads to faster cyclization but also in this case it was necessary to twist the linkers unrealistically. Transition states on both the hydrated ($Zr_6O_4(OH)_4(HCOO)_{12}$) and dehydrated ($Zr_6O_6(HCOO)_{12}$) cluster could only be obtained when a substantial deformation of at least one of the linkers was introduced and it was furthermore even necessary to break a chemical bond between the linker and the zirconium atom.

Acceptable kinetic data and transition states without substantial steric restrictions or unrealistic twisting of linkers, are only obtained for clusters C and D which have either one or three missing carboxylate linkers. Throughout this study we will work further with active sites of type C with one missing linker. Indeed, the experiments evidenced that the reaction rates are independent of crystal size. There is hence no need to invoke active sites at the outer surface (like the model cluster D) to explain the catalytic observations. A cluster with one missing carboxylate, like the one in C, will be cut from the periodic structure, preserving two terephthalate linkers closest to the active site (see further in the computational methods section of the supporting information).

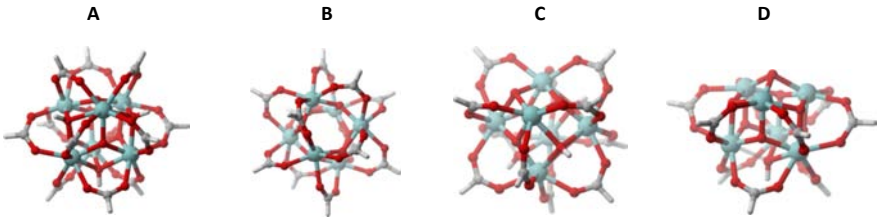

Figure S5. Different clusters used for the modeling of the citronellal cyclization. **A**) the fully hydrated cluster ($Zr_6O_4(OH)_4(HCOO)_{12}$); **B**) a fully dehydrated cluster ($Zr_6O_6(HCOO)_{12}$); **C**) a mono-decarboxylated cluster ($Zr_6O_5(OH)_3(HCOO)_{11}$); **D**) a tri-decarboxylated cluster ($Zr_6O_7(OH)_1(HCOO)_9$).

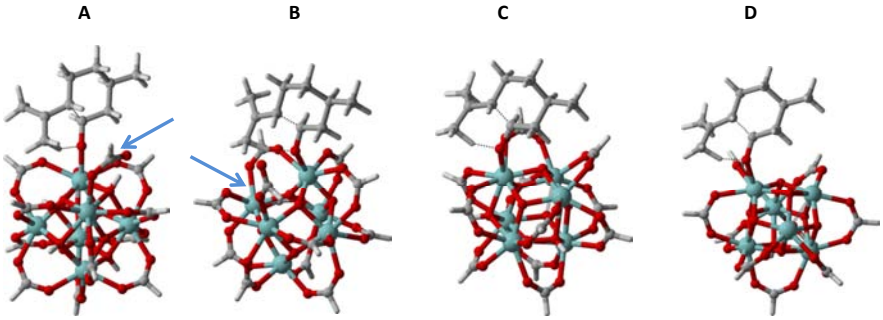

Figure S6. Different transition states for the cyclization of citronellal towards isopulegol modeled on the four different clusters A-D. In cases A and B, it was necessary to twist away one formate group of the cluster model (indicated with a blue arrow), a situation which seems unlikely in a perfectly crystalline UiO-66. On sites C and D, missing respectively 1 and 3 carboxylate groups, cyclization of citronellal occurs much more readily.

Table S3. Apparent bimolecular kinetic coefficients k_{app}^{fwd} are given at 373 K. The apparent Gibbs free energy barriers ($\Delta G_{373}^{\ddagger}$) are split up in an enthalpic part ($\Delta H_{373}^{\ddagger}$) and an entropic part ($-\mathrm{T}.\Delta S_{373}^{\ddagger}$). The used level of theory is b3lyp/4-31g*-D3.

Cluster	k_{app}^{fwd} ($m^3\ mol^{-1}\ s^{-1}$)	$\Delta G_{373}^{\ddagger}$ (kJ/mol)	$\Delta H_{373}^{\ddagger}$ (kJ/mol)	$-\mathrm{T}.\Delta S_{373}^{\ddagger}$ (kJ/mol)
A	1.65E-10	151.1	59.0	92.1
B	6.09E-06	118.5	25.5	93.0
C	5.85E-05	111.5	15.8	95.6
D	8.38E+01	67.5	-25.0	92.5

7.2. Details on the extended cluster study discussed in the manuscript

An overview of the most important geometrical parameters of the structures in Figure 5 in the main text is given in **Table S4**. The percentages of increase or decrease in these geometrical parameters of pre-TS reactants and post-TS products in comparison with the TS are also given in **Table S5**.

T**able S4.** Overview of some typical bond lengths and angles in the transition states for the citronellal cyclization. The increased Lewis acidity of our UiO-66-NO_2 model can be perceived in a shorter Zr-O distance and a further advanced transition state, indicated by several of the distances.

	Pre-TS		**Transition state**		**Post-TS**	
	UiO-66	UiO-66-NO_2	UiO-66	UiO-66-NO_2	UiO-66	UiO-66-NO_2
Zr-O (Å)	2.367	2.320	2.248	2.191	2.386	2.317
C_1-C_2 (Å)	2.991	2.960	1.697	1.671	**1.542**	**1.546**
H-O (Å)	3.129	3.004	1.562	1.503	**0.981**	**0.982**
C_3-H (Å)	**1.096**	**1.098**	1.209	1.233	2.563	3.435
O-C_1 (Å)	**1.228**	**1.230**	1.352	1.366	**1.451**	**1.456**
Zr-O-C_1 (°)	131.6	139.0	130.9	130.5	132.4	136.9

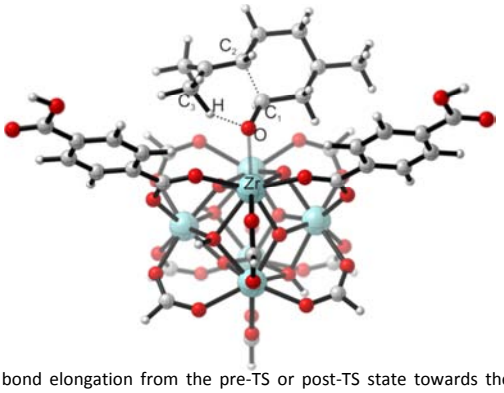

Table S5. Percentages of bond elongation from the pre-TS or post-TS state towards the TS. The percentages indicated in **bold** can be compared to see differences between UiO-66 and UiO-66-NO_2 since there, the initial distances (either in pre-TS or in post-TS) are more or less the same.

	Evolution pre-TS -> TS		Evolution post-TS -> TS	
	UiO-66	UiO-66-NO_2	UiO-66	UiO-66-NO_2
Zr-O (Å)	-5.03	-5.56	-5.78	-5.44
C_1-C_2 (Å)	-43.26	-43.55	**10.05**	**8.09**
H-O (Å)	-50.08	-49.97	**59.23**	**53.05**
C_3-H (Å)	**10.31**	**12.3**	-52.83	-64.1
O-C_1 (Å)	**10.1**	**11.06**	**-6.82**	**-6.18**
Zr-O-C_1 (°)	-0.53	-6.12	-1.13	-4.67

8. Computational methods

All clusters used in this paper were constructed by starting from the fully hydrated UiO-66 unit cell which was optimized with periodic DFT calculations carried out in the Vienna Ab Initio Simulation Package (VASP) [5-8]. For all the simulations, the Brillouin zone sampling was restricted to the **Γ**-point. Furthermore, the PBE exchange correlation functional of Perdew, Burke and Ernzerhof was used for the periodic calculations [9, 10]. The projector augmented wave approximation (PAW) [11] was used together with a plane wave basis set, with a general kinetic energy cutoff of 600 eV. To improve convergence, a Gaussian smearing of 0.02 eV was also applied [8]. A cell optimization with the quasi-newton algorithm was performed to converge the atomic forces below 0.04 eV/Å, with an accuracy on the energy of 10^{-4} eV.

Then a structural defect was introduced by the removal of one carboxylic acid from the unit cell; to compensate the charge created by removing the carboxylate anion, one of the hydroxyl groups in the cluster was converted to an oxo ligand, resulting in a net RCOOH removal. Next the cell was reoptimized with the same parameters. Afterwards a periodic cluster was cut out in Zeobuilder [12] and then saturated with hydrogen atoms, a frequently used approach in zeolite modeling [13-15]. To keep the computational expense within feasible limits, most of the terephthalates were replaced by formates except for two linkers positioned closest to the active zirconium site (Figure S7a). Outer hydrogen atoms connected to a carbon atom, and outer carboxyl oxygen atoms of the two terephthalic linkers were fixed to prevent unphysical deformations of the clusters. The extended UiO-66-NO_2 cluster was then constructed by substituting nitro groups on the two terephthalic linkers of the extended UiO-66 cluster. This was done both in *ortho* and *meta* position with respect to the active zirconium site (Figure S7b). This cluster should give an average effect of introduction of nitro groups on the activity of the studied reaction.

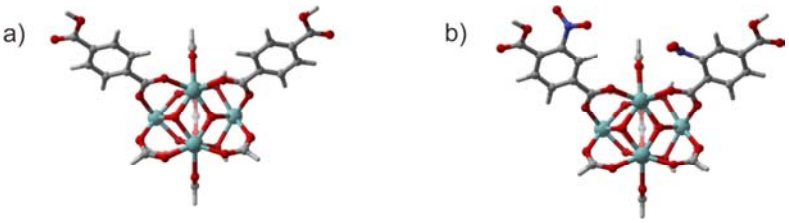

Figure S7. Extended cluster models used in the paper for a) UiO-66 and b) UiO-66(NO_2). The terephthalic linkers closest to the active site are maintained.

Geometry optimizations were performed with the Gaussian09 package [16] using the B3LYP hybrid functional [17, 18]. The double-zeta Pople basis set 4–31g* was used for all atoms except for Zr, for which the LANL2DZ effective core potential and basis set were applied [19]. For the sake of clarity, we will use the abbreviation BS1 for this combined basis set in the following. Afterwards single point energy refinements at the B3LYP/6-31+g(d) level of theory were performed to account for the electronic energy effects of the substituents on the terephthalate linkers, maintaining the LANL2DZ effective core potential and basis set for Zr. Furthermore, van der Waals corrections in conjunction with the B3LYP functional as developed by Grimme [20] were computed. In this paper, the D3-version [21] of the dispersion corrections was calculated using the program distributed by Grimme. Using standard notation "LOT-E"//"LOT-G" (LOT-E and LOT-G being the electronic levels of theory used for the energy and geometry optimizations, respectively), all results discussed in this paper are obtained with the method denoted as "B3LYP/6-31+g(d)-D3//B3LYP/BS1". Starting from transition state geometries, the quasi-IRC approach allowed to locate the product geometries. In the quasi-IRC approach, the geometry of the transition

state is slightly perturbed in the direction of the reactants and products followed by full geometry optimizations. The PHVA method [22-24], applied also previously for kinetics [15], was then used to investigate the kinetics of the citronellal cyclization on the extended UiO-66 clusters.

References

[1] Y. W. Chen, L. Chen, W. H. Zhou, D. J. Zha, D. Zhou, F. L. Bai, M. X. Wan, *Synth. Met.* **2009**, *159*, 1649-1656.

[2] T. Devic, P. Horcajada, C. Serre, F. Salles, G. Maurin, B. Moulin, D. Heurtaux, G. Clet, A. Vimont, J. M. Greneche, B. Le Ouay, F. Moreau, E. Magnier, Y. Filinchuk, J. Marrot, J. C. Lavalley, M. Daturi, G. Ferey, *Journal of the American Chemical Society* **2010**, *132*, 1127-1136.

[3] J. H. Cavka, S. Jakobsen, U. Olsbye, N. Guillou, C. Lamberti, S. Bordiga, K. P. Lillerud, *Journal of the American Chemical Society* **2008**, *130*, 13850-13851.

[4] C. Lamberti, L. Valenzano, B. Civalleri, S. Chavan, S. Bordiga, M. H. Nilsen, S. Jakobsen, K. P. Lillerud, *Chemistry of Materials* **2011**, *23*, 1700-1718.

[5] a) G. Kresse, J. Hafner, *Phys. Rev. B* **1994**, *49*, 14251; b) G. Kresse, J. Hafner, *Phys. Rev. B* **1993**, *47*, 558; c) G. Kresse, J. Furthmüller, *Phys. Rev. B* **1996**, *54*, 11169; dG. Kresse, J. Furthmüller, *Comput. Mat. Sci.* **1996**, *6*, 15.

[6] a J. P. Perdew, K. Burke, M. Ernzerhof, *Phys. Rev. Lett.* **1996**, *77*, 3865; b J. P. Perdew, K. Burke, M. Ernzerhof, *Phys. Rev. Lett.* **1997**, *78*, 1396.

[7] P. E. Blöchl, *Phys. Rev. B* **1994**, *50*, 17953.

[8] T. Verstraelen, V. Van Speybroeck, M. Waroquier, *J. Chem Inf. Model.* **2008**, *48*, 1530-1541.

[9] a) V. Van Speybroeck, J. Van der Mynsbrugge, M. Vandichel, K. Hemelsoet, D. Lesthaeghe, A. Ghysels, G. B. Marin, M. Waroquier, *Journal of the American Chemical Society* **2011**, *133*, 888-899; b) D. Lesthaeghe, J. Van der Mynsbrugge, M. Vandichel, M. Waroquier, V. Van Speybroeck, *Chemcatchem* **2011**, *3*, 208-212; c) M. Vandichel, D. Lesthaeghe, J. Van der Mynsbrugge, M. Waroquier, V. Van Speybroeck, *J. Catal.* **2010**, *271*, 67-78.

[10] H. E. B. Lempers, A. R. I. Garcia, R. A. Sheldon, *Journal of Organic Chemistry* **1998**, *63*, 1408-1413.

[11] a) A. D. Becke, *Journal of Chemical Physics* **1993**, *98*, 5648-5652; b) C. T. Lee, W. T. Yang, R. G. Parr, *Physical Review B* **1988**, *37*, 785-789.

[12] P. J. Hay, W. R. Wadt, *Journal of Chemical Physics* **1985**, *82*, 270-283.

[13] S. Grimme, *Journal of Computational Chemistry* **2004**, *25*, 1463-1473.

[14] S. Grimme, J. Antony, S. Ehrlich, H. Krieg, *Journal of Chemical Physics* **2010**, *132*.

[15] a) A. Ghysels, D. Van Neck, M. Waroquier, *Journal of Chemical Physics* **2007**, *127*, 164108; b) A. Ghysels, V. Van Speybroeck, T. Verstraelen, D. Van Neck, M. Waroquier, *Journal of Chemical Theory and Computation* **2008**, *4*, 614-625; c) A. Ghysels, V. Van Speybroeck, E. Pauwels, D. Van Neck, B. R. Brooks, M. Waroquier, *Journal of Chemical Theory and Computation* **2009**, *5*, 1203-1215.

Paper 9

Insight into the activity and diastereoselectivity of various Lewis acid catalysts for the citronellal cyclization

Matthias Vandichel, Frederik Vermoortele, Stijn Cottenie, Dirk E. De Vos, Michel Waroquier and Veronique Van Speybroeck

in preparation

Insight into the activity and diastereoselectivity of various Lewis acid catalysts for the citronellal cyclization

Matthias Vandichel[a], *Frederik Vermoortele*,[b] *Stijn Cottenie*,[a] *Dirk E. De Vos*,[b,*] *Michel Waroquier*[a] *and Veronique Van Speybroeck*[a,*]

[a]Center for Molecular Modeling (CMM), Ghent University, Technologiepark 903, 9052 Zwijnaarde, Belgium, and QCMM-Alliance, Ghent-Brussels, Belgium

[b]Centre for Surface Chemistry and Catalysis, Katholieke Universiteit Leuven, Kasteelpark Arenberg 23, 3001 Leuven, Belgium

*Corresponding authors: veronique.vanspeybroeck@ugent.be, dirk.devos@biw.kuleuven.be

RECEIVED DATE (to be automatically inserted after your manuscript is accepted if required according to the journal that you are submitting your paper to)

TITLE RUNNING HEAD Kinetics of the Lewis acid catalyzed citronellal cyclization

ABSTRACT

One of the important flavoring chemicals used today and produced on a large scale in the fine chemical industry, is (-)-menthol, which constitutes a particular stereoisomer of menthol. Most synthetic production processes rely on the hydrogenation of (-)-isopulegol, which in turn may be produced with high selectivity using the cyclization of (+)-citronellal on a Lewis acid catalyst. In this paper, the activity and selectivity of $ZnBr_2$, aluminum tris(2,6-diphenylphenoxide) (ATPH) and Cu-BTC is investigated by means of a combined theoretical and experimental approach. $ZnBr_2$ is the standard homogeneous catalyst used for this stereoselective cyclization, ATPH is also a homogeneous catalyst with very bulky sterically hindering ligands that provides very high selectivities (>99 %) and Cu-BTC is a heterogeneous metal organic framework. The performance of the catalysts was particularly evaluated in terms of temperature, which revealed that higher selectivities are obtained at lower temperatures. As such a higher catalyst activity allows working at lower temperatures and improves the selectivity. ATPH is the most active catalyst due to its stronger Lewis acidity, which allows stronger activation of the carbonyl bond in the citronellal molecule. Furthermore, introduction of steric factors may additionally increase the selectivity, as is the case for ATPH. The selectivity distribution is kinetically driven for $ZnBr_2$ and ATPH, and seems thermodynamically driven for Cu-BTC, due to diffusion limitations of the products out of the pores. In addition the experiments seems to indicate that mainly the Cu-sites in a surface shell with an approximately average thickness of 1μm are catalytically active. The theoretically determined selectivity distributions rely on the determination of an extensive set of stereoselective transition states, for which the differences in free energies have been calculated using a complementary set of ab initio techniques. Given the sensitivity of the selectivity on small Gibbs free energy differences, the agreement between experimental and theoretical selectivities is satisfactory. On basis of the obtained insights rational design of new catalysts may be obtained. As proof of concept, the hypothetically Cu-BTC-NO_2 Lewis catalyst is predicted to be very selective.

KEYWORDS. Lewis acids, selectivity, activity, heterogeneous catalysis, chemical kinetics, citronellal cyclization, Cu-BTC, ATPH, $ZnBr_2$, asymmetric catalysis.

1. INTRODUCTION

The cyclization of citronellal towards isopulegol is an important intermediate reaction in the production route towards menthol. Quantitatively, menthol is the most important aroma chemical worldwide used in many consumer products such as chewing gums, toothpastes, pharmaceutical and personal care products. The overall demand of menthol is still largely met by isolation from natural sources, but it is also produced on a large scale in the fine chemical industry. In 2010, 19300 tons of (-)-menthol were produced naturally or synthetically, making this product one of the largest volume chiral chemicals in the world [1]. Besides those facts, it is noteworthy to mention that citronellal is also a key compound in the synthesis of other organic compounds [2]. Of the eight stereoisomers of menthol, only (-)-menthol possesses the characteristic peppermint odor and physiological cooling effect which makes it valuable. Therefore various asymmetric synthesis procedures have been designed for the preparation of (-)-menthol [3]. Currently these processes rely on the synthesis from m-cresol (the Haarmann & Reimer process) and synthesis from myrcene (the Takasago process). Recently, BASF has also established a process for the production of menthol from neral [4-8]. The Takasago process [9,10] and BASF process,[4] have the cyclization of (+)-citronellal as an intermediate step. This reaction is usually conducted over a Lewis acid catalyst, and leads in principle to the formation of four diastereoisomers, namely isopulegol, iso-isopulegol, neo-isopulegol and neoiso-isopulegol (Scheme 1). With Lewis acids, high selectivities may be obtained especially when using metal halogenides. For several years the cyclization step has been carried out in the presence of $ZnBr_2$ as catalyst. The selectivity amounts to about 86.4% at 110 °C and 92.9% at 25 °C [10]. With Brønsted acids the selectivity is significantly lower but still (-)-isopulegol is the most abundant one. The reaction may also be prone to the occurrence of side reactions such as subsequent estherifications, crackings or dehydrations [11-13].

The Takasago process [9] uses traditionally an aqueous solution of $ZnBr_2$ as catalyst, obtaining a selectivity of > 90%, making further purification steps via crystallization necessary. The more recent

BASF process uses a tris(aryloxy)aluminium catalyst in the presence of an acid [4]. The latter process could for example work with a catalyst similar to the tris(2,6-diarylphenyloxy)aluminum catalyst (ATPH, Scheme 2) which has a (-)-isopulegol selectivity of more than 99% [4]. Purification of the unwanted isomers is thus much easier or not needed anymore. The sterically hindered aluminum site in aluminum tris(2,6-diphenylphenoxide) or ATPH was first designed to protect an aldehyde function during a nucleophilic addition [14]. The bulky, oxygenophilic ATPH can be used for precise recognition and activation of structurally similar aldehydes by selective Lewis acid-base formation [15]. This behavior of ATPH has been applied for chemoselective hetero-Diels-Alder and aldol condensation reactions [16,17] or even in the asymmetric conjugate 1,4-addition via organolithium compounds [18]. Modifications of ATPH were patented as catalyst for the citronellal cyclization by the Takasago corporation [10] in 2002, obtaining a selectivity higher than 99% towards isopulegol with slightly modified versions of this catalyst. Later, this patent was refined by researchers of the BASF group [4]. Furthermore, other ligands were patented [5] and the recovery of catalyst ligands from the reaction mixture was also patented [6,8]. Finally, the whole process from neral and/or geranial to (-)-menthol is taken up in the patent of Heydrich et al. [7]. Very recently, Itoh and Hori found that the combination of aryl binol ligands in combination with Al also forms a selective catalyst for the citronellal cyclization [19]. This type of linkers has an enormous potential, as they can be incorporated in Metal Organic Frameworks, forming a stable heterogeneous catalyst.

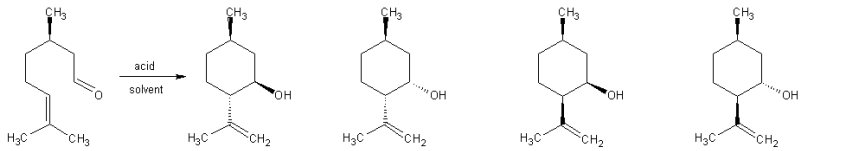

(+)-citronellal (**1**) (-)-isopulegol (**2**) (+)-neoisopulegol (**3**) (+)-isoisopulegol (**4**) (+)-neoisoisopulegol (**5**)

Scheme 1: The acid catalyzed cyclization of (+)-citronellal (1) yields four different isopulegol isomers: (-)-isopulegol (2), (+)-neoisopulegol (3), (+)-isoisopulegol (4), and (+)-neoisoisopulegol (5)

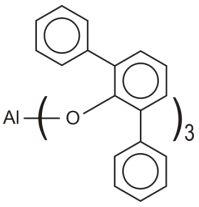

Scheme 2: Structural formula of ATPH

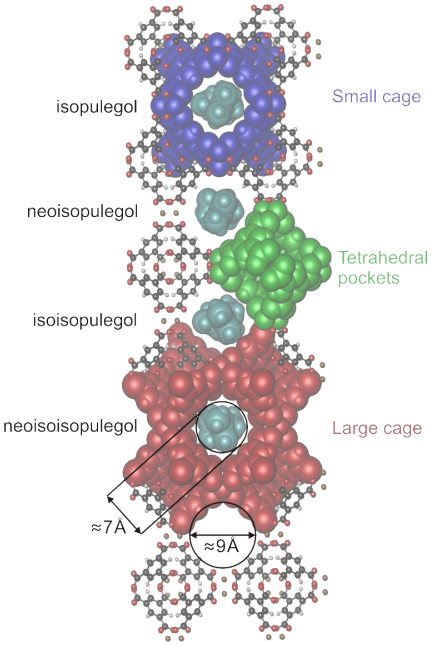

Figure 1: Cu-BTC, the cut through the crystals shows that two types of cages are altered;

Apart from these homogeneous catalysts, several solid acid materials have been explored for their potential to conduct the stereoselective cyclization step. An interesting overview is given in the work of

Boronat et al [20,21]. Promising concepts have been explored that rely on zeolites containing isolated and well-defined Lewis acid centers, such as Sn and Zr atoms [22,23].

Recently, the spectrum of nanoporous materials such as zeolites and zeotype structures has been further expanded through the discovery of a new class of hybrid porous solids. Those materials, nowadays also known as metal organic frameworks or MOFs, consist of both inorganic and organic moieties. Those materials have been applied in many different areas, ranging from gas storage,[24-30] gas separation,[31-34] luminescent properties,[35-37] magnetical properties,[30,38] etc. Also in the field of heterogeneous catalysis [24,30,39-42] there have been taken gigantic leaps by initial experimental case studies investigating the catalytic properties of MOFs. Different MOFs or modified related materials have already been tested for a wide variety of catalytic reactions and have been nicely tabulated in different reviews [24,39,40]. Within this respect some of the present authors, investigated the cyclization of racemic citronellal on Cu_3BTC_2 [43] [BTC=benzene-1,3,5-tricarboxylate] and found selectivities to the desired product isopulegol of 65% up to 69% dependent on the solvent used. Cu_3BTC_2 (hereafter abbreviated with Cu-BTC), also known as HKUST-1 [44] or MOF-199 [45], has taken a prominent role within the field of MOF research for various applications, because of accessible Cu^{2+} sites in combination with a structure exhibiting both large and small cages (Figure 1). The structure consists of Cu^{2+} paddlewheel complexes with free coordination sites on the Cu^{2+} ions and it has a typical zeolite-like structure consisting of three types of cages and two types of windows separating these cages. The octahedral large cages, respectively 13 and 11 Å in diameter, are interconnected by six 9 Å windows (measured from atom to atom) of square cross-section which penetrate the structure in the three different crystal directions (Figure 1). The large cages are also connected to tetrahedral-shaped pockets of ca. 6 Å size through triangular-shaped windows of ca. 4.6 Å size [40,46]. Based on the pore size, this structure seems to allow diffusion of reactants and products, such as citronellal and isopulegol isomers out of the cages with channel diameters of 9 Å in the three crystal directions (Figure 1). Previous studies on the catalytic activity of Cu-BTC, for other type of catalytic reactions have shown the hard Lewis acid behavior of the material [43,47-51].

The principal goal of this paper is the study of the industrially important citronellal cyclization [1,52] on various catalysts, i.e. $ZnBr_2$, ATPH and Cu-BTC, to achieve insight into the factors controlling the activity and selectivity for this diastereoselective reaction. Such insight is of utmost importance to rationally design new catalysts for this important industrial process. A combined theoretical and experimental approach has been followed. Experimentally all catalysts were synthesized and the reaction rates were determined in various temperature intervals. For each of the catalysts the selectivity towards the major isomer was determined and when possible also the temperature dependence of the selectivity was measured. To obtain insight into the molecular factors controlling both activity and selectivity a thorough molecular modeling approach was conducted. The full reactive profile was calculated by means of first-principles calculations, including the adsorption and desorption steps. A theoretical selectivity model is set up that relies on the construction of a stereoselective set of transition states. The combined approach followed here, is a first step in the rational design of diastereoselective catalysts for the citronellal cyclization. As a proof of concept, the hypothetical Cu-BTC-NO_2 MOF structure is introduced. The modification of the linkers with nitro groups is inspired by our previous study on the electronic modulation of MOF catalysts for the citronellal cyclization. Functionalized linkers could greatly enhance the catalyst performance of the coordinative unsaturated Lewis acid sites [53] in a series of functionalized Zr terephthalate materials with UiO-66 structure. Nitro-group substitution resulted in a 56-fold increase in rate. This effect was confirmed by theoretical modeling on a well chosen defect site, and resulted in substantial lowering of both the apparent and intrinsic free-energy barrier [53].

2 COMPUTATIONAL AND EXPERIMENTAL METHODS

2.1 Computational methods

All cluster calculations and extended cluster calculations were performed with the Gaussian09 package [54], while the periodic calculations were executed with the Vienna Ab Initio Simulation Package (VASP) [55-58]. The more extended systems were modeled with the well-established ONIOM-scheme, in

which a smaller part of the system is described at a higher level of theory and the rest at a lower level of theory. This multi-layer method allows for a fast optimization of the geometries, which can be followed by an energy refinement at a higher level of theory.

2.1.1 Cluster calculations

Different conformations for the (+)-citronellal cyclization were tested on a Cu-paddle wheel. The optimization of the transition states is done on B3LYP/6-31+g(d) [59,60] with the LANL2DZ pseudo potential and basis set for Cu [61]. As it is only important to distinguish between the transition states, the whole system was modeled with spin multiplicity 1 and no further energy refinement was performed. Nevertheless, D3 dispersion corrections [62] for the B3LYP functional were added.

For the homogeneous catalysts ($ZnBr_2$, ATPH) different levels of theory were used for both the activity determination (Section 3.2) as for the selectivity determination (Section 3.3). Geometry optimizations are carried out at the B3LYP/6-311++g(3df,2p) level of theory for $ZnBr_2$ and at the ONIOM(M06-2X/6-31+g(d):M06-2X/3-21g) level of theory for ATPH. In the case of ATPH, the M06-2X hybrid functional [63,64] is a good choice to accurately quantify the adsorbate-ligand interactions and ligand-ligand interactions because it is used especially for medium range non-covalent interactions. In this functional, double Hartree−Fock exchange is included to improve the description of non-covalent interactions which is extremely useful here [65,66]. Furthermore, the double-zeta Pople basis set 6–311+g(d,p) was applied for subsequent energy refinements in case of ATPH. For the activity determination only the most stable transition state towards (-)-isopulegol was selected and for all catalysts optimized at a very similar level of theory to make comparison possible

In all cases Grimme dispersion corrections [62] were added afterwards to refine the energies, using the dftd3 program available from the authors' web site.

2.1.2 Extended cluster calculations (Cu-BTC and Cu-BTC-NO_2)

The extended cluster (Cu_2BTC_4) was cut from the optimized Cu-BTC unit cells after periodic extension in Zeobuilder [67] and saturated by hydrogen atoms. Analogously, the Cu-BTC-NO_2-cluster was constructed arbitrarily by substituting all hydrogen atoms on the phenyl groups of the extended cluster by NO_2-groups. The applied level of theory was the same for both the activity as for the selectivity determination (Section 3.2 and 3.3 respectively) and the two systems were modeled at a maximum spin multiplicity of 3 (total spin = 1).

An ONIOM approach was then used to accurately describe the active site ($Cu_2(COO)_4$) and the adsorbed citronellal on a high level of theory and the surrounding linkers at a lower level of theory (Figure 2). Within the high level, the double-zeta Pople basis set 6–31+G(d) was used for all high level atoms except for Cu, for which the LANL2DZ effective core potential and basis set was applied [61]. For the sake of clarity, this combined basis will be abbreviated as BS1. The clusters were then optimized at the ONIOM(B3LYP/BS1:B3LYP/3-21g) level of theory, keeping the outer carbonyl oxygen atoms fixed. In a subsequent step, the energies were further refined by single-point calculations on the optimized structures at the B3LYP/6-311+g(d,p) level of theory. Furthermore, van der Waals corrections in conjunction with the B3LYP functional as developed by Grimme [68] are computed. For the extended cluster models, the D3-version [62] of the dispersion corrections was calculated. To account for the rigidity of this hypothetical framework, the low level oxygen atoms of the carboxyl groups were kept fixed preventing the deformation of the cluster. A similar procedure was also applied previously for the description of active sites within the Metal Organic Framework MIL-47 [69].

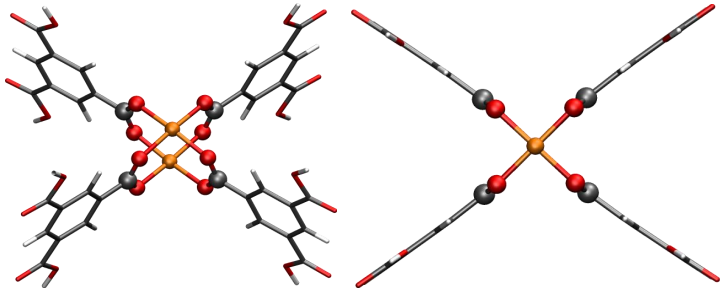

Figure 2: The extended Cu-BTC cluster and the applied ONIOM-scheme. The high level (B3LYP/BS1) indicated in ball and stick; low level (B3LYP/3-21g) in sticks; outer carboxylic oxygen atoms were fixed upon optimization.

2.1.3 Periodic calculations

Periodic calculations were performed on the metal organic framework Cu-BTC. The transition states from the extended cluster calculations are taken as starting geometries to find the transition states in the periodic model. An optimized Cu-BTC unit-cell was obtained from Nachtigall et al. [70] and was re-optimized with periodic DFT-D2 calculations. For those simulations, the Brillouin zone was restricted to the Γ-point. We employed the PBE exchange correlation functional [71,72] and the projector augmented wave approximation (PAW) [73] together with a plane wave basis set (kinetic energy cutoff of 600 eV). The RMM-DIIS algorithm was chosen as optimizer to converge the atomic forces below 0.01 eV/Å. To improve convergence, a Gaussian smearing [58] of 0.02 eV was also applied. Furthermore, van der Waals corrections [74] for the PBE functional are used throughout the optimization, as implemented in the VASP 5.2.11 code. The convergence criterion for the electronic self-consistent field (SCF) problem is set to 10^{-8} eV. Displacements in a, b and c-axis of ±0.015 Å are used in a subsequent partial Hessian calculation, where only the atoms of the $Cu_2(COO)_4$ paddle wheel and the reacting citronellal are taken into account. De Moor et al. [75] have shown that this type of procedure is sufficient to obtain a well conditioned partial

hessian, which has only positive eigenmodes in case of a minimum and only one imaginary eigenmode in case of a transition state.

2.1.4 Normal mode analysis and thermochemistry

A normal mode analysis was carried out to verify the nature of the transitions states and local minima. The PHVA method [54,76,77] was used for cluster and periodic models as implemented in the in-house developed post processing toolkit TAMkin [78]. TAMkin has already proved its efficiency in the computation of reaction kinetics [53,79-81]. This program is used to investigate the kinetics, the activation barriers of the citronellal cyclization. Finally, the initial theoretical selectivity towards the isopulegol isomers could be determined.

2.1.5 Construction of the transition states on the catalyst

In each case, we optimized the four transition states to the different isopulegol diastereomers exhibiting a chair conformation during the C-C coupling. Additionally, we varied the adsorption possibilities of citronellal on the catalyst (different positioning denoted with 1 and 2 as will be further discussed in Section 3). Sometimes, the transition states, starting from different adsorption geometries, eventually result in the same transition state (e.g. transition state towards neo-isopulegol **3** and neoiso-isopulegol **4** on $ZnBr_2$, Table S.5 and Figure S.3). In this case, only a single adsorption geometry was taken up in the selectivity analysis.

2.2 Theoretical methods to determine the selectivity

The computational prediction of enantioselectivities of metal catalyzed asymmetric reactions is a very challenging topic, as it requires the calculation of small free energy differences between diastereomeric transition states [82]. To do this in an accurate way, a full conformational search of the stereoselective transition states is required. Overlooking one important free energetically favorable transition state may lead to an erroneous selectivity pattern. A complete sampling of the free energy surface in the vicinity of

plausible transition states, can in principle be done using Monte Carlo or molecular dynamics methods. On the other hand it is also essential to take the full catalytic structure into account to model appropriately the molecular environment and therefore such methods are computationally not feasible with the current first-principles methods. One could opt for reliable molecular mechanics methods but unfortunately the parameters for transition metals are not readily available [83]. In view of previous considerations, we performed static calculations on the full catalytic system, but generated a representative set of plausible transition states in a very systematic way for each catalyst. Thus our selectivity predictions are based on free energy differences between a large set of stereoselective transition states. More explanation on how we constructed this set for each catalyst is given in Section 2.1.5. Following this protocol, the selectivities towards the different isopulegol isomers can be calculated using the Curtin Hammett principle. Hereby, we assume that all reactant conformations are in thermodynamic equilibrium and that only the free energy differences between the transition states are important [84]. As such a measure for the relative selectivity towards a specific isomer i is given by the ratio defined by the rate of formation of isomer i relative to the total rate of formation:

$$S_{\text{i,ini}} = \frac{k_i^{app}}{\sum_j k_j^{app}} = \frac{k_i^{\text{int}}}{\sum_j k_j^{\text{int}}} \qquad (1)$$

Herein, k_i^{app} is the apparent bimolecular rate coefficient (m^3 mol^{-1} s^{-1}) for the cyclization reaction towards i-pulegol with $i \in \langle \text{iso}, \text{neoiso}, \text{isoiso}, \text{neoisoiso} \rangle$. The apparent kinetics differs from the intrinsic kinetics. In the former, the kinetic data are referred to the catalyst and the citronellal molecule in gas phase, while in the latter the intrinsic kinetic data are referred to the whole adsorbed complex (an energy profile is displayed in Scheme 3). If we assume that each reaction leading to a specific isopulegol i starts from the same reactant complex, the relative selectivity may even be expressed in terms of the intrinsic and unimolecular rate coefficients k_i^{int} (s^{-1}). The equality in Eq.(1) can easily be proved by introducing Gibbs free energies for the transition states and by making use of a constant free

energy of adsorption ΔG_{ads} for the fully adsorbed citronellal-catalyst complex. As the rate constant k_i is proportional to $\exp(-\frac{\Delta G_i^{\ddagger}}{RT})$ the relative selectivity may also be written as:

$$S_{\text{i,ini}} = \frac{\exp(-\frac{\Delta G_i^{\ddagger}(app)}{RT})}{\sum_j \exp(-\frac{\Delta G_j^{\ddagger}(app)}{RT})} = \frac{\exp(-\frac{\Delta G_i^{\ddagger}(\text{int})}{RT})}{\sum_j \exp(-\frac{\Delta G_j^{\ddagger}(\text{int})}{RT})} \quad (2)$$

Eqs. (1) and (2) are valid in the initial stages of the reaction, as they take only the forward reaction rates into consideration. So if we can assume that the cyclization reactions are irreversible, the initial selectivity will be the global selectivity at a certain conversion.

An alternative method to calculate the selectivities is based on thermodynamical grounds: the specific nature of the transition states is not taken into account but the method is solely based on the thermodynamic product equilibrium (TPE). One assumes that the mixture of isopulegol isomers equilibrates towards the concentrations dictated by the free energy differences of the products after a sufficient long time. As such the selectivity towards isomer i of pulegol becomes:

$$S_{\text{i,TPE}} = \frac{c_{i,E}}{\sum_j c_{j,E}} = \frac{\exp(-\frac{\Delta G_i^{prod}}{RT})}{\sum_j \exp(-\frac{\Delta G_j^{prod}}{RT})} \quad (3)$$

with $c_{i,E}$ the equilibrium concentration of the i–pulegol and G_j^{prod} the free energy of isopulegol j in the product state. As the product concentration increases, the backward reaction becomes more and more important and the selectivity is expected to be more and more thermodynamically driven. It is expected that the experimental selectivity on each catalyst will take a value between the initial selectivity $S_{i,\text{ini}}$ and the product determined selectivity $S_{i,\text{TPE}}$.

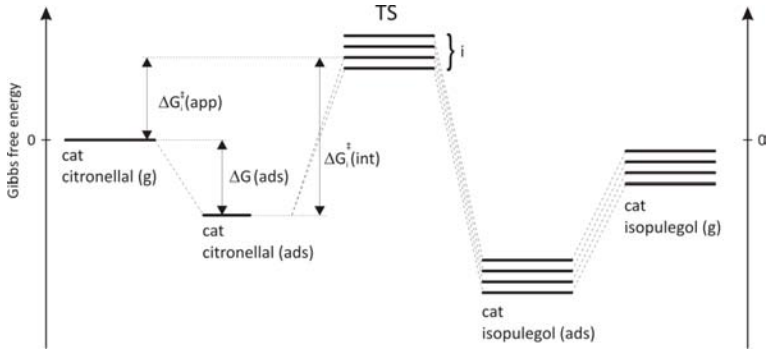

Scheme 3. Gibbs free-energy profile showing the difference between apparent (app) and intrinsic (int) activation barrier $\Delta G_i^{\ddagger}$.

2.3 Experimental catalyst preparation

ATPH was synthesized according to patent EP1225163: 240 mg 2,6-diphenylphenol was dissolved in 5 ml of (dry) toluene and flushed with argon at room temperature. Under Ar-atmosphere (in the nitrogen bag) 150 mg of a 25wt% solution triethylaluminium in toluene was added and the mixture was stirred at room temperature for 30min.

Cu-BTC was synthesized in the MW-oven using a procedure published by Y.K.Seo et al. [85]. Two different solutions were made:

(1) 1.764 g $Cu(NO_3)_2$ trihydrate in 24 ml H_2O

(2) 0.840 g BTC in 24 ml EtOH

The two clear solutions were mixed together and put in the microwave oven. The solution was heated to 140 °C in 10 min and kept at this temperature for 2 hours. After synthesis, the materials were thoroughly washed with an ethanol water mixture and dried at 100 °C.

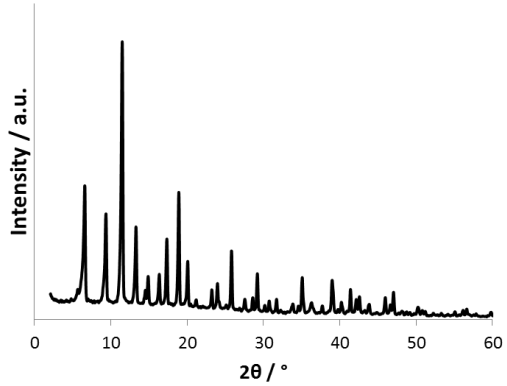

Figure 3: XRD pattern of Cu-BTC

$ZnBr_2$

Anhydrous $ZnBr_2$ (98%, Fluka) was used as received.

2.4 Experimental determination of the initial selectivity

Experimental initial selectivities were determined at low citronellal conversion (5-15 %) on ATPH, $ZnBr_2$, and Cu-BTC. The experimental reactions were carried out at different temperatures and the experimental selectivity was corrected with the thermal reaction using the following equations:

$$c_i = c_{i,cat} - c_{i,0} \quad (5)$$

in which $c_{i,cat}$ is the obtained concentration of compound i with the catalyst while $c_{i,0}$ is the concentration of compound i obtained with a thermal reaction. The initial experimental selectivity $S_{i,\mathrm{ini,exp}}$ was computed as follows:

$$S_{i,ini,\mathrm{exp}} = \frac{S_{i,cat}c_{i,cat} - S_{i,0}c_{i,0}}{c_{i,cat} - c_{i,0}} \quad (6)$$

In Eq. 6, $S_{i,\mathrm{cat}}$ is the selectivity towards isopulegol with the catalyst while $S_{i,o}$ represents the selectivity towards $i-$pulegol ($i \in \langle \mathrm{iso}, \mathrm{neoiso}, \mathrm{isoiso}, \mathrm{neoisoiso} \rangle$) in the thermal reaction. The experimental details about the experimental procedure are listed below for the investigated catalysts.

ATPH

2.5 g citronellal was added dropwise to a stirred solution of 0.164 mmol ATPH in 2.5 ml toluene at 25 °C. After a short reaction time (between 5-15 minutes), the reaction was stopped by adding 2 ml of a 4% sodium hydroxide solution. 0.2 ml of the organic layer was dissolved in 1 ml of toluene and analyzed using gas-chromatography.

$ZnBr_2$

1g citronellal was added to 0.1 g $ZnBr_2$. The reaction was carried out at 25°C and 100°C. 0.2 ml of the reaction solution was dissolved in 1 ml of toluene and analyzed using gas-chromatography.

Cu-BTC

Before the reaction, Cu-BTC was activated overnight at 150°C. 1g of citronellal was added to 0.1 g of activated Cu-BTC. The reaction was carried out in a broad temperature range (100-200°C). After reaction, the reaction slurry was filtered through a 0.45µm HPLC filter to remove the catalyst. 0.2 ml of the solution was dissolved in 1 ml of toluene and analyzed using gas-chromatography.

3. RESULTS AND DISCUSSION

3.1 Mechanism of the citronellal cyclization on Lewis acid catalysts

The cyclization of citronellal towards the various isomers of pulegol is a typical example of a carbonyl-ene reaction [86], where an ene group reacts with the enophilic carbonyl group. From a mechanistic point of view, such ene reaction can proceed in a concerted fashion through a cyclic transition state but can also proceed through a stepwise mechanism involving carbocation or biradical intermediates [87]. To distinguish between the concerted and stepwise mechanism, the kinetic isotope effect (KIE) may be used, where the reaction rate of the carbonyl-ene reaction is compared to the rate where the hydrogens of the ene group are replaced with deuterium [88,89]. In this way, the effect of the hydrogen transfer on the C-C coupling can be estimated. When the reaction rate changes upon substitution, this is an indication

that the hydrogen atom plays an important role in the rate determining step. For some intermolecular carbonyl-ene reactions, this ratio (KIE=k_H/k_D) is estimated about 1.1-1.3 [89], indicating that the hydrogen transfer has only a minor effect on the reaction rate. Molecular modeling studies are also ideally suited to further unravel mechanistic details. Recently, several computational studies appeared which investigated the addition of propene to formaldehyde, in MOF-11 [90], several homogeneous Lewis acids [91] and in metal exchanged FAU-zeolites [92]. These studies indicate that the reaction occurs in a concerted fashion although with a highly asymmetric transition state on a Lewis acid catalyst, where the carbon-carbon bond is almost formed, while the proton still needs to be transferred. Due to the asynchronous transition state, these results may also explain the kinetic isotope effects of Snider et al. [89]. Specifically for the citronellal cyclization also some theoretical studies have been performed which point in the same direction. Special attention goes to the work of Boronat et al. [20,21] studying the citronellal cyclization at Lewis acid sites (namely tin atoms) incorporated into framework positions of Beta zeolite (Sn-Beta) and of a more confined MFI zeolite. The Lewis acid properties of these catalysts have been investigated by means of DFT calculations and IR spectroscopy, and more in particular the diastereoselectivity of the citronellal cyclization to isopulegol. They found that the substrate was activated by coordination of the carbonyl group to the Lewis acid Sn centre, and that this was confirmed by *in situ* FT-IR spectroscopy by means of the two adsorption modes of the carbonyl group.

The diastereoselective cyclization of citronellal derivatives has also been investigated in a combined experimental-theoretical work by Kikukawa et al. [93] with Lewis acid sites generated in aluminum compounds, more specifically dialuminum-substituted silicotungstate. This compound showed a high catalytic activity for the cyclization and selectivity for the various isopolegol isomers including a very high diastereoselectivity toward **2**. Also relevant within the frame of the theme of this paper is the theoretical study of the kinetics of the cyclization of citronellal in the gas phase using DFT methods [94]. These calculations revealed that the reaction proceeds through an asynchronous concerted mechanism. Very recently, we demonstrated by means of a combined theoretical and experimental study that electronic linker modulations of the UiO-66 (UiO-66-X) material have a remarkable influence on the

catalytic activity for the citronellal cyclization [53]. Functionalized linkers were able to enhance the catalyst performance of the coordinative unsaturated Lewis acid sites. Our theoretical modeling results on the UiO-66 material also confirmed the concerted mechanism.

In this study a thorough investigation is performed on the cyclization of citronellal on various catalysts to assess their relative selectivity towards (-)-isopulegol and their relative activity. The transition states towards the major isomer, (-)-isopulegol, for the reaction occurring in gas phase and on the Lewis acid catalysts $ZnBr_2$, Cu-BTC and ATPH are shown in Figure 4.

All localized transition state geometries confirm the concerted nature of the reaction, during which a nucleophilic attack occurs of the C=C double bond to the carbonyl oxygen forming a new carbon-carbon bond and with simultaneous transfer of a hydrogen of one of the methyl groups towards the carbonyl group, yielding a hydroxyl group. Furthermore, the concerted nature of the transition states was confirmed by IRC calculations. In order to obtain reasonable reaction rates, the carbonyl group needs to be activated on a Lewis acid metal center. The various transition states depicted in Figure 4 show clear differences with respect to some critical distances: the amount of elongation of the carbonyl group is largest on the ATPH catalyst (1.39 Å) while being only slightly elongated for the reaction in the gas phase. In accordance therewith, the length of the forming C-C bond is the shortest on ATPH. Thus for ATPH the transition state is more product-like while being more reactant like for the reaction in gas phase. These geometrical observations are very useful in providing preliminary insight into the differences in activity of the various catalysts. On ATPH, the carbonyl bond is strongest activated, yielding the highest positive charge on the carbon of the carbonyl group and favoring therefore the nucleophilic attack of the C=C bond. We expect therefore strongest adsorption of citronellal and highest activity towards formation of (-)-isopulegol on ATPH, followed by $ZnBr_2$ and Cu-BTC. In the next section the activity of the various catalysts is discussed on basis of free energy differences, which will allow confirming these findings.

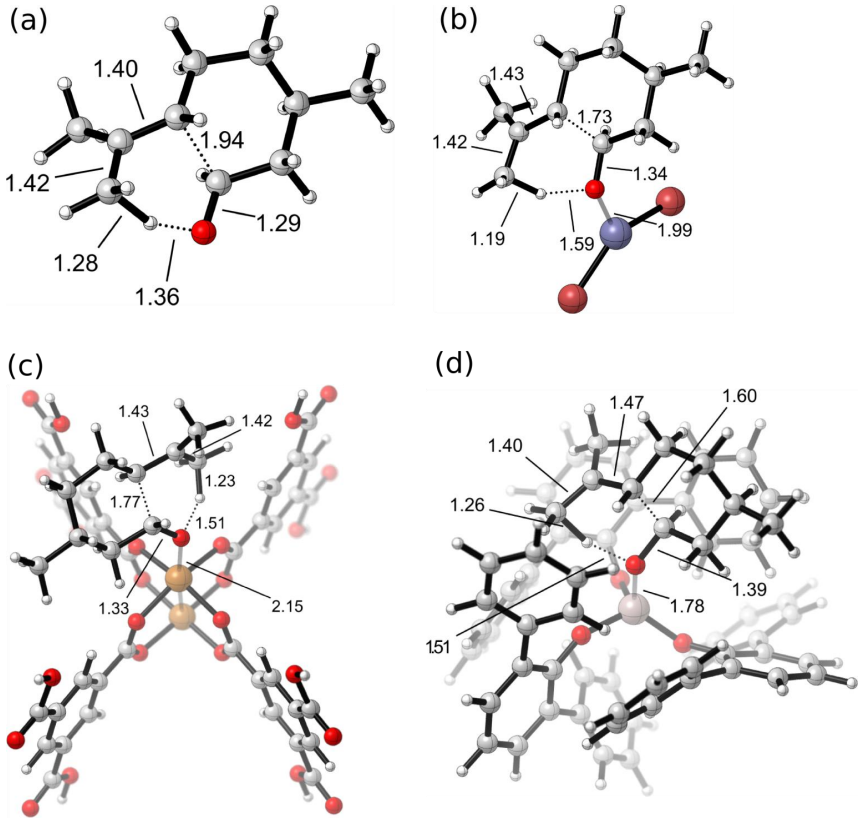

Figure 4: Transition states for cyclization of (+)-citronellal towards (-)-isopulegol (a) in the gas phase (b) on $ZnBr_2$ (c) on Cu-BTC and (d) on ATPH. All transition states were localized at the B3LYP/6-31+g(d). Some critical distances in Å are explicitly shown.

As our final aim is the study of both activity of the catalyst and selectivity towards the major product (-)-isopulegol, it is of utmost importance to explore the free energy surface in the region of the transition states properly to ensure that all important transition states for the determination of the selectivity calculations are taken into account (vide supra). A first explorative transition state search was performed on the $Cu_2(HCOO)_4$ paddle-wheel (Cu-PDWL), which is a metal dimer, forming a four-coordinate

square planar vertex. This is a typical secondary building unit (SBU) for various MOFs and has been extensively studied experimentally and theoretically [44,70,95,96]. The Cu-PDWL is seemingly easier to treat due to the smaller number of atoms in the metal-dimer, but has proven to be quite ambitious from theoretical point of view. This is due to various reasons such the electronic structure of open-shell transition metal cations (Cu_2^+) and the presence of unpaired electrons on two adjacent Cu_2^+ cations, which justifies the usage of multireference wavefunction based methods. This is especially true for the study of adsorption processes as was nicely shown in the recent paper of Nachtigall et al. to study the CO adsorption in Cu-BTC [96]. Herein, we are mainly interested in exploring the potential energy surface in the neighborhood of the transition state, therefore we opted for computationally feasible DFT methods. Selectivity predictions for the Cu-PDWL are not performed in this paper. A profound study on the assessment of high level multireference methods to determine the kinetics on the PDWL and other catalysts studied in this paper, is beyond the scope of this study.

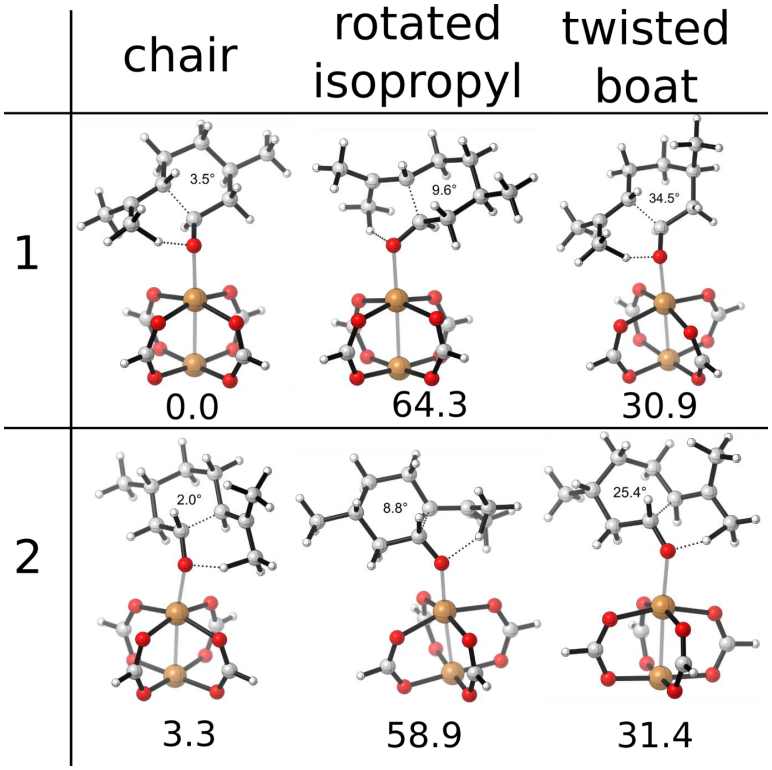

Figure 5: Transition state geometries for cyclization of (+)-citronellal towards (-)-isopulegol on a Cu-PDWL. All transition states were localized on the B3LYP/6-31+g(d) level of theory (LANL2DZ pseudopotential and basis for Cu). Also indicated are the relative free energy differences (at 383K) between the various transition states, referred to the most stable transition state “iso-1-chair”. All energy values were calculated at the B3LYP/6-31+g(d)-D3 level of theory (LANL2DZ pseudopotential and basis for Cu).

As the carbonyl oxygen has two free electron pairs, two possible adsorption geometries are possible on the Cu-PDWL, which are labeled with “1” and “2” in Figure 5 in which the various located transition

states for cyclization towards (-)-isopulegol are shown. Furthermore, the isopropyl may also be rotated which gives another two transition states labeled with rotated isopropyl. Additionally the forming cyclohexane ring can have various conformations, such as twisted-boat, boat or half-chair. To investigate the possible occurrence of transition states with another configuration for the cyclohexane ring, we located also the twisted-boat form as this one is a stable minimum on the potential energy surface (of a cyclohexane ring) in the gas phase. Following this procedure, six transition states were located which are shown in Figure 5. For the cyclization towards the other isomers of pulegol a similar investigation was performed and all activated complexes are shown in Figure S.1 of the Supporting information (SI). From the relative free energy differences between the various transition states (these are also indicated in Figure 5), it is immediately clear that rotated isopropyl and twisted-boat conformers are much higher in free energy (30 to 60 kJ/mol), and that only chair-like transition states need to be taken up in the further activity and selectivity study. On the other hand, it is necessary to take into account two possible adsorption positions for the carbonyl oxygen, as there is only a difference of 3.3 kJ/mol difference between the iso-chair-1 and iso-chair-2 transition state. For the study on the other Lewis acid catalyst, we will systematically consider all possible adsorption geometries, but we will only consider the chair conformations.

3.2 Theoretical and experimental investigation of the catalyst activity.

To accelerate the citronellal cyclization, it is important to use a catalyst which may activate the carbonyl group and for which reasonable rates of reaction can be obtained. Herein we investigate the activity of $ZnBr_2$, Cu-BTC and ATPH in terms of their activity towards citronellal cyclization to (-)-isopulegol both experimentally and theoretically.

Experimentally, the relative activity of the catalysts was investigated by measuring and comparing the reaction rates on the various catalysts. As the studied catalysts, show a large difference in activity, the reaction rates could not be determined at one temperature. The reaction rates were thus compared at two different temperatures: at 298 K for ATPH and $ZnBr_2$ and at 375 K for $ZnBr_2$ and Cu-BTC. An equal

amount (in moles) of each catalyst was used in the reaction (Table 1). The reaction rates reported in Table 1 were calculated from initial kinetic observations, i.e. at low conversion of citronellal. For each catalyst, a plot was constructed of -ln[A] versus time (Figures S.4-S.7, Supporting Information) in which [A] represents the concentration of citronellal. Subsequently, first order rate constants k_x were calculated from the slope using following formula:

$\ln [A] = \ln [A]_0 - k_X t$. The obtained reaction rates are tabulated in Table 1.

Table 1: Summary of the experimentally measured reaction rate constants (k_X) for the different catalysts at given temperature. Also reported are the initial quantities of catalyst and citronellal used in the experiment.

catalyst	**gram catalyst**	**mmol metal sites**	**gram citronellal**	**mmol citronellal**	**temperature (K)**	**k_x (h^{-1})**
Cu-BTC	0.1	0.496	1	6.5	373	0.0087
$ZnBr_2$	0.112	0.496	1	6.5	373	2.1977
$ZnBr_2$	0.037	0.164	2.5	16.2	298	0.1934
ATPH	0.126	0.164	2.5	16.2	298	0.8293

A relative order of activity can be established from comparing the relative rates k_x obtained for the catalysts at the same temperature. ATPH is the most active catalyst, catalyzing the reaction roughly 4 times faster than when using the same molar amount of $ZnBr_2$. Cu-BTC is the slowest catalyst and $ZnBr_2$ catalyzes the reaction about 270 times faster at 373 K than Cu-BTC. As Cu-BTC is a heterogeneous catalyst, one could expect that adsorption and desorption effects also play a major role.

Table 1 also tabulates the initial quantities of the Cu-BTC catalyst (in crystalline structure) and citronellal (in liquid phase) used during the experiment. The volume of the reactant is much larger than the total volume occupied by the Cu-BTC crystals. The measured reaction rates should be correctly interpreted in the sense that a double concentration of the catalyst will lead to a double rate k_X in the initial stage.

In Table 1 0.1 g catalyst is associated to 0.496 mmol of metal sites. This is a valid assumption if each Cu-atom is catalytically active, or in other words is accessible for citronellal conversion. However, this assumption is speculative and should be verified by changing the size of the crystalline catalyst particles in the experiment. If the citronellal cyclization rate does not vary, one may assume that roughly each Cu-atom participates at the reaction, as the total volume has not changed. In the experimental data reported in Table 1 the sample contains cubic catalyst particles with size of 20 μm, as approximately measured by TEM. In a second experiment the total amount of catalyst has been kept fixed, but now particles of size 10 μm have been used. Measuring the isopulegol production after a certain time at 393 K, the citronellal conversion doubles from 13 % to 26 %. This is a clear indication that the reaction happens at the surface layer of the catalyst and that not all Cu-sites are catalytically active or reachable by the citronellal reactant. We illustrate with a crude but realistic model in which the crystalline cubic particle has an inner core of volume c^3 in which the metal sites are inaccessible and an outer shell of a certain thickness d = (b-c)/2 in which we assume that all metal sites are accessible from the surface. The cubic particle with size b is composed of cubic unit cells of the Cu-BTC MOF crystal having a composition of 48 Cu , 192 O, 288 C and 96 H-atoms and a size a of 26.288 Å. In this model the crystal particle contains n^3 cells with n=b/a and the inactive inner core n'^3 cells with n'=c/a. Let us assume that the citronellal molecules can penetrate into the pores of the Cu-BTC frame work and interact with the metal centers up to 1 μm. We assume in our model that further diffusion has become inhibited due to pores which are blocked by the formed isopulegol stereomers or other obstacles, and that d = 1 μm is an average of the thickness of the outer shell. This implies that for crystal particles of size 20 μm the effectiveness coefficient $\alpha = \frac{\text{active metal sites}}{\text{total metal sites}}$ amounts to 0.271 and that each particle consists of 11.9 10^{10} active "unit cells" in the outer shell. In the second experiment with use of particles of size 10 μm, the same model, applying the same diffusion shell thickness of 1 μm, leads to an effectiveness coefficient α of 0.488 or 2.69 10^{10} active "unit cells". For a same quantity of catalyst (0.1 gram) we

have 8 times more particles of size 10 μm than of size 20 μm. Hence in the last scenario the number of active sites increases with almost a factor 2 ($\frac{8\times 2.69\ 10^{10}}{11.9\ 10^{10}} = 1.89$). In the initial stage the citronellal conversion will double, as in the experiment. This simple model is able to explain quite adequately the experimental observation of a double conversion of citronellal when cutting the crystal particles in half. It indicates that only the Cu-sites in an outer shell of thickness 1μm of the heterogeneous catalyst may be regarded as "active".

It implies that not all Cu-sites in Cu-BTC participate at the citronellal cyclization, in contrary to the homogeneous catalyst $ZnBr_2$, where each metal is considered as active site. A fair comparison would require an experiment over Cu-BTC with particles of size 2 μm. In this experimental set-up all Cu-sites may be regarded as catalytically active and the efficiency of the catalyst will increase with a factor of 3.7. In this context the results taken up in Table 1 for Cu-BTC and ZnBr2 should be interpreted with care as they are not based on an equal amount of "active" metal sites.

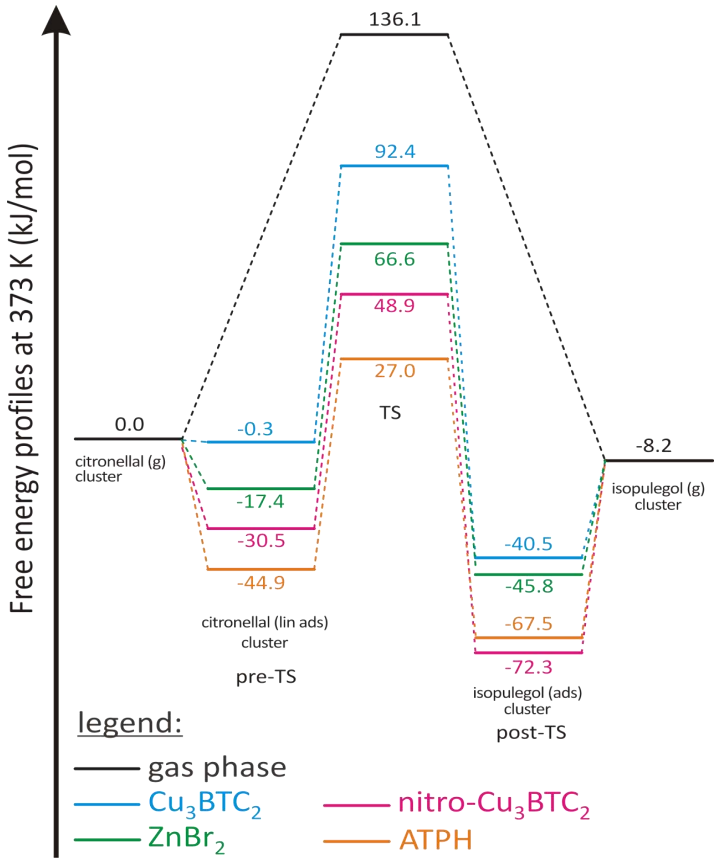

Figure 6: Gibbs free energy profiles, calculated at 383 K, for citronellal cyclization to (-)-isopulegol on various catalysts. The used level of theory for the energetics was B3LYP/6-311+g(d,p)-D3 and the profile is based on the most stable transition state for each catalyst, the "iso-chair" configuration. For CuBTC the geometry optimization is done using an ONIOM approach outlined in the computational methodology section.

Preliminary indications on the relative activity of the various catalysts, were obtained by studying the geometries of the transition states for cyclization towards (-)-isopulegol (vide supra). To obtain a thorough quantitative understanding of the relative activity, the free energy profiles of the citronellal cyclization towards (-)-isopulegol, were constructed for all catalysts, including the adsorption and desorption steps. The free energy profiles are shown in Figure 6 and the obtained theoretical results are given in Table 2, where also the contributions from enthalpy and entropy are separately listed. The gas phase results are included for the sake of completeness. The free energy profile is constructed based on the most stable transition state, i.e. the iso-chair conformation as explained in previous section. In addition to the experimentally tested catalysts, we have additionally taken up a hypothetical Cu-BTC material in our theoretical test set. It concerns a Cu-BTC material which is functionalized with electron withdrawing nitro groups on the BTC linkers, as explained in Section 2.1.2. The proposal for this material is inspired by the enhanced activity of the UiO material when functionalizing the linkers with nitro groups. The increase of activity for the UiO-66-NO_2, was ascribed to a stronger adsorption and additional preferential electrostatic interactions in the transition states between the adsorbent and the nitro groups [53]. This hypothetical material will further be referred as Cu-BTC-NO_2 catalyst.

As expected the uncatalyzed reaction has a high free energy barrier of 136.1 kJ/mol, which consists of an enthalpic barrier of 105.7 kJ/mol and entropic barrier of 30.4 kJ/mol. During a cyclization step the entropy typically decreases yielding an additional contribution $T\Delta S$ to the free energy barrier.

When the reaction takes place on a catalyst, the first step of the reaction profile consists of an adsorption process. The various catalysts show distinct differences for the adsorption of a linear citronellal molecule (cfr. Table 2). The strongest adsorption is found on ATPH (-44.9 kJ/mol), followed by $ZnBr_2$ (-17.4) and for Cu-BTC a slightly negative free energy of adsorption (-0.3) is obtained. The free energies of adsorption may be decomposed in an enthalpic and entropic contribution. A stronger the Lewis acidity of the metal center gives a more negative value for the enthalpy of adsorption. The entropy contribution ($-T\Delta S$) is positive as the molecule looses three translational and three rotational degrees of freedom during adsorption and higher values are expected for catalysts which impose more

steric constraints on the adsorbent. Indeed for $ZnBr_2$ the lowest value of $-T\Delta S$ is found as this catalyst imposes nearly no steric constraints on the citronellal molecule. The hypothetical Cu-BTC-NO_2 material has indeed stronger Lewis acidity due to the presence of the electron withdrawing nitro groups. The adsorption enthalpy amounts to -115.8 kJ/mol which is comparable to the value found for ATPH, whereas the entropic barrier for adsorption is almost the same as in the unsubstituted Cu-BTC (compare 79.3 with 85.3 kJ/mol for $-\mathrm{T}.\Delta S_{383}^{ads,citro}$) material.

After adsorption the cyclization can take place, during which the citronellal molecule first takes a non-linear conformation that is properly aligned to allow ring closure. The intrinsic kinetic data are also taken up in Table 2. These data refer to the adsorbed state of citronellal. The intrinisic free energy barriers vary within a limited range from 71.9 to 92.7 kJ/mol. The lowest value is found for ATPH and the highest value is found for Cu-BTC. Despite these seemingly moderate variations, strong differences are found for the enthalpic and entropic contributions, giving values of 33, 45 and 74 kJ/mol for ATPH, $ZnBr_2$ and Cu-BTC. These larger differences may be understood by referring back to the transition state geometries shown in Figure 4. A longer elongation of the carbonyl bond, gives a partially positive charge on the carbon atom which is larger and which facilitates the nucleophilic attack of the C=C bond.

Interestingly the intrinsic free energy barrier for Cu-BTC-NO_2, is about 10 kJ/mol lower than for Cu-BTC. This can be ascribed to stabilization of the transition state by preferred electrostatic interactions between the adsorbate and the nitro groups, as was the case for the UiO-NO_2 material. The transition state with indication of key geometrical parameters is taken up in Figure S.15 of the SI.

Table 2. Kinetic data for the citronellal cyclization to (-)-isopulegol at 373 K. Free energy, enthalpic and entropic contributions in the adsorbed state (ads) are given for linearly adsorbed citronellal (ads,citro) and adsorbed isopulegol (ads,iso) and for the transition state (‡) (kJ/mol). The rate constants (k_{373}^{fwd}) are given in units of $m^3.mol^{-1}.s^{-1}$ for the apparent kinetics and in s^{-1} for the intrinsic kinetics.

Adsorption				
	$\Delta G_{373}^{ads,citro}$	$\Delta H_{373}^{ads,citro}$	$-T.\Delta S_{373}^{ads,citro}$	
Cu-BTC	-0.28	-79.57	79.29	
$ZnBr_2$	-17.36	-58.39	41.03	
Cu-BTC-NO_2	-30.50	-115.81	85.31	
ATPH	-44.93	-113.40	68.47	
Desorption				
	$\Delta G_{373}^{des,iso}$	$\Delta H_{373}^{des,iso}$	$-T.\Delta S_{373}^{des,iso}$	
Cu-BTC	32.31	99.34	-67.03	
$ZnBr_2$	37.72	83.30	-45.58	
Cu-BTC-NO_2	64.02	137.85	-73.83	
ATPH	59.33	165.50	-70.90	
Intrinsic kinetics				
	$\Delta G_{373}^{\ddagger,intr}$	$\Delta H_{373}^{\ddagger,intr}$	$-T.\Delta S_{373}^{\ddagger,intr}$	$k_{373}^{fwd,intr}$
Cu-BTC	92.66	77.55	15.11	8.22E-01
$ZnBr_2$	83.97	45.30	38.67	1.36E+01
Cu-BTC-NO_2	79.39	60.90	18.49	5.92E+01
ATPH	71.91	33.30	38.61	6.62E+02
Apparent kinetics				
	$\Delta G_{373}^{\ddagger,app}$	$\Delta H_{373}^{\ddagger,app}$	$-T.\Delta S_{373}^{\ddagger,app}$	$k_{373}^{fwd,app}$
Gas phase	136.06	105.66	30.40	6.88E-07
Cu-BTC	92.38	-2.02	94.40	2.75E-02
$ZnBr_2$	66.61	-13.10	79.71	1.12E+02
Cu-BTC-NO_2	48.89	-54.91	103.80	3.38E+04
ATPH	26.98	-80.10	107.08	3.96E+07

In an attempt to quantify the relative rates for citronellal cyclization on the various catalysts, both intrinsic and apparent reaction kinetics were calculated. These values are also taken up in Table 2. The procedure applied here is similar than the one applied for the UiO-66 and the UiO-66-NO_2 catalysts. [53] There it was shown that the experimental acceleration between the catalysts lies closest to the ratio of intrinsic kinetic coefficients, while apparent kinetic data give an overestimation (Table 3). The experiments conducted here confirmed first order kinetics in citronellal concentration and therefore a comparison between intrinsic calculated rates and experimental rates is warranted.

The correct qualitative trends are found for the activities of the studied catalyst: Cu-BTC is the least active whereas ATPH gives the highest rates for the citronellal cyclization. On the quantitative level, one notices some discrepancies. The experimental relative rate is a factor of 15 larger in favor of the Lewis acid catalyst $ZnBr_2$ with respect of Cu-BTC. However, the measured experimental k_x value of 0.0087 s^{-1} for the Cu-BTC catalyst has been associated to the use of 0.496 mmol of active Cu-sites. When augmenting the efficiency of the catalyst by using crystal particles of size 2µm, the theoretical agreement with experiment drastically improves: instead of a factor of 15 the discrepancy decreases to a factor of 4. For ATPH an overestimation of about 40 is found. This is probably due to the various assumptions made in the theoretical model for the description of the transition states due to the extensive number of degrees of freedom arising from the flexibility of the three (2,6-dephenyl)phenoxide ligands (see further).

Table 3: Comparison of experimental and theoretical ratios of kinetic rate constants between the various catalysts. Theoretical results are on the B3LYP/6–311+g(d,p)-D3 level of theory and are based on the intrinsic rate coefficients. The number between brackets is hypothetical and is obtained when augmenting the efficiency of the Cu-BTC catalyst by using crystal particles of size 2µm.

	exp	theory
$k_{ZnBr2}/k_{Cu\text{-}BTC}$ (T=373 K)	252 (68)	16.5
k_{ATPH}/k_{ZnBr2} (T=298 K)	4	129

3.3 Theoretical and experimental investigation of the catalyst selectivity

A good catalyst for the citronellal cyclization needs to have both a high activity and a high selectivity towards the major isomer ((-)-isopulegol). As the various studied catalysts are active within another temperature window, it is important to assess the selectivity in terms of temperature. Experimentally, the initial selectivities at low conversion (5-15 %) for the citronellal cyclization were determined for ATPH, $ZnBr_2$, and Cu-BTC. Further experimental details are given in the Supporting Information and Methods section. The experimental results for the selectivity are given in Table 4 at various temperatures. It is immediately clear that the highest selectivities are obtained with ATPH . After 10 minutes at 298 K 11.4 % of citronellal was converted with a selectivity of 97.9 % towards the (-) isopulegol isomer. The diastereoselectivity distribution becomes 97.9/1/1.1. For the reaction conducted with $ZnBr_2$ at 298 K the diastereoselectivity towards isopulegol 2 drops to 87.5 %. The citronellal cyclization was also performed using the same catalyst but at a higher temperature of 373 K and our results show that the selectivity remains more or less the same (88 %). The lowest selectivities are obtained using Cu-BTC which reveals a diastereoselectivity of only 73% towards the desired isopolegol diastereomer. For this heterogeneous catalyst, we also explored the dependence of the selectivities as a function of temperature and the results at low conversion (5-15 %) are taken up in Table 5. It is immediately clear that the selectivity towards the major isopulegol isomer drops when increasing the temperature.

Table 4: Overview of the theoretical and experimental stereoselectivity distributions ((-)-isopulegol/(+)-neoisopulegol/(+)-isoisopulegol/neisoisopulegol) on various catalysts.

	Temperature (K)	Experimental selectivity	S_{ini}	S_{TPE}
Without catalyst	298	-	90.6/8.4/0.9/0.1	77.0/20.0/2.7/0.3
	373	-	80.1/15.3/3.9/0.7	71.2/23.3/4.8/0.7
Cu-BTC	373	73/20.8/6.2	85.9/4.4/9.6/0.1[a]	
			83.5/12.1/4.1/0.2[b]	
$ZnBr_2$	373	88/7.4/4.6	81.6/15.3/2.8/0.2	
	298	87.5/7.4/5.1	86.9/11.8/1.3/0.1	
ATPH	298	97.9/1.1/1.0	95.4/0.1/4.6/0.0	
Selectivity distribution for [a] the periodic model [b] the extended cluster model				

Table 5. Selectivities at different temperatures towards the isopulegol isomers in the citronellal cyclization with Cu-BTC as a catalyst.

T (K)	**S_{iso}**	**S_{neoiso}**	**$S_{(isoiso+neoisoiso)}$**
373	73.0	20.8	6.2
423	67.5	24.8	7.7
443	66.9	24.5	8.6
463	66.2	24.8	9
483	65.6	24.8	9.6

To rationalize the factors contributing to the diastereoselectivity and to understand the influence of temperature, a thorough molecular modeling study was conducted. As explained in the Methods section, selectivities were calculated using the Curtin Hammett principle giving initial selectivities $S_{i,ini}$ or using the product stabilities giving $S_{i,TPE}$. The computational results on the initial selectivities are critically dependent on the construction of a representative set of stereoselective transition states. Our study on the Cu-PDWL (vide supra) revealed insight into the most important transition states. For $ZnBr_2$, we started with eight initial transition states corresponding to two possible adsorption positions of the free electron pair of the carbonyl oxygen for each of the isomers under consideration. The final optimized transition states and corresponding energies are given in Figure S.3 and Table S.5 of the SI.

For Cu-BTC, the set of stereoselective transition states is larger as there are also two possible orientations of the isopropyl group into the big or large pocket of Cu-BTC. Taking also the two possible adsorption sites into account of the carbonyl bond, 16 initial transition structures were constructed which led to a set of 14 stereoselective transition states (procedure is briefly described in Section 2.1.5). Since the Cu-BTC material exhibits a periodic structure, we explored the set of transition states both in the cluster and periodic model, in order to evaluate the influence of the molecular environment of the active site on the selectivity. Geometrical parameters and energetic data are taken up in Tables S.4 and S.9 of the SI.

ATPH is a homogeneous catalyst that possesses an extensive number of degrees of freedom due to the flexibility of the three (2,6-diphenyl)phenoxide ligands. Accurate theoretical selectivity models for flexible homogeneous catalysts, are extremely challenging from theoretical point of view, as one needs to scan the relevant part of the free energy surface in the neighborhood of the stereoselective transition states with molecular dynamics methods or monte carlo methods [97]. These calculations are extremely time consuming and need accurate force fields which are generally not available for the systems under study. Such study is beyond the scope of the present paper and herein we limit ourselves to a crude estimation of the selectivity for ATPH based on four plausible transition states.

Figure 7 shows the selectivity for the desired (-)-isopulegol, obtained using the selectivity expression (Eqs. 2 and 3) and for the different catalysts in terms of temperature. We have also taken up the selectivity curves for the reaction performed in gas phase, both based on the Curtin Hammett principle (labeled with $S_{i,ini,gas}$ phase) and based on the product stabilities (labeled with $S_{i,TPE}$). Thermodynamically a selectivity of 77 % towards (-)-isopulegol is obtained at 298K, which steadily decreases with increasing temperature. These values give the basic selectivity levels which are inherently characteristic for this system. The free energy differences ($G_j^{product} - G_{iso}^{product}$) , with j one of the other diastereomers of isopulegol, are nearly independent of temperature (see Table S.10 of SI) and thus the observed temperature dependence can be drawn back to the 1/RT factor in the exponential function of the selectivity equation (Eq. 3). If the free energy difference between (-)-isopulegol and the

other diastereomers would increase with temperature the selectivity would decrease less fast in terms of temperature. However the small increase in the free energy differences noticed here imposes only a marginal effect on the overall temperature dependence.

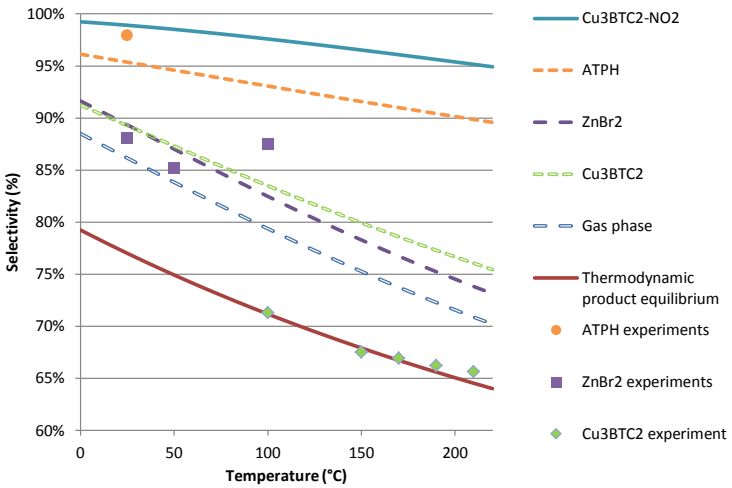

Figure 7: Theoeretical diastereoselectivity towards (-)-isopulegol on various catalysts (ATPH, $ZnBr_2$, Cu-BTC, gas phase kinetic + thermodynamic, Cu-BTC-NO_2). On each catalyst, the thermodynamic selectivity, based on the free energy difference between the isopulegol isomers should form the lower limit, and the calculated initial selectivity the upper limit.

Theoretical modeling predicts that introducing a Lewis acid catalyst increases the initial selectivities towards (-)- isopulegol. Theoretical values for the diastereoselectivity distributions are also taken up in Table 4 together with the experimental values to allow a straightforward comparison. Additionally the relative free energy differences between the stereoselective transition states are given in Table 6. Compared to the thermodynamic predictions, the most significant increase is found for ATPH, giving an initial theoretical selectivity at 298 K of 95%. Apart from being the most active catalyst, it also improves the diastereoselectivity towards the desired product as the differences in free energy of

activation between the (-)-isopulegol and the other stereomers is most pronounced (6.32 kJ/mol). For the other Lewis acid catalysts the free energy differences amount to about the same value (≈ 5kJ/mol) but both for $ZnBr_2$ and for Cu-BTC additional transition states leading to isopulegol give a slight increase in the selectivity. As Cu-BTC is a heterogeneous catalyst, it is important to assess the sensitivity of the values with respect to the description of the molecular environment. Therefore also periodic calculations have been performed taking into account the full molecular environment around the Lewis acid site. The selectivities using the periodic model are also taken up in Table 5. The periodic calculations don't predict large deviations of the observed selectivities with respect to the extended cluster model.

Table 6: Relative free energy differences ($\Delta(\Delta G^{\ddagger}_{383})$, kJ/mol) at 383 K between the different transition states towards the various pulegol isomers.

	Gas phase	**$ZnBr_2$**	**ATPH**	**Cu-BTC**
iso	0.00	0.00	0.00	0.00
		1.06		2.82
				7.20
				8.04
neoiso	5.15	4.53	19.56	5.61
				10.52
				12.55
				12.76
isoiso	9.35	8.50	6.32	11.01
		8.86		11.11
				12.74
				16.87
neoisoiso	14.81	13.51	37.76	17.85
				20.82

Interestingly the diastereoselectivity seems to decrease less fast in terms of temperature for ATPH than for the other catalysts. This originates from the difference in free energies between the stereoselective transition states, which increases in terms of temperature for ATPH (the values are taken up in Table S.11 of the SI). This effect is mainly due to the variations in entropic barrier. In any case, the entropy barrier for this system is quite high due to the strong steric hindrance of the bulky ligands around the catalytic center. For the sake of completeness additional selectivity profiles for all catalysts have been taken up in the SI (Figures S.8-S.12).

In what follows, we will compare the theoretical and experimental diastereoselectivities. Before doing so, one must realize that predicting selectivities is highly ambitious from theoretical point of view as the final obtained quantitative data depend on small energy differences, i.e. in our study the differences between the various stereomers ranges between 5 and 10 kJ/mol. The prediction of such data is very sensitive to the used model, such as the level of theory. We calculated the selectivities using various contempory functionals (TPSS, M06-2X, M06-L and B3LYP) and found that the B3LYP functional yielded the closest approximation with experimental results for $ZnBr_2$, Cu-BTC and we have therefore retained these results. The differences in free energies between the set of stereoselective transition states at other levels of theory is taken up in Tables S.13 and S.14 of the SI. A second consideration when comparing theoretical with experimental selectivities concerns the differences between the initial selectivies ($S_{i,ini}$) and thermodynamic controlled selectivies ($S_{i,TPE}$), which constitute a lower limit. For example in the case where diffusion limitations exist for the products, the measured values are expected to lie closer to the thermodynamic controlled selectivities.

For ATPH, only one experimental data point in terms of temperature could be obtained as this catalyst is extremely active and thus is was not possible to retrieve points at higher temperatures. Even in the simplified model taken into consideration here, which is based on only four stereoselective transition states, the obtained theoretical selectivities are in quite good agreement with the experimental values (cfr. Table 4 and Figure 7).

Also for $ZnBr_2$ the agreement with $S_{i,ini}$ is more than satisfactory and the agreement proves that the observed selectivities are kinetically controlled by the forward reactions. For this catalyst there is no diffusion limitation which could mask the initial selectivities in the measured data.

For Cu-BTC the experimental values do not coincide with the initial selectivities but are much closer to the thermodynamically determined selectivities. Cu-BTC is a typical example where diffusion limitations might play an important role, at least when the citronellal conversion takes place at metal centers inside the pores of the MOF. This is illustrated in Figure 1 where the pore size of Cu-BTC can be compared with the size of the various formed isomers of pulegol. Diffusion of linear citronellal

molecules into the different pores imposes no problem but diffusion of the various diastereomers out of the Cu-BTC framework poses more problems. In this context we refer to the discussion made in previous subsection where the experiment clearly indicated that mainly the Cu-sites in an outer shell with a thickness of about 2 μm are catalytically active. In the case of diffusion limitations with the escape of products out of the pores, a thermodynamic equilibrium may be installed between the measured products, explaining the better agreement between the experimental selectivities with the $S_{i,\mathrm{TPE}}$ values. Another issue that warrants attention is the fact that the available space around the active center is more restricted inside the pores than at the surface. In the case of the cyclization it has been shown that a reduced space favours the formation of the desired diastereomer [21]. This could partly explain the rather moderate experimental Cu-BTC selectivity towards (-)-isopulegol.

Finally it is interesting to comment on the theoretical predictions for the selectivities of a hypothetical nitro substituted version of the Cu-BTC material. The initial selectivities towards (-)-isopulegol are very high with values larger than 95 %. This catalyst has similarities with the highly selective homogeneous ATPH catalyst. The additional nitro groups, enhance the Lewis acidity of the metal centers, thus making this material more active than the unsubstituted Cu-BTC material and additionally the nitro groups impose additional steric hindrance which favors formation of the desired (-)-isopulegol. Also for this catalyst a high entropic barrier is found as in ATPH (Table S.6 of SI). However the Cu-BTC framework is not ideally suited for high selectivities towards isopulegol in reality due to pore restrictions, which inhibit fast diffusion of the various products. A realistic catalyst for practical purposes would need bigger pores. Modifying the dimensions of the linkers without truly altering the active site, is actively explored within the MOF community [98-101,102].

4. CONCLUSIONS

In this paper, we evaluated the performance of various Lewis acid catalysts for the enantioselective cyclization of (+)-citronellal towards (-)-isopulegol. The last compound is an important intermediate in most synthetic production routes towards (-)-menthol, which is an important aroma chemical compound worldwide. A clear understanding of the catalytic mechanisms and characteristics of plausible asymmetric catalysts, is of utmost importance to rationalize both the activity of the catalyst and selectivity towards the desired stereomer. Herein, we have performed a combined experimental and theoretical study to rationalize the factors contributing to the activity and selectivity of the catalyst. Our test set contains $ZnBr_2$, the standard homogeneous catalyst used for the citronellal cyclization; ATPH, a more recently proposed homogeneous catalyst which is characterized by selectivities more than 99% and Cu-BTC, a heterogeneous metal organic framework with open metal sites available for Lewis catalysis. ATPH is the most active catalyst, characterized by the highest reaction rates towards (-)-isopulegol and Cu-BTC is the least active. The activity is directly related to the strength of the Lewis acid metal centers. A stronger acidity activates the carbonyl bond more strongly, leading to a transition state which is more product-like and a larger positive charge on the carbonyl carbon which favors nucleophilic attack of the carbon-carbon double bond. The Lewis acidity of the metal centers can be tuned by functionalizing the organic linkers in case of Cu-BTC. Adding electron withdrawing groups on the BTC linkers, enhances the acidity and the activity of the catalyst. The selectivity is controlled by the free energy differences between the stereoselective transition states towards the various isomers of pulegol. ATPH is very selective towards (-)-isopulegol with an experimental determined selectivity at 298 K of about 98%. $ZnBr_2$ has a selectivity of 87.5% at 298 K, whereas Cu-BTC turns out to be the least selective. The high selectivity of ATPH may be traced back to a favorable free energy barrier towards (-)-isopulegol compared with the other isomers and more specifically a large entropic barrier was found that favors the major diastereomer. For $ZnBr_2$ and Cu-BTC various experiments were conducted in terms of temperature, which revealed that the selectivities towards (-)-isopulegol decrease for higher temperature. Thus a more active catalyst, allows to work at lower temperatures and will

therefore be more selective towards the major isomer. Based on these insights we simulated the selectivities of a hypothetical Cu-BTC material which was additionally functionalized with nitro groups. As such more steric hindrance was introduced which indeed predicts a higher selectivity towards (-)-isopulegol.

Overall the agreement between the theoretically predicted selectivities and experimentally measured values is very good. The theoretical prediction of enantioselectivities is highly ambitious within computational chemistry as it depends on a representative set of stereoselective transition states and the ability of theoretical methods to calculate accurately the free energy differences between the various activated complexes. The combined experimental and theoretical approach followed here is a case study for rational design of asymmetric catalysts as it reveals the major factors contributing to selectivity and activity of the Lewis acid catalyst.

ACKNOWLEDGMENT This work is supported by the Research Board of Ghent University (BOF), the Fund for Scientific Research; Flanders (FWO), and BELSPO in the frame of IAP/6/27. Funding was also received from the European Research Council under the European Community's Seventh Framework Programme [FP7(2007-2013) ERC grant agreement number 240483]. We would also like to thank Petr Nachtigall and Lukáš Grajciar for providing us with the optimized Cu-BTC unit cell. The computational resources (Stevin Supercomputer Infrastructure) and services used in this work were provided by Ghent University.

SUPPORTING INFORMATION PARAGRAPH

This material is available free of charge via the Internet at http://pubs.acs.org.

TOC : Table of contents figure

REFERENCES

(1) Leffingwell, J. C.; Leffingwel, D. *Speciality Chemicals Magazine* **2011**, 30.
(2) Lenardao, E. J.; Botteselle, G. V.; de Azambuja, F.; Perin, G.; Jacob, R. G. *Tetrahedron* **2007**, *63*, 6671.
(3) Lawrence, B.; Hopp, R. *Natural and Synthetic Menthol*; CRC Press, 2006.
(4) Friedrich, M.; Ebel, K.; Götz, N.; BASF SE, Ludwigshafen (DE): 2009; Vol. US 7,550,633 B2, p 9.
(5) Friedrich, M.; Ebel, K.; Gotz, N.; Krausee, W.; Zahm, C.; BASF SE, US 7,608,742 B2: 2009; Vol. US 7,608,742 B2.
(6) Heydrich, G.; Gralla, G.; Ebel, K.; Friedrich, M.; BASF SE, US 8,003,829 B2: 2011; Vol. US 8,003,829 B2.
(7) Heydrich, G.; Gralla, G.; Rauls, M.; Schmidt-Leithoff, J.; Ebel, K.; Krause, W.; Oehlenschlager, S.; Jakel, C.; Friedrich, M.; Bergner, J.; Kashani-Shirazi, N.; Paciello, R.; BASF SE, US 2010/0249467 A1: 2010; Vol. US 2010/0249467 A1.
(8) Heydrich, G.; Gralla, G.; Ebel, K.; BASF SE, US 2010/0010253 A1: 2010; Vol. US 2010/0010253 A1.
(9) Misono, M.; Nojiri, N. *Applied Catalysis* **1990**, *64*, 1.
(10) Iwata, T.; Okeda, Y.; Hori, Y.; Takasago International Corporation: United States, 2002; Vol. US 2002/0133046 A1, p 9.
(11) Milone, C.; Gangemi, C.; Neri, G.; Pistone, A.; Galvagno, S. *Appl. Catal. A-Gen.* **2000**, *199*, 239.
(12) Milone, C.; Perri, A.; Pistone, A.; Neri, G.; Galvagno, S. *Appl. Catal. A-Gen.* **2002**, *233*, 151.
(13) Kropp, P. J.; Breton, G. W.; Craig, S. L.; Crawford, S. D.; Durland, W. F.; Jones, J. E.; Raleigh, J. S. *J. Org. Chem.* **1995**, *60*, 4146.
(14) Maruoka, K.; Imoto, H.; Saito, S.; Yamamoto, H. *J Am Chem Soc* **1994**, *116*, 4131.
(15) Saito, S.; Nagahara, T.; Shiozawa, M.; Nakadai, M.; Yamamoto, H. *J Am Chem Soc* **2003**, *125*, 6200.
(16) Maruoka, K.; Saito, S.; Yamamoto, H. *Synlett* **1994**, 439.
(17) Saito, S.; Shiozawa, M.; Nagahara, T.; Nakadai, M.; Yamamoto, H. *J Am Chem Soc* **2000**, *122*, 7847.
(18) Ito, H.; Nagahara, T.; Ishihara, K.; Saito, S.; Yamamoto, H. *Angew. Chem.-Int. Edit.* **2004**, *43*, 994.
(19) Itoh, H.; Hori, Y. 2011; Vol. US 2011/0082308 A1.
(20) Boronat, M.; Concepcion, P.; Corma, A.; Navarro, M. T.; Renz, M.; Valencia, S. *Physical Chemistry Chemical Physics* **2009**, *11*, 2876.
(21) Boronat, M.; Corma, A.; Renz, M. *Turning Points in Solid-State, Materials and Surface Science*; The Royal Society of Chemistry, 2008; Vol. 10.1039/9781847558183-00639, pages 639-650.
(22) Corma, A.; Renz, M. *Chem Commun* **2004**, 550.
(23) Yongzhong, Z.; Yuntong, N.; Jaenicke, S.; Chuah, G.-K. *J Catal* **2005**, *229*, 404.
(24) Czaja, A. U.; Trukhan, N.; Muller, U. *Chemical Society Reviews* **2009**, *38*.
(25) Férey, G.; Serre, C.; Devic, T.; Maurin, G.; Jobic, H.; Llewellyn, P. L.; De Weireld, G.; Vimont, A.; Daturi, M.; Chang, J.-S. *Chemical Society Reviews* **2011**, *40*, 550.
(26) Han, S. S.; Mendoza-Cortes, J. L.; Goddard Iii, W. A. *Chemical Society Reviews* **2009**, *38*, 1460.
(27) Murray, L. J.; Dinca, M.; Long, J. R. *Chemical Society Reviews* **2009**, *38*, 1294.

(28) Rowsell, J. L. C.; Millward, A. R.; Park, K. S.; Yaghi, O. M. *J Am Chem Soc* **2004**, *126*, 5666.
(29) Suh, M. P.; Park, H. J.; Prasad, T. K.; Lim, D.-W. *Chemical Reviews* **2012**, *112*, 782.
(30) Kuppler, R. J.; Timmons, D. J.; Fang, Q. R.; Li, J. R.; Makal, T. A.; Young, M. D.; Yuan, D. Q.; Zhao, D.; Zhuang, W. J.; Zhou, H. C. *Coordin Chem Rev* **2009**, *253*, 3042.
(31) Li, J. R.; Kuppler, R. J.; Zhou, H. C. *Chemical Society Reviews* **2009**, *38*, 1477.
(32) Li, J.-R.; Kuppler, R. J.; Zhou, H.-C. *Chemical Society Reviews* **2009**, *38*, 1477.
(33) Li, J.-R.; Sculley, J.; Zhou, H.-C. *Chemical Reviews* **2012**, *112*, 869.
(34) Liu, Y.; Xuan, W.; Cui, Y. *Advanced Materials* **2010**, *22*, 4112.
(35) Allendorf, M. D.; Bauer, C. A.; Bhakta, R. K.; Houk, R. J. T. *Chemical Society Reviews* **2009**, *38*, 1330.
(36) Carlos, L. D.; Ferreira, R. A. S.; de Zea Bermudez, V.; Julian-Lopez, B.; Escribano, P. *Chemical Society Reviews* **2011**, *40*, 536.
(37) Rocha, J.; Carlos, L. D.; Paz, F. A. A.; Ananias, D. *Chemical Society Reviews* **2011**, *40*, 926.
(38) Kurmoo, M. *Chemical Society Reviews* **2009**, *38*, 1353.
(39) Lee, J.; Farha, O. K.; Roberts, J.; Scheidt, K. A.; Nguyen, S. T.; Hupp, J. T. *Chemical Society Reviews* **2009**, *38*, 1450.
(40) Farrusseng, D.; Aguado, S.; Pinel, C. *Angew. Chem.-Int. Edit.* **2009**, *48*, 7502.
(41) Ma, L.; Abney, C.; Lin, W. *Chemical Society Reviews* **2009**, *38*, 1248.
(42) Yoon, M.; Srirambalaji, R.; Kim, K. *Chemical Reviews* **2012**, *112*, 1196.
(43) Alaerts, L.; Seguin, E.; Poelman, H.; Thibault-Starzyk, F.; Jacobs, P. A.; De Vos, D. E. *Chem.-Eur. J.* **2006**, *12*, 7353.
(44) Chui, S. S. Y.; Lo, S. M. F.; Charmant, J. P. H.; Orpen, A. G.; Williams, I. D. *Science* **1999**, *283*, 1148.
(45) Tranchemontagne, D. J.; Hunt, J. R.; Yaghi, O. M. *Tetrahedron* **2008**, *64*, 8553.
(46) Chmelik, C.; Karger, J.; Wiebcke, M.; Caro, J.; van Baten, J. M.; Krishna, R. *Microporous Mesoporous Mat.* **2009**, *117*, 22.
(47) De Rosa, S.; Giordano, G.; Granato, T.; Katovic, A.; Siciliano, A.; Tripicchio, F. *J. Agric. Food Chem.* **2005**, *53*, 8306.
(48) Perez-Mayoral, E.; Cejka, J. *ChemCatChem* **2011**, *3*, 157.
(49) Schlichte, K.; Kratzke, T.; Kaskel, S. *Microporous Mesoporous Mat.* **2004**, *73*, 81.
(50) Wu, Y.; Qiu, L. G.; Wang, W.; Li, Z. Q.; Xu, T.; Wu, Z. Y.; Jiang, X. *Transit. Met. Chem.* **2009**, *34*, 263.
(51) Marx, S.; Kleist, W.; Baiker, A. *J Catal* **2011**, *281*, 76.
(52) BASF June 1, 2010; Vol. P 282/10e.
(53) Vermoortele, F.; Vandichel, M.; Van de Voorde, B.; Ameloot, R.; Waroquier, M.; Van Speybroeck, V.; De Vos, D. E. *Angew. Chem.-Int. Edit.* **2012**, *51*, 4887.
(54) Ghysels, A.; Van Neck, D.; Waroquier, M. *Journal of Chemical Physics* **2007**, *127*, 164108.
(55) Kresse, G.; Hafner, J. *Phys. Rev. B* **1994**, *49*, 14251.
(56) Kresse, G.; Hafner, J. *Phys. Rev. B* **1993**, *47*, 558.
(57) Kresse, G.; Furthmüller, J. *Phys. Rev. B* **1996**, *54*, 11169.
(58) Kresse, G.; Furthmüller, J. *Comput. Mat. Sci.* **1996**, *6*, 15.
(59) Becke, A. D. *Journal of Chemical Physics* **1993**, *98*, 5648.
(60) Lee, C. T.; Yang, W. T.; Parr, R. G. *Phys. Rev. B* **1988**, *37*, 785.
(61) Hay, P. J.; Wadt, W. R. *Journal of Chemical Physics* **1985**, *82*, 270.
(62) Grimme, S.; Antony, J.; Ehrlich, S.; Krieg, H. *Journal of Chemical Physics* **2010**, *132*.
(63) Zhao, Y.; Truhlar, D. G. *Theor Chem Acc* **2008**, *120*, 215.
(64) Zhao, Y.; Truhlar, D. G. *Accounts Chem. Res.* **2008**, *41*, 157.

(65) Catak, S.; Hemelsoet, K.; Hermosilla, L.; Waroquier, M.; Van Speybroeck, V. *Chem.-Eur. J.* **2011**, *17*, 12027.
(66) Catak, S.; D'Hooghe, M.; De Kimpe, N.; Waroquier, M.; Van Speybroeck, V. *Journal of Organic Chemistry* **2010**, *75*, 885.
(67) Verstraelen, T.; Van Speybroeck, V.; Waroquier, M. *J. Chem Inf. Model.* **2008**, *48*, 1530.
(68) Grimme, S. *J. Comput. Chem.* **2004**, *25*, 1463.
(69) Leus, K.; Vandichel, M.; Liu, Y. Y.; Muylaert, I.; Musschoot, J.; Pyl, S.; Vrielinck, H.; Callens, F.; Marin, G. B.; Detavernier, C.; Wiper, P. V.; Khimyak, Y. Z.; Waroquier, M.; Van Speybroeck, V.; Van der Voort, P. *J Catal* **2012**, *285*, 196.
(70) Grajciar, L.; Bludsky, O.; Nachtigall, P. *The Journal of Physical Chemistry Letters* **2010**, *1*, 3354.
(71) Perdew, J. P.; Burke, K.; Ernzerhof, M. *Phys. Rev. Lett.* **1996**, *77*, 3865.
(72) Perdew, J. P.; Burke, K.; Ernzerhof, M. *Phys. Rev. Lett.* **1997**, *78*, 1396.
(73) Blöchl, P. E. *Phys. Rev. B* **1994**, *50*, 17953.
(74) Grimme, S. *J. Comput. Chem.* **2006**, *27*, 1787.
(75) De Moor, B. A.; Ghysels, A.; Reyniers, M.-F. o.; Van Speybroeck, V.; Waroquier, M.; Marin, G. B. *Journal of Chemical Theory and Computation* **2011**, *7*, 1090.
(76) Ghysels, A.; Van Speybroeck, V.; Verstraelen, T.; Van Neck, D.; Waroquier, M. *Journal of Chemical Theory and Computation* **2008**, *4*, 614.
(77) Ghysels, A.; Van Speybroeck, V.; Pauwels, E.; Van Neck, D.; Brooks, B. R.; Waroquier, M. *Journal of Chemical Theory and Computation* **2009**, *5*, 1203.
(78) Ghysels, A.; Verstraelen, T.; Hemelsoet, K.; Waroquier, M.; Van Speybroeck, V. *J. Chem Inf. Model.* **2010**, *50*, 1736.
(79) Vandichel, M.; Lesthaeghe, D.; Van der Mynsbrugge, J.; Waroquier, M.; Van Speybroeck, V. *J Catal* **2010**, *271*, 67.
(80) Van Speybroeck, V.; Van der Mynsbrugge, J.; Vandichel, M.; Hemelsoet, K.; Lesthaeghe, D.; Ghysels, A.; Marin, G. B.; Waroquier, M. *J Am Chem Soc* **2011**, *133*, 888.
(81) Vandichel, M.; Leus, K.; Van Der Voort, P.; Waroquier, M.; Van Speybroeck, V. *J Catal* **2012**, *294*, 1.
(82) Reetz, M. T.; Meiswinkel, A.; Mehler, G.; Angermund, K.; Graf, M.; Thiel, W.; Mynott, R.; Blackmond, D. G. *J Am Chem Soc* **2005**, *127*, 10305.
(83) Donoghue, P. J.; Helquist, P.; Norrby, P.-O.; Wiest, O. *Journal of Chemical Theory and Computation* **2008**, *4*, 1313.
(84) Seeman, J. I. h. o. w. c. d. c. p. *Chemical Reviews* **1983**, *83*, 83.
(85) Seo, Y. K.; Hundal, G.; Jang, I. T.; Hwang, Y. K.; Jun, C. H.; Chang, J. S. *Microporous Mesoporous Mat.* **2009**, *119*, 331.
(86) Mikami, K.; Shimizu, M. *Chemical Reviews* **1992**, *92*, 1021.
(87) Clarke, M. L.; France, M. B. *Tetrahedron* **2008**, *64*, 9003.
(88) Snider, B. B. *Accounts Chem. Res.* **1980**, *13*, 426.
(89) Snider, B. B.; Ron, E. *J Am Chem Soc* **1985**, *107*, 8160.
(90) Choomwattana, S.; Maihom, T.; Khongpracha, P.; Probst, M.; Limtrakul, J. *The Journal of Physical Chemistry C* **2008**, *112*, 10855.
(91) Yang, Q. W.; Tong, X. L.; Zhang, W. Q. *Theochem-J. Mol. Struct.* **2010**, *957*, 84.
(92) Wannakao, S.; Khongpracha, P.; Limtrakul, J. *The Journal of Physical Chemistry A* **2011**, *115*, 12486.
(93) Kikukawa, Y.; Yamaguchi, S.; Nakagawa, Y.; Uehara, K.; Uchida, S.; Yamaguchi, K.; Mizuno, N. *J Am Chem Soc* **2008**, *130*, 15872.
(94) Zardoost, M. R.; Gholami, M. R.; Irani, M.; Siadati, S. A. *Prog. React. Kinet. Mech.* **2012**, *37*, 173.
(95) Sun, D.; Ma, S.; Ke, Y.; Collins, D. J.; Zhou, H.-C. *J Am Chem Soc* **2006**, *128*, 3896.

(96) Rubes, M.; Grajciar, L.; Bludsky, O.; Wiersum, A. D.; Llewellyn, P. L.; Nachtigall, P. *ChemPhysChem* **2012**, *13*, 488.
(97) Donoghue, P. J.; Helquist, P.; Norrby, P. O.; Wiest, O. *Journal of Chemical Theory and Computation* **2008**, *4*, 1313.
(98) Chen, B. L.; Eddaoudi, M.; Hyde, S. T.; O'Keeffe, M.; Yaghi, O. M. *Science* **2001**, *291*, 1021.
(99) Furukawa, H.; Go, Y. B.; Ko, N.; Park, Y. K.; Uribe-Romo, F. J.; Kim, J.; O'Keeffe, M.; Yaghi, O. M. *Inorganic Chemistry* **2011**, *50*, 9147.
(100) Wenzel, S. E.; Fischer, M.; Hoffmann, F.; Froba, M. *Inorganic Chemistry* **2009**, *48*, 6559.
(101) Cychosz, K. A.; Wong-Foy, A. G.; Matzger, A. J. *Journal of the American Chemical Society* **2008**, *130*, 6938.
(102) Vimont, A.; Thibault-Starzyk, F.; Daturi, M. *Chem. Soc. Rev.* **2010**, *39*, 4928.

Supporting Information:

Matthias Vandichel,[1,*] Frederik Vermoortele,[2] Stijn Cottenie,[1] Dirk E. De Vos,[2] Michel Waroquier[1] and Veronique Van Speybroeck,[1,*]

[1]Center for Molecular Modeling (CMM), Ghent University, Technologiepark 903, 9052 Zwijnaarde, Belgium, and QCMM-Alliance, Ghent-Brussels, Belgium

[2]Centre for Surface Chemistry and Catalysis, Katholieke Universiteit Leuven, Kasteelpark Arenberg 23, 3001 Leuven, Belgium

*Corresponding authors: Veronique.VanSpeybroeck@ugent.be, dirk.devos@biw.kuleuven.be

Table of contents:

1. Preliminary cluster study on a copper paddle wheel: determination of relevant transition states 2
2. Overview tables of geometrical transition state parameters for the non-periodic simulations 5
2.1 Gas phase: B3LYP/6-311+g(3df,2p)-D3 5
2.2 Cu_3BTC_2: Extended cluster system on B3LYP/6-311+g(d,p)-D3* 6
2.3 $ZnBr_2$: B3LYP/6-311++g(3df,2p)-D3 7
2.4 nitro-Cu_3BTC_2: Extended cluster system on B3LYP/6-311+g(d,p)-D3* 9
2.5 ATPH: M06-2X/6-311+g(d)-D3* 9
3. Overview tables periodic calculation 11
3.1 Gas phase calculations with PBE-D2, in VASP 11
3.2 Cu_3BTC_2: PBE-D2 11
4. Detailed analysis of some free energy differences in function of temperature 13
5. Catalyst activity 14
6. Overview experimental results for the initial selectivity distribution 16
7. Detailed modeled selectivity profiles for all catalysts in this study 17
8. Level of theory study: influence of the functional on the selectivity 21

1. Preliminary cluster study on a copper paddle wheel: determination of relevant transition states

Table S.1: Overview of the bimolecular kinetic parameters for the citronellal cyclization. A (m^3 mol^{-1} s^{-1}) and E_a (kJ/mol) are fitted between 273 K and 473 K. The bimolecular kinetic coefficient (**$k_{fwd,383}$**, m^3 mol^{-1} s^{-1}) and free energy barrier (**$\Delta G^{\ddagger}_{383}$,** kJ/mol) are given. The used level of theory is B3LYP/6-31+g(d)-D3, with LanL2DZ effective core potential and basis set for Cu.

	A (m^3 mol^{-1} s^{-1})	**E_a (kJ/mol)**	**$k_{fwd,383}$ (m^3 mol^{-1} s^{-1})**	**$\Delta G^{\ddagger}_{383}$ (kJ/mol)**
Iso-1	2.98E+00	43.3	3.71E-06	123.4
Iso-1*	2.57E+00	112.3	1.24E-15	192.9
Iso-1**	5.06E+00	76.4	1.91E-10	154.9
Iso-2	2.68E+00	42.4	4.36E-06	122.9
Iso-2*	2.57E+00	98.3	9.86E-14	179.0
Iso-2**	5.57E+00	75.1	3.19E-10	153.2
neoiso-1	3.51E+00	47.0	1.34E-06	126.7
neoiso-1*	7.31E+00	114.4	1.80E-15	191.7
neoiso-1**	6.04E+00	67.5	3.69E-09	145.4
neoiso-2	6.71E+00	52.8	4.21E-07	130.3
neoiso-2*	1.42E+00	97.0	8.19E-14	179.5
neoiso-2**	-	-	-	-
isoiso-1	4.13E+00	51.9	3.38E-07	131.0
isoiso-1*	1.99E+00	119.4	1.02E-16	200.8
isoiso-1**	5.45E+00	68.5	2.47E-09	146.7
isoiso-2	2.08E+00	50.6	2.59E-07	131.9
isoiso-2*	3.26E+00	107.9	6.22E-15	187.8
isoiso-2**	1.55E+01	74.0	1.22E-09	148.9
neoisoiso-1	2.04E+00	54.1	8.43E-08	135.5
neoisoiso-1*	2.30E+01	119.7	1.07E-15	193.3
neoisoiso-1**	2.77E+00	65.4	3.27E-09	145.8

* = rotated isopropyl group

** = twisted boat

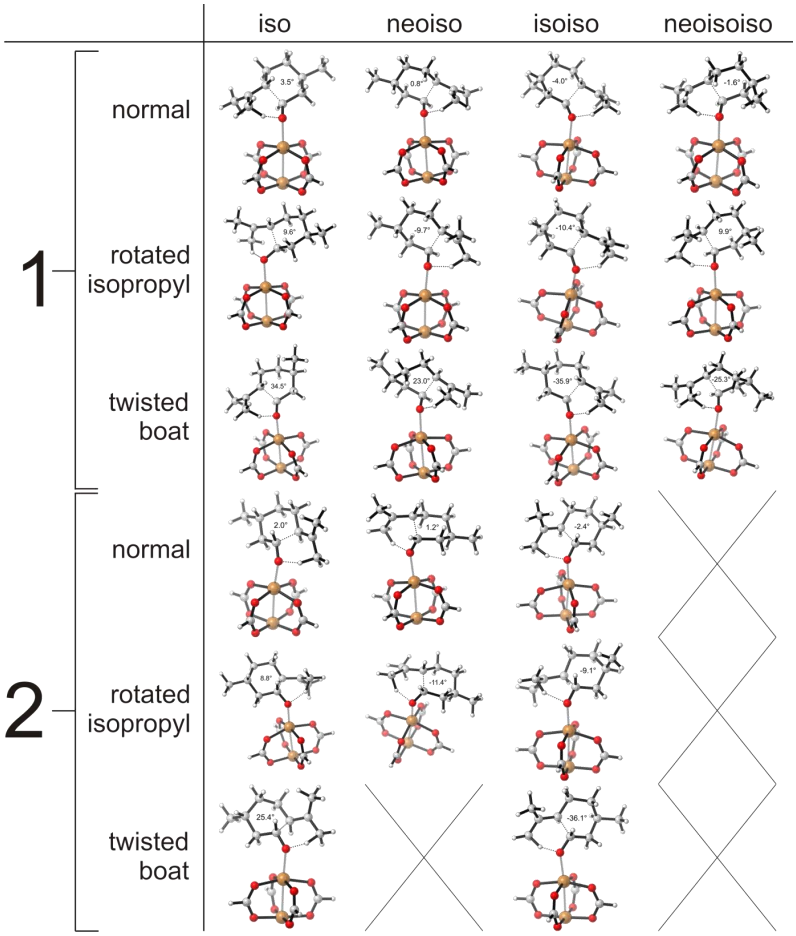

Figure S.1: Geometries of the transition states towards various isomers on a Cu-paddle wheel. Besides the two normal adsorption possibilities of citronellal on Cu (1 and 2), the isopropyl-group can be rotated or the forming cyclohexane ring can be twisted into a boat form. A cross in the figure represents that the transition state could not be found. The dihedral angle, connecting the bond forming carbon atoms in the cyclohexane ring with two opposite carbon atoms represent the deviation from planarity and is indicated in the figure.

Table S.2: Geometric parameters for the modeled transition states on a $Cu_2(HCOO)_4$ paddle wheel. The apparent free energy barrier at 383 K is given relative to the most stable transition state ($\Delta(\Delta G^{\ddagger}_{383})$).

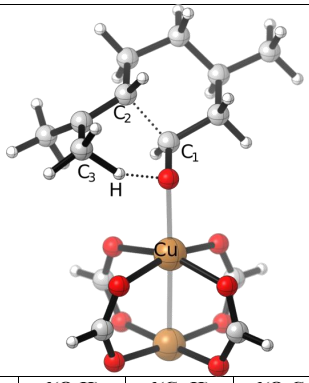

	d(C_1-C_2) (Å)	d(O-H) (Å)	d(C_3-H) (Å)	d(O-Cu) (Å)	$\gamma^{\ddagger}$ (cm^{-1})	$\Delta(\Delta G^{\ddagger}_{383})$ (kJ/mol)
Iso-1	1.78	1.5	1.22	2.14	-716.35	0.00
Iso-1*	1.74	1.72	1.19	2.11	-522.76	64.3
Iso-1**	1.79	1.49	1.23	2.14	-761.83	30.95
Iso-2	1.79	1.5	1.23	2.16	-778.43	3.26
Iso-2*	1.72	1.73	1.18	2.1	-440.13	58.93
Iso-2**	1.78	1.47	1.24	2.15	-865.93	31.42
neoiso-1	1.75	1.48	1.24	2.14	-806.06	4.13
neoiso-1*	1.79	1.66	1.19	2.13	-622.26	64.91
neoiso-1**	1.78	1.46	1.24	2.14	-858.11	25.01
neoiso-2	1.78	1.48	1.24	2.13	-835.67	6.17
neoiso-2*	1.8	1.59	1.21	2.12	-725.35	64.69
neoiso-2**	-	-	-	-	-	-
isoiso-1	1.78	1.5	1.22	2.14	-720.43	9.61
isoiso-1*	1.74	1.71	1.19	2.12	-533.29	76.38
isoiso-1**	1.79	1.49	1.23	2.14	-763.99	21.36
isoiso-2	1.79	1.49	1.23	2.16	-776.36	14.59
isoiso-2*	1.72	1.75	1.18	2.09	-415.73	69.26
isoiso-2**	1.81	1.47	1.23	2.16	-829.87	22.06
neoisoiso-1	1.75	1.49	1.24	2.14	-795.29	17.64
neoisoiso-1*	1.8	1.64	1.2	2.13	-656.42	70.13
neoisoiso-1**	1.78	1.46	1.24	2.14	-849.31	27.48

* = rotated isopropyl group
** = twisted boat

2. Overview tables of geometrical transition state parameters for the non-periodic simulations

The following section gives the most important distances of various transition state geometries, the transition state vibration and relative free energy at 383 K (in kJ/mol) for the specific catalyst. The level of theory corresponding with energy refinements will also be displayed in the title. In the case of Cu_3BTC_2, nitro-Cu_3BTC_2 and ATPH, the level of theory for the energy refinements was different from the level of theory for optimization. An ONIOM approach was used for those optimizations, describing the copper paddle wheel and the reacting citronellal at B3LYP/6-31+g(d) and the surroundings at B3LYP/3-21g. For the Cu atoms located in the high level part, a LanL2DZ basis set and effective core potential was applied. For ATPH, an ONIOM approach was used, describing the Al-site and the reacting citronellal at the M06-2X/6-31+g(d) and the 2,6-diphenylphenoxy linkers at M06-2X/3-21g. In the following, this whole procedures for the geometry optimization will be defined more shortly, by putting an extra star "*" behind the level of theory.

2.1 Gas phase: B3LYP/6-311+g(3df,2p)-D3

Table S.3: Geometric parameters for the modeled transition states in gas phase. The apparent free energy barrier is given relative to the most stable transition state ($\Delta(\Delta G^{\ddagger}_{383})$). The enthalpy and entropy contributions ($\Delta H^{\ddagger}_{383}$ and $-T.\Delta S^{\ddagger}_{383}$) to the apparent free energy barrier $\Delta G^{\ddagger}_{383}$ are also given separately at 383 K.

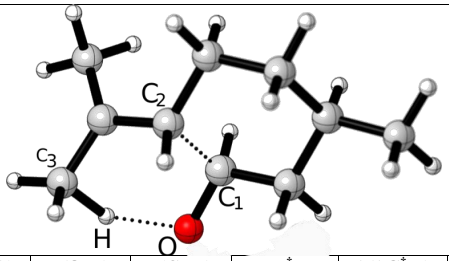

	$d(C_1\text{-}C_2)$ (Å)	**d(O-H) (Å)**	**$d(C_3\text{-}H)$ (Å)**	**$\gamma^{\ddagger}$ (cm^{-1})**	**$\Delta(\Delta G^{\ddagger}_{383})$ (kJ/mol)**	**$\Delta H^{\ddagger}_{383}$ (kJ/mol)**	**$-T.\Delta S^{\ddagger}_{383}$ (kJ/mol)**
iso	1.94	1.36	1.28	-1179.44	0.00	107.25	31.24
neoiso	1.95	1.36	1.29	-1256.02	5.15	112.22	31.42
isoiso	1.94	1.37	1.28	-1181.82	9.35	116.20	31.64
neoisoiso	1.95	1.36	1.29	-1250.95	14.81	121.41	31.89

2.2 Cu_3BTC_2: Extended cluster system on B3LYP/6-311+g(d,p)-D3*

At maximum, there exist 4 different new transition state geometries, when the gas phase cyclization is transferred to the catalyst (**Figure S.2**), the iso-propyl group can either be located in the big pocket (α) or in the small pocket (β) of the Cu_3BTC_2-cluster. Dependent on the way the carbonyl oxygen atom is adsorbed onto the cluster, the vector constructed from the carbon of the carbonyl group to the hydrogen bonded on that carbonyl group is either directed in (1) or out (2) of the plane of this papers.

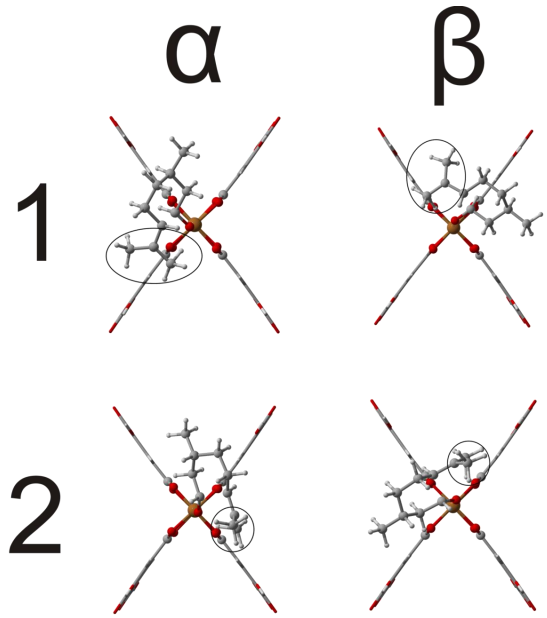

Figure S.2. Definition of the four different transition states possible for isopulegol. There are two adsorption possibilities corresponding with which free electron pair the carbonyl group of citronellal (1 and 2) is adsorbed on Cu. Seen from the top, the isopropyl-group of citronellal can be in the big pocket (α), but also in the small pocket (β).

Table S.4: Geometric parameters for the modeled transition states on an extended Cu_3BTC_2 cluster. The apparent free energy barrier is given relative to the most stable transition state ($\Delta(\Delta G^{\ddagger}_{383})$). The enthalpy and entropy contributions ($\Delta H^{\ddagger}_{383}$ and $-T.\Delta S^{\ddagger}_{383}$) to the apparent free energy barrier $\Delta G^{\ddagger}_{383}$ are also given separately at 383 K.

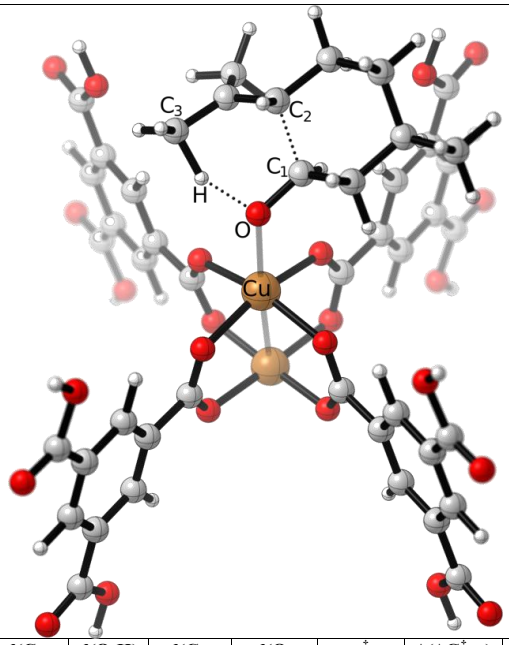

	d(C_1-C_2) (Å)	d(O-H) (Å)	d(C_3-H) (Å)	d(O-Cu) (Å)	$\gamma^{\ddagger}$ (cm^{-1})	$\Delta(\Delta G^{\ddagger}_{383})$ (kJ/mol)	$\Delta H^{\ddagger}_{383}$ (kJ/mol)	$-T.\Delta S^{\ddagger}_{383}$ (kJ/mol)
iso/1/alpha	1.75	1.54	1.22	2.17	-646.73	8.04	2.41	100.57
iso/1/beta	1.75	1.54	1.21	2.14	-633.96	7.20	0.69	101.44
iso/2/alpha	1.77	1.51	1.23	2.15	-743.05	0.00	-2.04	96.97
iso/2/beta	1.77	1.52	1.23	2.15	-741.99	2.82	-5.74	103.49
isoiso/1/alpha	1.76	1.54	1.21	2.13	-648.39	16.87	13.09	98.72
isoiso/1/beta	1.76	1.50	1.23	2.15	-731.85	12.74	4.09	103.59
isoiso/2/alpha	1.77	1.51	1.23	2.17	-770.53	11.11	7.56	98.48
isoiso/2/beta	1.77	1.51	1.22	2.14	-741.17	11.01	6.14	99.80
neoiso/1/alpha	1.73	1.54	1.23	2.14	-678.04	12.55	4.34	103.15
neoiso/1/beta	1.74	1.57	1.21	2.12	-604.16	12.76	6.83	100.86
neoiso/2/alpha	1.75	1.50	1.24	2.15	-830.38	5.61	1.39	99.15
neoiso/2/beta	1.75	1.50	1.24	2.14	-814.34	10.52	4.01	101.45
neoisoiso/1/alpha	1.71	1.53	1.23	2.15	-713.91	20.82	12.74	103.01
neoisoiso/1/beta	1.73	1.57	1.21	2.14	-593.69	17.85	12.75	100.04

2.3 $ZnBr_2$: B3LYP/6-311++g(3df,2p)-D3

The different modeled transition states are displayed in **Figure S.2**. $ZnBr_2$ has a smaller eigen-set of transition states to account then Cu_3BTC_2 because there are no different adsorption pockets. Transition state geometries with adsorption position 2 for neo- and neoiso-isopulegol were constructed, they however ended up to the same transition state as was obtained for adsorption position 1.

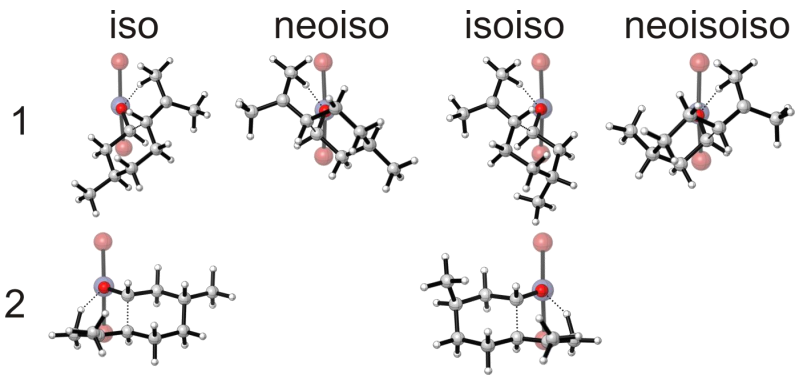

Figure S.3. Modeled transition states for the cyclization of citronellal on $ZnBr_2$ given at B3LYP/6-311+g(d,p). For neo- and neoiso-isopulegol the transition states with adsorption position 2 resulted in adsorption position 1 after optimization on the B3LYP/6-311+g(3df,2p) level of theory.

Table S.5: Geometric parameters for the modeled transition states on $ZnBr_2$. The apparent free energy barrier is given relative to the most stable transition state ($\Delta(\Delta G^{\ddagger}_{383})$). The enthalpy and entropy contributions ($\Delta H^{\ddagger}_{383}$ and $-T.\Delta S^{\ddagger}_{383}$) to the apparent free energy barrier $\Delta G^{\ddagger}_{383}$ are also given separately at 383 K.

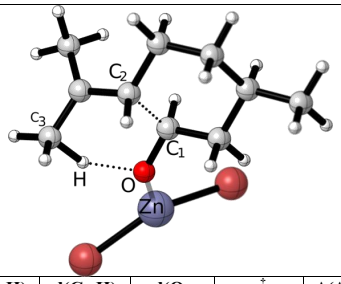

	d(C_1-C_2) (Å)	**d(O-H) (Å)**	**d(C_3-H) (Å)**	**d(O-Cu) (Å)**	**$\gamma^{\ddagger}$ (cm^{-1})**	**$\Delta(\Delta G^{\ddagger}_{383})$ (kJ/mol)**	**$\Delta H^{\ddagger}_{383}$ (kJ/mol)**	**$-T.\Delta S^{\ddagger}_{383}$ (kJ/mol)**
iso/1	1.67	1.52	1.22	1.99	-496.64	1.06	-3.79	78.72
iso/2	1.68	1.50	1.23	2.00	-591.36	0.00	-8.90	82.77
neoiso/1	1.68	1.52	1.23	1.98	-595.59	4.53	-0.94	79.34
isoiso/1	1.70	1.58	1.20	1.98	-500.04	8.50	3.74	78.63
isoiso/2	1.67	1.50	1.24	1.99	-589.54	8.86	-0.65	83.39
neoisoiso/1	1.68	1.52	1.23	1.99	-586.80	13.51	7.29	80.09

2.4 nitro-Cu_3BTC_2: Extended cluster system on B3LYP/6-311+g(d,p)-D3*

Table S.6: Geometric parameters for the modeled transition states on an extended cluster model for nitro-Cu_3BTC_2. The apparent free energy barrier is given relative to the most stable transition state ($\Delta(\Delta G^{\ddagger}_{383})$). The enthalpy and entropy contributions ($\Delta H^{\ddagger}_{383}$ and $-T.\Delta S^{\ddagger}_{383}$) to the apparent free energy barrier $\Delta G^{\ddagger}_{383}$ are also given separately at 383 K.

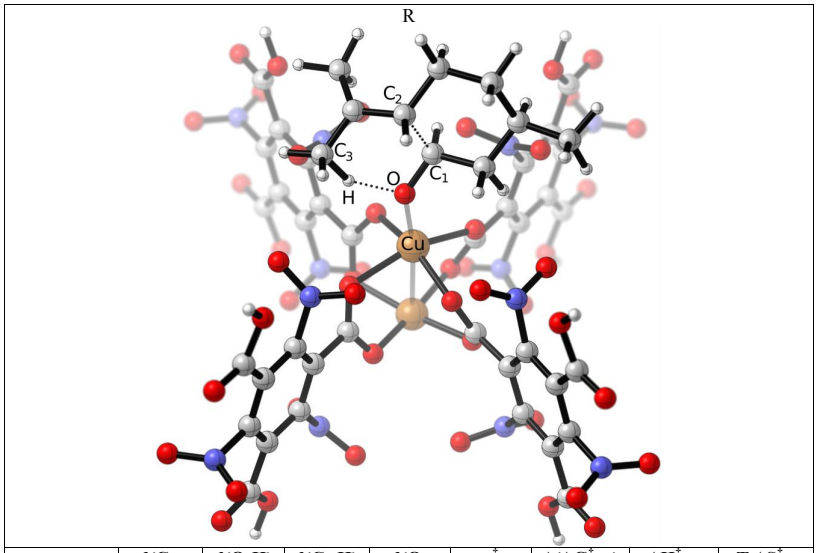

	$d(C_1$-$C_2)$ (Å)	**d(O-H) (Å)**	**$d(C_3$-H) (Å)**	**d(O-Cu) (Å)**	**$\gamma^{\ddagger}$ (cm^{-1})**	**$\Delta(\Delta G^{\ddagger}_{383})$ (kJ/mol)**	**$\Delta H^{\ddagger}_{383}$ (kJ/mol)**	**$-T.\Delta S^{\ddagger}_{383}$ (kJ/mol)**
iso/1	1.75	1.60	1.18	2.02	-421.29	0.00	-54.38	105.39
iso/2	1.70	1.54	1.22	2.05	-593.24	28.39	-28.84	108.24
neoiso/1	1.69	1.55	1.22	2.02	-556.98	13.29	-45.51	109.80
isoiso/1	1.75	1.60	1.18	2.01	-429.91	14.24	-43.14	108.39
neoisoiso/1	1.70	1.52	1.23	2.12	-629.29	74.67	12.71	112.96

2.5 ATPH: M06-2X/6-311+g(d)-D3*

Table S.7: Geometric parameters for the modeled transition states on an extended cluster model for ATPH. The apparent free energy barrier is given relative to the most stable transition state ($\Delta(\Delta G^{\ddagger}_{383})$). The enthalpy and entropy contributions ($\Delta H^{\ddagger}_{383}$ and $-T.\Delta S^{\ddagger}_{383}$) to the apparent free energy barrier $\Delta G^{\ddagger}_{383}$ are also given separately at 383 K.

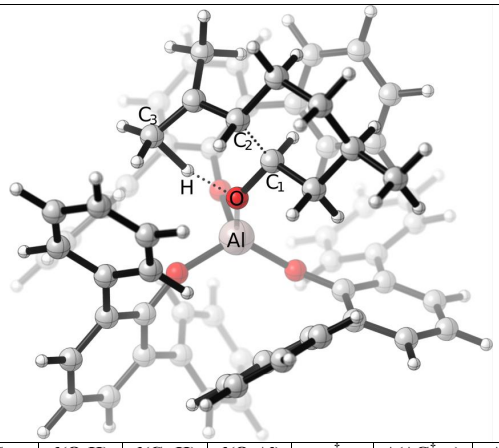

	d(C_1-C_2) (Å)	d(O-H) (Å)	d(C_3-H) (Å)	d(O-Al) (Å)	$\gamma^{\ddagger}$ (cm^{-1})	$\Delta(\Delta G^{\ddagger}_{383})$ (kJ/mol)	$\Delta H^{\ddagger}_{383}$ (kJ/mol)	$-T.\Delta S^{\ddagger}_{383}$ (kJ/mol)
iso	1.60	1.51	1.26	1.78	-780.26	0.00	-103.45	109.56
neoiso	1.61	1.52	1.26	1.77	-706.30	19.56	-90.15	115.81
isoiso	1.60	1.55	1.24	1.78	-732.29	6.32	-100.08	112.52
neoisoiso	1.61	1.52	1.25	1.80	-719.78	37.76	-75.54	119.41

3. Overview tables periodic calculation

3.1 Gas phase calculations with PBE-D2, in VASP

Table S.8: Geometric parameters for the modeled transition states in gas phase. The apparent free energy barrier is given relative to the most stable transition state ($\Delta(\Delta G^{\ddagger}_{383})$). The enthalpy and entropy contributions ($\Delta H^{\ddagger}_{383}$ and $-T.\Delta S^{\ddagger}_{383}$) to the apparent free energy barrier $\Delta G^{\ddagger}_{383}$ are also given separately at 383 K.

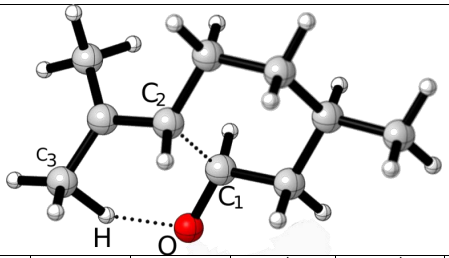

	$d(C_1-C_2)$ (Å)	**d(O-H) (Å)**	**$d(C_3-H)$ (Å)**	**$\gamma^{\ddagger}$ (cm^{-1})**	**$\Delta(\Delta G^{\ddagger}_{383})$ (kJ/mol)**	**$\Delta H^{\ddagger}_{383}$ (kJ/mol)**	**$-T.\Delta S^{\ddagger}_{383}$ (kJ/mol)**
iso	1.96	1.41	1.25	-808.37	0.00	61.31	48.28
neoiso	1.94	1.4	1.27	-879.96	3.81	65.89	47.51
isoiso	1.95	1.42	1.25	-792.6	8.96	69.47	49.08
neoisoiso	1.94	1.41	1.27	-863.44	12.46	74.42	47.63

3.2 Cu_3BTC_2: PBE-D2

Table S.9: Geometric parameters for the modeled transition states in Cu_3BTC_2. The apparent free energy barrier is given relative to the most stable transition state ($\Delta(\Delta G^{\ddagger}_{383})$). The enthalpy and entropy contributions ($\Delta H^{\ddagger}_{383}$ and $-T.\Delta S^{\ddagger}_{383}$) to the apparent free energy barrier $\Delta G^{\ddagger}_{383}$ are also given separately at 383 K.

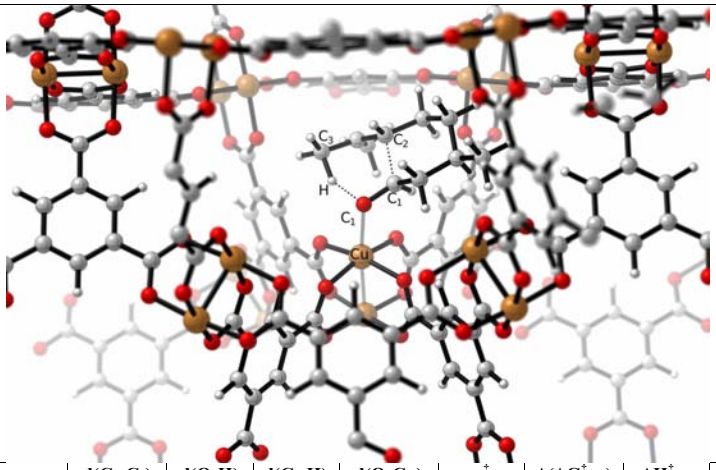

	d(C_1-C_2) (Å)	d(O-H) (Å)	d(C_3-H) (Å)	d(O-Cu) (Å)	$\gamma^{\ddagger}$ (cm^{-1})	$\Delta(\Delta G^{\ddagger}_{383})$ (kJ/mol)	$\Delta H^{\ddagger}_{383}$ (kJ/mol)	$-T.\Delta S^{\ddagger}_{383}$ (kJ/mol)
iso/1/alpha	1.83	1.56	1.21	2.17	-519.22	0.00	-51.23	117.83
iso/1/beta	1.83	1.55	1.21	2.16	-529.11	8.35	-50.48	125.43
iso/2/alpha	1.83	1.55	1.21	2.17	-528.64	4.79	-47.67	119.07
iso/2/beta	1.84	1.55	1.21	2.17	-527.94	4.22	-49.33	120.15
isoiso/1/alpha	1.85	1.59	1.19	2.12	-457.84	15.11	-33.28	114.99
isoiso/1/beta	1.84	1.56	1.20	2.14	-485.80	11.02	-41.86	119.49
isoiso/2/alpha	1.84	1.55	1.21	2.16	-545.36	15.36	-36.54	118.51
isoiso/2/beta	1.84	1.55	1.20	2.16	-515.80	6.41	-47.62	120.63
neoiso/1/alpha	1.78	1.57	1.21	2.12	-487.00	15.45	-42.07	124.12
neoiso/1/beta	1.78	1.57	1.21	2.10	-477.64	14.19	-38.74	119.53
neoiso/2/alpha	1.82	1.51	1.23	2.12	-613.61	15.76	-36.00	118.36
neoiso/2/beta	1.82	1.52	1.22	2.11	-603.81	8.84	-38.95	114.40
neoisoiso/1/alpha	1.77	1.59	1.20	2.11	-456.98	22.20	-28.24	117.05
neoisoiso/1/beta	1.77	1.58	1.21	2.11	-467.64	24.88	-27.12	118.60

4. Detailed analysis of some free energy differences in function of temperature

Table S.10: Free energy differences between the various products at different temperatures (in K). The level of theory used is B3LYP/6-311+g(3df,2p).

T (in K)	isopulegol	neoisopulegol	isoisopulegol	neoisoisopulegol
0	0.0	4.2	10.5	17.0
323	0.0	4.3	10.5	17.2
373	0.0	4.4	10.6	17.4
423	0.0	4.5	10.6	17.5
473	0.0	4.5	10.7	17.7

Table S.11: Free energy differences between the various products at different temperatures (in K) for the cyclization of citronellal on ATPH. The level of theory used is M06-2X/6-311+g(3df,2p)-D3/ONIOM(M06-2X/6-31+g(d)//M06-2X/3-21g).

	Temperature (K)	**$\Delta(\Delta G^{\ddagger}_{383})$ (kJ/mol)**	**$\Delta(\Delta H^{\ddagger}_{383})$ (kJ/mol)**	**$-T.\Delta(\Delta S^{\ddagger}_{383})$ (kJ/mol)**	**$\Delta H^{\ddagger}_{383}$ (kJ/mol)**	**$-T.\Delta S^{\ddagger}_{383}$ (kJ/mol)**
iso	0	0.00	0.00	0.00	-102.63	77.38
neoiso	0	17.75	13.27	4.48	-89.36	81.87
isoiso	0	5.42	3.08	2.35	-99.56	79.73
neoisoiso	0	34.94	28.01	6.93	-74.62	84.31
iso	323	0.00	0.00	0.00	-103.11	92.08
neoiso	323	18.57	13.28	5.30	-89.83	97.38
isoiso	323	5.85	3.19	2.66	-99.92	94.74
neoisoiso	323	36.22	27.93	8.29	-75.18	100.37
iso	373	0.00	0.00	0.00	-103.41	106.66
neoiso	373	19.39	13.30	6.10	-90.11	112.76
isoiso	373	6.25	3.33	2.91	-100.08	109.57
neoisoiso	373	37.51	27.91	9.60	-75.50	116.25
iso	423	0.00	0.00	0.00	-103.55	121.11
neoiso	423	20.21	13.32	6.88	-90.23	127.99
isoiso	423	6.63	3.50	3.13	-100.06	124.24
neoisoiso	423	38.79	27.93	10.86	-75.62	131.97
iso	473	0.00	0.00	0.00	-103.56	135.43
neoiso	473	21.02	13.36	7.66	-90.20	143.10
isoiso	473	6.99	3.66	3.32	-99.90	138.76
neoisoiso	473	40.07	27.98	12.09	-75.58	147.52

5. Catalyst activity

In **Figures S.4-S.7** the plots are given that were used to determine the experimental reaction rates k_x.

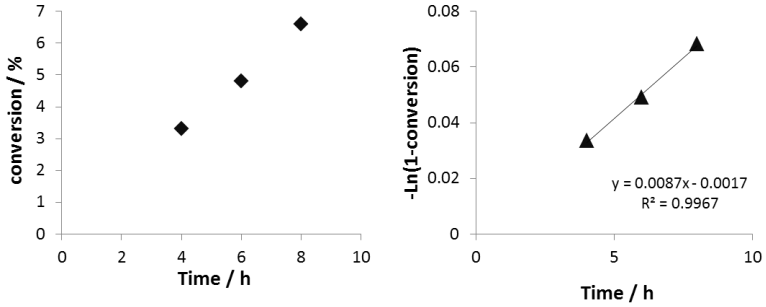

Figure S.4. Conversion curve of citronellal over CuBTC at 373K (left) and –Ln(1-conversion) *vs* time plot (right).

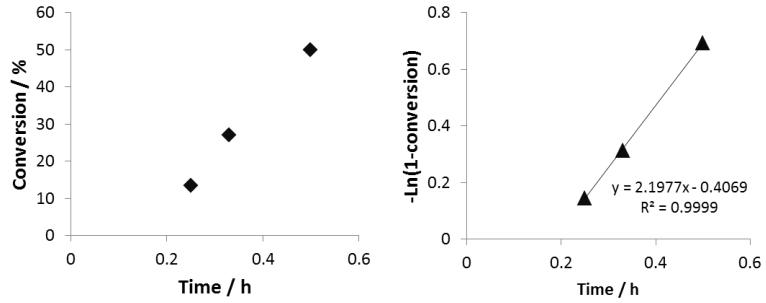

Figure S.5. Conversion curve of citronellal over $ZnBr_2$ at 373K (left) and –Ln(1-conversion) *vs* time plot (right).

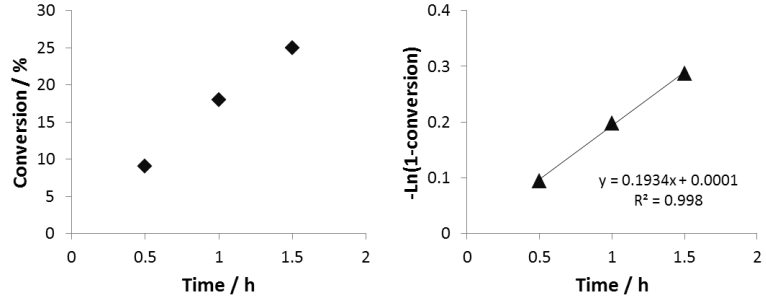

Figure S.6. Conversion curve of citronellal over $ZnBr_2$ at 298K (left) and –Ln(1-conversion) *vs* time plot (right).

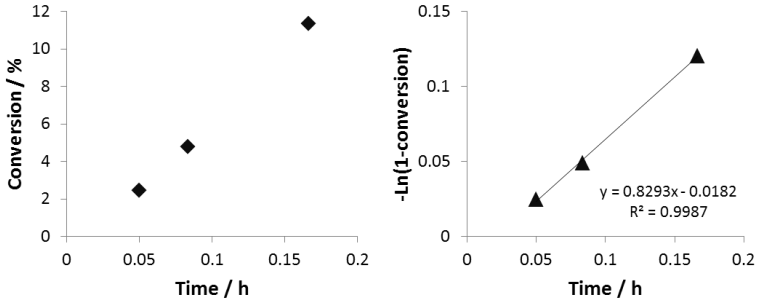

Figure S.7. Conversion curve of citronellal over ATPH at 298K (left) and -Ln(1-conversion) *vs* time plot (right).

6. Overview experimental results for the initial selectivity distribution

In a typical reaction run, 1g of citronellal was added to 0.1g of activated Cu_3BTC_2. The reaction was carried out at different temperatures. The selectivity and conversion at 373 K was corrected with the thermal reaction.

Table S.12 :

	Conversie (%)	S_{ISO} (%)	S_{NEOISO} (%)	S_{ISOISO} + $S_{NEOISOISO}$ (%)
373 K 8u substr kata 10/1	5.9	71.3	23.1	5.6
423 K 30 min substr/kata 10/1	11.2 11.5	67.1 67.9	25.0 24.6	8.0 7.5
443 K 10 min substr/kata 20/1	7.3 7.2 7.3	67.0 66.7 67.0	24.5 24.5 24.4	8.5 8.8 8.6
463 K 5 min substr/kata 20/1	4.9 4.9 4.9	66.3 66.2 66.1	24.8 24.6 24.9	8.9 9.3 9.1
483 K 3 min substr/kata 20/1	5.1 5.1 5.1	65.9 65.6 65.4	24.8 24.8 24.8	9.4 9.6 9.7

The highest selectivities were obtained using ATPH as a catalyst.

After 10 minutes at 298 K a 11.4 % of citronellal was converted with a selectivity of 98.1% towards the isopulegol isomers. The selectivity of isopulegol to other isomers is 97.9% (ratio: 97.9/1/1.1).

Using $ZnBr_2$ as a catalyst at 298 K the selectivity of isopulegol to the other isomers drops to 88%. When increasing the temperature to 373 K this selectivity remains more or less the same at 87.5%.

The lowest selectivities are obtained using CuBTC as a catalyst. In Table S.12 the selectivities in function of the temperature at low conversion (5-15 %) are given.

From this table it is clear that the selectivity towards the desired isopulegol slightly drops when increasing the temperature.

7. Detailed modeled selectivity profiles for all catalysts in this study

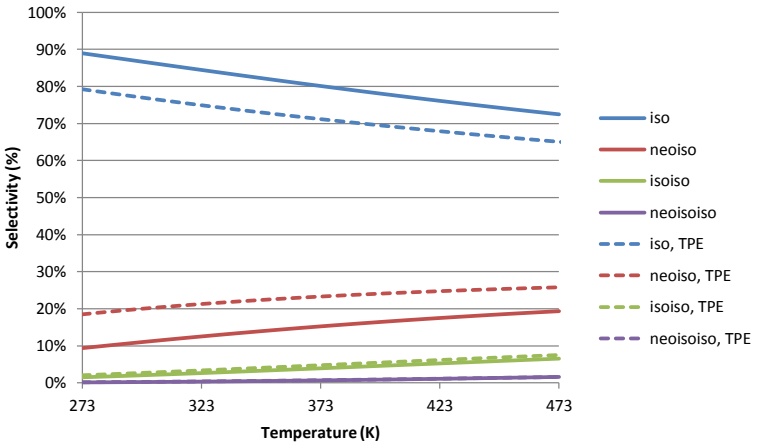

Figure S.8: Initial gas phase selectivity based Curtin Hammett principle (full lines) versus the thermodynamic product selectivity (dotted lines, TPE=Thermodynamic Product Equilibrium). Results at the B3LYP/6-311+g(3df,2p)-D3 level of theory.

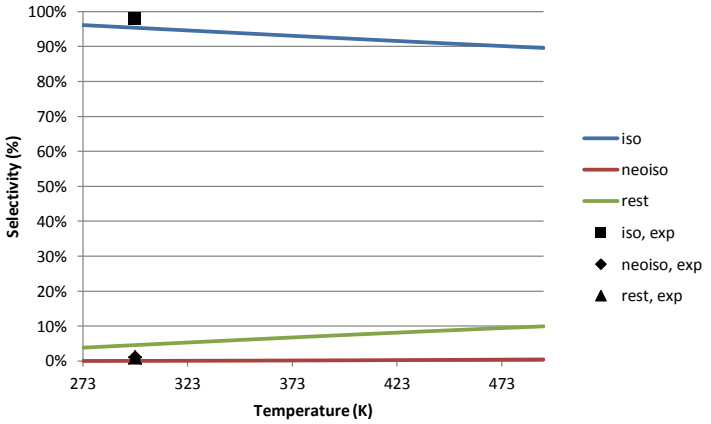

Figure S.9: Selectivity profiles of the citronellal cyclization on ATPH. Results at the m06-2X/6-311+g(d,p)-D3 level of theory.

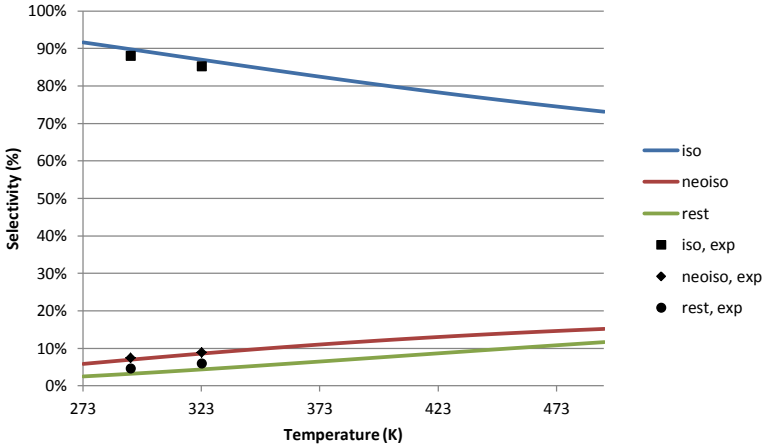

Figure S.10: Selectivity profiles of the citronellal cyclization on $ZnBr_2$. Results at the B3LYP/6-311++g(3df,2p)-D3 level of theory. Rest = isoisopulegol + neoisoisopulegol.

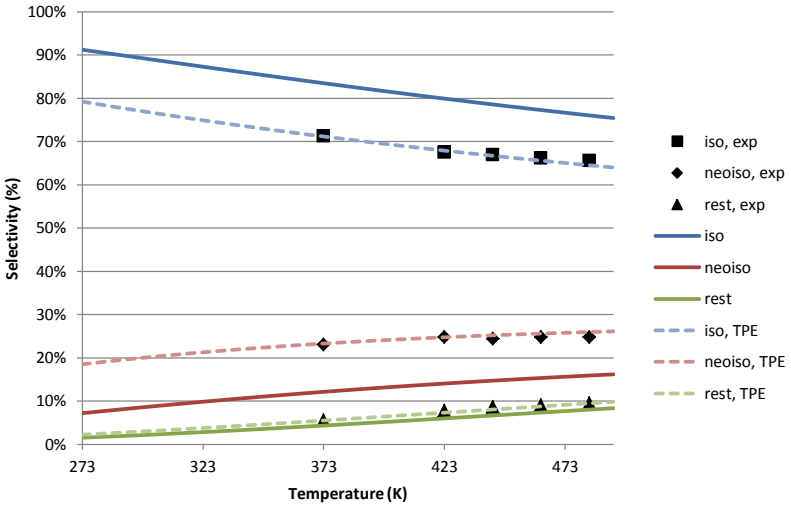

Figure S.11: Selectivity profiles of the citronellal cyclization on Cu_3BTC_2; the experimental selectivities are compared with those of the extended cluster model. Results at the B3LYP/6-311+g(3df,2p)-D3 level of theory. Rest = isoisopulegol + neoisoisopulegol. TPE = Thermodynamic Product Equilibrium.

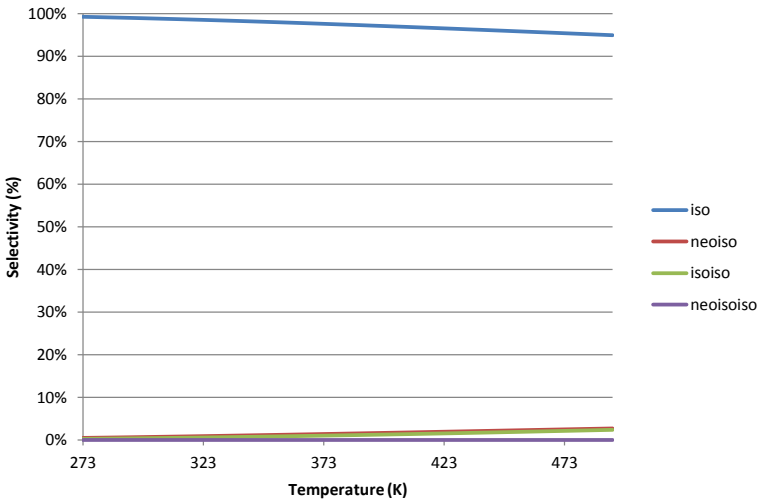

Cu_3BTC_2-NO_2. Results at the B3LYP/6-311+g(3df,2p)-D3 level of theory.

8. Level of theory study: influence of the functional on the selectivity

Table S.13: Overview of the free energy differences between the transition states at different levels of theory for the citronellal cyclization in gas phase. Those are given for the level of theory used during the optimization and also after the addition of dispersion corrections (D3) according to Grimme.

Level of theory	iso	neoiso	isoiso	neoisoiso
b3lyp/6-311+g(3df,2p)	0.0	5.9	11.4	18.2
b3lyp/6-311+g(3df,2p)-D3	0.0	5.1	9.4	14.8
M06L/6-311+g(3df,2p)	0.0	4.2	7.8	13.8
M06L/6-311+g(3df,2p)-D3	0.0	4.2	7.7	13.7
M062X/6-311+g(3df,2p)	0.0	2.9	8.7	12.8
M062X/6-311+g(3df,2p)-D3	0.0	2.9	8.6	12.7
TPSS/6-311+g(3df,2p)	0.0	5.2	10.4	16.8
TPSS/6-311+g(3df,2p)-D3	0.0	4.4	8.5	13.7

Table S.14: Overview of the free energy differences between the transition states at different levels of theory for the citronellal cyclization on $ZnBr_2$ (383 K). Those are given for the level of theory used during the optimization and also after the addition of dispersion corrections (D3) according to Grimme.

Level of theory	iso/1	iso/2	neoiso/1	isoiso/1	isoiso/2	neoisoiso/1
b3lyp/6-311+g(3df,2p)	0.0	7.0	4.9	10.4	17.9	17.9
b3lyp/6-311+g(3df,2p)-D3	1.1	0.0	4.5	8.5	8.9	13.5
M06L/6-311+g(3df,2p)	1.7	0.0	5.7	6.6	5.8	14.0
M06L/6-311+g(3df,2p)-D3	1.5	0.0	5.4	6.2	5.8	13.6
M062X/6-311+g(3df,2p)	0.6	0.0	1.5	7.1	8.1	10.2
M062X/6-311+g(3df,2p)-D3	0.5	0.0	1.3	6.8	8.1	10.0
TPSS/6-311+g(3df,2p)	0.0	5.9	4.9	3.9	14.6	17.9
TPSS/6-311+g(3df,2p)-D3	1.5	0.0	5.3	2.5	7.0	14.8

9. Level of theory study: influence of the functional on the selectivity

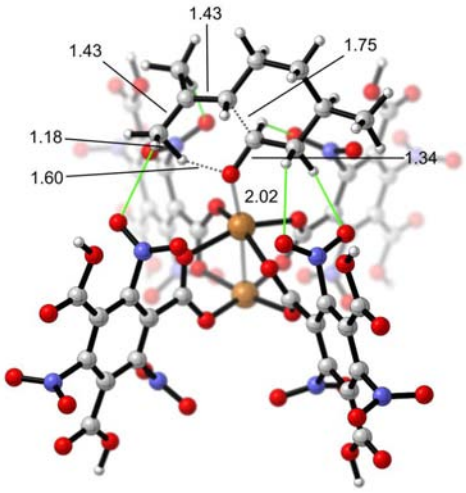

Figure S.13: The transition state of the citronellal cyclization towards isopulegol with indication of key geometrical parameters. Green lines indicate possible Interactions (<3 Å) between the hydrogens of citronellal and the nitro groups.

Paper 10

Host-guest and guest-guest interactions between xylene isomers confined in the MIL-47(V) pore system

An Ghysels, Matthias Vandichel, Toon Verstraelen, Monique A. van der Veen, Dirk E. De Vos, Michel Waroquier and Veronique Van Speybroeck

Theoretical Chemistry Accounts, 2012, 131, 1234 - 1246

Copyright 2012 by Springerlink.

Theor Chem Acc (2012) 131:1234
DOI 10.1007/s00214-012-1234-7

REGULAR ARTICLE

Host–guest and guest–guest interactions between xylene isomers confined in the MIL-47(V) pore system

An Ghysels · Matthias Vandichel · Toon Verstraelen · Monique A. van der Veen · Dirk E. De Vos · Michel Waroquier · Veronique Van Speybroeck

Received: 1 March 2012 / Accepted: 8 May 2012
© Springer-Verlag 2012

Abstract The porous MIL-47 material shows a selective adsorption behavior for para-, ortho-, and meta-isomers of xylenes, making the material a serious candidate for separation applications. The origin of the selectivity lies in the differences in interactions (energetic) and confining (entropic). This paper investigates the xylene–framework interactions and the xylene–xylene interactions with quantum mechanical calculations, using a dispersion-corrected density functional and periodic boundary conditions to describe the crystal. First, the strength and geometrical characteristics of the optimal xylene–xylene interactions are quantified by studying the pure and mixed pairs in gas phase. An extended set of initial structures is created and optimized to sample as many relative orientations and distances as possible. Next, the pairs are brought in the pores of MIL-47. The interaction with the terephthalic linkers and other xylenes increases the stacking energy in gas phase (−31.7 kJ/mol per pair) by roughly a factor four in the fully loaded state (−58.3 kJ/mol per xylene). Our decomposition of the adsorption energy shows various trends in the contributing xylene–xylene interactions. The absence of a significant difference in energetics between the isomers indicates that entropic effects must be mainly responsible for the separation behavior.

Keywords Adsorption · MIL-47 · DFT-D · Xylenes · Separation

Published as part of the special collection of articles celebrating theoretical and computational chemistry in Belgium.

Electronic supplementary material The online version of this article (doi:10.1007/s00214-012-1234-7) contains supplementary material, which is available to authorized users.

A. Ghysels (✉) · M. Vandichel · T. Verstraelen · M. Waroquier · V. Van Speybroeck (✉)
Center for Molecular Modeling, Quantum Chemistry-Molecular Modeling Alliance, Ghent University, Technologiepark 903, 9052 Ghent, Belgium
e-mail: an.ghysels@ugent.be

V. Van Speybroeck
e-mail: veronique.vanspeybroeck@ugent.be

M. A. van der Veen · D. E. De Vos
Centre for Surface Chemistry and Catalysis, KU Leuven, Kasteelpark Arenberg 23, 3001 Heverlee, Belgium

1 Introduction

Since a couple of years, metal organic frameworks (MOFs) are a topical theme; they represent a new class of porous materials with extraordinary physicochemical and mechanical properties due to their hybrid architecture of organic and inorganic building blocks [1–3]. Their applications in the field of gas adsorption, storage, gas separation, and catalysis are almost inexhaustible due to the specificity of the hybrid organic–inorganic composition [4–7]. Examples of their fascinating properties are the flexibility of the framework, the appearance of catalytic sites in the pores, etc. These are a consequence of the unique combination of properties typical for metals and organic species.

In previous work, some of the authors showed that metal organic frameworks could be successfully used as selective adsorbents for the industrially relevant separations of para-xylene (pX) versus meta-xylene (mX) and ortho-xylene (oX) versus ethylbenzene (eB) [8–10]. The separation of mixed C8 alkylaromatic compounds is one of the most challenging issues in the chemical industry, for example because of its direct link with PET production [11]. Among the various types of MOFs that have been tested, the MIL-47 material proved to be very successful. This MOF

Published online: 21 June 2012

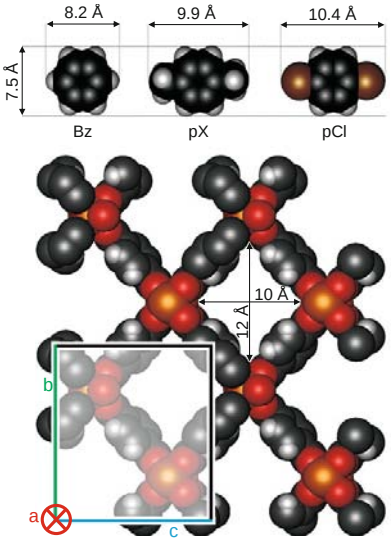

Fig. 1 MIL-47 consists of terephthalic linkers connected by VO^{2+} ions. Xylenes adsorb well in the one-dimensional pore channels. View along the *a* direction; four unit cells are displayed. The pore dimensions of MIL-47 and the characteristic dimensions of the adsorbates are estimated by assigning van der Waals radii to the atoms

consists of one-dimensional pores in which terephthalate ligands are connected by VO^{2+} ions (Fig. 1). MIL-47 is one of an impressive series of MOFs that were synthesized by Férey et al. [12]. It is not completely clear what mechanism is responsible for the preference of adsorption between the three types of xylene isomers and ethylbenzene. In this paper, we try to unravel the molecular interactions between pairs of adsorbed xylenes and between xylenes and organic linkers using in silico experiments. The interactions are studied with quantum mechanical periodic modeling. Once the mechanism of selectivity in adsorption has been understood, the obtained knowledge can be used for designing new materials with tailor-made properties toward gas separation and to possibly modify the organic linkers to control the affinity for specific aromatic adsorbates.

Long-range dispersion interactions and more particularly π–π stacking interactions will manifestly play an important role for the organization of xylenes in the pore. Basically, only very advanced ab initio correlated wave function methods are able to account for these effects, but they are computationally too demanding to apply to our system. Nowadays, density functional theory (DFT) is the most widely used method for electronic structure calculations for extended molecular systems, but without modifications, these methods are not able to account for long-range electrostatic correlations that are responsible for the dispersion forces. Grimme et al. [13–15] proposed the DFT-D method in which an empirical C_6R^{-6} correction is added to the standard density functionals. This method is able to account for the π–π interactions in MOFs [14].

Several molecular modeling studies investigated various adsorbates with grand canonical Monte Carlo techniques (GCMC) on MIL-47: N_2 [16], CO_2 [17], CH_4 [18], H_2 [19], and xylenes [20]. GCMC techniques usually rely on fast classical force field descriptions of the global potential energy of the system. So, GCMC techniques allow a fast computation of thermodynamic quantities and they have been frequently and successfully applied to explain separations over MOFs [16, 20–24]. The force fields required to perform the molecular simulations are taken from the literature. The accuracy of these classical approaches will certainly be improved in the near future when more advanced force fields are available for these particular MOFs that also account for the flexibility of the framework [25]. In the MIL-47 study by Castillo et al. [20], good agreement is found with isotherm experiments using a model with partial atomic charges and the Lennard-Jones potential for the van der Waals interactions. The framework is kept rigid during the simulations. The computed mixture isotherms of the xylene isomers lead to separation factors in MIL-47 predicting a preferential adsorption for ortho-xylene (oX), closely followed by para (pX), and then meta (mX). The adsorption selectivity was found to increase with pressure and the results agree with the experimental findings. The computed adsorption isotherms manifestly overestimate the loading of para- and ortho-xylene at the lowest temperatures. The authors attribute this discrepancy to small changes in the framework structure with temperature. The saturation loading reached in their simulations was about 4 molecules per unit cell, while experimentally the maximum loading was 3.4 molecules per unit cell [8, 9].

The selectivity of xylene isomers in MIL-47 most likely originates from packing effects, as suggested by Alaerts and Finsy et al. [8, 9]. It has been speculated that molecules are adsorbed by pairs at high loadings, their benzene rings facing each other and approximately parallel to the aromatic rings of the terephthalate linkers. Additionally, the spatial arrangement of the methyl groups of each xylene should play a significant role in the determination of the preferential adsorption. It is suspected that the crude force field used in the work of Castillo et al. cannot properly describe these packing effects. With the current lack of

suitable more accurate force fields, quantum chemical DFT-D calculations can give some added value in the underlying mechanism for the selective adsorption of xylene isomers. Stacking effects are more accurately described when taking into account the long-range dispersion interactions by using the empirical Grimme corrections [13] complementary to the standard density functionals. A DFT-D approach also has the advantage that the adsorption and stacking energy can be decoupled in various contributions elucidating the interactions responsible for the observed different adsorption behavior. In contrast to the molecular simulations of Castillo et al. [20], we also incorporate in this study the packing of mixed xylene pairs such as pX–oX, pX–mX and oX–mX.

In this work, we first investigate xylene–xylene interactions in the gas phase. The strength of the xylene stacking energy is compared to the stacking energy of benzene pairs and dichlorobenzene pairs. Benzene stacking is well studied [26–28], and dichlorobenzene adsorption shows experimentally a similar selectivity behavior in MIL-47 as xylenes [29]. Next, the pairs are embedded in the MIL-47 framework respecting the maximum loading of two xylene pairs in one unit cell. An extensive set of configurations for the adsorbed xylenes is generated. As such, we are able to validate the effect of the confined environment and interaction with the walls of the material. The adsorption energy of the most stable configuration is studied in detail using an energy decomposition scheme to achieve more insight into the host–guest and guest–guest interactions.

2 Computational methods

2.1 Characterization of a xylene pair

A thorough study on the interaction between xylene pairs will be performed, and thus it is essential to give a good definition of their relative position with respect to each other. The relative position and orientation of a xylene pair is characterized by attaching a Cartesian coordinate frame to each xylene (Fig. 2a) [30] denoted as $(O_1, \boldsymbol{x}_1, \boldsymbol{y}_1, \boldsymbol{z}_1)$ and $(O_2, \boldsymbol{x}_2, \boldsymbol{y}_2, \boldsymbol{z}_2)$ for the two xylenes, X_1 and X_2, respectively. The $\boldsymbol{x}$-axis always coincides with the twofold rotational symmetry axis of each xylene. Note that in the three-dimensional structure, the orientation of the methyl groups may prevent the existence of this C_2 symmetry, but the symmetry axis is always present in the projection on paper (Fig. 2a). The sense of $\boldsymbol{z}_2$ is chosen such that the angle between $\boldsymbol{z}_1$ and $\boldsymbol{z}_2$ is less than 90°. In principle, the relative orientation of two molecules is completely characterized by six parameters. For this work, we only consider the four most important internal coordinate parameters to describe

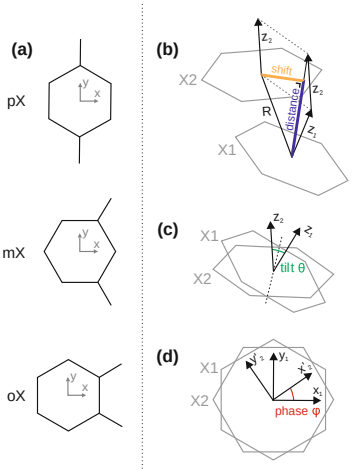

Fig. 2 A coordinate system is attached to each xylene (X_1 and X_2) in a xylene pair. Four parameters are defined to describe their relative position and orientation: shift (s), distance (d), tilt (θ), and phase (φ)

their relative orientation: distance (d), shift (s), tilt (θ), and phase (φ). These are defined below such that an interchange of X_1 and X_2 or a point inversion results in the same values for these four parameters.

The distance parameter d is the length of the projection of the vector $\boldsymbol{R}$ (connecting the centers of the six-membered rings) on the vector $\boldsymbol{z}_1 + \boldsymbol{z}_2$ (Fig. 2b). The length of the orthogonal complement in this projection is called the shift s. Next, X_2 is translated over the vector $\boldsymbol{R}$ to bring the geometric centers of the six-membered rings on top of each other (Fig. 2c). The tilt θ is defined as the angle between the $\boldsymbol{z}_1$- and $\boldsymbol{z}_2$-axis. X_2 is then rotated over θ about the vector $\boldsymbol{z}_1 \times \boldsymbol{z}_2$, such that $(O_2', \boldsymbol{x}_2, \boldsymbol{y}_2, \boldsymbol{z}_2) \rightarrow (O_2', \boldsymbol{x}_2', \boldsymbol{y}_2', \boldsymbol{z}_1)$; the $\boldsymbol{z}$-axes of the xylenes are now aligned and the $\boldsymbol{x}$-axes and $\boldsymbol{y}$-axes lie in the same plane (Fig. 2d). Finally, the phase φ is determined as the absolute value of the angle between the $\boldsymbol{x}_1$- and $\boldsymbol{x}_2'$-axis.

The above procedure is also applied to a benzene pair and dichlorobenzene pairs.

2.2 Quantumchemical modeling

Density functional theory calculations are carried out using the CPMD code, which allows to simulate systems with periodic boundary conditions [31]. The BP exchange correlation functional [32] is used with ultrasoft Vanderbilt pseudopotentials [33], especially designed to work with a

25 Ry cut off for the auxiliary plane wave grid. To include the possible effects of π–π interactions, the BP functional is combined with the Grimme dispersion correction for van der Waals interactions [13]. Three types of systems are simulated: xylenes in vacuum, the empty MIL-47 framework, and the fully loaded MIL-47 framework with four xylenes per unit cell.

Vacuum calculations of a xylene molecule or a pair of xylenes are performed in a large box of $20 \times 20 \times 20$ Å^3 and are labeled with 'vac'. The investigated molecules are para-xylene (pX), ortho-xylene (oX), and meta-xylene (mX). In addition, benzene (Bz) and dichlorobenzenes in para-, ortho-, and meta-configuration (pCl, oCl, mCl) are simulated in vacuum for comparison.

The initial framework geometry of the empty MIL-47 is taken directly from the refined structure obtained by X-ray diffraction (Supp. Info. of Ref. [12], CCDC-166785, orthorhombic unit cell with $a = 6.8179$ Å, $b = 16.1433$ Å, $c = 13.9392$ Å). In the energy minimization, the internal coordinates are optimized while the unit cell parameters are kept fixed at the experimental values. The metal V^{4+} ions in MIL-47 have each spin ½. The unit cell containing four vanadium centers can have a total spin of 0, 1, or 2. The most stable structure corresponds with $S = 1$, and the gain in energy with respect to the $S = 0$ system amounts to 80 kJ/mol per unit cell. As adsorption energies require the computation of differences in energy, the differences due to the usage of another spin state cancel out if we consistently use the same total spin for the framework. In view of the computational cost, all calculations were performed with $S = 0$.

In the fully loaded state, two xylene pairs are inserted in the pores of MIL-47 with the Zeobuilder package [34], and the geometry is optimized with CPMD [31]. The experimental unit cell parameters are used when MIL-47 is fully loaded with pure pX, oX, or mX (codes CCDC-632101, CCDC-632102, CCDC-632103, respectively [8]). Because of lack of experimental values during multicomponent adsorption experiments, the cell parameters are chosen somewhat arbitrarily when MIL-47 is fully loaded with a mixture of the xylene isomers: the pure oX experimental parameters for the pX–oX mixture (code CCDC-632102 [8]) and the empty framework parameters for pX–mX and oX–mX mixtures (code CCDC-166785 [12]). The variation in cell parameters among the structures is minimal, and keeping them fixed during the geometry optimization is an approximation whose effect is expected to largely cancel when calculating energy differences. The coordinate files of the optimized structures are available in the Supporting Information for the empty framework and the various fully loaded states. The decomposition of adsorption energies in Sect. 3 is derived from static calculations, where xylenes or framework atoms are removed from the fully loaded state and the energy is calculated without prior geometry optimization. These energies are labeled with 'stat'.

3 Results and discussion

3.1 Guest–guest interactions in gas phase

Before tackling the xylenes interactions in the MIL-47 pore system, it is useful to have an understanding of the stacking of xylenes in the gas phase. Therefore, we construct a series of xylene pairs, and the geometry and the stacking energy are investigated for each of them. The geometry is characterized by the four geometry parameters in Fig. 2: shift, distance, tilt, and phase. The stacking energy is calculated from the optimized geometry of the individual xylene molecules X_1 and X_2 and of a xylene pair P_{12}. The *stacking energy* is defined as

$$\Delta E^{\text{vac}}_{\text{stack}}(P_{12}) = E^{\text{vac}}(P_{12}) - E^{\text{vac}}(X_1) - E^{\text{vac}}(X_2) \quad (1)$$

Six pairs are studied: 'pure' pairs (pX–pX, oX–oX, mX–mX) and 'mixed' pairs (oX–mX, oX–pX, pX–mX). An extensive set of initial structures (Fig. 3) is generated by varying the distance d and the phase φ between the pairs: d varies between 2.8 and 4.6 Å with steps of 0.2 Å, while φ is increased with steps of 30° until a symmetrically equivalent structure is met. The initial shift s and tilt θ are set to zero. The geometries of these 330 initial structures are optimized in a large box (vacuum). For each pair, the optimized geometries are ordered according to increasing energy (E_1, E_2,…).

Table 1 presents the geometrical properties and stacking energies for the following two cases. First, the geometrical properties are calculated for the geometry with the lowest energy E_1. Second, in case of thermal equilibrium, the thermal average of a property A is obtained by weighting the contribution of each geometry by its Boltzmann probability $p(E_i)$,

$$p(E_i) = \exp\left(-\frac{E_i}{k_B T}\right) \Big/ \sum_j \exp\left(-\frac{E_j}{k_B T}\right) \quad (2)$$

$$\langle A \rangle = \sum_i p(E_i) A(i) \quad (3)$$

with T the temperature and k_B the Boltzmann constant. Due to temperature, not only the lowest energy state E_1 of a pair is populated, but also nearby minima can be reached. It should be noted, however, that our formula only sums over local minima but no nearby non-equilibrium states, which would be required for accurate thermodynamics.

The probability distribution $p(E_i)$ favors the lowest energy geometry E_1 largely at 300 K (highly peaked distribution in Supp. Info. Fig. 1), making this geometry the

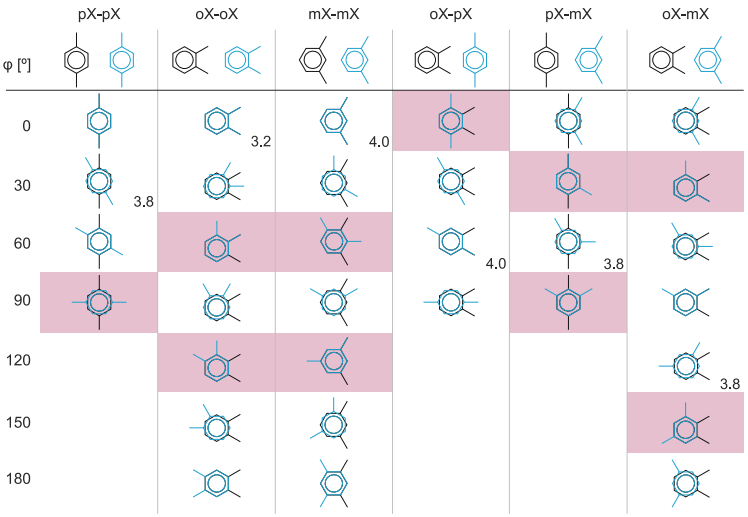

Fig. 3 Initial geometries of six xylene pairs are obtained by varying the phase φ and the distance d. A similar study is performed for dichlorobenzene pairs. Orientations that do not fit in the MIL-47 pores are given a *red* background. The initial geometries leading to the most stable structure are labeled with the initial distance

dominant contribution to the sum in Eq. (3). Indeed, the lowest energy properties correlate well with the thermal average properties in Table 1. Figure 4 illustrates the shift and distance parameters in the optimized benzene pair and the most stable pure xylene pairs. Clearly, the pairs take the parallel-displaced configuration.

The stacking energy $\Delta E^{\text{vac}}_{\text{stack}}$ is favorable for benzene, xylenes, and dichlorobenzenes. Xylene pairs are the most stable with an average stacking energy of −31.7 kJ/mol, followed by the dichlorobenzene pairs with −24.3 kJ/mol and benzene pairs with −19.7 kJ/mol. Aromatic π–π stacking has been extensively studied for benzene pairs [35–43], and it was found that T-shaped and parallel-displaced configurations have nearly equal stacking energy, being slightly more stable than the face-to-face sandwich configuration [26–28]. The benzene pair geometry in Table 1 is the parallel-displaced configuration. These studies also indicate that substituents typically make the stacking stronger with respect to benzene stacking, which is confirmed in our results for methyl and chlorine substituents [44–46].

Moreover, Table 1 suggests a relationship between the stacking energy and some of the geometrical parameters. The absolute value of the stacking energy correlates negatively with the distance (Fig. 5) and positively with the shift, whereas it appears to be relatively independent of the tilt and the phase. This means that the most favorable stacking is obtained when the rings lie close to each other and are somewhat shifted. Indeed, perfectly stacked rings with zero shift are less stable than parallel-displaced rings. The xylenes have higher shifts and lower distances than the dichlorobenzenes, thus explaining the systematically stronger stacking energy of the xylenes. The benzene pair is an outlier and does not follow this trend.

3.2 MIL-47 packed with four xylenes: decomposition of the adsorption energy

The stacking of xylenes is a favorable interaction in the gas phase of the order of −31.7 kJ/mol. Since the walls of the MIL-47 pores contain aromatic rings in the terephthalic linkers, it is expected that adsorbed xylenes are stabilized by an additional stacking energy: the interaction between the adsorbed xylenes and the framework, that is, the so-called host–guest interactions. We have investigated the geometrical characteristics and adsorption energy when MIL-47 is loaded with a xylene pair in each of its pores, which amounts to a total of four xylenes (two pairs) per unit cell. The adsorption energy is calculated as the difference in energy between the framework wherein two

Table 1 The geometrical parameters (shift s, distance d, tilt θ, and phase φ) and stacking energy (Eq. 1) calculated for the optimized structure with lowest energy and calculated as a thermal average

	Lowest energy geometry					300 K	Thermal average 300 K				
	Shift (Å)	Distance (Å)	Tilt (°)	Phase (°)	ΔE^{vac}_{stack} (kJ/mol)	$p(E_1)$	⟨Shift⟩ (Å)	⟨Distance⟩ (Å)	⟨Tilt⟩ (°)	⟨Phase⟩ (°)	$\langle \Delta E^{vac}_{stack} \rangle$ (kJ/mol)
Bz–Bz	1.66	3.22	5.5	9.0	−19.7	1.0	1.66	3.22	5.5	9.0	−19.7
pX–pX	0.8	3.27	3.3	38.5	−31.1	0.3	0.6	3.31	4.0	80.3	−28.5
oX–oX	1.3	3.25	2.6	41.9	−32.6	0.8	1.1	3.30	3.3	47.6	−30.3
mX–mX	1.5	3.22	4.7	104.9	−33.0	0.4	1.2	3.28	5.3	75.1	−30.6
pX–oX	1.3	3.34	4.2	102.5	−34.5	0.3	1.3	3.30	3.6	162.7	−32.7
pX–mX	1.4	3.20	8.9	−15.8	−36.3	0.5	1.3	3.23	7.5	29.0	−33.8
oX–mX	1.5	3.28	1.0	−26.9	−37.1	0.5	1.3	3.27	2.4	−25.3	−34.4
Average	*1.3*	*3.26*	*4.1*	*40.8*	*−34.1*	*0.4*	*1.1*	*3.28*	*4.4*	*61.6*	*−31.7*
pCl–pCl	1.1	3.17	4.1	59.4	−28.0	0.3	0.5	3.30	3.2	80.5	−24.1
oCl–oCl	0.9	3.27	2.9	124.6	−27.8	0.2	0.6	3.33	2.4	140.5	−25.2
mCl–mCl	0.4	3.40	9.6	64.0	−24.8	0.1	0.3	3.40	5.0	85.8	−21.6
pCl–oCl	0.9	3.28	1.9	152.5	−25.1	0.1	0.5	3.36	4.9	168.8	−22.5
pCl–mCl	0.9	3.23	5.9	91.7	−28.3	0.2	0.8	3.29	4.2	84.5	−25.3
oCl–mCl	1.0	3.24	2.5	−149.5	−29.9	0.3	0.8	3.29	2.3	−123.1	−27.0
Average	*0.9*	*3.27*	*4.5*	*57.1*	*−27.3*	*0.2*	*0.6*	*3.33*	*3.7*	*72.8*	*−24.3*

The probability $p(E_1)$ to find the structure in the lowest energy state at 300 K is also listed. Averages in the table are taken over the six xylene pairs and over the six dichlorobenzene pairs

pairs (P_{12}, P_{34}) are adsorbed, the empty framework (F), and the individual xylene molecules (X_1, X_2, X_3, X_4),

$$\Delta E_{ads}(P_{12}, P_{34}) = E(F, P_{12}, P_{34}) - E(F) - E^{vac}(X_1) - E^{vac}(X_2) - E^{vac}(X_3) - E^{vac}(X_4) \quad (4)$$

Both guest–guest and guest–host interactions contribute to this adsorption energy.

In order to find the most favorable configurations of xylene pairs in the framework, an extensive set of initial structures is generated in a similar fashion as in the gas phase analysis in Sect 2.1. Each unit cell contains two pores, and each pore is filled with a xylene pair. As in the gas phase, the list of pair geometries is generated systematically by varying the distance d between 2.8 and 4.0 Å in steps of 0.2 Å and by varying the phase φ in steps of 30°. This gives 231 initial pair geometries, as shown in Fig. 3. However, the confinement in the pore prevents some of the proposed pairs to be adsorbed (these orientations are given a red background in Fig. 3), leaving 161 plausible initial pair geometries. We adopt now the following procedure, as depicted in Fig. 6: for each of the plausible pair geometries, a duplicate is placed in the center of the first pore and another in the center of the second pore. This procedure results in 161 initial structures for fully loaded MIL-47.

An extra degree of freedom in the adsorbed state, compared to the gas phase, is the relative orientation of a pair as a whole with respect to the framework. Whereas rotating a pair or applying symmetry operations does not affect the energy in vacuum, this symmetry is broken when a pair is brought in the pores. Our 161 initial structures only represent 23 possible pair orientations. Unfortunately, a full sampling of this orientational degree of freedom is computationally not feasible. Nevertheless, we have added 15 orientations to improve the sampling, mainly for the mixed pairs which have lower symmetry than the pure pairs. In total, 266 initial structures for the fully loaded MIL-47 are created and optimized.

The geometry of each initial structure for the fully loaded state is optimized. Figure 7 shows the resulting geometries of the adsorbed pure pairs, and the mixed pairs are given in Figures 6–8 of the Supp. Info. For a given pore filling, the geometries are ordered according to increasing energy and the probability distribution is calculated (Eq. 2). Since the Boltzmann distribution is peaked (Supp. Info. Fig. 2), only the dominant geometry with the lowest energy is considered in the remainder of this section.

Comparison of the geometrical parameters of the adsorbed pairs (Table 2) with the pairs in vacuum (Table 1) shows that the distance is similar to the values for the adsorbed pairs in vacuum and that the shift has increased. Whereas the tilt takes values up to 34.1° in the adsorbed state, it remains close to zero in vacuum. In gas phase, this could be a consequence of our selection of initial structures where the tilt has been put to zero

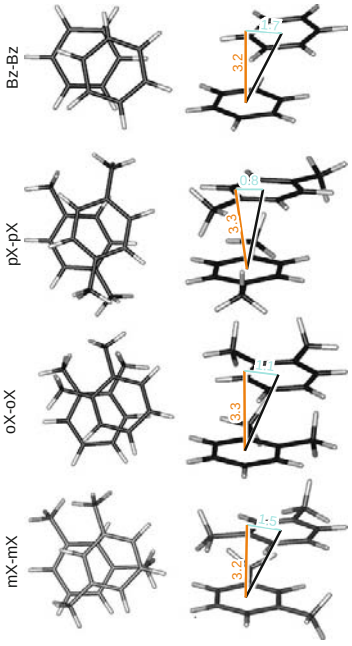

Fig. 4 Some stacked pairs in the gas phase viewed along the z_1 axis and sideways: benzene pair and pure pX, oX, and mX xylene pairs. The *orange* and *blue line* indicate the distance d and shift s parameters, respectively

systematically. When the pair is brought into the pore, the xylenes have to reorient themselves to attain optimal stacking with the terephthalic framework linkers, thus causing the large rotation.

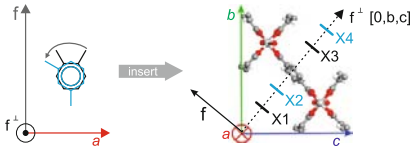

Fig. 6 The initial geometries of the fully loaded framework are created by inserting the xylene pairs of Fig. 3 into the MIL-47 pores. The vectors f and $f^{\perp}$ denote the diagonals in the (b, c) plane, orthogonal to the a direction. The pairs are inserted at the origin and translated over the vector $0.5a$. Subsequently, one pair is translated over the vector $0.25f^{\perp}$ and the other over the vector $0.75f^{\perp}$

The selectivity of xylene isomers in MIL-47 has earlier been attributed to geometrical packing effects [8, 9]. From X-ray data at high loadings [8, 9], it was suggested that molecules are adsorbed by pairs, with their aromatic rings facing each other. The occurrence of certain geometrical effects for single-component adsorption obtained by Rietveld refinement is as follows [8].

1. pX: The methyl groups within a stacked para-xylene pair are perfectly staggered.
2. oX: Structure refinement of ortho-xylene pairs reveals that the stacking of these isomers is analogous to that of para-xylene, but ring alignment is slightly less effective: the rings are shifted with respect to each other.
3. mX: Within pairs of meta-xylene, a steric interaction arises between an aromatic ring of one molecule and a methyl group of a molecule in the neighboring unit cell in the a direction. This interaction causes a tilt and a rotation of the aromatic molecules, preventing the optimal stacking of the rings.

In the three cases, the methyl groups dictate the spatial arrangement of the pairs. However, these experimental geometries differ from our most stable optimized structures (visualized in Fig. 7 and Figures 6–8 of Supp. Info.): the rings of the energetically most stable structures are often

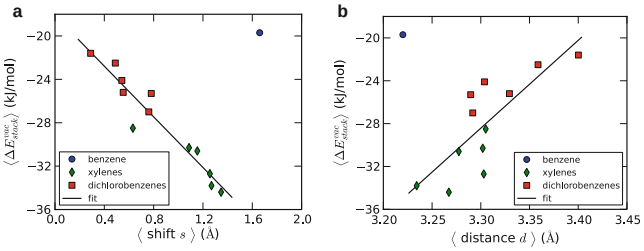

Fig. 5 The stacking energy of the pairs becomes stronger with increasing shift s and decreasing distance d. The benzene pair is an outlier; the linear fits are based on the thermal average values at 300 K of the xylene and dichlorobenzene pairs

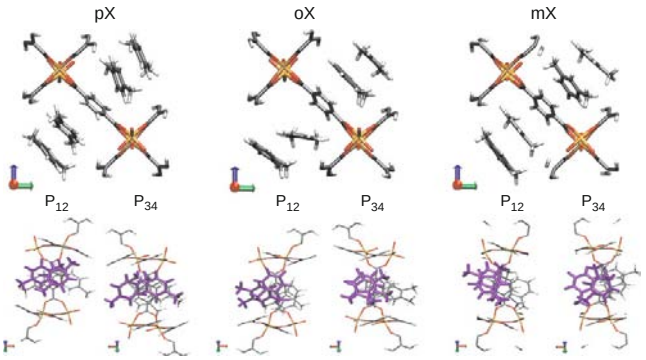

Fig. 7 The most stable geometry of the pure pX, oX, and mX pairs adsorbed in MIL-47. *Top* one unit cell viewed along the one-dimensional channels, in the *a* direction (*red arrow*), loaded with four xylenes. *Bottom* for each adsorbed state, the geometry of the P_{12} and P_{34} pairs is highlighted in purple in a view along the vector $f^{\perp}$, as defined in Fig. 6, for P_{12} and in the opposite sense (vector $-f^{\perp}$) for P_{34}

Table 2 Geometrical parameters of individual xylene pairs P_{12} and P_{34} in their adsorbed state

	Pair P_{12} in first pore				Pair P_{34} in second pore			
	Shift (Å)	Distance (Å)	Tilt (°)	Phase (°)	Shift (Å)	Distance (Å)	Tilt (°)	Phase (°)
pX–pX	3.8	3.17	23.0	246.5	2.1	3.26	24.8	21.1
oX–oX	1.2	3.20	6.3	109.2	3.2	3.03	26.3	69.1
mX–mX	2.8	3.11	23.3	154.3	1.3	3.26	6.5	140.3
pX–oX	1.3	3.27	5.1	216.3	1.8	3.14	5.8	219.9
pX–mX	1.8	3.57	33.3	3.0	1.7	3.24	3.1	−23.0
oX–mX	2.9	3.33	34.1	56.7	1.6	3.21	9.2	49.6
Average	*2.3*	*3.3*	*20.9*	*131.0*	*2.0*	*3.2*	*12.6*	*79.5*

not parallel (tilt θ) and are shifted (shift s). Such a more random ordering was also observed by Castillo et al. [20] in GCMC simulations of a fully packed 4 × 2 × 2 unit cell. Their unordered embedding of the ortho-xylenes in the pores resembles the configuration of our oX pair P_{34} [20]. They only found ordering for the pX pairs, in which all CH_3 groups between neighboring cells have the same orientation, resembling the geometry of our pX pair P_{12}.

3.3 Decomposition of adsorption energy in MIL-47

The adsorption energy is influenced by three effects: framework deformation, interaction of xylenes with the pore walls, and stacking of xylenes. The adsorption energy is thus decomposed into three terms

$$\Delta E_{\text{ads}} = E_{\text{deform}} + E_{\text{inter}} + E_{\text{stack}} \quad (5)$$

The physical interpretation of the terms is visualized in Fig. 8, and the calculated values are reported in Table 3.

A first contribution is the framework deformation. In order to accommodate the xylene pairs in the pores, the structure needs to relax and the linkers may need to reorient. This effect is quantified by the deformation energy E_{deform}, which is defined as the difference in energy between the empty framework with its geometry as in the fully adsorbed state (F, stat) and the empty framework with its geometry relaxed (F),

$$E_{\text{deform}} = E^{\text{stat}}(F) - E(F) \quad (6)$$

The framework deformation due to the loading requires energy ($E_{\text{deform}} > 0$).

A second contribution is the host–guest interactions. The xylenes are physisorbed in the pores due to interactions with the framework. The interaction energy E_{inter} is defined as the energy difference of the fully loaded framework (F, P_{12}, P_{34}) with respect to the energy of the empty host (F, stat) and the energy of the xylenes pairs (P_{12}, P_{34}, stat).

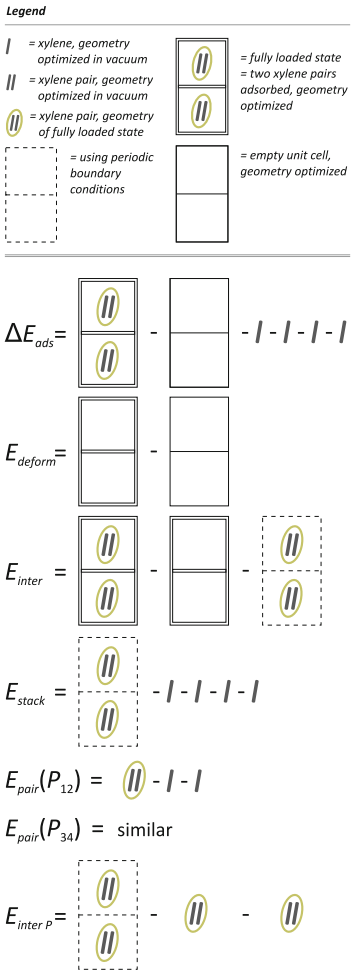

Fig. 8 Visualization of the decomposition of the adsorption energy (Eq. 5): the deformation energy (Eq. 6), the xylene–framework interaction (Eq. 7), and the stacking energy (Eq. 10) are calculated by deleting the xylenes or the framework from the fully loaded framework, and performing static calculations. The stacking energy is further decomposed in pair energies (Eq. 8) and the inter-pair energy (Eq. 9)

$$E_{\text{inter}} = E(F, P_{12}, P_{34}) - E^{\text{stat}}(F) - E^{\text{stat}}(P_{12}, P_{34}) \quad (7)$$

The latter two static calculations are simple single-point energy computations using the same geometry as in the fully loaded host (no geometry optimization is performed) from which the xylenes or the framework are removed (Fig. 8). The interaction of the xylenes with the pore walls, in this case mainly the terephthalic linkers, is attractive ($E_{\text{inter}} < 0$).

The third contribution in Eq. (5) is the interaction E_{stack} between the xylene molecules. As the xylenes appear in pairs in the pores, a large part of these xylene interactions per unit cell is the stacking energy of the first pair E_{pair} (P_{12}) and the stacking energy of the second pair E_{pair} (P_{34}). Due to the interaction with the host, the xylene pairs have different geometries than in vacuum. Instead of using Eq. (1), these pair stacking energies should be calculated by comparing the energy of an isolated pair in vacuum with the energies of two individual xylenes in vacuum. For instance, the geometry of the isolated pair P_{12} is obtained by removing the framework and pair P_{34} from the optimized fully loaded state. The static energy of this P_{12} geometry is then calculated with a single-point computation in a large box (vacuum, P_{12}, stat),

$$E_{\text{pair}}(P_{12}) = E^{\text{stat,vac}}(P_{12}) - E^{\text{vac}}(X_1) - E^{\text{vac}}(X_2) \quad (8)$$

and similarly for pair P_{34}. The pair stacking energy is schematically visualized in Fig. 8.

The remainder of the adsorption energy represents interactions between xylene pairs due to the periodicity of the material and is labeled as the inter-pair interaction $E_{\text{inter}P}$. A xylene pair interacts with other adsorbed xylene pairs in its own channel as well as with xylene pairs in adjacent channels. The interaction is calculated from the static energy of the pairs in the fully loaded geometry, where the framework has been removed, with the periodicity set to the framework lattice parameters (P_{12}, P_{34}, stat). This energy is compared with the static energy of the individual pairs, still in the same geometry, using a large box (vacuum, P_{12}, stat and vacuum, P_{34}, stat).

$$E_{\text{inter}P} = E^{\text{stat}}(P_{12}, P_{34}) - E^{\text{stat,vac}}(P_{12}) - E^{\text{stat,vac}}(P_{34}) \quad (9)$$

This procedure measures the interaction between the two pairs and the interaction with the periodic images of the pairs. Similar to the stacking energy of two molecules, the inter-pair interaction is favorable for the adsorption ($E_{\text{inter}P} < 0$). The total stacking energy in Eq. (5), which is also a negative contribution, can now be calculated as the sum of the pair stacking energies and the inter-pair stacking:

Table 3 Energy contributions to the adsorption energy of the fully loaded framework: deformation energy of the framework (E_{deform}), interaction energy between xylenes and framework (E_{inter}), and xylene stacking energy (E_{stack})

	ΔE_{ads}			E_{stack}			ΔE_{ads}	$\Delta E_{ads}/4$
	E_{deform}	E_{inter}	E_{stack}	E_{pair} (P_{12})	E_{pair} (P_{34})	E_{interP}		
MIL-47 + 4pX	19.3	−120.8	−131.2	−29.1	−18.4	−83.7	−232.7	−58.2
MIL-47 + 4oX	29.3	−120.1	−137.4	−26.9	−34.1	−76.5	−228.3	−57.1
MIL-47 + 4mX	18.8	−138.3	−109.2	−31.8	−37.2	−40.3	−228.8	−57.2
MIL-47 + 2pX–oX	15.6	−134.4	−103.9	−30.9	−35.9	−37.2	−222.8	−55.7
MIL-47 + 2pX–mX	8.0	−147.0	−116.0	−28.8	−22.3	−65.0	−255.0	−63.8
MIL-47 + 2oX–mX	5.9	−141.9	−95.0	−27.6	−25.2	−42.2	−231.0	−57.7
Average	16.2	−133.8	−115.5	−29.2	−28.9	−57.5	−233.1	−58.3

The stacking energy consists of the stacking energies of the individual pairs and the inter-pair stacking energy. The adsorption energy per xylene is obtained by division by four. All energies in kJ/mol

$$E_{stack} = E_{pair}(P_{12}) + E_{pair}(P_{34}) + E_{interP} \quad (10)$$

The predicted total adsorption energies are on average −233.1 kJ/mol per unit cell (Table 3), which amounts to −58.3 kJ/mol per adsorbed xylene molecule. On average, the host–xylene interaction E_{inter} and the xylene stacking energy E_{stack} contribute equally. But in individual cases, we notice some significant deviations: the total stacking energy can vary by more than 40 kJ/mol. Nevertheless, this effect is mostly compensated by the interaction energy between the xylenes and the walls of the host. A large stacking energy of the xylenes is accompanied systematically by a higher repulsive deformation energy of the framework. This feature could be understood by assuming that some framework relaxation is required to accommodate the xylene pair in its most favorable stacked conformation.

Within the category of pure pairs, the xylene–framework interaction energy is by far the strongest for the adsorption of pure mX pairs (−138.3 kJ/mol). The trend to favor mX is maintained when using mixed pairs, since the adsorption of mixed pairs oX–mX or pX–mX shows by far the largest interaction energies with the host. However, these favorable interactions are partially cancelled out by the lower stacking energies. Note also that more favorable energies for pure pairs not systematically lead to more favorable energies in the mixed pairs. For instance, mixing with the xylene isomer with the strongest stacking energy (oX) does not result in the strongest stacking energies for the mixed pairs (oX–mX, oX–pX). From Table 3, we conclude that the data for pure pairs are insufficient to predict adsorption energetics for mixed pairs.

The decomposition of the stacking energy in Table 3 shows that the pair stacking energies of the adsorbed pairs are less favorable than those of the pairs in vacuum (average −31.7 kJ/mol). Nevertheless, the pair stacking attains an average stacking efficiency of (−29.2 − 28.9)/2 = −29.0 kJ/mol. The inter-pair stacking energy can be very large, up to −83.7 kJ/mol for pX. The variation in the inter-pair stacking is explained by the organization of the xylenes in the pores, which may be derived from the geometrical parameters as follows. It is clear from Fig. 6 that X_1 and X_2 are nearest neighbors in the channel, and X_3 and X_4 are nearest neighbors in the adjacent channel. The interaction of a xylene with its nearest neighbors is included in the pair stacking energies E_{pair} (P_{12}) and E_{pair} (P_{34}). The interaction of xylenes with their next nearest neighbors is then of course included in the E_{interP}. According to our geometry versus energy analysis in vacuum (Fig. 5), the strength of the xylene–xylene interaction is mainly determined by the distance between the two molecules. To see the effect of the distance on the inter-pair energy, we determined the distance from the xylenes to their second nearest neighbor, which should be the dominant contribution. This distance is calculated as the root of $s^2 + d^2$ (s and d as defined in Fig. 2), which equals the distance between the centers of their rings. For pX, the second neighbors are separated by 4.96 and 5.77 Å, and these relatively short separations result in the strong inter-pair stacking energy of −83.7 kJ/mol. In contrast, the second neighbors for mX are separated by 5.75 and 7.40 Å, resulting in a much weaker inter-pair energy of −40.3 kJ/mol.

The typical stacking energy in vacuum, about −31.7 kJ/mol (Table 1), may be used as a 'unit for energy' to compare the importance of the energy contributions. The interaction energy of two pairs with the framework is worth over four units, the stacking of the pairs is worth one unit each, the inter-pair stacking is worth two units, and the deformation diminishes the total by half a unit. This brings the adsorption energy to nearly eight vacuum stacking energy equivalents (−233.1 kJ/mol). The attractive stacking between xylene molecules is here of the same importance as the attractive interaction energy between xylenes and framework.

Summarizing, the pure pairs deform the framework more (larger positive E_{deform}) and interact more weakly

with the framework (weaker E_{inter}) than the mixed pairs. However, the pure xylene pairs stack more efficiently in the pores (stronger E_{stack}). Overall, the values of adsorption energy for the various xylene pairs all have the same order of magnitude and appear not to explain the different adsorption selectivity of the pX, oX, and mX isomers. If the pure adsorption isotherms were to be solely determined by the strength of the adsorption energy, one would need a strong adsorption energy for pX, followed by oX, and a considerably weaker adsorption energy for mX. Since this is not the case, our results indicate that the selective adsorption behavior cannot be explained purely energetically. This means that temperature and entropy are expected to play a determining role for the selectivity.

The entropy arises from the many possible configurations the xylenes can take when adsorbed in the pores. In general, the more configurations the xylenes can take within the pores, the higher the entropy, and the more favorable the adsorption. A first contribution to the entropy is the relative orientation of the molecules in a xylene pair. The presence of the methyl groups can here reduce the number of configurational states. The fewer states are prohibited (because of overlapping methyl groups), the more states are available, and the more entropy is available. A second contribution to the entropy is the positioning of the pair in the channels. Likewise, the pair may take a number of different orientations and positions inside the channels. Bulkier pairs show a more limited number of available configurations, leading to a lower entropy. A third entropic contribution arises in the process of multicomponent adsorption, referred to as mixing entropy. Many ways exist to distribute the xylenes of each kind over the pores. The information about entropy is lacking in adsorption energy calculations, but could be obtained by a vibrational analysis [47, 48], Monte Carlo or Molecular Dynamics simulations. GCMC calculations, as those by Castillo et al. [20], include energetic and entropic effects and agree with experimental single-component isotherms. Our study now shows that the energetics of the pure and mixed xylene adsorption at high loadings are not alone responsible for the selectivities between isomers, such that the separation is also entropically driven.

4 Conclusions

The molecular packing effects of xylene isomers inside the confining environment of the MIL-47 pore system have been studied by quantumchemical calculations. The guest–guest interactions are first quantified in the gas phase. Xylenes show a high stacking energy in vacuum, such that xylenes are expected to stack efficiently with the rings of the MIL-47 linkers. When the xylenes are inserted in the MIL-47 pores, not only guest–guest interactions contribute to the adsorption energy, but also host–guest interactions. The adsorption energy for high loadings of para-, ortho-, and meta-xylene has thus been decomposed in three contributions: the deformation energy of the framework, the framework–xylene interaction, and the stacking energy. The stacking energy has been found to be equally important as the framework–xylene interaction, hence confirming the hypothesis that π–π stacking is responsible for the adsorption. The average stacking energy of xylene pairs in vacuum can be used as a unit for the interactions. The adsorption energy in the fully loaded state amounts to nearly two vacuum stacking equivalents per adsorbed xylene, which explains the efficient adsorption at room temperature.

The energetics could not explain the experimentally observed separation of xylene isomers with a preferential adsorption for ortho-xylene and para-xylene, since all adsorption energies lie in the same range. Therefore, entropic effects are likely the main driving force for the adsorption selectivity. This has two implications. First, sampling of configurational space should be adequately performed to assess the entropic effects, which can only be obtained with molecular dynamics or Monte Carlo simulations. Second, since the accuracy of the energetics is of subordinary importance to the sampling, it is expected that reasonable results can be obtained with classical force fields. Whereas force fields are less accurate than an ab initio treatment, they allow considerably longer sampling times because of the reduced computational cost.

Acknowledgments This work was supported by the Fund for Scientific Research—Flanders (FWO), the research Board of Ghent University, and BELSPO in the frame of IAP 6/27. Funding was also received from the European Research Council under FP7 with ERC grant agreement number 240483. A.G., T.V., and M.A.vdV. are postdoctoral researchers of the Fund for Scientific Research—Flanders (FWO). The computational resources and services used were provided by Ghent University (Stevin Supercomputer Infrastructure).

References

1. Férey G (2008) Hybrid porous solids: past, present, future. Chem Soc Rev 37:191–214
2. Long JR, Yaghi OM (2009) The pervasive chemistry of metal-organic frameworks. Chem Soc Rev 38:1213–1214
3. Perry JJ, Perman JA, Zaworotko MJ (2009) Design and synthesis of metal-organic frameworks using metal-organic polyhedra as supermolecular building blocks. Chem Soc Rev 38:1400–1417
4. Eddaoudi M, Kim J, Rosi N, Vodak D, Wachter J, O'Keeffe M, Yaghi OM (2002) Systematic design of pore size and functionality in isoreticular MOFs and their application in methane storage. Science 295:469–472
5. Férey G, Serre C, Devic T, Maurin G, Jobic H, Llewellyn PL, De Weireld G, Vimont A, Daturi M, Chang JS (2011) Why

hybrid porous solids capture greenhouse gases? Chem Soc Rev 40:550–562
6. Meek ST, Greathouse JA, Allendorf MD (2011) Metal-organic frameworks: a rapidly growing class of versatile nanoporous materials. Adv Mater 23:249–267
7. Tranchemontagne DJ, Mendoza-Cortes JL, O'Keeffe M, Yaghi OM (2009) Secondary building units, nets and bonding in the chemistry of metal-organic frameworks. Chem Soc Rev 38:1257–1283
8. Alaerts L, Kirschhock CEA, Maes M, van der Veen MA, Finsy V, Depla A, Martens JA, Baron GV, Jacobs PA, Denayer JEM, De Vos DE (2007) Selective adsorption and separation of xylene isomers and ethylbenzene with the microporous vanadium(IV) terephthalate MIL-47. Angew Chem Int Edit 46:4293–4297
9. Finsy V, Verelst H, Alaerts L, De Vos D, Jacobs PA, Baron GV, Denayer JFM (2008) Pore-filling-dependent selectivity effects in the vapor-phase separation of xylene isomers on the metal-organic framework MIL-47. J Am Chem Soc 130:7110–7118
10. Vermoortele F, Maes M, Moghadam PZ, Lennox MJ, Ragon F, Boulhout M, Biswas S, Laurier KGM, Beurroies I, Denoyel R, Roeffaers M, Stock N, Düren T, Serre C, De Vos DE (2011) p-xylene-selective metal–organic frameworks: a case of topology-directed selectivity. J Am Chem Soc 133:18526–18529
11. Fritz Ullmann's encyclopedia of industrial chemistry, 6th edn. In: Electronic release, 2000
12. Barthelet K, Marrot J, Riou D, Férey G (2002) A breathing hybrid organic-inorganic solid with very large pores and high magnetic characteristics. Angew Chem Int Edit 41:281
13. Grimme S (2006) Semiempirical GGA-type density functional constructed with a long-range dispersion correction. J Comput Chem 27:1787–1799
14. Grimme S, Antony J, Schwabe T, Muck-Lichtenfeld C (2007) Density functional theory with dispersion corrections for supramolecular structures, aggregates, and complexes of (bio)organic molecules. Org Biomol Chem 5:741–758
15. Schwabe T, Grimme S (2008) Theoretical thermodynamics for large molecules: walking the thin line between accuracy and computational cost. Acc Chem Res 41:569–579
16. Liu B, Smit B (2009) Comparative molecular simulation study of CO_2/N_2 and CH_4/N_2 separation in zeolites and metal—organic frameworks. Langmuir 25:5918–5926
17. Ramsahye NA, Maurin G, Bourrelly S, Llewellyn PL, Devic T, Serre C, Loiseau T, Férey G (2007) Adsorption of CO_2 in metal organic frameworks of different metal centres: grand Canonical Monte Carlo simulations compared to experiments. Adsorpt J Int Adsorpt Soc 13:461–467
18. Rosenbach N, Jobic H, Ghoufi A, Salles F, Maurin G, Bourrelly S, Llewellyn PL, Devic T, Serre C, Férey G (2008) Quasi-elastic neutron scattering and molecular dynamics study of methane diffusion in metal organic frameworks MIL-47(V) and MIL-53(Cr). Angew Chem Int Edit 47:6611–6615
19. Salles F, Jobic H, Maurin G, Koza MM, Llewellyn PL, Devic T, Serre C, Férey G (2008) Experimental evidence supported by simulations of a very high H-2 diffusion in metal organic framework materials. Phys Rev Lett 100(24):245901
20. Castillo JM, Vlugt TJH, Calero S (2009) Molecular simulation study on the separation of xylene isomers in MIL-47 metal—organic frameworks. J Phys Chem C 113:20869–20874
21. Wang S, Yang Q, Zhong C (2008) Adsorption and separation of binary mixtures in a metal-organic framework Cu-BTC: a computational study. Sep Purif Technol 60:30–35
22. Hamon L, Llewellyn PL, Devic T, Ghoufi A, Clet G, Guillerm V, Pirngruber GD, Maurin G, Serre C, Driver G, Beek WV, Jolimaître E, Vimont A, Daturi M, Férey GR (2009) Co-adsorption and separation of CO_2–CH_4 mixtures in the highly flexible MIL-53(Cr) MOF. J Am Chem Soc 131:17490–17499
23. Gallo M, Glossman-Mitnik D (2009) Fuel gas storage and separations by Metal—organic frameworks: simulated adsorption isotherms for H_2 and CH_4 and their equimolar mixture. J Phys Chem C 113:6634–6642
24. Pan L, Olson DH, Ciemnolonski LR, Heddy R, Li J (2006) Separation of hydrocarbons with a microporous metal-organic framework. Angew Chem Int Edit 45:616–619
25. Vanduyfhuys L, Verstraelen T, Vandichel M, Waroquier M, Van Speybroeck V (2012) Ab initio parametrized force field of the metal-organic framework MIL-53(Al) for use in molecular simulations including lattice dynamics. J Chem Theory Comput (submitted)
26. Sinnokrot MO, Sherrill CD (2003) Unexpected substituent effects in face-to-face π-stacking interactions. J Phys Chem A 107:8377–8379
27. Sinnokrot MO, Sherrill CD (2004) Highly accurate coupled cluster potential energy curves for the benzene dimer: sandwich, T-shaped, and parallel-displaced configurations. J Phys Chem A 108:10200–10207
28. Sinnokrot MO, Sherrill CD (2004) Substituent effects in π–π interactions: sandwich and T-shaped configurations. J Am Chem Soc 126:7690–7697
29. Alaerts L, Maes M, Jacobs PA, Denayer JFM, De Vos DE (2008) Activation of the metal-organic framework MIL-47 for selective adsorption of xylenes and other difunctionalized aromatics. Phys Chem Chem Phys 10:2979–2985
30. Cremer D, Pople JA (1975) General definition of ring puckering coordinates. J Am Chem Soc 97:1354–1358
31. Car R, Parrinello M (1985) Unified approach for molecular dynamics and density-functional theory. Phys Rev Lett 55:2471–2474
32. Becke AD (1988) Density-functional exchange-energy approximation with correct asymptotic behavior. Phys Rev A 38:3098
33. Vanderbilt D (1990) Soft self-consistent pseudopotentials in a generalized eigenvalue formalism. Phys Rev B 41:7892
34. Verstraelen T, Van Speybroeck V, Waroquier M (2008) ZEOBUILDER: a GUI toolkit for the construction of complex molecular structures on the nanoscale with building blocks. J Chem Inf Model 48:1530–1541
35. Gu J, Wang J, Leszczynski J, Xie Y, Schaefer HF (2008) Chem Phys Lett 459:164
36. McGaughey GB, Gagne M, Rappe AK (1998) J Biol Chem 273:15458
37. Morgado C, Vincent MA, Hillier IH, Shan X (2007) Phys Chem Chem Phys 9:448
38. Pavone M, Rega N, Barone V (2008) Chem Phys Lett 452:333
39. Piacenza M, Grimme S (2004) J Comput Chem 25:83
40. Podeszwa R, Bukowski R, Szalewicz K (2006) J Phys Chem A 110:10345
41. Waller MP, Robertazzi A, Platts JA, Hibbs DE, Williams PA (2006) J Comput Chem 27:491
42. Zhao Y, Truhlar DG (2005) Phys Chem Chem Phys 7:2701
43. Zhao Y, Truhlar DG (2006) J Chem Theory Comput 2:1009
44. Lee EC, Hong BH, Lee JY, Kim JC, Kim D, Kim Y, Tarakeshwar P, Kim KS (2005) Substituent effects on the edge-to-face aromatic interactions. J Am Chem Soc 127:4530–4537
45. Raju RK, Bloom JWG, An Y, Wheeler SE (2011) Substituent effects on non-covalent interactions with aromatic rings: insights from computational chemistry. ChemPhysChem 12:3116–3130
46. Hohenstein EG, Duan JN, Sherrill CD (2011) Origin of the surprising enhancement of electrostatic energies by electron-donating substituents in substituted sandwich benzene dimers. J Am Chem Soc 133:13244–13247

47. De Moor BA, Ghysels A, Reyniers M-F, Van Speybroeck V, Waroquier M, Marin GB (2011) Normal mode analysis in zeolites: toward an efficient calculation of adsorption entropies. J Chem Theory Comput 7:1090–1101

48. Van der Mynsbrugge J, Hemelsoet K, Vandichel M, Waroquier M, Van Speybroeck V (2012) An efficient approach for the computational study of alcohol and nitrile adsorption in H-ZSM-5. J Phys Chem C 116:5499–5508

Paper 11

A new V^{IV} based metal-organic framework having framework flexibility and high CO_2 adsorption capacity

Ying-Ya Liu, Sarah Couck, Matthias Vandichel, Maciej Grzywa, Karen Leus, Shyam Biswas, Dirk Volkmer, Jorge Gascon, Freek Kapteijn, Joeri F. M. Denayer, Michel Waroquier, Veronique Van Speybroeck and Pascal Van Der Voort

Inorganic Chemistry, in revision

Copyright 2012 by the American Chemical Society.

A new V^{IV} based metal-organic framework having framework flexibility and high CO_2 adsorption capacity

Ying-Ya Liu,[†] Sarah Couck,[‡] Matthias Vandichel,[§] Maciej Grzywa,[‖] Karen Leus,[†] Shyam Biswas,[†] Dirk Volkmer, [‖] Jorge Gascon,[⊥] Freek Kapteijn,[⊥] Joeri F. M. Denayer, [‡] Michel Waroquier, [§] Veronique Van Speybroeck,[§] and Pascal Van Der Voort[†]*

[†] COMOC - Center for Ordered Materials, Organometallics and Catalysis, Department of Inorganic and Physical Chemistry, Ghent University, Krijgslaan 281-S3, 9000 Ghent; Belgium

[‡]Department of Chemical Engineering, Vrije Universiteit Brussel, Pleinlaan 2, 1050 Brussels, Belgium

[§]Center for Molecular Modeling, Ghent University, Technologiepark 903, 9052 Zwijnaarde, Belgium

[‖]Solid State and Materials Chemistry, Institute of Physics, Augsburg University, Universitaetsstrasse 1, 86159 Augsburg, Germany

[⊥]Catalysis and Engineering, Delft University of Technology, Julianalaan 136, 2628 BL Delft, The Netherlands

ABSTRACT: A vanadium based metal-organic framework, VO(BPDC) ($BPDC^{2-}$ = biphenyl-4,4'-dicarboxylate), adopting an expanded MIL-47 structure type, has been synthesized via solvothermal and microwave methods. Its stuctural and gas/vapor sorption properties have been studied. This compound displays a distinct breathing effect towards certain adsorptives at workable temperatures. The sorption isotherms of CO_2 and CH_4 indicate a different sorption behavior at specific temperatures. *In-situ* synchrotron X-ray powder diffraction measurements and molecular simulations have been utilized to characterize the structural transition. The experimental measurements clearly suggest the existence of both narrow pore and large pore forms. Theoretically, by determination of a free energy profile along the pore angle in an empty host framework, apart from a regular large pore and a regular narrow pore form, an overstretched narrow pore form has also been found. Additionally, a variety of spectroscopic techniques combined with N_2 adsorption/desorption isotherms measured at 77K demonstrate that the existence of the mixed oxidation states V^{III}/V^{IV} in the titled MOF structure compared to pure V^{IV} increases the difficulty in triggering the flexibility of the framework.

Introduction

Metal-organic frameworks (MOFs) are highly crystalline and porous compounds, which are being intensively studied among other reasons for their potential applications in adsorption and separation technologies and in catalysis.[1] They are built up of metal-oxide clusters or metal ions interconnected by polydentate organic ligands, thus forming two- or three-dimensional porous frameworks. Most of the porous MOFs exhibit a rigid framework

under workable conditions and have therefore fixed pore dimensions. However, a few intriguing structures are those whose pore dimensions may change without breaking chemical bonds within the framework, triggered by host-guest interactions at a certain temperature or pressure. This phenomenon has often been termed as 'breathing'[2] and the flexible frameworks have been referred to as 'dynamic frameworks'[3] or 'soft porous crystals'.[4]

The best studied example of such flexible coordination compounds is the series of MIL-53, originally developed by Férey's group (MIL stands for Materials of Institute Lavoisier), $M^{III}(OH)(BDC)$ (M^{III}= Al, Cr, Fe, Ga, Sc and In; BDC^{2-} = 1,4-benzenedicarboxylate).[5] This series of compounds shows a reversible structural change between a large pore (*lp*) form and a narrow pore (*np*) or even a very narrow pore (*vnp*) form upon gas- or solvent-host interactions.[2a,5a,6] This transition is highly dependent on the adsorbate (i.e. CO_2, CH_4, various hydrocarbons etc.).[1b,7] Furthermore, functionalization of the organic ligand can significantly influence and therefore tune the flexibility of the network.[8] An isostructural analogue of MIL-53 is MIL-47. The main difference between both isostructures lies in the nature of the metal centres and in the presence of -OH groups. Compared to MIL-53, MIL-47 was believed to be relatively rigid. The difference in flexibility between both structures was explained [9] by the presence of -OH groups on M^{III} sites, whereas the V^{IV} has a V=O bond. These -OH groups may strongly interact with different adsorbents, inducing structural transformations. Recently, it was shown that a certain degree of flexibility can be induced in the MIL-47 structure by controlling the oxidation state of the V-centers, going from pure V^{III} to mixed V^{IV}/V^{III} valence states.[9] A very recent report [10] demonstrated that a structural change can even be observed in MIL-47(V^{IV}) by applying high external mechanical pressure(180-350

MPa). Such flexible frameworks and a fortiori those with a designable flexibility are very promising candidates for applications including selective storage/separation,[11] molecular sensing[4,12] and drug delivery.[13] Recently, attempts for a complete elucidation of the underlying mechanisms that trigger the breathing effects of flexible MOFs have been made by several groups.[14]

In this paper, we report on the first MOF bearing a V^{IV}–carboxylate coordination unit exhibiting flexibility under mild conditions. This new MOF denoted as COMOC-2 (COMOC = Center for Ordered Materials, Organometallics and Catalysis, Ghent University) features an extended MIL-47 structure $[V^{IV}O(BPDC)]$ ($BPDC^{2-}$ = biphenyl-4,4'-dicarboxylate). Noteworthy, in contrast to this vanadium analogue, an isostructure Aluminium biphenyl-4,4'-dicarboxylate, known as DUT-5 (Al(OH)(BPDC), DUT denoted as Dresden University of Technology), showed to be a rigid structure, as demonstrated by the gas (H_2, N_2, CO_2, CH_4) sorption and solvent exchange experiments.[15] Spectroscopic characterization demonstrated that COMOC-2 consists exclusively of V^{IV} centers. It will be refered to as COMOC-2(V^{IV}) hereafter. It shows a distinct breathing effect towards certain adsorptives, and exhibits highly selective adsorption of CO_2 over CH_4 at workable temperatures. In situ synchrotron XRD patterns were collected to capture the structure change upon certain gas pressures. Furthermore, the free energy profile was determined along the breathing mode of the empty COMOC-2(V^{IV}) by means of first principles calculations. Two other variants of COMOC-2(V^{IV}) were obtained by slight variation of the reaction parameters: one is in a mixed valence V^{IV}/V^{III} state labeled as COMOC-2(V^{IV}/V^{III}), the other displays a pure large pore phase labeled as COMOC-2(*lp*). Due to the difference in oxidation states,

COMOC-2(V^{IV}/V^{III}) shows a different adsorption behavior compared to COMOC-2(V^{IV}). The crystal structure of the large pore phase of COMOC-2 has been determined by Rietveld refinement from the powder XRD data of COMOC-2(*lp*).

Experimental section

Materials and general methods. All starting materials were commercially available reagents of analytical grade and used without further purification. Microwave-assisted syntheses were carried out on a microwave synthesizer (Discover, CEM Inc.). Fourier transform infrared (FT-IR) spectra were recorded in the region of 400-4000 cm^{-1} on a Bruker EQUINOX 55 FTIR spectrometer. Diffuse-reflectance infrared Fourier transform (DRIFT) spectra were recorded on a Thermo Nicolet 6700 FT-IR spectrometer, equipped with a nitrogen-cooled MCT detector and a KBr beam splitter. The in-situ DRIFT cell was connected to a vacuum manifold and a controlled gas inlet system. Each spectrum was recorded at 120 ˚C under vacuum. Raman spectra were collected with the RXN1 Raman spectrometer (Kaiser Optical Systems) fitted with a 532 nm laser operating at 40 mW using optical probe. Elemental analyses were carried out on a Thermo Scientific Flash 2000 CHNS-O Analyzer. Thermogravimetric analysis (TGA) on COMOC-2 was performed with a Netzsch STA 449 F3 Jupiter-Simultaneous TG-DSC analyzer in the temperature range of 25-700 ˚C under nitrogen atmosphere at a heating rate of 10 ˚C min^{-1}. Laboratory X-Ray powder diffraction (XRPD) patterns were recorded on a Seifert XRD 3003 TT diffractometer outfitted with a Meteor 1D detector (for Rietveld Refinement of COMOC-2) or a Thermo Scientific ARL X'Tra diffractometer (for all other compounds), both operated at 40 kV, 40 mA using Cu-Kα (λ = 1.5406 Å). Temperature programmed XRPD (TP-XRPD) patterns

were collected on a Bruker D8 Discover X-ray diffractometer equipped with a linear detector using Cu-Kα radiation; the XRD patterns were recorded from room temperature to 620 ˚C at a heating rate of 0.2 ˚C s^{-1} under helium atmosphere. The X-ray photoelectron spectroscopy (XPS) measurements were recorded on a Kratos AXIS Ultra spectrometer, equipped with a monochromatic X-ray source and a delay-line detector (DLD). Spectra were obtained using the aluminum anode (Al K α = 1486.6 eV) operating at 150 W. Analysis of XPS data was performed using the XPSPEAK 4.1 program, using the Shirley function to substract the background.

Syntheses

1. Synthesis of COMOC-2-as ([VO(BPDC)] $(DMF)_{0.1}(H_2O)_{0.5}$)

a) Method 1: solvothermal synthesis

0.5 g of $VOSO_4 \cdot H_2O$ and 1.02 g of 4,4'-biphenyldicarboxylic acid (H_2BPDC) were added into 70 mL DMF. The mixture was transferred to a 100 mL round bottom flask equipped with a magnetic stirrer. The flask was sealed, heated slowly to 147 ^oC under stirring and kept at this temperature for 15-20 h. After completion of the reaction, a yellowish green powder was collected over a membrane filter, washed thoroughly first with DMF, then with methanol to remove the green vanadium impurities, and finally with acetone, and subsequently dried at room temperature under vacuum. Yield: 0.31 g, 34.7%, based on vanadium. Elemental analysis for $[VO(C_{14}H_8O_4)](C_3H_7NO)_{0.1}$ $(H_2O)_{0.5}$: calcd: C: 53.1; H: 3.02 ; N: 0.43 (%); found: C: 53.75 ; H: 2.97 ; N: 0.28 (%).

b) Method 2: microwave-assisted synthesis

0.05 g of $VOSO_4 \cdot H_2O$ and 0.102 g of H_2BPDC were added into 3 mL of DMF, heated to 150 °C under microwave irradiation for 20 min with magnetic stirring. The maximum irradiation power was set to 150 W, with the 'powermax' active (air cooling was used during the irradiation). After completion of the reaction, a yellowish green powder was collected over a membrane filter, washed thoroughly first with DMF, then with methanol to remove the green vanadium impurities, and finally with acetone, and subsequently dried at room temperature under vacuum. Yield: 0.015g, 16.8%, based on vanadium.

Important: COMOC-2 is sensitive to air and moisture, and should be stored under argon atmosphere.

c) Activation of COMOC-2-as

The COMOC-2-as compound was activated by heating up the sample at a heating rate of 1 $^{\circ}C\ min^{-1}$ under vacuum up to 120 ^{o}C and held at this temperature for 3 h. This activation temperature was optimized based on the results of nitrogen sorption experiments and powder XRD data.

2. Syntheses of COMOC-2(V^{IV}/V^{III})-as and COMOC-2(*lp*)-as

COMOC-2(V^{IV}/V^{III})-as can be obtained by a slight variation of the solvothermal reaction parameters described above for COMOC-2-as. The compound was synthesized by prolongation of the reaction time to 24 h or by increasing the reaction temperature to 160 °C. Probably the decomposition products of DMF partially reduce V^{IV} to V^{III}, producing the mixed-valence COMOC-2(V^{IV}/V^{III})-as. In a typical reaction, 0.5 g of $VOSO_4 \cdot H_2O$ and 1.02 g of 4,4'-biphenyldicarboxylic acid (H_2BPDC) were added into 70 mL DMF. The mixture was transferred to a 100 mL round bottom flask equipped with a magnetic stirrer. The flask was

sealed, heated to 150 ^{o}C with a heating rate of ~1 ^{o}C min^{-1} under stirring and kept at this temperature for 22 h. After cooling to room temperature, a yellowish green powder was collected over a membrane filter, washed thoroughly first with DMF, then with methanol to remove the green vanadium impurities, and finally with acetone, and subsequently dried at room temperature under vacuum.

Moreover, the use of a more concentrated reaction mixture (50 mL of DMF instead of 70 mL) with all other solvothermal reaction parameters unaltered, results in the formation the COMOC-2(*lp*)-as, which contains small amount of free linker, as evidenced by elemental analysis on activated COMOC-2(*lp*) sample: $[VO(C_{14}H_8O_4)](C_3H_7NO)_{0.05}$ $(C_{14}H_{10}O_4)_{0.07}$: calcd: C: 55.44; H: 2.78 ; N: 0.21 (%); found: C:55.36 ; H:2.78 ; N: 0.23 (%).

XRPD data collection and Rietveld refinement for COMOC-2. For the determination of crystal structure of COMOC-2 from XRPD data, a microcrystalline sample was ground using an agate mortar and pestle, and was deposited in the hollow of a zero-background sample holder. Diffraction data were collected at room temperature in the 2θ range of 4.5-90˚ with 0.02˚ steps, with a scan speed of 1000 s step^{-1} using a Seifert XRD 3003 TT diffractometer equipped with a Meteor 1D detector, operated at 40 kV, 40 mA for Cu target (λ = 1.5418 Å). The structure of Al(OH)(BPDC)[15] was used as a model for refinement of the crystal structure. Lattice parameters were determined using the PROSZKI package[16]. The Rietveld refinement was carried out using the Jana2006 program[17]. Weak geometric restraints on bond distances were used during the refinement process. The preferred orientation was refined applying the March-Dollase formula. The preferred orientation was chosen along the [101] direction. After calculation of the difference Fourier maps no additional peaks were detected, which could be

ascribed to the small amount (according to the elemental analysis data) of occluded free linker. The crystal data and details of refinement, atomic coordinates, and bond distances for COMOC-2 are listed in Table S1, S2 and S3, respectively. The Rietveld refinement plot is shown in Figure S3.

Measurement of gas and vapor sorption isotherms. Prior to the sorption measurements, the samples were outgassed at 353K. N_2 sorption experiments were carried out with a Belsorp Mini (Bel Japan, Inc.) apparatus. Equilibrium isotherms of CO_2 and CH_4 were measured using the static volumetric method with an HPA-100 device from VTI Corporation. The vapor phase isotherm of hexane was measured with the gravimetric method on a microbalance of VTI Corporation.

Synchrotron X-ray powder diffraction measurements and analysis. In-situ synchrotron powder diffraction patterns were collected at the Swiss Norwegian beamline (station BM01A) of the European Synchrotron Radiation Facility (Grenoble, France) using an MAR345 image plate detector and a monochromatic beam with a wavelength of 0.75276 Å. The sample-to-detector distance was 400 mm and parameters of the detector were calibrated using a silica standard sample. The diffraction patterns were integrated by Fit2D software[18]. The well-ground powder sample was filled in a 0.4 mm glass capillary. A gas dosing system was used to admit CO_2 from vacuum to 17.5 bar of pressure into the capillary filled with sample and exposed to the X-ray beam. Prior to the measurement, the sample was degassed at 80 ^oC for 30 min (heating rate: 2 ^oC min^{-1}) under vacuum. The in-situ XRPD data upon CO_2 dosing was collected at -40 ^oC. The temperature was controlled by Oxford Cryostream Cooler. A typical data set at each pressure point was collected. The XRPD patterns of

COMOC-2 under CO_2 pressure of 7.5 bar and 15 bar were selected for the determination of lattice parameters of *np* and *lp* phase, respectively. The lattice parameters were determined using the DICVOL program[19] and refined using the STOE's WinXPow[20] software package.

First-Principles calculations - Methodology. To further unravel the mechanism inducing the breathing, the free energy profile along the breathing mode of the empty COMOC-2(V^{IV}) is computed by means of first principles calculations. For MIL-53, Walker et al. showed that a subtle interplay between dispersion forces and entropic factors controlled the inherent bi-stable behaviour of the material.[21] Along the same line, Stavitski et al. used dispersion corrected first principles calculations to describe the breathing in the amine modified MIL-53(Al) framework.[22] Very recently, Triguero et al. presented a stochastic model of "breathing" transitions in MIL-53. They concluded that (at the level of the crystal) these transformations occur via layer-by-layer shear.[23]

Periodic DFT-D calculations on the entire COMOC-2(V^{IV}) unit cell containing 112 atoms were carried out in the Vienna Ab Initio Simulation Package (VASP 5.2.11) [24], using the PBE exchange-correlation functional [25] and a plane-wave basis set with a general kinetic energy cutoff of 700 eV. The projector augmented wave approximation (PAW) [26] was used. Brillouin zone sampling was restricted to the Γ-point. Gaussian smearing [24b] was applied to improve convergence: 0.05 eV for cell optimizations, 0.02 eV for the subsequent geometry and frequency calculations. Furthermore, D2 van der Waals corrections [27] for the PBE functional are used throughout the optimization, as implemented in the VASP 5.2.11.

Firstly, the most stable open and closed structures are determined using the climbing Nudged Elastic Band (cNEB) methodology [28] with a varying unit cell between constructed

cell optimized structures. Then the minima of the narrow pore (*np*) and large pore (*lp*) shape were selected and submitted to a cell optimization. By swapping/switching the two unit cell vectors, an overstretched narrow pore (*np*') form was constructed. For the cell optimizations, the convergence criterion for the electronic self-consistent field (SCF) problem is set to 10^{-6} eV while the force convergence criterion is put to 0.01 eV/Å. Between the minimum energy structures, a very detailed climbing NEB-run has been performed. [28] The intermediate points were cell optimized, until the force convergence criterion of 0.02 eV/Å was reached. In this way, an electronic energy profile could be constructed between the three observed phases. Electronic barriers between the phases could be estimated, based on this profile.

In order to get free-energy differences between these forms, frequency calculations have been performed on the various intermediate structures, in order to estimate the zero point vibrational energy and the entropy. To avoid imaginary frequencies, the structures were submitted to tighter convergence criteria, using the unit cell parameters for the previous cell optimization. The general kinetic energy cutoff is lowered to 600 eV for those tight optimizations. The convergence criterion for the electronic self-consistent field (SCF) problem is set to 10^{-7} eV while the force convergence criterion is put to either 0.001 or 0.002 eV/Å. Displacements of ±0.015 Å in the *a*, *b* and *c*-axis are used in the subsequent Hessian calculation, while the vibrational modes are extracted using the normal mode analysis as implemented in the in-house developed post-processing toolkit TAMKIN. [29]

Results and discussion

Synthesis and structrual characterization

COMOC-2 can be synthesized solvothermally and under microwave irradiation. The material is thermally stable up to 350 ^{o}C, as verified by thermogravimetric analysis (TGA) (Figure S1) and temperature programmed X-ray powder diffraction (TP-XRD) measurements (Figure S2). In COMOC-2(V^{IV}), the vanadium is exclusively V^{IV}, as verified by the ν(V=O) bands observed at 898 cm^{-1} from Raman spectrum and the absence of ν(OH) bands in diffuse reflectance infrared Fourier transform (DRIFT) spectrum (Figure 1 and 2). However, by varying the reaction conditions, two other variants of COMOC-2 were obtained. The V^{III} on COMOC-2(V^{IV}/V^{III}) was evidenced by a weak band at 3637 cm^{-1} which is assigned to the ν(OH) from V^{III}-OH. COMOC-2(*lp*) is in V^{IV} state, but still contains a small amount of free linker in the porous structure (not detectable by means of powder diffraction).

The oxidation state of the vanadium sites was further verified by XPS measurements. The spectra for COMOC-2(*lp*), COMOC-2(V^{IV}) and COMOC-2(V^{IV}/V^{III}) samples are shown in Figure S4. These spectra further confirm that COMOC-2(*lp*) and COMOC-2(V^{IV}) contain exclusively V^{IV}-sites, wheres the COMOC-2(V^{IV}/V^{III}) indeed shows a mixed valence.

COMOC-2(V^{IV}) and COMOC-2(V^{IV}/V^{III}) always show a mixture of *lp* and *np* phase as compared to COMOC-2(*lp*) in powder XRD measurements (Figure S5). It should be mentioned that COMOC-2(V^{IV}/V^{III}) and COMOC-2(*lp*) are two extreme variants synthesized under poorly reproducible conditions. The attempts to realize a more precise control over the ratio of the oxidation state were not successful. COMOC-2(V^{IV}) is the main focus of this article.

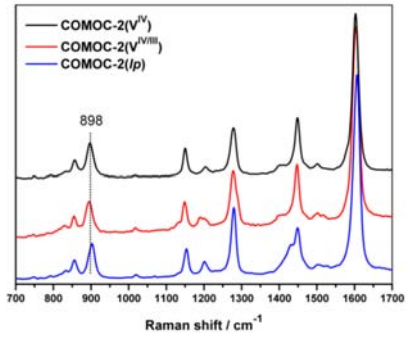

Figure 1. Raman spectra of COMOC-2(V^{IV}), COMOC-2(V^{IV}/V^{III}) and COMOC-2(*lp*). The band centered at 898 cm^{-1}, observed for COMOC-2 and its variants, is assigned to the ν (V=O) mode of the asymmetric V–O–V bond formed by sharing of two consecutive VO_6 octahedra.

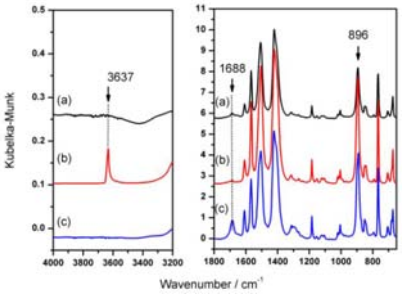

Figure 2. Comparison among the DRIFT spectra of (a) COMOC-2(V^{IV}), (b) COMOC-2(V^{IV}/V^{III}) and (c) COMOC-2(*lp*). The band centered at 896 cm^{-1}, observed for COMOC-2 and its variants, is assigned to the ν (V=O) mode of the asymmetric V–O–V bond formed by sharing of two consecutive VO_6 octahedra. The band at 1688 cm^{-1} is assigned to the stretching vibration of –COOH group of the free linker. The latter is clearly observed in

the IR spectrum of COMOC-2(*lp*) A weak band at 3637 cm^{-1} which is assigned to the ν (OH) from V^{III}-OH, this has only been observed from COMOC-2(V^{IV}/V^{III}).

A Rietveld refinement was performed on COMOC-2(*lp*) (Figure S3). The XRD pattern shows that COMOC-2(*lp*) is isostructural with the rigid microporous aluminium biphenyl-4,4'-dicarboxylate DUT-5. [15] COMOC-2 structure (Figure 3) contains chains of [30] octahedra cross-linked by $BPDC^{2-}$ organic linkers. The octahedral chains have a -O=V-O=V- coordination mode. The equatorial corners of the {VO_6} octahedra are shared with $BPDC^{2-}$ ligands. The 1D orthorhombic channels parallel to the octahedral chains have an aperture of ~18.9 × 19.4 Å. The refined *lp* structure has an accessible pore volume of 68.2% (2092.7 $Å^3$ per 3068.6 $Å^3$), as calculated by PLATON. [31]

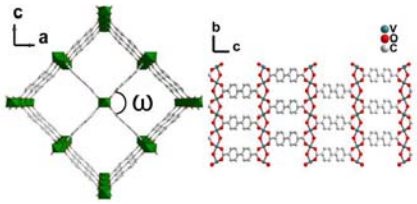

Figure 3. The *lp* form of COMOC-2 structure (*left*). The chains of corner-sharing {VO_6} octahedra (*right*). The pore angle ω corresponds to the dihedral angle between the two phenyl rings (*left*) and is defined according to tg ω/2 = c/a.

To study the role of oxidation state in determining the extent of framework flexibility, the N_2 adsorption/desorption isotherms (Figure 4) of COMOC-2(V^{IV}) and COMOC-2(V^{IV}/V^{III}) at 77 K were measured and compared. Both samples reveal a two-step sorption behavior, typical for flexible MOFs. For COMOC-2(V^{IV}), a gradual adsorption occurs until P/P_0 = 0.5,

when the isotherm reaches its first plateau. Then a very strong uptake of N_2 can be observed, rising steeply in the area P/P_0= 0.5~1.0; leading to a final uptake volume of 510 cm^3/g at P/P_0 = 0.98 (The maximum N_2 uptake volume of COMOC-2(V^{IV}) with different batches is around 510±40 cm^3/g). This sorption amount is similar to that of DUT-5, that has a Langmuir surface area of about 2335 $m^2\ g^{-1}$, and a total N_2 sorption amount of ~600 $cm^3\ g^{-1}$. A hysteresis occurs upon desorption. For COMOC-2(V^{IV}/V^{III}), the N_2 sorption isotherms at 77K also reveal a two-step sorption behavior. However, the first plateau is maintained until P/P_0 = 0.6, then followed by a large nitrogen uptake at higher relative pressures, leading to almost the same sorption amount as for COMOC-2(V^{IV}) at P/P_0 = 0.98. It is interesting to note that the presence of V^{III} in COMOC-2(V^{IV}/V^{III}) compared to pure COMOC-2(V^{IV}) increases the difficulty in triggering the flexibility of the framework. This phenomenon is contrary to MIL-47, in which the presence of V^{IV} centers inhibits the flexibility to a large extent.[932] The reason that COMOC-2(V^{III}/V^{IV}) needs a higher nitrogen pressure to open up the pores, might be due to remaining internal stabilization effects (e.g. H-bonding).

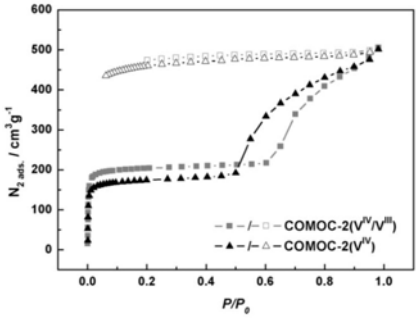

Figure 4. N_2 adsorption (solid symbols) and desorption (open symbols) isotherms of COMOC-2(V^{IV}) (black) and COMOC-2(V^{IV}/V^{III}) (gray) at 77 K.

Gas / vapor sorption isotherms

To further verify the structural transformation of COMOC-2(V^{IV}), CO_2, CH_4 and *n*-hexane sorption isotherms were measured. As shown in Figure 5a, the adsorption isotherms at 303 K for both CO_2 and CH_4 show a classical type I shape, with a capacity of 4.8 mmol CO_2 g^{-1} at 25 bar and 1.4 mmol CH_4 g^{-1} at 27 bar. At 265K however, the CO_2 and CH_4 isotherms become distinctively different. In the CO_2 sorption isotherm at around 12.5 bar, a sudden increase in adsorption is observed, reaching 14 mmol g^{-1} at 28 bar, corresponding to almost complete pore filling based on the nitrogen porosimetry data. Two distinct steps are clearly observed, revealing a breathing of the framework. Desorption occurs with a large hysteresis loop. This loop is explained with the stress model developed by Neimark et al. [33] According to this model, structural transition or phase transformation, i.e. the breathing effect, occurs when a certain critical stress threshold is reached. As a consequence, the structural transition pressure depends on the stress threshold. As the stress threshold is different for the various phases, a hysteresis occurs in the adsorption-desorption process. Also at this lower temperature, CH_4 presents a type I isotherm. The desorption curve for CH_4 almost coincides with adsorption isotherm without the occurrence of any hysteresis. The adsorption profile of COMOC-2(V^{IV}) shows a distinctive adsorption step at 265 K for CO_2 but not for CH_4. This is similar to the CO_2 and CH_4 adsorption behavior of MIL-53 at 304 K. [7]

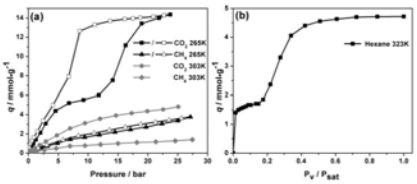

Figure 5. (a) Adsorption (solid symbol) isotherms of COMOC-2(V^{IV}) for CO_2 and CH_4 at 303 and 265 K. Desorption isotherms (open symbol) of CO_2 and CH_4 at 265 K are also included. (b) Adsorption isotherm for *n*-hexane at 323 K on COMOC-2(V^{IV}).

n-Hexane, having larger molecular weight and thus comparatively larger van der Waals interactions, shows the two-step adsorption behavior associated with framework breathing at 323 K. As shown in Figure 5b, in the first plateau, when COMOC-2(V^{IV}) is in the *np* form, the adsorption capacity is ca. 2 mmol g^{-1}. The framework opens up at P/P_0 = 0.2 to reach a final hexane adsorption capacity of 4.7 mmol g^{-1} or almost 40 w% at saturation pressure.

Analysis of in situ synchrotron XRD Patterns

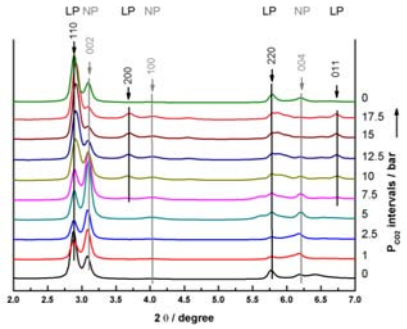

Figure 6. In-situ synchrotron XRD patterns of COMOC-2(V^{IV}) (λ = 0.75276 Å) in the 2θ range 2-7° measured at a certain CO_2 pressure at 233 K. The apparent phase changes and peak indices are marked with arrows.

In order to correlate this intriguing breathing adsorption behavior to structural changes in the COMOC-2(V^{IV}) sample, we have performed *in-situ* synchrotron XRD studies at 233 K

using the Swiss-Norwegian beamline at the European Synchrotron Radiation Facility (ESRF) equipped with a pressure controlled apparatus dosing CO_2 gas up to a pressure of 17.5 bar. In Figure 6 and Figure S6 we show this series of in-situ XRPD patterns in a different view. The XRD patterns collected as a function of the CO_2 pressure clearly show the reversible structural changes that accompany the breathing effect. The first XRD pattern of the sample recorded in vacuum shows mainly a *lp* phase, with a fraction of *np* phase. When the pressure is increased up to 1 bar of CO_2, the *lp* to *np* transition occurs immediately, as shown by the sudden decrease in intensity of the *lp* reflections and the appearance of the *np* reflections. The *lp* to *np* transformation process continues until the CO_2 pressure reaches 7.5 bar. Above this pressure, the structure opens again, accompanied by the reversible intensity change in the representative *np* to *lp* reflection peaks. After the high pressure measurements, upon removal of CO_2, the final degassed sample shows peaks entirely consistent with the original phase, confirming the reversibility of this transition process. As shown in Figure S6 (top), the background intensity increases with the amount of CO_2 molecules adsorbed, due to the increment of the electron density when pressure rises.

Table 1. The calculated and empirically determined lattice parameters for the different forms of COMOC-2(V^{IV}).

phase	Crystal system	*a* (Å)	*b* (Å)	*c* (Å)	*α* (deg)	*β* (deg)	*γ* (deg)	*V*(Å^3)
np (exp.)[a]	monoclinic	6.651(4)	27.94(4)	10.735(13)	97.06(8)	90	90	1979.4(47)
np (cal.)	orthorhombic	6.991	28.111	6.809	90	90	90	1338.13
lp (exp.)[b]	orthorhombic	6.776(3)	23.087(19)	18.897(9)	90	90	90	2956.1(32)

lp (cal.)	orthorhombic	6.927	21.642	20.498	90	90	90	3073.00
lp (exp.)[c]	orthorhombic	6.957(4)	21.443(3)	20.570(2)	90	90	90	3069(5)
lp' (cal.)	orthorhombic	6.981	7.946	27.275	90	90	90	1512.97

[a] Determined based on synchrotron XRPD pattern with 7.5 bar CO_2 pressure at 233 K; [b] Determined based on synchrotron XRPD pattern with 15 bar CO_2 pressure at 233 K; [c] Crystal data obtained from Rietveld structure refinement on laboratory XRPD pattern of COMOC-2(*lp*) at 293 K.

Since all the *in-situ* synchrotron XRD patterns contain both *lp* and *np* phases, we were unable to select a pattern of pure phase for Rietveld refinement. To estimate the flexibility of the framework, two XRD patterns were selected and used to index the unit cell parameters (Table 1). The *np* phase was indexed to a monoclinic cell with V~1979 Å^3, whereas the *lp* phase was indexed to a orthorhombic cell with V~2956 Å^3. For comparison, also the lattice parameters determined from theoretical calculations and laboratory XRPD patterns are taken up in Table 1. However, we should stress that the theoretical predictions for the lattice parameters are based on an empty host system, while the experimental values are resulting from synchrotron XRD patterns under certain CO_2 pressure. We must be very careful when comparing both results. Due to the adsorption of CO_2 molecules in the structure, the free energy profile can change significantly, especially in the region of the narrow pore phases. The minima around 27 ° and 148 ° coresponding respectively with *np* and *np'* , as observed in Figure 7, can never be reached as the presence of guest molecules in the pores will obviously lead to larger pore angles. However, when we compare the experimental data recorded at ambient conditions (COMOC-2(*lp*)) with the theoretical *lp* predictions, the data match perfectly.

Full free energy profile for the empty COMOC-2(V^{IV}) structure :

Following the methodology, as oulined before, a full free energy profile has been constructed for the empty COMOC-2(V^{IV}) structure in function of the breathing angle ω. As indicated in Figure 7, three stable minima were found in the empty host framework: the *np*, the *lp* and an overstretched narrow pore (*np'*) form. The two modeled narrow pore forms are different in geometry- they are displayed in Figures S8-S9- and their unit cell topology may be compared with the *vnp* structure as observed in anhydrous MIL-53(Fe) by the group of Férey,[34] as the theoretical models have been modeled in the complete absence of water. The pore angles for the different structures are shown in Table 2. As only indexed lattice parameters are provided from the synchrotron XRD experiments, a unified force field (UFF) is used to generate structures for the *np* and *lp* phases which fit the experimental XRPD patterns with the cell parameters a, b, c and the angles α, β and γ as degrees of freedom. Please note that a direct one-to-one correspondence with the ab-initio determined lattice parameters should be considered with care, since the XRPD patterns have been measured with the presence of CO_2 adsorbate molecules, while the periodic VASP calculations have been performed in the empty host. As shown in table 2, all theoretical phases are found to be orthorhombic. The small pore angle for the *np* phase requires some additional clarification. The angle $O_{ca,1}$-V-$O_{ca,3}$ (α) is more or less constant in the two models (ab-initio and empirical) around 85 °, which is realistic, and thus plays no significant role in shrinking of the pore angle. The dihedral motion V-O_{ca}-C_{ca}-C_{pc} (χ) determines the rotation of the linker about the O_{ca}-O_{ca} axes of the carboxyl groups. This rotation enables shrinkage or expansion of the entire unit cell. The dihedral angle O_{ca}-C_{ca}-C_{pc}-C_{ph} controls the tilting of the plane of the linker (see Figure S8). Table 2 also reports the average χ of these tilting angles.

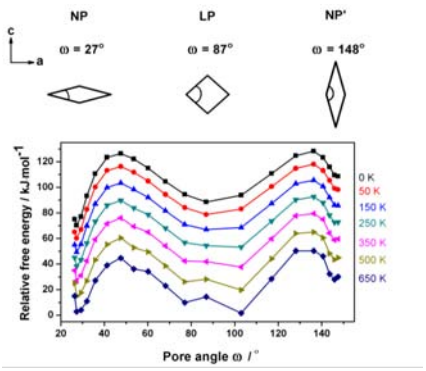

Figure 7. The modelled free energy profiles as a function of temperature for the empty COMOC-2(V^{IV}). Three different minima are observed, representing the different pore shapes: *np, lp* and *np*'. Profiles at different temperatures are shifted by 10 kJ/mol.

Table 2. The pore angle ω (as defined in Figure 3) and the angle χ being the average of the two dihedral angles V-O_{ca}-C_{ca}-C_{pc} for the different structures (for the atomic labeling: see Figure S7). α stands for the angle $O_{ca,1}$-V-$O_{ca,3}$ in the equatorial plane of the four carboxyl oxygens coordinated with V. The deviation from planarity is the angle between the planes of the two phenyl groups within the biphenyl linker.

phase	Crystal system	*ω* (deg)	χ (deg)	α (deg)	deviation planarity biphenyl (deg)
np (emp.)[a]	Monoclinic	42.0	143.7	84.4	0.9
np (cal.)	Orthorhombic	27.2	142.5	84.5	46.3
lp (emp.)[b]	Orthorhombic	78.6	-	-	-
lp (cal.)	Orthorhombic	86.9	165.5	87.5	46.7
lp (exp.)[c]	Orthorhombic	87.6	164.1	80.6	1.9

lp' (cal.)	Orthorhombic	147.5	139.6	85.8	49.1

[a] Empirically determined based on synchrotron XRPD pattern with 7.5 bar CO_2 pressure at 233 K; [b] Empirically determined based on synchrotron XRPD pattern with 15 bar CO_2 pressure at 233 K; [c] Determined based on the crystal data obtained from Rietveld structure refinement on laboratory XRPD pattern of COMOC-2(*lp*) at 293 K.

Table 3. Free energy barriers ($\Delta G^{\ddagger}$(*lp*→*np*) and $\Delta G^{\ddagger}$(*lp*→*np'*) in kJ mol^{-1} required for the shape transformations.

Temperature (K)	$\Delta G^{\ddagger}$ (*lp*→*np*)	$\Delta G^{\ddagger}$ (*lp*→*np*')
0	37.9	39.8
50	37.6	39.4
150	36.5	38.6
250	36.6	39.4
350	38.3	41.7
500	40.7	45.2
650	43.1	48.7

In complete agreement with earlier work of Walker et al.,[35] addition of dispersion corrections [27,36] is needed to get realistic energy differences between *lp* and *np* forms. Without dispersion interactions, the three minima are not found. As frequency calculations were performed for every point along the profile, we were able to determine also the vibrational entropic contributions of the smallest unit cell and to plot the free energy profiles for various temperatures. The numerical results reveal that the free energy barrier for the *lp* → *np* phase transition is more or less constant with temperature, with a value varying between 36 and 42 kJ mol^{-1} (Table 3). The free energy difference between the *np* forms

decreases from 38.3 to 27.2 kJ mol^{-1} when increasing the temperature from 0 to 650 K. The theoretically determined free energy profiles of the empty host give evidence for a tri-stable behavior of COMOC-2(V^{IV}), favoring the large pore structure when temperature rises. Experimentally, the breathing behavior is only observed at a certain CO_2 pressure. No phase transitions are taken place with CH_4. The occurrence of a breathing behavior depends on the strength of the host-guest interactions. For a molecule as CO_2 exhibiting strong interactions with the pore walls, the free energy barrier towards the *np* may already be overcome at 1 bar, as demonstrated by the experiment. As our simulations were performed without guest molecules, we cannot correlate exactly the pore angle and lattice parameters for the *np* and *lp* shapes with the experimental values given in Table 1. In particular, the theoretical lattice parameter along the *c*-axis for the *np* form is smaller compared to the experimental value, since the *np* form may not fully close due to the presence of adsorbate molecules. Our simulations do however clearly show that COMOC-2(V^{IV}) has an intrinsic tri-stable behavior.

Conclusions

In conclusion, a V^{IV} carboxylate MOF COMOC-2 having the same framework topology as MIL-47 was synthesized and fully characterized. Unlike MIL-47, COMOC-2(V^{IV}) shows a breathing effect upon gas and vapor sorption at mild conditions. Similar to MIL-53, the sorption isotherms of CO_2 and CH_4 display a different shape at specific temperatures. Compared to COMOC-2(V^{IV}), COMOC-2(V^{III}/V^{IV}) increases the difficulty in triggering the flexibility of the framework. The theoretically determined free energy profile along the pore angle points toward a tri-stable behavior of the material. Apart from a regular *np* form, an overstretched narrow pore configuration was theoretically found. Future work will focus on

the understanding of the phase transitions induced within COMOC-2(V^{IV}) by various other adsorbates, targeting potential applications in selective gas adsorption and molecular sensing.

Supporting Information. Crystallographic information file (CIF) of COMOC-2(*lp*), general information on additional structural information in the free energy profile, detailed XPS data analysis, TGA, Rietveld refinement plot, powder XRD measurements and ab initio simulated structure information. This material is available free of charge via the Internet at http://pubs.acs.org."

AUTHOR INFORMATION

Corresponding Author

*** E-mail: pascal.vandervoort@ugent.be**

Acknowledgements

The ESRF is acknowledged for providing access to the Swiss-Norwegian beamline. The authors acknowledge the financial support from the Ghent University BOF Grant (Nr. 01P02911T and 01D31608), GOA Grant (Nr. 01G00710), the Long Term Structural Methusalem Grant (Nr. 01M00409), BELSPO in the frame of IAP 6/27 and the European Research Council (FP7(2007-2013) ERC Grant (Nr. 240483). Computational resources (Stevin Supercomputer Infrastructure) and services were provided by Ghent University.

REFERENCES

(1) (a) Denayer, J. F. M.; Finsy, V.; Ma, L.; Alaerts, L.; De Vos, D. E.; Baron, G. V. *Microporous Mesoporous Mater.* **2009**, *120*, 221; (b) Trens, P.; Trung, T. K.; Tanchoux, N.; Bourrelly, S.; Llewellyn, P. L.; Loera-Serna, S.; Serre, C.; Loiseau, T.; Fajula, F.; Ferey,

G. *J. Am. Chem. Soc.* **2008**, *130*, 16926; (c) De Weireld, G.; Hamon, L.; Serre, C.; Devic, T.; Loiseau, T.; Millange, F.; Ferey, G. *J. Am. Chem. Soc.* **2009**, *131*, 8775; (d) Rosi, N. L.; Eckert, J.; Eddaoudi, M.; Vodak, D. T.; Kim, J.; O'Keeffe, M.; Yaghi, O. M. *Science* **2003**, *300*, 1127; (e) Tonigold, M.; Lu, Y.; Mavrandonakis, A.; Puls, A.; Staudt, R.; Möllmer, J.; Sauer, J.; Volkmer, D. *Chem. Eur. J.* **2011**, *17*, 8671.

(2) (a) Barthelet, K.; Marrot, J.; Riou, D.; Ferey, G. *Angew. Chem. Int. Ed.* **2001**, *41*, 281; (b) Ferey, G.; Serre, C. *Chem. Soc. Rev.* **2009**, *38*, 1380.

(3) Uemura, K.; Kitagawa, S.; Kondo, M.; Fukui, K.; Kitaura, R.; Chang, H. C.; Mizutani, T. *Chem. Eur. J.* **2002**, *8*, 3586.

(4) Horike, S.; Shimomura, S.; Kitagawa, S. *Nat. Chem.* **2009**, *1*, 695.

(5) (a) Loiseau, T.; Serre, C.; Huguenard, C.; Fink, G.; Taulelle, F.; Henry, M.; Bataille, T.; Ferey, G. *Chem. Eur. J.* **2004**, *10*, 1373; (b) Serre, C.; Millange, F.; Thouvenot, C.; Nogues, M.; Marsolier, G.; Louer, D.; Ferey, G. *J. Am. Chem. Soc.* **2002**, *124*, 13519; (c) Whitfield, T. R.; Wang, X. Q.; Liu, L. M.; Jacobson, A. J. *Solid State Sci.* **2005**, *7*, 1096; (d) Jacobson, A. J.; Vougo-Zanda, M.; Huang, J.; Anokhina, E.; Wang, X. Q. *Inorg. Chem.* **2008**, *47*, 11535; (e) Anokhina, E. V.; Vougo-Zanda, M.; Wang, X. Q.; Jacobson, A. J. *J. Am. Chem. Soc.* **2005**, *127*, 15000; (f) Mowat, J. P. S.; Miller, S. R.; Slawin, A. M. Z.; Seymour, V. R.; Ashbrook, S. E.; Wright, P. A. *Microporous Mesoporous Mater.* **2011**, *142*, 322.

(6) (a) Serre, C.; Bourrelly, S.; Vimont, A.; Ramsahye, N. A.; Maurin, G.; Llewellyn, P. L.; Daturi, M.; Filinchuk, Y.; Leynaud, O.; Barnes, P.; Ferey, G. *Adv. Mater.* **2007**, *19*, 2246;

(b) Liu, Y.; Her, J. H.; Dailly, A.; Ramirez-Cuesta, A. J.; Neumann, D. A.; Brown, C. M. *J. Am. Chem. Soc.* **2008**, *130*, 11813; (c) Thallapally, P. K.; Tian, J.; Kishan, M. R.; Fernandez, C. A.; Dalgarno, S. J.; McGrail, P. B.; Warren, J. E.; Atwood, J. L. *J. Am. Chem. Soc.* **2008**, *130*, 16842; (d) Trung, T. K.; Trens, P.; Tanchoux, N.; Bourrelly, S.; Llewellyn, P. L.; Loera-Serna, S.; Serre, C.; Loiseau, T.; Fajula, F.; Ferey, G. *J. Am. Chem. Soc.* **2008**, *130*, 16926; (e) Volkringer, C.; Loiseau, T.; Guillou, N.; Ferey, G.; Elkaim, E.; Vimont, A. *Dalton Trans.* **2009**, 2241.

(7) Bourrelly, S.; Llewellyn, P. L.; Serre, C.; Millange, F.; Loiseau, T.; Ferey, G. *J. Am. Chem. Soc.* **2005**, *127*, 13519.

(8) (a) Wang, Z. Q.; Cohen, S. M. *J. Am. Chem. Soc.* **2009**, *131*, 16675; (b) Ramsahye, N. A.; Trung, T. K.; Bourrelly, S.; Yang, Q. Y.; Devic, T.; Maurin, G.; Horcajada, P.; Llewellyn, P. L.; Yot, P.; Serre, C.; Filinchuk, Y.; Fajula, F.; Ferey, G.; Trens, P. *J. Phys. Chem. C* **2011**, *115*, 18683; (c) Biswas, S.; Ahnfeldt, T.; Stock, N. *Inorg. Chem.* **2011**, *50*, 9518.

(9) Leclerc, H.; Devic, T.; Devautour-Vinot, S.; Bazin, P.; Audebrand, N.; Ferey, G.; Daturi, M.; Vimont, A.; Clet, G. *J. Phys. Chem. C* **2011**, *115*, 19828.

(10) Yot, P. G.; Ma, Q.; Haines, J.; Yang, Q.; Ghoufi, A.; Devic, T.; Serre, C.; Dmitriev, V.; Ferey, G.; Zhong, C.; Maurin, G. *Chem. Sci.* **2012**.

(11) (a) Finsy, V.; Kirschhock, C. E. A.; Vedts, G.; Maes, M.; Alaerts, L.; De Vos, D. E.; Baron, G. V.; Denayer, J. F. M. *Chem. Eur. J.* **2009**, *15*, 7724; (b) Finsy, V.; Ma, L.; Alaerts, L.; De Vos, D. E.; Baron, G. V.; Denayer, J. F. M. *Microporous Mesoporous Mater.*

2009, *120*, 221; (c) Couck, S.; Denayer, J. F. M.; Baron, G. V.; Remy, T.; Gascon, J.; Kapteijn, F. *J. Am. Chem. Soc.* **2009**, *131*, 6326; (d) De Vos, D. E.; Maes, M.; Vermoortele, F.; Alaerts, L.; Couck, S.; Kirschhock, C. E. A.; Denayer, J. F. M. *J. Am. Chem. Soc.* **2010**, *132*, 15277; (e) Denayer, J. F. M.; Couck, S.; Remy, T.; Baron, G. V.; Gascon, J.; Kapteijn, F. *Phys. Chem. Chem. Phys.* **2010**, *12*, 9413.

(12) Serra-Crespo, P.; van der Veen, M. A.; Gobechiya, E.; Houthoofd, K.; Filinchuk, Y.; Kirschhock, C. E. A.; Martens, J. A.; Sels, B. F.; De Vos, D. E.; Kapteijn, F.; Gascon, J. *J. Am. Chem. Soc.* **2012**, *134*, 8314.

(13) (a) Serre, C.; Horcajada, P.; Maurin, G.; Ramsahye, N. A.; Balas, F.; Vallet-Regi, M.; Sebban, M.; Taulelle, F.; Ferey, G. *J. Am. Chem. Soc.* **2008**, *130*, 6774; (b) Horcajada, P.; Chalati, T.; Serre, C.; Gillet, B.; Sebrie, C.; Baati, T.; Eubank, J. F.; Heurtaux, D.; Clayette, P.; Kreuz, C.; Chang, J. S.; Hwang, Y. K.; Marsaud, V.; Bories, P. N.; Cynober, L.; Gil, S.; Ferey, G.; Couvreur, P.; Gref, R. *Nat. Mater.* **2010**, *9*, 172.

(14) (a) Llewellyn, P. L.; Maurin, G.; Devic, T.; Loera-Serna, S.; Rosenbach, N.; Serre, C.; Bourrelly, S.; Horcajada, P.; Filinchuk, Y.; Ferey, G. *J. Am. Chem. Soc.* **2008**, *130*, 12808; (b) Boutin, A.; Springuel-Huet, M. A.; Nossov, A.; Gedeon, A.; Loiseau, T.; Volkringer, C.; Ferey, G.; Coudert, F. X.; Fuchs, A. H. *Angew. Chem. Int. Ed.* **2009**, *48*, 8314; (c) Devautour-Vinot, S.; Maurin, G.; Henn, F.; Serre, C.; Devic, T.; Ferey, G. *Chem. Commun.* **2009**, 2733; (d) Yang, C.; Wang, X. P.; Omary, M. A. *Angew. Chem. Int. Ed.* **2009**, *48*, 2500; (e) Boutin, A.; Couck, S.; Coudert, F. X.; Serra-Crespo, P.; Gascon, J.;

Kapteijn, F.; Fuchs, A. H.; Denayer, J. F. M. *Microporous Mesoporous Mater.* **2011**, *140*, 108.

(15) Senkovska, I.; Hoffmann, F.; Froba, M.; Getzschmann, J.; Bohlmann, W.; Kaskel, S. *Microporous Mesoporous Mater.* **2009**, *122*, 93.

(16) Lasocha, W.; Lewinski, K. *J. Appl. Crystallogr.* **1994**, *27*, 437.

(17) V. Petricek; M. Dusek; Palatinus, L. *Jana2006. The crystallographic computing system.* **2006**.

(18) Hammersley, A. P., ESRF Internal Report.

(19) Boultif, A.; Louer, D. *J. Appl. Crystallogr.* **1991**, *24*, 987.

(20) STOE WinXPOW version 2.11.

(21) Walker, A. M.; Civalleri, B.; Slater, B.; Mellot-Draznieks, C.; Cora, F.; Zicovich-Wilson, C. M.; Roman-Perez, G.; Soler, J. M.; Gale, J. D. *Angew. Chem. Int. Ed.* **2010**, *49*, 7501.

(22) Stavitski, E.; Pidko, E. A.; Couck, S.; Remy, T.; Hensen, E. J. M.; Weckhuysen, B. M.; Denayer, J.; Gascon, J.; Kapteijn, F. *Langmuir* **2011**, *27*, 3970.

(23) Triguero, C.; Coudert, F. X.; Boutin, A.; Fuchs, A. H.; Neimark, A. V. *J. Phys. Chem. Lett.* **2011**, *2*, 2033.

(24) (a) Kresse, G.; Furthmuller, J. *Phys. Rev. B* **1996**, *54*, 11169; (b) Kresse, G.; Furthmuller, J. *Comput. Mater. Sci.* **1996**, *6*, 15; (c) Kresse, G.; Hafner, J. *Physical Review B* **1993**, *47*, 558; (d) Kresse, G.; Hafner, J. *Phys. Rev. B* **1994**, *49*, 14251.

(25) (a) Perdew, J. P.; Burke, K.; Ernzerhof, M. *Phys. Rev. Lett.* **1996**, *77*, 3865; (b) Perdew, J. P.; Burke, K.; Ernzerhof, M. *Phys. Rev. Lett.* **1997**, *78*, 1396.

(26) Blochl, P. E. *Phys. Rev. B* **1994**, *50*, 17953.

(27) Grimme, S. *J. Comput. Chem.* **2006**, *27*, 1787.

(28) Henkelman, G.; Uberuaga, B. P.; Jonsson, H. *J. Chem. Phys.* **2000**, *113*, 9901.

(29) Ghysels, A.; Verstraelen, T.; Hemelsoet, K.; Waroquier, M.; Van Speybroeck, V. *J. Chem. Inf. Model.* **2010**, *50*, 1736.

(30) Ouellette, W.; Yu, M. H.; O'Connor, C. J.; Zubieta, J. *Inorg. Chem.* **2006**, *45*, 7628.

(31) Spek, A. *J. Appl. Crystallogr.* **2003**, *36*, 7.

(32) Serra-Crespo, P.; Gobechiya, E.; Ramos-Fernandez, E. V.; Juan-Alcañiz, J.; Martinez-Joaristi, A.; Stavitski, E.; Kirschhock, C. E. A.; Martens, J. A.; Kapteijn, F.; Gascon, J. *Langmuir* **2012**, *28*, 12916.

(33) Neimark, A. V.; Coudert, F. X.; Boutin, A.; Fuchs, A. H. *J. Phys. Chem. Lett.***2010**, *1*, 445.

(34) Llewellyn, P. L.; Horcajada, P.; Maurin, G.; Devic, T.; Rosenbach, N.; Bourrelly, S.; Serre, C.; Vincent, D.; Loera-Serna, S.; Filinchuk, Y.; Ferey, G. *J. Am. Chem. Soc.* **2009**, *131*, 13002.

(35) Walker, A. M.; Civalleri, B.; Slater, B.; Mellot-Draznieks, C.; Corà, F.; Zicovich-Wilson, C. M.; Román-Pérez, G.; Soler, J. M.; Gale, J. D. *Angew. Chem. Int. Ed.* **2010**, *49*, 7501.

(36) (a) Grimme, S. *J. Comput. Chem.* **2004**, *25*, 1463; (b) Grimme, S.; Antony, J.; Ehrlich, S.; Krieg, H. *J. Chem. Phys.* **2010**, *132*.

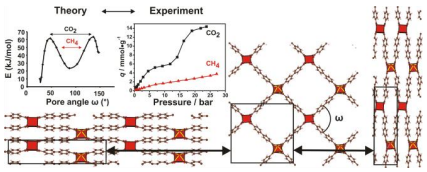

A flexible V^{IV} based metal-organic framework VO(BPDC) featuring MIL-47 topology was synthesized. This framework shows a different profile in CO_2 and CH_4 sorption at 265 K. The in- situ XRD measurements are coupled to climbing Nudged Elastic Band calculations to find the free energy profile of the different phases.

Supporting information for

A new V^{IV} based metal-organic framework having framework flexibility and high CO_2 adsorption capacity

Ying-Ya Liu, Sarah Couck, Matthias Vandichel, Maciej Grzywa, Karen Leus, Shyam Biswas, Dirk Volkmer, Jorge Gascon, Freek Kapteijn, Joeri F. M. Denayer, Michel Waroquier, Veronique Van Speybroeck and Pascal Van Der Voort*

**COMOC - Centre for Ordered Materials, Organometallics and Catalysis, Department of Inorganic and Physical Chemistry, Ghent University, Krijgslaan 281-S3, 9000 Ghent; Belgium.*

E-mail: pascal.vandervoort@ugent.be

Contents

1. Figure S1. TG and DTA curves of COMOC-2 in air flow.
2. Figure S2. Top: TP-XRD patterns of COMOC-2 at selected temperatures. Bottom: variation of intensities of the Bragg peaks as a function of temperature (λ = 1.5406 Å).
3. Figure S3. The Rietveld refinement plots for COMOC-2(*lp*).
4. Figure S4. The V 2p XPS spectra as well as the wide scan spectra of the COMOC-2(*lp*), COMOC-2(V^{IV}) and COMOC-2(V^{IV}/V^{III}) samples.
5. The detailed interpretation of XPS spectra.
6. Figure S5. Comparison among the experimental powder XRD patterns of COMOC-2(V^{IV}), COMOC-2(V^{IV}/V^{III}), COMOC-2(*lp*) and the simulated XRD pattern of COMOC-2(*lp*) obtained from Rietveld refinement data (λ = 1.5406 Å).
7. Figure S6. Full range (top) and selected range (bottom) of *in-situ* synchrotron XRD patterns measured at 233 K (λ = 0.75276 Å).
8. Additional structural information about the appearance of three minima in the free energy profile.
9. Figure S7. Schematic picture of a partial structure of COMOC-2 with labelling of the different atom types.
10. Figure S8. Ab initio simulated structures of COMOC-2(V^{IV}), representing the three phases: *np*, *lp* and *np'*.
11. Figure S9. Ab initio simulated structures of COMOC-2(V^{IV}), representing the three phases: *np*, *lp* and *np'*.
12. Table S1. Crystal data and structure refinement summary for the *lp* form of COMOC-2.
13. Table S2. Atomic coordinates for the *lp* form of COMOC-2.
14. Table S3. Bond distances for the *lp* form of COMOC-2.

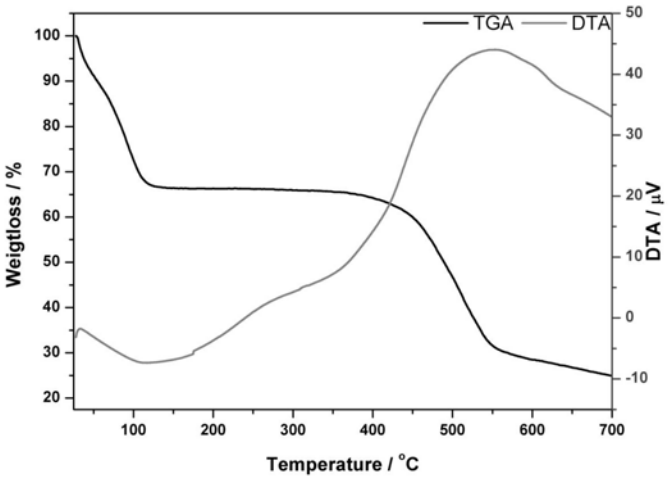

Figure S1. TG and DTA curves of COMOC-2 in air flow.

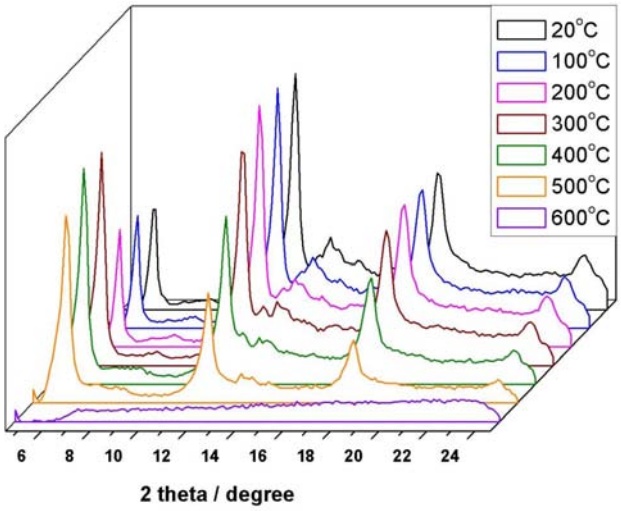

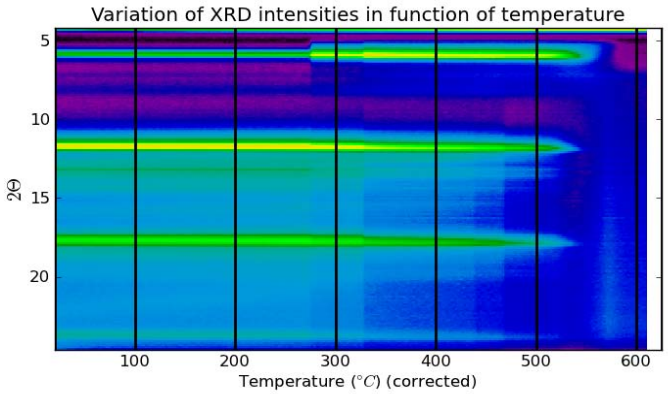

Figure S2. Top: TP-XRD patterns of COMOC-2 at selected temperatures. Bottom: variation of intensities of the Bragg peaks as a function of temperature (λ = 1.5406 Å).

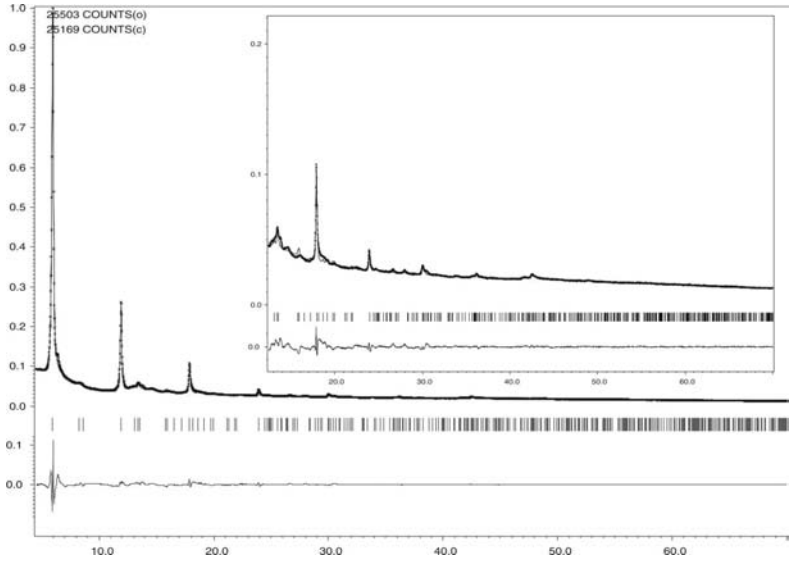

Figure S3. The Rietveld refinement plots for COMOC-2(*lp*). Dotted and solid lines represent observed and calculated patterns, respectively, with peak markers and the difference plot shown at the bottom. For clarity, the insert shows an expanded view of the 2θ range 12-70 °. (λ = 1.5406 Å)

The detailed interpretation of XPS spectra

As shown in Figure S4d, the binding energis for O 1s for COMOC-2(*lp*) and COMOC-2(V^{IV}) have the same value of 531.58 eV. For the COMOC-2(V^{IV}/V^{III}) sample, the binding energy for O 1s has shifted to a higher energy of 531.88 eV. It should be noted that O1s is shown to be the best calibration signal for V2p core level spectra of vanadium oxides[1], therefore, the difference of binding energy (Δ) between the O1s and $V2p_{3/2}$ level is the best measure to determine the oxidation state of the vanadium species[1-2], as it is not sensitive to small changes in absolute energy. The analysis of the V 2p portion of the spectrum shows that the $V2p_{3/2}$ binding energy of COMOC-2(*lp*) (Figure S4a) and COMOC-2(V^{IV}) (Figure S4b) can both be fitted with a single component at 516.98 eV, the Δ between the O1s and $V2p_{3/2}$ levels is 14.6 eV, which exactly points to V^{IV} $V2p_{3/2}$[1]. The $V2p_{1/2}$ of COMOC-2(*lp*) and COMOC-2(V^{IV}) are centered at 524.28 eV and 524.78 eV respectively. These results clearly demonstrate that the COMOC-2(*lp*) and COMOC-2(V^{IV}) are in a pure V^{IV} state. The V2p portion of COMOC-2(V^{IV}/V^{III}) spectrum (Figure S4c) cannot be fitted to a single component. The parameter fitting shows the binding energy of V $2p_{3/2}$ at 517.5 eV and V $2p_{3/2}$ at 516.8 eV, while the Δ between the O1s and $V2p_{3/2}$ levels is 14.4 eV and 15.0 eV, which corresponds to the binding energy of a mixed V^{IV} and V^{III} state[1]. Also, $V2p_{1/2}$ of COMOC-2(V^{IV}/V^{III}) needs to be fitted with two oxidation states, centered at 523.4 eV and 522.2 eV. All these values show that COMOC-2(V^{IV}/V^{III}) sample indeed contains a mixed V^{IV} and V^{III} oxidation state.

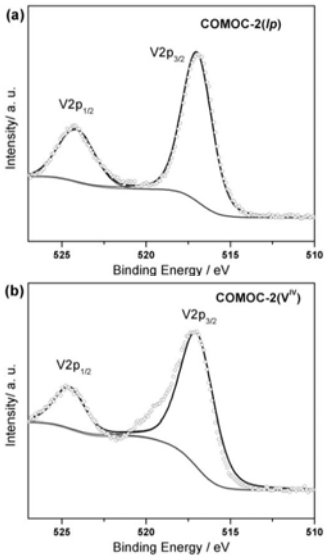

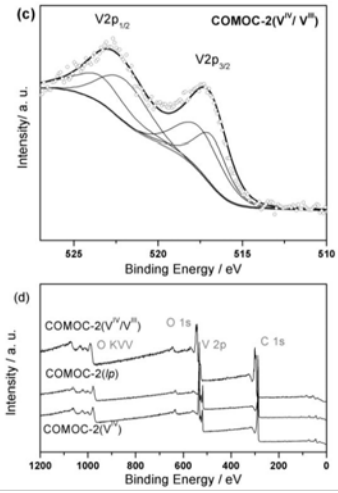

Figure S4. The V 2p XPS spectra as well as the wide scan spectra of the COMOC-2(*lp*), COMOC-2(V^{IV}) and COMOC-2(V^{IV}/V^{III}) samples.

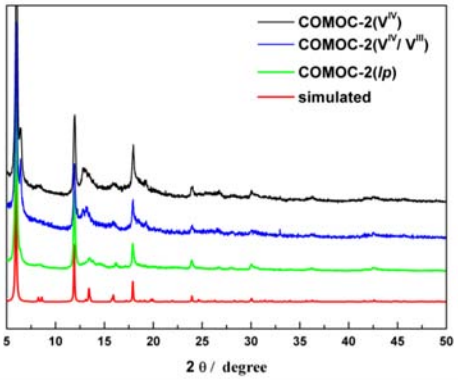

Figure S5. Comparison among the experimental powder XRD patterns of COMOC-2(V^{IV}), COMOC-2(V^{IV}/V^{III}), COMOC-2(*lp*) and the simulated XRD pattern of COMOC-2(*lp*) obtained from Rietveld refinement data (λ = 1.5406 Å).

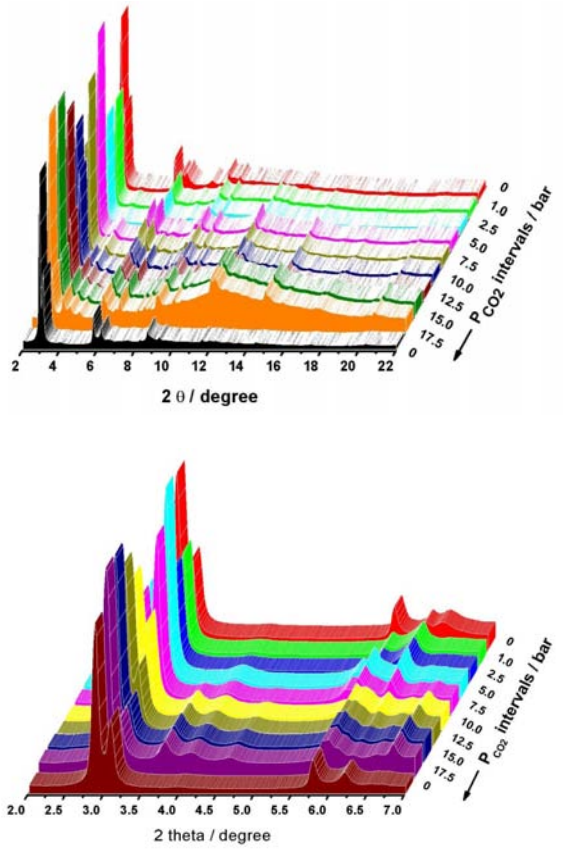

Figure S6. Full range (top) and selected range (bottom) of *in-situ* synchrotron XRD patterns measured at 233 K (λ = 0.75276 Å). Each pattern was measured at a certain CO_2 pressure. Note that all the XRD patterns contain both *lp* and *np* phases.

Additional structural information about the appearance of three minima in the free energy profile for COMOC-2(V^{IV}) representing the narrow pore (*np*), large pore (*lp*) and overstretched narrow pore (*np'*) in the empty frame.

To facilitate the discussion, different atom types have been introduced and defined in Figure S7. Figure S8 displays the three different simulated phase structures of COMOC-2(V^{IV}) in the bc-plane as obtained in the periodic ab initio calculation. Four equatorial oxygens O_{ca} coordinate with the same vanadium to form a square (example of such a square is shown in Figure S7). Together with the closest vanadyl oxygen O_{va}, a square-pyramid is formed (red colored in the Figures S8 and S9). The cross in the square indicates that the vanadyl oxygen lies above the plane. The vanadium metal always lies in the interior of the pyramid close to the square basis. Similarly, the three structures are also visualized in the ac-plane (Figure S9). The real situation of the *np* structure is sketched in Figure S9, where the four equatorial O_{ca} oxygens coordinated with the vanadium are shown as squares.

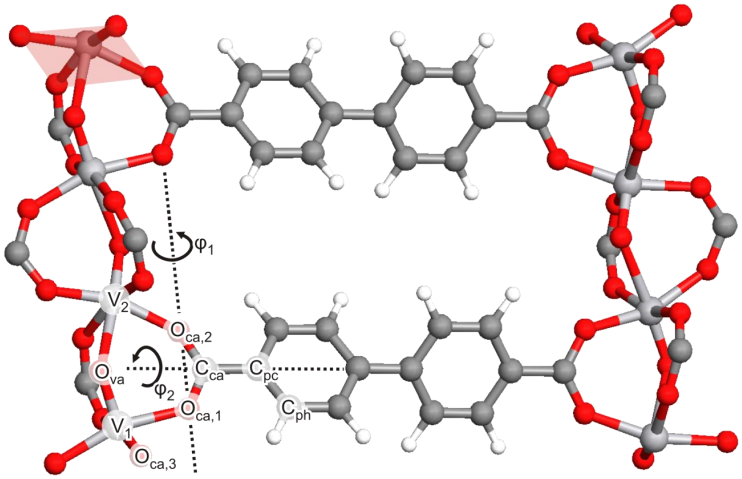

Figure S7. Schematic picture of a partial structure of COMOC-2 with labelling of the different atom types. Illustration of some dihedral motions. Dashed lines indicate rotation axes. Also shown is the square (blue coloured) connecting the four equatorial O_{ca} oxygens forming a pyramid with the vanadyl oxygen O_{va}.

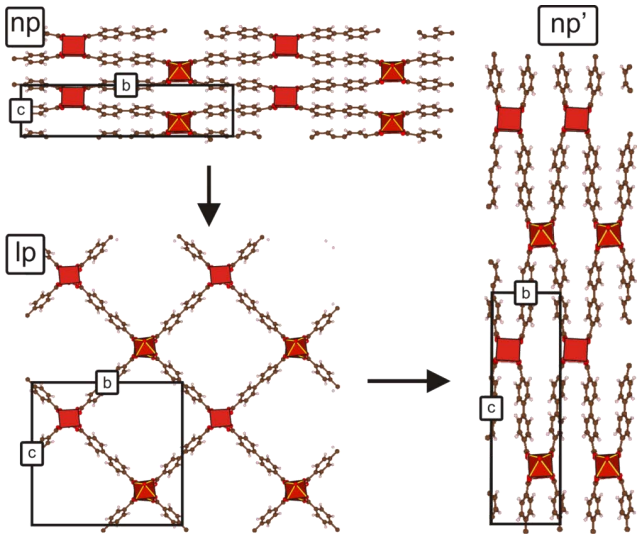

Figure S8. Ab initio simulated structures of COMOC-2(V^{IV}), representing the three phases: *np*, *lp* and *np'*. View along the crystallographic *bc* plane.

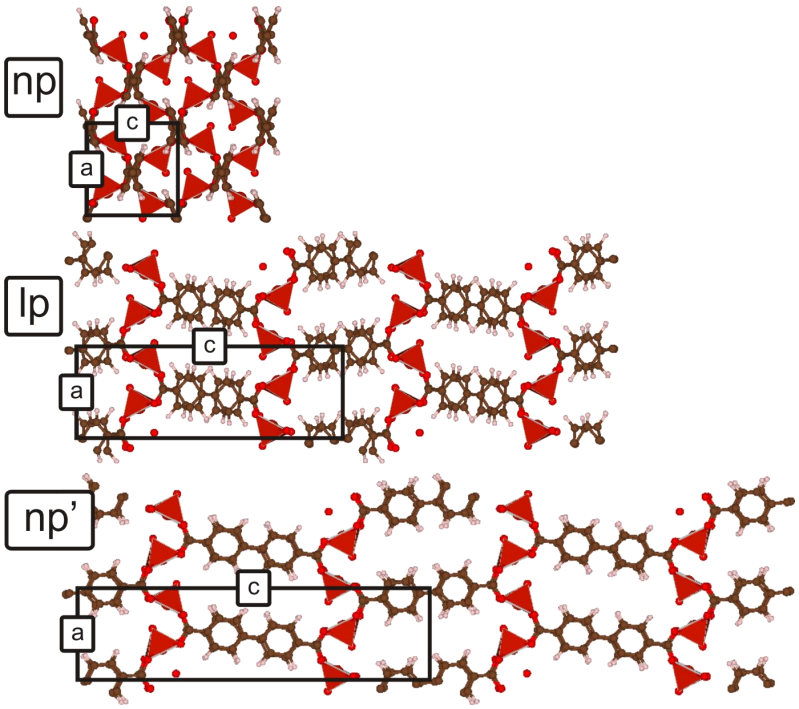

Figure S9. Ab initio simulated structures of COMOC-2(V^{IV}), representing the three phases: *np*, *lp* and *np'*. View along the crystallographic ac plane.

Table S1. Crystal data and structure refinement summary for the *lp* form of COMOC-2.

Compound	VO(BPDC)
Empirical formula	$C_{14}O_5V$
M	299.1
Crystal system	Orthorhombic
Space group	*I*mma (no. 74)
a/ Å	21.443(3)
b/ Å	6.957(4)
c/ Å	20.570(2)
V/ Å^3	3069(5)
Z	8
D/ g cm^{-3}	1.2944
2θ/°	4.5-70
Number of observations	3276
R_{wp}	5.07
a	8.75

Table S2. Atomic coordinates for the *lp* form of COMOC-2.

Atom	x	y	z	u
V1	0;	0.5;	0;	0.018(7)
O2	0;	0.25;	0.038(4);	0.017(10)
O1	0.0645(9);	0.577(2);	0.051(2);	0.017(10)
C1	0.082(3);	0.75;	0.074(2);	0.0631(10)
C2	0.129(3);	0.75;	0.130(3);	0.0631(10)
C3	0.151(2);	0.5664(8);	0.155(2);	0.0631(10)
C4	0.201(2);	0.5640(8);	0.204(3);	0.0631(10)
C5	0.224(6);	0.75;	0.226(7);	0.0631(10)

Table S3. Bond distances for the *lp* form of COMOC-2.

V1-O2;	1.91(3)
V1-O2^{i};	1.91(3)
V1-O1;	1.81(3)
V1-O1^{ii};	1.81(3)
V1-O1^{iii};	1.81(3)
V1-O1^{iv};	1.81(3)
O1-C1;	1.35(3)
C1-C2;	1.52(8)
C2-C3;	1.46(4)
C2-C3^{v};	1.46(4)
C3-C4;	1.46(7)
C4-C5;	1.46(7)
C5-C5^{vi};	1.50(19)
O2-V1-O2^{i};	180.0(5)
O2-V1-O1;	91.9(16)
O2-V1-O1^{ii};	88.1(16)
O2-V1-O1^{iii};	88.1(16)
O2-V1-O1^{iv};	91.9(16)
O2^{i}-V1-O1;	88.1(16)
O2^{i}-V1-O1^{ii};	91.9(16)
O2^{i}-V1-O1^{iii};	91.9(16)
O2^{i}-V1-O1^{iv};	88.1(16)
O1-V1-O1^{ii};	80.6(14)
O1-V1-O1^{iii};	180.0(5)
O1-V1-O1^{iv};	99.4(14)
O1^{ii}-V1-O1^{iii};	99.4(14)
O1^{ii}-V1-O1^{iv};	180.0(5)
O1^{iii}-V1-O1^{iv};	80.6(14)
V1-O2-V1^{vii};	132(5)
V1-O1-C1;	133(3)
O1-C1-O1^{v};	126(4)
O1-C1-C2;	117(2)
O1^{v}-C1-C2;	117(2)
C1-C2-C3;	119(3)
C1-C2-C3^{v};	119(3)
C3-C2-C3^{v};	122(5)
C2-C3-C4;	120(3)

C3-C4-C5; 117(5)
C4-C5-C4^{v}; 125(10)
C4-C5-C5^{vi}; 118(5)
C4^{v}-C5-C5^{vi}; 118(5)

(i) -x+1,y+1/2,-z+1
(ii) x+1,-y+2,-z+1
(ii) -x,-y+1,-z
(iv) -x+1,y+1,z+1
(v) x+1,-y+3/2,z+1
(vi) -x+1/2,y,-z+1/2
(vii) -x,-y+1/2,z

References

[1] G. Silversmit, D. Depla, H. Poelman, G. B. Marin, R. De Gryse, *J. Electron Spectrosc. Relat. Phenom.* **2004**, *135*, 167-175.
[2] J. Mendialdua, R. Casanova, Y. Barbaux, *J. Electron Spectrosc. Relat. Phenom.* **1995**, *71*, 249-261.

Paper 12

Ab initio parametrized force field for the flexible metal-organic framework MIL-53(Al)

Louis Vanduyfhuys, Toon Verstraelen, Matthias Vandichel, Michel Waroquier and Veronique Van Speybroeck

Journal of Chemical Theory and Computation, 8, 3217 - 3231

Copyright 2012 by the American Chemical Society.

JCTC Journal of Chemical Theory and Computation
Article
pubs.acs.org/JCTC

Ab Initio Parametrized Force Field for the Flexible Metal−Organic Framework MIL-53(Al)

L. Vanduyfhuys, T. Verstraelen,* M. Vandichel, M. Waroquier, and V. Van Speybroeck*

Center for Molecular Modeling (CMM), Ghent University (Member of the QCMM Ghent-Brussels Alliance Group), Technologiepark 903, 9052 Ghent, Belgium

Supporting Information

ABSTRACT: A force field is proposed for the flexible metal−organic framework MIL-53(Al), which is calibrated using density functional theory calculations on nonperiodic clusters. The force field has three main contributions: an electrostatic term based on atomic charges derived with a modified Hirshfeld-I method, a van der Waals (vdW) term with parameters taken from the MM3 model, and a valence force field whose parameters were estimated with a new methodology that uses the gradients and Hessian matrix elements retrieved from nonperiodic cluster calculations. The new force field predicts geometries and cell parameters that compare well with the experimental values both for the large and narrow pore phases. The energy profile along the breathing mode of the empty material reveals the existence of two minima, which confirms the intrinsic bistable behavior of the MIL-53. Even without the stimulus of external guest molecules, the material may transform from the large pore (lp) to the narrow pore (np) phase [Liu et al. *J. Am. Chem. Soc.* **2008**, *120*, 11813]. The relative stability of the two phases critically depends on the vdW parameters, and the MM3 dispersion interaction has the tendency to overstabilize the np phase.

1. INTRODUCTION

The discovery of metal−organic frameworks (MOFs)—a new class of nanoporous materials with exceptional physicochemical and mechanical properties—may be regarded as one of the major achievements within science in the past decade.[1−5] The chemistry and exploration of the properties of these materials is developing at an extraordinary pace with a huge number of research articles and reviews that appeared in the literature.[6−10] These materials consist of inorganic moieties connected by organic linkers and form a three-dimensional porous framework. There is an almost unlimited number of structures that may be proposed due to the chemical variety of both organic linkers and metal units at the nodal points. The resulting framework has very attractive features like high pore volumes with a diameter of up to 98 Å for IRMOF-74-XI[11] and a high Brunauer−Emmett−Teller surface area of up to 6240 m^2/gr for MOF-210.[12] It is especially this highly porous structure that makes these materials prime candidates for various industrial applications such as gas storage, purification or separation,[6,13−20] or liquid separation (e.g., fuels, xylenes).[21,22] The applications within catalysis are extensively investigated nowadays.[23−25] Excellent reviews on this topic appeared recently from the groups of Corma and Farrusseng.[26,27] Apart from these attractive features, some MOFs also exhibit intriguing flexible behavior, in which the pores can open or close reversibly upon external stimuli such as temperature,[28] electric or magnetic fields, mechanical pressure,[29] light,[30] or gas and liquid exposure.[15,31,32] Some of the typical examples showing this flexible or breathing behavior include MIL-88 and MIL-53, where cell parameters may vary drastically while the material retains its crystallinity.[33,34] The breathing is studied most extensively for the series of MIL-53 frameworks, which were originally synthesized and characterized by Férey and coworkers. A variety of compounds with chemical formula $M^{III}(OH)(BDC)$ (M^{III}= Al, Cr, Fe, Ga, Sc, and In; BDC^{2-} = terephthalate or 1,4-benzenedicarboxylate) have been synthesized.[31,33,35−39] This paper focuses on the MIL-53 framework with aluminum at the nodal points. MIL-53(Al) is built of long aluminum oxide chains connected to each other by terephthalic linkers, which results in a one-dimensional structure with a channel diameter of almost 10 Å, as schematically indicated by the green and blue tubes in Figure 1. This one-dimensional structure lies at the origin of the flexibility of some MOFs: the material can shrink or expand because the rigid linkers can hinge on the oxide chains. Most often the breathing behavior

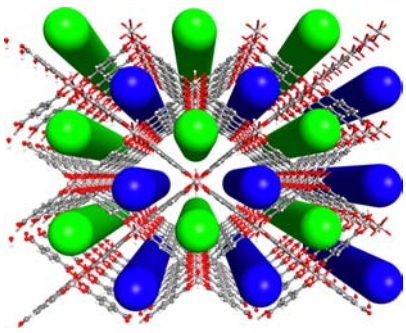

Figure 1. MIL-53(Al) and its 1D channels.

Received: February 29, 2012
Published: July 13, 2012

ACS Publications © 2012 American Chemical Society

has been observed upon the adsorption of guest molecules.[15,31,32] However, Liu et al. recently reported the transition between two phases, i.e., a large pore (lp) and a narrow pore (np) without guest molecules but stimulated by temperature only.[28] The work of Liu et al. shows the intrinsic bistable behavior of the MIL-53(Al) host. Recently, Walker et al. were able to show the existence of two minima on the potential energy surface for the framework using density functional theory including an empirical dispersion term.[40] The np phase could only be retrieved by calculations including dispersive interactions.

DFT calculations are attractive due to their transferability to chemically very diverse systems, although they are also computationally very expensive and are not ideally suited to be used in molecular dynamics (MD) or Monte Carlo (MC) simulations, since such simulations typically run over longer length and time scales. MD and MC simulations are attractive to use in the study of adsorption and diffusion of guest molecules.[41−44] Apart from computational considerations, DFT is still hampered by the lack of dispersion effects in most of the frequently used functionals. The DFT-D method is the most commonly used approach nowadays to include these long-range interactions in which an empirical dispersion term is added to the DFT energy.[45,46] Another approach to address the dispersion interactions is the use of new density functionals that explicitly include dispersion interactions, such as M06-2X,[47,48] ωB97X-D,[49] vdW-DF,[50] and vdW-DF2.[51] Recently, the PBE-D2 method and vdW-DF, vdW-DF2, and some additional functionals have been tested for their performance in reproducing adsorption enhalpies of carbon dioxide in MOFs, and it was found that PBE-D2, vdW-DF, and vdW-DF2 compare extremely well with experimental results.[52]

An attractive approach used to perform atomistic simulations in which larger length and time scales are involved is the usage of a force field that neglects the detailed electronic structure of the MOF but approximates the potential energy surface (PES) as an analytical function of the nuclear coordinates. Such an approach is attractive as it allows one to perform a broad variety of simulations at a low computational cost. However, the approach is only successful if one possesses an accurate theoretical model for all the interactions that govern the behavior of the framework. Specifically stated, one needs a good mathematical model for the potential energy of the MOF framework as a function of its nuclear coordinates and cell parameters. Each analytical function of the force field corresponds to a certain internal degree of freedom and contains unknown parameters. These parameters can be recycled from existing force fields such as UFF,[53] DREIDING,[54] CVFF,[55] MM3,[56] and so on. For example, the group of Férey developed a force field for MIL-53(Cr) based on the CVFF and DREIDING force fields.[57] Another way to fix the unknown parameters would be to estimate them from a set of training data. One can either use experimental data such as geometries, vibrational modes, enthalpies of formation, or adsorption isotherms, or one can choose to use ab initio calculations performed on representative systems. Schmid and co-workers developed a force field for MOF-5 using DFT calculations on two representative clusters.[58] They also developed a genetic algorithm to derive force field parameters[59] and used it to derive a force field for the metal organic framework Cu-BTC.[60]

Another important aspect of a MOF force field is whether it treats the framework as rigid or flexible. In a simulation with a rigid framework, the atoms of the MOF are kept fixed while the guest molecules are allowed to move. Only the electrostatic and van der Waals interactions of the MOF with the guest molecules and the mutual interactions between the guest molecules are relevant. In a simulation with a flexible framework, the atoms of the framework are also allowed to move. The covalent interactions between the MOF atoms must also be addressed, and hence such a force field is called a covalent force field. Until recently, most of the MOF force-field simulations made use of a rigid framework. Schmid and co-workers pioneered the development of a force field for a MOF (MOF-5 in this case) in which the framework was flexible.[58] They showed that, for their force field, allowing the framework atoms to move during the simulation is crucial to correctly reproducing the diffusion coefficients of guest molecules in the MOF.[61] However, Ford et al. performed simular calculations with another force field[62] and found that the diffusion coefficient of benzene in MOF-5 is only mildly dependent on the framework flexibility.[63] It is clear that more research is needed to make a general conclusion on the influence of framework flexibility on the diffusion coefficients.

The purpose of this work is to derive a new force field for MIL-53(Al) from first principles and to develop new methodologies that facilitate the determination of the parameters. The force field has three main contributions: an electrostatic term, a van der Waals (vdW) term, and a conventional valence force field. The electrostatic part of the model is based on atomic point charges. Several methodologies used to assign atomic charges are tested and compared. The vdW term and the corresponding parameters are taken from the MM3 model of Allinger et al.[56] For the derivation of the valence parameters, i.e., the rest values and force constants, a new methodology is proposed. The force field is validated by comparing geometrical properties and cell parameters of the MIL-53(Al) framework with experimental data both for the lp and np phase. Additionally the force field is tested for its ability to reproduce the breathing phenomenon and more particularly to what extent the transition between the two phases can be predicted. This paper is a step toward the development of force fields that enable the predictive modeling of host−guest molecules in MOFs using a systematic methodology.

In the following two sections, we will outline the computational methods and the theoretical aspects of the force-field development. In the fourth section, the MIL-53(Al) force field is validated and applied to study the breathing effect. The fifth section summarizes our main conclusions. The Appendix discusses the technical details of the new calibration procedure for the valence force field.

2. COMPUTATIONAL DETAILS

Three kinds of calculations were performed in this work. Ab initio calculations on two nonperiodic clusters, ab initio calculations on the periodic MIL-53(Al), and force field calculations on the periodic MIL-53(Al).

The calculations on the nonperiodic clusters were performed as follows. The geometries of the isolated cluster models were fully optimized using Density Functional Theory (DFT) with the B3LYP[64−66] exchange correlation functional, which is an appropriate functional for the reproduction of molecular geometries.[67,68] Most of the atoms were described using a 6-311++G(d,p) basis set,[69−71] which includes diffuse functions for an improved description of the electron distribution in the oxygen anions. For the C−H atom pairs outside the core region

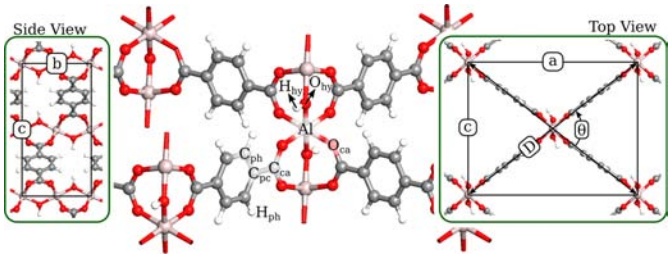

Figure 2. Definition of the force-field atom types in the periodic Mil-53(Al). The indentations visualize a side and top view together with the definition of the pricincipal axes of the unit cell, the diagonal D, and the interdiagonal angle θ.

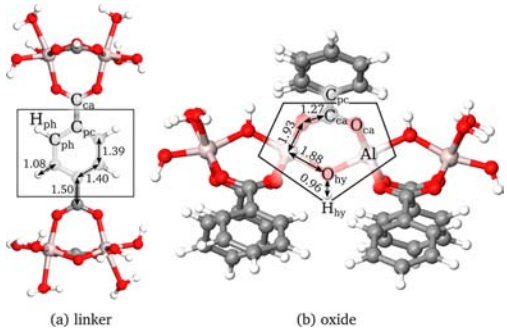

Figure 3. Nonperiodic clusters used to derive force field parameters for MIL-53. The core region of the cluster is indicated by a box, and some representative bond lengths are also given (in Ångströms). These were derived from the DFT calculations as specified in the Computational Details.

of the oxide cluster (explicit definition of the core region is given further in this paper), the computationally less expensive 6-31G(d,p) basis set[71,72] was used. The optimized clusters were confirmed to be true minima on the potential energy surface by performing a vibrational frequency analysis. These calculations also provide the Ab Initio (AI) forces and the Hessian matrix, i.e., the matrix with analytical second order derivatives of the energy toward the Cartesian coordinates, which are needed for the calibration of the force-field parameters. All cluster computations were carried out with Gaussian 09.[73]

In addition to these cluster calculations, we also performed periodic calculations on MIL-53(Al) with DFT, using the PBE[74,75] exchange correlation functional. A full geometry optimization of the periodic structure was performed using the GPAW[76−78] program with the projector-augmented wave method (PAW).[79,80] The pseudowave function in the PAW method was represented on a cubic real-space grid with a spacing of 0.2 Å. This wave function was used to derive atomic charges directly for the periodic structure. Furthermore, a DFT scan of the potential energy surface of the periodic structure was performed using the VASP[81−83] program. A Γ-point calculation was used with an energy cutoff of 600 eV, and the convergence criterion for the electronic self-consistent field (SCF) calculation was set to 10^{-6} eV. Furthermore, a Gaussian smearing[81] of 0.01 eV was applied. The reason we use different programs for the different periodic calculations is purely technical. We have chosen GPAW for the calculation of the periodic atomic charges because we found it more convenient to access the necessary quantities while we chose VASP for the periodic scan because it was found to be computationally more efficient to calculate a complete energy scan.

To validate the force field, several geometry optimizations were carried out with the new MIL-53(Al) force field. All these computations were performed with YAFF, a force field code developed in house. The simulations were performed using a supercell consisting of two unit cells aligned in the direction of the shortest cell vector. All derived properties are further given per unit cell. The electrostatic interactions were computed using an Ewald summation with a real space cutoff of 15 Å, α = 0.213, and a reciprocal space cutoff of 0.32 $Å^{-1}$.[84] The van der Waals interactions were also calculated with a smooth cutoff of 15 Å. A smooth cutoff for pairwise interactions indicates that the pairwise interaction energy is not simply truncated at the cutoff. Instead, we introduce a small transition region in which the energy smoothly evolves from the original expression to zero by means of a smoothing function, for which we used a cosine function. This smoothing avoids ill defined force components.

Journal of Chemical Theory and Computation Article

3. FORCE FIELD DEVELOPMENT

3.1. Choice of the Cluster Model Systems. In this work, Density Functional Theory (DFT) computations on two nonperiodic clusters are used to derive force-field parameters that can be applied to the periodic MIL-53(Al) system. There are two principal reasons to use cluster models: DFT computations on these clusters are computationally less demanding, and several well-established ab initio codes for isolated systems are available that can compute the Cartesian Hessian accurately. With the current computational resources, it is possible to extract the Cartesian Hessian matrix from periodic calculations, but such calculations come with a very high computational cost, especially when all normal modes need to have a positive frequency.[85] Therefore, preference was given to cluster models. However, one can only use these cluster models if the Hessian matrix elements are transferable to the periodic system. Therefore, one must carefully construct the isolated clusters such that they capture all the essential features of the periodic structure.

The structural topology of MIL-53 consists of tilted chains of $AlO_4(OH)_2$ octahedra, which are linked via carboxylate groups of the terephthalate ions (1,4-benzenedicarboxylate, BDC) creating a three-dimensional structure with an array of one-dimensional large pore channels shown in Figure 1. The chemical formula of the MIL-53(Al) is $Al(OH)(O_2C{-}C_6H_4{-}CO_2)$. A single unit cell is depicted in Figure 2, clearly showing the individual organic linkers connecting the metal-oxide chains. The nonperiodic clusters introduced in this study are shown in Figure 3. The first cluster contains a terephthalate linker at its center, while the second cluster is constructed around a segment of the metal-oxide chain. In order to select proper isolated cluster models, we considered the following guidelines:

1. The charge of the clusters should be as small as possible in order to avoid the introduction of electrostatic interactions that are unrealistic for the periodic structure.
2. The electronic structure of both clusters must be closed-shell systems, in line with the periodic MIL-53(Al) system.
3. The cluster should be large enough to capture all essential features of the periodic MOF structures. Not all force components and Hessian elements of the clusters are relevant for the periodic structure. Therefore, a core region was introduced as schematically depicted in Figure 3. Only force components of atoms in the core and Hessian elements of atom pairs of which at least one atom lies in the core are used for the further derivation of the force field. In this respect, the termination of the clusters must be well-separated from the core region (linker or oxide) of interest. In our cluster, the atoms belonging to the core regions are separated from terminating atoms by at least four bonds.
4. Each atom in the periodic MIL-53 structure must have an equivalent counterpart in the core region of one of the cluster models.

The proposed clusters in Figure 3, which were constructed using Zeobuilder,[86] fulfill these basic conditions. In the linker model (Figure 3a), the hydrogen atoms are removed from the bridging μ_2(OH) groups, and the oxide moieties are terminated by water molecules and hydroxyl groups to obtain a neutral closed-shell system.

The choice of a cluster which is representative for the inorganic building unit of MIL-53(Al) is less straightforward due to the occurrence of the one-dimensional chains formed by corner-sharing aluminum octahedra which are linked through μ_2(OH) bridging groups. Each aluminum center has two distinct types of Al−O linkages in the MIL-53 structure: four "equatorial" bonds to oxygens of the carboxylate ligands which are denoted by O_{ca} and two "axial" bonds along the chain direction which are denoted as O_{hy} (Figure 2). A first proposal for the inorganic cluster contained three aluminum atoms of the one-dimensional chain, as shown in Figure S1 of the Supporting Information. The oxide chain is terminated with water molecules and hydroxyl groups, while the linkers are terminated by replacing a carboxyl group by a hydrogen atom. We found that this first model is inadequate for a realistic description of the MIL-53 structure due to a poor description of the strong 1−5 electrostatic interactions between two O_{ca} atoms (separated by four covalent bonds) as indicated in Figure S1 in the Supporting Information. One of the atoms in this pairwise interaction is always close to the boundary of the cluster, leading to interactions that are not representative for the periodic system. Moreover the inorganic cluster with three aluminum atoms is not symmetric with respect to the central six-membered unit connecting two aluminum octahedra. At least four aluminum atoms are necessary to avoid these problems and to obtain a proper description of the periodic MIL-53 structure. The final cluster, shown in Figure 3b, has a total spin of zero and a total charge of +1 and fulfills other basic conditions as introduced before.

3.2. Force Field Energy Expression. The development of a force field (FF) consists of two steps: (i) the proposal of a suitable energy expression that depends on all internal coordinates and (ii) the estimation of the parameters figuring in the FF expression. The analytical expression for the force-field energy used in this work is given by

$$V^{\mathrm{ff}} = \underbrace{V_{\mathrm{bond}} + V_{\mathrm{bend}} + V_{\mathrm{torsion}}}_{V^{\mathrm{ff}}_{\mathrm{cov}}} + \underbrace{V_{\mathrm{el}} + V_{\mathrm{vdW}}}_{V^{\mathrm{ff}}_{\mathrm{noncov}}} \tag{1}$$

with

$$V_{\mathrm{bond}} = \sum_{i=1}^{N_r} \frac{1}{2} K_{r,i}(r_i - r_{i,0})^2 \tag{2}$$

$$V_{\mathrm{bend}} = \sum_{i=1}^{N_\theta} \frac{1}{2} K_{\theta,i}(\theta_i - \theta_{i,0})^2 \tag{3}$$

$$V_{\mathrm{torsion}} = \sum_{i=1}^{N_\phi} \frac{1}{2} K_{\phi,i}[1 - \cos(m_i\phi_i)] \tag{4}$$

$$V_{\mathrm{el}} = \frac{1}{2} \sum_{i\neq j}^{N_{\mathrm{at}}} \frac{q_i q_j}{4\pi\varepsilon_0 r_{ij}} \tag{5}$$

$$V_{\mathrm{vdW}} = \frac{1}{2} \sum_{i\neq j}^{N_{\mathrm{at}}} \varepsilon_{ij} \left[1.84 \times 10^5 \exp\left(-12\frac{r_{ij}}{\sigma_{ij}} \right) - 2.25 \left(\frac{\sigma_{ij}}{r_{ij}} \right)^6 \right] \tag{6}$$

with N_r being the total number of stretch bonds, N_θ the total number of bending angles, N_ϕ the total number of torsions, and N_{at} the total number of atoms. This potential energy expression

consists of a part describing the *covalent* interactions (V^{ff}_{cov}), which are related to the presence of chemical bonds, and a part originating from *noncovalent* interactions (V^{ff}_{noncov}), which are governed by electrostatic and van der Waals interactions.

The harmonic model is not immediately applicable to the octahedral environment of aluminum. In particular, the four equatorial bonds with the oxygens of the carboxylate ligands have angular minima at 90° and 180°. Therefore, we used the improved Fourier-type angle-bending potential as proposed by Tafipolsky et al.[60,87,88] instead of the harmonic angle-bending term for the O_{ca}−Al−O_{ca} angle:

$$V_{O_{ca}-Al-O_{ca}}(\theta) = \frac{K_\theta}{2}[1 + \cos(\theta)][1 + \cos(2\theta)] \quad (7)$$

Although the partitioning of energy terms into covalent and noncovalent parts seems trivial, it is merely an empirical and somewhat ambiguous convention. Using density functional theory, or any other electronic structure method, one cannot derive the covalent and noncovalent contributions separately. Electrostatic interactions are also present between bonded atoms, certainly when considering bonds with a strong ionic character. This is especially true for the bonds in the inorganic part of the MIL-53. Therefore, we choose to include electrostatic interactions between all pairs of atoms, as opposed to the conventional exclusion of certain pairs of atoms from the summation in eq 5 used in many other force fields. As such, the energy associated with chemical bonding will be determined by an electrostatic contribution and a residual covalent part.

The electrostatic interaction V_{el} is modeled by using constant atomic charges, and the sum runs over all atom pairs excluding self-interactions. More information on the determination of the atomic charges is given in section 3.3.

The van der Waals part of the noncovalent energy is modeled by the MM3-vdW[56] term in eq 6; the numbers 1.84×10^5 and 2.25 originate from the work of Allinger and coworkers.[56] σ_{ij} denotes the sum of the van der Waals radii: $\sigma_i + \sigma_j$. The energy parameter, ε_{ij}, is derived from atomic parameters by taking the geometric mean, i.e., $\varepsilon_{ij} = (\varepsilon_i\varepsilon_j)^{1/2}$. In this equation, the summation in the vdW interactions runs over all atom pairs excluding pairs involved in bonds (so-called 1−2 pairs) and valence angles (1−3 pairs). Without such exclusion rules, one would get strongly overestimated repulsion terms that would distort bond lengths and valence angles.

To limit the number of independent parameters in the energy expression, force-field atom types are introduced as shown in Figure 2. For the covalent interactions, unique parameters are associated with each pair (for bonds), triplet (for angles), or quadruplet (for torsions) of force-field atom types. Each atom type is associated with a unique set of atomic vdW parameters and an atomic charge.

3.3. Atomic Charges for the Electrostatic Interactions. Atomic charges are a key ingredient to modeling the electrostatic interactions and are also convenient properties to understand chemical interactions. However, they are nontrivial to define from a quantum-mechanical perspective: many different theoretical schemes have been proposed in the literature over the past 60 years to derive Atom-in-Molecule (AIM) charges, which do not necessarily lead to consistent results. Some of the more popular schemes are Mulliken population analysis,[89] natural population analysis,[90] (iterative) Hirshfeld partitioning,[91,92] ESP-fitted charges,[93−95] and QTAIM charges.[96]

For the development of force-field models, one often relies on ESP-fitted charges because they reproduce the electrostatic potential surrounding the molecule.[97,98] Ramsahye et al.[99] calculated ESP-fitted charges for MIL-53(Al). Especially the RESP[95] method is popular in limiting the statistical deficiencies of ESP-fitted charges. Despite the restraining techniques used in the RESP scheme, RESP charges are still very sensitive to conformational changes.[100] One can also reduce the rank deficiency[101] of ESP-fitted charges by using a limited set of bond-charge-increment (BCI)[102] parameters associated with certain pairs of atom types.[97]

Recently, the Hirshfeld-I[92] partitioning scheme was proposed, which relies on a partitioning of the electron density. Several studies showed that this new scheme results in charges that reproduce the electrostatic potential with nearly the same accuracy as ESP-fitted charges for organic molecules.[103] Moreover, the Hirshfeld-I charges are very robust with respect to conformational changes, which is clearly an advantage over the ESP-fitted charges,[100,104] and only show a weak dependence on the basis set used in the quantum mechanical calculations.[92] Nevertheless, also the Hirshfeld-I method has its deficiencies. A recent study of charge equilibration models for silicates revealed that the Hirshfeld-I method overestimates (in absolute value) the charges of systems with a strong ionic character. For example, this error leads to systematically overestimated dipole moments for a large set of silica clusters.[105] Therefore, we suggest herein a modified version of the method, hereafter called *valence Hirshfeld-I* (VHI), where the core electrons are assigned to their native atoms and only the valence electrons are partitioned with the Hirshfeld-I scheme.

In what follows, MIL-53(Al) charges are derived from the isolated cluster computations and from the periodic DFT calculation using GPAW (see Computational Details). The charges derived from the periodic system serve as a validation of the results obtained with the cluster computations. For the derivation of the valence parameters in the following section, we need the charges on all atoms in the cluster models to subtract the electrostatic interactions from the DFT training data.

Three sets of charges are derived from the cluster computations: Hirshfeld-I charges (HI), valence Hirshfeld-I charges (VHI), and ESP-fitted charges (ESP); the hirshfeld-based charges are included in Tables S1−S3 of the Supporting Information. The ESP cost function is taken from ref 105. To derive charges for the periodic system from these data, one cannot simply transfer the charges obtained for the core regions of both linker and oxide cluster to the periodic system, because this procedure would not result in a neutral MIL-53(Al) framework. To circumvent this problem, we introduce bond-charge-increments (BCIs),[102] p_{ij}, which are defined as charge tranfers along neighboring atoms and which are related to atomic charges, q_i, as follows:

$$q_i = \sum_j {}' p_{ij} + q_i^0 \quad \forall\ i \text{ with } p_{ij} = -p_{ji} \quad (8)$$

where the sum is limited to atoms j that are bonded to atom i. The precharge q_i^0 is introduced to treat systems that are not neutral.[97] The introduction of this precharge is only needed for the oxide cluster, where all precharges are set equal to the total charge divided by the number of atoms.[105] The procedure to transfer the charges from the cluster calculations to the periodic structure is as follows: first, the HI and VHI charges are transformed to BCIs associated with pairs of atom types (see

Figure 2), by inverting eq 8 using a least-squares method. Second, the fitted BCIs of the core of each cluster are transferred to the periodic system. This uniquely defines all BCIs of the periodic system, except for $C_{ca}-C_{pc}$ pairs because it crosses the core boundary in both clusters. However, the BCIs deduced from both clusters are very similar and thus it does not make much difference which one we use in the periodic system. We have chosen the one from the oxide cluster. One should avoid to transform ESP-fitted charges a posteriori to BCIs due to the statistical noise on the charges. Instead, BCI parameters were fitted directly to ESP grid data.[97] The atomic charges for the MIL-53(Al) framework in its large pore form, obtained by applying the BCIs derived from the clusters, are shown in the first three columns of Table 1.

Table 1. Atomic Charges for the MIL-53(Al) Framework in Its Large Pore Form (in e) Calculated Using Different Methods[a]

	cluster-based			periodic	
atom type	HI	VHI	ESP	AHI	AESP
Al	2.939	2.078	2.002	2.058	2.075
C_{ca}	0.996	0.885	0.899	0.839	0.664
C_{pc}	−0.154	−0.111	−0.041	−0.106	0.067
C_{ph}	−0.071	−0.091	−0.145	−0.099	−0.180
H_{hy}	0.566	0.515	0.418	0.508	0.422
H_{ph}	0.124	0.127	0.148	0.133	0.161
O_{ca}	−0.879	−0.740	−0.810	−0.699	−0.702
O_{hy}	−1.882	−1.322	−0.906	−1.368	−1.081

[a]HI refers to the Hirshfeld-I method, VHI to the valence Hirshfeld-I method, and ESP stands for ESP-fitted charges. AHI are Hirshfeld-I charges obtained by partitioning the auxiliary density, and AESP stands for charges derived from the electrostatic potential due to the auxiliary density. The atom types are depicted in Figure 2.

Charges were also derived from periodic calculations on the lp variant of the Mil-53(Al) using the GPAW[76−78] method to validate the accuracy of the cluster-based charges. In the projector augmented wave (PAW) scheme,[79,80] the auxiliary density only accounts for a fraction of the total electron density, which roughly corresponds to the density of the valence electrons. This auxiliary density was partitioned using the Hirshfeld-I scheme (AHI), and the electrostatic potential due to the auxiliary density was used to fit ESP-charges (AESP). Both types of charges were corrected with the atomic compensation charges, which account for the contributions that are missing in the auxiliary density of the PAW scheme. The results are given in the last two columns of Table 1.

The charges for Al and O_{hy} obtained with the HI method deviate significantly from the other methods, which agrees with earlier work where similar deviations were observed for charges in silicates.[105] The four other schemes lead to much more consistent results. The good correspondence between the periodic and cluster results confirms the robustness of the transformation between atomic charges and bond-charge increments. We already mentioned that we need charges for all atoms in the clusters; hence we need to choose a cluster-based scheme. We choose to proceed with the VHI charges because the differences between ESP and AESP charges are larger than the differences between VHI and AHI, indicating that the ESP-based charges are not as robust.

3.4. van der Waals Parameters. The van der Waals (vdW) parameters are taken from the MM3 force field of Allinger et al.[56,106] and are given in Table 2. The accuracy of the repulsion between apolar hydrogen atoms is problematic in the MM3 model and may be improved by displacing the interaction site for the van der Waals interaction of such hydrogen atoms along the R−H bond.[56] However, comparison of the force-field interaction energy, consisting of nonbonded contributions only, of two benzene molecules with DFT revealed that the repulsion between hydrogen atoms of nearby linkers is acceptable when the MM3 vdW parameters are used without any correction. Hence the displacement of the van der Waals interaction site of the aromatic hydrogen atoms was not implemented. Such corrections may become relevant when studying the adsorption of guest molecules in the MIL-53 framework. Therefore, an extended recalibration of the repulsion and dispersion interactions will be considered in future work. In this paper, we focus on testing new methods to derive electrostatic and valence parameters, which will be discussed in the following subsections.

Table 2. MM3 van der Waals Parameters[a]

atom type	σ_i [Å]	ε_i [kJ mol^{-1}]	MM3 atom type
Al	2.36	0.485	aluminum (-)
C_{ca}	1.94	0.234	sp^2 carbon (2)
C_{pc}	1.94	0.234	sp^2 carbon (2)
C_{ph}	1.94	0.234	sp^2 carbon (2)
H_{hy}	1.60	0.067	alcohol hydrogen (21)
H_{ph}	1.62	0.084	aromatic hydrogen (5)
O_{ca}	1.82	0.247	oxygen in carboxyl anion(47)
O_{hy}	1.82	0.247	alcohol oxygen (75)

[a]The aluminum parameters are taken from ref 106. All other parameters are taken from the mm3.prm file from the TINKER[107] package, which is based on ref 56. The number between parentheses is the atom type number from the mm3.prm file.

3.5. Covalent Parameters. As discussed above, the electrostatic interactions in this work are treated differently compared to most conventional force-field models: pairwise electrostatic interactions are included between all atom pairs without applying any scaling or exclusion rules. This approach can be well motivated in our case since the bonds in the oxide moiety of the system have a strong ionic character. In the total force field expression, both covalent and electrostatic terms are present and the sum of both needs to be described accurately. This implies that the covalent terms must be fitted to reproduce the differences between the ab initio training data and the electrostatic term (V_{el}). This mainly affects the oxide parameters in the model, where the electrostatic term is strongly attractive for bonded atoms (such as the pair $Al-O_{ca}$) and the corresponding covalent terms will be repulsive at small interatomic distances. There is no need to subtract the van der Waals terms from the DFT computations because (i) the vdW contribution is excluded for 1−2 and 1−3 pairs and (ii) the long-range dispersion effects are absent in DFT reference data due to the known limitations of the B3LYP functional.[45]

Several schemes exist to estimate the covalent parameters from training data generated from first principles. We can group these schemes according to the training data that are used for the fitting procedure. A first class uses only information directly related to the potential energy surface (e.g., gradient, Hessian, ...),[108−112] and a second class also uses information from derived quantities (e.g., geometry, normal modes, ...)[59,113] or even statistical observables.[114−116] It is conceptually attractive

to calibrate force-field parameters to reproduce the (derived) observables of interest, but such schemes are computationally demanding and provide little insight into the topology of the parameter space. The deduction of the parameters is not straightforward: one has to perform multiple force field simulations at each iteration of the parameter calibration, and it is hardly possible to compute analytical derivatives of the cost function toward the force field parameters. In that case, one can only use Monte Carlo methods or genetic algorithms to optimize the parameters.[59]

In this work, the parameters are calibrated using the gradients and Hessian matrix elements from the ab initio calculations. Only gradients that belong to atoms of the core region of the clusters and Hessian matrix elements for which at least one of the involved atoms belong to the core region for the clusters are used. Basically, the valence parameters are deduced by solving the following sets of equations

$$G^{\mathrm{ai}} = G^{\mathrm{ff}}_{\mathrm{cov}} + G^{\mathrm{ff}}_{\mathrm{el}} \tag{9}$$

$$H^{\mathrm{ai}} = H^{\mathrm{ff}}_{\mathrm{cov}} + H^{\mathrm{ff}}_{\mathrm{el}} \tag{10}$$

where G^{ai} is the ab initio energy gradient corresponding to the derivative of the ab initio energy toward the Cartesian coordinates. $G^{\mathrm{ff}}_{\mathrm{cov}}$ and $G^{\mathrm{ff}}_{\mathrm{el}}$ are Cartesian derivatives of the force-field energy contributions $V^{\mathrm{ff}}_{\mathrm{cov}}$ and V_{el} of eq 1, respectively. H^{ai} is the ab initio Hessian, containing the second derivatives of the ab initio energy toward the Cartesian coordinates, and similar definitions hold for $H^{\mathrm{ff}}_{\mathrm{cov}}$ and $H^{\mathrm{ff}}_{\mathrm{el}}$. Such equations can be solved using a least-squares technique to obtain the optimal parameters using the Levenberg−Marquardt algorithm. Two crucial modifications of these equations were needed, which will be briefly discussed below. More information on the procedure may be found in the Appendix.

Both modifications mainly affect the gradient equations (eq 9). Without any modifications, the gradient equations are compatible with the force-matching method that is often used in conjunction with ab initio molecular dynamics simulations.[108] Since both isolated clusters are optimized at the DFT level, the left-hand side of these equations is zero ($G^{\mathrm{ai}} = 0$).

In the hypothetical case that parameters are found such that the force-field gradient also becomes zero for both clusters, the force field would exactly reproduce the ab initio geometries. However, in reality the gradient equations are only solved approximately, and the errors on the force-field gradient will lead to errors in the force-field geometry. Because this error is distributed equally over all components of the Cartesian gradient, the error on the geometry will be especially large (or small) along shallow (or steep) modes of the potential energy surface. Since our primary goal is the construction of a force-field that correctly reproduces geometries, we have introduced additional weight factors in the gradient equations which depend on the Hessian and which give higher weights to the gradient along shallow modes. This ensures that the PES is more accurately determined along shallow modes of the surface. More details about the mathematical derivation can be found in the Appendix.

The second adjustment is an additional set of equations to address the strong correlations between the rest parameters, i.e., the parameters $r_{i,0}$ and $\theta_{i,0}$ in eqs 2 and 3. A well-known difficulty with force field calibrations is the redundancy of the internal coordinates.[111,117] The number of internal coordinates usually largely exceeds the number of Cartesian degrees of freedom. Due to this redundancy, certain linear combinations of internal coordinates do not have a corresponding Cartesian degree of freedom. Consider for example the angles in a planar six-membered ring. It is not possible to increase all six angles equally, and hence an angular force that tries to increase all angles would cancel out when transformed to Cartesian coordinates. This is a direct result from the fact that there are only five independent angles, while the sixth is constrained by the geometrical requirement that the sum of the angles is 720°. The gradient equations above (or any of its variants) are not sensitive to such internal strains, i.e., combinations of internal forces that cancel each other out when transformed to Cartesian coordinates, because they only consider the Cartesian gradient. In case of the six-membered ring, the gradient equations would not be able to fix the rest value of the angle bending term. The additional equations introduced in this work require that all of the internal strains, i.e., linear combinations of derivatives of covalent energy terms that do not contribute to the Cartesian forces, are equal to zero. More details on how this is precisely done are given in the Appendix.

In order to find the optimal covalent parameters, a cost function is constructed that takes the errors on the three sets of equations discussed above into account: (i) transformed gradient equations, (ii) Hessian equations, and (iii) internal strain equations. The parameters that minimize this cost function are given in Table 3 and will be used in the covalent contributions of the force field. The optimization of the covalent parameters was done using the in-house developed software packages FFit2 and MolMod.[118] It is immediately clear that the rest parameters of the bonds in the oxide chain are larger than the typical equilibrium value of the corresponding internal coordinates (see Figure 3). These are ionic bonds that have a significant attractive electrostatic contribution due to the large and opposite charges on the atoms involved. At the equilibrium bond length, this is compensated by a repulsive covalent bond term. Similarly, the rest angles of the Al−O_{ca}−C_{ca} and Al−O_{hy}−Al bends are lower than the equilibrium values due to the repulsion of, respectively, Al−C_{ca} and Al−Al. A more prominent illustration can be found in the force constant of the O_{ca}−Al−O_{ca} bend, which is equal to zero. Apparently, the electrostatic repulsion of the O_{ca} atoms can fully account for the interaction energy of the angle bending.

3.6. Ab Initio Scan of the Periodic Cell. Table 3 reveals that the force constants of the dihedral angles Al−O_{ca}−C_{ca}−C_{pc} (K_c) and Al−O_{ca}−C_{ca}−O_{ca} (K_o) are relatively small. This is an indication that these torsions may show anharmonic behavior and hence that the proposed energy term (eq 4) is not the most suitable term to describe these torsional motions. Furthermore, the force constants (K_c and K_o) are prone to statistical noise: small deviations on the weights in the cost function (see Appendix) result in significant deviations on these force constants. In order to investigate the validity of the harmonic terms for these dihedral motions, we performed additional periodic DFT computations with VASP (see Computational Details) from which also K_c and K_o are deduced.

Figure 4 gives a visual representation of the dihedral motions of interest. The dihedral angle Al−O_{ca}−C_{ca}−C_{pc} determines the rotation of a linker about the two O_{ca}−O_{ca} axes of the carboxyl groups in the linkers (φ_1). This rotation enables shrinkage or expansion of the entire unit cell. The dihedral angle Al−O_{ca}−C_{ca}−O_{ca} controls the tilting of the plane of the linker (illustrated by the rectangular shaded area) around the C_{ca}−C_{pc}−C_{pc}−C_{ca} axis (φ_2). This tilting also induces an opposite rotation of two neighboring Al(O_{ca})$_4$ planes (illustrated by the

Table 3. Parameters of the Covalent Contributions to the Force Field[a]

bonds	K [kJ mol^{-1} Å^{-2}]	r_0 [Å]
Al–O_{ca}	1079	2.151
Al–O_{hy}	1738	2.137
C_{ca}–O_{ca}	5466	1.337
C_{ca}–C_{pc}	2580	1.508
C_{ph}–C_{pc}	2897	1.398
C_{ph}–H_{ph}	3420	1.086
C_{ph}–C_{ph}	3413	1.386
O_{hy}–H_{hy}	7030	1.046
bends	K [kJ mol^{-1} rad^{-2}]	θ_0 [deg]
Al–O_{ca}–C_{ca}	58	87.7
Al–O_{hy}–Al	173	73.5
Al–O_{hy}–H_{hy}	104	85.0
O_{ca}–Al–O_{ca}	0	
O_{ca}–Al–O_{hy}	121	91.1
O_{ca}–C_{ca}–O_{ca}	672	122.9
O_{ca}–C_{ca}–C_{pc}	136	123.8
O_{hy}–Al–O_{hy}	0	
C_{ca}–C_{pc}–C_{ph}	678	120.7
C_{pc}–C_{ph}–C_{ph}	448	121.6
C_{pc}–C_{ph}–H_{ph}	297	121.4
C_{ph}–C_{pc}–C_{ph}	345	118.4
C_{ph}–C_{ph}–H_{ph}	351	122.0
dihedrals	K [kJ mol^{-1}]	
Al–O_{ca}–C_{ca}–C_{pc}	3 (14)[a]	
Al–O_{ca}–C_{ca}–O_{ca}	14 (11)[a]	
C_{pc}–C_{ph}–C_{ph}–H_{ph}	36	
C_{pc}–C_{ph}–C_{ph}–C_{pc}	41	
C_{ph}–C_{ph}–C_{pc}–C_{ph}	32	
C_{ph}–C_{ph}–C_{pc}–C_{ca}	58	
C_{ph}–C_{pc}–C_{ca}–O_{ca}	23	
H_{ph}–C_{ph}–C_{ph}–H_{ph}	23	
H_{ph}–C_{ph}–C_{pc}–C_{ph}	27	
H_{ph}–C_{ph}–C_{pc}–C_{ca}	29	

[a]The values between brackets are determined using the ab initio scan (see section 3.6).

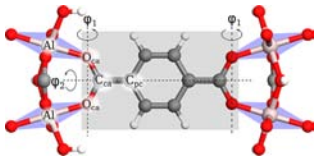

Figure 4. Illustration of the dihedral motions. The dashed lines indicate rotation axes. The rectangular shaded area highlights all the atoms that take part in the rotations, and the blue parallelograms show the Al(O_{ca})$_4$ planes.

blue parallelograms) about the Al–Al axis. Both the linker rotation and tilting are strongly influenced by the constraints imposed by the periodic structure of the MOF. Therefore, it may be anticipated that periodic calculations are necessary to get a good estimate of the force constants of these dihedral motions. This was investigated by performing a scan in terms of the interdiagonal angle θ, which is defined in Figure 2. To limit the computational complexity of the scan, we generated a trajectory using the force field (instead of using an ab initio trajectory) and calculated the DFT energy for every frame in the trajectory. Constrained geometry optimizations, using the initial parameters of the force field as tabulated in Table 3, were performed, in which the interdiagonal angle θ was varied from 30° to 90° with a step of 1°. The interdiagonal angle θ and the diagonal length D are indicated in Figure 2 and are defined as

$$D = \sqrt{a^2 + c^2} \tag{11}$$

$$\theta = 2\arctan\left(\frac{a}{c}\right) \tag{12}$$

It is the intention to estimate new values for the two dihedral force constants K_c and K_o that reproduce the DFT energy along the trajectory as well as possible. For that purpose, we decompose the force field energy into three parts:

$$V_{dft} = V_{res} + V_{vdw} + V_{dih} \tag{13}$$

with

$$V_{dih} = K_c V_c + K_o V_o \tag{14}$$

V_{dih} contains the two contributions to the dihedral force-field energy that relate to the parameters K_c and K_o which need to be determined. V_c and V_o represent these two contributions with the value of their respective force constant set at 1 kJ mol^{-1}. V_{vdw} is the MM3-vdW contribution to the force-field energy, and V_{res} contains all of the remaining contributions (bonds, bends, remaining dihedrals, and electrostatic interactions) of V^{ff}. By investigating all contributions to the force-field energy, we notice that dispersion interactions and Pauli repulsion both have a large influence on the energy profile. However, dispersion is neglected in most DFT functionals. Recently, new functionals were suggested that include dispersion, and additionally the popular DFT-D method is regularly used in which an empirical van der Waals correction is added to the DFT energy.[45−47,119] As it is unclear at this point to what extent the MM3-vdW contribution performs well at reproducing the dispersion interaction of these new DFT approaches, we performed the scan with regular PBE but drop the dispersion contribution from the FF energy during the scan. This will enhance the Pauli repulsion contribution in the force field because at short internuclear distances, dispersion compensates Pauli repulsion. To correct for this, we uniformly scale the Pauli interactions, V_{pauli}, with a factor ζ which will be determined hereafter before finding the most optimal values for K_c and K_o.

The result from the energy scan and the various energy contributions are shown in Figure 5. The torsional energies V_c and V_o are more or less constant in a small range of interdiagonal angles (30−36°), giving rise to a constant contribution $K_cV_c + K_oV_o = V_{dih}$ (green curve in Figure 5). Hence, we can use this tail to estimate ζ by solving

$$\Delta V_{dft} = \Delta V_{res} + \zeta \Delta V_{pauli} \tag{15}$$

for all interdiagonal angles in the range of 30−36° using a least-squares technique. This leads to a scaling factor ζ = 0.65. In a second step, we can use this ζ and solve eq 13 (in which all contributions are expressed relative to θ = 90°) in the least-squares sense over the entire range of the interdiagonal angle to estimate the force constants K_c and K_o. This procedure results in the following values for K_c and K_o:

$$K_c = 13.6 \text{ kJ mol}^{-1} \tag{16}$$

$$K_o = 11.1 \text{ kJ mol}^{-1} \tag{17}$$

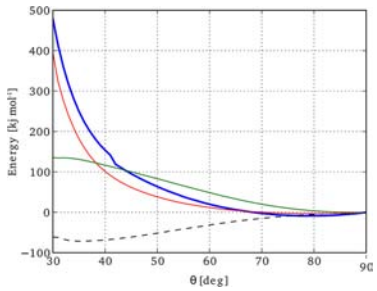

Figure 5. Relevant energies of the periodic ab initio scan: total DFT energy V_{dft} (bold blue), force-field residual energy V_{res} (dashed black), ζ-scaled Pauli energy ζV_{pauli} (red), fitted dihedral energy V_{dih} (green). All energies are expressed relative to $\theta = 90°$.

Figure 5 shows the results of the fit using these new values for K_c and K_0. Using these force constants, we calculated the root-mean-square-deviation Δ between the DFT energy and the total force-field energy and found $\Delta = 0.94$ kJ mol^{-1}. This small deviation indicates that the functional form proposed in eq 4 is a good choice, and there is no need for additional anharmonic contributions. Comparing the new force constants with their original values from Table 3, we see that there is a large difference, especially for the dihedral Al−O_{ca}−C_{ca}−C_{pc}, indicating that the equilibrium forces and Hessian of the two clusters do not contain enough information about these dihedral motions. The scan of the periodic unit cell is indeed mandatory in order to describe the dihedrals accurately. The new force constants are indicated in Table 3. From now on, we will use these values in the force-field simulations. In the remainder of the paper, the van der Waals parameters are reset to their former MM3 values, including Pauli and dispersion. No scaling is applied anymore, because the scaling procedure was only necessary to compensate for the neglect of dispersion interactions in this section.

4. FORCE FIELD APPLICATIONS AND VALIDATION

4.1. Geometry Optimization. A first validation of the force field is the correct prediction of the geometry in both the np and lp form. The cell parameters and the fractional coordinates of the periodic structure were optimized using the new force field. The final geometry obtained in lp is shown in Figure 6. Some essential internal coordinates from the core region of both isolated clusters are compared with their force-field counterparts in the optimized periodic structure (see Table 4). The table also shows a force-field simulation in which MM3-vdW interactions are switched off (see column *ForceField(no-vdW)*). Such a comparative study can be very instructive to explore the main differences in the optimized geometry by taking into account vdW interactions or not. Since only the covalent and electrostatic interactions of the FF are fitted to the DFT calculations—and not the vdW interactions—we could expect that the FF-no-vdW simulation will generate geometrical parameters close to the DFT values. This is indeed the case. The largest discrepancies are noticed in the predictions of the bond Al−O_{hy} and the bending angles Al−O_{ca}−C_{ca} and Al−O_{hy}−Al, which are severely underestimated.

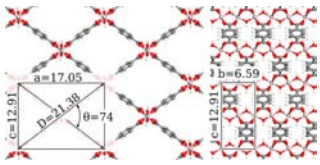

Figure 6. Top and side view of the unit cell in the lp phase after a geometry optimization using the force field (with MM3 vdW). The unit cell and its dimensions are also shown; lengths are in angstroms and angles in degrees.

Table 4. Some Key Bond Distances and Angles Obtained in the Force Field and DFT Optimized Cluster Geometries[a]

	force field		
	MM3-vdW	*no-vdW*	DFT-cluster
bond lengths [Å]			
Al−O_{ca}	1.932	1.927	1.927
Al−O_{hy}	1.878	1.861	1.882
O_{ca}−C_{ca}	1.267	1.266	1.268
C_{ca}−C_{pc}	1.503	1.489	1.496
C_{ph}−C_{ph}	1.391	1.387	1.389
C_{ph}−C_{pc}	1.409	1.398	1.399
bending angles [deg]			
Al−O_{ca}−C_{ca}	132.0	127.8	134.5
Al−O_{hy}−Al	122.7	121.0	126.4
O_{ca}−Al−O_{hy}	90.0	90.0	89.7
O_{ca}−Al−O_{ca}	90.0	90.0	90.0
O_{ca}−C_{ca}−O_{ca}	123.5	124.1	124.5

[a]The force-field internal coordinates are given both for a force-field optimization with MM3-vdW interactions switched on (*MM3-vdW*) and with vdW interactions switched off (*no-vdW*).

This is not completely surprising since the Pauli repulsion in the metal oxide chain is not involved in the FF-no-vdW results. The three geometrical variables under consideration are much better reproduced in the MM3-vdW simulations, and this confirms our expectations. In general, the agreement is very satisfactory, and this provides good evidence that the covalent and electrostatic interactions succeed in reproducing the ab initio calculations.

In the next step, we compared the simulated cell dimensions of both lp and np phases with the experimental values of the empty host at 77 K from ref 28 (see Table 5). The interdiagonal angle θ and diagonal length D defined in Figure 2 are also tabulated. For the lp, the agreement between simulation and experiment is very good: the simulation predicts an orthorhombic shape, in agreement with the experiment, and the deviation between simulation and experiment on the interdiagonal angle θ and the diagonal length D is around 1%. Furthermore, the force field also performs reasonably well at reproducing the unit cell of the np phase; especially the reproduction of the interdiagonal angle θ is very good. There is however a rather large deviation in the diagonal length (6.3%), and at this point, we do not have a clear explanation for this discrepancy. The force field also predicts a nonorthorhombic shape of the unit cell, in agreement with the experiment, albeit a diclinic shape with smaller angles instead of a monoclinic shape. However, overall we can conclude that the force field succeeds in predicting the geometries of both lp and np phases.

Table 5. Comparison of Cell Parameters[a]

	experimental (77 K)		simulated	
	lp	np	lp	np
a [Å]	16.913	20.824	17.046	19.565
b [Å]	6.624	6.607	6.593	6.527
c [Å]	12.671	6.871	12.905	6.245
α [deg]	90.000	90.000	90.000	87.891
β [deg]	90.000	90.000	90.000	89.434
γ [deg]	90.000	113.949	90.632	97.150
D [Å]	21.133	21.928	21.380	20.537
θ [deg]	73.680	36.522	74.254	35.407

[a]The experimental values of the empty host (at 77 K) are taken from ref 28. Simulated cell parameters are obtained by minimizing the force-field energy of the MIL-53(Al) structure.

This is especially promising since the information on the np phase was only used for fine-tuning two dihedral force constants. The force field was additionally tested for its sensitivity with respect to some crucial parameters. We selected K_c and K_ω, as these are the two dihedral force constants which are crucial to describing the structural transition of the material. The results may be found in the Supporting Information. We found that the interdiagonal angle in the narrow pore and the diagonal length in both phases are insensitive to changes in these force constants, while the interdiagonal angle in the large pore is more sensitive.

4.2. Energy Profile during Breathing. MIL-53(Al) is the most studied example of a flexible MOF with its specific breathing behavior. Upon adsorption of guest molecules, the framework can switch reversibly between a large pore (lp) and a narrow pore (np) form.[15,31,32] In the case of H_2O as an adsorbent, the observed structural transition is mainly due to the hydrogen bond interaction between water and the oxygens of the MOF carboxylates.[31] However, there is experimental evidence that these structural transitions also take place in the absence of guest molecules, indicating that the framework is intrinsically bistable.[28] The energy barrier between the two forms is very low, allowing for thermally induced transitions between the two forms. The intrinsic bistability of MIL-53(Al) has already been investigated in the literature by Walker et al.[40] based on DFT-D computations. These calculations showed that the np form is more stable than the lp form with values ranging from 34 to 42 kJ mol^{-1} per unit cell. These energy differences include a large fraction of dispersion interaction (ranging from 150 to 184 kJ mol^{-1} per unit cell). The authors conclude that dispersion interactions are primarily responsible for the existence of the np form even without guest molecules.

A crucial test of our force field is its ability to also simulate the bistable behavior of the MIL-53(Al). Additionally, a force field is able to provide insight into the governing terms that lie on the origin of the breathing behavior. Therefore, we performed a scan that is representative for the breathing mode of MIL-53(Al) using the force field. The scan consists of a series of geometry optimizations in which we constrain the interdiagonal angle θ to values between 30° and 90° with steps of 1°, relaxing all other degrees of freedom during the geometry optimization. The procedure is similar to the one applied in section 3.6. To further investigate the importance of the vdW interactions, the scan procedure was repeated several times, but for each scan, another scale factor is used for the σ and/or ε parameters of the vdW expression (eq 6) relative to the tabulated MM3 values. The various energy profiles are displayed in Figure 7. Most curves show two minima, one at small interdiagonal angles that we can associate with the narrow pore phase (np) and one at higher interdiagonal angles that we can associate with the large pore phase (lp).

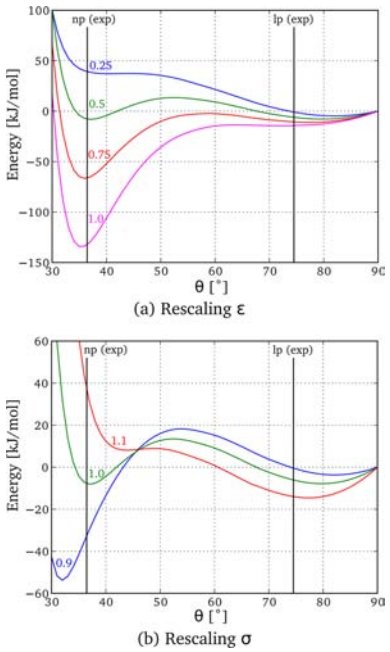

Figure 7. Energy profiles of the breathing mode for different sets of van der Waals parameters with indication of the interdiagonal angle of the experimental narrow pore and large pore phases.[31] (a) Total energy after uniformly rescaling the ε parameters of the vdW interactions and a σ scale factor of 1.0. (b) Total energy after uniformly rescaling the σ parameters and an ε scale factor of 0.5. The experimental values for the two local minima are taken from ref 28.

Without discussing the quantative features, this result is very promising, as apparently all curves indeed yield two minima. To further analyze the results, we first focus on the unscaled MM3 results in Figure 7a (scale factor = 1). We observe that the np is much more stable than the lp phase, by more than 60 kJ mol^{-1} per unit cell. This energy difference is too large compared to the result of Walker et al.[40] of 42 kJ mol^{-1}. The lp minimum is located around 74.3°, which is in good agreement with the experimental value of 73.7°,[28] but with an extremely low barrier. The interdiagonal angle of the np is predicted at 35.4°, also in good agreement with the experimental value of 36.5°.[28] In other words, the force-field simulation with unscaled MM3 parameters predicts two minima, lp and np, which are located at interdiagonal angles that are in very good agreement with the

experiment. However, the relative stability of the two minima does not agree with the results of Walker et al.

Next, we examine the sensitivity of the energy profile to the scaling factors of the van der Waals interactions. The upper figure (Figure 7a) displays the influence of decreasing the strength of the vdW interactions:

- The np becomes less stable, while its position remains unaffected.
- The position of the lp phase seems to shift slightly to larger interdiagonal angles, and its energy increases.

Rescaling the σ parameters induces other larger effects on the energy profile:

- The position of both the np and lp minimum are strongly dependent on the scale factor.
- Similar conclusions can be drawn for the stability of the two local minima. For a scale factor of 1.1, the relative stability is interchanged. The lp phase becomes more stable with respect to the np phase.

Another noteworthy feature is that also the shape of the unit cell is strongly dependent on the van der Waals interactions. This observation is confirmed by the current scan: varying both scales over the proposed range induces a variation in D of 0.4 Å and a variation in b of 0.16 Å in the large pore phase and even more in the narrow pore phase (see Table S4 in the Supporting Information).

Our tests with rescaled MM3-vdW parameters point out that it is crucial to have an accurate set of van der Waals parameters, in order to get a realistic energy profile of the breathing mode. The unscaled parameters of the MM3 force field are not entirely satisfactory as the relative stability of the two minima does not agree with Walker et al. Nevertheless, the two minima are present. Further model development is necessary to deduce more accurate forms for the van der Waals part of the force field. However, based on the results of Walker et al., we can propose a scale factor for the ε parameters that more accurately reproduces the relative stability. A linear interpolation between the results at ε scale factors 1.0 and 0.75 results in a scale factor of 0.86 with a corresponding relative stability of 42 kJ mol^{-1}.

5. CONCLUSIONS

A force field was developed for the metal organic framework MIL-53(Al) using density functional theory calculations on small nonperiodic clusters. Atomic partial charges, calculated using a Hirshfeld-I scheme on the valence molecular electron density, were used to calculate the electrostatic interactions of all atom pairs without any scaling, including 1−2, 1−3, and 1−4 pairs. The covalent parameters of the force field were fitted to reproduce the ab initio Hessian and forces using a least-squares cost function with two crucial adjustments that address mismatches in the geometry and strong correlations in the parameters. Two parameters figuring in the dihedral terms which contribute to the breathing behavior of the structure were refined using an ab initio scan in terms of the breathing angle using periodic DFT calculations. The van der Waals parameters of all atoms were taken from the MM3 force field.

The force field was validated for its ability to reproduce the geometry and cell parameters. The new force field predicts a geometry of the periodic MOF in its large pore form that closely matches the ab initio geometries of the core region in two well-chosen clusters, representative for the system of interest. The force field predicts unit cells of both the large pore and narrow pore phases with a shape that shows good agreement with the reported experimental data. Furthermore, the energy profile of the breathing mode was revealed to be highly dependent on the van der Waals parameters. The MM3 parameters succeed in reproducing a profile with two minima, although the np phase is predicted to be more stable than the theoretical data of Walker et al. By varying the van der Waals parameters, we showed that the energy profile can be tuned to predict also quantitatively the energies of the two phases more accurately.

In conclusion, the new force field was parametrized using a novel scheme for the covalent and electrostatic interactions and as such succeeds in predicting the geometries of the lp and np phases. However, to accurately describe the energy profile of the breathing mode, we need an improved set of van der Waals parameters. In the future, we plan to estimate van der Waals parameters specifically for MIL-53(Al) to overcome this deficiency. Additionally, future work is warranted to test the ability of the force field when also guest molecules are present in the material.

APPENDIX

We will now discuss in full detail how the parameters of the covalent interactions are estimated. Initially, the discussion is limited to a training set containing a single molecule. An extension with multiple molecules is trivial and will be discussed later. The calibration of the valence parameters is based on energy gradient and Hessian data derived from an ab initio computation on an isolated cluster that is representative for the system of interest. In practice, the geometry of the cluster is first optimized. However, we explicitly include the ab initio energy gradient in the equations to keep the derivation as general as possible.

Some conventions on the notation are systematically used below. The indices i and j are used for internal coordinates and runs from 1 to N_{ic}, the number of internal coordinates. μ and ν are indices used for Cartesian components and run from 1 to $3N_{at}$, with N_{at} being the total number of atoms. The potential energy is denoted by V, the gradient by G, and the Hessian by H. The model (force field or ab initio) in which this observable is calculated is specified in the superscript; e.g., V^{ff} represents the potential energy in the force field model. A contribution to these observables is specified in the subscript; e.g., V^{ff}_{cov} represents the covalent contribution to the potential energy in the force field model. Vector and matrix elements are denoted by means of brackets, e.g., $[G]_\mu$ and $[H]_{\mu\nu}$.

The most straightforward way to obtain valence parameters is to solve the following sets of equations:

$$G^{ai} = G^{ff}_{cov} + G^{ff}_{el} \tag{18}$$

$$H^{ai} = H^{ff}_{cov} + H^{ff}_{el} \tag{19}$$

where G^{ai}, G^{ff}_{cov}, and G^{ff}_{el} are $3N_{at} \times 1$ vectors containing the ab initio, covalent force-field, and electrostatic force-field gradients at the cluster geometry. Similarly, H^{ai}, H^{ff}_{cov}, and H^{ff}_{el} are the corresponding Hessian matrices with $3N_{at}$ by $3N_{at}$ second order derivatives. In these equations, only the covalent contributions depend on the valence parameters. The remaining contributions are constant matrices because the charges for the electrostatic term can be determined a priori. The total number of equations is in practice always larger than the number of parameters, certainly when information from multiple molecules is combined, which implies that the equations can only be

solved approximately using a least-squares procedure. Our experience is that these basic equations (with simple first and second order Cartesian derivatives of the energy) are not suitable for the calibration of valence parameters. Some crucial modifications are needed and discussed in the remainder of the Appendix.

A generic expression is used for the covalent force field to simplify the derivation:

$$V^{\mathrm{ff}}_{\mathrm{cov}} = \sum_i^{N_{ic}} f_i(z_i, \alpha_{i1}, \alpha_{i2}, ...) \tag{20}$$

The sum runs over all internal coordinates, z_i, used in the force field model, e.g., bond lengths, bending angles, and dihedral angles. The internal coordinates, z_i, are known functions of $3N_{at}$ Cartesian coordinates, x_μ. With each internal coordinate, an energy term, f_i, is associated, which contains a set of empirical parameters: α_{i1}, α_{i2}, and so on. These empirical parameters are calibrated to obtain an optimal correspondence between ab initio and force field data. The chain rule can be used to relate the Cartesian derivatives of the covalent energy in eqs 18 and 19 with derivatives of individual energy terms:

$$[G^{\mathrm{ff}}_{\mathrm{cov}}]_\mu = \frac{\partial V^{\mathrm{ff}}_{\mathrm{cov}}}{\partial x_\mu} = \sum_i^{N_{ic}} \frac{\partial f_i(z_i, \alpha_{i1}, \alpha_{i2}, ...)}{\partial z_i} \frac{\partial z_i}{\partial x_\mu} \tag{21}$$

$$\begin{aligned}[H^{\mathrm{ff}}_{\mathrm{cov}}]_{\mu\nu} &= \frac{\partial V^{\mathrm{ff}}_{\mathrm{cov}}}{\partial x_\mu \partial x_\nu} \\ &= \sum_i^{N_{ic}} \frac{\partial^2 f_i(z_i, \alpha_{i1}, \alpha_{i2}, ...)}{\partial z_i^2} \frac{\partial z_i}{\partial x_\mu} \frac{\partial z_i}{\partial x_\nu} \\ &\quad + \frac{\partial f_i(z_i, \alpha_{i1}, \alpha_{i2}, ...)}{\partial z_i} \frac{\partial^2 z_i}{\partial x_\mu \partial x_\nu}\end{aligned} \tag{22}$$

These equations can be written in matrix form as follows:

$$G^{\mathrm{ff}}_{\mathrm{cov}} = J\mathcal{G}^{\mathrm{ff}}_{\mathrm{cov}} \tag{23}$$

$$H^{\mathrm{ff}}_{\mathrm{cov}} = J\mathcal{H}^{\mathrm{ff}}_{\mathrm{cov}}J^T + \sum_i^{N_{ic}} C_i[\mathcal{G}^{\mathrm{ff}}_{\mathrm{cov}}]_i \tag{24}$$

with

$$[J]_{\mu i} = \frac{\partial z_i}{\partial x_\mu} \tag{25}$$

$$[C_i]_{\mu\nu} = \frac{\partial^2 z_i}{\partial x_\mu \partial x_\nu} \tag{26}$$

$$[\mathcal{G}^{\mathrm{ff}}_{\mathrm{cov}}]_i = \frac{\partial f_i(z_i, \alpha_{i1}, \alpha_{i2}, ...)}{\partial z_i} \tag{27}$$

$$[\mathcal{H}^{\mathrm{ff}}_{\mathrm{cov}}]_{ij} = \delta_{ij} \frac{\partial^2 f_i(z_i, \alpha_{i1}, \alpha_{i2}, ...)}{\partial z_i^2} \tag{28}$$

The Jacobian, J, and the matrices, C_i, are constant during the calibration procedure. They depend on the molecular geometry and the choice of internal coordinates, which are fixed. All empirical parameters are found in the matrices with the first and second order derivatives of the energy terms, $\mathcal{G}^{\mathrm{ff}}_{\mathrm{cov}}$ and $\mathcal{H}^{\mathrm{ff}}_{\mathrm{cov}}$, respectively. Because each energy term only depends on one internal coordinate, the matrix $\mathcal{H}^{\mathrm{ff}}_{\mathrm{cov}}$ is diagonal. If cross terms would be present, it would also contain off-diagonal terms.

The two extensions discussed below are mainly related to the gradient equations (see eq 18), while the Hessian equations (see eq 19) are not modified. In both extensions, the Jacobian, J, plays a central role. In order to avoid any dependence on the choice of units for bond lengths and angles in the remainder of the Appendix, we rewrite equation eq 23 as follows:

$$G^{\mathrm{ff}}_{\mathrm{cov}} = \tilde{J}S\mathcal{G}^{\mathrm{ff}}_{\mathrm{cov}} \tag{29}$$

where S is a diagonal matrix with the norms of the columns of J and $\tilde{J}$ is a dimensionless matrix that contains the normalized columns of the Jacobian. Two matrices, which can be derived from $\tilde{J}$ with singular value decomposition (SVD), are used below: (i) a projection matrix P and (ii) an orthogonal complement $\tilde{J}_\perp$. The projection matrix P has orthonormal columns that form a basis for the columns of $\tilde{J}$. These basis vectors represent small changes in Cartesian coordinates that correspond to small changes in internal coordinates. It is not possible to write a small global translation or rotation as a linear combination of these basis vectors. The matrix $\tilde{J}_\perp$ has as rows an orthonormal basis for the orthogonal complement of the rows of $\tilde{J}$.

1. Transformed Gradient Equations

The first weakness of the gradient equations is that—when used in a least-squares context—the residual contribution is distributed equally over all components of the gradient, except for random fluctuations. In order to obtain parameters that accurately predict the molecular geometry, the gradient along shallow modes of the potential energy surface has to be more accurately determined than along modes with high curvature. This means that we have to introduce weights in the gradient equations to account for the variable sensitivity of the geometry to errors in the gradient. In order to give a higher weight to the gradient along shallow modes, one could multiply both sides of the gradient equations with the inverse of the ab initio Hessian.

$$(H^{\mathrm{ai}})^{-1}G^{\mathrm{ai}} = (H^{\mathrm{ai}})^{-1}(G^{\mathrm{ff}}_{\mathrm{cov}} + G^{\mathrm{ff}}_{\mathrm{el}}) \tag{30}$$

However, because the Hessian is a singular matrix, the inverse can only be defined in a subspace of the Cartesian coordinates. Therefore, we use the projection matrix P, which projects the Cartesian coordinates to the subspace of the internal coordinates. The final transformed gradient equations become:

$$(PH^{\mathrm{ai}}P^T)^{-1}PG^{\mathrm{ai}} = (PH^{\mathrm{ai}}P^T)^{-1}P(G^{\mathrm{ff}}_{\mathrm{cov}} + G^{\mathrm{ff}}_{\mathrm{el}}) \tag{31}$$

One could also interpret this transformation as a single step from the Newton optimization algorithm. In practice, one uses ab initio optimized geometries for the parameter calibration, which implies that the left-hand side is zero. The right-hand side is then an approximate error on the force-field geometry in a coordinate space that excludes global rotation and translation. Hence, these equations impose a good force-field geometry without having to perform the actual geometry optimization during the calibration procedure. In principle, one could also use the force-field Hessian on the right-hand side of eq 31, but this would introduce a strong nonlinear dependence of the equations in the parameters, leading to a much harder nonlinear least-squares problem.

2. Internal Strain Equations

A second weakness of the gradient equations is that the Jacobian in eq 23 transforms the vector with derivatives of energy terms to a lower dimensional space to obtain the

Cartesian energy derivatives. It is therefore unavoidable that the Cartesian gradient of the covalent energy becomes insensitive to some linear combinations of derivatives of energy terms. The simplest example can be found in cyclopropane, where it is impossible to increase or reduce the three C−C−C angles simultaneously. If a cyclopropane force field would have a C−C−C rest-angle different from 60°, the equilibrium angle would still be 60°. We will denote such internal forces that cancel each other out as *internal strain*. In the case of cyclopropane, it is impossible to determine the value of the C−C−C rest angle from Cartesian training data. One has two options to solve this type of problem: (i) introduce constraints to fix such parameters or (ii) introduce additional equations in the least-squares fit to fix these parameters. We propose a solution in line with the second option.

One can quantify the amount of internal strain using the orthogonal complement $\tilde{J}_\perp$ as follows:

$$Y_{\mathrm{cov}}^{\mathrm{ff}} = \tilde{J}_\perp S \mathcal{G}_{\mathrm{cov}}^{\mathrm{ff}} \tag{32}$$

A new symbol, $Y_{\mathrm{cov}}^{\mathrm{ff}}$, is used to stress that the internal strain is complementary to the Cartesian gradient. All the degrees of freedom that are discarded (projected out) when computing the Cartesian gradient of the covalent energy are present in $Y_{\mathrm{cov}}^{\mathrm{ff}}$. The additional least-squares equations are obtained by simply requiring that the internal strains are equal to zero:

$$Y_{\mathrm{cov}}^{\mathrm{ff}} = 0 \tag{33}$$

In the example of cyclopropane, such equations force the rest value parameter to be 60°. Also in more complex cases, these equations impose realistic values for the rest parameters.

3. Total Cost Function

So far, three sets of least squares equations are defined, all having different units: transformed gradient (tg) equations in Å, Hessian (h) equations in kJ mol^{-1} Å^{-2}, and internal strain (is) equations in kJ mol^{-1} Å^{-1}. For each set of equations, we write the difference between the left-hand and right-hand side of the kth equation as $\mathrm{Err}_k^{\mathrm{XX}}$ where XX is tg, h, or is. One can find a set of covalent force-field parameters that approximately solves all equations by minimizing a total cost function:

$$X = \frac{1}{\sigma_{\mathrm{tg}}^2 N_{\mathrm{tg}}} \sum_{k=1}^{N_{\mathrm{tg}}} (\mathrm{Err}_k^{\mathrm{tg}})^2 + \frac{1}{\sigma_{\mathrm{h}}^2 N_{\mathrm{h}}} \sum_{k=1}^{N_{\mathrm{h}}} (\mathrm{Err}_k^{\mathrm{h}})^2 + \frac{1}{\sigma_{\mathrm{is}}^2 N_{\mathrm{is}}} \sum_{k=1}^{N_{\mathrm{is}}} (\mathrm{Err}_k^{\mathrm{is}})^2 \tag{34}$$

where the *scales* (σ_{tg}, σ_{h}, and σ_{is}) have the same unit as the corresponding equations. They must be tuned to obtain a well-defined least-squares problem. We could not find universal values for these scales. We experience that a good choice for the scales depends on the system for which a force field is being developed. There are two criteria that can be used as a guidance to tune the scales: (i) one should obtain a condition number for the least squares fit that is as low as possible, and (ii) the scales should roughly correspond to acceptable orders of magnitude for the root-mean-square errors on each set of equations. (The condition number is defined as the ratio of the highest and lowest eigenvalue of the Hessian of the cost function at the optimal parameters.)

When one uses a training set with multiple molecules for the force-field calibration, one can simply minimize the sum of the corresponding cost functions. For the calibration of the MIL-53(Al) force field, only the core regions were used from two clusters. Equations that are not related to the atoms in the core region were omitted from the cost function. Because the force field contains nonlinear parameters, one should carefully choose reasonable initial values prior to the calibration procedure.

■ ASSOCIATED CONTENT

Supporting Information

The following additional information is included: an unused deficient oxide cluster, the atomic coordinates and Hirshfeld-based charges of the DFT-optimized clusters, the cell dimensions as a function of the van der Waals scale factors, and a sensitivity analysis of D and θ toward K_c and K_o. This material is available free of charge via the Internet at http://pubs.acs.org/.

■ AUTHOR INFORMATION

Corresponding Author

*E-mail: Toon.Verstraelen@Ugent.be; Veronique.VanSpeybroeck@Ugent.be.

Notes

The authors declare no competing financial interest.

■ ACKNOWLEDGMENTS

This work is supported by the Fund for Scientific Research; Flanders (FWO), the Research Board of Ghent University (BOF) and BELSPO in the frame of IAP/6/27. Funding was also received from the European Research Council under the European Community's Seventh Framework Programme [FP7(2007-2013) ERC grant agreement number 240483]. Computational resources (Stevin Supercomputer Infrastructure) and services were provided by Ghent University.

■ REFERENCES

(1) Li, H.; Eddaoudi, M.; O'Keeffe, M.; Yaghi, O. *Nature* **1999**, *402*, 276−279.
(2) Eddaoudi, M.; Kim, J.; Rosi, N.; Vodak, D.; Wachter, J.; O'Keeffe, M.; Yaghi, O. *Science* **2002**, *295*, 469−472.
(3) Long, J.; Yaghi, O. *Chem. Soc. Rev.* **2009**, *38*, 1213−1214.
(4) Kitagawa, S.; Noro, S.-I.; Kitaura, R. *Angew. Chem., Int. Ed.* **2004**, *43*, 2334−2375.
(5) Kitagawa, S.; Noro, S.-I.; Nakamura, T. *Chem. Commun.* **2006**, 701−707.
(6) Trung, T.; Trens, P.; Tanchoux, N.; Bourrelly, S.; Llewellyn, P.; Loera-Serna, S.; Serre, C.; Loiseau, T.; Fajula, F.; Férey, G. *J. Am. Chem. Soc.* **2008**, *130*, 16926−16932.
(7) Férey, G. *Chem. Soc. Rev.* **2008**, *37*, 191−214.
(8) Perry, J.; Perman, J.; Zaworotko, M. *Chem. Soc. Rev.* **2009**, *38*, 1400−1417.
(9) Tranchemontagne, D. J.; Mendoza-Cortes, J. L.; O'Keeffe, M.; Yaghi, O. *Chem. Soc. Rev.* **2009**, *38*, 1257−1283.
(10) Meek, S.; Greathouse, J.; Allendorf, M. *Adv. Mater.* **2011**, *23*, 249−267.
(11) Deng, H.; Grunder, S.; Cordova, K. E.; Valente, C.; Furukawa, H.; Hmadeh, M.; Gándara, F.; Whalley, A. C.; Liu, Z.; Asahina, S.; Kazumori, H.; O'Keeffe, M.; Terasaki, O.; Stoddart, J. F.; Yaghi, O. M. *Science* **2012**, *336*, 1018−1023.
(12) Furukawa, H.; Ko, N.; Go, Y. B.; Aratani, N.; Choi, S. B.; Choi, E.; Yazaydin, A. O.; Snurr, R. Q.; O'Keeffe, M.; Kim, J.; Yaghi, O. M. *Science* **2010**, *329*, 424−428.
(13) Mulder, F.; Dingemans, T.; Schimmel, H.; Ramirez-Cuesta, A.; Kearley, G. *Chem. Phys.* **2008**, *351*, 72−76.
(14) Himsl, D.; Wallacher, D.; Hartmann, M. *Angew. Chem., Int. Ed.* **2009**, *48*, 4639−4642.

(15) Bourrelly, S.; Llewellyn, P.; Serre, C.; Millange, F.; Loiseau, T.; Férey, G. *J. Am. Chem. Soc.* **2005**, *127*, 13519−13521.
(16) Millward, A.; Yaghi, O. *J. Am. Chem. Soc.* **2005**, *127*, 17998−17999.
(17) Li, Y.; Yang, R. *Langmuir* **2007**, *23*, 12937−12944.
(18) Couck, S.; Denayer, J.; Baron, G.; Remy, T.; Gascon, J.; Kapteijn, F. *J. Am. Chem. Soc.* **2009**, *131*, 6326−6327.
(19) D'Alessandro, D.; Smit, B.; Long, J. *Angew. Chem., Int. Ed.* **2010**, *49*, 6058−6082.
(20) Férey, G.; Serre, C.; Devic, T.; Maurin, G.; Jobic, H.; Llewellyn, P.; De Weireld, G.; Vimont, A.; Daturi, M.; Chang, J. *Chem. Soc. Rev.* **2011**, *40*, 550−562.
(21) Alaerts, L.; Kirschhock, C.; Maes, M.; van der Veen, M.; Finsy, V.; Depla, A.; Martens, J.; Baron, G.; Jacobs, P.; Denayer, J.; De Vos, D. *Angew. Chem., Int. Ed.* **2007**, *46*, 4293−4297.
(22) Alaerts, L.; Maes, M.; Giebeler, L.; Jacobs, P.; Martens, J.; Denayer, J.; Kirschhock, C.; De Vos, D. *J. Am. Chem. Soc.* **2008**, *130*, 14170−14178.
(23) Leus, K.; Muylaert, I.; Vandichel, M.; Marin, G.; Waroquier, M.; Van Speybroeck, V.; Van der Voort, P. *Chem. Commun.* **2010**, *46*, 5085−5087.
(24) Leus, K.; Vandichel, M.; Liu, Y.-Y.; Muylaert, I.; Musschoot, J.; Pyl, S.; Vrielinck, H.; Callens, F.; Marin, G.; Detavernier, C.; Wiper, P.; Khimyak, Y.; Waroquier, M.; Van Speybroeck, V.; Van der Voort, P. *J. Catal.* **2012**, *285*, 196−207.
(25) Vermoortele, F.; Vandichel, M.; Van de Voorde, B.; Ameloot, R.; Waroquier, M.; Van Speybroeck, V.; De Vos, D. E. *Angew. Chem., Int. Ed.* **2012**, *51*, 4887−4890.
(26) Corma, A.; García, H.; Llabrés i Xamena, F. X. *Chem. Rev.* **2010**, *110*, 4606−4655.
(27) Farrusseng, D.; Aguado, S.; Pinel, C. *Angew. Chem., Int. Ed.* **2009**, *48*, 7502−7513.
(28) Liu, Y.; Her, J.; Dailly, A.; Ramirez-Cuesta, A.; Neumann, D.; Brown, C. *J. Am. Chem. Soc.* **2008**, *130*, 11813−11818.
(29) Beurroies, I.; Boulhout, M.; Llewellyn, P. L.; Kuchta, B.; Férey, G.; Serre, C.; Denoyel, R. *Angew. Chem., Int. Ed.* **2010**, *49*, 7526−7529.
(30) Murray, K.; Kepert, C. *Top. Curr. Chem.* **2004**, *233*, 195−228.
(31) Loiseau, T.; Serre, C.; Huguenard, C.; Fink, G.; Taulelle, F.; Henry, M.; Bataille, T.; Férey, G. *Chem.—Eur. J.* **2004**, *10*, 1373−1382.
(32) Llewellyn, P.; Bourrelly, S.; Serre, C.; Filinchuk, Y.; Férey, G. *Angew. Chem., Int. Ed.* **2006**, *45*, 7751−7754.
(33) Serre, C.; Millange, F.; Thouvenot, C.; Noguès, M.; Marsolier, G.; Louër, D.; Férey, G. *J. Am. Chem. Soc.* **2002**, *124*, 13519−13526.
(34) Serre, C.; Mellot-Draznieks, C.; Surblé, S.; Audebrand, N.; Filinchuk, Y.; Férey, G. *Science* **2007**, *315*, 1828−1831.
(35) Anokhina, E. V.; Vougo-Zanda, M.; Wang, X.; Jacobson, A. J. *J. Am. Chem. Soc.* **2005**, *127*, 15000−15001.
(36) Whitfield, T. R.; Wang, X.; Liu, L.; Jacobson, A. J. *Solid State Sci.* **2005**, *7*, 1096−1103.
(37) Vougo-Zanda, M.; Huang, J.; Anokhina, E.; Wang, X.; Jacobson, A. J. *Inorg. Chem.* **2008**, *47*, 11535−11542.
(38) Bauer, S.; Serre, C.; Devic, T.; Horcajada, P.; Marrot, J.; Férey, G.; Stock, N. *Inorg. Chem.* **2008**, *47*, 7568−7576.
(39) Mowat, J. P.; Miller, S. R.; Slawin, A. M.; Seymour, V. R.; Ashbrook, S. E.; Wright, P. A. *Microporous Mesoporous Mater.* **2011**, *142*, 322−333.
(40) Walker, A.; Civalleri, B.; Slater, B.; Mellot-Draznieks, C.; Corà, F.; Zicovich-Wilson, C.; Román-Pérez, G.; Soler, J.; Gale, J. *Angew. Chem., Int. Ed.* **2010**, *49*, 7501−7503.
(41) Smit, B.; Maesen, T. L. M. *Chem. Rev.* **2008**, *108*, 4125−4184.
(42) Walton, K. S.; Millward, A. R.; Dubbeldam, D.; Frost, H.; Low, J. J.; Yaghi, O. M.; Snurr, R. Q. *J. Am. Chem. Soc.* **2008**, *130*, 406−407.
(43) Dubbeldam, D.; Krishna, R.; Snurr, R. Q. *J. Phys. Chem. C* **2009**, *113*, 19317−19327.
(44) Duren, T.; Bae, Y.-S.; Snurr, R. Q. *Chem. Soc. Rev.* **2009**, *38*, 1237−1247.
(45) Grimme, S. *J. Comput. Chem.* **2006**, *27*, 1787−1799.
(46) Grimme, S.; Antony, J.; Ehrlich, S.; Krieg, H. *J. Chem. Phys.* **2010**, *132*, 154104.
(47) Zhao, Y.; Truhlar, D. *Theor. Chem. Acc.* **2008**, *120*, 215−241.
(48) Zhao, Y.; Truhlar, D. *Acc. Chem. Res.* **2008**, *41*, 157−167.
(49) Chai, J.-D.; Head-Gordon, M. *Phys. Chem. Chem. Phys.* **2008**, *10*, 6615−6620.
(50) Dion, M.; Rydberg, H.; Schröder, E.; Langreth, D.; Lundqvist, B. *Phys. Rev. Lett.* **2004**, *92*, 246401−246404.
(51) Lee, K.; Murray, E. D.; Kong, L.; Lundqvist, B. I.; Langreth, D. C. *Phys. Rev. B* **2010**, *82*, 081101−081104.
(52) Poloni, R.; Smit, B.; Neaton, J. *J. Phys. Chem. A* **2012**, *116*, 4957−4964.
(53) Rappé, A.; Casewit, C.; Colwell, K.; Goddard, W.; Skiff, W. *J. Am. Chem. Soc.* **1992**, *114*, 10024−10035.
(54) Mayo, S.; Olafson, B.; Goddard, W. *J. Phys. Chem.* **1990**, *94*, 8897−8909.
(55) Dauber-Osguthorpe, P.; Roberts, V.; Osguthorpe, D.; Wolff, J.; Genest, M.; Hagler, A. *Proteins: Struct., Funct., Genet.* **1988**, *4*, 31−47.
(56) Allinger, N.; Lii, J.; Yuh, Y. *J. Am. Chem. Soc.* **1989**, *111*, 8551−8566.
(57) Salles, F.; Ghoufi, A.; Maurin, G.; Bell, R.; Mellot-Draznieks, C.; Férey, G. *Angew. Chem., Int. Ed.* **2008**, *47*, 8487−8491.
(58) Tafipolsky, M.; Amirjalayer, S.; Schmid, R. *J. Comput. Chem.* **2007**, *28*, 1169−1175.
(59) Tafipolsky, M.; Schmid, R. *J. Phys. Chem. B* **2009**, *113*, 1341−1352.
(60) Tafipolsky, M.; Amirjalayer, S.; Schmid, R. *J. Phys. Chem. C* **2010**, *114*, 14402−14409.
(61) Tafipolsky, M.; Amirjalayer, S.; Schmid, R. *Angew. Chem., Int. Ed.* **2007**, *46*, 463−466.
(62) Dubbeldam, D.; Walton, K. S.; Ellis, D. E.; Snurr, R. Q. *Angew. Chem., Int. Ed.* **2007**, *46*, 4496−4499.
(63) Ford, D. C.; Dubbeldam, D.; Snurr, R. Q.; Künzel, V.; Wehring, M.; Stallmach, F.; Kärger, J.; Müller, U. *J. Phys. Chem. Lett.* **2012**, *3*, 930−933.
(64) Becke, A. *Phys. Rev. A* **1988**, *38*, 3098.
(65) Becke, A. *J. Chem. Phys.* **1993**, *98*, 5648−5652.
(66) Lee, C.; Yang, W.; Parr, R. *Phys. Rev. B* **1988**, *37*, 785.
(67) Zygmunt, S.; Mueller, R.; Curtiss, L.; Iton, L. *THEOCHEM* **1998**, *430*, 9−16.
(68) Sousa, S.; Fernandes, P.; Ramos, M. *J. Phys. Chem. A* **2007**, *111*, 10439−10452.
(69) Krishnan, R.; Binkley, J. S.; Seeger, R.; Pople, J. A. *J. Chem. Phys.* **1980**, *72*, 650−654.
(70) McLean, A. D.; Chandler, G. S. *J. Chem. Phys.* **1980**, *72*, 5639−5648.
(71) Frisch, M. J.; Pople, J. A.; Binkley, J. S. *J. Chem. Phys.* **1984**, *80*, 3265−3269.
(72) Ditchfield, R.; Hehre, W. J.; Pople, J. A. *J. Chem. Phys.* **1971**, *54*, 724−728.
(73) Frisch, M.; Trucks, G.; Schlegel, H.; Scuseria, G.; Robb, M.; Cheeseman, J.; Scalmani, G.; Barone, V.; Mennucci, B.; Petersson, G.; Nakatsuji, H.; Caricato, M.; Li, X.; Hratchian, H.; Izmaylov, A.; Bloino, J.; Zheng, G.; Sonnenberg, J.; Hada, M.; Ehara, M.; Toyota, K.; Fukuda, R.; Hasegawa, J.; Ishida, M.; Nakajima, T.; Honda, Y.; Kitao, O.; Nakai, H.; Vreven, T.; Montgomery, J.; Peralta, J.; Ogliaro, F.; Bearpark, M.; Heyd, J.; Brothers, E.; Kudin, K.; Staroverov, V.; Kobayashi, R.; Normand, J.; Raghavachari, K.; Rendell, A.; Burant, J.; Iyengar, S.; Tomasi, J.; Cossi, M.; Rega, N.; Millam, J.; Klene, M.; Knox, J.; Cross, J.; Bakken, V.; Adamo, C.; Jaramillo, J.; Gomperts, R.; Stratmann, R.; Yazyev, O.; Austin, A.; Cammi, R.; Pomelli, C.; Ochterski, J.; Martin, R.; Morokuma, K.; Zakrzewski, V.; Voth, G.; Salvador, P.; Dannenberg, J.; Dapprich, S.; Daniels, A.; Farkas, O.; Foresman, J.; Ortiz, J.; Cioslowski, J.; Fox, D. *Gaussian 09*, revision A.02; Gaussian Inc.: Wallingford, CT, 2009.
(74) Perdew, J.; Burke, K.; Ernzerhof, M. *Phys. Rev. Lett.* **1996**, *77*, 3865−3868.
(75) Perdew, J.; Burke, K.; Ernzerhof, M. *Phys. Rev. Lett.* **1997**, *78*, 1396−1396.

(76) Mortensen, J.; Hansen, L.; Jacobsen, K. *Phys. Rev. B* **2005**, *71*, 035109−035119.
(77) Enkovaara, J.; Rostgaard, C.; Mortensen, J.; Chen, J.; Dulak, M.; Ferrighi, L.; Gavnholt, J.; Glinsvad, C.; Haikola, V.; Hansen, H.; Kristoffersen, H.; Kuisma, M.; Larsen, A.; Lehtovaara, L.; Ljungberg, M.; Lopez-Acevedo, O.; Moses, P.; Ojanen, J.; Olsen, T.; Petzold, V.; Romero, N.; Stausholm-Møller, J.; Strange, M.; Tritsaris, G.; Vanin, M.; Walter, M.; Hammer, B.; Häkkinen, H.; Madsen, G.; Nieminen, R.; Nørskov, J.; Puska, M.; Rantala, T.; Schiøtz, J.; Thygesen, K.; Jacobsen, K. *J. Phys.: Condens. Matter* **2010**, *22*, 253202−253225.
(78) Bahn, S.; Jacobsen, K. *Comput. Sci. Eng.* **2002**, *4*, 56−66.
(79) Blöchl, P. E. *Phys. Rev. B* **1994**, *50*, 17953−17979.
(80) Blöchl, P. E.; Först, C. J.; Schimpl, J. *Bull. Mater. Sci.* **2003**, *26*, 33−41.
(81) Kresse, G.; Furthmuller, J. *Comput. Mater. Sci.* **1996**, *6*, 15−50.
(82) Hafner, J. *J. Comput. Chem.* **2008**, *29*, 2044−2078.
(83) Kresse, G.; Joubert, D. *Phys. Rev. B* **1999**, *59*, 1758.
(84) Ewald, P. P. *Ann. Phys.* **1921**, *369*, 253−287.
(85) De Moor, B.; Ghysels, A.; Reyniers, M.; Van Speybroeck, V.; Waroquier, M.; Marin, G. *J. Chem. Theory Comput.* **2011**, *7*, 1090−1101.
(86) Verstraelen, T.; Van Speybroeck, V.; Waroquier, M. *J. Chem. Inf. Model.* **2008**, *48*, 1530−1541.
(87) Allured, V.; Kelly, C.; Landis, C. *J. Am. Chem. Soc.* **1991**, *113*, 1.
(88) Rappe, A.; Bormann-Rochotte, L.; Wiser, D.; Hart, J.; Pietsch, M.; Casewit, C.; Skiff, W. *Mol. Phys.* **2007**, *105*, 301.
(89) Mulliken, R. S. *J. Chem. Phys.* **1955**, *23*, 1833−1840.
(90) Reed, A. E.; Weinstock, R. B.; Weinhold, F. *J. Chem. Phys.* **1985**, *83*, 735−746.
(91) Hirshfeld, F. *Theor. Chim. Acta* **1977**, *44*, 129.
(92) Bultinck, P.; Van Alsenoy, C.; Ayers, P. W.; Carbo-Dorca, R. *J. Chem. Phys.* **2007**, *126*, 144111.
(93) Singh, U. C.; Kollman, P. A. *J. Comput. Chem.* **1984**, *5*, 129−145.
(94) Breneman, C. M.; Wiberg, K. B. *J. Comput. Chem.* **1990**, *11*, 361−373.
(95) Bayly, C.; Cieplak, P.; Cornell, W.; Kollman, P. *J. Phys. Chem.* **1993**, *97*, 10269−10280.
(96) Bader, R. F. W. *Chem. Rev.* **1991**, *91*, 893−928.
(97) Bush, B. L.; Bayly, C. I.; Halgren, T. A. *J. Comput. Chem.* **1999**, *20*, 1495−1516.
(98) Ponder, J. W.; Case, D. A. *Adv. Protein Chem.* **2003**, *66*, 27−85.
(99) Ramsahye, N.; Maurin, G.; Bourrelly, S.; Llewellyn, P.; Férey, G. *Phys. Chem. Chem. Phys.* **2007**, *9*, 1059−1063.
(100) Verstraelen, T.; Pauwels, E.; De Proft, F.; Van Speybroeck, V.; Geerlings, P.; Waroquier, M. *J. Chem. Theory Comput.* **2012**, *8*, 661−676.
(101) Press, W. H.; Teukolsky, S. A.; Vetterling, W. T.; Flannery, B. P. *Numerical Recipes: The Art of Scientific Computing*, 3rd ed.; Cambridge University Press: New York, NY, 2007; Chapter Solution of Linear Algebraic Equations, pp 65−75.
(102) Halgren, T. A. *J. Comput. Chem.* **1996**, *17*, 520−552.
(103) Van Damme, S.; Bultinck, P.; Fias, S. *J. Chem. Theory Comput.* **2009**, 334−340.
(104) Catak, S.; D'hooghe, M.; Verstraelen, T.; Hemelsoet, K.; Van Nieuwenhove, A.; Ha, H.-J.; Waroquier, M.; De Kimpe, N.; Van Speybroeck, V. *J. Org. Chem.* **2010**, *75*, 4530−4541.
(105) Verstraelen, T.; Sukhomlinov, S. V.; Van Speybroeck, V.; Waroquier, M.; Smirnov, K. S. *J. Phys. Chem. C* **2012**, *116*, 490−504.
(106) Allinger, N. L.; Zhou, X.; Bergsma, J. *THEOCHEM* **1994**, *312*, 69−83.
(107) Ponder, J. W. *TINKER − Software Tools for Molecular Design*; Washington University in Saint Louis: Saint Louis, MO, 2011. http://dasher.wustl.edu/ffe/ (accessed on January 11, 2012).
(108) Ercolessi, F.; Adams, J. B. *Europhys. Lett.* **1994**, *26*, 583−588.
(109) Xie, T.; Bowman, J. M. *J. Chem. Phys.* **2002**, *117*, 10487−10492.
(110) Carbonniere, P.; Begue, D.; Dargelos, A.; Pouchan, C. *Chem. Phys.* **2004**, *300*, 41−51.
(111) Verstraelen, T.; Van Neck, D.; Ayers, P. W.; Van Speybroeck, V.; Waroquier, M. *J. Chem. Theory Comput.* **2007**, *3*, 1420−1434.
(112) Sparta, M.; Hansen, M. B.; Matito, E.; Toffoli, D.; Christiansen, O. *J. Chem. Theory Comput.* **2010**, *6*, 3162−3175.
(113) van Duin, A. C. T.; Dasgupta, S.; Lorant, F.; Goddard, W. A. *J. Phys. Chem. A* **2001**, *105*, 9396−9409.
(114) Martin, M. G.; Siepmann, J. I. *J. Phys. Chem. B* **1998**, *102*, 2569−2577.
(115) Liu, B.; Smit, B.; Rey, F.; Valencia, S.; Calero, S. *J. Phys. Chem. C* **2008**, *112*, 2492−2498.
(116) Maerzke, K. A.; Siepmann, J. I. *J. Phys. Chem. B* **2011**, *115*, 3452−3465.
(117) Hill, J.-R.; Sauer, J. *J. Phys. Chem.* **1995**, *99*, 9536−9550.
(118) CMM Software. http://molmod.ugent.be/software (accessed on July 24, 2012).
(119) Chai, J.-D.; Head-Gordon, M. *J. Chem. Phys.* **2008**, *128*, 084106.

Paper 13

Synthesis, characterization and adsorption properties of an amino functionalized Metal Organic Framework: NH_2-MIL-47(V)

Karen Leus, Sarah Couck, Matthias Vandichel, Gauthier Vanhaelewyn, Ying-Ya Liu, Guy B. Marin, Isabel Van Driessche, Diederik Depla, Michel Waroquier, Veronique Van Speybroeck, Joeri F. M. Denayer and Pascal Van Der Voort

Physical Chemistry Chemical Physics, in press.

Copyright 2012 by the The Royal Society of Chemistry.

Journal Name Physical Chemistry Chemical Physics Dynamic Article Links ► Page 10 of 63

Cite this: DOI: 10.1039/c0xx00000x

www.rsc.org/xxxxxx

ARTICLE TYPE

Synthesis, Characterization and Sorption Properties of NH_2-MIL-47

Karen Leus[a], Sarah Couck[b], Matthias Vandichel[c], Gauthier Vanhaelewyn[d], Ying-Ya Liu[a], Guy B. Marin[c], Isabel Van Driessche[f], Diederik Depla[d], Michel Waroquier[c], Veronique Van Speybroeck[c], Joeri F.M. Denayer[b], Pascal Van Der Voort[a*]

Received (in XXX, XXX) Xth XXXXXXXXX 20XX, Accepted Xth XXXXXXXXX 20XX
DOI: 10.1039/b000000x

An amino functionalized vanadium-containing Metal Organic Framework, NH_2-MIL-47 has been synthesized by a hydrothermal reaction in an autoclave. Alternatively, a synthesis route via microwave enhanced irradiation has been optimized to accelerate the synthesis. The NH_2-MIL-47 exhibits the same topology as MIL-47, in which the V center is octahedrally coordinated. After an exchange procedure in DMF the V^{+III} center is oxidized to V^{+IV}, which is confirmed by EPR and XPS measurements. The CO_2 and CH_4 adsorption properties have been evaluated and compared to MIL-47, showing that both MOFs have an almost similar adsorption capacity and affinity for CO_2. DFT- based molecular modeling calculations were performed to obtain more insight into the adsorption positions for CO_2 in NH_2-MIL-47. Furthermore our calculated adsorption enthalpies agree well with the experimental values.

1. Introduction

Metal Organic Frameworks (MOFs) are crystalline porous solids built up by metal atoms linked together by multifunctional organic ligands. The possibility of designing a MOF with a desired structure, pore size and shape has made them very attractive in many applications. MOFs have been extensively studied for gas storage and separations[1-18], catalysis[19-27] and luminescence[28]. Also in biomedical applications they become more and more a subject of interest [29]. The rigidity of the structure allows further functionalization without changing the original topology. Thus, a series of functional groups can be grafted onto the linker, giving perspectives for different applications. The prototype, MOF-5, constructed from octahedral Zn-O-C clusters and benzene linkers, was used to demonstrate that its three-dimensional porous system can be functionalized with the organic groups -Br, $-NH_2$, $-OC_3H_7$, $-OC_5H_{11}$,$-C_2H_4$, and $-C_4H_4$ [30]. Recently, Biswas et al. reported an isoreticular series of Al-MIL-53-X (X=Cl, Br, CH_3, NO_2, OH) [31]. Another paper reports on the isoreticular series of UiO-66 with an extra NH_2, NO_2 or Br substituent on the organic linker compared to the parent MOF [32]. These extra functional groups, embedded in the structure, can have a significant effect in the outcome for many applications ranging from adsorption to catalysis. The functionalization of porous materials with $-NH_2$ groups is of particular interest for the adsorptive separation of CO_2. For silica-based materials it was already demonstrated that functionalization of the surface of the mesopores with $-NH_2$ groups enhances the affinity toward CO_2 adsorption. This points to a strong interaction between CO_2 and the amino groups in the pores. Sometimes this even resulted in chemisorption, with the formation of carbonate, bicarbonate or carbamate species[33-38].

For MOF materials, the effect of $-NH_2$ groups is less straightforward and is still the subject of many discussions [39, 40]. For IRMOF-3 it was shown that the amino functionalization only had a marginal effect on the CO_2 sorption capacity and selectivity[39, 40]. Arstad et al. prepared three amino functionalized materials (USO-1-Al, USO-2-Ni, and USO-3-In) and they concluded that the capacity toward CO_2 is increased in comparison with the non-functionalized materials [41]. Pure phase amine functionalized MIL-101(Al) has been synthesized in the work of Serra-Crespo et al.[42] The separation properties have been assessed in terms of single component adsorption and mixture separation. The authors found that NH_2-MIL-101(Al) is an excellent candidate for the selective adsorption of CO_2 from methane and N_2. The functionalized material also displays a high CO_2 capacity, but lower than the unfunctionalized MIL-101 with Cr instead of Al. On the other hand NH_2-MIL-101(Al) performs better in CO_2/CH_4 separation than MIL-101(Cr) at low CO_2 pressures[42]. An amine-functionalized ZIF (ZIF-96) displays again higher CO_2 adsorption capacities.[43]

In the specific case of MIL-53(Al), the functionalization of the framework with $-NH_2$ groups leads to a drastic increase in selectivity for CO_2 in mixtures with CH_4 as compared to the non-functionalized material, but this is not caused by a direct interaction (chemisorption) between CO_2 and the NH_2 groups [44-46]. Lescouet et al. have shown that the adsorption capacity varies according to the fraction of amine functionalized linker [47].

Furthermore, the flexibility of the frameworks plays also an important role in adsorption processes. Several papers studied the difference in adsorption behavior between the rigid MIL-47 in comparison to the flexible and breathing MIL-53. In a recent paper of Trung et al[48], MIL-53(Cr) and MIL-47(V) were studied for the adsorption of the apolar species, n-hexane and n-nonane. While MIL-53(Cr) exhibits a sub-step during the sorption process

explained by a structural transition of the framework, one obtains a I-type isotherm for MIL-47 as typically observed for non flexible microporous materials [48, 49]. In the recent paper of Leclerc et al[49], it has been shown that the oxidation state of the vanadium is decisive for the MIL-47 to show a breathing effect. If the vanadium resides in an +III state, a similar breathing effect as in MIL-53 has been observed whereas the presence of V^{+IV} centers inhibits the flexibility to a large extent.[49] Conversely, the use of amine groups may also inhibit CO_2 adsorption, as observed on the modified MIL-53 (Fe), when strong bonds maintain the structure in its closed form[50].

To the best of our knowledge, amino functionalized MIL-47 has not yet been investigated. As can be seen from Fig. 1, NH_2-MIL-47 has a three-dimensional framework, where each V^{+IV} center is coordinated to four oxygen atoms from four carboxylate groups, and to two oxygen atoms on the O–V–O axis, thus forming a saturated octahedral coordination node.

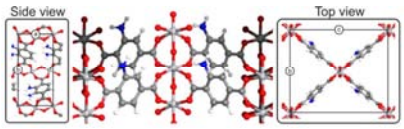

Figure 1. Side, front and top view of the structure of NH_2-MIL-47.

The parent MIL-47 has already demonstrated to possess good catalytic and adsorption properties[24, 25, 49, 51-53].

In this contribution, we report on the synthesis and the characterization of the amino functionalized V-MOF with MIL-47 topology. The CO_2 and CH_4 adsorption properties of this NH_2-MIL-47 have been investigated and are compared to the parent MIL-47. Theoretical modeling can assist us in explaining the differences observed in adsorption behavior between both materials.

2. Experimental Section

2.1 Synthesis of NH_2-MIL-47 and MIL-47

NH_2-MIL-47 *as* has been synthesized in 2 possible manners. The first route was carried out in an autoclave. The molar ratio of VCl_3/ 2-aminoterephthalic acid/ H_2O was 1/1/100. Typically 9 mmol vanadium(III)chloride and 9 mmol 2-aminoterephthalic acid were mixed in a Teflon insert with 16.60 mL H_2O and placed in an autoclave for 4 days at 150 °C. Moreover, to accelerate the synthesis time, a procedure under microwave irradiation has been developed. For the microwave assisted synthesis 1.7 mmol VCl_3 was mixed with 1.7 mmol 2-aminoterephthalic acid in 3.02 mL H_2O. The reaction was carried out at 150 °C for 20 minutes, reducing the synthesis time significantly from 4 days to 20 minutes without loss in crystallinity. In a second step, an exchange procedure in DMF at 125 °C has been done for 90 minutes to remove unreacted linker. MIL-47 was synthesized according to a synthesis route described in literature [54].

2.2 Characterization

All the chemicals were bought from Sigma Aldrich and used without further purification. The microwave assisted synthesis was carried out on a microwave synthesizer (Discover, CEM Inc.). Scanning electron microscopy (SEM) images were taken on a FEI Quanta 200FEG microscope with 4 nm resolution operating at 30 kV. Nitrogen adsorption experiments were measured at -196 °C using a Belsorp mini II gas analyzer. Diffuse Reflectance Infrared Fourier Transform Spectroscopy (DRIFTS) were measured on a Thermo Nicolet 6700 FT-IR spectrometer equipped with a N_2 cooled MCT-A (mercury–cadmium–tellurium) detector. Thermo Gravimetric Analysis (TGA) was performed on an SDT 2960 from TA Instruments. X-ray powder diffraction (XRPD) patterns were collected on a ARL X'TRA X-ray diffractometer with Cu Ka radiation of 0.15418 nm wavelength and a solid state detector. Elemental analyses (C, H, N) were performed on a Thermo Scientific Flash 2000 CHNS-O Analyzer. The EPR spectra were recorded at room temperature using a Bruker ESP300E X-band spectrometer with a maximum microwave power of 200 mW. The measurements were performed using a Bruker ER 4114-HT (high temperature) cavity. The latter is a cylindrical cavity resonating in the TE_{011} mode. The magnetic field was modulated at 100 kHz with a peak-to-peak amplitude of 0.1 mT. The spectra were averaged 4 times with a sweep time of 335.5 s and a time constant of 81.92 ms. The magnetic field sweep width was 1.5 T and the center field was set close to the free electron g-value (2.0023). All spectra contained 2048 data points. The samples were transferred into ER 222 G-type quartz tubes with an outer diameter of 4 mm for recording. The samples masses were about 20 mg. All EPR spectra have been normalized to a microwave frequency of 9.51 GHz for comparison. The magnetic field and microwave frequency were measured using a Bruker ER035M gaussmeter and a HP 5350 B microwave frequency counter, respectively. The XPS measurements were recorded on a X-ray photoelectron spectroscopy S-Probe XPS spectrometer with monochromated Al (1486 eV) exciting radiation from Surface Science Instruments (VG). The powder was pressed into a Sn substrate. A flood gun set at 3 eV and a Ni grid placed 3 mm above the sample surface were used for charge compensation. The following spectra were recorded survey spectrum, V2p, O1s and C1s. In short subsequent measurements of the V2p region no signs of peak shift during the measurement were observed. The binding energy was calculated with respect to the C1s adventitious carbon fixed at 284.6 eV.

2.3 Adsorption tests

Adsorption isotherms of pure CO_2 (purity of 99,99%) and CH_4 (purity of 99,95%) were determined at 30 °C, using the volumetric technique. About 0.5 g of MIL-47 or NH_2-MIL-47 was loaded in the sample container. Prior to the measurement the sample was out-gassed by heating it up to 80 °C under vacuum.

Breakthrough experiments have been performed using a column with a length of 30 cm and an internal diameter of 0.216 cm packed with 600 mg of MOF pellets. Pellets were obtained by pressing the powder to a solid disk, crushing the disk followed by sieving to the desired fraction of 500-630 μm. The adsorption capacity was calculated via the method of *Malek and Farooq (1996)*.[55] The same column was used for obtaining pulse gas chromatographic (pulse GC) data, i.e. Henry constants and adsorption enthalpies of CO_2 and CH_4. More details of this technique are reported elsewhere [56]. Additional information about

This journal is © The Royal Society of Chemistry [year]

the breakthrough setup and the pulse gas chromatography measurements are given in the supporting information.

2.4 Computational details

The computational study comprises two types of ab initio calculations: first non-periodic cluster calculations to obtain initial insight into the active site of adsorption on the terephthalic linkers with and without amino functionalization. Secondly periodic calculations on the parent MIL-47 and NH_2-MIL-47 were done. The cluster geometries were optimized with the Gaussian09 package[57] using Density Functional Theory (DFT) with the hybrid M06-2X functional [58, 59] to study the initial adsorption of CH_4 and CO_2 on both linkers. This functional is the best choice to quantify the interactions of CH_4 and CO_2 with the organic linkers because it is utilized especially for medium range non-covalent interactions. The double-zeta Pople basis set 6–311+g(d,p) was applied. The optimized clusters were confirmed to be true minima on the potential energy surface by performing a vibrational frequency analysis, which confirmed that only positive frequencies were present. Afterwards, van der Waals corrections for the M06-2X functional were added to the energy [60, 61]. The thermal corrections were added to the energy to determine the enthalpy, by an in-house developed software module TAMkin[62].

Secondly, the adsorbate molecules CH_4 and CO_2 were placed within the periodic V-MOF structures, in a position which corresponds to the most optimal geometries obtained with the cluster calculations. The geometry of the periodic system with inclusion of the guest molecules has been optimized by means of the Vienna Ab Initio Simulation Package (VASP) [63-66] making use of the PBE exchange correlation functional[67, 68]. For more details we refer to the Computational Section of the Supporting Information. In order to prevent self interactions between the adsorbates in neighbouring cells the unit cell has been doubled along the **a** direction. The orientation of the amino group on the linkers is taken as in the crystallographic structure of NH_2-MIL-53(Fe) as reported in ref [69].

3. Results and discussion

3.1. Structure analysis

XRD measurements (Bragg-Brentano configuration) of both V-MOFs were executed. Based on the obtained XRD spectra the corresponding d-spacings were calculated. The comparison between both samples together with the lines calculated from the MIL-47 structure as published by Barthelet et al.[54] (shown in grey) is presented in Fig. 2.

Detailed analysis of both spectra shows that 20 lines of 21 lines of the modified MIL-47 structure correspond (within the error of the measurement) with the MIL-47 lines for which 26 lines were detected. This nice agreement is shown in Fig. 2 (top). From this XRD analysis one can conclude that the molecular structure of the modified MIL-47 is very similar with the original MIL-47 structure. The addition of the amino group hardly influences the molecular structure. The *as*-synthesized sample is formulated as $V^{+III}OH(C_8H_5NO_4)$ $x(C_8H_7NO_4)$ (x~0.58) on the basis of the elemental analysis (calcd: C 43.11, H 2.88, N 6.28; found: C 43.10, H 2.86, N 6.39). After exchange with DMF, the elemental formula is $V^{+IV}O(C_8H_5NO_4)$ denoted as NH_2-MIL-47.

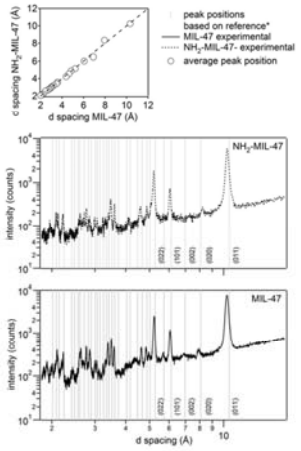

Figure 2. Calculated d-spacings for MIL-47 and NH_2-MIL-47 (*reference[54]).

3.2 N_2 sorption measurements

Major efforts have been done to find the appropriate pre-treatment of the V-MOF. An exchange procedure in DMF has been optimized to remove unreacted linkers and to obtain the highest surface area without loss of the integrity of the framework. The results of the exchange procedure are summarized in Table 1.

Table 1. Optimization of the exchange procedure in DMF for NH_2-MIL-47.

Time (minutes)	Exchange temperature (°C)	Langmuir surface area (m^2/g)
90	150	572
240	150	-
60	100	287
90	100	280
60	125	257
90	125	672
150	125	647
180	125	386

The optimal surface area was obtained at an exchange temperature of 125 °C during 90 minutes. Exchange experiments at 150 °C caused already significant damage to the structural integrity. If the exchange experiment was carried out at 150°C for 240 minutes the MOF structure was completely dissolved.

However, at a lower temperature (100 °C), we were unable to completely remove the free linker from the pores. Longer exchange times at this temperature gave no improvement. An exchange temperature of 125 °C for 90 minutes gave the highest surface area without structural damage, whereas a longer exchange time at 125 °C lead already to damage of the structure. Furthermore, the presence of water and long exposure times to ambient conditions (in absence of any solvent) should be avoided as gradual decomposition will take place. The Langmuir surface area of MIL-47 was approximately 1200 m^2/g, which was comparable to the value reported in literature[54]. The BET values, determined in the P/P_0 pressure interval between 0.05 and 0.2, for MIL-47 and NH_2-MIL-47 are respectively 809 m^2/g and 535 m^2/g. The isotherms of MIL-47 and the optimized NH_2-MIL-47 are shown in Fig. S.2 in the supporting information.

3.3 Thermal behavior

To examine the thermal stability of NH_2-MIL-47, a TGA experiment has been carried out with a heating rate of 2°C/min in air. The resulting TGA curve is shown in Fig. 3. Prior to this measurement the sample was dried under vacuum to remove DMF and H_2O molecules.

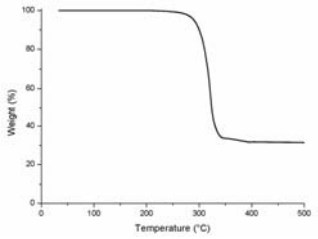

Figure 3. TGA curve of NH_2-MIL-47 obtained under an air flow with a heating rate of 2°C/min.

As can be seen from this figure, the first and only weight loss starts at 280°C, indicating that the V-MOF is stable up to 280°C. Afterwards, the framework starts to decompose. The thermostability is in agreement with the earlier reported MIL-47 [54]. Thus, the introduction of functional groups does not influence the thermal stability. Moreover, we can conclude that the pretreatment step was successful to remove occluded guest molecules.

3.4 Determination of the oxidation state

EPR measurements were performed to determine the oxidation state of the V in NH_2-MIL-47 *as* and NH_2-MIL-47. The measurements were carried out with a rectangular High Temperature EPR Cavity (HTC). In Fig. 4, the spectra of both samples are shown.

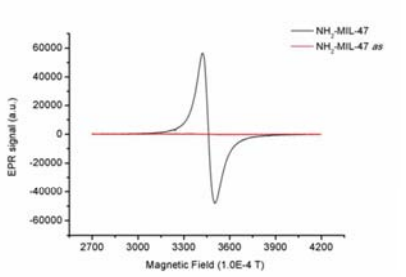

Figure 4. EPR X-band spectrum of NH_2-MIL-47 *as* (red) and NH_2-MIL-47 (black).

As expected, the NH_2-MIL-47 *as* spectrum does not show any signal due to V^{+IV}. From this observation one can conclude that the metal is in the +III oxidation state. On the other hand, a manifest signal is observed in the NH_2-MIL-47 spectrum which can be attributed to V^{+IV}. The latter is the result of the exchange procedure in DMF. In the recent report of Leclerc et al. it was already suggested that the presence of DMF molecules could oxidize the V center in MIL-47 [49]. Moreover both observations are in agreement with the proposed structural formula obtained from elemental analysis. In addition, XPS measurements were performed (Fig. 5). The binding energy for a V2p3/2 peak in NH_2-MIL-47 is observed at 516.8 eV. This coincides with the spectrum for MIL-47 (BE: 516.8 eV) and $VO(acac)_2$ (BE: 516.2 eV) both known as V^{+IV} [54, 70].

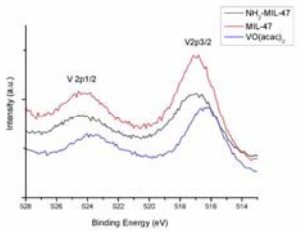

Figure 5. XPS spectra of V 2p3/2 and V 2p1/2 region of MIL-47, NH_2-MIL-47 and $VO(acac)_2$.

3.5 IR and SEM measurements

In Fig. 6, the DRIFT spectrum is shown of NH_2-MIL-47 *as* and NH_2-MIL-47. A distinct difference between both spectra, is the broad band at around 3630-3680 cm^{-1}, which is only present in the *as*-synthesized sample. This rather broad band represents a combination of both the stretching vibration of the μ_2-OH group (the V^{III}O-H) and the free OH groups of the trapped linker [69]. The total disappearance of this band in the NH_2-MIL-47 clearly demonstrates the complete removal of free linker after the

This journal is © The Royal Society of Chemistry [year]

optimized exchange procedure and the oxidation of the V^{III}O-H towards V^{IV}=O groups.

The doublet at 3494 and 3386 cm^{-1} corresponds to the asymmetrical and symmetrical stretching of the amine groups, the vibration at 1630 cm^{-1} can be attributed to the N-H bending (scissoring) vibration. The C-N stretching absorption of the aromatic amines is located at 1338 cm^{-1} [21, 32]. Typical vibrations, due to the benzene linker can be observed: 1510-1450 cm^{-1} (aromatic ring stretch), 1225-950 cm^{-1} (aromatic C-H in plane bend) and 900-670 cm^{-1} (aromatic C-H out of plane bend)[71]. The vibrations in the region 1597-1616 cm^{-1} and 1415-1463 cm^{-1} can be assigned to the asymmetric and symmetric $–CO_2$ stretching vibrations respectively [72].

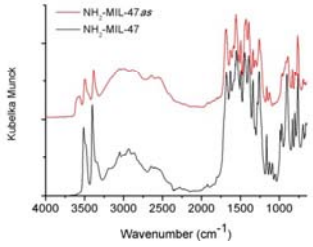

Figure 6. DRIFT spectrum of NH_2-MIL-47 *as* (top) and NH_2-MIL-47 (bottom).

In Fig. 7, the SEM pictures of the materials obtained via microwave and autoclave procedure are presented. It can be seen that the structure, crystal size and morphology of the materials obtained *via* both synthesis routes are very similar (Fig. 7a and Fig. 7c). There are no significant changes observed of the materials after the exchange procedure compared to the non treated sample (Fig. 7b and Fig. 7d). It is hard to give an exact size of the crystals because of the very broad crystal size distribution.

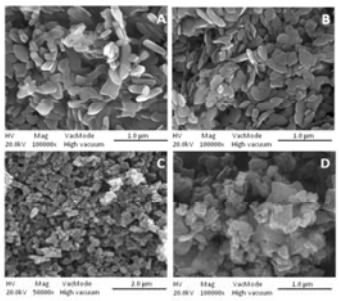

Figure 7**.** SEM pictures of NH_2-MIL-47 (a) synthesized via autoclave (b) after exchange via autoclave synthesis (c) synthesized via microwave (d) after exchange via microwave synthesis.

3.6 Adsorption tests: experimental and computational results

Adsorption isotherms of CO_2 and CH_4 on MIL-47 and NH_2-MIL-47 are displayed is Fig. 8. The experimentally obtained isotherms for CO_2 and CH_4 on MIL-47 show a somewhat lower capacity than was previously reported. Literature specifies a capacity for CO_2 and CH_4 of 10.1 and 5.5 mmol/g respectively, compared to 7.7 and 4.1 mmol/g obtained in this study.[53, 73] This difference should be attributed to differences in preparation methods and sample pretreatment, resulting in different micropore volumes. Calculated micropore volume for this material is 0.40 ml/g while for MIL-47 in literature it is 0.46 ml/g.[54]

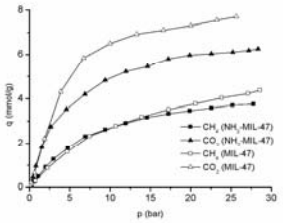

Figure 8. Adsorption isotherms of CO_2 and CH_4 on MIL-47 (open symbols) and NH_2-MIL-47 (closed symbols) at 30 °C.

An interesting observation is the decrease in capacity (per gram adsorbent) for the amino version of the material, corresponding to 20% for CO_2 and 10% for CH_4 at 25 bar. This is in agreement with other amino functionalized MOFs [42, 44, 46] where a capacity drop has also taken place per mass of sample. The presence of free-standing amino-groups in the pores results in a decrease in available pore volume. Even more interestingly is that the isotherms on both materials strongly coincide in the low-pressure regime; thus the presence of $–NH_2$ groups does not result in a significant increase in affinity for CO_2 or CH_4. This is confirmed by low coverage pulse-chromatography experiments. As shown in Table 2, adsorption enthalpies, Henry adsorption constants and separation factors of CO_2 and CH_4 are comparable on both materials. This strongly differs from what is observed with the MIL-53(Al) material, where functionalization with $–NH_2$ groups results in an increase in CO_2 adsorption enthalpy of 18 kJ/mol and a multiplication of the CO_2/CH_4 separation factor by orders of magnitude[44, 46]. This is related to the structure of the materials. Pore size in the low coverage area can be estimated by using the pulse gas chromatographic technique[74]. In the paper of Couck et al. it was shown that the MIL-53 structure is probably in the large pore (lp) form when performing low coverage experiments[75] while NH_2-MIL-53 has narrower pores in this low coverage region[46, 75]. The narrower pore size is the reason for the higher adsorption enthalpy present in NH_2-MIL-53. As for MIL-47, it is know that this material does not show a flexible behavior in the present experimental conditions, meaning that MIL-47 and MIL-53 have the same adsorption properties in the low coverage domain. Also NH_2-MIL-47 does not show flexibility and as a consequence behaves the same as its parent material MIL-47.

Table 2. Adsorption enthalpy (ΔH), Henry constant (K') at 30 °C of CO_2 and CH_4 and zero coverage separation factor ($\alpha_{K'}$) defined as the ratio of Henry adsorption constants of CO_2 over CH_4.

	ΔH (kJ/mol)		K' (mol/kg/Pa)		$\alpha_{K'}$
	CO_2	CH_4	CO_2	CH_4	
MIL-47	-17.8	-11.1	$1.19\ 10^{-5}$	$4.68\ 10^{-6}$	2.5
NH_2-MIL-47	-22.0	-13.0	$9.83\ 10^{-6}$	$2.65\ 10^{-6}$	3.7

Finally, the adsorption behavior of the parent MIL-47 and functionalized form of MIL-47 was evaluated in breakthrough adsorption experiments, in which CO_2/CH_4 mixtures of different composition, at a total pressure of 1 bar, were separated. Fig. 9 shows the amount of adsorbed CO_2 and CH_4 and the separation factor as a function of mixture composition. Capacity (per mass) for both CO_2 and CH_4, is slightly lower on NH_2-MIL-47 than on MIL-47. Again the selectivity, calculated from the breakthrough experiments, is comparable on both materials and is also in good agreement with the Henry selectivity (Table 2).

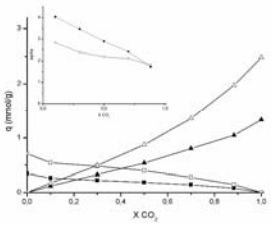

Figure 9. Adsorption capacity for NH_2-MIL-47 (closed symbols: q CH_4 (■) and q CO_2 (▲)) and MIL-47 (open symbols: q CH_4 (□) and q CO_2 (△)). In the inset the selectivity for MIL-47 (○) and NH_2-MIL-47 (●) obtained via breakthrough experiments at 30 °C and a total pressure of 1 bar is shown.

In addition to the experiments, the adsorption strength of CH_4 and CO_2 within the materials MIL-47 and NH_2-MIL-47 is investigated theoretically. Ramsahye et al. studied the adsorption behaviour of CO_2 in the unsubstituted materials MIL-53(Al,Cr) and MIL-47(V). By means of periodic DFT calculations on the MIL-47(V) they concluded that there are no preferential adsorption sites for CO_2[76]. In a second publication, previous authors used grand canonical monte carlo simulations to study the adsorption mechanism. These simulations were based on partial atomic charges extracted from periodic DFT calculations and interatomic potentials between the adsorbate and host framework[77]. Simulation of adsorption phenomena can indeed be performed using molecular dynamics and Monte Carlo simulations with suitable force fields providing us information on the distribution on the position of adsorbates within the framework and giving average adsorption data. The derivation of a proper force field is a non-trivial taks and is beyond the scope of this study. This is especially true for the derivation of polarisable force fields which are not standard available.[78, 79] Herein, we performed static calculations, based on DFT and complemented with dispersion corrections, to study the qualitative differences between adsorbate-host interactions. The computational protocol is outlined in section 2.4. A large number of adsorption structures has been investigated in the finite cluster model in order to determine the most stable configuration of the absorbate with respect to the linker. The most favorable positions are displayed in Figure 10 both for CH_4 and CO_2. The amino group has the largest effect on the position of the CO_2 adsorbate. The polar character of CO_2 lies at the origin of a stronger electrostatic attractive interaction between the adsorbate carbon and the negative charge of the nitrogen.

The electronic adsorption energy ΔE and adsorption enthalpy ΔH_{30} at 30 °C for both the terephthalic linkers and full periodic MIL-47 type materials are tabulated in Table 3. For both adsorbates the adsorption is stronger for the amino functionalized linker and CO_2 is more adsorbed than CH_4 by about 7 kJ/mol. Qualitatively this is in nice agreement with the experiment (Table 2). When taking into account the full topology of the MIL-47 the qualitative differences between CO_2 and CH_4 remain nearly the same, although overall the guest molecules are stronger adsorbed. This is probably the result of additional dispersion interactions between the adsorbate and the other linkers in the framework. For the periodic calculations the adsorption enthalpies have not been calculated in view of the difficulties encountered in the VASP calculations to obtain positive frequencies. To get an idea about the position of the CO_2 adsorbate in the periodic structure we refer to Figure 11. Compared to the geometry obtained using the small cluster calculations CO_2 now takes a configuration in between the amino group of the one linker and the aromatic nucleus of another linker.

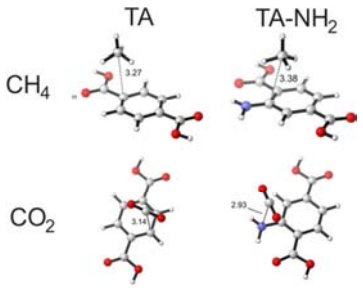

Figure 10. An overview of the most stable adsorption positions of CO_2 and CH_4 on terephthalic acid (TA) and 2-aminoterephthalic acid (TA-NH_2) (cluster model). Shortest distances between the carbon of the adsorbate and the nearest linker atom are displayed in Ångström.

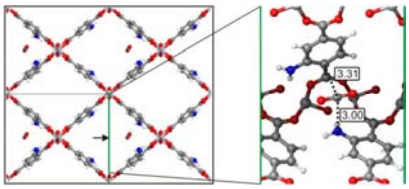

Figure 11. Most stable adsorption position of CO_2 in the periodic structure of NH_2-MIL-47. Distances displayed in Ångström.

Table 3. The calculated electronic adsorption energy (ΔE in kJ/mol) and adsorption enthalpy at 30 °C (ΔH_{30} in kJ/mol). Unit cell parameters in the periodic calculations have been optimized for the parent MIL-47 and for

This journal is © The Royal Society of Chemistry [year]

the NH_2-MIL-47 (NH_2-TA represents the 2-aminoterephthalic acid linker and TA the terephthalic acid linker).

	ΔE (kJ/mol)		ΔH303 (kJ/mol)	
	CO_2	CH_4	CO_2	CH_4
TA	-13.3	- 11.0	-9.8	-5.9
NH_2-TA	-19.1	- 12.4	-14.8	-7.2
MIL-47	-24.7	- 13.2	-	-
NH_2-MIL-47	-25.6	- 14.5	-	-

Summarizing, we have shown that the experimental adsorption enthalpies obtained from pulse chromatographic experiments (Table. 2) follow the same trend as the corresponding adsorbate-linker interactions. Also within the framework, our geometrically similar adsorption spots show the same trend. We can thus conclude that the difference in linker-adsorbate interaction is the main driving force between CO_2/CH_4 separation within MIL-47 and MIL-47-NH_2 rather than an interaction with the amino groups. On specific MOFs, presence of NH_2 indirectly enhances CO_2 adsorption. In particular, for NH_2-MIL-53(Al), the amino groups play a key role in framework flexibility, and lead to the closure of the NH_2-MIL-53(Al) pores, hereby enhancing CO_2 adsorption due to stronger aspecific interactions on the one hand and exclusion of CH_4 molecules on the other hand[45]. Since MIL-47 and NH_2-MIL-47 are rather rigid and non-flexible, presence of amino groups does not result in pore contraction, and accordingly not in an increase in CO_2 affinity either.

4. Conclusions

An amino functionalized V-MOF, with MIL-47 topology, has been successfully synthesized via both autoclave and microwave enhanced irradiation. The NH_2-MIL-47 shows a similar thermal stability in comparison to the parent MIL-47, decomposing in one step at 280 °C. An optimization of the exchange procedure in DMF was performed, resulting in a Langmuir surface area of approximately 672 m^2/g. CO_2 and CH_4 adsorption measurements have shown that the presence of additional NH_2 groups does not have a beneficial effect on the adsorption properties, which was also confirmed by the theoretical modeling results. For the NH_2-MIL-47, both experiment and theory clearly show that the amination of the linker does not result in an increased adsorption capacity per mass of adsorbent, nor in an increased CH_4/CO_2 separation factor. The slight increase in adsorption enthalpy for the NH_2-MIL-47 does not compensate for the loss in pore volume compared to the parent MIL-47. Contrary to other MOFs, the NH_2-MIL-47 and the MIL-47 are not triggered into breathing behavior at the experimental conditions.

Acknowledgements

The authors acknowledge dr. Els Bruneel for the XPS measurements and ing. Danny Vandeput and ing. Tom Planckaert for their aid in the N2-sorption, CHNS analysis and XRD measurements. Karen Leus is grateful to the Long Term Structural Methusalem Grant Nr. 01M00409 Funding by the Flemish Government. Furthermore, this research is co-funded by the Ghent University, GOA Grant Nr. 01G00710, BELSPO in the frame of IAP 6/27 and the European Research Council (FP7(2007-2013) ERC Grant Nr. 240483). Computational resources (Stevin Supercomputer Infrastructure) and services were provided by Ghent University. Joeri Denayer is grateful to the Hercules foundation for funding for medium-scale research infrastructure.

Notes and references

[a] *Dept. Inorganic and Physical Chemistry, Centre for Ordered Materials, Organometallics and Catalysis, Ghent University, Krijgslaan 281-S3, 9000 Ghent, Belgium Phone: +32 964 44 42*
E-mail: pascal.vandervoort@ugent.be
[b] *Vrije Universiteit Brussel, Department of Chemical Engineering, Belgium.*
[c] *Ghent University, Center for Molecular Modeling, Technologiepark 903, 9052 Zwijnaarde, Belgium.*
[d] *Ghent University, Department of Solid State Sciences, Krijgslaan 281-S1, 9000 Ghent, Belgium.*
[e] *Ghent University, Laboratory for Chemical Technology, Krijgslaan 281-S5, 9000 Ghent, Belgium.*
[f] *Ghent University, Department of Inorganic and Physical Chemistry, Sol-gel Center for Research on Inorganic Powders and Thin films Synthesis (SCRiPTS), Krijgslaan 281-S3, 9000 Gent, Belgium*

† Electronic Supplementary Information (ESI) available: Nitrogen adsorption isotherms of NH_2-MIL-47 and MIL-47. Detailed information about the breakthrough setup, pulse gas chromatography measurements and VASP calculations. Adsorption geometries of CO_2 and CH_4 on the (amino-) terephthalate linker, NH_2-MIL-47 and MIL-47. See DOI: 10.1039/b000000x/

1. Y. H. Hu and L. Zhang, *Adv Mater*, 2010, **22**, E117-E130.
2. J. R. Li, Y. G. Ma, M. C. McCarthy, J. Sculley, J. M. Yu, H. K. Jeong, P. B. Balbuena and H. C. Zhou, *Coordin Chem Rev*, 2011, **255**, 1791-1823.
3. S. Q. Ma and H. C. Zhou, *Chem Commun*, 2010, **46**, 44-53.
4. L. J. Murray, M. Dinca and J. R. Long, *Chem Soc Rev*, 2009, **38**, 1294-1314.
5. Z. Chang, D. S. Zhang, Q. Chen, R. F. Li, T. L. Hu and X. H. Bu, *Inorg Chem*, 2011, **50**, 7555-7562.
6. S. M. Xie, Z. J. Zhang, Z. Y. Wang and L. M. Yuan, *J Am Chem Soc*, 2011, **133**, 11892-11895.
7. Y. Ling, Z. X. Chen, H. Zheng, Y. M. Zhou, L. H. Weng and D. Y. Zhao, *Cryst Growth Des*, 2011, **11**, 2811-2816.
8. Y. G. Zhao, H. H. Wu, T. J. Emge, Q. H. Gong, N. Nijem, Y. J. Chabal, L. Z. Kong, D. C. Langreth, H. Liu, H. P. Zeng and J. Li, *Chem-Eur J*, 2011, **17**, 5100-5108.
9. M. T. Luebbers, T. J. Wu, L. J. Shen and R. I. Masel, *Langmuir*, 2010, **26**, 11319-11329.
10. L. Alaerts, M. Maes, P. A. Jacobs, J. F. M. Denayer and D. E. De Vos, *Phys Chem Chem Phys*, 2008, **10**, 2979-2985.
11. L. Alaerts, C. E. A. Kirschhock, M. Maes, M. A. van der Veen, V. Finsy, A. Depla, J. A. Martens, G. V. Baron, P. A. Jacobs, J. E. M. Denayer and D. E. De Vos, *Angew Chem Int Edit*, 2007, **46**, 4293-4297.
12. X. L. Si, C. L. Jiao, F. Li, J. Zhang, S. Wang, S. Liu, Z. B. Li, L. X. Sun, F. Xu, Z. Gabelica and C. Schick, *Energ Environ Sci*, 2011, **4**, 4522-4527.

13. J. M. Simmons, H. Wu, W. Zhou and T. Yildirim, *Energ Environ Sci*, 2011, **4**, 2177-2185.
14. J. Sculley, D. Q. Yuan and H. C. Zhou, *Energ Environ Sci*, 2011, **4**, 2721-2735.
15. D. A. Yang, H. Y. Cho, J. Kim, S. T. Yang and W. S. Ahn, *Energ Environ Sci*, 2012, **5**, 6465-6473.
16. S. Choi, T. Watanabe, T. H. Bae, D. S. Sholl and C. W. Jones, *J Phys Chem Lett*, 2012, **3**, 1136-1141.
17. H. Liu, Y. G. Zhao, Z. J. Zhang, N. Nijem, Y. J. Chabal, H. P. Zeng and J. Li, *Adv Funct Mater*, 2011, **21**, 4754-4762.
18. J. P. S. Mowat, S. R. Miler, J. M. Griffin, V. R. Seymour, S. E. Ashbrook, S. P. Thompson, D. Fairen-Jimenez, A. M. Banu, T. Duren and P. A. Wright, *Inorg Chem*, 2011, **50**, 10844-10858.
19. F. N. Shi, A. R. Silva and J. Rocha, *J Solid State Chem*, 2011, **184**, 2196-2203.
20. F. X. L. I. Xamena, A. Abad, A. Corma and H. Garcia, *J Catal*, 2007, **250**, 294-298.
21. J. Gascon, U. Aktay, M. D. Hernandez-Alonso, G. P. M. van Klink and F. Kapteijn, *J Catal*, 2009, **261**, 75-87.
22. J. Lee, O. K. Farha, J. Roberts, K. A. Scheidt, S. T. Nguyen and J. T. Hupp, *Chem Soc Rev*, 2009, **38**, 1450-1459.
23. D. Y. Hong, Y. K. Hwang, C. Serre, G. Ferey and J. S. Chang, *Adv Funct Mater*, 2009, **19**, 1537-1552.
24. K. Leus, I. Muylaert, M. Vandichel, G. B. Marin, M. Waroquier, V. Van Speybroeck and P. Van der Voort, *Chem Commun*, 2010, **46**, 5085-5087.
25. K. Leus, M. Vandichel, Y. Y. Liu, I. Muylaert, J. Musschoot, S. Pyl, H. Vrielinck, F. Callens, G. B. Marin, C. Detavernier, P. V. Wiper, Y. Z. Khimyak, M. Waroquier, V. Van Speybroeck and P. Van Der Voort, *J Catal*, 2012, **285**, 196–207.
26. Y. Y. Liu, K. Leus, M. Grzywa, D. Weinberger, K. Strubbe, H. Vrielinck, R. Van Deun, D. Volkmer, V. Van Speybroeck and P. Van der Voort, *Eur J Inorg Chem*, 2012, **16**, 2819–2827.
27. D. Farrusseng, S. Aguado and C. Pinel, *Angew Chem Int Edit*, 2009, **48**, 7502-7513.
28. M. D. Allendorf, C. A. Bauer, R. K. Bhakta and R. J. T. Houk, *Chem Soc Rev*, 2009, **38**, 1330-1352.
29. S. Keskin and S. Kizilel, *Ind Eng Chem Res*, 2011, **50**, 1799-1812.
30. M. Eddaoudi, J. Kim, N. Rosi, D. Vodak, J. Wachter, M. O'Keeffe and O. M. Yaghi, *Science*, 2002, **295**, 469-472.
31. S. Biswas, T. Ahnfeldt and N. Stock, *Inorg Chem*, 2011, **50**, 9518-9526.
32. M. Kandiah, M. H. Nilsen, S. Usseglio, S. Jakobsen, U. Olsbye, M. Tilset, C. Larabi, E. A. Quadrelli, F. Bonino and K. P. Lillerud, *Chem Mater*, 2010, **22**, 6632-6640.
33. H. Y. Huang, R. T. Yang, D. Chinn and C. L. Munson, *Ind Eng Chem Res*, 2003, **42**, 2427-2433.
34. N. Hiyoshi, K. Yogo and T. Yashima, *Micropor Mesopor Mat*, 2005, **84**, 357-365.
35. Y. Belmabkhout, R. Serna-Guerrero and A. Sayari, *Ind Eng Chem Res*, 2010, **49**, 359-365.
36. C. Chen, W. J. Son, K. S. You, J. W. Ahn and W. S. Ahn, *Chem Eng J*, 2010, **161**, 46-52.
37. V. Zelenak, M. Badanicova, D. Halamova, J. Cejka, A. Zukal, N. Murafa and G. Goerigk, *Chem Eng J*, 2008, **144**, 336-342.
38. A. C. C. Chang, S. S. C. Chuang, M. Gray and Y. Soong, *Energ Fuel*, 2003, **17**, 468-473.
39. J. R. Karra and K. S. Walton, *J Phys Chem C*, 2010, **114**, 15735-15740.
40. A. R. Millward and O. M. Yaghi, *J Am Chem Soc*, 2005, **127**, 17998-17999.
41. B. Arstad, H. Fjellvag, K. O. Kongshaug, O. Swang and R. Blom, *Adsorption*, 2008, **14**, 755-762.
42. P. Serra-Crespo, E. V. Ramos-Fernandez, J. Gascon and F. Kapteijn, *Chem Mater*, 2011, **23**, 2565-2572.
43. W. Morris, B. Leung, H. Furukawa, O. K. Yaghi, N. He, H. Hayashi, Y. Houndonougbo, M. Asta, B. B. Laird and O. M. Yaghi, *J Am Chem Soc*, 2010, **132**, 11006-11008.
44. S. Couck, J. F. M. Denayer, G. V. Baron, T. Remy, J. Gascon and F. Kapteijn, *J Am Chem Soc*, 2009, **131**, 6326-+.
45. E. Stavitski, E. A. Pidko, S. Couck, T. Remy, E. J. M. Hensen, B. M. Weckhuysen, J. Denayer, J. Gascon and F. Kapteijn, *Langmuir*, 2011, **27**, 3970-3976.
46. S. Couck, E. Gobechiya, C. E. A. Kirschhock, P. Serra-Crespo, J. Juan-Alcaniz, A. M. Joaristi, E. Stavitski, J. Gascon, F. Kapteijn, G. V. Baron and J. F. M. Denayer, *Chemsuschem*, 2012, **5**, 740-750.
47. T. Lescouet, E. Kockrick, G. Bergeret, M. Pera-Titus and D. Farrusseng, *Dalton T*, 2011, **40**, 11359-11361.
48. T. K. Trung, I. Deroche, A. Rivera, Q. Y. Yang, P. Yot, N. Ramsahye, S. D. Vinot, T. Devic, P. Horcajada, C. Serre, G. Maurin and P. Trens, *Micropor Mesopor Mat*, 2011, **140**, 114-119.
49. H. Leclerc, T. Devic, S. Devautour-Vinot, P. Bazin, N. Audebrand, G. Ferey, M. Daturi, A. Vimont and G. Clet, *J Phys Chem C*, 2011, **115**, 19828-19840.
50. T. Devic, F. Salles, S. Bourrelly, B. Moulin, G. Maurin, P. Horcajada, C. Serre, A. Vimont, J. C. Lavalley, H. Leclerc, G. Clet, M. Daturi, P. L. Llewellyn, Y. Filinchuk and G. Ferey, *J Mater Chem*, 2012, **22**, 10266-10273.
51. A. Phan, A. U. Czaja, F. Gandara, C. B. Knobler and O. M. Yaghi, *Inorg Chem*, 2011, **50**, 7388-7390.
52. N. A. Khan, J. W. Jun, J. H. Jeong and S. H. Jhung, *Chem Commun*, 2011, **47**, 1306-1308.
53. N. Rosenbach, A. Ghoufi, I. Deroche, P. L. Llewellyn, T. Devic, S. Bourrelly, C. Serre, G. Ferey and G. Maurin, *Phys Chem Chem Phys*, 2010, **12**, 6428-6437.
54. K. Barthelet, J. Marrot, D. Riou and G. Ferey, *Angew Chem Int Edit*, 2001, **41**, 281-+.
55. A. Malek and S. Farooq, *J Chem Eng Data*, 1996, **41**, 25-32.
56. R. A. Ocakoglu, J. F. M. Denayer, G. B. Marin, J. A. Martens and G. V. Baron, *J Phys Chem B*, 2003, **107**, 398-406.
57. M. J. T. Frisch, G. W.; Schlegel, H. B.; Scuseria, G. E.; Robb, M. A.; Cheeseman, J. R.; Scalmani, G.; Barone, V.; Mennucci, B.; Petersson, G. A.; Nakatsuji, H.; Caricato, M.; Li, X.; Hratchian, H. P.; Izmaylov, A. F.; Bloino, J.; Zheng, G.; Sonnenberg, J. L.; Hada, M.; Ehara, M.; Toyota, K.; Fukuda, R.; Hasegawa, J.; Ishida, M.; Nakajima, T.; Honda, Y.; Kitao, O.; Nakai, H.; Vreven, T.; Montgomery, Jr., J. A.; Peralta, J. E.; Ogliaro, F.; Bearpark, M.; Heyd, J. J.; Brothers, E.; Kudin, K. N.; Staroverov, V. N.; Kobayashi, R.; Normand, J.;

 This journal is © The Royal Society of Chemistry [year]

Raghavachari, K.; Rendell, A.; Burant, J. C.; Iyengar, S. S.; Tomasi, J.; Cossi, M.; Rega, N.; Millam, N. J.; Klene, M.; Knox, J. E.; Cross, J. B.; Bakken, V.; Adamo, C.; Jaramillo, J.; Gomperts, R.; Stratmann, R. E.; Yazyev, O.; Austin, A. J.; Cammi, R.; Pomelli, C.; Ochterski, J. W.; Martin, R. L.; Morokuma, K.; Zakrzewski, V. G.; Voth, G. A.; Salvador, P.; Dannenberg, J. J.; Dapprich, S.; Daniels, A. D.; Farkas, O.; Foresman, J. B.; Ortiz, J. V.; Cioslowski, J.; Fox, D. J. Gaussian 09, {R}evision {A}.02, Gaussian, Inc., Wallingford CT: , 2009.

58. Y. Zhao and D. G. Truhlar, *Theor Chem Acc*, 2008, **120**, 215-241.
59. Y. Zhao and D. G. Truhlar, *Accounts Chem Res*, 2008, **41**, 157-167.
60. S. Grimme, *J Comput Chem*, 2004, **25**, 1463-1473.
61. S. Grimme, J. Antony, S. Ehrlich and H. Krieg, *J Chem Phys*, 2010, **132**.
62. A. Ghysels, T. Verstraelen, K. Hemelsoet, M. Waroquier and V. Van Speybroeck, *J Chem Inf Model*, 2010, **50**, 1736-1750.
63. G. Kresse and J. Hafner, *Phys Rev B*, 1994, **49**, 14251-14269.
64. G. Kresse and J. Hafner, *Phys Rev B*, 1993, **47**, 558-561.
65. G. Kresse and J. Furthmuller, *Phys Rev B*, 1996, **54**, 11169-11186.
66. G. Kresse and J. Furthmuller, *Comp Mater Sci*, 1996, **6**, 15-50.
67. J. P. Perdew, K. Burke and M. Ernzerhof, *Phys Rev Lett*, 1996, **77**, 3865-3868.
68. J. P. Perdew, K. Burke and M. Ernzerhof, *Phys Rev Lett*, 1997, **78**, 1396-1396.
69. T. Devic, P. Horcajada, C. Serre, F. Salles, G. Maurin, B. Moulin, D. Heurtaux, G. Clet, A. Vimont, J. M. Greneche, B. Le Ouay, F. Moreau, E. Magnier, Y. Filinchuk, J. Marrot, J. C. Lavalley, M. Daturi and G. Ferey, *J Am Chem Soc*, 2010, **132**, 1127-1136.
70. B. Jarrais, A. R. Silva and C. Freire, *Eur J Inorg Chem*, 2005, 4582-4589.
71. J. Coates, ed., *Interpretation of Infrared Spectra, A Practical Approach*, 2000.
72. T. Loiseau, C. Serre, C. Huguenard, G. Fink, F. Taulelle, M. Henry, T. Bataille and G. Ferey, *Chem-Eur J*, 2004, **10**, 1373-1382.
73. S. Bourrelly, P. L. Llewellyn, C. Serre, F. Millange, T. Loiseau and G. Ferey, *J Am Chem Soc*, 2005, **127**, 13519-13521.
74. J. F. M. Denayer and G. V. Baron, *Adsorption*, 2005, **11**, 85-90.
75. S. Couck, T. Remy, G. V. Baron, J. Gascon, F. Kapteijn and J. F. M. Denayer, *Phys Chem Chem Phys*, 2010, **12**, 9413-9418.
76. N. A. Ramsahye, G. Maurin, S. Bourrelly, P. L. Llewellyn, C. Serre, T. Loiseau, T. Devic and G. Ferey, *J Phys Chem C*, 2008, **112**, 514-520.
77. N. A. Ramsahye, G. Maurin, S. Bourrelly, P. L. Llewellyn, T. Devic, C. Serre, T. Loiseau and G. Ferey, *Adsorption*, 2007, **13**, 461-467.
78. J. M. Castillo, T. J. H. Vlugt and S. Calero, *J Phys Chem C*, 2009, **113**, 20869-20874.
79. L. Vanduyfhuys, T. Verstraelen, M. Vandichel, M. Waroquier and V. Van Speybroeck, *J Chem Theory Comput*, 2012, **8**, 3217-3231.

Paper 14

Efficient approach for the computational study of alcohol and nitrile adsorption in H-ZSM-5

Jeroen Van der Mynsbrugge, Karen Hemelsoet, Matthias Vandichel, Michel Waroquier and Veronique Van Speybroeck

Journal of Physical Chemistry, 2012, 116, 5499 - 5508

Copyright 2012 by the American Chemical Society.

THE JOURNAL OF PHYSICAL CHEMISTRY C

Article

pubs.acs.org/JPCC

Efficient Approach for the Computational Study of Alcohol and Nitrile Adsorption in H-ZSM-5

Jeroen Van der Mynsbrugge, Karen Hemelsoet, Matthias Vandichel, Michel Waroquier, and Veronique Van Speybroeck*

Center for Molecular Modeling, Ghent University, Technologiepark 903, 9052 Zwijnaarde, Belgium and QCMM Alliance, Ghent-Brussels, Belgium

Supporting Information

ABSTRACT: Since many industrially important processes start with the adsorption of guest molecules inside the pores of an acidic zeolite catalyst, a proper estimate of the adsorption enthalpy is of paramount importance. In this contribution, we report ab initio calculations on the adsorption of water, alcohols, and nitriles at the bridging Brønsted sites of H-ZSM-5, using both cluster and periodic models to account for the zeolite environment. Stabilization of the adsorption complexes results from hydrogen bonding between the guest molecule and the framework, as well as from embedding, i.e., van der Waals interactions with the pore walls. Large-cluster calculations with different DFT methods, in particular B3LYP(-D), PBE(-D), M062X(-D), and ωB97X-D, are tested for their ability to reproduce the experimental heats of adsorption available in the literature (*J. Phys. Chem. B* **1997**, *101*, 3811−3817). A proper account of dispersion interactions is found to be crucial to describe the experimental trend across a series of adsorbates of increasing size, i.e., an increase in adsorption enthalpy by 10−15 kJ/mol for each additional carbon atom. The extended-cluster model is shown to offer an attractive alternative to periodic simulations on the entire H-ZSM-5 unit cell, resulting in virtually identical final adsorption enthalpies. Comparing calculated stretch frequencies of the zeolite acid sites and the adsorbate functional groups with experimental IR data additionally confirms that the cluster approach provides an appropriate representation of the adsorption complexes.

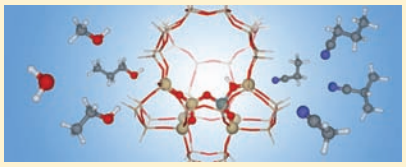

1. INTRODUCTION

Catalytic conversions on acidic zeolite catalysts are applied in a whole range of industrial production processes.[1] In recent years, theoretical modeling has been proven a highly useful tool to complement experimental studies in gaining a deeper understanding of the complex reaction mechanisms taking place inside the zeolite pores. Theoretical simulations allow obtaining information about individual reaction steps, which is highly difficult to achieve through experiments, due to many side reactions occurring simultaneously. A prominent example is the methanol-to-olefin process (MTO).[2,3] Several computational studies have provided invaluable insights into the catalytic cycles responsible for olefin production[4−9] and the origin of catalyst deactivation.[10,11] While earlier studies were primarily aimed at obtaining a better mechanistic insight, current research efforts tend to focus on developing efficient theoretical procedures to accurately predict experimentally observed reaction barriers and rate coefficients.[12,13] Experimental studies typically start from gas phase reactants that diffuse into the zeolite pores and adsorb onto the active sites before undergoing reaction. A proper estimate of the initial heat of adsorption is therefore necessary for the precise theoretical description of an entire reaction path.[12,13]

In this work, a set of adsorbate molecules were selected for which experimentally determined differential heats of adsorption on H-ZSM-5 are available.[14] The test set (Figure 1) consists of water, primary alcohols (methanol, ethanol, and propanol), and nitriles (acetonitrile, propionitrile, butyronitrile, and isobutyronitrile), all of which preferentially interact through hydrogen bonds with the Brønsted acid sites inside the zeolite. If these acid sites are sufficiently isolated, well-defined complexes of one adsorbate molecule per active site will be formed. These adsorption complexes are additionally stabilized by dispersive interactions with the pore walls, resulting in an increase in adsorption enthalpy of 10−15 kJ/mol for each additional carbon atom.[14] A similar effect has been

H–OH	CH_3–C≡N
CH_3–OH	CH_3–CH_2–C≡N
CH_3–CH_2–OH	CH_3–$(CH_2)_2$–C≡N
CH_3–$(CH_2)_2$–OH	$(CH_3)_2$–CH–C≡N

Figure 1. Adsorbate molecules considered in this study: water, methanol, ethanol, propanol, acetonitrile, propionitrile, butyronitrile, and isobutyronitrile.

Received: December 22, 2011
Revised: February 7, 2012
Published: February 10, 2012

ACS Publications © 2012 American Chemical Society

dx.doi.org/10.1021/jp2123828 | *J. Phys. Chem. C* 2012, 116, 5499−5508

reported for the adsorption of *n*-alkanes and *n*-alkenes in different zeolites; the adsorption enthalpy was found to increase by 10−12 kJ/mol per carbon atom, depending on the zeolite topology, the silicon−aluminum ratio, and the temperature.[15−18]

At 400 K, primary alcohols and nitriles are fairly unreactive, such that accurate adsorption enthalpies can be obtained from calorimetric measurements,[14] which are ideally suited as reference data for a theoretical benchmarking study. Furthermore, our selection comprises two series of structural analogues with identical functionality, enabling a systematic investigation of the different contributions to the adsorption enthalpy with increasing adsorbate size.

As long-range interactions and topological characteristics of the zeolite are of paramount importance to the stabilization of various adsorbates, computational models need to take the zeolite framework into account. Many current studies on adsorption and/or catalysis in zeolites employ methods with periodic boundary conditions to treat the complete system.[13,17−25] However, rate coefficients and barriers for methylation reactions have been successfully predicted using an extended-cluster model in which only a fragment of the zeolite structure is considered.[12] Provided the selected fragment is large enough, the cluster approach allows accounting for all relevant confinement effects. Besides a better computational efficiency, cluster calculations have the additional advantage over periodic simulations that the vibrational analysis is much more straightforward, which is vital for the calculation of thermodynamic properties and kinetic coefficients.

In both finite-cluster and periodic studies, density functional theory (DFT) methods[26,27] are nowadays frequently used; they offer a favorable balance between accuracy and computational efficiency and can therefore be applied to large systems of chemical relevance. A serious drawback, however, is their lack of a proper description of long-range electron correlation effects that cause dispersive or van der Waals interactions.[28,29] Previous studies have shown that neglecting these van der Waals interactions has only a limited effect on intrinsic barriers (about 10−20 kJ/mol), such that the general picture of reaction routes determined with standard DFT methods (e.g., the popular B3LYP functional[30,31]) remains largely unaltered for most reactions, although one must be careful when generalizing this conclusion.[7,8,10] This is no longer the case for adsorption steps, for which the effect of dispersive interactions can become highly significant and may result in differences in adsorption energy of up to 70 kJ/mol.[12,13,19]

Many efforts have been made in recent years to include van der Waals interactions within the framework of DFT, allowing a substantial decrease in computational expense.[32−35] Several of these methods will be employed in this paper and are briefly highlighted.

One of the most effective and most widely applied methods, is the so-called DFT-D scheme proposed by Grimme[28,36,37] In this method, an empirical damped-potential term is added to energies obtained with standard functionals, at a negligible computational cost. Since its first introduction, the DFT-D method has been successfully applied on a wide variety of systems, demonstrating its robustness.[37] In the latest version (referred to as DFT-D3), ab initio data have to a large extent replaced the empirical input, such that dispersion corrections are now available for all elements, with improved overall performance.[37]

Other attempts to include dispersive interactions involve developing new functionals which are specifically parametrized for systems in which weak interactions play a prominent role. The most well-known example of such a functional is found in the M06 family, developed by the Truhlar group.[38,39] In the hybrid M06−2X functional, double Hartree−Fock exchange is included to improve the description of noncovalent interactions. Successful applications of this functional include the study of π-stacking interactions on aromatic systems.[40,41] Recently, M06−2X has also been employed to investigate zeolite-catalyzed reactions.[42,43]

While the DFT-D approach proposed by Grimme has the advantage of allowing us to improve the results obtained with commonly used DFT methods without changing the original functionals, the addition of the separate dispersion term to the regular DFT energy can lead to some amount of double-counting of total energy in the intermediate range. This can be avoided by self-consistently parametrizing dispersion-corrected functionals in their entirety. Examples of this approach include Grimme's B97-D functional[44] and Chai and Head-Gordon's ωB97X-D functional.[45] The latter is a long-range corrected hybrid density functional, which was reoptimized to include dispersion corrections. A recent benchmarking study by Goerigk and Grimme on an extensive database dubbed GMTKN30 found the ωB97X-D functional to be a promising method for main group thermochemistry, kinetics, and noncovalent interactions.[35]

All investigated adsorbate molecules (Figure 1) are weak bases, which makes them attractive probe molecules for zeolite acidity since their interactions with the Brønsted acid sites cause measurable shifts in the vibrational spectra.[46] Thus far, a lot of attention was given to the issue whether in different zeolite systems the adsorbed complex is physisorbed (hydrogen bonded) or chemisorbed. The interpretation of experimental IR spectra based on theoretical simulations has overall been subject to debate as it turns out that the final outcome depends on both the applied theoretical procedure and the model. In this context, mainly water and alcohol adsorption have been examined.[47−51] Experimental IR spectra of the smallest investigated compounds, i.e., water,[52] methanol,[53] ethanol,[54] and acetonitrile[55−59] adsorbed in H-ZSM-5, are available, which can be compared to theoretical values to further validate proposed models. The assignment of the various bands has proven challenging, and several studies focused on the observed (A,B,C) triplet of infrared OH bands around 2800, 2400, and 1700 cm^{-1}.[46,52,53] In the case of acetonitrile, theoretical computations of the IR spectra can serve as a useful tool to discuss acid−base interactions. Pelmenschikov pointed out that the CN stretching frequency is an efficient probe to distinguish different adsorption sites in zeolites, in particular Lewis acid sites, terminal silanol groups, and the bridging Brønsted acid site, which will be discussed in this work.[55,56] Related work of Simperler et al. obtained a ranking of seven different high silica zeolites based on the hydrogen-bond strength as a predictor of acidity.[60] In this study, the shift in the ν(OH) region will be investigated for all adsorption complexes. For the nitrile series, the ν(CN) frequency will also be examined.

In this paper, the adsorption of the selected alcohols and nitriles in H-ZSM-5 is studied using both cluster and periodic models. The cluster approach will be combined with different contemporary DFT methods to test their ability to account for dispersion. A complete vibrational analysis will enable the calculation of adsorption enthalpies at 400 K, which are directly

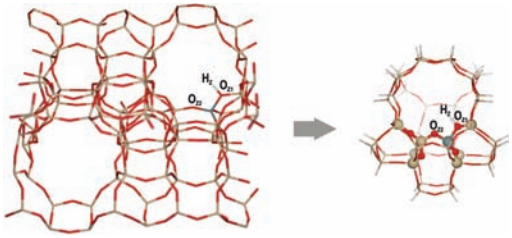

Figure 2. Theoretical model for the H-ZSM-5 catalyst. The aluminum defect is located at the T12 position. The full periodic structure (left) is reduced to an extended cluster model containing 46T atoms (right). In ONIOM calculations, a central 8T fragment of the catalyst (indicated in ball-and-stick representation) is included in the high-level region.

comparable to the experimentally measured values.[14] Investigation of characteristic IR frequencies and comparison with available experimental data will help to validate whether realistic representations of H-ZSM-5 at low loadings of weak bases can be obtained using the cluster model. Additionally, adsorption enthalpies are calculated based on the periodic simulations in which the entire unit cell is taken into account and compared to those obtained from the cluster approach.

2. ZEOLITE MODELS AND COMPUTATIONAL METHODS

2.1. Selection of the Brønsted Acid Site. In this study, we focus on a single active site within an H-ZSM-5 catalyst to investigate the adsorption complexes formed at low coverages. The zeolite model is constructed by introducing an aluminum defect at the T12 crystallographic position of an orthorhombic MFI unit cell.[61] This position, at the intersection of the straight and sinusoidal channels, offers maximum available space and creates the most accessible active site to accommodate various guest molecules.[62,63] While several studies[64−67] have attempted to determine the most favorable position for aluminum substitution, ultimately little preference for any specific position was found, and a distribution of T-sites hosting aluminum defects can be expected in a realistic zeolite crystal.[63] Additionally, recent experimental and theoretical evidence has confirmed that the framework position of aluminum defects and their distribution throughout the material is determined by kinetic effects occurring during zeolite synthesis, rather than on thermodynamic grounds.[68−70]

In this paper, the acidic proton H_Z is located on the bridging oxygen O_{Z1} (Figure 2), as in our previous work. The proton is well-known to easily migrate from one oxygen bridge to another,[71,72] especially when aided by assisting adsorbate species such as, e.g., water molecules.[73] However, a detailed investigation of all possible Brønsted sites would require a molecular dynamics approach, which is clearly beyond the scope of the current study and which is currently still limited by the lack of force-field methods offering the required accuracy for both host and guest species.

2.2. Cluster Calculations. In the majority of the calculations presented in this work, a large cluster model was used to represent the zeolite catalyst. A fragment containing 46 tetrahedral atoms (46T) was cut from the crystallographic structure, such that the model includes a sufficiently large portion of the framework surrounding the active site to account for relevant confinement effects (Figure 2).

Dangling bonds at the cluster edges were saturated with hydrogen atoms (Si−H termination). The terminating hydrogens were fixed in space to avoid unrealistic deformations of the cluster throughout geometry optimizations. Stationary points were localized using a two-level ONIOM scheme, in which a central 8T cluster is treated at the B3LYP/6-31+g(d) level of theory, while the remainder of the system is described using the semiempirical MNDO method. In a subsequent step, the energies were further refined by single-point calculations on the optimized structures. Full DFT calculations on the complete 46T cluster were performed at the B3LYP/6-31+g(d), M06−2X/6-31+g(d), ωB97X-D/6-31+g(d), and PBE/6-31+g(d) levels of theory. Dispersion corrections according to Grimme were added to the B3LYP, M06−2X, and PBE energies.[37,44] All cluster calculations were performed using the Gaussian03 and Gaussian09 packages,[74,75] and Grimme corrections were calculated with the dftd3 program available from the authors' Web site.[76]

2.3. Periodic Calculations. Periodic DFT-D calculations on the entire H-ZSM-5 unit cell containing 288 atoms (Figure 2) were carried out in the Vienna Ab Initio Simulation Package (VASP 5.2.11),[77−80] using the PBE exchange-correlation functional[81,82] and a plane-wave basis set with a general kinetic energy cutoff of 600 eV. The projector augmented wave (PAW) approximation[83] was used. Brillouin zone sampling was restricted to the Γ-point. Gaussian smearing[78] was applied to improve convergence: 0.05 eV for geometry optimizations, 0.03 eV for frequency calculations, and 0.005 eV for energy calculations on the optimized geometries. van der Waals corrections according to Grimme were used throughout all periodic calculations.[44]

The unit cell parameters of H-ZSM-5 were determined, starting from crystallographic data for silicalite,[84] using a similar procedure as Svelle et al.[13] The silicalite unit cell was fully optimized at the start but was also allowed to relax during subsequent geometry optimizations, i.e., after the aluminum defect, proton, and adsorbates had been introduced. Geometry optimizations of the adsorption complexes were carried out in two steps, similar to the approach proposed by De Moor et al.[25] An initial relaxation using the conjugate gradient algorithm was performed until the forces on all atoms are smaller than 0.01 eV/Å. This was followed by a second optimization with fixed cell parameters, in which the quasi-Newton algorithm is

applied. Geometries are considered to be converged once the forces on the atoms drop below 0.005 eV/Å. For some of the adsorption complexes, even tighter criteria were required to eliminate all imaginary frequencies (cf. Section 2.4). Specific convergence criteria applied for each individual case are included in the Supporting Information (Table S1). The convergence criterion for the electronic self-consistent field (SCF) problem was set to 10^{-8} eV.

2.4. Normal-Mode Analysis and Thermochemistry. A normal-mode analysis was performed to verify the nature of the optimized structures (true energy minima should only have real frequencies) for both the cluster and periodic calculations, using Partial Hessian Vibrational Analysis (PHVA), as implemented in the in-house developed postprocessing toolkit TAMKIN.[85,86] In the cluster calculations, PHVA was used to exclude the terminating hydrogen atoms with constrained positions from the analysis. In the periodic calculations, vibrational modes are calculated numerically (using displacements in x, y, and z-directions of $\pm$0.01 Å), and only a partial Hessian was calculated to reduce the computational cost. PHVA was applied on the adsorbate and the 8T atoms from the zeolite framework that are included in the high-level region in the ONIOM calculations on the cluster model. The strong hydrogen bond interactions between the alcohol or nitrile and the zeolite justify the application of the "immobile adsorbate" method, in which only harmonic frequencies are considered.[17,18,25]

The vibrational analysis also supplies the necessary thermochemistry data to allow the calculation of theoretical adsorption enthalpies at 400 K, the temperature at which the experimental reference data were obtained.[14] The adsorption enthalpy was calculated by subtracting the enthalpies of the empty zeolite and the gas phase adsorbate from the enthalpy of the adsorption complex

$$\Delta H_{ads} = H_{complex} - H_{zeolite} - H_{adsorbate}$$

Since we are using a flexible model[87] that is allowed to relax during geometry optimizations, in the cluster calculations the enthalpy of the empty zeolite was recalculated for each adsorbate, starting from the optimized geometry of the corresponding adsorption complex. The adsorbate molecule is removed from the complex, and the empty zeolite is subsequently optimized. This approach avoids nonreproducible errors on the calculated adsorption enthalpy caused by spurious enthalpy differences due to deformations of the zeolite host that are unrelated to interactions between the zeolite and the adsorbate under consideration.

IR spectra of all adsorption complexes were also investigated within the cluster model. Computed harmonic frequencies are typically larger than the experimentally observed values due to the neglect of anharmonic effects, the incomplete incorporation of electron correlation, and the use of a finite basis set. For this reason, a scale factor of 0.9648 was applied, which is common practice when using the B3LYP functional.[88]

3. RESULTS AND DISCUSSION

3.1. Geometrical Aspects of the Adsorption Complexes.

(A). Interaction with the Brønsted Acid Sites. At low coverages (up to one per active site), the investigated adsorbate molecules are known to form well-defined physisorption complexes at the Brønsted sites through hydrogen bonds; i.e., proton transfer between the zeolite and the adsorbates does not occur.[14] A complete overview of the critical distances and hydrogen bond angles in the adsorption complexes is included in the Supporting Information (Table S2).

Water and alcohols allow the formation of two hydrogen bond interactions with the active site, as the hydroxyl group can act simultaneously as hydrogen bond donor and acceptor (Figure 3a). In the cluster model the interaction between the zeolite proton (H_Z) and the oxygen atom of the hydroxyl group (O_A) results in a hydrogen bond of on average 1.52 Å. At the same time, the hydrogen end of the hydroxyl group (H_A) coordinates with a nearest-neighbor framework oxygen bridge with respect to the acid proton (O_{Z2}), resulting in a slightly longer hydrogen bond of about 1.89 Å. On the basis of the O–O distances ($d(O_A–O_{Z2}) \approx 2.72$ Å, $d(O_A–O_{Z1}) \approx 2.53$ Å), the hydrogen bonds can be classified as "strong" and "medium", respectively.[89] Clearly, the two hydrogen bonds could easily "switch places", thereby shuffling the acid proton between framework oxygen bridges. This observation is in agreement with previous theoretical results on the adsorption of methanol in zeolites by Sauer et al., which showed that complexes with methanol interacting in different configurations with the active site are very similar in energy and exist in a wide and shallow potential well. Ion-pair complexes in which the zeolite proton is fully transferred to methanol to form a methoxoniom ion were found to be slightly higher in energy, and these authors therefore considered them as transition states connecting different hydrogen bonded complexes.[20,73,90] In the periodic calculations performed in our current study, which included dispersion corrections throughout the optimizations, ion-pair complexes were obtained for methanol, ethanol and propanol, resulting in two fairly similar hydrogen bonds (average length 1.50 Å) between the protonated alcohol and two framework oxygens adjacent to the aluminum defect. Whether ion-pair complexes appear as stationary points or not most likely depends at least in part on the level of theory used. In particular, the addition of D-corrections and the kinetic energy cutoff might have an important influence on the result. Nguyen et al. recently reported both hydrogen bonded and protonated complexes for primary alcohols in H-ZSM-5, based on periodic PBE alculations using a cutoff energy of 400 eV.[22] In their study these authors included dispersion corrections as an energy refinement on the optimized geometries. More importantly, however, they also showed that the calculated adsorption

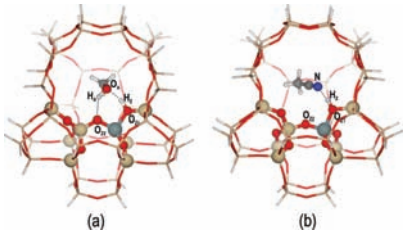

Figure 3. Hydrogen bond interactions with the Brønsted acid site in H-ZSM-5 in alcohol and nitrile adsorption complexes, e.g., methanol (a) and acetonitrile (b).

energy is very similar for the neutral and ion-pair complexes, differing by less than 6 kJ/mol.[22]

In contrast, the nitriles can form only one hydrogen bond between the zeolite proton and the nitrogen end of the cyanide group, with an average length of about 1.66 Å in the cluster simulations (see Figure 3b). Consequently, these adsorbates cannot assist in transferring the zeolite proton to different positions in the framework. The final geometries obtained from the periodic calculations were very similar; the average length of the H_Z−N hydrogen bond was only slightly shorter, about 1.52 Å, which might again be due to the inclusion of dispersion corrections in the optimization.

(B). Orientation within the Zeolite Channels. In the gas phase, adsorbate molecules will preferentially assume conformations in which their carbon chains are fully staggered, thereby eliminating steric hindrance. Inside the zeolite pores, however, this might be prohibited by confinement effects, especially when larger adsorbates are concerned. While all adsorbates in the current study can still assume fully staggered conformations (cf. Figure S1 in Supporting Information), comparing the largest members of each series – propanol and butyronitrile – indicates that confinement effects will play a more important role with alcohols compared to nitriles (Figure 4). Larger nitriles can avoid steric hindrance by moving into the straight channel of the MFI structure. Alcohols, on the other hand, are more constrained by the double hydrogen bond interaction with the active site, such that larger ones will be forced to assume a more folded conformation to align their carbon chain with the straight channel.

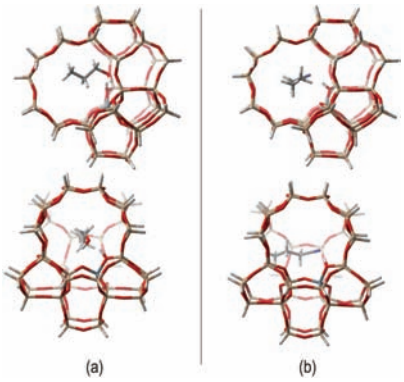

Figure 4. Optimized geometry of the adsorption complexes of propanol (a) and butyronitrile (b), viewed along sinusoidal (top) and straight (bottom) channels.

3.2. IR Spectroscopy. Calculated frequencies and relevant shifts resulting from adsorption of the weak bases are listed in Table 1. The scaled OH stretching frequency of the Brønsted acid site of the empty H-ZSM-5 cluster is on average 3600 cm^{-1}, in excellent agreement with reported experimental data (3610 cm^{-1}).[53] Upon physisorption of the bases, a clear red shift of the zeolite OH stretch (varying between 708 and 1360 cm^{-1}) is observed, due to the aforementioned hydrogen bonding. For a particular molecular type, the calculated shift roughly correlates with the proton affinity (PA) of the base, as depicted in Figure S2 (cf. Supporting Information). As a result, the red shift is the largest in the case of the alcohol series and increases with increasing molecular size. Comparison with available data for methanol adsorbed in H-ZSM-5 shows that the calculated shift of 1183 cm^{-1} (Table 1) is in good agreement with MP2-based results obtained on small cluster models of Haase and Sauer, reporting a shift of 1159 cm^{-1},[47] whereas periodic PBE simulations lead to a shift as large as 2233 cm^{-1}.[22] Notably, based on our large-cluster simulations the calculated OH stretch in adsorbed methanol equals 3426 cm^{-1}, which is in significantly better agreement with the experimentally reported[53] value of 3550 cm^{-1} compared to the MP2-based calculations using small clusters[47] and also to the PBE-based periodic simulations.[22]

For the nitrile series, several studies have reported on the influence of acetonitrile on the IR spectrum of initially unloaded H-ZSM-5.[55−59] The observed CN stretching frequency in the adsorption complex equals 2300 cm^{-1}, which is very well reproduced using our large-cluster approach (Table 1). Pelmenschikov et al.[55] reported calculated frequencies using small cluster models, and similar values were obtained. The shift of the CN stretch frequency in the adsorbed complex compared to the gas phase ranges from 9 to 24 cm^{-1}. The agreement with available data for acetonitrile is also satisfactory in this case (experimental shift equals 35 cm^{-1}[55]), suggesting that our theoretical model results in realistic structures for H-ZSM-5 at low loadings with weak bases.

3.3. Adsorption Enthalpy. For the complete series of adsorbate molecules, adsorption enthalpies at 400 K were calculated at the different levels of theory, as explained in Section 2.2. The majority of the calculations were performed using the extended-cluster model. To validate this approach, some additional fully periodic calculations were carried out. The final adsorption enthalpies obtained using the various methods are summarized in Table 2. Thermal corrections at 400 K are fairly similar for all adsorbates considered and add about +6 kJ/mol to the electronic energy differences. A complete breakdown of different contributions to the calculated adsorption enthalpies – i.e., electronic energies, dispersion corrections (where applicable), thermal corrections – is included in the Supporting Information (Table S3). Scatter plots depicting the correlation between calculated and experimental enthalpy values are shown in Figure 5.

First of all, adsorption enthalpies were calculated using the standard B3LYP functional. This functional does not include a proper description of dispersion interactions and was found to be completely inadequate for the calculation of adsorption enthalpies. The theoretical values predicted from the B3LYP energies significantly underestimate the experimental reference data[14] and are almost the same for all adsorbates considered, regardless of their size or chemical characteristics (Figure 5a). This is in complete contradiction with the experimental observation that across a series of similar compounds of increasing size (in this case alcohols or nitriles) the adsorption enthalpy increases steadily by about 10−15 kJ/mol with each additional C-atom in the carbon chain.[14] The outcome is significantly improved when D-corrections are added to the electronic energies: at the B3LYP-D level of theory, the experimentally observed trend in adsorption enthalpies is recovered across the series of alcohols and nitriles (Figure 5a).

Table 1. Zeolite OH and Adsorbate CN Vibrational Stretching Frequencies in cm^{-1} for the Various Adsorption Complexes Obtained from Cluster Calculations[a]

	$\nu(O_ZH_Z)$			ν(CN)		
	empty cluster[b]	adsorbed complex	shift	adsorbed complex	gas phase	shift
H_2O	3604	2687	917			
CH_3OH	3601	2418	1183			
CH_3CH_2OH	3602	2363	1239			
$CH_3(CH_2)_2OH$	3598	2238	1360			
CH_3CN	3600	2893	708	2307	2282	24
CH_3CH_2CN	3602	2845	757	2295	2271	24
$CH_3(CH_2)_2CN$	3597	2885	712	2280	2271	9
$(CH_3)_2CHCN$	3598	2809	790	2278	2263	15

[a]Frequencies are evaluated at the ONIOM(B3LYP/6-31+G(d):MNDO) level of theory. [b]The small differences result from the optimization of the empty cluster for all different adsorbates (see Section 2.4).

Table 2. Adsorption Enthalpies at 400 K Calculated Using Different DFT Methods, With and Without Dispersion Corrections (in kJ/mol)[a]

	B3LYP	B3LYP-D2	B3LYP-D3	M06−2X	M06−2X-D3	ωB97X-D	PBE	PBE-D2	PBE-D3	PBE-D2 pbc[b]	experimental[c]
H_2O	−71	−91	−90	−84	−88	−100	−80	−87	−91	−89	−90 ± 10
CH_3OH	−69	−108	−111	−93	−101	−102	−91	−108	−112	−125	−115 ± 5
CH_3CH_2OH	−82	−129	−132	−108	−120	−122	−97	−124	−129	−141	−130 ± 5
$CH_3(CH_2)_2OH$	−85	−148	−152	−119	−134	−139	−102	−140	−148		−145 ± 5
CH_3CN	−72	−104	−110	−89	−98	−101	−84	−102	−104	−108	−110 ± 5
CH_3CH_2CN	−72	−120	−127	−95	−108	−116	−87	−116	−120	−112	−120 ± 5
$CH_3(CH_2)_2CN$	−64	−137	−144	−105	−121	−130	−83	−128	−137	−139	−145 ± 5
$(CH_3)_2CHCN$	−69	−130	−139	−99	−115	−125	−86	−125	−130		−130 ± 5

[a]All cluster calculations were performed using the 6-31+g(d) basis set. [b]Periodic results obtained using a kinetic energy cutoff of 600 eV. [c]Experimental values from ref 14.

For completeness, we calculated dispersion corrections according to both the D2-scheme,[44] as used in our previous work,[11,12,91] and the more recent D3-version.[37] Overall, only minor differences were found between the two approaches.

Next, adsorption enthalpies were calculated based on M06−2X energies (Figure 5b). The numerical values show that, compared to B3LYP, some of the weak interactions between the zeolite host and the adsorbate molecule are accounted for by the M06−2X functional. However, the deviation from the reference data increases for the larger adsorbates, which is probably due to the specific way the M06−2X functional was parametrized. While this functional performs very well on systems with noncovalent interactions in the medium range, it does not possess the correct asymptotic behavior to describe long-range dispersion interactions.[35] The remaining deficiency can be remedied by adding an empirical dispersion correction term,[35] resulting in the recovery of the correct experimental trend. The M06−2X functional has recently been used for the study of zeolite-catalyzed processes.[42,43] However, our results reported in this paper indicate caution is required when using this method in cases for which dispersion interactions are important.

Subsequently, adsorption enthalpies were also evaluated using the ωB97X-D functional, resulting in a very good correlation with the experimental values (Figure 5c). This functional tends to predict a slightly lower interaction strength between adsorbate and zeolite compared to B3LYP-D, which can probably be ascribed to the simultaneous determination of all parameters in the ωB97X-D functional, thereby avoiding double counting in the intermediate range.[45] Although this functional has thus far not been used in the field, it could be a promising candidate for use in future research on zeolite-catalyzed reactions. Goerigk et al. reported on its good performance for main-group thermochemistry, kinetics, and noncovalent interactions based on a benchmarking study on the GMTKN30 database.[35] The performance of the ωB97X-D functional to describe the kinetics of methylation reactions is currently being investigated in our group.

Finally, enthalpies of adsorption were calculated based on fully periodic simulations in which the entire H-ZSM-5 unit cell is taken into account (see Section 2.3) to verify the validity of the extended-cluster model. To enable a direct comparison between periodic and cluster calculations, the PBE functional was used to evaluate adsorption enthalpies in both the cluster and periodic approach (Figure 5d). Considering only the cluster results, the qualitative performance of PBE appears similar to that of B3LYP, as it critically depends on the addition of dispersion corrections to recover the experimental trend across the series of adsorbates. Comparing periodic PBE-D with cluster PBE-D adsorption enthalpies, periodic simulations clearly do not offer a significant improvement over the cluster approach. Adsorption enthalpies for methanol and ethanol are predicted to be slightly larger by the periodic calculations, which could be related to protonated complexes being obtained for these adsorbates. For propanol and isobutyronitrile, no adsorption enthalpy at 400 K could be calculated, as even with the strong convergence criteria imposed the partial Hessian still contained imaginary frequencies. In general, the extended-cluster approach was found to offer a reliable alternative for the much more demanding periodic calculations, combining lower computational costs with less technical complications and a more straightforward vibrational analysis.

The overall performance of the different methods across the test set is summarized in Figure 6, displaying the mean

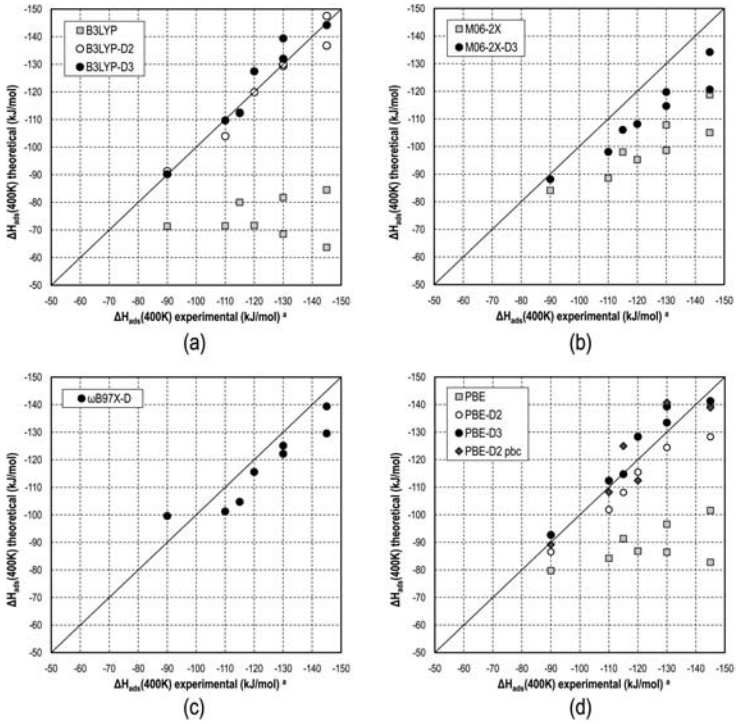

Figure 5. Correlation between theoretical (*y*-axis) and experimental (*x*-axis) values for adsorption enthalpies evaluated at different levels of theory: (a) B3LYP(-D), (b) M06−2X(-D), (c) ωB97X-D, (d) PBE(-D). Dispersion corrections on B3LYP, M06−2X, and PBE values were calculated according to the Grimme D2- and D3-schemes. All cluster calculations were performed using the 6-31+g(d) basis set. Periodic results (PBE-D2 pbc) were obtained using a kinetic energy cutoff of 600 eV. [a]Experimental values from ref 14.

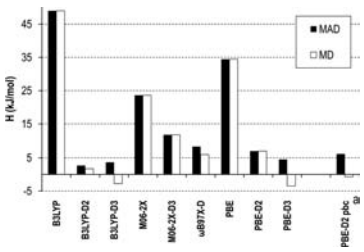

Figure 6. Mean deviation (MD) and mean absolute deviation (MAD) between theoretical and experimental adsorption enthalpies. [a]Based on the reduced data set for which periodic results were available.

deviation (MD) and mean absolute deviation (MAD) between theoretical and experimental values. Dispersion-corrected functionals are clearly essential to obtain reliable trends for the adsorption enthalpies. B3LYP and PBE perform very poorly, exhibiting a mean absolute deviation of 49 and 34 kJ/mol, respectively, when comparing calculated and experimental adsorption enthalpies at 400 K. For M06−2X, a slightly better result is obtained (MAD of 24 kJ/mol), which is mainly due to the reasonable performance for the smallest adsorbates (cf. supra). The results improve substantially by adding dispersion corrections, reducing MADs to 3−4, 5−7, and 12 kJ/mol for B3LYP-D, PBE-D, and M06−2X-D respectively. ωB97X-D performs generally well across the entire series of alcohols and nitriles (MAD of 8 kJ/mol). MADs for PBE-D values obtained using periodic calculations (6 kJ/mol) and using the cluster approach (7 kJ/mol) are comparable, confirming that periodic simulations do not offer a substantial advantage. The adsorbates for which the adsorption enthalpies could not be determined

dx.doi.org/10.1021/jp2123828 | J. Phys. Chem. C 2012, 116, 5499−5508

based on the periodic model (i.e., propanol and isobutyronitrile) were excluded in the calculation of the MD and MAD values for the periodic PBE-D results.

3.4. Framework–Adsorbate Interplay. The total heat of adsorption of the alcohols or nitriles results from the interplay of different effects: on one hand, the adsorption complex is stabilized by hydrogen bonds and dispersive interactions with the zeolite walls; on the other hand, deformations of both the zeolite host and the adsorbate molecule have a destabilizing effect. Calculating the different contributions separately provides a more detailed insight into their relative importance.

The interactions between adsorbate and the zeolite (ΔE_{inter}) can be calculated from

$$\Delta E_{inter} = E_{complex} - E^{c}_{zeolite} - E^{c}_{adsorbate}$$

Herein, energies of the zeolite and adsorbate are evaluated at the geometries found in the adsorption complex without further optimization (denoted by the superscript 'c'). As a result, contributions due to deformation of the zeolite host and the adsorbate are excluded. These can be calculated separately from

$$\Delta E^{zeo}_{deform} = E^{c}_{zeolite} - E_{zeolite}$$

$$\Delta E^{ads}_{deform} = E^{c}_{adsorbate} - E_{adsorbate}$$

The total adsorption energy (ΔE_{ads}) is now given by

$$\Delta E_{ads} = \Delta E_{inter} + \Delta E^{zeo}_{deform} + \Delta E^{ads}_{deform}$$

The various contributions at the B3LYP-D level of theory are listed in Table 3. Note that these are purely electronic energies, differing slightly from the adsorption enthalpies at 400 K presented in Table 2.

Table 3. Different Contributions to the Adsorption Energy[a]

	ΔE_{inter}	ΔE^{zeo}_{deform}	ΔE^{ads}_{deform}	ΔE_{ads}
H_2O	−109.0	10.3	1.0	−97.7
CH_3OH	−135.1	14.6	1.6	−118.9
CH_3CH_2OH	−156.2	15.8	2.3	−138.1
$CH_3(CH_2)_2OH$	−177.3	17.1	1.7	−158.5
CH_3CN	−118.3	2.9	0.3	−115.2
CH_3CH_2CN	−140.6	6.8	0.5	−133.3
$CH_3(CH_2)_2CN$	−159.2	6.2	2.2	−150.8
$(CH_3)_2CHCN$	−154.7	8.7	0.6	−145.4

[a] ΔE_{inter}: interaction between zeolite and adsorbate. ΔE^{zeo}_{deform}: deformation of the zeolite host. ΔE^{ads}_{deform}: deformation of the adsorbate. ΔE_{ads}: total adsorption energy. Level of theory: B3LYP-D/6-31+g(d). All values in kJ/mol.

While the interaction between the zeolite host and the adsorbate molecules dominates the final adsorption energy, destabilization due to deformation of the zeolite host clearly increases with increasing size of the adsorbate molecule and is generally more prominent for water and the alcohols (10–17 kJ/mol), compared to the nitriles (3–9 kJ/mol). The latter could be due to the stronger hydrogen bond interactions between two hydroxyl groups in the case of the alcohols, compared to the somewhat weaker hydrogen bond between the cyanide and zeolite hydroxyl group formed upon nitrile adsorption. A stronger hydrogen bond results in slightly more local deformation of the framework surrounding the active site. Destabilization due to deformation of the adsorbate molecule is virtually negligible for the alcohols and nitriles considered in this study (less than 3 kJ/mol), in agreement with the earlier conclusion that the current adsorbates are not yet hindered by confinement effects in the zeolite pore (cf. Section 3.1).

4. CONCLUSIONS

Adsorption enthalpies of a series of alcohols and nitriles on the zeolite catalyst H-ZSM-5 were calculated using different DFT-based methods. Water, methanol, ethanol, propanol, acetonitrile, propionitrile, butyronitrile, and isobutyronitrile were selected based on the availability of experimental reference data for their differential heats of adsorption in H-ZSM-5, which makes them ideally suited for benchmarking computational methodologies. In addition, the adsorption of weak bases in acidic zeolite materials is a crucial step for many industrial processes, such as the MTO conversion.

Large-cluster calculations on the adsorption complexes indicate that all adsorbates are found to be physisorbed in the H-ZSM-5 cluster, in agreement with experimental IR data for low adsorbate coverage in H-ZSM-5. The alcohols form two and the nitriles one hydrogen bond with the bridging Brønsted acid sites. It was moreover shown that deformation of the zeolite host has a non-negligible destabilizing effect, which increases with the size of the adsorbate molecule and is more prominent for alcohols than for nitriles, as the former interact more strongly with the zeolite.

The performance of different DFT-methods, i.e., B3LYP(-D), PBE(-D), M062X(-D), and ωB97X-D, to reproduce the experimental adsorption enthalpies was assessed, with special emphasis on the influence of dispersion interactions. A proper account of dispersion interactions was found to be indispensable to describe the experimental trend across a series of adsorbates of increasing size, i.e., an increase in adsorption enthalpy by 10–15 kJ/mol for each additional carbon atom. The well-known B3LYP and PBE functionals are completely inadequate to determine adsorption enthalpies for the alcohols and nitriles and are effectively unable to distinguish between alcohols or nitriles of different size. M06–2X, which was parametrized to include weak interactions, was still found to underestimate the adsorption enthalpy for the adsorbates considered in this study. Moreover, the deviation from the experimental trend increases with increasing adsorbate size. For all three functionals, however, the deficiency can be remedied by adding dispersion correction terms as proposed by Grimme. The recent ωB97X-D functional, which combines custom parametrization with Grimme-like dispersion terms, was found to perform well for the calculation of adsorption enthalpies across the series of compounds. Comparing calculated with experimental adsorption enthalpies, B3LYP-D, PBE-D, and ωB97X-D all result in MAD values below 8 kJ/mol for the complete set of alcohols and nitriles.

Comparison with periodic simulations using the PBE-D functional on the full H-ZSM-5 unit cell confirmed that the extended-cluster model offers an attractive alternative, resulting in virtually identical final adsorption enthalpies while avoiding both the larger computational expense and technical difficulties associated with periodic calculations.

■ ASSOCIATED CONTENT

Supporting Information

Complete Gaussian references, convergence criteria used in periodic simulations, critical hydrogen bond lengths and angles for all adsorption complexes, OH-stretch frequency shifts vs gas

phase proton affinities for selected adsorbates, additional figures, and complete coordinates of all optimized adsorption complexes. This material is available free of charge via the Internet at http://pubs.acs.org.

AUTHOR INFORMATION

Corresponding Author

*E-mail: veronique.vanspeybroeck@ugent.be.

Notes

The authors declare no competing financial interest.

ACKNOWLEDGMENTS

This work was supported by the Fund for Scientific Research Flanders (FWO), the Research Board of Ghent University (BOF), and BELSPO in the frame of IAP/6/27. Funding was also received from the European Research Council under the European Community's Seventh Framework Programme [FP7(2007-2013) ERC grant agreement number 240483]. Computational resources and services used in this work were provided by Ghent University.

REFERENCES

(1) *Zeolites for Cleaner Technologies*; Guisnet, M., Gilson, J.-P., Eds.; Imperial College Press: London, 2002; *Vol. 3*.
(2) Stocker, M.; Weitkamp, J. *Microporous Mesoporous Mater.* **1999**, *29*, 1−1.
(3) Haw, J. F.; Song, W.; Marcus, D. M.; Nicholas, J. B. *Acc. Chem. Res.* **2003**, *36*, 317−326.
(4) Svelle, S.; Arstad, B.; Kolboe, S.; Swang, O. *J. Phys. Chem. B* **2003**, *107*, 9281−9289.
(5) Svelle, S.; Kolboe, S.; Olsbye, U.; Swang, O. *J. Phys. Chem. B* **2003**, *107*, 5251−5260.
(6) Svelle, S.; Kolboe, S.; Swang, O. *J. Phys. Chem. B* **2004**, *108*, 2953−2962.
(7) Lesthaeghe, D.; Horre, A.; Waroquier, M.; Marin, G. B.; Van Speybroeck, V. *Chem.—Eur. J.* **2009**, *15*, 10803−10808.
(8) Lesthaeghe, D.; Van der Mynsbrugge, J.; Vandichel, M.; Waroquier, M.; Van Speybroeck, V. *ChemCatChem* **2011**, *3*, 208−212.
(9) McCann, D. M.; Lesthaeghe, D.; Kletnieks, P. W.; Guenther, D. R.; Hayman, M. J.; Van Speybroeck, V.; Waroquier, M.; Haw, J. F. *Angew. Chem., Int. Ed.* **2008**, *47*, 5179−5182.
(10) Hemelsoet, K.; Nollet, A.; Vandichel, M.; Lesthaeghe, D.; Van Speybroeck, V.; Waroquier, M. *ChemCatChem* **2009**, *1*, 373−378.
(11) Hemelsoet, K.; Nollet, A.; Van Speybroeck, V.; Waroquier, M. *Chem.—Eur. J.* **2011**, *17*, 9083−9093.
(12) Van Speybroeck, V.; Van der Mynsbrugge, J.; Vandichel, M.; Hemelsoet, K.; Lesthaeghe, D.; Ghysels, A.; Marin, G. B.; Waroquier, M. *J. Am. Chem. Soc.* **2011**, *133*, 888−899.
(13) Svelle, S.; Tuma, C.; Rozanska, X.; Kerber, T.; Sauer, J. *J. Am. Chem. Soc.* **2009**, *131*, 816−825.
(14) Lee, C. C.; Gorte, R. J.; Farneth, W. E. *J. Phys. Chem. B* **1997**, *101*, 3811−3817.
(15) Denayer, J. F.; Souverijns, W.; Jacobs, P. A.; Martens, J. A.; Baron, G. V. *J. Phys. Chem. B* **1998**, *102*, 4588−4597.
(16) Arik, I. C.; Denayer, J. F.; Baron, G. V. *Microporous Mesoporous Mater.* **2003**, *60*, 111−124.
(17) De Moor, B. A.; Reyniers, M. F.; Marin, G. B. *Phys. Chem. Chem. Phys.* **2009**, *11*, 2939−2958.
(18) De Moor, B. A.; Reyniers, M.-F. o.; Gobin, O. C.; Lercher, J. A.; Marin, G. B. *J. Phys. Chem. C* **2011**, *115*, 1204−1219.
(19) Tuma, C.; Sauer, J. *Phys. Chem. Chem. Phys.* **2006**, *8*, 3955−3965.
(20) Tuma, C.; Sauer, J. *Chem. Phys. Lett.* **2004**, *387*, 388−394.
(21) Tuma, C.; Sauer, J. *Angew. Chem., Int. Ed.* **2005**, *44*, 4769−4771.
(22) Nguyen, C. M.; Reyniers, M. F.; Marin, G. B. *Phys. Chem. Chem. Phys.* **2010**, *12*, 9481−9493.
(23) Nguyen, C. M.; Reyniers, M. F.; Marin, G. B. *J. Phys. Chem. C* **2011**, *115*, 8658−8669.
(24) De Moor, B. A.; Reyniers, M.-F. o.; Sierka, M.; Sauer, J.; Marin, G. B. *J. Phys. Chem. C* **2008**, *112*, 11796−11812.
(25) De Moor, B. A.; Ghysels, A.; Reyniers, M.-F. o.; Van Speybroeck, V.; Waroquier, M.; Marin, G. B. *J. Chem. Theory Comput.* **2011**, *7*, 1090−1101.
(26) Hohenberg, P.; Kohn, W. *Phys. Rev.* **1964**, *136*, B864.
(27) Kohn, W.; Sham, L. J. *Phys. Rev.* **1965**, *140*, A1133.
(28) Grimme, S. *J. Comput. Chem.* **2004**, *25*, 1463−1473.
(29) Grimme, S.; Antony, J.; Schwabe, T.; Muck-Lichtenfeld, C. *Org. Biomol. Chem.* **2007**, *5*, 741−758.
(30) Becke, A. D. *J. Chem. Phys.* **1993**, *98*, 5648−5652.
(31) Lee, C.; Yang, W.; Parr, R. G. *Phys. Rev. B* **1988**, *37*, 785.
(32) Grafenstein, J.; Cremer, D. *J. Chem. Phys.* **2009**, *130*, 124105.
(33) Johnson, E. R.; Mackie, I. D.; DiLabio, G. A. *J. Phys. Org. Chem.* **2009**, *22*, 1127−1135.
(34) Sato, T.; Nakai, H. *J. Chem. Phys.* **2009**, *131*, 224104.
(35) Goerigk, L.; Grimme, S. *Phys. Chem. Chem. Phys.* **2011**, *13*, 6670−6688.
(36) Grimme, S.; Antony, J.; Schwabe, T.; Muck-Lichtenfeld, C. *Org. Biomol. Chem.* **2007**, *5*, 741−758.
(37) Grimme, S.; Antony, J.; Ehrlich, S.; Krieg, H. *J. Chem. Phys.* **2010**, *132*, 154104.
(38) Zhao, Y.; Truhlar, D. G. *Theor. Chem. Acc.* **2008**, *120*, 215−241.
(39) Zhao, Y.; Truhlar, D. G. *Acc. Chem. Res.* **2008**, *41*, 157−167.
(40) Catak, S.; D'Hooghe, M.; De Kimpe, N.; Waroquier, M.; Van Speybroeck, V. *J. Org. Chem.* **2010**, *75*, 885−896.
(41) Catak, S.; Hemelsoet, K.; Hermosilla, L.; Waroquier, M.; Van Speybroeck, V. *Chem.—Eur. J.* **2011**, *17*, 12027−12036.
(42) Boekfa, B.; Choomwattana, S.; Khongpracha, P.; Limtrakul, J. *Langmuir* **2009**, *25*, 12990−12999.
(43) Boekfa, B.; Pantu, P.; Probst, M.; Limtrakul, J. *J. Phys. Chem. C* **2010**, *114*, 15061−15067.
(44) Grimme, S. *J. Comput. Chem.* **2006**, *27*, 1787−1799.
(45) Chai, J.-D.; Head-Gordon, M. *Phys. Chem. Chem. Phys.* **2008**, *10*, 6615−6620.
(46) Zecchina, A.; Spoto, G.; Bordiga, S. *Phys. Chem. Chem. Phys.* **2005**, *7*, 1627−1642.
(47) Haase, F.; Sauer, J. *J. Am. Chem. Soc.* **1995**, *117*, 3780−3789.
(48) Krossner, M.; Sauer, J. *J. Phys. Chem.* **1996**, *100*, 6199−6211.
(49) Sauer, J.; Ugliengo, P.; Garrone, E.; Saunders, V. R. *Chem. Rev.* **1994**, *94*, 2095−2160.
(50) Blaszkowski, S. R.; van Santen, R. A. *J. Phys. Chem.* **1995**, *99*, 11728−11738.
(51) Hemelsoet, K.; Ghysels, A.; Mores, D.; De Wispelaere, K.; Van Speybroeck, V.; Weckhuysen, B. M.; Waroquier, M. *Catal. Today* **2011**, *177*, 12−24.
(52) Jentys, A.; Warecka, G.; Derewinski, M.; Lercher, J. A. *J. Phys. Chem.* **1989**, *93*, 4837−4843.
(53) Mirth, G.; Lercher, J. A.; Anderson, M. W.; Klinowski, J. *J. Chem. Soc., Faraday Trans.* **1990**, *86*, 3039−3044.
(54) Zecchina, A.; Bordiga, S.; Spoto, G.; Scarano, D.; Spano, G.; Geobaldo, F. *J. Chem. Soc., Faraday Trans.* **1996**, *92*, 4863−4875.
(55) Pelmenschikov, A. G.; van Santen, R. A.; Janchen, J.; Meijer, E. *J. Phys. Chem.* **1993**, *97*, 11071−11074.
(56) Pelmenschikov, A. G.; van Wolput, J. H. M. C.; Jaenchen, J.; van Santen, R. A. *J. Phys. Chem.* **1995**, *99*, 3612−3617.
(57) Florian, J.; Kubelkova, L. *J. Phys. Chem.* **1994**, *98*, 8734−8741.
(58) Kubelkova, L.; Kotrla, J.; Florian, J. *J. Phys. Chem.* **1995**, *99*, 10285−10293.
(59) Trombetta, M.; Armaroli, T.; Alejandre, A. G.; Solis, J. R.; Busca, G. *Appl. Catal., A* **2000**, *192*, 125−136.
(60) Simperler, A.; Bell, R. G.; Foster, M. D.; Gray, A. E.; Lewis, D. W.; Anderson, M. W. *J. Phys. Chem. B* **2004**, *108*, 7152−7161.
(61) van Koningsveld, H. *Acta Crystallogr., Sect. B: Struct. Sci.* **1990**, *46*, 731−735.
(62) Lesthaeghe, D.; Van Speybroeck, V.; Waroquier, M. *Phys. Chem. Chem. Phys.* **2009**, *11*, 5222−5226.

(63) Bhan, A.; Joshi, Y. V.; Delgass, W. N.; Thomson, K. T. *J. Phys. Chem. B* **2003**, *107*, 10476−10487.
(64) Alvarado-Swaisgood, A. E.; Barr, M. K.; Hay, P. J.; Redondo, A. *J. Phys. Chem.* **1991**, *95*, 10031−10036.
(65) Lonsinger, S. R.; Chakraborty, A. K.; Theodorou, D. N.; Bell, A. T. *Catal. Lett.* **1991**, *11*, 209−217.
(66) Redondo, A.; Hay, P. J. *J. Phys. Chem.* **1993**, *97*, 11754−11761.
(67) Grau-Crespo, R.; Peralta, A. G.; Ruiz-Salvador, A. R.; Gomez, A.; Lopez-Cordero, R. *Phys. Chem. Chem. Phys.* **2000**, *2*, 5716−5722.
(68) Sklenak, S.; Dedecek, J.; Li, C.; Wichterlova, B.; Gabova, V.; Sierka, M.; Sauer, J. *Phys. Chem. Chem. Phys.* **2009**, *11*, 1237−1247.
(69) Sklenak, S.; Dedecek, J.; Li, C.; Wichterlova, B.; Gabova, V.; Sierka, M.; Sauer, J. *Angew. Chem., Int. Ed.* **2007**, *46*, 7286−7289.
(70) Dedecek, J.; Kaucky, D.; Wichterlova, B. *Chem. Commun. (Cambridge, U. K.)* **2001**, 970−971.
(71) Baba, T.; Komatsu, N.; Ono, Y.; Sugisawa, H. *J. Phys. Chem. B* **1998**, *102*, 804−808.
(72) Ryder, J. A.; Chakraborty, A. K.; Bell, A. T. *J. Phys. Chem. B* **2000**, *104*, 6998−7011.
(73) Franke, M. E.; Sierka, M.; Simon, U.; Sauer, J. *Phys. Chem. Chem. Phys.* **2002**, *4*, 5207−5216.
(74) Frisch, M. J.; et al., *Gaussian 03*, revision E.01 ed.; Gaussian, Inc.: Wallingford CT, 2004.
(75) Frisch, M. J.; et al., *Gaussian 09*, revision A.02 ed.; Gaussian, Inc.: Wallingford CT, 2009.
(76) Grimme, S., http://toc.uni-muenster.de/DFTD3/.
(77) Kresse, G.; Furthmuller, J. *Phys. Rev. B* **1996**, *54*, 11169.
(78) Kresse, G.; Furthmuller, J. *Comput. Mater. Sci.* **1996**, *6*, 15−50.
(79) Kresse, G.; Hafner, J. *Phys. Rev. B* **1993**, *47*, 558.
(80) Kresse, G.; Hafner, J. *Phys. Rev. B* **1994**, *49*, 14251.
(81) Perdew, J. P.; Burke, K.; Ernzerhof, M. *Phys. Rev. Lett.* **1996**, *77*, 3865.
(82) Perdew, J. P.; Burke, K.; Ernzerhof, M. *Phys. Rev. Lett.* **1997**, *78*, 1396.
(83) Blochl, P. E. *Phys. Rev. B* **1994**, *50*, 17953.
(84) Structure Commision of the International Zeolite Association (IZA-SC), Database of Zeolite Structures, http://www.iza-structure.org/databases/.
(85) CMM Code, http://molmod.ugent.be/code/wiki.
(86) Ghysels, A.; Verstraelen, T.; Hemelsoet, K.; Waroquier, M.; Van Speybroeck, V. *J. Chem. Inf. Model.* **2010**, *50*, 1736−1750.
(87) Fermann, J. T.; Moniz, T.; Kiowski, O.; McIntire, T. J.; Auerbach, S. M.; Vreven, T.; Frisch, M. J. *J. Chem. Theory Comput.* **2005**, *1*, 1232−1239.
(88) Merrick, J. P.; Moran, D.; Radom, L. *J. Phys. Chem. A* **2007**, *111*, 11683−11700.
(89) Gilli, P.; Bertolasi, V.; Ferretti, V.; Gilli, G. *J. Am. Chem. Soc.* **1994**, *116*, 909−915.
(90) Sierka, M.; Sauer, J. *J. Phys. Chem. B* **2001**, *105*, 1603−1613.
(91) Vandichel, M.; Lesthaeghe, D.; Van der Mynsbrugge, J.; Waroquier, M.; Van Speybroeck, V. *J. Catal.* **2010**, *271*, 67−78.

Paper 15

The effect of confined space on the growth of naphthalenic species in a chabazite-type catalyst: A molecular modeling study

Karen Hemelsoet, Arno Nollet, Matthias Vandichel, David Lesthaeghe, Veronique Van Speybroeck and Michel Waroquier

ChemCatChem, 2009, 1, 373 - 378

Copyright 2009 by Wiley-VCH Verlag GmbH& Co. KGaA, Weinheim.

FULL PAPERS

DOI: 10.1002/cctc.200900208

The Effect of Confined Space on the Growth of Naphthalenic Species in a Chabazite-Type Catalyst: A Molecular Modeling Study

Karen Hemelsoet,* Arno Nollet, Matthias Vandichel, David Lesthaeghe, Veronique Van Speybroeck,* and Michel Waroquier[a]

Methylation reactions of naphthalenic species over the acidic microporous zeolite with chabazite topology have been investigated by means of two-layered ab initio computations. Large cluster results combined with van der Waals contributions provide thermodynamic and kinetic results of successive methylation steps. The growth of fused bicyclic species is important as these can act as hydrocarbon pool species within the methanol-to-olefin (MTO) process, but ultimately leads to the deactivation of the catalyst. The influence of the confined space of the zeolite pore on the resulting transition state or product shape selectivity is investigated in detail.

Introduction

The increasing demand for light olefins in the petrochemical industry, combined with the limited reserves of crude oil have raised interest in the methanol-to-olefin (MTO) process.[1,2] This process is the transformation of methanol (often made from natural gas or coal through synthesis gas) into light olefins (i.e., ethene and propene) over microporous solid acids, such as zeolites and zeotype materials. Silicoaluminophosphate with a CHA topology (H-SAPO-34) and H-ZSM-5 are the most applied and studied catalysts for the MTO process. The architectural characteristics of the CHA topology are optimal for commercialization as the 8-ring narrow windows provide selectivity towards small molecules such as ethene and propene.[3] Recently, other promising catalysts were tested, such as ZSM-22.[4,5] Particular shape selectivity of this catalyst results in a unique product spectrum, that is, branched C_{5+} species are mainly formed. In the last decades, the complex reaction mechanism of the MTO process has been intensely debated,[6–8] but experimental and computational findings have finally confirmed the hydrocarbon pool (HP) mechanism. In this hypothesis, organic reaction centers act as cocatalysts inside the zeolite pores.[9–11] The actual active catalyst is thus the combined organic–inorganic supramolecular complex of the HP and zeolite framework. The MTO conversion results from the repeated methylation of the organic compounds and cations derived thereof, followed by olefin elimination, which forms a full catalytic cycle.

Aromatics, typically polymethylbenzenes, and alkenes,[12–14] were so far found to be crucial HP species, differentiating between the aromatic and alkene routes, respectively. It can not be ruled out, however, that other HP species are also active. The aromatic route comprises the paring and sidechain mechanisms. The latter mechanism involves the deprotonation of an alkyl group on an alkylbenzenium species and the formation of an exocyclic double bond. This double bond is further methylated, which reforms a benzenium ion with a higher alkyl chain. The higher alkyl chains are subsequently eliminated as alkenes. The paring mechanism involves ring contractions or expansions to extend an alkyl group on the cationic species. It is currently understood that ethene is predominantly formed from the lower methylbenzenes, whereas propene formation is favored by methylbenzenes with four to six methyl groups. Modeling results combined with experimental findings recently led to the first example of a complete cycle in H-ZSM-5.[15] The alkene-based cycle was also studied in this catalyst, which indicated that this route contributes insignificantly to ethene, but is a highly relevant mode of propene formation.[12–14] The role of branched organics as the active species is also under investigation. The high selectivity to triptane in another methanol conversion process, catalyzed by ZnI_2 and InI_3, was recently reported.[16] All recent studies have enforced our vision that the MTO conversion is a very complex process during which various routes occur simultaneously.

To obtain additional insight, it is important to isolate one particular parameter at a time. Theoretical calculations are ideally suited to achieve this goal.[17] In this contribution, we investigate the effects of confined spaces on the growth of the naphthalenic species. Their role during the MTO process is not straightforward. They might be important in active routes towards formation of olefins but also in passive routes, which

[a] Dr. K. Hemelsoet, A. Nollet,[+] M. Vandichel, Dr. D. Lesthaeghe, Prof. Dr. V. Van Speybroeck, Prof. Dr. M. Waroquier
Center for Molecular Modeling, QCMM Alliance Ghent-Brussels
Ghent University, Technologiepark 903, 9052 Zwijnaarde (Belgium)
Fax: (+32) 9-264-66-97
E-mail: karen.hemelsoet@ugent.be
veronique.vanspeybroeck@ugent.be

[+] Present address:
Shell/NAM, Schepersmaat 2, Postbus 28000
9400 HH Assen (The Netherlands)

Supporting information for this article is available on the WWW under http://dx.doi.org/10.1002/cctc.200900208.

 © 2009 Wiley-VCH Verlag GmbH & Co. KGaA, Weinheim

lead to the deactivation of the catalyst. We focus on a high-silicon chabazite catalyst for which we have developed a well-established procedure to calculate the kinetics from first principles.[18] We also found that methylations of benzene-like species could be dramatically sped up in the chabazite topology.[18] Important geometrical characteristics of this CHA catalyst are illustrated in Figure 1. The methylated species are quite

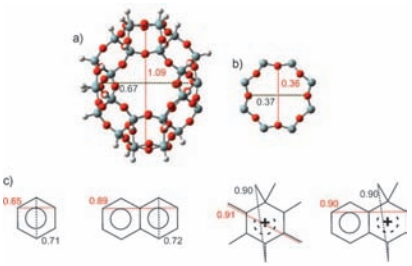

Figure 1. Geometrical characteristics of a) the CHA zeolite pore, b) 8-membered ring window, and c) some illustrative HP species. Free diameters (taking into account van der Waals radii, that is, 0.11 nm for H, 0.17 nm for C and 0.15 nm for O) are indicated in nm.

bulky compared to the free pore diameters and thus the stabilizing and steric effects of the zeolite topology are essential. Interestingly, the naphthalenic species investigated here are of the same size as the traditional benzenic HP species, such as the heptamethylbenzenium ion. The confinement effects of the zeolite pore might nevertheless be different, especially in the case of voluminous transition state structures.

A previous theoretical study by our group elucidated the influence of zeolite topology, which compared the MFI, CHA, and BEA frameworks for the crucial *ipso*-methylation reaction of hexamethylbenzene.[18] The following order of reactivity according to topology was found: CHA $\gg$ MFI $>$ BEA. Park and Seo compared the performance of CHA, LTA, MFI, BEA, MOR, and FAU topologies by using in situ IR spectroscopy.[19] The number of strong acidic sites within the zeolite and the topology were found to be determining factors for the deactivation. Seo and co-workers investigated the effects of shape and size of the cage on the deactivation during the MTO process, comparing four eight-membered ring molecular sieves with an Si/Al molar ratio of 5–6:1[20] Although the initial activity and selectivity of the catalysts were very similar, the deactivation behavior differed to a large extent and the following order was found: CHA $\ll$ LTA $<$ ERI $<$ UFI. UV/Vis spectra indicated that the formation of large polycyclic aromatics in the CHA cages for a short time was not detectable.[20] Bleken et al. recently addressed the influence of acid strength, comparing H-SAPO-34 with the more acidic H-SSZ-13 variant at similar conditions.[21] Both catalysts were found to act similarly, however, a lower optimal operation temperature and increased ethene/propene ratio were found for H-SSZ-13.

The role of naphthalenic species during the MTO process was experimentally investigated by Haw and co-workers. Using the cryogenic grinding method,[22] it was found that in SAPO-34, methylnaphthalenes become significantly present after the addition of 1 or 2 mL of methanol for 0.3 g of catalyst. A careful comparison showed the naphthalenic species to be approximately one third as active as their benzenic counterparts. However, a higher ethene selectivity was obtained,[23] which could be related to the observation that methylnaphthalenes in H-SAPO-34 never contain more than four methyl groups.[24] Methylphenanthrenes are restricted to two groups, whereas their catalytic activity is almost non-existent. They are still able to age to pyrene with no methyl groups, which is seen as the final state of the degenerated catalyst cage.[24] Bjørgen and co-workers investigated the formation of coke precursors from hexamethylbenzene reacting over H-beta at 325 °C. They found that the large hexamethylnaphthalene compounds could easily be formed from dihydrotrimethylnaphthalene by methylations and hydrogen transfers.[25] In general, the deactivation was fast. The latter observations relate to the deactivation of the catalyst by coking, which naturally influences both activity and selectivity. Many uncertainties regarding this deactivation process remain, partially due to the generally poor characterization of coke. Bordiga et al. applied ex situ spectroscopic techniques (i.e., DR-UV/Vis and IR) to study the nature of the carbonaceous species formed in H-ZSM-5.[26] They found that methylated aromatic carbocationic species slowly evolve into precursors of graphitic coke. Weckhuysen et al. recently focused on the differences between the coking behavior in H-ZSM-5 and H-SAPO-34, by using in situ UV/Vis spectroscopy combined with confocal fluorescence microspectroscopy.[27] Graphitic coke on H-ZSM-5 crystals is initially formed at the edges of the crystal, whereas in H-SAPO-34 aromatic coke compounds are mainly formed inside the crystals. A recent study on the deactivation of H-SAPO-34 by Olsbye and co-workers, using isotopic switch experiments, revealed that an increased ethene/propene ratio results from product shape selectivity rather than transition-state shape selectivity as the diffusion of small molecules are hindered through the presence of bulky species inside the zeolite pores.[28]

Results and Discussion

Methylation scheme

To study the potential activity of the naphthalenic species during an active MTO cycle, we concentrated on the methylation reactions of the aromatic unit. This step was previously shown to be one of the slowest of the overall reaction cycle;[15] moreover, it is the crucial step before any olefin producing cycle (sidechain or paring) can be initiated. The influence of acidity, through comparison of the protonated aluminosilicate CHA and H-SAPO-34 catalysts, is the focus of another study. The overall studied reaction scheme consists of several types of methylations (Scheme 1). Firstly, a distinction is made between α and β sites (Scheme 1 and Scheme 2), defined by the position of the carbon atom undergoing electrophilic attack.

 © 2009 Wiley-VCH Verlag GmbH & Co. KGaA, Weinheim

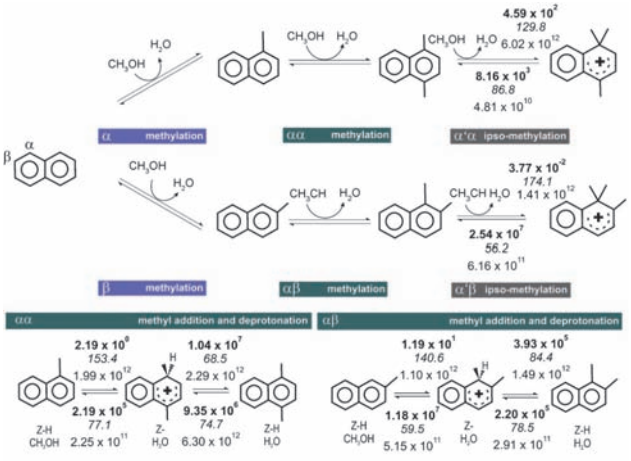

Scheme 1. Methylations and *ipso*-methylations of naphthalenic compounds; rate constants *k* at 670 K (bold) are given in s^{-1}, activation barriers E_a (italics) in kJ mol^{-1}, and pre-exponential factors *A* in s^{-1}.

Secondly, *ipso*-methylations are considered since the created *gem*-methylated species lead to the onset of the olefin-producing routes.[18] The growth of HP species within the confined space of a zeolite cage is represented by two routes resulting in the formation of a trimethylnaphthalenium ion (Scheme 1). The first route consists of three successive α-methylations. The first step is a normal α-methylation of naphthalene (α), followed by a second normal methylation step (αα), and thirdly an *ipso*-methylation (α'α). The second route consists of a normal β-methylation of naphthalene followed by a second normal methylation step (αβ) and an *ipso*-methylation (α'β). Unlike many other theoretical studies, all of our conclusions are based on rate constants at the actual temperature of operation.

These values and the kinetic parameters derived in the 620 to 770 K temperature interval are given in Scheme 1 and Scheme 2. A new code developed in our group was used to efficiently perform the kinetic analysis.[29–31] Reaction barriers and reaction energies for all reaction steps are given in Table 1.

As shown previously for the MFI topology,[15] the stabilizing effect of the zeolite framework on carbenium ions leads to a stepwise methylation behavior as opposed to the concerted gas-phase results. A relatively slow methylation step is followed by a much faster deprotonation, which leads to a neutral aromatic and regeneration of an acidic site in the zeolite framework. The energy barriers at 0 K immediately reveal that there is a non-negligible effect of the confined space; the obtained values are relatively high.

The first methyl addition is more difficult compared to a second addition of a methyl group. At 670 K, $k_{\alpha\alpha}/k_{\alpha}$ equals 77 and $k_{\alpha\beta}/k_{\beta}$ equals 3. The α versus β results indicate that the position of the electrophilic attack is important ($k_{\beta}/k_{\alpha}=122$, at 670 K), although not determining. The methylation at the β position is more hindered by the confinement of the pore, as the large organic compounds are pushed out of the chabazite cage. Moreover, this methylation results in a charged product

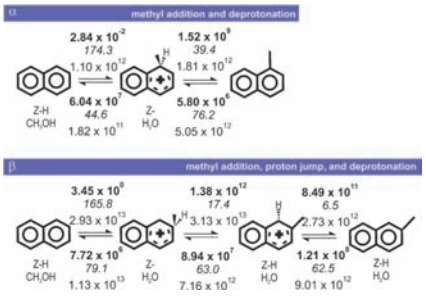

Scheme 2. First methylation (α and β) of naphthalene; rate constants *k* at 670 K (bold) are given in s^{-1}, activation barriers E_a (italics) in kJ mol^{-1}, and pre-exponential factors *A* in s^{-1}.

Table 1. Energy barriers $\Delta E^{\neq}$ and reaction energies ΔE_r (based on electronic energies at the ONIOM(b3lyp/dgtzvp:hf/dgtzvp) level) and corresponding van der Waals corrections. All values in kJ mol^{-1}.

	$\Delta E^{\neq}$	ΔE_r	vdW ($\Delta E^{\neq}$)	vdW (ΔE_r)
α methyl addition	171.7	126.3	−23.4	−15.9
β methyl addition	165.3	85.6	−18.3	−2.0
αα methyl addition	150.6	73.6	−18.3	−6.6
αβ methyl addition	138.3	78.9	−23.0	−8.1
β proton jump	23.3	−43.3	2.0	0.7
α deprotonation	49.6	−39.2	−2.9	2.9
β deprotonation	14.3	−57.7	1.1	−3.2
αα deprotonation	78.8	−8.5	−3.5	0.4
αβ deprotonation	93.9	1.8	−19.2	0.3
α'α *ipso* addition	127.5	40.6	−15.7	−3.4
α'β *ipso* addition	170.2	113.4	−30.2	−18.2
exocyclic deprotonation	96.2	48.3	−8.1	6.8
exocyclic methylation	197.9	162.7	−28.0	−35.6

 © 2009 Wiley-VCH Verlag GmbH & Co. KGaA, Weinheim

species which can not directly be deprotonated due to an unfavorable position of the proton towards an oxygen atom near the aluminum (Scheme 2). A proton jump to a neighboring ring carbon atom is thus needed, which can then be followed by a deprotonation step. The calculated energetics and rate constants indicate that the barriers for this proton shift are very low (i.e., 23.3 kJ mol^{-1}), with a corresponding rate coefficient of 1.38×10^{12} s^{-1} at 670 K. Overall, the methyl additions exhibit high barriers and are highly endothermic leading to slow
reactions.

The α and $\alpha\alpha$ deprotonation reactions are found to be exothermic and the barriers are much lower. Comparison with previous work indicates that the average barrier for deprotonation of the bicyclic compounds is much higher compared to that of the benzenic species within an H-ZSM-5 zeolite.[15] The catalyst acidity (CHA > MFI[32]), proton affinity of the aromatic molecule,[33,34] and topology are responsible for these differences. The chabazite stabilizes the carbenium ions to a large extent[18] and thus deprotonation is less favorable compared to the MFI structure. β deprotonation has a very low barrier and occurs very fast. On the contrary, the $\alpha\beta$ deprotonation exhibits a higher barrier at 0 K since the methyl group at the β position prohibits the transition state structure to take on the optimal geometry. However, conduits, such as water and methanol, which are present inside the zeolite pores, assist the deprotonation. These reactions represent the fastest reaction type studied in this contribution.

For the *ipso*-methylation reactions, the influence of the zeolite confinement is also found to be important. The $\alpha'\alpha$ *ipso* reaction shows an energetically favorable transition-state geometry, whereas the transition state of $\alpha'\beta$ *ipso* reaction differs from the optimal geometry and the barrier increases (127.5 versus 170.2 kJ mol^{-1}). The $\alpha'\beta$-resulting cationic product species is less stabilized by the zeolite framework. The resulting effect on the rate coefficients is very large (difference of approximately four orders of magnitude at 670 K). In Figure 2, the optimized transition state structure of the $\alpha'\beta$ reaction is depicted.

Overall, the methyl addition reactions are found to be the rate-limiting step, which is in accordance with previous reports for the reactions of benzenic species in H-ZSM-5.[15]

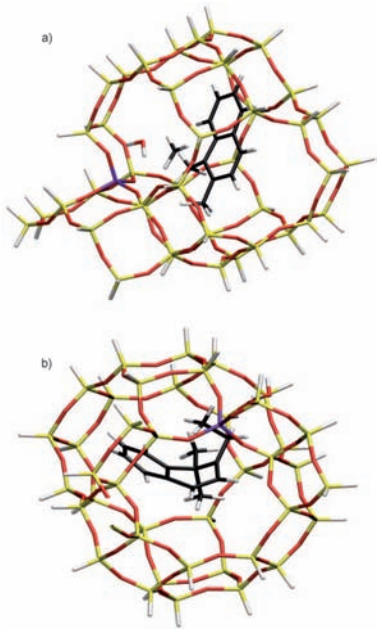

Figure 2. Optimized geometries in the 46T cluster: a) Transition state of the $\alpha'\beta$ *ipso*-methylation; b) product state of the exocyclic methylation.

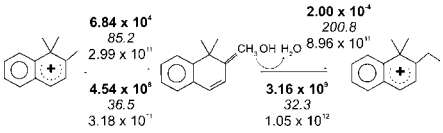

Scheme 3. Exocyclic deprotonation and methylation of the 1,1,2-trimethylnaphthalenium ion; rate constants *k* at 670 K (bold) are given in s^{-1}, activation barriers E_a (italics) in kJ mol^{-1}, and pre-exponential factors *A* in s^{-1}.

Onset of the sidechain route

We previously detected the increased activity of the *ortho*-methylated benzenium species as opposed to the *para*-methylated compound,[35] and therefore the 1,1,2-trimethylnaphthalenium ion is used as a starting point for 2 additional reactions. An exocyclic deprotonation resulting in the formation of a double bond and a final exocyclic (sidechain) methylation are considered (Scheme 3). These reactions form the onset of the sidechain route.

The rate coefficients show that the exocyclic deprotonation is slower than the deprotonation of a ring carbon atom due to a substantially larger energy barrier (Table 1). The final methylation reaction results in the largest compound investigated in this study and clearly challenges the dimensions of the zeolite pore. The calculated barrier and reaction energy are found to be the highest of all reactions investigated in this study. These results suggest that the sidechain path is not an active ethene-producing path for naphthalenic HP species since the CHA cage is found to impose constraints on the transition and product state. The optimized geometry of the latter shows a curled up structure for the bicyclic compound (Figure 2b). Moreover, we recently came to the same conclusion for benzenic HP species in H-ZSM-5.[35] These results show that even for small- or medium-pore systems, bicyclic compounds should

 © 2009 Wiley-VCH Verlag GmbH & Co. KGaA, Weinheim

be regarded as coke precursors rather than active compounds within the sidechain mechanism, as transition and product shape selectivity prohibit the subsequent reactions.

Van der Waals contributions

Since the investigated naphthalenic compounds are bulky organics, van der Waals effects become important. The contributions to the reaction barriers and energies are listed in Table 1. Not surprisingly, the contributions to the energy barriers amount to a decrease of $\pm 20\ kJ\,mol^{-1}$ in the case of methyl additions. For deprotonation reactions, the van der Waals corrections on the reaction energies are smaller, and the small positive values result from the more compact product compared to the reactant structure. The large van der Waals correction for the reaction energy, in the case of the methyl addition to the exocylic double bond, indicates the bulkiness of the product state (Figure 2). Although not negligible, the qualitative picture is not altered by incorporating van der Waals corrections. The influence of the dispersion contributions on the rate coefficients at 670 K is further exemplified (see the Supporting Information, Table S1). The largest effect is found in the case of the $\alpha'\beta$ *ipso*-methylation, for which the rate coefficient of the forward reaction is enlarged by a factor of 226.

Comparison with benzenic HP species

Comparison with the benzenic species (i.e., traditional HP species) is not straightforward as little computational information is available for the CHA topology. We previously calculated the *ipso*-methylation of hexamethylbenzene (HMB),[18] and the reaction barrier and reaction energy for HMB were found to equal 60.8 and $-8.4\ kJ\,mol^{-1}$. Not surprisingly, these values differ to a large extent from those obtained in this work and point out the differences between the presence of additional methyl groups versus an extra aromatic ring. To allow a more direct comparison, we calculated the *ipso*-methylation of *ortho*-xylene, which can directly be compared with the $\alpha'\beta$ *ipso*-methylation of the bicyclic compound. The reaction barrier at 0 K amounts to $129.3\ kJ\,mol^{-1}$, which is indeed smaller than its bicyclic counterpart of $170.2\ kJ\,mol^{-1}$ (Table 1). The reaction energies are 81.2 and $113.4\ kJ\,mol^{-1}$ for the benzenic and naphthalenic compound, respectively. The rate coefficients of the forward reactions differ by four orders of magnitude (1.61×10^{2} versus $3.77\times10^{-2}\ s^{-1}$), whereas the reverse reactions occur at similar rates (3.31×10^{7} versus $2.54\times10^{7}\ s^{-1}$).

Conclusions

We have demonstrated, by means of ab initio computations, that the growth of naphthalenic compounds within a zeolite with chabazite topology is feasible through successive methylation reactions although the rates are smaller compared to benzenic compounds. Our results are in line with earlier experimental observations.

Trimethylated bicyclic molecules should still be considered as active HP intermediates for the MTO process since steric effects between the bulky organic compounds, on one hand, and the zeolite framework on the other hand, do not prohibit the formation of reactive intermediates. This study also indicates that the sidechain mechanism should not be considered as an active ethene-producing cycle for naphthalenic hydrocarbon pool species within the MTO process.

Computational Methods

The investigated zeolite is of the CHA topology and a 46T cluster (with the active site represented by a 8T high level region) was applied. The models were constructed using Zeobuilder.[36] The computations are performed with the Gaussian 03 package[37] using a well-established multilayered method, which combines a ONIOM(b3lyp/dgtzvp:hf/dgtzvp) energy and ONIOM(b3lyp/dgtzvp: MNDO) geometry. Due to the size of our HP species and cluster model, van der Waals contributions were taken into account by using the DFT-D approach as implemented in the Orca software package.[38] Using the optimized ONIOM(b3lyp/dgtzvp:MNDO) geometries, the b3lyp-d method was used to quantify the order of magnitude of the dispersion interactions. In this method, the dispersive energy is described by damped interatomic potentials of the form C_6R^{-6}.[39,40] Rate coefficients and kinetic parameters were computed applying transition state theory as implemented in the TAMkin program, which is a post-processing toolkit for thermochemistry and kinetics analyses.[29–31] For the computation of the kinetic properties, the ONIOM energies (without consideration of the van der Waals corrections) were used. The influence of the dispersion corrections on the rate coefficients can be found in the Supporting Information (Table S1).

Acknowledgements

This work was supported by the Fund for Scientific Research Flanders (FWO), the Research Board of the Ghent University (BOF) and BELSPO, in the frame of the network IAP 6/27. Computational resources and services were provided by Ghent University.

Keywords: ab initio calculations · hydrocarbons · methylation · transition states · zeolites

[1] M. Stöcker, *Microporous Mesoporous Mater.* **1999**, *29*, 3.
[2] J. F. Haw, W. G. Song, D. M. Marcus, J. B. Nicholas, *Acc. Chem. Res.* **2003**, *36*, 317.
[3] B. Yilmaz, U. Müller, *Top. Catal.* **2009**, *52*, 888.
[4] Z.-M. Cui, Q. Liu, Z. Ma, S.-W. Bian, W.-G. Song, *J. Catal.* **2008**, *258*, 83.
[5] S. Teketel, S. Svelle, K. P. Lillerud, U. Olsbye, *ChemCatChem* **2009**, *1*, 78.
[6] W. G. Song, D. M. Marcus, H. Fu, J. O. Ehresmann, J. F. Haw, *J. Am. Chem. Soc.* **2002**, *124*, 3844.
[7] D. M. Marcus, K. A. McLachlan, M. A. Wildman, J. O. Ehresmann, P. W. Kletnieks, J. F. Haw, *Angew. Chem.* **2006**, *118*, 3205; *Angew. Chem. Int. Ed.* **2006**, *45*, 3133.
[8] D. Lesthaeghe, V. Van Speybroeck, G. B. Marin, M. Waroquier *Angew. Chem.* **2006**, *118, 1746; Angew. Chem. Int. Ed.* **2006**, *45*, 1714.
[9] I. M. Dahl, S. Kolboe, *Catal. Lett.* **1993**, *20*, 329.

 © 2009 Wiley-VCH Verlag GmbH & Co. KGaA, Weinheim

[10] I. M. Dahl, S. Kolboe, *J. Catal.* **1994**, *149*, 458.
[11] I. M. Dahl, S. Kolboe, *J. Catal.* **1996**, *161*, 304.
[12] R. M. Dessau, *J. Catal.* **1986**, *99*, 111.
[13] S. Svelle, F. Joensen, J. Nerlov, U. Olsbye, K. P. Lillerud, S. Kolboe, M. Bjørgen, *J. Am. Chem. Soc.* **2006**, *128*, 14770.
[14] M. Bjørgen, F. Joensen, K.-P. Lillerud, U. Olsbye, S. Svelle, *Catal. Today* **2009**, *142*, 90.
[15] D. M. McCann, D. Lesthaeghe, P. W. Kletnieks, D. R. Guenther, M. J. Hayman, V. Van Speybroeck, M. Waroquier, J. F. Haw, *Angew. Chem.* **2008**, *120*, 5257; *Angew. Chem. Int. Ed.* **2008**, *47*, 5179.
[16] N. Hazari, J. A. Labinger, V. J. Scott, *J. Catal.* **2009**, *263*, 266.
[17] D. Lesthaeghe, V. Van Speybroeck, M. Waroquier, *Phys. Chem. Chem. Phys.* **2009**, *11*, 5222.
[18] D. Lesthaeghe, B. De Sterck, V. Van Speybroeck, G. B. Marin, M. Waroquier, *Angew. Chem.* **2007**, *119*, 1333; *Angew. Chem. Int. Ed.* **2007**, *46*, 1311.
[19] J. W. Park, G. Seo, *Appl. Catal. A* **2009**, *356*, 180.
[20] J. W. Park, J. Y. Lee, K. S. Kim, S. B. Hong, G. Seo, *Appl. Catal. A* **2008**, *339*, 36.
[21] F. Bleken, M. Bjørgen, L. Palumbo, S. Bordiga, S. Svelle, K.-P. Lillerud, U. Olsbye, *Top. Catal.* **2009**, 52, 218.
[22] H. Fu, W. Song, J. F. Haw, *Catal. Lett.* **2001**, *76*, 89.
[23] W. Song, H. Fu, J. F. Haw, *J. Phys. Chem. B* **2001**, *105*, 12839.
[24] J. F. Haw, D. M. Marcus, *Top. Catal.* **2005**, *34*, 41.
[25] M. Bjørgen, U. Olsbye, S. Kolboe, *J. Catal.* **2003**, *215*, 30.
[26] L. Palumbo, F. Bonino, P. Beato, M. Bjørgen, A. Zecchina, S. Bordiga, *J. Phys. Chem. C* **2008**, *112*, 9710.
[27] D. Mores, E. Stavitski, M. H. F. Kox, J. Kornatowski, U. Olsbye, B. M. Weckhuysen, *Chem. Eur. J.* **2008**, *14*, 11320.
[28] B. P. C. Hereijgers, F. Bleken, M. H. Nilsen, S. Svelle, K.-P. Lillerud, M. Bjørgen, B. M. Weckhuysen, U. Olsbye, *J. Catal.* **2009**, *264*, 77.
[29] TAMkin is available at http://molmod.ugent.be/code.
[30] A. Ghysels, D. Van Neck, V. Van Speybroeck, T. Verstraelen, M. Waroquier, *J. Chem. Phys.* **2007**, *126*, 224102.
[31] A. Ghysels, V. Van Speybroeck, T. Verstraelen, D. Van Neck, M. Waroquier, *J. Chem. Theory Comput.* **2008**, *4*, 614.
[32] M. Brändle, J. Sauer, *J. Am. Chem. Soc.* **1998**, *120*, 1556.
[33] E. P. Hunter, S. G. Lias, *J. Phys. Chem. Ref. Data* **1998**, *27*, 413.
[34] M. Eckert-Maksić, I. Antol, M. Klessinger, Z. B. Maksić, *J. Phys. Org. Chem.* **1999**, *12*, 597.
[35] D. Lesthaeghe, A. Horré, M. Waroquier, G. B. Marin, V. Van Speybroeck, *Chem. Eur. J.* **2009**, DOI: 10.1002/chem.200901723.
[36] T. Verstraelen, V. Van Speybroeck, M. Waroquier, *J. Chem. Inf. Model.* **2008**, *48*, 1530.
[37] *Gaussian 03*, Revision C.02, M. J. Frisch, G. W. Trucks, H. B. Schlegel, G. E. Scuseria, M. A. Robb, J. R. Cheeseman, J. A. Montgomery, Jr., T. Vreven, K. N. Kudin, J. C. Burant, J. M. Millam, S. S. Iyengar, J. Tomasi, V. Barone, B. Mennucci, M. Cossi, G. Scalmani, N. Rega, G. A. Petersson, H. Nakatsuji, M. Hada, M. Ehara, K. Toyota, R. Fukuda, J. Hasegawa, M. Ishida, T. Nakajima, Y. Honda, O. Kitao, H. Nakai, M. Klene, X. Li, J. E. Knox, H. P. Hratchian, J. B. Cross, V. Bakken, C. Adamo, J. Jaramillo, R. Gomperts, R. E. Stratmann, O. Yazyev, A. J. Austin, R. Cammi, C. Pomelli, J. W. Ochterski, P. Y. Ayala, K. Morokuma, G. A. Voth, P. Salvador, J. J. Dannenberg, V. G. Zakrzewski, S. Dapprich, A. D. Daniels, M. C. Strain, O. Farkas, D. K. Malick, A. D. Rabuck, K. Raghavachari, J. B. Foresman, J. V. Ortiz, Q. Cui, A. G. Baboul, S. Clifford, J. Cioslowski, B. B. Stefanov, G. Liu, A. Liashenko, P. Piskorz, I. Komaromi, R. L. Martin, D. J. Fox, T. Keith, M. A. Al-Laham, C. Y. Peng, A. Nanayakkara, M. Challacombe, P. M. W. Gill, B. Johnson, W. Chen, M. W. Wong, C. Gonzalez, and J. A. Pople, Gaussian, Inc., Wallingford CT, **2004**.
[38] Orca, Version 2.6, An Ab Initio, DFT and Semiempirical Electronic Structure package, F. Neese, University of Bonn, Germany, **2008**.
[39] S. Grimme, *J. Comput. Chem.* **2004**, *25*, 1463.
[40] S. Svelle, C. Tuma, X. Rozanska, T. Kerber, J. Sauer, *J. Am. Chem. Soc.* **2009**, *131*, 816.

Received: July 26, 2009
Published online on October 20, 2009

 © 2009 Wiley-VCH Verlag GmbH & Co. KGaA, Weinheim

A

List of publications

Updated October 2012

A.1 International peer-reviewed journals

1. K. Hemelsoet, A. Nollet, M. Vandichel, D. Lesthaeghe, V. Van Speybroeck, and M. Waroquier.
   The effect of confined space on the growth of naphthalenic species in a chabazite-type catalyst: A molecular modeling study.
   Chemcatchem **2009**, *1*, 373-378,
   Times Cited: 12, first IF (2011): 5.207, 24/134 [Q1].

2. K. Leus, I. Muylaert, M. Vandichel, G. B. Marin, M. Waroquier, V. Van Speybroeck, and P. Van der Voort.
   The remarkable catalytic activity of the saturated metal organic framework V-MIL-47 in the cyclohexene oxidation.
   Chemical Communications **2010**, *46*, 5085-5087,
   Times Cited: 12, IF (2011): 6.169, 17/152 [Q1].

3. M. Vandichel, D. Lesthaeghe, J. Van der Mynsbrugge, M. Waroquier, and V. Van Speybroeck.
   Assembly of cyclic hydrocarbons from ethene and propene in acid zeolite catalysis to produce active catalytic sites for MTO conversion.
   Journal of Catalysis **2010**, *271*, 67-78,
   Times Cited: 19, IF (2011): 6.002, 5/133 [Q1].

4. D. Lesthaeghe, J. Van der Mynsbrugge, M. Vandichel, M. Waroquier, and V. Van Speybroeck.

Full theoretical cycle for both ethene and propene formation during methanol-to-olefin conversion in H-ZSM-5.
Chemcatchem **2011**, *3*, 208-212,
Times Cited: 13, first IF (2011): 5.207 , 24/134 [Q1].

5. V. Van Speybroeck, J. Van der Mynsbrugge, M. Vandichel, K. Hemelsoet, D. Lesthaeghe, A. Ghysels, G. B. Marin, and M. Waroquier.
First principle kinetic studies of zeolite-catalyzed methylation reactions.
Journal of the American Chemical Society **2011**, *133*, 888-899,
Times Cited: 16, IF (2011): 9.907, 11/152 [Q1].

6. K. Leus,* M. Vandichel,* Y. Y. Liu, I. Muylaert, J. Musschoot, S. Pyl, H. Vrielinck, F. Callens, G. B. Marin, C. Detavernier, P. V. Wiper, Y. Z. Khimyak, M. Waroquier, V. Van Speybroeck, and P. Van der Voort.
* = equal first author
The coordinatively saturated vanadium MIL-47 as a low leaching heterogeneous catalyst in the oxidation of cyclohexene.
Journal of Catalysis **2012**, *285*, 196-207,
Times Cited: 2, IF (2011): 6.002, 5/133 [Q1].

7. F. Vermoortele, M. Vandichel, B. Van de Voorde, R. Ameloot, M. Waroquier, V. Van Speybroeck, and D.E. De Vos.
Electronic effects of linker substitution on lewis acid catalysis with metal-organic frameworks.
Angewandte Chemie-International Edition **2012**, *51*, 4887-4890,
Times Cited: 1, IF (2011): 13.455, 7/152 [Q1].

8. J. Van der Mynsbrugge, K. Hemelsoet, M. Vandichel, M. Waroquier, V. Van Speybroeck.
Efficient Approach for the Computational Study of Alcohol and Nitrile Adsorption in H-ZSM-5.
Journal of Physical Chemistry C **2012**, *116*, 5499-5508,
Times Cited: 3, IF (2011): 4.805, 23/231 [Q1].

9. A. Ghysels, M. Vandichel, T. Verstraelen, D.E. De Vos, M. Van der Veen, M. Waroquier, and V. Van Speybroeck.
Host-guest and guest-guest interactions between xylene isomers.
Theoretical Chemistry Accounts **2012**, *131*, 1234-1246,
Times Cited: 0, IF (2011): 2.162, 63/134 [Q2].

10. M. Vandichel, K. Leus, P. Van Der Voort, M. Waroquier, and V. Van Speybroeck.
Mechanistic insight into the cyclohexene epoxidation with $VO(acac)_2$ and *tert*-butyl hydroperoxide.
Journal of Catalysis **2012**, *294*, 1-18,
Times Cited: 0, IF (2011): 6.002, 5/133 [Q1].

11. L. Vanduyfhuys, T. Verstraelen, M. Vandichel, M. Waroquier, V. Van Speybroeck.
Ab initio parametrized force field for the flexible metal-organic framework MIL-53(Al).
Journal of Chemical Theory and Computation **2012**, *8*, 3217 - 3231.
Times Cited: 0, IF (2011): 5.215, 2/32 [Q1].

12. Y.-Y. Liu, S. Couck, M. Vandichel, M. Grzywa, K. Leus, S. Biswas, D. Volkmer, J. Gascon, F. Kapteijn, J.F.M. Denayer, M. Waroquier, V. Van Speybroeck and P. Van Der Voort.
A new V^{IV} based metal-organic framework having framework flexibility and high CO_2 adsorption capacity.
Inorganic Chemistry **2012**, in revision,
Times Cited: 0, IF (2011): 4.601, 3/43 [Q1].

13. K. Leus, S. Couck, M. Vandichel, G. Vanhaelewyn, Y.-Y. Liu, G.B. Marin, I. Van Driessche, D. Depla, M. Waroquier, V. Van Speybroeck, J.F.M. Denayer, P. Van Der Voort.
Synthesis, characterization and adsorption properties of an amino functionalized Metal Organic Framework: NH_2-MIL-47(V).
Physical Chemistry Chemical Physics **2012**, in press.
Times Cited: 0, IF (2012): 3.573, 5/32 [Q1].

14. M. Vandichel, S. Biswas, K. Leus, J. Paier, J. Sauer, P. Van Der Voort, M. Waroquier, and V. Van Speybroeck.
Performance of Vanadium MIL-47 and linker substituted variants as catalysts for oxidation reactions: a combined theoretical and experimental approach.
2012, in preparation.

15. M. Vandichel, F. Vermoortele, S. Cottenie, D.E. De Vos, M. Waroquier, and V. Van Speybroeck.
Kinetic insight on the diastereoselectivity of the citronellal cyclization on various catalysts.
2012, in preparation.

A.2 Oral contributions

16. M. Vandichel, Frederik Vermoortele, Dirk De Vos, Michel Waroquier, Veronique Van Speybroeck.
Modeling Lewis acid catalyzed reactions in MOFs: How to solve the challenges?
MOF2012, Edinbrugh, Scotland, 17 September 2012

17. K. Leus and M. Vandichel.
Synthesis of new Vanadium containing Metal Organic Frameworks (V-MOFs) for applications in oxidation catalysis and adsorption/separation processes.
Doctoral Symposium WE, Ghent, Belgium, 22 March 2012

18. M. Vandichel, S. Cottenie, F. Vermoortele, D. De Vos, M. Waroquier, V. Van Speybroeck.
Modeling Lewis catalyzed reactions in Metal Organic Frameworks.
NCCC XII, Noordwijkerhout, Noordwijkerhout, The Netherlands, 28 February - 2 March 2011

19. V. Van Speybroeck, J. Van der Mynsbrugge, M. Vandichel, K. Hemelsoet, D. Lesthaeghe, M. Waroquier.
First principle kinetic studies of zeolite-catalyzed methylation reactions: towards kinetic accuracy for rate constants. 1st International Workshop of the European Nanoporous Materials Institute of Excellence (ENMIX), Antwerp, Belgium, 4 October 2010

20. M. Vandichel, J. Van der Mynsbrugge, T. Verstraelen, M. Maes, L. Alaerts, D. De Vos, M. Waroquier, V. Van Speybroeck.
Insights on the adsorption behavior of aromatics in MIL-47 and MIL-53 from a theoretical perspective.
NCCC XI, Noordwijkerhout, Noordwijkerhout, The Netherlands, 1-3 March 2010

A.3 Poster contributions

Research results were presented as poster presentations on several international conferences.

Bibliography

[1] Cronstedt, A. F. *Akad. Handl. Stockholm* **1756**, *18*, 120.

[2] Maesen, T. in *Introduction to Zeolite Science and Technology*, Vol. 168 of *Studies in Surface Science and Catalysis*, 3^{rd} ed., Čejka, J.; van Bekkum, H.; Corma, A.; Schüth, F. , Eds.; Elsevier; Radarweg 29, PO Box 211, 1000 AE Amsterdam, The Netherlands, 2007, pp. 1–12.

[3] Barrer, R. M.; Denny, P. J. *Journal of the Chemical Society* **1961**, 971.

[4] Kerr, G. T.; Kokotailo, G. T. *Journal of the American Chemical Society* **1961**, *83*, 4675.

[5] Martínez, C.; Corma, A. *Coordination Chemistry Reviews* **2011**, *255*, 1558.

[6] Cundy, C. S.; Cox, P. A. *Chemical Reviews* **2003**, *103*, 663.

[7] Baerlocher, C.; McCusker, L. B.; Oslon, D. *Atlas of Zeolite Framework Types*; Elsevier; 3^{rd} ed., 2007.

[8] McCusker, L. B.; Baerlocher, C. in *Introduction to Zeolite Science and Technology*, Vol. 168 of *Studies in Surface Science and Catalysis*, 3^{rd} ed., Čejka, J.; van Bekkum, H.; Corma, A.; Schüth, F. , Eds.; Elsevier; Radarweg 29, PO Box 211, 1000 AE Amsterdam, The Netherlands, 2007, pp. 13–38.

[9] http://www.iza-structure.org/databases. Last accessed May 2012.

[10] Chen, N. Y. *Industrial & Engineering Chemistry Research* **2001**, *40*, 4157.

[11] Argauer, R.J.; Landolt, G.R. Crystalline zeolite ZSM-5 and method of preparing the same, *US Patent 3,702,886*, **1972**.

[12] Verstraelen, T. , Ph.D. thesis, Center for Molecular Modeling, University of Gent, Molecular Modeling of the Synthesis of Zeolites and Related Nanoporous Materials, 2009.

[13] Yilmaz, B.; Müller, U. *Topics in Catalysis* **2009**, *52*, 888.

[14] Vermeiren, W.; Gilson, J. P. *Topics in Catalysis* **2009**, *52*, 1131.

[15] Kresge, C. T.; Leonowicz, M. E.; Roth, W. J.; Vartuli, J. C.; Beck, J. S. *Nature* **1992**, *359*, 710.

[16] Beck, J. S.; Vartuli, J. C.; Roth, W. J.; Leonowicz, M. E.; Kresge, C. T.; Schmitt, K. D.; Chu, C. T. W.; Olson, D. H.; Sheppard, E. W.; McCullen, S. B.; Higgins, J. B.; Schlenker, J. L. *Journal of the American Chemical Society* **1992**, *114*, 10834.

[17] Van Der Voort, P. Nanoporous Materials, optional course for the 2nd Master Chemistry, 2009.

[18] Zhao, D.; Feng, J.; Huo, Q.; Melosh, N.; Fredrickson, G. H.; Chmelka, B. F.; Stucky, G. D. *Science* **1998**, *279*, 548.

[19] Melero, J. A.; van Grieken, R.; Morales, G. *Chemical Reviews* **2006**, *106*, 3790.

[20] Mizoshita, N.; Tani, T.; Inagaki, S. *Chemical Society Reviews* **2011**, *40*, 789.

[21] Hoffmann, F.; Fröba, M. *Chemical Society Reviews* **2011**, *40*, 608.

[22] Yang, Q. H.; Liu, J.; Zhang, L.; Li, C. *Journal of Materials Chemistry* **2009**, *19*, 1945.

[23] Soler-Illia, G. J. A. A.; Azzaroni, O. *Chemical Society Reviews* **2011**, *40*, 1107.

[24] Hoskins, B. F.; Robson, R. *Journal of the American Chemical Society* **1989**, *111*, 5962.

[25] Hoskins, B. F.; Robson, R. *Journal of the American Chemical Society* **1990**, *112*, 1546.

[26] Yaghi, O. M.; Li, G.; Li, H. *Nature* **1995**, *378*, 703.

[27] Rowsell, J. L. C.; Yaghi, O. M. *Microporous and Mesoporous Materials* **2004**, *73*, 3.

[28] O'Keeffe, M. *Chemical Society Reviews* **2009**, *38*, 1215.

[29] Tomic, E. A. *Journal of Applied Polymer Science* **1965**, *9*, 3745.

[30] Biondi, C.; Bonamico, M.; Torelli, L.; Vaciago, A. *Chemical Communications* **1965**, 191.

[31] Czaja, A. U.; Trukhan, N.; Müller, U. *Chemical Society Reviews* **2009**, *38*, 1284.

[32] Li, H.; Eddaoudi, M.; O'Keeffe, M.; Yaghi, O. M. *Nature* **1999**, *402*, 276.

[33] Wells, A. F. *Structural Inorganic Chemistry*; Oxford [Oxfordshire]; Clarendon Press, 1984.

[34] Eddaoudi, M.; Kim, J.; Rosi, N.; Vodak, D.; Wachter, J.; O'Keeffe, M.; Yaghi, O. M. *Science* **2002**, *295*, 469.

[35] Rowsell, J. L. C.; Millward, A. R.; Park, K. S.; Yaghi, O. M. *Journal of the American Chemical Society* **2004**, *126*, 5666.

[36] Férey, G. *Chemical Society Reviews* **2008**, *37*, 191.

[37] Chui, S. S. Y.; Lo, S. M. F.; Charmant, J. P. H.; Orpen, A. G.; Williams, I. D. *Science* **1999**, *283*, 1148.

[38] Serre, C.; Millange, F.; Thouvenot, C.; Noguès, M.; Marsolier, G.; Loueër, D.; Férey, G. *Journal of the American Chemical Society* **2002**, *124*, 13519.

[39] Li, J.-R.; Sculley, J.; Zhou, H.-C. *Chemical Reviews* **2012**, *112*, 869.

[40] Kitagawa, S.; Kitaura, R.; Noro, S. *Angewandte Chemie-International Edition* **2004**, *43*, 2334.

[41] Ma, S.; Zhou, H.-C. *Journal of the American Chemical Society* **2006**, *128*, 11734.

[42] Liu, Y.; Kravtsov, V. C.; Larsen, R.; Eddaoudi, M. *Chemical Communications* **2006**, 1488.

[43] Park, K. S.; Ni, Z.; Côté, A. P.; Choi, J. Y.; Huang, R.; Uribe-Romo, F. J.; Chae, H. K.; O'Keeffe, M.; Yaghi, O. M. *Proceedings of the National Academy of Sciences* **2006**, *103*, 10186.

[44] Mantion, A.; Massüger, L.; Rabu, P.; Palivan, C.; McCusker, L. B.; Taubert, A. *Journal of the American Chemical Society* **2008**, *130*, 2517.

[45] Lin, J.-B.; Zhang, J.-P.; Chen, X.-M. *Journal of the American Chemical Society* **2010**, *132*, 6654.

[46] El-Kaderi, H. M.; Hunt, J. R.; Mendoza-Cortés, J. L.; Côté, A. P.; Taylor, R. E.; O'Keeffe, M.; Yaghi, O. M. *Science* **2007**, *316*, 268.

[47] Imaz, I.; Rubio-Martínez, M.; An, J.; Solé-Font, I.; Rosi, N. L.; Maspoch, D. *Chemical Communications* **2011**, *47*, 7287.

[48] IUPAC project: "Coordination polymers and metal organic frameworks: terminology and nomenclature guidelines"; **2009**, http://www.iupac.org/web/ins/2009-012-2-200.

[49] Batten, S. R.; Champness, N. R.; Chen, X.-M.; Garcia-Martinez, J.; Kitagawa, S.; Öhrström, L.; O'Keeffe, M.; Suh, M. P.; Reedijk, J. *CrystEngComm* **2012**, *14*, 3001.

[50] Cavka, J. H.; Jakobsen, S.; Olsbye, U.; Guillou, N.; Lamberti, C.; Bordiga, S.; Lillerud, K. P. *Journal of the American Chemical Society* **2008**, *130*, 13850.

[51] Barthelet, K.; Marrot, J.; Riou, D.; Férey, G. *Angewandte Chemie-International Edition* **2002**, *41*, 281.

[52] Liu, Y.-Y.; Couck, S.; Vandichel, M.; Grzywa, M.; Leus, K.; Biswas, S.; Volkmer, D.; Gascon, J.; Kapteijn, F.; Denayer, J.; Waroquier, M.; Van Speybroeck, V.; Van Der Voort, P. *Inorganic Chemistry* **2012**, , in revision.

[53] Dhakshinamoorthy, A.; Alvaro, M.; Garcia, H. *Catalysis Science & Technology* **2011**, *1*, 856.

[54] Jiang, J. W.; Babarao, R.; Hu, Z. Q. *Chemical Society Reviews* **2011**, *40*, 3599.

[55] Coster, D.; Blumenfeld, A. L.; Fripiat, J. J. *The Journal of Physical Chemistry* **1994**, *98*, 6201.

[56] Han, S. S.; Choi, S.-H.; van Duin, A. C. T. *Chemical Communications* **2010**, *46*, 5713.

[57] Low, J. J.; Benin, A. I.; Jakubczak, P.; Abrahamian, J. F.; Faheem, S. A.; Willis, R. R. *Journal of the American Chemical Society* **2009**, *131*, 15834.

[58] Zhou, H.-C.; Long, J. R.; Yaghi, O. M. *Chemical Reviews* **2012**, *112*, 673.

[59] Müller, U.; Schubert, M.; Teich, F.; Pütter, H.; Schierle-Arndt, K.; Pastré, J. *Journal of Materials Chemistry* **2006**, *16*, 626.

[60] Kuppler, R. J.; Timmons, D. J.; Fang, Q. R.; Li, J. R.; Makal, T. A.; Young, M. D.; Yuan, D. Q.; Zhao, D.; Zhuang, W. J.; Zhou, H. C. *Coordination Chemistry Reviews* **2009**, *253*, 3042.

[61] Horike, S.; Shimomura, S.; Kitagawa, S. *Nat Chem* **2009**, *1*, 695.

[62] Qiu, S.; Zhu, G. *Coordination Chemistry Reviews* **2009**, *253*, 2891.

[63] Janiak, C.; Vieth, J. K. *New Journal of Chemistry* **2010**, *34*, 2366.

[64] Meek, S. T.; Greathouse, J. A.; Allendorf, M. D. *Advanced Materials* **2011**, *23*, 249.

[65] O'Keeffe, M.; Yaghi, O. M. *Chemical Reviews* **2012**, *112*, 675.

[66] Tranchemontagne, D. J.; Mendoza-Cortés, J. L.; O'Keeffe, M.; Yaghi, O. M. *Chemical Society Reviews* **2009**, *38*, 1257.

[67] O'Keeffe, M.; Peskov, M. A.; Ramsden, S. J.; Yaghi, O. M. *Accounts of Chemical Research* **2008**, *41*, 1782.

[68] Delgado-Friedrichs, O.; O'Keeffe, M.; Yaghi, O. M. *Physical Chemistry Chemical Physics* **2007**, *9*, 1035.

[69] O'Keeffe, M.; Eddaoudi, M.; Li, H. L.; Reineke, T.; Yaghi, O. M. *Journal of Solid State Chemistry* **2000**, *152*, 3.

[70] Yaghi, O. M.; O'Keeffe, M.; Ockwig, N. W.; Chae, H. K.; Eddaoudi, M.; Kim, J. *Nature* **2003**, *423*, 705.

[71] Alaerts, L. , Ph.D. thesis, Centre for Surface Chemistry and Catalysis, Katholieke Universiteit Leuven, Application of Metal-Organic Frameworks in Catalysis and Adsorption, 2008.

[72] Yaghi, O. M.; O'Keeffe, M.; Kanatzidis, M. *Journal of Solid State Chemistry* **2000**, *152*, 1.

[73] Eberhart, M. E.; Clougherty, D. P. *Nature Materials* **2004**, *3*, 659.

[74] Jansen, M.; Schön, J. C. *Angewandte Chemie International Edition* **2006**, *45*, 3406.

[75] Barthelet, K.; Marrot, J.; Férey, G.; Riou, D. *Chemical Communications* **2004**, 520.

[76] Vandichel, M. Research ideas which are currently explored, 2012.

[77] Biswas, S.; Couck, S.; Grzywa, M.; Denayer, J. F. M.; Volkmer, D.; Van Der Voort, P. *European Journal of Inorganic Chemistry* **2012**, 2481.

[78] Volkringer, C.; Loiseau, T.; Guillou, N.; Férey, G.; Haouas, M.; Taulelle, F.; Elkaim, E.; Stock, N. *Inorganic Chemistry* **2010**, *49*, 9852.

[79] Stavitski, E.; Goesten, M.; Juan-Alcañiz, J.; Martinez-Joaristi, A.; Serra-Crespo, P.; Petukhov, A. V.; Gascon, J.; Kapteijn, F. *Angewandte Chemie International Edition* **2011**, *50*, 9624.

[80] Barthelet, K.; Adil, K.; Millange, F.; Serre, C.; Riou, D.; Férey, G. *Journal of Materials Chemistry* **2003**, *13*, 2208.

[81] Guillou, N.; Livage, C.; Drillon, M.; Férey, G. *Angewandte Chemie-International Edition* **2003**, *42*, 5314.

[82] Livage, C.; Forster, P. M.; Guillou, N.; Tafoya, M. M.; Cheetham, A. K.; Férey, G. *Angewandte Chemie International Edition* **2007**, *46*, 5877.

[83] Forster, P. M.; Stock, N.; Cheetham, A. K. *Angewandte Chemie International Edition* **2005**, *44*, 7608.

[84] Bauer, S.; Stock, N. *Angewandte Chemie International Edition* **2007**, *46*, 6857.

[85] Stock, N.; Biswas, S. *Chemical Reviews* **2012**, *112*, 933.

[86] Czaja, A. U.; Leung, E.; Trukhan, N.; Müller, U. in *Metal-Organic Frameworks*, Farrusseng, D. , Eds.; Wiley-VCH Verlag GmbH & Co. KGaA; Bochstr. 12, 69469 Weinheim, Germany, 2011, pp. 339–352.

[87] Yilmaz, B.; Trukhan, N.; Müller, U. *Chinese Journal of Catalysis* **2012**, *33*, 3.

[88] Gaab, M.; Trukhan, N.; Maurer, S.; Gummaraju, R.; Müller, U. *Microporous and Mesoporous Materials* **2012**, *157*, 131.

[89] Bétard, A.; Fischer, R. A. *Chemical Reviews* **2012**, *112*, 1055.

[90] Shekhah, O.; Liu, J.; Fischer, R. A.; Wöll, C. *Chemical Society Reviews* **2011**, *40*, 1081.

[91] Gascon, J.; Kapteijn, F. *Angewandte Chemie International Edition* **2010**, *49*, 1530.

[92] Zacher, D.; Shekhah, O.; Wöll, C.; Fischer, R. A. *Chemical Society Reviews* **2009**, *38*, 1418.

[93] Lohe, M. R.; Rose, M.; Kaskel, S. *Chemical Communications* **2009**, 6056.

[94] Ameloot, R.; Vermoortele, F.; Vanhove, W.; Roeffaers, M. B. J.; Sels, B. F.; De Vos, D. E. *Nat Chem* **2011**, *3*, 382.

[95] Halper, S. R.; Do, L.; Stork, J. R.; Cohen, S. M. *Journal of the American Chemical Society* **2006**, *128*, 15255.

[96] Kitaura, R.; Onoyama, G.; Sakamoto, H.; Matsuda, R.; Noro, S.-i.; Kitagawa, S. *Angewandte Chemie International Edition* **2004**, *43*, 2684.

[97] Cohen, S. M. *Chemical Reviews* **2012**, *112*, 970.

[98] Farrusseng, D.; Canivet, J.; Quadrelli, A. in *Metal-Organic Frameworks*, Farrusseng, D. , Eds.; Wiley-VCH Verlag GmbH & Co. KGaA; Bochstr. 12, 69469 Weinheim, Germany, 2011, pp. 23–48.

[99] Tanabe, K. K.; Cohen, S. M. *Chemical Society Reviews* **2011**, *40*, 498.

[100] Wang, Z.; Cohen, S. M. *Chemical Society Reviews* **2009**, *38*, 1315.

[101] Wang, Z.; Tanabe, K. K.; Cohen, S. M. *Inorganic Chemistry* **2008**, *48*, 296.

[102] Garibay, S. J.; Wang, Z.; Cohen, S. M. *Inorganic Chemistry* **2010**, *49*, 8086.

[103] Garibay, S. J.; Cohen, S. M. *Chemical Communications* **2010**, *46*, 7700.

[104] Canivet, J.; Aguado, S.; Daniel, C.; Farrusseng, D. *Chemcatchem* **2011**, *3*, 675.

[105] Volkringer, C.; Cohen, S. M. *Angewandte Chemie-International Edition* **2010**, *49*, 4644.

[106] Morris, W.; Doonan, C. J.; Furukawa, H.; Banerjee, R.; Yaghi, O. M. *Journal of the American Chemical Society* **2008**, *130*, 12626.

[107] Mulfort, K. L.; Farha, O. K.; Stern, C. L.; Sarjeant, A. A.; Hupp, J. T. *Journal of the American Chemical Society* **2009**, *131*, 3866.

[108] Goto, Y.; Sato, H.; Shinkai, S.; Sada, K. *Journal of the American Chemical Society* **2008**, *130*, 14354.

[109] Bernt, S.; Guillerm, V.; Serre, C.; Stock, N. *Chemical Communications* **2011**, *47*, 2838.

[110] Goesten, M. G.; Juan-Alcañiz, J.; Ramos-Fernandez, E. V.; Sai Sankar Gupta, K. B.; Stavitski, E.; van Bekkum, H.; Gascon, J.; Kapteijn, F. *Journal of Catalysis* **2011**, *281*, 177.

[111] Goesten, M. G.; Sai Sankar Gupta, K. B.; Ramos-Fernandez, E. V.; Khajavi, H.; Gascon, J.; Kapteijn, F. *CrystEngComm* **2012**, *14*, 4109.

[112] Yoon, M.; Srirambalaji, R.; Kim, K. *Chemical Reviews* **2012**, *112*, 1196.

[113] Ma, L.; Abney, C.; Lin, W. *Chemical Society Reviews* **2009**, *38*, 1248.

[114] Lee, J.; Farha, O. K.; Roberts, J.; Scheidt, K. A.; Nguyen, S. T.; Hupp, J. T. *Chemical Society Reviews* **2009**, *38*, 1450.

[115] Farrusseng, D.; Aguado, S.; Pinel, C. *Angewandte Chemie-International Edition* **2009**, *48*, 7502.

[116] Dhakshinamoorthy, A.; Garcia, H. *Chemical Society Reviews* **2012**, *41*, 5262.

[117] Liu, Y.; Xuan, W.; Cui, Y. *Advanced Materials* **2010**, *22*, 4112.

[118] Sumida, K.; Rogow, D. L.; Mason, J. A.; McDonald, T. M.; Bloch, E. D.; Herm, Z. R.; Bae, T.-H.; Long, J. R. *Chemical Reviews* **2012**, *112*, 724.

[119] Suh, M. P.; Park, H. J.; Prasad, T. K.; Lim, D.-W. *Chemical Reviews* **2012**, *112*, 782.

[120] Wu, H.; Gong, Q.; Olson, D. H.; Li, J. *Chemical Reviews* **2012**, *112*, 836.

[121] Férey, G.; Serre, C.; Devic, T.; Maurin, G.; Jobic, H.; Llewellyn, P. L.; De Weireld, G.; Vimont, A.; Daturi, M.; Chang, J.-S. *Chemical Society Reviews* **2011**, *40*, 550.

[122] Murray, L. J.; Dinca, M.; Long, J. R. *Chemical Society Reviews* **2009**, *38*, 1294.

[123] Han, S. S.; Mendoza-Cortés, J. L.; Goddard III, W. A. *Chemical Society Reviews* **2009**, *38*, 1460.

[124] Li, J.-R.; Kuppler, R. J.; Zhou, H.-C. *Chemical Society Reviews* **2009**, *38*, 1477.

[125] Cui, Y.; Yue, Y.; Qian, G.; Chen, B. *Chemical Reviews* **2012**, *112*, 1126.

[126] Kreno, L. E.; Leong, K.; Farha, O. K.; Allendorf, M.; Van Duyne, R. P.; Hupp, J. T. *Chemical Reviews* **2012**, *112*, 1105.

[127] Wang, C.; Zhang, T.; Lin, W. *Chemical Reviews* **2012**, *112*, 1084.

[128] Rocha, J.; Carlos, L. D.; Paz, F. A. A.; Ananias, D. *Chemical Society Reviews* **2011**, *40*, 926.

[129] Allendorf, M. D.; Bauer, C. A.; Bhakta, R. K.; Houk, R. J. T. *Chemical Society Reviews* **2009**, *38*, 1330.

[130] Zhang, W.; Xiong, R.-G. *Chemical Reviews* **2012**, *112*, 1163.

[131] Clemente-León, M.; Coronado, E.; Martí-Gastaldo, C.; Romero, F. M. *Chemical Society Reviews* **2011**, *40*, 473.

[132] Kurmoo, M. *Chemical Society Reviews* **2009**, *38*, 1353.

[133] Horcajada, P.; Gref, R.; Baati, T.; Allan, P. K.; Maurin, G.; Couvreur, P.; Férey, G.; Morris, R. E.; Serre, C. *Chemical Reviews* **2012**, *112*, 1232.

[134] Getman, R. B.; Bae, Y.-S.; Wilmer, C. E.; Snurr, R. Q. *Chemical Reviews* **2012**, *112*, 703.

[135] Düren, T.; Bae, Y.-S.; Snurr, R. Q. *Chemical Society Reviews* **2009**, *38*, 1237.

[136] Zhang, J.-P.; Zhang, Y.-B.; Lin, J.-B.; Chen, X.-M. *Chemical Reviews* **2012**, *112*, 1001.

[137] Gagnon, K. J.; Perry, H. P.; Clearfield, A. *Chemical Reviews* **2012**, *112*, 1034.

[138] Shimizu, G. K. H.; Vaidhyanathan, R.; Taylor, J. M. *Chemical Society Reviews* **2009**, *38*, 1430.

[139] Smaldone, R. A.; Forgan, R. S.; Furukawa, H.; Gassensmith, J. J.; Slawin, A. M. Z.; Yaghi, O. M.; Stoddart, J. F. *Angewandte Chemie International Edition* **2010**, *49*, 8630.

[140] Pu, F.; Liu, X.; Xu, B.; Ren, J.; Qu, X. *Chemistry A European Journal* **2012**, *18*, 4322.

[141] http://climate.nasa.gov/evidence/. Last accessed May 2012.

[142] D'Alessandro, D.; Smit, B.; Long, J. *Angewandte Chemie International Edition* **2010**, *49*, 6058.

[143] Keskin, S.; van Heest, T.; Sholl, D. *Chemsuschem* **2010**, *3*, 879.

[144] Caskey, S. R.; Wong-Foy, A. G.; Matzger, A. J. *Journal of the American Chemical Society* **2008**, *130*, 10870.

[145] Dietzel, P. D. C.; Panella, B.; Hirscher, M.; Blom, R.; Fjellvåg, H. *Chemical Communications* **2006**, 959.

[146] Dietzel, P. D. C.; Morita, Y.; Blom, R.; Fjellvåg, H. *Angewandte Chemie International Edition* **2005**, *44*, 6354.

[147] Rosi, N. L.; Kim, J.; Eddaoudi, M.; Chen, B.; O'Keeffe, M.; Yaghi, O. M. *Journal of the American Chemical Society* **2005**, *127*, 1504.

[148] Zhou, W.; Wu, H.; Yildirim, T. *Journal of the American Chemical Society* **2008**, *130*, 15268.

[149] Trukhan, N.; Müller, U.; Panchenko, A.; Malkowski, I.M.; Fisher, A. Novel metal-organic frameworks as electrode material for lithium ion accumulators, *International Patent WO 2011/132147 A1*, **2011**.

[150] Deng, H.; Grunder, S.; Cordova, K. E.; Valente, C.; Furukawa, H.; Hmadeh, M.; Gndara, F.; Whalley, A. C.; Liu, Z.; Asahina, S.; Kazumori, H.; OKeeffe, M.; Terasaki, O.; Stoddart, J. F.; Yaghi, O. M. *Science* **2012**, *336*, 1018.

[151] Chae, H. K.; Siberio-Pérez, D. Y.; Kim, J.; Go, Y.; Eddaoudi, M.; Matzger, A. J.; O'Keeffe, M.; Yaghi, O. M. *Nature* **2004**, *427*, 523.

[152] Yazaydin, A. O.; Snurr, R. Q.; Park, T.-H.; Koh, K.; Liu, J.; LeVan, M. D.; Benin, A. I.; Jakubczak, P.; Lanuza, M.; Galloway, D. B.; Low, J. J.; Willis, R. R. *Journal of the American Chemical Society* **2009**, *131*, 18198.

[153] Park, J.; Kim, H.; Han, S. S.; Jung, Y. *The Journal of Physical Chemistry Letters* **2012**, *3*, 826.

[154] Fu, Y.; Sun, D.; Chen, Y.; Huang, R.; Ding, Z.; Fu, X.; Li, Z. *Angewandte Chemie International Edition* **2012**, *51*, 3364.

[155] http://teslatech.info/ttevents/prgframe.htm and http://globalbem.com/conference/. Last accessed October 2012.

[156] Bhatia, S. K.; Myers, A. L. *Langmuir* **2006**, *22*, 1688.

[157] Vermoortele, F.; Maes, M.; Moghadam, P. Z.; Lennox, M. J.; Ragon, F.; Boulhout, M.; Biswas, S.; Laurier, K. G. M.; Beurroies, I.; Denoyel, R.; Roeffaers, M.; Stock, N.; Düren, T.; Serre, C.; De Vos, D. E. *Journal of the American Chemical Society* **2011**, *133*, 18526.

[158] Alaerts, L.; Kirschhock, C. E. A.; Maes, M.; Van der Veen, M. A.; Finsy, V.; Depla, A.; Martens, J. A.; Baron, G. V.; Jacobs, P. A.; Denayer, J. E. M.; De Vos, D. E. *Angewandte Chemie-International Edition* **2007**, *46*, 4293.

[159] Finsy, V.; Verelst, H.; Alaerts, L.; De Vos, D.; Jacobs, P. A.; Baron, G. V.; Denayer, J. F. M. *Journal of the American Chemical Society* **2008**, *130*, 7110.

[160] Alaerts, L.; Maes, M.; Giebeler, L.; Jacobs, P. A.; Martens, J. A.; Denayer, J. F. M.; Kirschhock, C. E. A.; De Vos, D. E. *Journal of the American Chemical Society* **2008**, *130*, 14170.

[161] Maes, M.; Vermoortele, F.; Alaerts, L.; Couck, S.; Kirschhock, C. E. A.; Denayer, J. F. M.; De Vos, D. E. *Journal of the American Chemical Society* **2010**, *132*, 15277.

[162] Maes, M.; Vermoortele, F.; Alaerts, L.; Denayer, J. F. M.; De Vos, D. E. *Journal of Physical Chemistry C* **2011**, *115*, 1051.

[163] Bourrelly, S.; Llewellyn, P. L.; Serre, C.; Millange, F.; Loiseau, T.; Férey, G. *Journal of the American Chemical Society* **2005**, *127*, 13519.

[164] Llewellyn, P. L.; Bourrelly, S.; Serre, C.; Filinchuk, Y.; Férey, G. *Angewandte Chemie International Edition* **2006**, *45*, 7751.

[165] Finsy, V.; Ma, L.; Alaerts, L.; De Vos, D. E.; Baron, G. V.; Denayer, J. F. M. *Microporous and Mesoporous Materials* **2009**, *120*, 221.

[166] Hamon, L.; Llewellyn, P. L.; Devic, T.; Ghoufi, A.; Clet, G.; Guillerm, V.; Pirngruber, G. D.; Maurin, G.; Serre, C.; Driver, G.; Beek, W. v.; Jolimaître, E.; Vimont, A.; Daturi, M.; Férey, G. *Journal of the American Chemical Society* **2009**, *131*, 17490.

[167] Couck, S.; Denayer, J. F. M.; Baron, G. V.; Rémy, T.; Gascon, J.; Kapteijn, F. *Journal of the American Chemical Society* **2009**, *131*, 6326.

[168] Stavitski, E.; Pidko, E. A.; Couck, S.; Rémy, T.; Hensen, E. J. M.; Weckhuysen, B. M.; Denayer, J.; Gascon, J.; Kapteijn, F. *Langmuir* **2011**, *27*, 3970.

[169] Maes, M.; Alaerts, L.; Vermoortele, F.; Ameloot, R.; Couck, S.; Finsy, V.; Denayer, J. F. M.; De Vos, D. E. *Journal of the American Chemical Society* **2010**, *132*, 2284.

[170] Alaerts, L.; Seguin, E.; Poelman, H.; Thibault-Starzyk, F.; Jacobs, P. A.; De Vos, D. E. *Chemistry-a European Journal* **2006**, *12*, 7353.

[171] Ravon, U.; Chaplais, G.; Chizallet, C.; Seyyedi, B.; Bonino, F.; Bordiga, S.; Bats, N.; Farrusseng, D. *Chemcatchem* **2010**, *2*, 1235.

[172] Mellot-Draznieks, C.; Dutour, J.; Férey, G. R. *Angewandte Chemie-International Edition* **2004**, *43*, 6290.

[173] Wilmer, C. E.; Leaf, M.; Lee, C. Y.; Farha, O. K.; Hauser, B. G.; Hupp, J. T.; Snurr, R. Q. *Nature Chemistry* **2012**, *4*, 83.

[174] Liu, B.; Smit, B. *Langmuir* **2009**, *25*, 5918.

[175] Ramsahye, N. A.; Maurin, G.; Bourrelly, S.; Llewellyn, P. L.; Devic, T.; Serre, C.; Loiseau, T.; Férey, G. *Adsorption-Journal of the International Adsorption Society* **2007**, *13*, 461.

[176] Rosenbach, N.; Jobic, H.; Ghoufi, A.; Salles, F.; Maurin, G.; Bourrelly, S.; Llewellyn, P. L.; Devic, T.; Serre, C.; Férey, G. *Angewandte Chemie-International Edition* **2008**, *47*, 6611.

[177] Salles, F.; Jobic, H.; Maurin, G.; Koza, M. M.; Llewellyn, P. L.; Devic, T.; Serre, C.; Férey, G. *Physical Review Letters* **2008**, *100*, .

[178] Myers, A. L.; Prausnitz, J. M. *Aiche Journal* **1965**, *11*, 121.

[179] Benjamin, M. M. *Environmental Science Technology* **2009**, *43*, 2530.

[180] Vandichel, M.; Lesthaeghe, D.; Van der Mynsbrugge, J.; Waroquier, M.; Van Speybroeck, V. *Journal of Catalysis* **2010**, *271*, 67.

[181] Van Speybroeck, V.; Van der Mynsbrugge, J.; Vandichel, M.; Hemelsoet, K.; Lesthaeghe, D.; Ghysels, A.; Marin, G. B.; Waroquier, M. *Journal of the American Chemical Society* **2011**, *133*, 888.

[182] Lesthaeghe, D.; Van der Mynsbrugge, J.; Vandichel, M.; Waroquier, M.; Van Speybroeck, V. *Chemcatchem* **2011**, *3*, 208.

[183] Leus, K.; Muylaert, I.; Vandichel, M.; Marin, G. B.; Waroquier, M.; Van Speybroeck, V.; Van Der Voort, P. *Chemical Communications* **2010**, *46*, 5085.

[184] Vandichel, M.; Leus, K.; Van Der Voort, P.; Waroquier, M.; Van Speybroeck, V. *Journal of Catalysis* **2012**, *294*, 1.

[185] Leus, K.; Vandichel, M.; Liu, Y. Y.; Muylaert, I.; Musschoot, J.; Pyl, S.; Vrielinck, H.; Callens, F.; Marin, G. B.; Detavernier, C.; Wiper, P. V.; Khimyak, Y. Z.; Waroquier, M.; Van Speybroeck, V.; Van Der Voort, P. *Journal of Catalysis* **2012**, *285*, 196.

[186] Vermoortele, F.; Vandichel, M.; Voorde, Van de B.; Ameloot, R.; Waroquier, M.; Van Speybroeck, V.; De Vos, D. *Angewandte Chemie-International Edition* **2012**, *51*, 4887.

[187] Ghysels, A.; Vandichel, M.; Verstraelen, T.; De Vos, D.; Van der Veen, M.; Waroquier, M.; Van Speybroeck, V. *Theoretical Chemistry Accounts* **2012**, *131*, 1234.

[188] Vanduyfhuys, L.; Verstraelen, T.; Vandichel, M.; Waroquier, M.; Van Speybroeck, V. *Journal of Chemical Theory and Computation* **2012**, *8*, 3217.

[189] Leus, K.; Couck, S.; Vandichel, M.; Vanhaelewyn, G.; Liu, Y.-Y.; Marin, G.; Van Driessche, I.; Depla, D.; Waroquier, M.; Van Speybroeck, V.; Denayer, J.; Van Der Voort, P. *Physical Chemistry Chemical Physics* **2012**, , in press.

[190] Van der Mynsbrugge, J.; Hemelsoet, K.; Vandichel, M.; Waroquier, M.; Van Speybroeck, V. *Journal of Physical Chemistry C* **2012**, *116*, 5499.

[191] Hemelsoet, K.; Nollet, A.; Vandichel, M.; Lesthaeghe, D.; Van Speybroeck, V.; Waroquier, M. *Chemcatchem* **2009**, *1*, 373.

[192] Lesthaeghe, D. , Ph.D. thesis, Center for Molecular Modeling, University of Gent, Unraveling the Reaction Mechanism of Industrial Processes in Zeolite Catalysis: a Quantum Chemical Approach, 2007.

[193] De Moor, B. A.; Ghysels, A.; Reyniers, M. F.; Van Speybroeck, V.; Waroquier, M.; Marin, G. B. *Journal of Chemical Theory and Computation* **2011**, *7*, 1090.

[194] Dědeček, J.; Kaucký, D.; Wichterlová, B. *Chemical Communications* **2001**, 970.

[195] Sklenak, S.; Dědeček, J.; Li, C. B.; Wichterlová, B.; Gábová, V.; Sierka, M.; Sauer, J. *Angewandte Chemie-International Edition* **2007**, *46*, 7286.

[196] van Koningsveld, H.; Jansen, J. C.; van Bekkum, H. *Zeolites* **1990**, *10*, 235.

[197] Stöcker, M. *Microporous and Mesoporous Materials* **1999**, *29*, 3.

[198] Olsbye, U.; Svelle, S.; Bjørgen, M.; Beato, P.; Janssens, T. V. W.; Joensen, F.; Bordiga, S.; Lillerud, K. P. *Angewandte Chemie International Edition* **2012**, *51*, 5810.

[199] Jiang, Y.; Wang, W.; Reddy Marthala, V. R.; Huang, J.; Sulikowski, B.; Hunger, M. *Journal of Catalysis* **2006**, *238*, 21.

[200] Haw, J. F.; Marcus, D. M.; Kletnieks, P. W. *Journal of Catalysis* **2006**, *244*, 130.

[201] Jiang, Y.; Wang, W.; Reddy Marthala, V. R.; Huang, J.; Sulikowski, B.; Hunger, M. *Journal of Catalysis* **2006**, *244*, 134.

[202] Lesthaeghe, D.; Van Speybroeck, V.; Marin, G. B.; Waroquier, M. *Angewandte Chemie International Edition* **2006**, *45*, 1714.

[203] Lesthaeghe, D.; Van Speybroeck, V.; Marin, G. B.; Waroquier, M. *Chemical Physics Letters* **2006**, *417*, 309.

[204] Song, W.; Marcus, D. M.; Fu, H.; Ehresmann, J. O.; Haw, J. F. *Journal of the American Chemical Society* **2002**, *124*, 3844.

[205] Haw, J. F.; Marcus, D. M. *Topics in Catalysis* **2005**, *34*, 41.

[206] Dahl, I. M.; Kolboe, S. *Catalysis Letters* **1993**, *20*, 329.

[207] Dessau, R. M. *Journal of Catalysis* **1986**, *99*, 111.

[208] Haw, J. F.; Song, W. G.; Marcus, D. M.; Nicholas, J. B. *Accounts of Chemical Research* **2003**, *36*, 317.

[209] Svelle, S.; Joensen, F.; Nerlov, J.; Olsbye, U.; Lillerud, K. P.; Kolboe, S.; Bjørgen, M. *Journal of the American Chemical Society* **2006**, *128*, 14770.

[210] Barbera, K.; Bonino, F.; Bordiga, S.; Janssens, T. V. W.; Beato, P. *Journal of Catalysis* **2011**, *280*, 196.

[211] McCann, D. M.; Lesthaeghe, D.; Kletnieks, P. W.; Guenther, D. R.; Hayman, M. J.; Van Speybroeck, V.; Waroquier, M.; Haw, J. F. *Angewandte Chemie-International Edition* **2008**, *47*, 5179.

[212] Svelle, S.; Rønning, P. O.; Olsbye, U.; Kolboe, S. *Journal of Catalysis* **2005**, *234*, 385.

[213] Svelle, S.; Rønning, P. A.; Kolboe, S. *Journal of Catalysis* **2004**, *224*, 115.

[214] Svelle, S.; Tuma, C.; Rozanska, X.; Kerber, T.; Sauer, J. *Journal of the American Chemical Society* **2008**, *131*, 816.

[215] Bond, G. C.; Keane, M. A.; Kral, H.; Lercher, J. A. *Catalysis Reviews-Science and Engineering* **2000**, *42*, 323.

[216] Tuma, C.; Sauer, J. *Angewandte Chemie-International Edition* **2005**, *44*, 4769.

[217] Talsi, E. P.; Chinakov, V. D.; Babenko, V. P.; Zamaraev, K. I. *Journal of Molecular Catalysis* **1993**, *81*, 235.

[218] Gould, E. S.; Hiatt, R. R.; Irwin, K. C. *Journal of the American Chemical Society* **1968**, *90*, 4573.

[219] Stepovik, L.; Gulenova, M. *Russian Journal of General Chemistry* **2009**, *79*, 1663.

[220] Valenzano, L.; Civalleri, B.; Chavan, S.; Bordiga, S.; Nilsen, M. H.; Jakobsen, S.; Lillerud, K. P.; Lamberti, C. *Chemistry of Materials* **2011**, *23*, 1700.

[221] Kim, M.; Garibay, S. J.; Cohen, S. M. *Inorganic Chemistry* **2011**, *50*, 729.

[222] Zlotea, C.; Phanon, D.; Mazaj, M.; Heurtaux, D.; Guillerm, V.; Serre, C.; Horcajada, P.; Devic, T.; Magnier, E.; Cuevas, F.; Férey, G.; Llewellyn, P. L.; Latroche, M. *Dalton Transactions* **2011**, *40*, 4879.

[223] Vermoortele, F.; Ameloot, R.; Vimont, A.; Serre, C.; De Vos, D. *Chemical Communications* **2011**, *47*, 1521.

[224] Wang, C.; Xie, Z.; deKrafft, K. E.; Lin, W. *Journal of the American Chemical Society* **2011**, *133*, 13445.

[225] Hansch, C.; Leo, A.; Taft, R. W. *Chemical Reviews* **1991**, *91*, 165.

[226] Castillo, J. M.; Vlugt, T. J. H.; Calero, S. *Journal of Physical Chemistry C* **2009**, *113*, 20869.

[227] Férey, G.; Serre, C. *Chemical Society Reviews* **2009**, *38*, 1380.

[228] Coudert, F.-X. in *Metal-Organic Frameworks*, Farrusseng, D. , Eds.; Wiley-VCH Verlag GmbH & Co. KGaA; Bochstr. 12, 69469 Weinheim, Germany, 2011, pp. 51–68.

[229] Loiseau, T.; Serre, C.; Huguenard, C.; Fink, G.; Taulelle, F.; Henry, M.; Bataille, T.; Férey, G. *Chemistry-a European Journal* **2004**, *10*, 1373.

[230] Whitfield, T. R.; Wang, X.; Liu, L.; Jacobson, A. J. *Solid State Sciences* **2005**, *7*, 1096.

[231] Anokhina, E. V.; Vougo-Zanda, M.; Wang, X.; Jacobson, A. J. *Journal of the American Chemical Society* **2005**, *127*, 15000.

[232] Vougo-Zanda, M.; Huang, J.; Anokhina, E.; Wang, X.; Jacobson, A. J. *Inorganic Chemistry* **2008**, *47*, 11535.

[233] Mowat, J. P. S.; Miller, S. R.; Slawin, A. M. Z.; Seymour, V. R.; Ashbrook, S. E.; Wright, P. A. *Microporous and Mesoporous Materials* **2011**, *142*, 322.

[234] Leclerc, H.; Devic, T.; Devautour-Vinot, S.; Bazin, P.; Audebrand, N.; Férey, G.; Daturi, M.; Vimont, A.; Clet, G. *Journal of Physical Chemistry C* **2011**, *115*, 19828.

[235] Neimark, A. V.; Coudert, F. X.; Boutin, A.; Fuchs, A. H. *Journal of Physical Chemistry Letters* **2010**, *1*, 445.

[236] Walker, A. M.; Civalleri, B.; Slater, B.; Mellot-Draznieks, C.; Corà, F.; Zicovich-Wilson, C. M.; Román-Pérez, G.; Soler, J. M.; Gale, J. D. *Angewandte Chemie-International Edition* **2010**, *49*, 7501.

[237] Triguero, C.; Coudert, F. X.; Boutin, A.; Fuchs, A. H.; Neimark, A. V. *Journal of Physical Chemistry Letters* **2011**, *2*, 2033.

[238] Henkelman, G.; Uberuaga, B. P.; Jonsson, H. *Journal of Chemical Physics* **2000**, *113*, 9901.

[239] Llewellyn, P. L.; Horcajada, P.; Maurin, G.; Devic, T.; Rosenbach, N.; Bourrelly, S.; Serre, C.; Vincent, D.; Loera-Serna, S.; Filinchuk, Y.; Férey, G. *Journal of the American Chemical Society* **2009**, *131*, 13002.

[240] Grimme, S. *Journal of Computational Chemistry* **2006**, *27*, 1787.

[241] Grimme, S.; Antony, J.; Ehrlich, S.; Krieg, H. *Journal of Chemical Physics* **2010**, *132*, .

[242] Grimme, S. *Journal of Computational Chemistry* **2004**, *25*, 1463.

[243] Lee, C. C.; Gorte, R. J.; Farneth, W. E. *Journal of Physical Chemistry B* **1997**, *101*, 3811.

[244] Nguyen, C. M.; Reyniers, M. F.; Marin, G. B. *Phys Chem Chem Phys* **2010**, *12*, 9481.